Optimisation of Chemical Absorption for the Decarbonisation of the Iron and Steel Industry: An Integrated Simulation and Pilot-Scale Investigation to Benchmark Capture Performance from High-CO_2 Process Emissions

Jack Oliver Wells

A thesis submitted in partial fulfilment of the requirements for the degree of
Doctor of Engineering

The University of Sheffield
Faculty of Engineering
School of Mechanical, Aerospace and Civil Engineering
Energy 2050

March 2026

Declaration

I, the author, confirm that the thesis is my own work. I am aware of the University's Guidance on the Use of Unfair Means (https://www.sheffield.ac.uk/study-skills/assessment/academic-integrity/academic-integrity). This work has not previously been presented for an award at this, or any other, university.

Acknowledgements

The journey to submission has been long and, at times, challenging, and I would not have reached the finish line without the guidance, support, and encouragement of so many people.

I am deeply grateful to my supervisory team at the University of Sheffield for their expertise and enduring support over the years. First and foremost, I thank Professor Mohamed Pourkashanian for offering me the remarkable opportunity to join the Centre for Doctoral Training (CDT) programme and pursue my Engineering Doctorate. I am equally thankful to Professor Derek Ingham and Dr Kevin Hughes, whose mentorship during our weekly meetings helped to shape the direction of this thesis. Their academic guidance, coupled with their practical support during times of personal difficulty, has been invaluable. I also extend my thanks to Dr Muhammad Akram for generously sharing his technical expertise and for his assistance during the experimental stages of this work.

This thesis would not be what it is, indeed, it might not exist at all, without the mentorship and unwavering support of Dr Andy Heeley. He guided me through some of the most difficult periods of my doctoral journey, offering encouragement when I had moments of self-doubt. His constructive feedback, insightful questions, and commitment of time and energy were instrumental in bringing this project to completion, and I am sincerely grateful to him for all of his help.

I would also like to thank Professor Robin Irons and Dr Claudia Matz of the CDT in Resilient Decarbonised Fuel Energy Systems for their support throughout my studies. Whether during annual CDT schools, social events, course modules, or informal email exchanges, they were always approachable and willing to listen. Through the CDT, I had the privilege of meeting many wonderful and supportive colleagues, including Fernando, Rahima, Vincent, Jenny, and Marta, with whom I have shared moments of both celebration and commiseration. I am thankful for their friendship and look forward to seeing where the future takes us all.

To my closest friends from university, affectionately known as “The Gang”, I owe a debt of gratitude. My heartfelt thanks go especially to my best friend, Georgeos, whose own postgraduate journey allowed him to relate to my challenges on both academic and personal levels. I am equally grateful to Zac, Simon, Amalie, Jen, Josh, Matt, Jules, and Aymen for their resolute friendship, whether through technical knowledge, emotional support, or tough love when needed. I truly cherish the memories we have made together, and I thank you all for accompanying me on this journey.

As the first in my family to attend university, and later to pursue postgraduate education, I often navigated uncharted territory. Throughout this journey, my mother, father, grandmother, and three sisters all stood by me with love and encouragement. Their belief in me has been a constant source of strength, and I could not have reached this point without them.

Balancing my doctoral research with my ambitions as a competitive archer has been both challenging and rewarding. During my time with the CDT, I have become a county shooter for Yorkshire, climbed into the top 30 national rankings for 2024, secured several prestigious sponsorships, and earned many podium placements across university and external competitions up to national level. Archery has provided a much-needed balance to my academic life, and I am grateful for the CDT's flexibility in allowing me to pursue this passion. I extend my thanks to my fellow archer friends across the country for making training and competing such an enjoyable and fulfilling experience.

Finally, I wish to acknowledge the financial support provided by the Engineering and Physical Sciences Research Council, the International Flame Research Foundation, and my family, without which this work would not have been possible.

Abstract

Decarbonisation of critical hard-to-abate industrial sectors such as the iron and steel industry is crucial for meeting climate targets, with chemical absorption carbon capture identified as a key transitional technology. However, its application to these industrial sectors is hindered by a significant knowledge gap: the absence of publicly available and transparent performance benchmarks using a conventional capture plant under elevated CO_2 conditions that are typical of industrial process emissions.

This thesis addresses this gap through a synergistic methodology combining process simulation with pilot-scale experimentation. An initial process simulation model was developed in Aspen Plus to identify parametric trends and plant performance across a wide range of operating conditions. The results from this investigation were used to inform initial starting conditions for a targeted experimental campaign on a conventional packed bed system.

The experimental campaign established a novel performance baseline for the treatment of flue gas with CO_2 concentrations ranging from 10 to 25 mol.% CO_2, using a solvent of 35 wt.% monoethanolamine. The dataset was then used to calibrate and enhance the simulation model to create a high-fidelity predictive tool that forms the foundation of a digital twin for the capture plant. This was achieved using a novel Python automation framework developed to control Aspen Plus. The enhanced model was successfully used to interpolate and extrapolate performance of the capture plant, identifying optimal operating conditions beyond the experimental scope.

The novel baseline performance dataset can be used to compare the capture effectiveness of alternative and advanced process configurations in the treatment of heavy industry process emissions. In addition, the methodologies outlined in this thesis can serve as a guide for the development, validation, and enhancement of representative process simulations of other chemical absorption systems. This work ultimately seeks to accelerate the deployment of carbon capture for industrial decarbonisation.

Publications

i) The research from Chapter 3 of this thesis has been published and appears in Fuel as the following:

Wells J, Heeley A, Akram M, Hughes KJ, Ingham DB, Pourkashanian M. Simulation and modelling study of a chemical absorption plant to evaluate capture effectiveness when treating high CO_2 content iron and steel industry emissions. Fuel 2025;380:133189. https://doi.org/10.1016/j.fuel.2024.133189.

ii) The research from Chapter 4 of this thesis is under preparation for potential publication:

Wells J, Akram M, Heeley A, Hughes KJ, Ingham DB, Pourkashanian M. Performance campaign of a chemical absorption pilot plant to evaluate capture effectiveness with treating high CO_2 content process emissions from the iron and steel industry.

iii) The research from Chapter 5 of this thesis is also under preparation for potential publication:

Wells J, Bailey Ladd VJ, Hardo G, Heeley A, Hughes KJ, Ingham DB, Pourkashanian M. AspenAutoKit: Python based automation application for Aspen Plus.

Table of Contents

Declaration i

Acknowledgements ii

Abstract iv

Publications v

Table of Contents vi

List of Figures xii

List of Tables xv

Nomenclature xvii

Chapter 1: Introduction 1

1.1 Climate Change and the Need for Decarbonisation 1

1.1.1 Global Cooperation on Climate Change Prevention 3

1.1.2 The United Kingdom and The Climate Change Act 4

1.2 Barriers to Heavy Industry Decarbonisation 5

1.2.1 The Iron and Steel Industry: A Hard-To-Abate Sector 5

1.3 Carbon Capture Usage and Storage as a Key Abatement Strategy 8

1.3.1 The Primary Approaches to CO_2 Capture 8

1.3.2 Post-Combustion Capture Technologies 9

1.3.2.1 Chemical Absorption 9

1.3.2.2 Physical Absorption 9

1.3.2.3 Adsorption 9

1.3.2.4 Membrane Separation 10

1.3.2.5 Cryogenic Distillation 11

1.4 Chemical Absorption Carbon Capture for the Iron and Steel Industry 12

1.5 Overall Aim and Thesis Outline 13

1.6 References for Chapter 1 14

Chapter 2: Literature Review for Chemical Absorption Carbon Capture 18

2.1 Literature Review Overview 18

2.1.1 The Chemical Absorption Process 18

2.1.2 Definitions of Key Performance Indicators 19

2.1.3 The Energy Penalty from Solvent Regeneration 20

2.2 The Absorbent: Chemistry, Kinetics, and Selection 21

2.2.1 Solvent Characteristics for Chemical Absorption 21

2.2.2 Process Chemistry for Conventional Alkanolamine Solvents 22

2.2.2.1 Reaction Pathways for Primary Amines 23

2.2.2.2 Kinetics of Alkanolamines with CO_2 24

2.2.3 Solvent Degradation: Mechanisms and Consequences 25

2.2.3.1 Thermal Degradation 25
2.2.3.2 Oxidative Degradation 26
2.2.3.3 Heat-Stable-Salts 27
2.2.3.4 Pilot-Scale Degradation Studies 27
2.2.3.5 Corrosion 28
2.2.3.6 Environmental and Health Concerns 29
2.2.3.7 The Case for Novel Solvents 29
2.2.4 Solvent Developments 29
2.2.4.1 Functionalised Solvents 29
2.2.4.2 Solvent Blends 30
2.2.4.3 Phase Change Solvents 30
2.2.4.4 Water-Lean Solvents 31
2.2.4.5 Ammonia 31
2.2.4.6 Summary of Solvent Selection 32
2.3 The Process: Optimisation, Configuration, and Intensification 33
2.3.1 Process Optimisation Through Column Temperature Profiles 33
2.3.2 Absorber Operational Pinches 34
2.3.2.1 Lean-Pinched Operation 35
2.3.2.2 Rich-Pinched Operation 35
2.3.2.3 Bulge-Pinched Operation 35
2.3.3 Stripper Operational Regions 36
2.3.3.1 The Baseline Region 36
2.3.3.2 The Exponential Region 37
2.3.3.3 The Inflection Point 37
2.3.4 Summary of Column Temperature Profile Utilisation 38
2.3.5 Advanced Structural Configurations 38
2.3.5.1 Intercooled Absorber 38
2.3.5.2 Rich Solvent Split 39
2.3.5.3 Rich Solvent Pre-heating 40
2.3.5.4 Rich Solvent Flashing 40
2.3.5.5 Solvent Split Flow 40
2.3.5.6 Stripper Condensate Bypass 41
2.3.5.7 Stripper Condensate Heating 41
2.3.5.8 Lean Vapour Compression 41
2.3.5.9 Other Modifications 42
2.3.5.10 Combination of Process Modifications 42
2.3.6 Summary of Process Modifications 44
2.3.7 Process Intensification for Chemical Absorption Carbon Capture 45
2.3.7.1 The Conventional Baseline 45
2.3.7.2 Intensified Gas-Liquid Contacting 46
2.3.7.3 Intensified Heat Integration 47
2.3.7.4 Summary and Outlook for Process Intensification 47
2.4 Global Status of Commercial-Scale Iron and Steelmaking CCUS Projects 48
2.4.1 Pilot-Scale CCUS Projects for Iron and Steelmaking 49

2.5 The Challenge of Elevated CO_2 Concentrations 51
2.6 Process Simulation for Chemical Absorption Carbon Capture 52
2.6.1 Commercial Software for Process Simulation 53
2.6.1.1 Aspen Plus and Aspen HYSYS 53
2.6.1.2 gPROMS 53
2.6.1.3 ProMax 54
2.6.1.4 CHEMCAD 54
2.6.1.5 Simulation Software Selection 54
2.7 The Knowledge Gap, Research Novelty, Aim and Objectives 55
2.8 References for Chapter 2 56
Chapter 3: Simulation Model Development and Performance Predictions 64
3.1 The TERC ACP and Need for Process Simulation 64
3.1.1 Introduction to the TERC ACP 64
3.1.2 The TERC ACP Process Description 64
3.1.3 The Need for Process Simulation 66
3.2 DCC Model Development 67
3.2.1 Introduction 67
3.2.2 MEA Absorption Chemistry 67
3.2.3 Kinetic Model 67
3.2.4 Thermodynamic Model 68
3.2.5 Transport Property Models 69
3.2.6 The Aspen Plus Radfrac™ Model 69
3.2.6.1 Rate-Based Calculation Mode 69
3.2.6.2 Bulk Modelling 69
3.2.6.3 Film Modelling 70
3.2.6.4 Number of Stages 70
3.2.7 DCC Model Development Summary 71
3.2.8 Introduction to the CCSI Model 71
3.2.9 Model Convergence Logic 72
3.3 Model Validation 74
3.3.1 PACT ACP Validation 74
3.3.2 TERC ACP Validation 80
3.4 Sensitivity Analysis 82
3.4.1 Flue Gas Composition 82
3.4.2 Flue Gas Temperature 84
3.4.3 Lean Solvent Temperature 86
3.4.4 Lean Solvent Concentration 88
3.4.5 Solvent Mass Flow Rate 90
3.4.6 CO_2 Capture Efficiency 92
3.4.7 Stripper Column Pressure 94

3.4.8 Optimisation of an Example Case ... 96

3.4.9 Model Validation and Sensitivity Summary ... 99

3.5 Modelling Predictions for Flue Gases with Elevated CO_2 ... 99

3.5.1 Analysis and Discussion for 90% Capture Efficiency Conditions ... 100

3.5.2 Analysis and Discussion for 95% Capture Efficiency Conditions ... 105

3.5.3 Comparison Between 90% and 95% Capture Efficiency Conditions ... 108

3.6 Simulated Column Profiles ... 110

3.6.1 Absorber and Stripper Temperature Profiles ... 110

3.6.2 Absorber and Stripper Composition Profiles ... 113

3.6.3 Optimal Liquid to Gas Ratio Temperature Profiles ... 117

3.7 Stripping Column Pressure Implications ... 119

3.8 Conclusions for Chapter 3 ... 124

3.9 References for Chapter 3 ... 127

Chapter 4: Experimental Performance Campaign for Elevated CO_2 Conditions ... 129

4.1 Experimental Campaign Overview ... 129

4.2 Pilot Plant Technical Specifications ... 130

4.2.1 Process Description of the TERC ACP ... 130

4.3 Methodology ... 134

4.3.1 Sampling and Measurements Overview ... 134

4.3.2 Process Data Analysis ... 134

4.3.3 Flue Gas Analysis ... 134

4.3.4 Solvent Analysis ... 136

4.4 Operating Procedures ... 137

4.4.1 Standard Operating Procedure ... 137

4.4.2 Capture Condition Procedure ... 138

4.4.3 Data Processing Procedure ... 139

4.5 Data Calculations ... 140

4.5.1 Capture Efficiency Calculations ... 140

4.5.2 Specific Reboiler Heat Duty Calculations ... 142

4.5.3 Solvent Concentration Calculation ... 143

4.5.4 CO_2 Concentration Calculation ... 143

4.5.5 Solvent Loading Calculations ... 144

4.5.6 Solvent Component Mass Flow Calculations ... 144

4.6 Uncertainty Analysis Framework ... 147

4.7 Experimental Matrix ... 149

4.8 Experimental Results ... 150

4.8.1 Introduction to the Experimental Results ... 150

4.8.2 Limitations During the Campaign ... 150

4.8.3 25% CO_2 Flue Gas Capture Conditions ... 152

4.8.4 20% CO_2 Flue Gas Capture Conditions 156
4.8.5 15% CO_2 Flue Gas Capture Conditions 159
4.8.6 10% CO_2 Flue Gas Capture Conditions 162
4.8.7 Collated Results 165
4.8.8 Uncertainty Analysis for the Primary Experimental Results 170
4.8.9 Experimental Results Discussion 172
4.9 System Energy Balance for Capture Conditions 176
4.9.1 Introduction to the Energy Balance 176
4.9.2 Calculation Basis and Reference Values 177
4.9.2.1 General Stream Energy Calculations 177
4.9.2.2 Specific Heat Capacities 178
4.9.2.3 Latent Heat of Vaporisation 178
4.9.3 Condenser Duty Calculations 179
4.9.4 Steam Production Calculations 181
4.9.5 Additional Calculations 183
4.9.6 Energy Balance Discussion and Uncertainty Analysis 184
4.10 Solvent Regeneration Energy 188
4.10.1 Introduction to the Regeneration Energy 188
4.10.2 Sensible Heat of Solvent 189
4.10.3 Solvent Vaporisation 191
4.10.4 Heat of Desorption 193
4.10.5 Heat Recovery 196
4.10.6 Net Regeneration Energy, System Heat Loss, and Energy Distribution 199
4.10.7 Regeneration Energy Discussion 204
4.10.8 Heat Loss Discussion 206
4.11 Conclusions for Chapter 4 209
4.12 References for Chapter 4 211
Chapter 5: Simulation Model Enhancement and Utilisation 214
5.1 Introduction to the ECC Model 214
5.2 Comparison of Experimental Results to DCC Model 215
5.2.1 Specific Reboiler Duty 216
5.2.2 Solvent Loadings 218
5.2.3 Absorber Temperature Profiles 220
5.2.4 Stripper Temperature Profiles 223
5.2.5 DCC Model Comparison Summary 226
5.3 Alternative Packing Configurations 228
5.3.1 Alternative Packing Hypothesis 228
5.3.2 Python Automation Script Development 229
5.3.3 Optimal Packing Configuration Identification 232
5.4 Aspen Plus Tuning Factors 234

5.4.1 Tuning Factor Scope 234
5.4.2 Interfacial Area 234
5.4.3 Heat Transfer Factor 235
5.4.4 Mass Transfer Coefficient Factors 235
5.4.5 Liquid Holdup 236
5.4.6 Tuning Factor Conclusion 237
5.5 Simulation Tuning 237
5.5.1 Tuning Approach 237
5.5.2 Absorber Liquid Holdup Tuning 238
5.5.3 Absorber Interfacial Area Tuning 239
5.5.4 Stripper Liquid Holdup Tuning 241
5.5.5 Stripper Interfacial Area Tuning 242
5.5.6 Tuning Summary 243
5.6 Comparison of Tuned Column Packing Configurations 244
5.6.1 Specific Reboiler Duty Comparison 244
5.6.2 Lean Loading Comparison 246
5.6.3 Rich Loading Comparison 248
5.6.4 Solvent Cyclic Capacity Comparison 250
5.6.5 Absorber Temperature Profile Comparison 251
5.6.6 Stripper Temperature Profile Comparison 253
5.6.7 Selecting the Optimal Packing Configuration for the ECC Model 255
5.7 Expanding Experimental Campaign Results with ECC Model Predictions 258
5.7.1 SRD Predictions 259
5.7.2 Solvent Loadings Predictions 261
5.7.3 Stripper Temperature Profile Predictions 264
5.7.4 Expanding Experimental Campaign Results Conclusion 265
5.8 ECC Model Predictions for Capture Conditions with 30 mol.% CO_2 266
5.9 Conclusions for Chapter 5 269
5.10 References for Chapter 5 271
Chapter 6: Conclusions and Recommendations for Future Work 272
6.1 Thesis Reflection 272
6.2 Summary of Key Findings 273
6.2.1 Simulation Model Development and Performance Predictions 273
6.2.2 Experimental Performance Campaign for Elevated CO_2 Conditions 276
6.2.3 Simulation Model Enhancement and Utilisation 279
6.3 Overall Thesis Conclusions 281
6.4 Recommendations for Future Work 282
6.4.1 Future Experimental Work 282
6.4.2 Future Simulation Work 284

List of Figures

Chapter 1 Figures:

Figure 1.1: Atmospheric CO_2 in parts per million for the last 800,000 years based on ice-core data................................. 1

Figure 1.2: Historical CO_2 concentrations from the Mauna Loa Observatory.. 2

Figure 1.3: Blast furnace-basic oxygen furnace steelmaking. 6

Figure 1.4: Technical options for CO_2 capture dependent on feed pressure and CO_2 concentration. 12

Chapter 2 Figures:

Figure 2.1: Simplified process flow diagram of a chemical absorption process... 19

Figure 2.2: Status of global commercial-scale CCUS projects for iron and steelmaking... 48

Chapter 3 Figures:

Figure 3.1: Process flow diagram of the TERC ACP Aspen Plus V11.0. 66

Figure 3.2: Specific reboiler duty against flue gas CO_2 concentration. 74

Figure 3.3: Comparison of solvent loadings and capacities against flue gas CO_2 concentration....................................... 75

Figure 3.4: Temperature profiles with varying flue gas CO_2 concentrations for the PACT ACP....................................... 76

Figure 3.5: Predicted absorber temperature profiles with different flue gas CO_2 concentration cases. 77

Figure 3.6: Predicted stripper temperature profiles with different flue gas CO_2 concentration cases................................ 78

Figure 3.7: Specific reboiler duty against capture efficiency... 80

Figure 3.8: Key performance metrics for DCC model sensitivity with respect to flue gas temperature............................ 84

Figure 3.9: Key performance metrics for DCC model sensitivity with respect to lean solvent temperature...................... 86

Figure 3.10: Key performance metrics for DCC model sensitivity with respect to lean solvent concentration. 88

Figure 3.11: Key performance metrics for DCC model sensitivity with respect to pure solvent mass flow rate................ 90

Figure 3.12: Key performance metrics for DCC model sensitivity with respect to CO_2 capture efficiency....................... 92

Figure 3.13: Key performance metrics for DCC model sensitivity with respect to stripper column pressure.................... 94

Figure 3.14: Optimisation of an example case... 96

Figure 3.15: Specific reboiler duty against pure solvent flow rate for gas flow rates for a range of CO_2 concentrations at 90% capture efficiency.. 100

Figure 3.16: Specific reboiler duty against pure solvent flow rate for gas flow rates for a range of CO_2 concentrations at 95% capture efficiency.. 105

Figure 3.17: Column temperature profiles with a CO_2 concentration of 20 mol.%, using 35 wt.% MEA pure solvent flow rates to achieve 90% capture efficiency. 111

Figure 3.18: Absorber column profiles with different pure solvent flow rates for a gas flow rate of 170 Nm^3/h with a CO_2 concentration of 20 mol.%, achieving 90% capture efficiency using 35 wt.% MEA. 113

Figure 3.19: Stripper column profiles with different pure solvent flow rates for a gas flow rate of 170 Nm^3/h with a CO_2 concentration of 20 mol.%, achieving 90% capture efficiency using 35 wt.% MEA. 115

Figure 3.20: Optimal temperature profiles with varying CO_2 concentrations, treated with 35 wt.% MEA to achieve 90% capture efficiency. 117

Figure 3.21: Specific reboiler duty against stripper pressure for various gas flow rates with a CO_2 concentration of 20 mol.%, achieving 90% capture efficiency at an L_{pure}/G ratio of 3.9... 119

Figure 3.22: Stripper temperature profiles with gas flow of 210 Nm^3/h with a CO_2 concentration of 20 mol.% for a range of stripper pressures achieving 90% capture efficiency at an L_{pure}/G ratio of 3.9... 121

Figure 3.23: Specific reboiler duty against stripper pressure for 170 Nm^3/h gas flow rates with a range of CO_2 concentrations achieving 90% capture efficiency at identified optimal L_{pure}/G ratios. 122

Chapter 4 Figures:

Figure 4.1: Photograph of the TERC ACP. 129

Figure 4.2: Simplified flow diagram of the TERC ACP. 131

Figure 4.3: Photograph of the Gasmet DX4000 FTIR analyser used for gas analysis. 135

Figure 4.4: Photograph of the auto-titrator system for solvent analysis. 136

Figure 4.5: Key performance metrics for solvent flow rates treating 150 Nm^3/h flue gas containing 25 mol.% CO_2, targeting 90% capture efficiency. 153

Figure 4.6: Key performance metrics for solvent flow rates treating 150 Nm^3/h flue gas containing 20 mol.% CO_2, targeting 90% capture efficiency. 157

Figure 4.7: Key performance metrics for solvent flow rates treating 150 Nm^3/h flue gas containing 15 mol.% CO_2, targeting 90% capture efficiency. 160

Figure 4.8: Key performance metrics for solvent flow rates treating 150 Nm^3/h flue gas containing 10 mol.% CO_2, targeting 90% capture efficiency. 163

Figure 4.9: Specific reboiler duty against: (A) liquid to gas ratio and (B) solvent/CO_2 ratio, for solvent flow rates treating 150 Nm^3/h flue gas containing different CO_2 concentrations, targeting 90% capture efficiency. 165

Figure 4.10: Lean solvent loading against: (A) liquid to gas ratio and (B) solvent/CO_2 ratio, for solvent flow rates treating 150 Nm^3/h flue gas containing different CO_2 concentrations, targeting 90% capture efficiency. 167

Figure 4.11: Specific reboiler duty against: (A) lean solvent loading and (B) solvent capacity, for solvent flow rates treating 150 Nm^3/h flue gas containing different CO_2 concentrations, targeting 90% capture efficiency. 168

Figure 4.12: Energy balance around the overall stripper system. 176

Figure 4.13: Energy balance around the condenser. 179

Figure 4.14: Energy balance around the stripper column. 181

Figure 4.15: Solvent sensible heat against: (A) liquid to gas ratio and (B) solvent/CO_2 ratio, for solvent flow rates treating 150 Nm^3/h flue gas containing different CO_2 concentrations, targeting 90% capture efficiency. 190

Figure 4.16: Vaporisation energy against: (A) liquid to gas ratio and (B) solvent/CO_2 ratio, solvent flow rates treating 150 Nm^3/h flue gas containing different CO_2 concentrations, targeting 90% capture efficiency. 192

Figure 4.17: Desorption energy against: (A) liquid to gas ratio and (B) solvent/CO_2 ratio, solvent flow rates treating 150 Nm^3/h flue gas containing different CO_2 concentrations, targeting 90% capture efficiency. 195

Figure 4.18: Comparison of desorption energy values given by Q_{react} and Q_{de} for different capture conditions. 196

Figure 4.19: Condensation energy against: (A) liquid to gas ratio and (B) solvent/CO_2 ratio, solvent flow rates treating 150 Nm^3/h flue gas containing different CO_2 concentrations, targeting 90% capture efficiency. 197

Figure 4.20: Sensible heat of CO_2 against: (A) liquid to gas ratio and (B) solvent/CO_2 ratio, solvent flow rates treating 150 Nm^3/h flue gas containing different CO_2 concentrations, targeting 90% capture efficiency. 197

Figure 4.21: Sensible heat of steam against: (A) liquid to gas ratio and (B) solvent/CO_2 ratio, solvent flow rates treating 150 Nm^3/h flue gas containing different CO_2 concentrations, targeting 90% capture efficiency. 198

Figure 4.22: Comparison of energy values given by $Q_{reboiler}$ and $Q_{regen,net}$ for different capture conditions. 199

Figure 4.23: Energy distribution of Q_{sens}, Q_{vap}, and Q_{react} as percentages of the conventional regeneration energy for different capture conditions. 201

Chapter 5 Figures:

Figure 5.1: SRD against solvent flow rate for different CO_2 concentrations in a 150 Nm^3/h gas flow targeting 90% capture efficiency. 216

Figure 5.2: Difference in SRD between DCC model simulations and experimental results for capture conditions targeting 90% capture efficiency from a 150 Nm^3/h gas flow. 217

Figure 5.3: Solvent loadings against solvent flow rate for different CO_2 concentrations in a 150 Nm^3/h gas flow targeting 90% capture efficiency. 218

Figure 5.4: Difference in solvent loadings between DCC model simulations and experimental results for capture conditions targeting 90% capture efficiency from a 150 Nm^3/h gas flow. 219

Figure 5.5: Absorber temperature profiles from experimental measurements and DCC model predictions. 221

Figure 5.6: Difference in absorber MAPE between DCC model simulations and experimental results for capture conditions targeting 90% capture efficiency from a 150 Nm^3/h gas flow. 222

Figure 5.7: Stripper temperature profiles from experimental measurements and DCC model predictions. 224

Figure 5.8: Difference in stripper MAPE between DCC model simulations and experimental results for capture conditions targeting 90% capture efficiency from a 150 Nm^3/h gas flow. 225

Figure 5.9: Screenshot of example absorber column internals options in Aspen Plus V11.0. 229

Figure 5.10: Flowchart of the developed Python script. The blue pathway represents the initial column packing testing and the red pathway represents subsequent tuning factor testing for the selected packings. 231

Figure 5.11: Alternative packing arrangement investigation overview. 232

Figure 5.12: Fine tuning process steps to develop ECC model. 237

Figure 5.13: Difference in SRD between different column packing configurations and experimental results for capture conditions targeting 90% capture efficiency from a 150 Nm^3/h gas flow. 244

Figure 5.14: SRD against solvent flow rate for different CO_2 concentrations in a 150 Nm^3/h gas flow targeting 90% capture efficiency. 245

Figure 5.15: Difference in lean solvent loading between different column packing configurations and experimental results for capture conditions targeting 90% capture efficiency from a 150 Nm^3/h gas flow. 246

Figure 5.16: Lean solvent loading against solvent flow rate for different CO_2 concentrations in a 150 Nm^3/h gas flow targeting 90% capture efficiency. 247

Figure 5.17: Difference in rich solvent loading between different column packing configurations and experimental results for capture conditions targeting 90% capture efficiency from a 150 Nm^3/h gas flow. 248

Figure 5.18: Rich solvent loading against solvent flow rate for different CO_2 concentrations in a 150 Nm^3/h gas flow targeting 90% capture efficiency. 249

Figure 5.19: Difference in solvent cyclic capacity between different column packing configurations and experimental results for capture conditions targeting 90% capture efficiency from a 150 Nm^3/h gas flow. 250

Figure 5.20: Absorber MAPEs between different column packing configurations and experimental results for capture conditions targeting 90% capture efficiency from a 150 Nm^3/h gas flow. 251

Figure 5.21: Absorber temperature profiles for different column packing configurations and experimental results for capture conditions: (A) 25_1000, (B) 20_1100, and (C) 15_600. 252

Figure 5.22: Stripper MAPEs between different column packing configurations and experimental results for capture conditions targeting 90% capture efficiency from a 150 Nm^3/h gas flow. 253

Figure 5.23: Stripper temperature profiles for different column packing configurations and experimental results for capture conditions: (A) 25_900, (B) 20_800, and (C) 15_700. 254

Figure 5.24: SRD against solvent flow rate for different CO_2 concentrations in a 150 Nm^3/h gas flow targeting 90% capture efficiency for ECC model predictions and experimental results. 259

Figure 5.25: Solvent loadings against solvent flow rate for different CO_2 concentrations in a 150 Nm^3/h gas flow targeting 90% capture efficiency for ECC model predictions and experimental results 261

Figure 5.26: SRD against lean solvent loading for different CO_2 concentrations in a 150 Nm^3/h gas flow targeting 90% capture efficiency for ECC model predictions and experimental results. 262

Figure 5.27: Stripper temperature profiles from experimental measurements and ECC model predictions. 264

Figure 5.28: Predictions by the ECC model for a 150 Nm^3/h gas flow containing 30 mol.% CO_2, targeting 90% capture efficiency. 267

List of Tables

Chapter 1 Tables:

Table 1.1: Typical compositions of iron and steel industry process emissions. 7

Chapter 2 Tables:

Table 2.1: Other advanced structural configurations reported in the open literature. 42
Table 2.2: Positive and very positive interactions between process modifications. 43

Chapter 3 Tables:

Table 3.1: Technical specifications of the ACP. 65
Table 3.2: Parameter operating ranges of the ACP. 65
Table 3.3: Kinetic parameters used in Equation (3.10). 68
Table 3.4: Physical property models used in the simulation for liquid and gas phases. 69
Table 3.5: Summary of key design parameters used in the simulation. 71
Table 3.6: Suggested ranges for CCSI simulation variables. 72
Table 3.7: PACT ACP validation results. 79
Table 3.8: Base comparator case parameters for input to the DCC model. 82
Table 3.9: Sensitivity analysis parameters and operating ranges investigated for the DCC model. 82
Table 3.10: Key results for DCC model sensitivity with respect to flue gas composition. 83
Table 3.11: Optimisation of an example case. 97
Table 3.12: Optimal L_{pure}/G and solvent/CO_2 ratios for different CO_2 concentrations for gas flow rates of 130, 170, and 210 Nm^3/h achieving 90% capture efficiency using 35 wt.% MEA. 102
Table 3.13: Solvent loadings data at optimal L_{pure}/G ratios for different CO_2 concentrations for gas flow rates of 130, 170, and 210 Nm^3/h achieving 90% capture efficiency using 35 wt.% MEA. 103
Table 3.14: Comparison of percentage differences between solvent capacity and solvent/CO_2 ratio with respect to flue gas CO_2 concentration, achieving 90% capture efficiency using 35 wt.% MEA. 103
Table 3.15: SRD at identified optimal L_{pure}/G and solvent/CO_2 ratios for different CO_2 concentrations for gas flow rates of 130, 170, and 210 Nm^3/h achieving 90% capture efficiency using 35 wt.% MEA. 104
Table 3.16: Optimal L_{pure}/G and solvent/CO_2 ratios for different CO_2 concentrations for gas flow rates of 130, 170, and 210 Nm^3/h achieving 95% capture efficiency using 35 wt.% MEA. 106
Table 3.17: Solvent loadings data at optimal L_{pure}/G ratios for different CO_2 concentrations for gas flow rates of 130, 170, and 210 Nm^3/h achieving 95% capture efficiency using 35 wt.% MEA. 106
Table 3.18: Comparison of percentage differences between solvent capacity and solvent/CO_2 ratio with respect to flue gas CO_2 concentration, achieving 95% capture efficiency using 35 wt.% MEA. 107
Table 3.19: SRDs at identified optimal L_{pure}/G and solvent/CO_2 ratios for different CO_2 concentrations for gas flow rates of 130, 170, and 210 Nm^3/h achieving 95% capture efficiency using 35 wt.% MEA. 107
Table 3.20: SRDs at identified optimal L_{pure}/G and solvent/CO_2 ratios for different CO_2 concentrations for gas flow rates of 130, 170, and 210 Nm^3/h achieving 90% and 95% capture efficiency using 35 wt.% MEA. 108
Table 3.21: Optimal L_{pure}/G ratios, solvent/CO_2 ratios, lean loadings and solvent capacities for different CO_2 concentrations for 90% and 95% capture efficiency using 35 wt.% MEA. 108
Table 3.22: SRD, cross-heat exchanger duty, and hot rich solvent temperature across a range of stripper pressures for a constrained heat exchanger and an unconstrained heat exchanger with a minimised temperature approach. Cases conducted at an L/G ratio of 3.9 for a gas flow of 210 Nm^3/h gas with a CO_2 concentration of 20 mol.% achieving 90% capture efficiency, with solvent concentration of 35 wt.% MEA. 121

Chapter 4 Tables:

Table 4.1: Technical specifications of the TERC ACP. 133
Table 4.2: Parameter operating ranges of the TERC ACP. 133
Table 4.3: Description of flue gas sampling points, labelled in Figure 4.2. 135
Table 4.4: Description of solvent sampling points, labelled in Figure 4.2. 136
Table 4.5: Experimental matrix of solvent flow rates and CO_2 concentrations in gas flows of 150 Nm^3/h. 149
Table 4.6: Results summary for complete capture conditions with a flue gas CO_2 concentration of 25 mol.%. 152
Table 4.7: Results summary for complete capture conditions with a flue gas CO_2 concentration of 20 mol.%. 156
Table 4.8: Results summary for complete capture conditions with a flue gas CO_2 concentration of 15 mol.%. 159
Table 4.9: Results summary for complete capture conditions with a flue gas CO_2 concentration of 10 mol.%. 162
Table 4.10: Relative uncertainties in the primary experimental results for different capture conditions. 171
Table 4.11: Energy balances across the stripper for different capture conditions. 186
Table 4.12: Relative uncertainties in the energy balances across the stripper for different capture conditions. 187
Table 4.13: Regeneration energy components and other key values for different capture conditions. 202
Table 4.14: Relative uncertainties of the regeneration energy components for different capture conditions. 203

Chapter 5 Tables:

Table 5.1: Summary of performance improvement targets for the ECC model. 226
Table 5.2: DCC model simulation results of the experimental capture conditions. 227
Table 5.3: Column packing configurations selected for tuning. 233
Table 5.4: Summary of selected tuning factors for the two column packing configurations. 243
Table 5.5: ECC model simulation results of the experimental capture conditions. 257
Table 5.6: ECC model simulation results for flue gas CO_2 concentrations of 30 mol.%, under similar conditions to the experimental campaign. 268

Nomenclature

Acronyms:

ACP	Amine Capture Plant
AEEA	2-(2-Aminoethylamino)Ethanol
AMP	2-Amino-2-Methyl-1-Propanol
BF-BOF	Blast Furnace-Basic Oxygen Furnace
BFG	Blast Furnace Gas
BOFG	Basic Oxygen Furnace Gas
CCC	Committee on Climate Change
CCS	Carbon Capture and Storage
CCSI	Carbon Capture Simulation Initiative
CCSL	Carbon Clean Solutions Limited
CCU	Carbon Capture Utilisation
CCUS	Carbon Capture Usage and Storage
CDT	Centre for Doctoral Training
CHP	Combined Heat and Power
COG	Coke Oven Gas
COP	Conference of Parties
CSTR	Continuous Stirred-Tank Reactors
DCC	Developed Carbon Capture
DEA	Diethanolamine
DRI	Direct Reduced Iron
ECC	Enhanced Carbon Capture
EIC	Energy Innovation Centre
ELECNRTL	Electrolyte Non-Random Two-Liquid
EO	Equation-Oriented
EOS	Equation of State
ETF	Enhanced Transparency Framework
FDR	Film Discretization Ratio
FGD	Flue Gas Desulphurisation
FOQUS	Framework for Optimisation, Quantification of Uncertainty, and Surrogates
FPHE	Formed Plate Heat Exchanger
FTIR	Fourier Transform Infrared
GCCSI	Global CCS Institute
GHG	Greenhouse Gas Emission
GUI	Graphical User Interface
HHE	Hybrid Heat Exchanger
HSS	Heat-Stable-Salts

IA	Interfacial Area
IEA	International Energy Agency
IEEFA	Institute for Energy Economics and Financial Analysis
IFPEN	IFP Energies Nouvelles
IPCC	Intergovernmental Panel on Climate Change
IR	Infrared
L/G	Liquid-To-Gas
LH	Liquid Holdup
MAPE	Mean Absolute Percentage Error
MDA	1-8-p-Menthanediamine
MDEA	Methyldiethanolamine
MEA	Monoethanolamine
MHI	Mitsubishi Heavy Industries
MTU	Mobile Test Unit
NCCC	National Carbon Capture Centre
NDC	Nationally Determined Contributions
NOAA	National Oceanic Atmospheric Administration
PACT	Pilot-scale Advanced Capture Centre
PB	Packed Bed
PCHE	Printed Circuit Heat Exchanger
PC-SAFT	Perturbed-Chain Statistical Associating Fluid Theory
PE	2-Piperidine Ethanol
PHW	Pressurised Hot Water
PI	Process Intensification
PSTU	Pilot Solvent Test Unit
PZ	Piperazine
RCF	Reaction Condition Factor
RPB	Rotating Packed Bed
RTD	Resistance Temperature Detector
SHE	Spiral Heat Exchanger
SM	Sequential-Modular
SRD	Specific Reboiler Duty
TCM	Technology Centre Mongstad
TERC	Translational Energy Research Centre
TGR	Top Gas Recycling
TRL	Technological Readiness Level
UK	United Kingdom
UKCCSRC	UK Carbon Capture and Storage Research Centre
UNCED	United Nations Conference on Environment and Development
UNFCCC	United Nations Framework Convention on Climate Change
VLE	Vapour-Liquid Equilibrium

Latin Alphabet:

A	actual temperature of a column RTD (°C)
$c_{\mathrm{CO_2,0,vol.\%}}$	initial CO_2 percentage in the flue gas (vol.%)
$c_{\mathrm{CO_2,1,vol.\%}}$	volume of CO_2 in the exiting flue gas (vol.%)
$c_{\mathrm{CO_2,remaining,vol.\%}}$	uncaptured CO_2 (vol.%)
$c_{\mathrm{CO_2,removed,vol.\%}}$	captured CO_2 (vol.%)
$c_{\mathrm{CO_2,wt.\%}}$	concentration of captured CO_2 in the solvent by mass (wt.%)
$c_{\mathrm{exit\ gas,vol.\%}}$	exiting gas volume as a percentage of the inlet flue gas (vol.%)
$c_{\mathrm{MEA,wt.\%}}$	concentration of MEA in the solvent by mass (wt.%)
$C_{\mathrm{p,avg}}$	average specific heat capacity of the stream (kJ/(kg·K))
$C_{\mathrm{p,i}}$	specific heat capacity of a specific component ((kJ/(kg·K))
$C_{\mathrm{p,j}}$	specific heat capacity of a specific stream ((kJ/(kg·K))
$C_{\mathrm{p,PHW}}$	specific heat capacity of the PHW (kJ/(kg·K))
E	activation energy
h_{f}	specific enthalpy of saturated liquid (kJ/kg)
h_{fg}	specific enthalpy of vaporisation/condensation (kJ/kg)
h_{g}	specific enthalpy of saturated vapour (kJ/kg)
H_{abs}	average specific enthalpy of absorption/desorption (kJ/mol·CO_2)
k	Arrhenius factor
$k_{\mathrm{air,i}}$	air scaling factor for specific component in the flue gas
k_{removal}	CO_2 removal fraction (e.g. 0.9 for 90% capture)
k_{solvent}	solvent flow rate scaling factor (1/h)
m_{i}	mass of a specific component (kg)
$\dot{m}_{\mathrm{i}}$	mass flow rate of a specific component (kg/h)
$\dot{m}_{\mathrm{j}}$	mass flow rate of a specific stream (kg/h)
$m_{\mathrm{i,0}}$	initial mass of specific component (kg)
$m_{\mathrm{sample,1}}$	mass of first solvent sample (g)
$m_{\mathrm{sample,2}}$	mass of second solvent sample (g)
$m_{\mathrm{CO_2,0}}$	initial mass of CO_2 (kg)
$m_{\mathrm{H_2O,0}}$	initial mass of H_2O (kg)
$m_{\mathrm{MEA,0}}$	initial mass of MEA (kg)
$\dot{m}_{\mathrm{CO_2}}$	mass flow rate of CO_2 (kg/h)
$\dot{m}_{\mathrm{CO_2,captured}}$	mass flow rate of captured CO_2 (kg/h)
$\dot{m}_{\mathrm{CO_2,in}}$	mass flow rate of CO_2 entering the absorber (kg/h)
$\dot{m}_{\mathrm{CO_2,out}}$	mass flow rate of CO_2 exiting the absorber (kg/h)
$\dot{m}_{\mathrm{H_2O}}$	mass flow rate of H_2O (kg/h)
$\dot{m}_{\mathrm{MEA}}$	mass flow rate of MEA (kg/h)
$\dot{m}_{\mathrm{PHW}}$	mass flow rate of the PHW (kg/h)
$\dot{m}_{\mathrm{Solvent}}$	total mass flow rate of the solvent (kg/h)
$\dot{m}_{\mathrm{steam}}$	mass flow rate of steam (kg/h)
$\dot{m}_{\mathrm{steam,cond}}$	mass flow of condensing steam (kg/h)
M_{HCl}	molarity of HCl (mol/L)

M_{NaOH}	molarity of NaOH (mol/L)
$MW_{\mathrm{CO_2}}$	molecular weight of CO_2 (g/mol)
$MW_{\mathrm{H_2O}}$	molecular weight of H_2O (g/mol)
MW_{i}	molecular weight of a specific component (g/mol)
MW_{MEA}	molecular weight of MEA (g/mol)
n	temperature exponent
$n_{\mathrm{H_2O,0}}$	initial moles of H_2O (mol)
n_{gas}	number of moles of flue gas (mol)
n_{i}	number of moles of a specific component in the flue gas (mol)
N	number of species in the reaction
$P_{\mathrm{CO_2,eq}}$	equilibrium partial pressure of CO_2 (Pa)
$P_{\mathrm{CO_2,gas}}$	actual partial pressure of the gas phase (Pa)
P_{gas}	pressure of the flue gas (Pa)
P_{reboiler}	pressure of the reboiler (kPa)
$P_{\mathrm{saturation}}$	saturation pressure at the corresponding temperature (kPa)
q_{reboiler}	specific reboiler duty (MJ/(kg·CO_2))
q_{regen}	specific regeneration energy (MJ/kg·CO_2)
$Q_{\mathrm{column,steam}}$	sensible heat transferred from the steam cooling to the saturation temperature (kJ/h)
Q_{cond}	energy released from steam condensation within the column (kJ)
$Q_{\mathrm{condenser}}$	energy removed by the condenser (kJ/h)
Q_{de}	desorption energy (kJ/h)
Q_{i}	amount of energy flowing in a specific component (kJ/h)
Q_{j}	amount of energy flowing in a specific stream (kJ/h)
Q_{losses}	generalised heat losses across the system (kJ/h)
Q_{reboiler}	reboiler heat duty (kJ/h)
Q_{recovery}	total energy of internal heat recovery (kJ/h)
Q_{react}	total energy required in the desorption reaction (kJ/h)
Q_{regen}	conventional regeneration energy (kJ/h)
$Q_{\mathrm{regen,net}}$	net regeneration energy (kJ/h)
Q_{sens}	total sensible heat of the solvent (kJ/h)
$Q_{\mathrm{sens,bottom}}$	sensible heat to get the total solvent at the stripper bottom to the reboiler core temperature (kJ/h)
$Q_{\mathrm{sens,CO_2}}$	sensible heat transferred from the cooling of CO_2 within the column (kJ)
$Q_{\mathrm{sens,column}}$	sensible heat to get the column steam condensate to the stripper bottom temperature (kJ/h)
$Q_{\mathrm{sens,condenser}}$	sensible heat to get the condenser steam condensate to the stripper bottom temperature (kJ/h)
$Q_{\mathrm{sens,rich}}$	sensible heat to get the hot rich solvent component to the stripper bottom temperature (kJ/h)
$Q_{\mathrm{sens,steam}}$	sensible heat transferred from the cooling of steam within the column (kJ)
Q_{steam}	energy of flowing steam (kJ)
$Q_{\mathrm{top,H_2O}}$	sensible heat transferred from the water that exits the top of the stripper (kJ/h)
Q_{vap}	total energy required to vaporise the solvent from liquid (kJ/h)
r	rate of reaction (dependent)
R	universal gas constant (J/(mol·K))
S	simulated temperature at the same height as the RTD (°C)

SSG	specific steam generation (kg/kg)
T_0	reference temperature
T_{abs}	absolute temperature (K)
T_{gas}	temperature of the flue gas (K)
$T_{\mathrm{PHW,in}}$	inlet temperature of the PHW (°C)
$T_{\mathrm{PHW,out}}$	outlet temperature of the PHW (°C)
T_{sol}	temperature of the solvent (°C)
u	absolute uncertainty of a value (same units as the mean value)
u_{rel}	relative uncertainty of a mean value (unitless, %)
$\dot{V}_{\mathrm{PHW}}$	volumetric flow rate of the PHW (m^3/h)
$V_{\mathrm{exit\ gas,1}}$	preliminary volume of exiting flue gas (m^3)
$V_{\mathrm{exit\ gas,2}}$	final volume of exiting flue gas (m^3)
V_{gas}	volume of the flue gas (m^3)
V_{HCl}	volume of HCL required for titration (mL)
V_{i}	volume of a specific component in the flue gas (m^3)
V_{NaOH}	volume of NaOH required for titration (mL)
$w_{\mathrm{H_2O}}$	mass fraction of water (kg/kg)
w_{i}	mass fraction of a specific component (kg/kg)
$x_{\mathrm{H_2O}}$	mole fraction of water in the stream (mol/mol)
x_{i}	mole fraction of a specific component
$y_{\mathrm{CO_2}}$	volume fraction of CO_2 in the flue gas
$y_{\mathrm{H_2O}}$	volume fraction of H_2O in the flue gas
y_{i}	volume fraction of a specific component in the flue gas

Greek Alphabet:

β_{i}	the stoichiometric coefficient of a specific component in the reaction equation
γ_{i}	activity coefficient of a specific component
η_{capture}	capture efficiency of CO_2 (%)
λ	amount of CO_2 loading in the solvent (mol·CO_2/mol·MEA)
ρ_{PHW}	density of the PHW at the average temperature (kg/m^3)
ΔT_{i}	temperature change of a specific component (K)
ΔT_{j}	temperature change of a specific stream (K)

Chapter 1: Introduction

1.1 Climate Change and the Need for Decarbonisation

It has become undeniable that anthropogenic emissions in the post-industrialisation era are the primary driver of climate change today [1]. There are evidential links between rising global temperatures and atmospheric greenhouse gas (GHG) concentrations, which includes CH_4, N_2O, SF_6, HFCs, PFCs, and most significantly CO_2, which has been true through Earth's history [2]. GHGs are quantified by the amount of warming or cooling they can produce in the atmosphere, known as radiative forcing. CO_2 has a high radiative forcing value compared to other GHGs [3], meaning it has a significant impact on global warming. This is significant, as CO_2 is also the most abundant GHG, making up 74% of emitted GHGs in 2022 [4]. Annual CO_2 emissions have also increased rapidly over the last 50 years and have not yet peaked, with 92% of these emissions coming from fossil fuel use [4,5]. Over 37 billion tonnes of CO_2 were emitted in 2023 alone [6]. It is an urgent challenge for humanity to minimise and mitigate GHG emissions to safeguard future generations from the devastating effects of climate change [1].

The extent of human influence on atmospheric CO_2 concentrations has been revealed through analysis of ice core samples taken in Antarctica, where trapped air pockets have given insight into the historical CO_2 concentrations of earth's atmosphere, presented in Figure 1.1.

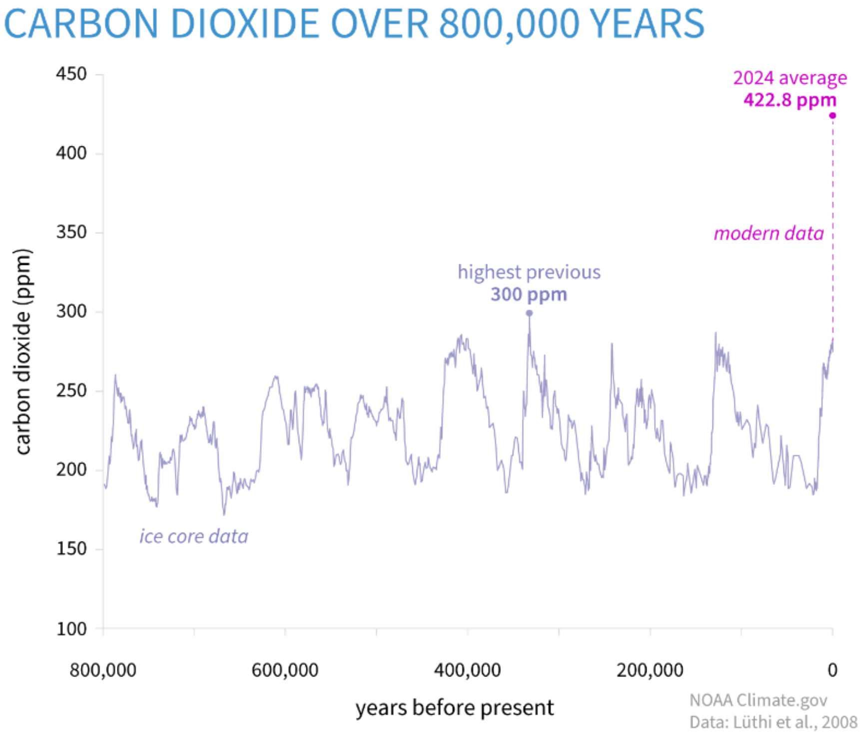

Figure 1.1: Atmospheric CO_2 in parts per million for the last 800,000 years based on ice-core data. Graph by the National Oceanic Atmospheric Administration (NOAA) [7] based on data by Lüthi et al. [8].

The historical data highlights warm interglacial periods, identified by higher CO_2 concentrations, and ice ages, identified by lower CO_2 concentrations. It can be seen that prior to human industrialisation in the 1750s, the CO_2 concentration never surpassed 300 ppm. Since the industrialisation period, the associated increase in CO_2 concentration occurred rapidly and appears instantaneous on a geological time scale.

This increase in CO_2 concentration has been closely monitored since 1958, when C. David Keeling of the Scripps Institution of Oceanography began taking monthly measurements of atmospheric CO_2 at the NOAA Mauna Loa Observatory in Hawaii [9]. This dataset represents the longest continuous record of direct atmospheric CO_2 and is presented in Figure 1.2.

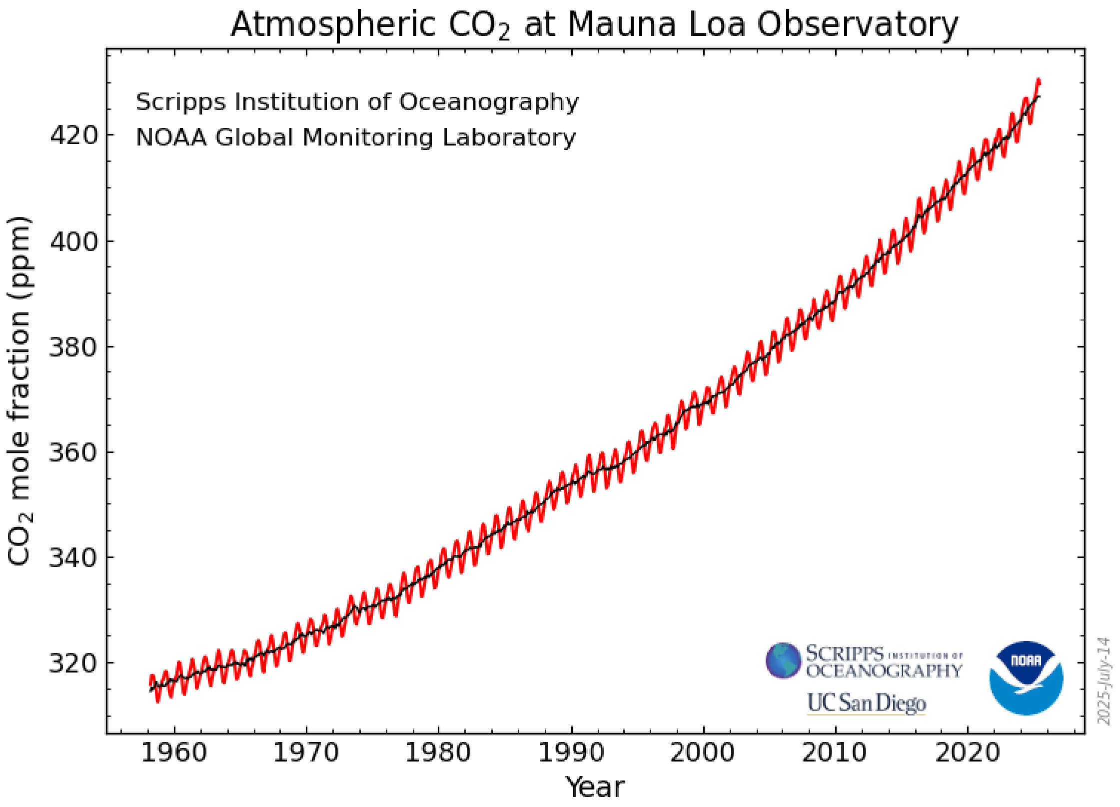

Figure 1.2: Historical CO_2 concentrations from the Mauna Loa Observatory. Graph by the NOAA Global Monitoring Laboratory [10].

During 2021 the atmospheric concentration of CO_2 breached 420 ppm for the first time in history. This peaked to approximately 430 ppm in March 2025 [10]. The Intergovernmental Panel on Climate Change (IPCC) uses a value of 278 ppm for the pre-industrial CO_2 baseline [1], indicating that CO_2 concentrations have already increased by over 50%. This concentration represents a global temperature increase of approximately 1.5 °C compared to 1850 [11]. This rate of temperature increase is unsustainable, and if CO_2 continues to be emitted at high concentrations, then a runaway temperature cascade could occur, causing catastrophic damage to the planet. Humanity must intervene to reduce and minimise CO_2 emissions to prevent further global warming.

1.1.1 Global Cooperation on Climate Change Prevention

The global threat posed by runaway climate change has not been ignored. The United Nations Framework Convention on Climate Change (UNFCCC) established an international environmental treaty with the ultimate objective of stabilising GHG concentrations at a level that would prevent interference with the climate system [12]. It was originally signed by 154 parties at the United Nations Conference on Environment and Development (UNCED) held in Rio de Janeiro in June 1992 and entered into force in 1994. Member parties have since met annually at Conferences of Parties (COP), and it was at the first COP in Berlin 1995 that current actions to mitigate climate change were described as inadequate [13], eventually leading to the establishment of the Kyoto Protocol in response. The Kyoto Protocol was an international treaty named after the Japanese city in which it was adopted in December 1997 at COP3, aiming to control anthropogenic emissions of GHGs in a way that can reflect underlying national differences in emissions, wealth, and capacity [14]. Focus was placed on four specific GHGs: CO_2, CH_4, N_2O, SF_6, alongside two broader groups of gases: HFCs and PFCs [15–17]. The Kyoto Protocol was succeeded by The Paris Agreement in 2015 [18].

The Paris Agreement is a legally binding treaty that commits signatory nations to a collective effort in combating climate change. It was adopted by 196 parties at COP21 held in Paris and officially entered into force on November 4th, 2016. The aim of the agreement is to restrict the global average temperature rise to well below 2 °C above pre-industrial levels, while pursuing efforts to limit the temperature increase to 1.5 °C. The scientific consensus indicates that achieving the more stringent 1.5 °C target is necessary to avert the most catastrophic impacts of climate change. This ambitious goal imposes a finite global carbon budget and demands a rapid and profound transformation of the global energy and industrial systems. To remain on this trajectory, global GHG emissions must peak no later than 2025 and decline by 43% by 2030 [19]. Member parties must aim to peak with their respective GHG emissions as soon as possible and reduce emissions to sustainable magnitudes, with it acknowledged that developing countries will take longer to reach their peak and achieve subsequent reductions. Implementation of the Paris Agreement requires economic and social transformation, based on the best available science. The Paris Agreement is built on five-year cycles of progressively increasing ambition, where each country communicates its planned actions for emissions mitigation, known as Nationally Determined Contributions (NDCs) [20], the first of which were submitted in 2020 [21]. To support developing member parties, a framework for financial, technical, and capacity building is available to pursue mitigation targets. Furthermore, from 2024 countries will report transparently on actions taken and progress made under an enhanced transparency framework (ETF) [19]. The ETF also highlights any additional support required or adaptations needing to be made.

1.1.2 The United Kingdom and The Climate Change Act

The United Kingdom (UK) has established one of the world's most ambitious climate policy frameworks, embedding its decarbonisation targets in national law. The foundation of this framework is the Climate Change Act 2008 [22], which originally set a target to achieve an 80% reduction in GHG emissions relative to 1990 levels by 2050. After the Paris Agreement entered into force, the UK amended its target in 2019 to bring all GHGs to net zero by 2050 [23], becoming the first major economy to commit to ending its contribution to global warming by 2050.

The Net Zero target is underpinned by a series of legally binding, five-year carbon budgets that set interim reduction goals on the pathway to 2050, while also complying with any international obligations [24]. The carbon budgets must be set 12 years in advance, with seven budgets set as of 2025, guiding pathways to emissions reductions up until 2042 [25]. The carbon budgets are advised by the appointed Committee on Climate Change (CCC), experts in scenario modelling and emissions mitigation tactics. Each carbon budget has a set amount of carbon units assigned, which can be in one of three forms: a reduction in emissions; removal of a specified amount of GHG from the atmosphere; or an arranged limit of emissions allowed under a scheme or agreement. Although CO_2 is a primary focus for the Climate Change Act, it also targets the other GHGs which the Kyoto Protocol originally accounted for, each with their own respective mitigation targets compared to their own baseline levels.

The CCC published a letter formally advising that the UK should commit to reducing GHG emissions by 68% by 2030, as part of the UK's NDC to the Paris Agreement. This target would "place the UK among the leading countries in climate ambition" [26]. This was formally acknowledged in the published NDC for the UK [27], where actions for achieving this target were outlined. In 2024 at COP29, the UK government formally adopted the CCC's recommendation for an emissions reduction target of 81% by 2035 as part of the UK's NDC to the Paris agreement [28]. In 2022, the UK became the first major economy to cut emissions by 50% compared to 1990 levels [29].

The government's strategic vision for achieving these reduction targets is articulated in key policy documents, most notably the "Net Zero Strategy: Build Back Greener" [30], "Industrial Decarbonisation Strategy" [31], and the UK's "Modern Industrial Strategy" [32]. These strategies outline a comprehensive, economy-wide approach that included the phasing out of coal-fired power stations, a milestone subsequently achieved in September 2024 [33], a massive expansion of offshore wind and other renewable energy sources, and significant investment in emerging low-carbon technologies, particularly hydrogen and Carbon Capture Usage and Storage (CCUS) [34]. The Net Zero Strategy explicitly acknowledges that certain sectors, including heavy industry, are inherently difficult to decarbonise, and identifies that CCUS will play an essential role in reducing emissions from these areas [30]. The Industrial Decarbonisation Strategy provides a more focused roadmap for these sectors, with a central pillar being the development of low-carbon industrial clusters. The strategy sets a target to establish at least four such clusters by 2030, which will co-locate existing key clusters of industrial facilities with shared infrastructure for CCUS and hydrogen production, thereby creating economies of scale with significant cost reduction [31]. The Modern Industrial Strategy, published in mid-2025, outlines a 10-year plan to foster industrial growth while supporting the transition to a low-carbon, globally competitive economy [32].

1.2 Barriers to Heavy Industry Decarbonisation

While the transition to renewable energy is effectively tackling emissions from the power generation sector, a significant portion of global GHG emissions originate from the industrial sector. Three primary sectors: cement, petrochemicals, and steel industries are notably referred to as hard-to-abate industries [35]. These sectors are fundamental pillars of a modern manufacturing economy but each present unique decarbonisation challenges. The difficulties stem from a combination of factors, including the need for high heat and high pressure processes, process emissions released from chemical reactions rather than fuel combustion, and the need for fossil fuels as feedstocks [36,37]. Additionally, these industrial sectors have large, capital-intensive facilities with long operational lifetimes, making replacement economically challenging [37]. These industries account for nearly 60% of total industrial energy consumption and contribute approximately 70% of industrial CO_2 emissions [35]. These foundational manufacturing industries accounted for approximately 30% of global CO_2 emissions in 2018 [36]. Therefore, the decarbonisation of these industries is an absolute necessity for meeting the goals of the Paris Agreement.

Among these, the iron and steelmaking industry is a critical focus area. It is one of the largest industrial sources of CO_2, accounting for approximately 7% of the global GHG emissions in 2023, producing 2.8 billion tonnes of CO_2 equivalent emissions [38]. Mitigating these emissions is therefore a cornerstone of any credible industrial decarbonisation strategy [39]. This thesis will focus specifically on the decarbonisation of the iron and steel industry to minimise process emissions, with the aim to generalise outcomes so they may be applied to other hard-to-abate industries.

1.2.1 The Iron and Steel Industry: A Hard-To-Abate Sector

The iron and steel industry is a foundational sector of the global economy, providing the essential materials for construction, infrastructure, transport, and the very technologies needed for the green energy transition, such as wind turbines and electric vehicles [40]. From 2012 to 2023, the global production of crude steel increased from 1.56 billion to 1.89 billion tonnes due to rising global demand [41], with associated process emissions rising by approximately 30% to reach a 7% global share of GHG emissions [38]. During 2022, an average of 20.99 GJ of energy was consumed with 1.91 tonnes of CO_2 emitted per tonne of crude steel cast [41], demonstrating the significant environmental impact of steelmaking.

The primary reason for such a large carbon footprint is the dominance of the conventional Blast Furnace-Basic Oxygen Furnace (BF-BOF) production route. This route, which was responsible for 71.1% of global steel production in 2023 [41], is inherently carbon intensive. The BF-BOF route involves chemically reducing iron ore to liquid iron using coke, a high purity carbon fuel derived from coal, as both a reducing agent and as a source of thermal energy [42]. This process generates enormous quantities of unavoidable CO_2, with emissions typically ranging from 1.6 to 2.2 tonnes of CO_2 for every tonne of crude steel produced [43]. China is the single largest producer of crude steel in the world, producing over one billion tonnes in 2023, a share exceeding 53% of global production [41], with approximately 90% of this production originating from the BF-BOF route [44]. Meaningful decarbonisation of the iron and steel industry should therefore focus on the BF-BOF production route.

In the BF-BOF route, iron ore is reduced to liquid iron in a blast furnace and then converted to steel in a basic oxygen furnace, before being cast and finally rolled into the desired products, as shown in Figure 1.3.

Figure 1.3: Blast furnace-basic oxygen furnace steelmaking, from The European Steel Association [45].

A key challenge in decarbonising the BF-BOF route is managing emissions from multiple distributed sources. The blast furnace is the single largest emitter in the production process, responsible for approximately 70% of an integrated steel mill's CO_2 emissions [46]. The basic oxygen furnace accounts for approximately 10% of emissions, and the coke ovens produce around 5%. Together, these core production processes account for approximately 85% of the mill's emissions and produce the primary steelmaking off-gases: Blast Furnace Gas (BFG), Basic Oxygen Furnace Gas (BOFG), and Coke Oven Gas (COG). Typical average compositions of these off-gases are presented in Table 1.1, excluding trace compounds [47,48]. These gases are captured and used as fuel to produce heat for other parts of the plant or to generate electricity to power the site [49]. The largest volume off-gas stream is typically the BFG, characterised by a high concentration of both CO_2 and CO. Decarbonisation efforts should primarily focus on reducing emissions from the blast furnace to achieve maximum impact [46].

Table 1.1: Typical compositions of iron and steel industry process emissions.

Flue Gas Component	BFG mol.%	BOFG mol.%	COG mol.%
CO_2	24.0	15.0	2.0
CO	23.5	68.0	5.5
H_2	3.5	1.0	65.0
CH_4	-	-	23.5
N_2	49.0	15.5	1.0
O_2	-	0.5	-

The long-term future for decarbonised steel production will likely remove blast furnaces entirely and instead rely on hydrogen-based direct reduced iron (DRI) reactors to produce liquid iron. Green hydrogen for the DRI process would be produced through electrolysis using renewable energy, with the potential to achieve CO_2 reductions of over 95% [50,51]. However, the global hydrogen economy has its own challenges, where the scaling up of green hydrogen production and rolling out supply chains will take time [52,53]. Even if the hydrogen economy improves, blast furnaces have long design lifetimes of up to 25 years [54,55], with 71% of the existing fleet needing major refurbishment by 2030, and the remainder by 2040 [56]. Consequently, many blast furnaces will continue operation for several decades before shutting down or needing replacement.

An intermediate solution is therefore required to decarbonise existing conventional blast furnaces and provide a transitional technology step between the existing process and potential green manufacturing process. The International Energy Agency (IEA) describes Carbon Capture and Storage (CCS) as a key component in achieving deep carbon emission reductions for the iron and steel industry [57–59], and it is likely to serve as an interim solution for foundation industries [60].

1.3 Carbon Capture Usage and Storage as a Key Abatement Strategy

CCUS is a term given to a portfolio of technologies designed to capture CO_2 emissions from industrial processes, power plants, and other sources, preventing their release to the atmosphere and contributing to climate change [61–63]. It is comprised of four major stages:

1) **Capture:** The separation of CO_2 from other emissions at large point sources. Capture technologies fall into three distinct categories: post-combustion capture, pre-combustion capture, and oxyfuel combustion systems [64,65].
2) **Transport:** The transportation of captured CO_2 to a storage site. The CO_2 is compressed and delivered in either gas, liquid, or solid form. Pipelines, ships, and road tankers are all typical transportation options [66].
3) **Storage:** Geological storage involves injecting CO_2 into deep underground rock formations. Saline formations and depleted gas and oil reservoirs are typical options for geological storage [67].
4) **Usage:** Captured CO_2 can also be used as a chemical feedstock to create valuable products such as fuels, chemicals, or building materials, or put into a process such as enhanced oil recovery [68].

CCUS has the potential to be applied to all major point emission sources in an integrated steel mill, however the blast furnace has been the primary focus for most existing studies [69]. This thesis therefore focuses on the separation and capture of CO_2 from iron and steelmaking process emissions.

1.3.1 The Primary Approaches to CO_2 Capture

Selecting the right form of capture technology is critical, as it represents the fundamental approach to how CO_2 will be abated. The applicability of these technologies is dictated by the challenge of retrofitting existing blast furnaces and other infrastructure [70]. Pre-combustion and oxyfuel combustion technologies require fundamental systematic changes to the steelmaking process itself. Pre-combustion capture involves reforming the fuel source before it enters the furnace, while oxyfuel would require a complete redesign of the blast furnace to operate with pure oxygen instead of air [71–73]. While these technologies hold promise for future, new build facilities, they are not economically or technically feasible as retrofits for the vast fleet of conventional blast furnaces currently operating.

Post-combustion capture stands as the most readily available and viable capture technology for achieving short term decarbonisation in the steel industry [74]. This technologically mature strategy is designed to capture CO_2 after it has been produced, ideal for handling BFG, and is easier to retrofit with existing facilities without fundamentally altering the core ironmaking process [75]. For this reason, this thesis will focus exclusively on the investigation of post-combustion capture technologies.

1.3.2 *Post-Combustion Capture Technologies*

Several different post-combustion capture technologies exist, including chemical absorption, physical absorption, adsorption, membrane separation, and cryogenic distillation [65,76]. Process descriptions for each of these technologies are given in the following subsections.

1.3.2.1 *Chemical Absorption*

A chemical solvent reacts selectively with a targeted gas species within a mixed flue gas stream [77]. The reaction is reversible at higher temperatures, allowing for desorption of the captured gas species and regeneration of the solvent. The capture process is carried out in a two-stage process that works on a temperature swing basis. The absorption favours low partial pressures of the targeted gas component at low temperatures, typically around 40 °C. During desorption, the solvent is heated to a higher temperature around 120 °C [78]. High purities and recoveries are possible because of the selective nature of the solvent, but solvent systems can exhibit volatile and corrosive behaviour and have high energy demands, requiring optimisation for economical operation. Amine-based solvents are the most commonly used chemical solvents in chemical absorption for the capture of CO_2, with extensive use of monoethanolamine (MEA) due to its maturity and commercialisation [79].

1.3.2.2 *Physical Absorption*

Physical absorption is based on the principle of gas dissolving into a solvent solution without a chemical reaction occurring, governed by Henry’s Law [80]. Operating in a two-step process, physical absorption favours high partial pressures of the desired gas component at a low temperature, then desorption occurs by flashing to lower pressures to release the captured gas component and regenerate the solvent [81]. The energy for solvent regeneration is much less than with chemical absorption: little or no heat input is required for regeneration as temperature is not as critical as pressure in this process, operation under reduced pressure consumes less energy than temperature swings, and the absence of chemical bonding means no energy input is required to reverse chemical reactions. However, physical absorption requires a high-pressure gas stream in addition to a high partial pressure of the targeted gas species to be economically feasible, meaning it is only applicable in specific use cases or after pressurisation takes place. Several commercialised physical solvent systems have emerged for the capture of CO_2, examples include Selexol, Fluor, Purisol, and Rectisol solvents [82].

1.3.2.3 *Adsorption*

Adsorption differs from absorption on the basis that gaseous components are selectively retained on the external surface of a porous solid (the adsorbent), rather than components penetrating to the interior of the capturing substance (the absorbent) [83]. Adsorption is controlled through two distinct mechanisms, either by chemisorption or physisorption. Chemisorption depends on chemical attraction and reactions between the surface and the surrounding molecules, and is often slower than physisorption, usually requiring higher temperatures so the activation energy can be met. Physisorption involves weak van der Waals forces of physical attraction between the solid adsorbent and the surrounding molecules, resembling the action of condensation from gases to liquids. Physisorption has no chemical specificity, with adsorption typically occurring at low temperatures or high gaseous pressure [83,84]. Adsorption, like absorption technologies, also occurs in a two-step process: the adsorption step puts the gaseous mixture in contact with the solid adsorbent for capture, and the desorption step regenerates the solid adsorbent by liberating the captured gas. Pressure swings, temperature swings, and electric swings are all options for adsorbent regeneration [76,85]. Adsorbents for CO_2 capture can be divided into two categories, chemical and physical. Chemical adsorbents for CO_2 capture include amine-based adsorbents, such as amine impregnated adsorbents and amine grafted adsorbents; and other examples such as hydrotalcites and double salts. Physical adsorbents for CO_2 capture include: activated carbon and carbon molecular sieves, metal oxides such as calcium oxide and magnesium oxide, metal carbonates such as calcium carbonate, metal salts such as lithium silicate and lithium zirconate, zeolites, mesoporous silica, and metal organic frameworks, among others [86].

1.3.2.4 Membrane Separation

Gas component separation can also be achieved with membranes, where the mixed gas is passed across a membrane to achieve selective permeation of the targeted gas component [76]. The driving force necessary for mass transport across the membrane can be achieved with either pressurised mixed gas contacting the surface of the membrane, or with a vacuum applied on the other side of the membrane. During the separation process, two outlet streams are made: the permeate steam, which is the enriched stream of gas components that have passed through the membrane, and the retentate stream, which contains the remaining gas components from the feed that are less permeable and do not traverse the membrane [76]. Membrane material choice is based on specific physical and chemical properties and need to be tailored for a given gas mixture. These properties include: the membrane material, the membrane structure and thickness, the membrane configuration, and the module and system design [87]. It is the permeability and selectivity of the material that determines the economics and efficiency of the separation process. Membranes can be broadly classified into three categories based on their selectivity and flux density: porous membranes, asymmetric membranes, and non-porous membranes [88]. Dense polymeric membranes, a type of non-porous membrane, are commonly used for commercialised gas separation at industrial scale [76,89].

1.3.2.5 Cryogenic Distillation

Cryogenic distillation is a relatively new idea for the capture of CO_2 from flue gases [90]. Desired gas components are separated from a mixture through their very low boiling points. A refrigeration system is coupled with a condenser set to the lowest possible temperature, making the process very energy intensive [91]. The main advantage of cryogenic distillation for CO_2 capture is the lack of a chemical systems requirement, and the ability to operate at ambient pressure. It also directly produces liquid CO_2, making it easy for economical transport to storage sites by either pipeline or vehicles [92]. Drawbacks with this technology include the cost of equipment and refrigeration, and the requirement of removing moisture to prevent plugging by solid CO_2 and ice [93]. Cryogenic distillation has been widely applied throughout the chemical, metal, and electronic industries to produce various high purity gases from either air or natural gas, in addition to producing or recovering carbon dioxide and hydrogen from industrial applications [94,95]. Commercially, however, it is only recommended for gas streams containing over 50% CO_2, applicable for oxyfuel scenarios, as CO_2 levels below this is usually uneconomical for the energy demand [92].

1.4 Chemical Absorption Carbon Capture for the Iron and Steel Industry

A review study by Ramirez-Santos et al. [76] explored the emerging developments and applications of these technologies for emission reductions within the iron and steel industry, highlighting the benefits and challenges each technological approach brings. While different projects have been investigated across these technologies, it is chemical absorption that has been identified as the most applicable technology to the capture of CO_2 from blast furnaces and should therefore be prioritised for research [76]. Chemical absorption is the most proven technology for the capture of CO_2 due to its maturity and widespread research carried out in the area [96], and a review study by Marques et al. shows that chemical absorption has been applied to 39% of the 49 industrial carbon capture facilities reviewed in Europe [75]. BFG has CO_2 concentrations and pressures that align closely with the use of chemical absorption [97], as presented in Figure 1.4, making it a prime candidate as a technology for the decarbonisation of the iron and steel industry.

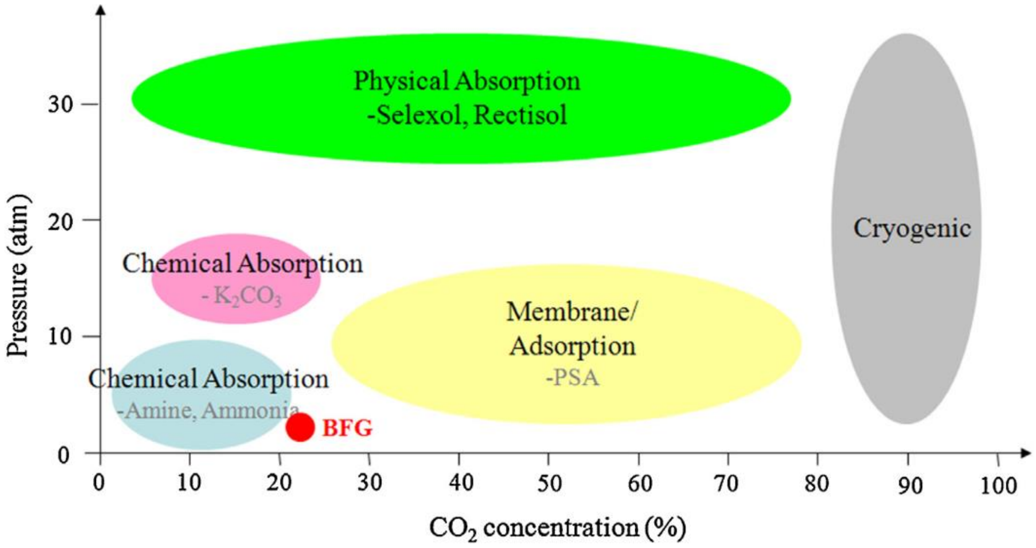

Figure 1.4: Technical options for CO_2 capture dependent on feed pressure and CO_2 concentration [97].

Decarbonisation technologies, specifically CCUS, must be rolled out in the near future in order to minimise the effects of climate change from iron and steel manufacturing. Chemical absorption lends itself strongly as the most readily applicable interim carbon capture technology whilst working towards the ultimate decarbonisation of the iron and steel industry. As such, this thesis will focus on chemical absorption for specific use with flue gases of elevated CO_2 concentrations, such as BFG and other steelmaking emissions.

Significant challenges related to energy consumption and process optimisation remain, particularly under the specific conditions of BFG and other process emissions. The following chapter presents a comprehensive review of the literature to identify the key knowledge gaps addressed in this research.

1.5 Overall Aim and Thesis Outline

The overall aim of this thesis is to investigate and optimise the chemical absorption process for carbon capture from flue gases with elevated CO_2 concentrations, representative of process emissions from the iron and steel industry. To achieve this, the thesis is organised into six chapters, including this one, where the contents of each chapter are outlined below:

- **Chapter 1** outlines the context and insight to the problem statement, explaining the need for global decarbonisation to combat the effects of climate change. The essential need of industrial decarbonisation is explored, with a focus on the iron and steel industry. CCUS is discussed as a solution for meaningful decarbonisation, where chemical absorption is identified as the technology of choice for this investigation.
- **Chapter 2** provides a comprehensive review of chemical absorption as a carbon capture technology and its application to the iron and steel industry, highlighting key research gaps in the open literature that this thesis will explore. Notably, the lack of real-world pilot plant data for elevated CO_2 concentrations typical of industrial processes is identified, which informs the objectives that this thesis sets out to achieve.
- **Chapter 3** describes the development, validation, and predictive use of a simulation model in Aspen Plus that is representative of a real-world capture plant. Performance trends and operational guidelines are identified, which are ultimately used to inform the initial conditions for an experimental campaign explored in the subsequent chapter.
- **Chapter 4** details the experimental campaign that was conducted to assess the performance of a conventional packed bed capture plant using standard MEA solvent. A baseline performance dataset was collected across the operational envelope of the capture plant, which was then used to determine the regeneration energy requirements for each capture condition.
- **Chapter 5** presents a comparison between the experimental data and predictions made by the simulation model. The model is then calibrated against the experimental data to align performance to expectations. The calibrated model is then used to expand the dataset of the experimental campaign, allowing for greater insight into the performance metrics of the capture plant. Finally, the model is used to extend predictions beyond the boundaries of the experimental campaign.
- **Chapter 6** summarises the conclusions from research Chapters 3,4, and 5, and provides recommendations for future work for both experimental and simulation-based studies.

1.6 References for Chapter 1

[1] Masson-Delmotte, V., P. Zhai, A. Pirani, S. L. Connors, C. Péan, S. Berger, N. Caud, Y. Chen L, Goldfarb, M. I. Gomis, M. Huang, K. Leitzell, E. Lonnoy, J.B.R. Matthews, T. K. Maycock TW, O. Yelekçi RY and BZ (eds.). Climate Change 2021: The Physical Science Basis. Contribution of Working Group I to the Sixth Assessment Report of the Intergovernmental Panel on Climate Change. Cambridge University; 2021.

[2] Lacis AA, Schmidt GA, Rind D, Ruedy RA. Atmospheric CO2: Principal Control Knob Governing Earth’s Temperature. Science 2010;330:356–9. https://doi.org/10.1126/science.1190653.

[3] Stocker, T.F., D. Qin, G.-K. Plattner, M. Tignor, S.K. Allen, J. Boschung, A. Nauels, Y. Xia VB and PMM (eds.). Summary for Policymakers. Climate Change 2013: The Physical Science Basis. Contribution of Working Group I to the Fifth Assessment Report of the Intergovernmental Panel on Climate Change. Cambridge and New York: 2013.

[4] Historical GHG Emissions | Climate Watch. Climate Watch n.d. https://www.climatewatchdata.org/ghg-emissions?breakBy=gas&chartType=percentage&end_year=2019&start_year=1990&ap3c=AGWUV9OohLwihokAAGbPPfu1uSNWxJOLVG2NtmDzhL5AJTijVg.

[5] Ritchie H, Rosado P, Roser M. CO_2 and Greenhouse Gas Emissions. Our World in Data 2023.

[6] Andrew RM, Peters GP. The Global Carbon Project’s fossil CO2 emissions dataset 2024. https://doi.org/10.5281/zenodo.13981696.

[7] NOAA Climate.gov. Carbon Dioxide Over 800,000 Years | NOAA Climate.gov n.d. https://www.climate.govhttps://www.climate.gov/media/16929.

[8] Lüthi D, Le Floch M, Bereiter B, Blunier T, Barnola JM, Siegenthaler U, et al. NOAA/WDS Paleoclimatology - EPICA Dome C - 800KYr CO2 Data n.d. https://doi.org/10.25921/xgzs-gd10.

[9] Keeling CD, Bacastow RB, Bainbridge AE, Ekdahl CA, Guenther PR, Waterman LS, et al. Atmospheric carbon dioxide variations at Mauna Loa Observatory, Hawaii. Tellus 1976;28:538–51. https://doi.org/10.1111/j.2153-3490.1976.tb00701.x.

[10] Global Monitoring Laboratory. Trends in CO2 - NOAA Global Monitoring Laboratory n.d. https://gml.noaa.gov/ccgg/trends/mlo.html.

[11] Hausfather Z. State of the climate: 2025 close behind 2024 as the hottest start to a year. Carbon Brief 2025. https://www.carbonbrief.org/state-of-the-climate-2025-close-behind-2024-as-the-hottest-start-to-a-year/.

[12] UNFCCC. United Nations Framework Convention on Climate Change United Nations. United Nations Framework Convention on Climate Change 1992:1–33.

[13] Depledge J. Tracing the origins of the Kyoto Protocol: an article by article textual history 2000:135.

[14] Grubb M. Kyoto and the Future of International Climate Change Responses: From Here to Where. International Review for Environmental Strategies 2004;5:15–38.

[15] UNFCCC. Kyoto Protocol - Targets for the first commitment period n.d. https://unfccc.int/process-and-meetings/the-kyoto-protocol/what-is-the-kyoto-protocol/kyoto-protocol-targets-for-the-first-commitment-period.

[16] Britannica. Kyoto Protocol | History, Provisions, & Facts n.d. https://www.britannica.com/event/Kyoto-Protocol.

[17] US EPA. Understanding Global Warming Potentials n.d. https://www.epa.gov/ghgemissions/understanding-global-warming-potentials.

[18] United Nations (UN). The Paris Agreement. 2015.

[19] The Paris Agreement | UNFCCC n.d. https://unfccc.int/process-and-meetings/the-paris-agreement.

[20] Key aspects of the Paris Agreement | UNFCCC n.d. https://unfccc.int/most-requested/key-aspects-of-the-paris-agreement.

[21] UNFCCC. The Paris Agreement n.d. https://unfccc.int/process-and-meetings/the-paris-agreement/the-paris-agreement.

[22] HM Government. Climate Change Act 2008. 2008.

[23] GOV.UK. UK becomes first major economy to pass net zero emissions law 2019. https://www.gov.uk/government/news/uk-becomes-first-major-economy-to-pass-net-zero-emissions-law (accessed August 25, 2021).

[24] Ministry of Justice. Net Zero Carbon Strategy 2024. n.d.

[25] Climate Change Committee. The Seventh Carbon Budget. 2025.

[26] Climate Change Committee. Letter: Advice on the UK’s 2030 Nationally Determined Contribution (NDC) 2020. https://www.theccc.org.uk/publication/letter-advice-on-the-uks-2030-nationally-determined-contribution-ndc/.

[27] HM Government. United Kingdom of Great Britain and Northern Ireland’s Nationally Determined Contribution. Comparative Politics 2020:32.

[28] UK Government. United Kingdom of Great Britain and Northern Ireland’s 2035 Nationally Determined Contribution. 2025.

[29] UK First Major Economy to Halve Emissions. GOVUK n.d. https://www.gov.uk/government/news/uk-first-major-economy-to-halve-emissions.

[30] HM Government. Net Zero Strategy: Build Back Greener. 2021.

[31] HM Government. Industrial Decarbonisation Strategy 2021.

[32] UK Government. The UK's Modern Industrial Strategy. 2025.

[33] Power Stations of the UK. Coal Countdown – Power Stations of the UK n.d. https://www.powerstations.uk/coal-countdown/.

[34] Hudspith J. The UK's Net Zero Target for 2050: A Guide to Strategy, Progress, and Challenges 2025. https://dbsne.com/post/net-zero-explained-the-uks-ambitious-target-and-challenges.

[35] UNFCCC. Integrating hard-to-abate industries in the process of preparing and implementing NDCs. n.d.

[36] Guo Y, Lu J, Zhang Q, Cao Y, Chen L, Mauzerall DL. Co-production of steel and chemicals to mitigate hard-to-abate carbon emissions. Nat Chem Eng 2024;1:365–75. https://doi.org/10.1038/s44286-024-00061-1.

[37] Office of Fossil Energy and Carbon Management. Scaling Carbon Capture for Hard-to-Abate Industries in the United States and Globally. EnergyGov n.d. https://www.energy.gov/fecm/articles/scaling-carbon-capture-hard-abate-industries-united-states-and-globally.

[38] Ian Tiseo. Steel Industry Emissions Worldwide. Statista n.d. https://www.statista.com/topics/13436/steel-industry-emissions-worldwide/.

[39] Swalec C. Guest post: These 553 steel plants are responsible for 9% of global CO2 emissions. Carbon Brief 2021. https://www.carbonbrief.org/guest-post-these-553-steel-plants-are-responsible-for-9-of-global-co2-emissions/.

[40] Innovation Zero. UK Industrial Strategy: Takeaways for Industrial / Hard to Abate Sectors. Innovation Zero 2025 n.d. https://www.innovationzero.com/news/uk-industrial-strategy-takeaways-industrial-hard-abate-sectors.

[41] World Steel in Figures 2024. WorldsteelOrg n.d. https://worldsteel.org/data/world-steel-in-figures/world-steel-in-figures-2024/.

[42] SAIL. Coke Ovens-Sinter-BF-BOF Route n.d. https://www.sail.co.in/learning-center/coke-ovens-sinter-bf-bof-route.

[43] Mio A, Petrescu L, Luca A-V, Galusnyak SC, Fermeglia M, Cormos C-C. Carbon Dioxide Capture in the Iron and Steel Industry: Thermodynamic Analysis, Process Simulation, and Life Cycle Assessment. Chemical and Biochemical Engineering Quarterly 2023. https://doi.org/10.15255/cabeq.2022.2123.

[44] World Steel Association. Steel Statistical Yearbook 2022 2022.

[45] The European Steel Association. What is steel and how is steel made? 2022. https://www.eurofer.eu/about-steel/learn-about-steel/what-is-steel-and-how-is-steel-made/.

[46] Wiley DE, Ho MT, Bustamante A. Assessment of opportunities for CO2 capture at iron and steel mills: An Australian perspective. Energy Procedia 2011;4:2654–61. https://doi.org/10.1016/j.egypro.2011.02.165.

[47] Rose JW, Cooper JR. Technical Data on Fuel. 7th Edition. The British National Committee, World Energy Conference; 1977.

[48] Heeley A. Typical iron and steel making process emission compositions 2024.

[49] IEAGHG. Iron and Steel CCS Study (Techno-Economics Integrated Steel Mill) 2013. https://ieaghg.org/docs/General_Docs/Reports/2013-04.pdf.

[50] Wallach O. Green Steel: Decarbonising with Hydrogen-Fueled Production. Visual Capitalist 2022. https://www.visualcapitalist.com/sp/green-steel-decarbonising-with-hydrogen-fueled-production/.

[51] H2 green steel. Green Steel production. H2 Green Steel 2022. https://www.h2greensteel.com/articles/green-steel-production.

[52] IEA. The Future of Hydrogen – Analysis. IEA 2019. https://www.iea.org/reports/the-future-of-hydrogen.

[53] Eh Christina L. M., Tiong Angnes N. T., Kansedo Jibrail, Lim Chun Hsion, How Bing Shen, Ng Wendy Pei Qin. Circular Hydrogen Economy and Its Challenges. Chemical Engineering Transactions 2022;94:1273–8. https://doi.org/10.3303/cet2294212.

[54] Nakano K, Inada T, Katayama K, Ujisawa Y, Oboso A. Advanced Technologies for Blast Furnace Life Extension 2020.

[55] Vogl V, Olsson O, Nykvist B. Phasing out the blast furnace to meet global climate targets. Joule 2021;5:2646–62. https://doi.org/10.1016/j.joule.2021.09.007.

[56] IRENA. Potential Green Hydrogen Uses In Industry And Related Barriers. Green hydrogen for industry: A guide to policy making, Abu Dhabi: 2022.

[57] IEA. Energy Technology Perspectives 2020 – Analysis. IEA 2020. https://www.iea.org/reports/energy-technology-perspectives-2020.

[58] IEA. Iron and Steel Technology Roadmap – Analysis. IEA 2020. https://www.iea.org/reports/iron-and-steel-technology-roadmap.

[59] IEA. Net Zero by 2050 – Analysis. IEA 2021. https://www.iea.org/reports/net-zero-by-2050.

[60] Element Energy. Deep Decarbonisation Pathways for UK Industry. Climate Change Committee (CCC) 2020.

[61] Global CCS Institute. What is CCS? n.d.

[62] Bui M, Adjiman CS, Bardow A, Anthony EJ, Boston A, Brown S, et al. Carbon capture and storage (CCS): the way forward. Energy Environ Sci 2018;11:1062–176. https://doi.org/10.1039/c7ee02342a.

[63] UK carbon capture, usage and storage (CCUS). GOVUK 2023. https://www.gov.uk/government/collections/uk-carbon-capture-usage-and-storage-ccus.

[64] Resources for the Future. Carbon Capture and Storage 101 n.d. https://www.rff.org/publications/explainers/carbon-capture-and-storage-101/.

[65] Rezaei S, Liu A, Hovington P. Emerging technologies in post-combustion carbon dioxide capture & removal. Catalysis Today 2023;423:114286. https://doi.org/10.1016/j.cattod.2023.114286.

[66] Working Group III of the Intergovernmental Panel on Climate Change. IPCC Special Report on Carbon Dioxide Capture and Storage. Intergovernmental Panel on Climate Change 2005:443.

[67] Global CCS Institute. Geological Storage of CO2: Safe, Permanent, and Abundant 2018.

[68] The CCUS Hub. Understanding Carbon Capture Use Storage (CCUS) 2021. https://ccushub.ogci.com/ccus-basics/understanding-ccus/.

[69] WorldSteel Association. Carbon capture and storage (CCS) n.d.

[70] Perpiñán J, Peña B, Bailera M, Eveloy V, Kannan P, Raj A, et al. Integration of carbon capture technologies in blast furnace based steel making: A comprehensive and systematic review. Fuel 2023;336:127074. https://doi.org/10.1016/j.fuel.2022.127074.

[71] Gibbins J. Capture overview: Pre-Combustion (Hydrogen) and Oxyfuel 2021.

[72] Calin-Cristian Cormos. Techno-economic and environmental analysis of hydrogen and power co-generation based on co-gasification of coal and biomass / solid wastes with carbon capture. Chemical Engineering Transactions 2014;37:139–44. https://doi.org/10.3303/CET1437024.

[73] Van Der Stel J, Louwerse G, Sert D, Hirsch A, Eklund N, Pettersson M. Top gas recycling blast furnace developments for ‘green’ and sustainable ironmaking. Ironmaking & Steelmaking 2013;40:483–9. https://doi.org/10.1179/0301923313z.000000000221.

[74] Tsupari E, Kärki J, Arasto A, Pisilä E. Post-combustion capture of CO2 at an integrated steel mill – Part II: Economic feasibility. International Journal of Greenhouse Gas Control 2013;16:278–86. https://doi.org/10.1016/j.ijggc.2012.08.017.

[75] Marques L, Monteiro M, Cenci C, Mateus M, Condeço J. Review of Post-Combustion Carbon Capture in Europe: Current Technologies and Future Strategies for Largest CO2-Emitting Industries. Energies 2025;18:3539. https://doi.org/10.3390/en18133539.

[76] Ramírez-Santos ÁA, Castel C, Favre E. A review of gas separation technologies within emission reduction programs in the iron and steel sector: Current application and development perspectives. Separation and Purification Technology 2018;194:425–42. https://doi.org/10.1016/j.seppur.2017.11.063.

[77] Fang M, Zhu D. Chemical Absorption. Handbook of Climate Change Mitigation and Adaptation, New York, NY: Springer New York; 2015, p. 1–109. https://doi.org/10.1007/978-1-4614-6431-0_38-2.

[78] Chowdhury FA, Yamada H, Higashii T, Goto K, Onoda M. CO2 Capture by Tertiary Amine Absorbents: A Performance Comparison Study. Industrial & Engineering Chemistry Research 2013;52:8323–31. https://doi.org/10.1021/ie400825u.

[79] Luis P. Use of monoethanolamine (MEA) for CO2 capture in a global scenario: Consequences and alternatives. Desalination 2016;380:93–9. https://doi.org/10.1016/j.desal.2015.08.004.

[80] Vega F, Cano M, Camino S, Fernández LMG, Portillo E, Navarrete B. Solvents for Carbon Dioxide Capture. Carbon Dioxide Chemistry, Capture and Oil Recovery, InTech; 2018. https://doi.org/10.5772/intechopen.71443.

[81] Stewart MI. Gas Sweetening. Surface Production Operations 2014:433–539. https://doi.org/10.1016/b978-0-12-382207-9.00009-3.

[82] Burr B, Lyddon L. A Comparison of Physical Solvents for Acid Gas Removal n.d.

[83] Adsorption | surface phenomenon | Britannica n.d. https://www.britannica.com/science/adsorption.

[84] Patterson HBW. Adsorption. Bleaching and Purifying Fats and Oils: Theory and Practice 2009:53–67. https://doi.org/10.1016/B978-1-893997-91-2.50008-0.

[85] Hinkov I, Lamari FD, Langlois P, Dicko M, Chilev C, Pentchev I. Carbon dioxide capture by adsorption (review). Journal of Chemical Technology and Metallurgy 2016;51:609–26.

[86] Ben-Mansour R, Habib MA, Bamidele OE, Basha M, Qasem NAA, Peedikakkal A, et al. Carbon capture by physical adsorption: Materials, experimental investigations and numerical modeling and simulations – A review. Applied Energy 2016;161:225–55. https://doi.org/10.1016/j.apenergy.2015.10.011.

[87] Bernardo P, Drioli E, Golemme G. Membrane Gas Separation: A Review/State of the Art. Industrial & Engineering Chemistry Research 2009;48:4638–63. https://doi.org/10.1021/ie8019032.

[88] Pandey P, Chauhan RS. Membranes for gas separation. Progress in Polymer Science 2001;26:853–93. https://doi.org/10.1016/S0079-6700(01)00009-0.

[89] Sanders DF, Smith ZP, Guo R, Robeson LM, McGrath JE, Paul DR, et al. Energy-efficient polymeric gas separation membranes for a sustainable future: A review. Polymer 2013;54:4729–61. https://doi.org/10.1016/j.polymer.2013.05.075.

[90] Spigarelli BP, Kawatra SK. Opportunities and challenges in carbon dioxide capture. Journal of CO2 Utilization 2013;1:69–87. https://doi.org/10.1016/j.jcou.2013.03.002.

[91] Alcántara-Avila JR, Gómez-Castro FI, Gabriel Segovia-Hernández J, Sotowa K-I, Horikawa T. Energy Minimization in Cryogenic Distillation Columns Through Intermediate Side Heat Exchangers. Computer Aided Chemical Engineering 2014;33:1501–6. https://doi.org/10.1016/b978-0-444-63455-9.50085-4.

[92] Mondal MK, Balsora HK, Varshney P. Progress and trends in CO2 capture/separation technologies: A review. Energy 2012;46:431–41. https://doi.org/10.1016/j.energy.2012.08.006.

[93] Meisen A, Shuai X. Research and development issues in CO2 capture. Energy Conversion and Management 1997;38:S37–42. https://doi.org/10.1016/S0196-8904(96)00242-7.

[94] Weisend JG. Cryogenic Technology. Kirk-Othmer Encyclopedia of Chemical Technology, Hoboken, NJ, USA: John Wiley & Sons, Inc.; 2012. https://doi.org/10.1002/0471238961.0318251501071801.a01.pub3.

[95] Kerry FG. Industrial Gas Handbook. Boca Raton: CRC Press; 2007. https://doi.org/10.1201/9781420008265.

[96] Gruenewald M, Radnjanski A. Gas–liquid contactors in liquid absorbent-based PCC. Absorption-Based Post-combustion Capture of Carbon Dioxide, Elsevier; 2016, p. 341–63. https://doi.org/10.1016/b978-0-08-100514-9.00014-7.

[97] Han K, Ahn CK, Lee MS. Performance of an ammonia-based CO2 capture pilot facility in iron and steel industry. International Journal of Greenhouse Gas Control 2014;27:239–46. https://doi.org/10.1016/j.ijggc.2014.05.014.

Chapter 2: Literature Review for Chemical Absorption Carbon Capture

2.1 Literature Review Overview

The decarbonisation of the iron and steel industry represents a critical challenge for achieving global climate targets. Carbon capture has been described as a crucial component in achieving deep carbon emission reductions for this sector [1–3], with chemical absorption identified as the most suitable, mature capture technology to be deployed for this purpose [4]. However, the application of chemical absorption to steelmaking is hindered by unique process emission compositions that differ from those in the power sector, where the technology was originally developed.

Consequently, this chapter provides a comprehensive and critical literature review to understand the complexities surrounding the application of chemical absorption carbon capture to steelmaking process emissions. It begins by examining the fundamental principles of solvent chemistry and process engineering that govern system performance, before analysing the global status of commercial and pilot-scale projects within the steel industry, culminating in the identification of key knowledge gaps and methodologies that form the basis for the research presented in this thesis.

2.1.1 The Chemical Absorption Process

Chemical absorption is a mature and widely applied post-combustion carbon capture technology in which CO_2 from flue gas is selectively removed by reacting with a liquid chemical solvent. The process operates cyclically in two main stages: absorption and desorption. During absorption, the flue gas is contacted with the solvent in a wet scrubbing column at low temperatures, at approximately 40 °C, enabling fast, reversible reactions that capture CO_2. The cleaned flue gas exits the top of the column, typically passing through a water wash to remove solvent carryover before being released to the atmosphere. The CO_2-rich solvent is then sent to a desorption column, also known as a stripper, passing through a cross-heat exchanger to be preheated. In the stripper, the rich solvent is further heated by steam generated in a reboiler to release the captured CO_2, which then exits the top of the column. The CO_2 then passes through a condenser and a reflux drum to remove any entrained water or solvent, before being compressed for transport or utilisation. The regenerated solvent, now CO_2-lean, leaves the reboiler and is passed through the cross-heat exchanger and then returned to the absorber, completing the cycle [5–7]. A simplified process flow diagram of the chemical absorption process is presented in Figure 2.1.

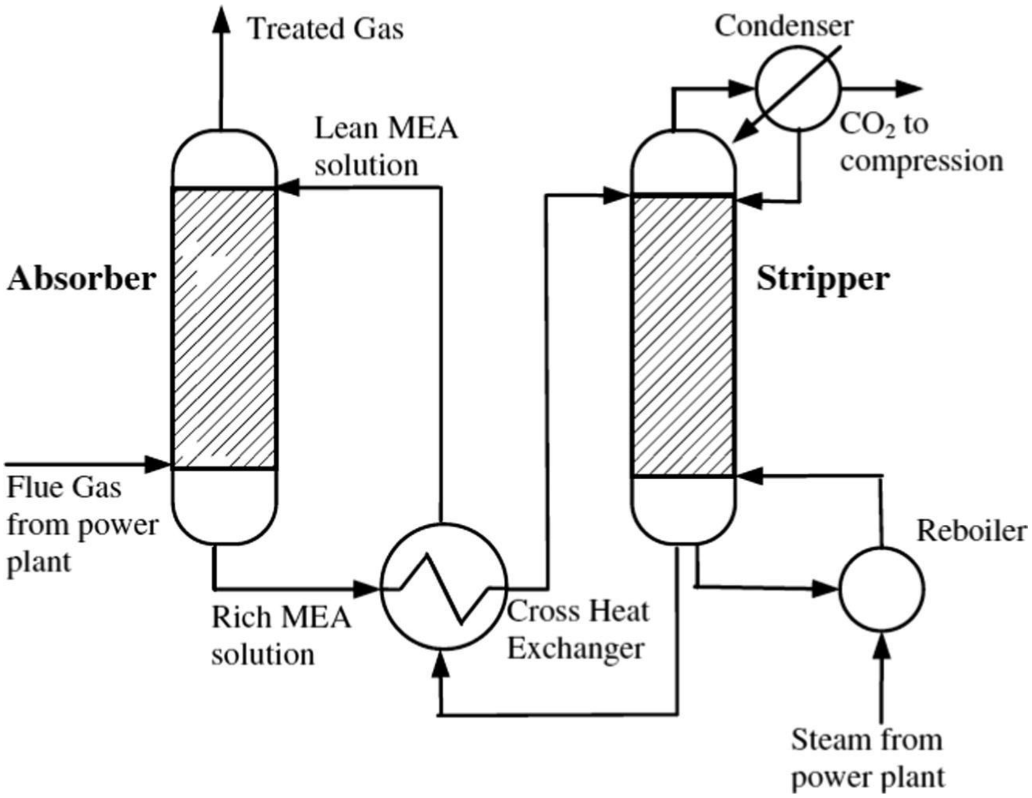

Figure 2.1: Simplified process flow diagram of a chemical absorption process [8].

This reversible reaction pathway enables high capture efficiencies and product purities [9], but also presents operational challenges, including high energy requirements, solvent volatility, corrosiveness, and degradation from the repeated heating and cooling cycles. Optimising process design, solvent management, and operation is therefore essential to achieve effective capture at a minimal cost.

2.1.2 Definitions of Key Performance Indicators

The performance of the chemical absorption process is evaluated using several key indicators, which will be used throughout this thesis and are defined as follows:

- **Specific reboiler duty (SRD):** The primary metric for process energy consumption, representing the energy supplied to the stripper reboiler per unit of CO_2 captured. It is typically expressed in units of either GJ/tonne·CO_2 or MJ/kg·CO_2.
- **Solvent loading:** A dimensionless measure of the amount of CO_2 absorbed into the solvent, defined as the ratio between the moles of CO_2 and the moles of solvent, formally in units of mol·CO_2/mol·MEA. The following solvent loading and capacity terms are also dimensionless with the same unit.
- **Lean loading:** The remaining loading of the solvent after regeneration has taken place. The solvent is referred to as lean solvent.

- **Rich loading:** The final loading of the solvent after CO_2 absorption has taken place. The solvent is referred to as rich solvent.
- **Solvent cyclic capacity:** The effective CO_2 carrying capacity of the solvent per cycle. It is calculated as the difference between the rich and lean loading.
- **Absorption capacity:** The theoretical maximum carrying capacity of a solvent.
- **Solvent regeneration:** The process of desorbing the CO_2 from the solvent, turning a rich solvent lean.
- **Liquid-to-gas (L/G) ratio:** A critical dimensionless operational parameter representing the ratio between the liquid solvent mass flow rate and the mass flow rate of the flue gas entering the absorber.
- **Approach temperature:** The approach temperature refers to the temperature difference between different streams around the cross-heat exchanger. For this thesis, the approach temperature refers solely to the temperature difference between the hot rich solvent and hot lean solvent streams on the stripper side.
- **Capture efficiency:** The percentage amount of CO_2 that is captured from the incoming flue gas stream.

2.1.3 The Energy Penalty from Solvent Regeneration

The high energy requirement for solvent regeneration is the main barrier to the financial viability of chemical absorption [10–12]. To understand and overcome this challenge, it is essential to deconstruct the total regeneration energy into its three fundamental thermodynamic components [13–17]:

- **Sensible heat:** The energy needed to raise the temperature of the entire circulating rich solvent from the absorber exit temperature to the stripper reboiler operating temperature.
- **Heat of vaporisation:** The latent heat demanded to boil the water from the aqueous solvent to generate the stripping steam to drive the desorption reaction.
- **Heat of desorption:** The energy required to overcome the reaction enthalpy and break the chemical bonds between the CO_2 and the solvent. It is an intrinsic part of the solvent's chemistry.

The vast landscape of research and development aimed at improving the energy efficiency of chemical absorption can be categorised based on which energy component is primarily targeted. This reveals a clear bifurcation of research efforts into two principal, yet increasingly interconnected, pillars of research.

The first pillar is solvent-centric, where innovations in solvent development primarily seek to reduce the heat of desorption. The second pillar is process-centric, where advances in process optimisation, configuration, and intensification are designed to minimise the process-dependent sensible heat and vaporisation duties. This review first provides a structured analysis of these two foundational pillars.

2.2 The Absorbent: Chemistry, Kinetics, and Selection

The performance, cost, and environmental impact of a chemical absorption process are fundamentally governed by the choice of solvent. To understand the challenges surrounding solvent selection, this section first outlines the characteristics of an ideal absorbent and examines the fundamental process chemistry and kinetics of amine-based capture. Subsequently, the discussion addresses the barriers associated with traditional solvents, leading to a review of recent developments in novel solvent technologies to overcome these limitations.

2.2.1 Solvent Characteristics for Chemical Absorption

The choice of solvent is central to the performance and economics of chemical absorption carbon capture. No single solvent possesses all ideal properties, and compromises must be made. Therefore, selection and development efforts focus on balancing reactivity, energy efficiency, stability, and environmental considerations to suit specific process conditions. The following key characteristics, summarised from the open literature [4,12,18–24], represent the primary criteria for assessing and comparing solvents:

- **High reactivity with CO_2:** A solvent's reaction kinetics with CO_2 is a critical factor that influences the size of the equipment and, consequently, the overall cost of the capture process. Solvents with faster reaction rates can reduce the required size of the absorber and stripper columns, leading to lower capital and operational expenses.
- **Low regeneration energy demand:** Minimising the energy required for solvent regeneration is critical for reducing the overall energy penalty of capture. Solvents with lower heats of absorption are generally preferred, provided they do not compromise reaction rates.
- **High CO_2 absorption capacity:** A solvent's capacity to absorb CO_2 directly impacts the efficiency and cost of the process. A higher capacity reduces the solvent needing to be circulated to capture the same amount of CO_2, which also reduces pumping and heating costs.
- **High thermal and oxidative stability:** Solvents can degrade under the high temperatures of the stripper, and in the presence of oxygen in the flue gas. Degradation products reduce capture efficiency and can be hazardous, posing operational issues and significant solvent make-up costs. Therefore, high stability is crucial for a viable solvent.
- **Low volatility and minimal corrosiveness:** Volatility leads to the loss of solvent to the atmosphere, while high corrosiveness damages plant equipment, increasing maintenance and capital costs.

- **Low foaming tendency and favourable viscosity:** Low viscosity ensures good mass transfer of CO_2 into the solvent and reduces pumping energy requirements, while resistance to foaming prevents operational disruptions in the absorber.
- **Low environmental impact, low toxicity, and low production cost:** Sustainable solvents should minimise toxicity, flammability, and environmental hazards, creating a safer working environment for operation, while also being inexpensive to produce and handle.
- **Tolerance to flue gas impurities:** Flue gases can contain impurities such as sulphur dioxides, nitrogen oxides, and metal particulates. These components can react irreversibly with solvents, causing degradation and forming heat-stable salts that reduce the efficiency of the solvent. An ideal solvent should be able to maintain performance in the presence of these impurities.

If a new solvent can be developed that sees universal improvements across all characteristics, it will quickly become the replacement solvent of choice for chemical absorption. Until then, amine-based solvents will continue to be the most commonly used absorbents in chemical absorption for the capture of CO_2, with MEA being the primary choice due to its maturity and commercialisation [4,25], with many studies focused on process optimisation of MEA-based capture systems [26].

MEA is non-toxic, relatively inexpensive, and has high reactivity, making it ideal for use in chemical absorption. However, MEA suffers from high energy consumption, with chemical and thermal stability issues causing solvent degradation [27–29]. Despite this, MEA is typically used as the benchmark solvent for research and development. For the application of MEA in the clean-up of BFG, separation costs have been estimated as \$71.7/tonne·CO_2 for MEA absorption of BFG with 30-40% CO_2, with an energy consumption in the order of 4 GJ/ tonne·CO_2 [4]. The following section explores process chemistry of MEA and other amine-based solvents that are traditionally used.

2.2.2 Process Chemistry for Conventional Alkanolamine Solvents

Alkanolamines are categorised into three classes based on their amine functional group: primary amines, such as MEA, secondary amines, such as diethanolamine (DEA), and tertiary amines, such as methyldiethanolamine (MDEA). These solvents represent the first generation of chemical solvents investigated for flue gas treatment [30]. They are regenerable, possess high CO_2 absorption capacity, provide good CO_2 selectivity for high purity streams, and exhibit fast kinetics that make them suitable for low CO_2 partial pressures. However, the reaction kinetics, heats of reaction, and corrosivity vary significantly across amine classes.

In general, the CO_2-amine reactivity follows a decreasing trend from primary to tertiary amines, which correlates with reduced regeneration energy requirements but also lower absorption rates [31]. Primary amines are the most reactive but also exhibit the highest heat of reaction and strongest corrosivity. These properties diminish progressively in secondary and tertiary amines [4]. Primary and secondary amines react with CO_2 to form carbamates [32], which have strong CO_2-amine bonds that require high energy input for solvent regeneration [33]. The typical heats of reaction for primary amines and secondary amines range from 80 to 90 kJ/mol·CO_2 and 70 to 75 kJ/mol·CO_2, respectively [34]. Tertiary amines instead hydrolyse the CO_2 to form bicarbonates [33,35], which have a reduced heat of reaction compared to primary and secondary amines, ranging from 40 to 55 kJ/mol·CO_2 [34]. The stoichiometric loading capacity of primary and secondary amines is limited to 0.5 mol·CO_2/mol·amine, while tertiary amines can achieve 1.0 mol·CO_2/mol·amine [36,37].

2.2.2.1 Reaction Pathways for Primary Amines

The process chemistry of CO_2 capture by primary alkanolamines can be divided into several steps, which are outlined below [7,38–40]:

The ionisation of water:

$$H_2O \leftrightarrow H^+ + OH^- \tag{2.1}$$

Hydrolysis of dissolved CO_2 to carbonic acid:

$$CO_2 + H_2O \leftrightarrow HCO_3^- + H^+ \tag{2.2}$$

Bicarbonate formation:

$$CO_2 + OH^- \leftrightarrow HCO_3^- \tag{2.3}$$

Bicarbonate dissociation:

$$HCO_3^- + H_2O \leftrightarrow CO_3^{2-} + H_3O^+ \tag{2.4}$$

Carbamate formation:

$$CO_2 + RNH_2 \leftrightarrow RNHCOO^- + H^+ \tag{2.5}$$

Carbamate reversion by hydrolysis:

$$RNHCOO^- + H_2O \leftrightarrow RNH_2 + HCO_3^- \tag{2.6}$$

Protonation of primary alkanolamines:

$$RNH_2 + H_3O^+ \leftrightarrow RNH_3^+ + H_2O \tag{2.7}$$

Overall balanced reaction for CO_2 capture by primary alkanolamines:

$$2RNH_2 + CO_2 \leftrightarrow RNH_3^+ + RNHCOO^- \tag{2.8}$$

The kinetics of the above reaction pathway are discussed in the following subsection.

2.2.2.2 *Kinetics of Alkanolamines with CO_2*

Three principal reaction mechanisms describe the reaction of CO_2 with alkanolamines [39]: the zwitterion mechanism [41], the termolecular mechanism [42], and the base-catalysed hydration mechanism [43]. The zwitterion and termolecular mechanisms are widely used to describe CO_2 absorption by primary and secondary amines, while the base-catalysed hydration mechanism is specific to tertiary amines [39].

This work is primarily concerned with the reaction between CO_2 and MEA, which proceeds via either the zwitterion or termolecular mechanism, both of which are discussed below. As MEA does not react via the base-catalysed hydration pathway, this mechanism is not considered further. Comprehensive discussions of this mechanism and the broader kinetics of CO_2-alkanolamine systems are available in Vaidya and Kenig [33].

The Zwitterion Mechanism

Originally proposed by Caplow [41] and then reintroduced by Danckwerts [44], this two-step mechanism suggests that the reaction between CO_2 and the amine (denoted as AmH) forms a zwitterion as an intermediate [33]:

$$\mathrm{AmH} + \mathrm{CO_2} \underset{k_{-1}}{\overset{k_1}{\leftrightharpoons}} \mathrm{AmH^+COO^-}\ \text{(zwitterion)} \tag{2.9}$$

The zwitterion is subsequently deprotonated with a base (denoted here as B), which can be another amine molecule, water, or hydroxide ion, to form carbamate:

$$\mathrm{B} + \mathrm{AmH^+COO^-} \overset{k_B}{\rightarrow} \mathrm{AmCOO^-}\ \text{(carbamate)} + \mathrm{BH^+} \tag{2.10}$$

Assuming steady state conditions for the zwitterion, the overall rate expression is:

$$r = \frac{k_1[\mathrm{CO_2}][\mathrm{AmH}]}{1 + \frac{k_{-1}}{k_B[\mathrm{B}]}} \tag{2.11}$$

Including parallel reactions with water and hydroxide from reactions (2.2) and (2.3), the total CO_2 consumption rate is:

$$r_{\mathrm{overall}} = \left[\frac{k_1[\mathrm{CO_2}][\mathrm{AmH}]}{1 + \frac{k_{-1}}{k_B[\mathrm{B}]}}\right] + \left[k_{\mathrm{H_2O}}[\mathrm{CO_2}][\mathrm{H_2O}] + k_{\mathrm{OH^-}}[\mathrm{CO_2}][\mathrm{OH^-}]\right] \tag{2.12}$$

When the rate of reaction is defined with respect to CO_2, the rate constant is derived as:

$$r_{\mathrm{CO_2}} = k_{\mathrm{CO_2}}[\mathrm{CO_2}] \tag{2.13}$$

Where:

$$k_{\mathrm{CO_2}} = \left[\frac{k_1[\mathrm{AmH}]}{1 + \frac{k_{-1}}{k_B[\mathrm{B}]}}\right] + \left[k_{\mathrm{H_2O}}[\mathrm{H_2O}] + k_{\mathrm{OH^-}}[\mathrm{OH^-}]\right] \tag{2.14}$$

Experimental studies in the open literature indicate that the zwitterion mechanism provides an accurate description of the reaction kinetics between MEA and CO_2 [45–47], widely regarded as the preferred model [38].

The Termolecular Mechanism

Originally proposed by Crooks and Donnellan [42] and later revisited by da Silva and Svendsen [48], this single step mechanism assumes a simultaneous reaction of CO_2, amine, and a base. The reaction proceeds via a loosely bound encounter complex as the intermediate [33], represented as:

$$CO_2 + AmH \cdots B \leftrightharpoons AmCOO^- \cdots BH^+ \qquad \textbf{(2.15)}$$

The complex can dissociate back to the original reactants, CO_2 and amine, although a small fraction reacts with a second water or amine molecule to produce ionic products. The rate constant for this mechanism is given by:

$$k_{CO_2} = \left[k_{H_2O}[H_2O] + k_{OH^-}[OH^-] + k_{AmH}[AmH]\right] \cdot [AmH] \qquad \textbf{(2.16)}$$

While this model can also fit experimental data, the zwitterion is generally preferred for primary amines due to stronger empirical support [38]. Irrespective of the mechanism used, formation of a carbamate and a protonated base are widely accepted as the products of CO_2-amine reactions [49].

While the reaction pathways described above are focused on the ideal chemistry and kinetics governing CO_2 absorption, in practice these solvents are subjected to harsh process conditions that can promote undesirable side reactions, causing irreversible degradation of the solvent and other consequences. The following section details the mechanisms and challenges surrounding solvent degradation.

2.2.3 Solvent Degradation: Mechanisms and Consequences

Solvent degradation refers to the irreversible chemical decomposition of the active solvent, which leads to a permanent loss of capture capacity and decrease in system performance. It is a major operational issue, estimated to be responsible for approximately 10% of the total cost of capture, owing to the continuous solvent make-up and management of problems such as fouling, foaming, and corrosion [23,50]. Degradation is broadly classified into three primary mechanisms: thermal degradation, oxidative degradation, and the formation of heat-stable-salts (HSS).

2.2.3.1 Thermal Degradation

Thermal degradation occurs in the highest temperature sections of the capture plant, primarily in the stripper and reboiler [6]. The process occurs in the presence of CO_2, where the prevalent formation mechanism for primary and secondary alkanolamines is the polymerisation of carbamates [23]. When carbamate is formed, the high stripping temperatures lead to the formation of oxazolidinones as a degradation product through the carbamate ring closure reaction. This compound is highly reactive and can react further with the amines to produce dimers, which go on to produce a variety of other degradation products [51]. The most important parameters to affect the thermal degradation rate have been identified as: temperature, solvent CO_2 loading, and solvent concentration [52]. Akram et al. [6]

reported that a third of thermal degradation occurs in the stripper where CO_2 loading is highest, with the rest occurring in the reboiler where the temperature is highest.

Zoannou et al. [52] found that thermal degradation at a temperature of 160 °C for eight weeks reduced the MEA concentration by 95%, with an earlier study by Davis [53] reporting a reduction of 65% at a temperature of 150 °C for the same time period. In practice, thermal degradation is a slow process at typical operating temperatures [52], where the impact can be significantly reduced if the reboiler temperature is held below 110 °C [54]. The degradation rate of MEA has been shown to quadruple every 17 °C or each time the stripper pressure is doubled [54], but significant degradation does not occur until around 130 °C [6,55]. The thermal degradation rate of MEA has been reported as varying between 2.5 and 6% per week at 135 °C [54].

2.2.3.2 Oxidative Degradation

Oxidative degradation occurs in the presence of O_2, primarily in the absorber where the solvent is in direct contact with oxygen-containing flue gas. Two main formation mechanisms, electron abstraction and hydrogen abstraction, have been proposed as formation pathways for degradation compounds [23]. While carboxylic acids have been identified as the most common degradation products from oxidative degradation in the presence of alkanolamines, MEA specifically degrades by electron abstraction to form aldehyde compounds and ammonia [23]. A review by Gouedard et al. [56] discussed the main oxidative and thermal degradation products for MEA and other solvents, noting that detailed reaction mechanisms are incomplete for some products. This has led to limitations in oxidative degradation modelling studies by authors such as Dickinson et al. [57], but various other studies have sought to address these knowledge gaps [58–62].

A study by Chi and Rochelle [60] directly investigated the oxidative degradation of MEA, which highlighted the influence of higher solvent CO_2 loading and iron content on increasing degradation rate. For 30 wt.% MEA solvent, the required solvent makeup rate was 0.68 kg/tonne CO_2, with a degradation rate of 7.4 mM/h noted. However, studies have shown that the degradation mechanisms, kinetics, and extent of degradation can vary between pilot plant studies and controlled lab conditions [63]. This is most likely the result of flue gas contaminants and industrial influences impacting the reaction pathways. The degradation of MEA has been shown to be dominated by oxidative degradation over thermal degradation in an industrial environment [63,64], owing to typical process operation conditions.

2.2.3.3 Heat-Stable-Salts

A major and detrimental consequence of both solvent degradation and the presence of flue gas impurities is the formation of HSS, formed from the reaction of the basic alkanolamine with strong acids [65]. These acids can be introduced via the flue gas, such as SO_x, NO_x, and HCl, or generated in situ as byproducts from oxidative degradation, such as formic and acetic acid [23,56,65]. A key characteristic of the HSS is that they have a high thermal stability, they do not break down or decompose during the solvent regeneration process, leading to accumulation in the system [66]. The HSS cannot easily be removed from the solvent and consequently reduce the CO_2 absorption capacity [67]. Furthermore, the presence of HSS increases the viscosity of the solvent, promotes foaming, and is a primary contributor to increased corrosion rates [50,66]. Consequently, management of HSS levels is a critical aspect of plant operation, with their removal centred around solvent reclamation, which separates the solvent from the HSS [68,69].

2.2.3.4 Pilot-Scale Degradation Studies

Large-scale testing of MEA degradation has been studied at the Technology Centre Mongstad (TCM) [70], where thermal and oxidative degradation was monitored, alongside HSS formation and nitrosamine production. Over 1960 hours of operation, solvent loss was 1.6 ± 0.1 kg·MEA/tonne·CO_2 captured, with 67% of this through ammonia emissions, 16% from identified degradation products, with the remainder attributed to mechanical losses. The study monitored the accumulation of major HSS, which included an unknown component, showing how concentrations steadily increased before reclamation took place. Degradation product formation was described as a function of temperature, solvent loading, and MEA concentration, and a simplified reaction pathway was proposed to describe these transformations.

An 18-month campaign was conducted on the post combustion capture plant in the Niederaussem power plant, using 30 wt.% MEA [71]. When the degradation process remained stable, solvent loss was less than 0.3 kg·MEA/tonne·CO_2. Very low MEA emissions were reported, which contributed to the overall low solvent loss in the study. The concentration of thermal degradation products remained low, at approximately 1 g/l after 8000 operating hours. The main oxidative degradation product was noted to be acetate, at approximately five times the amount of formate produced. This is an inversion of what was seen at the TCM, where five times more formate than acetate was reported [70]. Moser et al. theorised that trace flue gas components or organic reaction products may be acting as catalysts, leading to complex oxidative degradation pathways that preferentially produce acetate over formate [71]. They concluded that further investigation is needed to identify these dependencies and develop a more detailed understanding of the oxidative mechanisms.

Neerup et al. [72] provided a comprehensive summary of solvent degradation and emissions studies measured on pilot plants around the world. The summary included conventional alkanolamine solvents in addition to proprietary and novel solvents, documenting the measured degradation products where possible. Other studies have modelled large scale CO_2 capture units to assess solvent degradation [73,74].

2.2.3.5 Corrosion

Chemical absorption capture plants are notoriously susceptible to corrosion, which compromises equipment integrity, increases maintenance costs, and contributes to solvent degradation. Wang et al. [12] and Fleury et al. [75] summarised factors that influence corrosion rates, which includes: solvent CO_2 loading, solvent type and concentration, temperature, solvent recirculation rate and turbulence, and the presence of degradation products. MEA has been identified as one of the most corrosive solvents when compared with secondary and tertiary amines, with corrosion reducing in the order of MEA > DEA > MDEA [12].

The pathway for system corrosion is cyclical and self-reinforcing, which affects the energy penalty for capture. Both oxidative and thermal degradation pathways contribute to the production of corrosive HSS. The corrosion of plant equipment releases metal ions into the solvent, which in turn act as powerful catalysts for further oxidative degradation. The accumulation of these degradation products reduces the solvent’s absorption capacity, which forces the plant to circulate more solvent to achieve the same capture efficiency, which increases the regeneration energy requirements and worsens the overall energy penalty. This vicious cycle demonstrates how degradation, corrosion, and energy are inextricably linked, proving a challenge for capture operations to address.

This pathway was explicitly documented by Moser et al. [71] during their 18-month campaign. The solvent recirculation rate was slowly increased from 4000 kg/h to 6000 kg/h to maintain 90% capture efficiency as degradation products accumulated. They noted how the degradation products increased in a non-linear fashion, demonstrating how a runaway degradation cycle can occur in capture systems. To address the solvent contamination, two management strategies were employed: a solvent purge, where a portion of the contaminated solvent was removed and replaced with fresh solvent, was used twice during the campaign, followed by solvent reclamation, which was used towards the end of the campaign [71].

In an ideal operating environment, thermal and oxidative degradation would be negligible, with minimal acid content in the flue gas, which would prevent the production of corrosive HSS. However, the solvent itself is still typically corrosive, such as MEA, meaning that corrosion is difficult to eliminate entirely. Mitigation strategies to reduce this corrosion involves the use of alternative, less corrosive solvents, building the plant with corrosive resistant materials, and using corrosion inhibitors as additions to the solvent [76].

2.2.3.6 Environmental and Health Concerns

An additional concern surrounding the use of chemical absorption carbon capture is the emission of the solvent and degradation products to the atmosphere. These compounds may be present in the treated flue gas that exits the absorber column due to their high volatility [23]. Mitigation strategies to prevent the release of these emissions include washing treatments with either water or aqueous solutions, UV radiation, and thermal decomposition of nitro-compounds [23,77,78].

If released to the atmosphere, alkanolamines and degradation products can react with NO_x via photo-oxidation to form nitrosamines, nitramines, and nitramides [23]. Many of these compounds are known or suspected carcinogens, raising significant public health concerns about the deployment of chemical absorption plants near populated areas [79,80]. The formation, fate, and transport of these compounds are areas of active research and regulatory scrutiny.

2.2.3.7 The Case for Novel Solvents

The operational viability of chemical absorption is significantly impacted by a series of interconnected degradation challenges inherent to conventional alkanolamines. The mechanisms of thermal and oxidative degradation lead to the irreversible loss of active solvent and the formation of corrosive HSS. This triggers a cyclical cascade of equipment corrosion and further degradation, increasing operational costs from solvent make-up and equipment maintenance. Furthermore, emissions of volatile solvent components with the potential to form hazardous atmospheric byproducts such as nitrosamines pose significant environmental and health concerns. These profound drawbacks have established an urgent need for novel solvent developments to mitigate these challenges, which are discussed in the next section.

2.2.4 Solvent Developments

Having identified the need for novel solvent developments in the preceding section, the following subsections discuss several novel and alternative solvent types, and their application in post-combustion capture.

2.2.4.1 Functionalised Solvents

Functionalised solvents were first proposed by Sartori et al. [81,82], as alternatives to conventional alkanolamines. These solvents incorporate additional functional groups to their structure to alter their chemical behaviour, and act as sterically hindered amines. Consequently, the energy of regeneration is decreased, with significant impact on the absorption rate. Examples of sterically hindered amines include 2-amino-2-methyl-1-propanol (AMP), 2-piperidine ethanol (PE), and 1-8-p-menthanediamine (MDA) [81].

A prominent example is the proprietary solvent KS-1™, developed by Mitsubishi Heavy Industries (MHI) for its KM CDR Process™ [83]. Compared to MEA, KS-1™ offered lower corrosivity, higher stability, and high CO_2 loading. Subsequent research into a successor solvent demonstrated superior performance in terms of steam consumption, solvent degradation, and emissions, which outweighed a slight increase in electricity cost [84]. This development led to the new solvent KS-21™, which was tested at the TCM in 2021, where a capture efficiency between 95 and 98% was reported for flue gas from a gas turbine [85]. Under modified operating conditions, the KS-21™ solvent achieved an industry-leading capture efficiency of 99.8% and demonstrated CO_2 capture from flue gases with a CO_2 concentration lower than the atmosphere [85].

2.2.4.2 Solvent Blends

Amine blends, which combine different amine solvents to leverage and hybridise the complementary properties of each component, have also been investigated [31,86]. This practice is often referred to as "promoting" a solvent. For example, the absorption performance of slower-reacting tertiary amines can be enhanced by blending them with faster-reacting primary or secondary amines. MEA, DEA, and Piperazine (PZ), have all been used as promoters for solvents such as MDEA and AMP [87–90].

2.2.4.3 Phase Change Solvents

Phase change solvents are mixtures that undergo phase separation upon a change in process conditions, such as the absorption of CO_2 or a subsequent temperature increase [91]. This allows the CO_2-lean phase to be separated from the CO_2-rich phase via a non-thermal mechanical process [91]. As only the concentrated CO_2-rich phase undergoes thermal regeneration, this approach reduces the mass of solvent regenerated, substantially reducing energy consumption and equipment costs [92–94]

These solvents typically involve liquid-liquid or liquid-solid phase separation. While liquid-solid systems present significant technical challenges, liquid-liquid phase separation can be readily integrated into the capture process [91,95]. Various types have been developed, including mixed amine solvents, lipophilic-amine-based thermomorphic biphasic solvents, the DMX™ solvent, alkanolamine/ionic liquid emulsions, phase change amino acid salt solvents, and more [95]. A review by Zhang et al. [94] highlights the potential of aqueous and thermomorphic biphasic solvents, with solvents like DMX-1 approaching a target regeneration energy of 2 $GJ/tonne{\cdot}CO_2$ [91,94]. The DMX™ process has been tested with BFG, achieving capture costs competitive with MEA [28]. However, the fundamental theoretical and mechanistic principles of phase-change phenomena require further elucidation, alongside continued pilot plant testing [95].

2.2.4.4 *Water-Lean Solvents*

Water-lean solvents are formulated to retain the chemical selectivity of aqueous solvents while improving thermodynamic efficiency due to a lower heat requirement for regeneration [96]. These solvents consist of amines and organic diluents, with minimal water content [97]. Heldebrant et al. [98] noted that water-lean solvents can potentially reduce reboiler duties and exhibit high mass transfer rates, although this benefit is often offset by an increased solvent viscosity, presenting a key process engineering compromise.

Zheng et al. [99] evaluated a water-lean solvent, 2-EEMPA, and reported a potential regeneration energy demand of 2 GJ/tonne·CO_2 at a cost of $50.6/tonne·$CO_2$, with further cost reductions anticipated through process optimisation. However, Yuan and Rochelle [100] argued that water-lean solvents may not necessarily offer lower energy consumption than advanced aqueous amines. They highlighted that second-generation aqueous amines like KS-1™, DC103, and Piperazine achieve competitive regeneration energies in the range of 2.1-2.4 GJ/tonne·CO_2, and that advanced stripper configurations can mitigate water vapour losses as effectively as water-lean systems.

2.2.4.5 *Ammonia*

Aqueous ammonia processes represent another alternative to amines, as reviewed by Shakerian et al. [101] and Molina and Bouallou [102]. Studies have indicated that CO_2 capture efficiencies above 95% are possible when using ammonia [103]. Ammonia offers several advantages over MEA, including a higher absorption capacity, lower regeneration energy, negligible thermal degradation, lower corrosivity, high chemical stability, and lower cost [104]. While the technical feasibility of ammonia-based capture is established, several process challenges remain [104]. The chemical mechanisms are not fully understood, complicating process simulation and optimisation. Furthermore, ammonia volatility is a significant operational challenge due to potential ammonia slip, which can breach emissions limits and poses safety risks.

Ammonia is particularly suited for treating steelmaking emissions, as its regeneration temperature can be met using low-grade waste heat from the steelworks. Kim et al. [105] demonstrated in laboratory tests that for BFG treatment, ammonia concentrations above 5 wt.% achieved capture efficiencies comparable to MEA at regeneration temperatures of 86 °C or lower. Rhee et al. [106] later tested the process on a pilot facility at POSCO using real BFG with ammonia concentrations of 5, 7 and 9 wt.%, achieving regeneration temperatures of 87, 83, and 78 °C, respectively. CO_2 capture efficiencies exceeded 90% in all cases. They concluded that the technology is promising for this application, though further work on energy consumption and ammonia slip is needed. Subsequent work demonstrated 90% capture efficiency at over 98% purity, with a projected cost of $20/tonne·$CO_2$ assuming waste heat utilisation [107].

2.2.4.6 Summary of Solvent Selection

Overall, the regeneration energy demand remains the principal drawback of chemical absorption, presenting a multifaceted challenge. Traditional alkanolamines like MEA achieve the high absorption rates required for stringent CO_2 recovery targets, which is why they remain a benchmark for capture plants, despite being disadvantaged by high heats of absorption. This high heat of absorption can primarily be addressed through the utilisation of alternative solvents. Promoted solvents, such as MDEA with PZ, can achieve competitive absorption rates to MEA but introduce their own operational challenges.

Some in-development solvents suffer from several issues, such as chemical slippage as is the case for ammonia, or a lack of research and conflicting data like with water-lean solvents. Proprietary solvents such as KS-21™ and DMX™ show significant potential; however, publicly available performance data is limited, posing a challenge for independent academic assessment.

Compared to studies on coal or natural gas, literature on chemical absorption for BFG and other steelmaking emissions is sparse, consisting mainly of simulation and lab studies with limited pilot-scale campaigns. A clear research gap exists in pilot-scale testing to validate how the performance of MEA compares to proprietary solvents, particularly regarding energy demand.

In the absence of a commercially available, non-proprietary solvent that demonstrates superior performance to MEA without its associated drawbacks, research focus has also been directed towards process optimisation and intensification. These strategies to reduce the sensible heat and heat of vaporisation through advanced engineering techniques and are the focus of discussion in the following section.

2.3 The Process: Optimisation, Configuration, and Intensification

This section explores engineering approaches to reducing the energy penalty of chemical absorption, moving from process optimisation to fundamental process redesign and process intensification (PI). The discussion commences by examining the use of column temperature profiles to fine-tune the performance of fixed capture plant configurations. It then transitions to a review of advanced structural configurations that improve on conventional designs, before concluding with an assessment of emerging PI technologies.

2.3.1 Process Optimisation Through Column Temperature Profiles

The performance of chemical absorption capture systems is largely governed by the operation of the absorber and stripper columns. While a comprehensive understanding of column performance requires detailed knowledge of liquid and gas phase composition profiles along the packing height [108], obtaining such data during plant operation is often impractical. Composition analysis typically requires complex, slow, and expensive instrumentation that is not suited for continuous operational feedback. Temperature profiles, by contrast, offer a simple, robust, and continuous alternative for process monitoring.

Arrays of temperature sensors, such as Resistance Temperature Detectors (RTDs), can generate a real-time thermal map of the columns, providing indirect insight into column performance. The exothermic nature of CO_2 absorption and the endothermic nature of its desorption mean that temperature variations are intrinsically linked to the rate and location of the mass transfer processes. Consequently, temperature profiles can serve as effective tools for process optimisation, acting as a proxy for overall system performance.

Crucially, the temperature also governs the equilibrium behaviour of the system, where the equilibrium partial pressure of CO_2 above the solvent is a function of both temperature and solvent loading:

$$P_{\mathrm{CO_2,eq}} = f(\lambda, T_{\mathrm{sol}}) \tag{2.17}$$

Where:

$P_{\mathrm{CO_2,eq}}$ = equilibrium partial pressure of CO_2 (Pa)

λ = amount of CO_2 loading in the solvent (mol·CO_2/mol·MEA)

T_{sol} = temperature of the solvent (°C)

The driving force for mass transfer is the absolute difference between the equilibrium partial pressure of CO_2 and the actual gas partial pressure of CO_2.

$$\text{Driving Force} = \left|P_{\mathrm{CO_2,eq}} - P_{\mathrm{CO_2,gas}}\right| \tag{2.18}$$

Where:

$P_{\mathrm{CO_2,gas}}$ = actual partial pressure of the gas phase (Pa)

Absorption occurs when the gas partial pressure of CO_2 is higher than the equilibrium pressure:

$$P_{\mathrm{CO_2,gas}} > P_{\mathrm{CO_2,eq}} \tag{2.19}$$

The absorber is relatively cold compared to the stripper, giving it a low equilibrium pressure, meaning that the gas partial pressure dominates and causes the CO_2 to move from the gas phase into the liquid phase. As temperature increases, the equilibrium pressure also increases, reducing the driving force and making absorption less favourable.

Desorption occurs when the equilibrium pressure of CO_2 is higher than the gas partial pressure:

$$P_{\mathrm{CO_2,eq}} > P_{\mathrm{CO_2,gas}} \tag{2.20}$$

The stripper is hot compared to the absorber, which raises the equilibrium pressure, meaning that the equilibrium pressure dominates and causes the CO_2 to move from the liquid phase into the gas phase. As temperature increases, equilibrium pressure also increases, which increases the driving force and makes desorption more favourable.

The driving force will reduce to zero and no net absorption or desorption occurs if the equilibrium pressure is the same as the gas partial pressure:

$$P_{\mathrm{CO_2,eq}} = P_{\mathrm{CO_2,gas}} \tag{2.21}$$

The shape of a column temperature profile is directly determined by where the mass transfer is occurring. A region of rapid CO_2 absorption creates significant exothermic heat, leading to a localised temperature increase. This creates a feedback mechanism that governs the principle of CO_2 capture via chemical absorption: absorption generates heat, which raises the temperature, which in turn affects the local equilibrium and reaction kinetics, thereby influencing the subsequent rate of absorption. Consequently, a temperature profile can be mapped along the length of the columns to characterise the absorption process. Therefore, these profiles serve as an invaluable and readily available representation of the more complex composition and mass transfer rate profiles. Correct interpretation of these profiles allows for analysis of the operational states of the system, identification of system limitations, and the implementation of targeted optimisation strategies.

2.3.2 Absorber Operational Pinches

To understand how the absorber temperature profile relates to absorber efficiency, it is essential to first define the concept of a mass transfer “pinch”. As explained by Weiland et al. [108], a pinch occurs at a specific location in a column where the driving force for mass transfer approaches zero, meaning no further mass transfer can take place in that region. This is a critical concept, explaining why adding more packing height or improving mass transfer coefficients in the pinched region will yield no appreciable improvement in overall performance [109]. The location of this pinch determines the operational mode of the column and is dictated by the solvent flow and the corresponding L/G ratio. The different operational modes are outlined in the following subsections.

2.3.2.1 Lean-Pinched Operation

Lean-pinched operation occurs at high L/G ratios, where the mass flow rate of the solvent is high relative to the mass flow of flue gas [110]. In this mode, the solvent has an available cyclic capacity greatly exceeding the amount of CO_2 needing to be removed, meaning the solvent becomes only partially loaded. The pinch occurs at lean end of the process from the gas perspective, at the top of the column, where the driving force for absorption diminishes to zero as the treated gas becomes clean with a minimal partial pressure of CO_2. In simple terms, a lean pinch occurs when the gas is nearly CO_2 free and the solvent remains lean.

The temperature profile of a lean-pinched absorber is distinctive. The high solvent flow rate pushes the primary reaction region towards the bottom of the column, where the driving force for absorption is highest. As heat is released from the absorption reaction, a characteristic temperature bulge develops near the bottom of the absorber, indicative of the highest absorption occurring [110]. The magnitude of this bulge is often suppressed compared to the other operating regimes because the high solvent flow prevents a significant temperature buildup [111]. This mode of operation is typical for applications requiring deep CO_2 removal in excess of 90% capture efficiency, such as in liquefied natural gas production [109,112,113].

2.3.2.2 Rich-Pinched Operation

Rich-pinched operation occurs at low L/G ratios, where the mass flow rate of the solvent is low relative to the mass flow of the flue gas [110]. In this mode, the solvent has an available cyclic capacity approximating the amount of CO_2 needing to be removed, meaning that the solvent becomes fully loaded. The pinch occurs at the rich end of the process from the gas perspective, at the bottom of the column, where the driving force for absorption diminishes to zero as the solvent approaches maximum saturation. In simple terms, a rich pinch occurs when the gas is still CO_2 rich while the solvent is already fully loaded.

The corresponding temperature profile of a rich-pinched absorber is the inverse of the lean-pinched case. The low solvent flow rate leads to the primary reaction region with the highest driving force occurring towards the top of the column. The heat released from the absorption reaction causes a characteristic temperature bulge to develop near the top of the absorber [110]. This mode of operation is typical for bulk CO_2 removal applications such as post-combustion capture, where the aim is to achieve a specific capture efficiency with a saturated solvent flow [109,112].

2.3.2.3 Bulge-Pinched Operation

Between the well-defined lean-pinched and rich-pinched regimes lies a transitional state known as bulge-pinched operation [109,111]. This mode occurs at intermediate L/G ratios and is characterised by the mass transfer pinch occurring in the middle of the column, coinciding with the location of the maximum temperature bulge. This condition is highly detrimental to the performance and energy efficiency of the entire capture system [112]. In bulge-pinched operation, the middle of the absorber becomes excessively hot. This increases the equilibrium pressure of the CO_2, severely reducing the driving force for mass transfer, confining effective absorption to the colder top and bottom sections of the absorber where a driving force still exists [109,111].

This inefficiency in the absorber has system-wide consequences. In order to achieve the target capture efficiency with a significant part of the absorber being ineffective, the system must compensate by increasing the mass transfer rates at the ends of the column. The most direct way to do this is to supply a “leaner” lean solvent, one with a lower initial CO_2 loading. Producing a leaner solvent requires more intensive solvent regeneration in the stripper, achieved by increasing the heat input to the reboiler [112]. This directly leads to a higher SRD for the same amount of CO_2 captured. Consequently, the bulge-pinched mode should always be avoided in operation.

2.3.3 *Stripper Operational Regions*

The temperature profile of the stripper is fundamentally governed by the dynamics of the water vapour generated in the reboiler. When the steam rises and condenses on contact with the cooler incoming rich solvent, it transfers its latent heat, driving the endothermic desorption reaction. The efficiency of this heat transfer process is critical. The location and progression of the condensation process along the column’s height dictates how efficiently the energy input from the reboiler is utilised. These can be described as different operational regions, primarily influenced by the L/G ratio.

2.3.3.1 *The Baseline Region*

The baseline region of operation occurs at high L/G ratios, or more accurately, low steam-to-solvent ratios. Under these conditions, the steam generated by the reboiler is rapidly and completely condensed by the large mass of downflowing rich solvent near the bottom of the stripper, such that the CO_2 leaves the top of the stripper with as little water vapour as possible [114,115]. This rapid, localised condensation results in a characteristic temperature profile. The upper section of the column remains relatively cool, closely matching the temperature of the incoming rich solvent. Much further down in the column, a sharp and rapid temperature increase occurs in the region where the condensation takes place. This profile is indicative of poor heat distribution and inefficient use of the column. The majority of the column height is not actively participating in heat exchange or stripping, leading to suboptimal solvent regeneration. For a given energy input, a higher than necessary lean solvent loading will be produced when operating in the baseline region, reducing the capture efficiency of the process.

2.3.3.2 The Exponential Region

The exponential region is the opposite extreme, occurring at low L/G ratios, corresponding to a high steam-to-solvent ratios. This condition arises when an excessive amount of steam is generated by the reboiler relative to the solvent flow rate. The amount of steam produced is so large that it cannot fully condense within the column, leading to a significant quantity of steam exiting the top of the stripper alongside the liberated CO_2. This loss of water vapour represents an extreme energy inefficiency in the process. The energy put into the system to vaporise the solvent and generate steam is not fully recovered via condensation within the column to drive the desorption reaction. Instead, this energy is lost overhead, leading to an exponential increase in SRD as the L/G ratio decreases further [115,116].

The characteristic temperature profile for this condition is the opposite of the baseline region profile. The incoming rich solvent immediately incurs a sharp and rapid temperature increase as it enters the top of the column due to the excess steam condensing on the cooler solvent. The rich solvent now has a high temperature that is equilibrated with the rising steam and remains at this temperature as the solvent falls into the reboiler.

2.3.3.3 The Inflection Point

The inflection point represents the ideal operating condition where the stripper achieves the minimum SRD for a target lean loading and corresponding capture efficiency, and marks the transition between the inefficient baseline and exponential regions of the system [116]. It occurs at an intermediate L/G ratio and corresponding steam-to-solvent ratio, representing the locus of optimal energy performance for the system. At this point, the amount of stripping steam closely matches the heat demand of the incoming rich solvent. This allows the steam to condense progressively and efficiently along the entire height of the column to drive the desorption reaction, completing just before the top. The characteristic temperature profile shows a smooth gradient along the column, reflecting this smooth energy transition.

Minimal excess water vapour leaves the top of the stripper, and the entire packing height is effectively utilised for heat and mass transfer, avoiding both column underutilisation, as seen in the baseline region, and energy wastage, as seen in the exponential region. Therefore, it is crucial to operate the stripper as close to the inflection point as possible to minimise the SRD [114–116].

The inflection point is not only a function of L/G ratio but is also a strong function of stripper operating pressure. Research by Michailos and Gibbins has shown that increasing the stripper pressure shifts the inflection point to lower lean loadings [116]. This occurs because higher pressures, and corresponding temperatures, raise the equilibrium pressure of CO_2, so less stripping steam is required to achieve the same stripping effect [117].

2.3.4 Summary of Column Temperature Profile Utilisation

In summary, temperature profiles in both the absorber and stripper columns serve as practical and useful proxies for underlying mass transfer and energy phenomena. Distinct profile shapes are linked to specific operational modes. In the absorber, efficient operation occurs under lean-pinched or rich-pinched conditions, while the bulge-pinch regime must be avoided. In the stripper, optimal performance is achieved at the inflection point, avoiding baseline and exponential regions that indicate energy wastage. Recognising these characteristic patterns enables rapid diagnosis of inefficiencies and supports targeted adjustment of process parameters, such as the L/G ratio, reboiler duty, or stripper pressure, to optimise capture efficiency, thereby minimising energy consumption.

The optimisation strategies discussed above focus on adjusting process parameters for a fixed capture plant configuration, representing one primary approach to reducing energy consumption. A second, complementary approach involves fundamentally modifying the capture plant itself to improve heat integration and capture efficiency from the outset. The following section explores these advanced structural configurations.

2.3.5 Advanced Structural Configurations

Improving the efficiencies of CO_2 capture by chemical absorption extends beyond careful solvent consideration and process optimisation. As highlighted previously, the energy for solvent regeneration is the main challenge in the chemical absorption process. The desorption energy accounts for a significant amount of the energy requirement and is largely dependent on the solvent choice [118], as discussed throughout Section 2.2. The remaining energy input is comprised of the sensible heat and the heat of vaporisation, which can be reduced through modified structural configurations and process optimisation [119].

A wide range of alternative structural configurations have been proposed in the open literature to improve efficiency, minimise energy losses, and reduce the operating costs of chemical absorption carbon capture [55]. In the subsections below, various process modifications are discussed to assess their viability for improving capture plant performance, underpinned by the simulation work published by Xue et al. [120].

2.3.5.1 Intercooled Absorber

Absorber intercooling involves withdrawing a fraction of the semi-rich solvent from the absorber to cool it down before being reinjected into the column [121]. The exothermic absorption of CO_2 leads to a temperature increase within the absorber, creating a distinct temperature bulge within the column and reduces the thermodynamic driving force for absorption. This limits the maximum achievable rich loading of the solvent [120,122].

By using an intercooler, the gas-liquid equilibrium shifts, allowing for an increase in the rich solvent loading at the bottom of the absorber. Consequently, the required solvent circulation rate is reduced, leading to a lower reboiler duty [121]. However, it should be noted that a lower temperature also reduces the absorption rate due to the associated chemical kinetics. While the thermodynamic driving force increases with a temperature reduction, the time needed to reach equilibrium increases, which can necessitate larger equipment [122].

Absorber intercooling is a widely studied modification, with key contributions from Le Moullec and Kanniche [122], Karimi et al. [123], Tobiesen et al. [124], Freguia and Rochelle [125], and Chang and Shih [126], and is part of a patented process by Aroonwilas and Veawab [127]. In the study by Xue et al. [120] an intercooler placed at the 5th absorber stage cooled the solvent to 45 °C. For MEA, this increased the rich loading from 0.465 to 0.492, a 5.8% increase, reduced the solvent circulation rate by 11.5%, and lowered the reboiler duty by 7.1%. For DEA, the rich loading increased by 4.7%, but while the circulation rate dropped by 4.7%, the reboiler duty increased by 2.8%. This phenomenon occurred because the heat of absorption for MEA is higher than for DEA, meaning intercooling yields greater benefits for solvents with high heats of absorption.

Le Moullec and Kanniche [122] evaluated different intercooler placements and found that placement in the middle or toward the bottom of the absorber was most beneficial, reporting a 2.6% reduction in heat duty. Karimi et al. [123] determined the optimal position to be one-quarter to one-fifth of the column height from the bottom, reporting energy savings of 2.84% for MEA and 3.36% for DEA. They also noted that for MEA, energy savings increased with higher lean loadings, whereas for DEA, the savings decreased.

Rezazadeh et al. [128] investigated two intercooling configurations for a capture efficiency of 90% using MEA. At a lean loading of 0.34, the “in-and-out” and “recycle” configurations yielded 15.6% and 16.8% reductions in total equivalent work, respectively, compared to the standard process. They noted that intercooling offers limited benefits at very low or very high lean loadings.

2.3.5.2 Rich Solvent Split

The rich solvent split configuration is a relatively simple modification involving the division of the cold rich solvent into two streams. One stream is preheated by the hot lean solvent in the cross-heat exchanger, while the other stream is kept cold and injected at the top of the stripper. The heated stream is injected at a lower point in the stripper to create a smooth temperature profile and maximise heat recovery, leading to a reduction in the reboiler duty [121]. Xue et al. [120] simulated a 10% cold / 90% preheated split, achieving a reboiler duty reduction of 7.7% with MEA and 7% by DEA. Le Moullec and Kanniche [122] showed that this configuration could reduce energy consumption by operating at a higher lean solvent loading, reducing reboiler duty by 12.1% compared to the standard process.

2.3.5.3 Rich Solvent Pre-heating

Rich solvent preheating involves using heat from the hot vapour exiting the top of the stripper to help preheat the incoming cold rich solvent [121]. While this appears to be efficient, the temperature of the exiting vapour is often close to that of the rich solvent, which minimises the driving force for heat transfer, a conclusion reached by Xue et al. [120]. However, when combined with a rich solvent split, the process essentially functions as a modified rich solvent split configuration [129]. In this combined case, a reboiler reduction of 11.9% was achieved, with the demand on the stripper condenser reduced [129].

2.3.5.4 Rich Solvent Flashing

Rich solvent flashing involves flashing the rich solvent in a vessel before it enters the stripper [121]. This modification essentially adds a pre-stripping stage. However, the work by Le Moullec and Kanniche [122] suggested its performance is neutral compared to a standard plant configuration and is more appropriate for absorbers at pressures significantly above atmospheric, a conclusion corroborated by the findings of Xue et al. [120].

2.3.5.5 Solvent Split Flow

The solvent split flow process, originating from a patent by Shoeld [130], was first designed for H_2S removal but has since been adapted for CO_2 capture. The principle is to regenerate the solvent to two different levels of leanness. One fully lean solvent stream is fed to the top of the absorber as usual, while a second, semi-lean stream is drawn from an intermediate stage of the stripper and fed into the middle of the absorber [121,126].

In the simulation study by Xue et al. [120], the split flow configuration reduced reboiler duties by 7.6% with MEA and 7.8% DEA. They noted that larger equipment sizes would be required to handle the increased solvent circulation due to a lower solvent cyclic capacity. Similarly, Ahn et al. [129] found a reboiler duty reduction of 12.2% with MEA and reached the same conclusions regarding equipment sizing and solvent flow rates.

The most common variant of solvent split flow processes integrates the solvent split flow with rich solvent splitting to create a staged feed to the stripper, while also optimising heat integration by cooling the semi-lean solvent, as investigated by Aroonwilas and Veawab [131] and Leites et al. [132]. The performance of such a complex integrated system is highly sensitive to design and operational parameters [122], which include:

- The semi-lean solvent draw-off height in the stripper
- The injection height of semi-lean solvent into the absorber
- The flowrate of the semi-lean solvent
- The lean solvent loading

- The operating pressure of the stripper
- The height and split fraction of the rich split solvent injection in the stripper
- The rich solvent preheating strategy

Further performance improvements can be achieved through the addition of a dedicated reboiler for the semi-lean solvent stripping [133], although the primary energy savings are derived from the fundamental split flow design itself [129]. Notably, this modification is considered more effective for solvents with thermodynamically unfavourable solvents, such as tertiary amines, than for MEA [121].

2.3.5.6 Stripper Condensate Bypass

The stripper condensate bypass involves feeding condensate from the condenser directly to the absorber instead of the stripper. Oexmann and Kather [134] used this modification in their investigation of piperazine promoted potassium carbonate and MEA application to post combustion CO_2 capture from coal-fired power stations. The simulation study by Xue et al. [120] showed marginal reboiler duty savings of 0.6% for MEA and 0.4% for DEA, an almost negligible amount because the condensate flow rate is a minimal fraction of the total solvent recirculation.

2.3.5.7 Stripper Condensate Heating

Stripper condensate heating uses the hot stripper overhead vapour to preheat the condensate before it is returned to the reboiler for further heating [121]. This configuration was part of the process patented by Aroonwilas and Veawab [127]. Ahn et al. [129] found the reboiler duty increased by 0.3% with this configuration, as the low flow rate limited effective heat transfer. In contrast, Xue et al. [120] found minor reboiler duty reductions of 1% for MEA and DEA when using this configuration.

2.3.5.8 Lean Vapour Compression

Lean vapour compression involves flashing the hot lean solvent at a low pressure and then recompressing the resulting vapour before injecting it back into the bottom of the stripper [121]. The vapour can reach very high pressure and temperature using this process, which is beneficial for the stripping process. Patents by Reddy et al. [135] and Woodhouse and Rushfeldt [136] incorporate variations of this modification.

In the simulation study by Xue et al. [120], reboiler reductions of 12.8% for MEA and 11.9% for DEA were achieved. However, this modification requires significant additional electricity consumption, resulting in actual total savings in the range of 2.7 to 3.9% overall. Sanchez Fernandez et al. [137] reported energy reductions up to 18% when using lean vapour compression, with overall net savings of 7.3%. Other studies by Karimi et al. [138] and Le Moullec and Kanniche [122] found energy savings ranging from 7.8 to 9.3%, depending on the operating pressures.

2.3.5.9 Other Modifications

The configurations described above are not an exhaustive list. Many other potential modifications exist that can enhance absorption, improve heat integration, and reduce energy requirements [121]. Some modifications would be applicable for retrofitting to standard plant configurations, whereas more advanced configurations may require a complete rebuild. A list of some other potential configurations is presented in Table 2.1, with the detailed descriptions available in Le Moullec et al. [121], Le Moullec and Kanniche [122], and Oyenekan and Rochelle [139].

Table 2.1: Other advanced structural configurations reported in the open literature.

Other Advanced Structural Configurations	
Inter-heated Absorber	Intermediate Compression Stripper
Rich Solvent Recycle	Multi Pressure Stripper
Dual Loop Absorber	Multi Pressure Split Flow
Flue Gas Compression/Expansion	Multi Effect Stripper
Partial Flash Regeneration	Double Matrix Stripper
Triple Flash Regeneration	Flashing Feed Stripper
Rich Vapour Compression	Stripper Overhead Compression
Improved Economiser Arrangement	Integrated Heat Pumps
Inter-heated Stripper	Direct Steam Stripping
Internal Exchange Stripper	Flash of Boiler Condensate
Vacuum Operated Stripper	Flue Gas Pre-cooling

All of these modifications are fundamentally based on the principles of minimising excessive driving forces and maximising the thermodynamic potential of the system [132].

2.3.5.10 Combination of Process Modifications

Process modifications can be combined to achieve synergistic effects and significant performance enhancements. Table 2.2 summarises the “very positive” and “positive” interactions between different modifications, as outlined by Le Moullec and Kanniche [122].

Table 2.2: Positive and very positive interactions between process modifications [122].

Very Positive Interactions	Semi-lean Split Flow	+	Rich Solvent Split
	Direct Steam Stripping	+	Improved Economiser
	Direct Steam Stripping	+	Vacuum Stripper
	Rich Solvent Split	+	Improved Economiser
Positive Interactions	Semi-Lean Split Flow	+	Improved Economiser
	Partial Flash Regeneration	+	Improved Economiser
	Direct Steam Stripping	+	Rich Solvent Split
	Direct Steam Stripping	+	Atmospheric Stripper
	Intermediate Compression Stripper	+	Rich Solvent Split
	Intermediate Compression Stripper	+	Improved Economiser
	Stripper Overhead Compression	+	Improved Economiser
	Lean Vapour Compression	+	Atmospheric Stripper
	Atmospheric Stripper	+	Rich Solvent Split
	Atmospheric Stripper	+	Improved Economiser

Modifications to the absorber and stripper can often be considered independently, as they do not generally interact with each other. For absorber enhancements, focus is typically directed towards intercooling and pre-cooling systems, with further consideration for rich solvent recycling and flue gas compression/expansion modifications [121,122]. For the stripper, process modifications that optimise heat integration, such as split flow arrangements, rich solvent splitting, improved economisers, and partial flash regeneration all show considerable performance improvements over the standard configuration. In addition, any process modification that optimises heat integration around the stripper becomes more efficient with increasing stripper pressure, as more heat can be recovered, which leads to a deeper regeneration of the lean solvent [122]. Lean vapour compression, for instance, which transforms available sensible heat into latent heat for stripping, also exhibits improved performance at higher pressures.

However, the influence of stripper pressure is not universal, and represents a key area for optimisation. Xue et al. [120], after evaluating literature that showed benefits from reduced stripper pressure, concluded that the optimal pressure must be determined for each specific modification strategy. Their own study subsequently confirmed that higher pressure strippers were indeed beneficial when using MEA and DEA in the configurations they tested.

Synthesising the information from this review, an example of a highly integrated and beneficial “superstructure” design could consist of an intercooled absorber with flue gas pre-cooling, combined with a solvent split flow configuration using rich solvent and semi-lean splits from a high-pressure stripper.

Crucially, literature that considers combinations of process modifications specifically for the clean-up of steelmaking emissions is limited. Among the few available publications are key studies by Tobiesen et al. [124] and Choi et al. [119]. Tobiesen et al. investigated a configuration combining an intercooled absorber with flue gas pre-cooling while assessing the performance of different solvents. Choi et al. evaluated a more complex superstructure configuration with an MEA solvent, which consisted of flue gas splitting, absorbing intercooling, a semi-lean draw, and staged feeding of lean solvent to the absorber. The main conclusion from the work of Choi et al. was that while flue gases with lower CO_2 content may achieve sufficient energy reduction from a single modification, the impact of multiple modifications in combination becomes more prominent as the flue gas CO_2 concentration increases. As BFG has a high CO_2 content, this finding indicates that the investigation of combined configurations could be a promising route for achieving substantial energy savings in this application.

2.3.6 Summary of Process Modifications

This review of process modifications for a conventional chemical absorption plant highlights promising structural configurations that can improve heat integration and absorption efficiency. These enhancements lead to reduced energy consumption, which is critical for the effective treatment of flue gases with elevated CO_2 concentrations typical of hard-to-abate heavy industries.

However, most studies only consider the use of MEA in the evaluation of process configurations, often ignoring the crucial interactions between solvent choice and the process design. A comprehensive study on these interactions across a broad range of solvents has yet to be published [121]. Information regarding these interactions for the treatment of steelmaking emissions is even more limited, with studies by Tobiesen et al. [124] and Choi et al. [119] being among the only published works to investigate this specific area.

Critically, the review revealed few studies containing pilot plant data for these advanced process modifications, with the majority of projects focused on simulation and modelling. Obtaining comparable pilot plant data for different process configurations presents significant practical challenges, because it would require either a modular capture plant setup allowing “plug and play” process configurations, or multiple plants of similar design but equipped with unique process configurations. Modelling studies should therefore focus on finding optimal superstructure configurations for targeted applications, such that new pilot plants can be designed and commissioned for novel research campaigns.

Advanced process configurations are not the only option for process improvements. The application of process intensification to chemical absorption carbon capture can lead to alternative structural designs, which are discussed in the next section.

2.3.7 Process Intensification for Chemical Absorption Carbon Capture

Some of the main barriers for the widespread adoption of conventional PB systems for chemical absorption carbon capture include high capital and operating costs, and a large equipment footprint. Process intensification seeks to address these challenges by developing novel equipment and methods that lead to smaller, cheaper, safer, and energy efficient processes [140]. The core principle of PI is to reduce equipment volume by intensifying processes through enhanced heat and mass transfer rates [9].

While PI is often associated with novel equipment, the development of advanced solvents, as previously discussed, can also be considered a form of intensification at the chemical level. The focus of this section, however, is on equipment-based PI. This approach differs from the advanced configurations discussed earlier, which primarily modify the arrangement of conventional equipment, by instead seeking to fundamentally replace key unit operations with more compact and efficient technologies. Accordingly, the following subsections identify leading PI alternatives for the conventional absorber and stripper, and for the crucial cross-heat exchanger.

2.3.7.1 The Conventional Baseline

So far, the chemical absorption carbon capture process has been in the context of having absorber and stripper columns to capture CO_2 from flue gases. This conventional approach uses packed bed (PB) columns to increase the effective surface area and the liquid holdup for the absorption reaction [141,142]. This facilitates increased mass transfer through better surface contact between the gas and liquid phases for a longer residence time. A PB column contains a support plate, liquid distributor, a mist eliminator, and a packing of choice [142].

Packings come in two main types: structured and random. Structured packings are precisely engineered with regular geometric patterns, typically with corrugated layers or honeycomb-like discs. They are stacked in layers in an organised manner within the column, forcing fluids to follow complex paths to maximise the contact area between phases [143,144]. In contrast, random packings are irregularly shaped components that are arranged randomly in a column. Chaotic flow paths are induced as the packing components have no fixed arrangement [143,144]. Compared to random packings, structured packings offer a higher mass transfer efficiency with a more uniform flow distribution and a lower pressure drop [143]. However, random packings are typically more cost effective and are easier to install. Considerations into packing requirements include: adequate strength while not being too heavy, being chemically inert to the fluids used, high surface area, sufficient channels for fluids to travel, and being cost effective [145]. For further reading, LianChuang offers comprehensive guides for both structured and random packings [143,144].

2.3.7.2 Intensified Gas-Liquid Contacting

Wang et al. [9] performed a critical review into typical PI technologies, identifying the rotating packed bed (RPB), also known as a “HiGee” (High-Gravity) contactor, as the most promising and well-studied PI technology for chemical absorption carbon capture. First patented by Ramshaw and Mallinson [146], RPBs can be applied to distillation, absorption, and stripping processes. Instead of relying on gravity to pull solvent through a packed column, an RPB uses a strong centrifugal field generated by spinning the packing at high speeds, typically ranging from 500 to 2500 RPM [147]. The packed bed surrounds the rotor in a torus shape inside a cylindrical casing [148]. Solvent is introduced at the rotor centre and is flung radially outward by the intense centrifugal force. Flue gas typically flows counter-currently, entering at the outer edge and flowing inward to contact the solvent for absorption [148]. Under the high gravity, the solvent breaks into a fine spray of micro-droplets, significantly enhancing effective surface area for absorption [148]. The most significant advantage of an RPB over a conventional PB is the potential for drastic size reduction. The high mass transfer rates provided by the high gravity environment leads to a significant reduction in the required packing volume. A study by Jung et al. [149] reported a reduction in packing volume ranging from 8.5 to 23.6 times smaller than a conventional PB, with energy savings ranging from 13.4 to 25.0%. In addition, the overall gas phase mass transfer coefficient in an RPB can be significantly higher than in a conventional PB [150].

The use of RPBs to replace stripper columns has also been explored experimentally in studies by Cheng et al. [151] and Jassim et al. [152]. Cheng et al. reported that the volume of an RPB stripper could be at least ten times smaller than a conventional PB stripper, while also achieving a 64% reduction in regeneration energy [151]. Jassim et al. explored the performance of RPBs for solvent concentrations up to 100 wt.% MEA, investigating the governing mass transfer mechanisms. They found that an RPB stripper could have a height that is 8.4 times smaller and a diameter 11.3 times smaller than a comparable conventional PB stripper [152]. Despite these experimental advances, Wang et al. [9] have reported a lack of simulation and modelling studies for intensified strippers in the open literature, identifying a key research gap. Furthermore, Adamu et al. [153] suggested that while promising, the overall capture cost savings for RPB-based processes are currently marginal compared to conventional systems. They proposed that further capital cost reductions could be achieved by directly integrating the reboiler with the regenerating RPB.

The technological readiness level (TRL) of RPB installations typically ranges from 5 to 7 [154,155], indicating the technology has reached the operational prototype and demonstration phases. In contrast, conventional PB installations have seen TRLs up to 8 [156], highlighting the difference in development progression. While RPBs promise significant long-term potential for cost reduction, conventional PBs remain the typical technology for large commercial operations due to their long operational history and higher TRL.

2.3.7.3 Intensified Heat Integration

Conventional PB systems contain a cross-heat exchanger to improve the heat integration of the process. The hot lean solvent returning from the stripper preheats the incoming rich solvent from the absorber. This heat exchanger, and its accompanying pipework, often has a large equipment footprint, necessitating intensification [9].

As part of their critical review into PI technologies, Wang et al. [9] investigated alternative cross-heat exchanger technologies. Five different technologies were evaluated, which included: the printed circuit heat exchanger (PCHE), the formed plate heat exchanger (FPHE), the hybrid heat exchanger (HHE), the Marbond heat exchanger, and the spiral heat exchanger (SHE). The optimal selection of an intensified cross-heat exchanger requires consideration of several factors, including but not limited to: operating pressure, thermal performance, temperature working range, desired pressure drop, fluid mixture for heat transfer, fluid flow capacities, construction materials, and cost [157].

Wang et al. [9] recommended the PCHE and Marbond heat exchanger for use in intensified post combustion capture processes, citing their high efficiency, compactness, weight savings, low pressure drop, high operating temperatures, and potential for retrofitting [158]. The PCHE is compact plate-fin-type heat exchanger manufactured using chemical etching and diffusion bonding [159]. Fluid flow channels are chemical etched on flat metal plates, which are then stacked and diffusion bonded to produce a single block [9,159]. The volume of a PCHE is typically 4 to 6 times smaller than that of a conventional shell-and-tube heat exchangers, due to its compact design [157].

The Marbond heat exchanger has a similar manufacturing procedure. Slotted flat plates are chemically etched and then diffusion bonded together [158]. This method allows for the creation of single sub-streams by stacking several thinner, slotted plates, which provides the potential for very low hydraulic diameters [9,158].

2.3.7.4 Summary and Outlook for Process Intensification

PI offers a promising pathway to reduce the capital cost and physical footprint of chemical absorption plants. Technologies like RPBs have demonstrated the potential to replace the large columns of conventional capture plants with a compact and efficient alternative contacting unit, while advanced heat exchangers can significantly reduce the volume of ancillary equipment. However, while these technologies are developed further, research continues to focus on optimising and modifying the more mature, conventional PB systems for near term deployment.

Having established the fundamental challenges and potential solutions related to solvents and process engineering for chemical absorption carbon capture, the focus now shifts from theoretical potential to practical implementation. An overview of commercial and pilot-scale chemical absorption applications for the iron and steel industry is provided in the following sections to understand the current state of technological deployment.

2.4 Global Status of Commercial-Scale Iron and Steelmaking CCUS Projects

In their 2024 report on the global status of CCS, the Global CCS Institute (GCCSI) has listed 628 worldwide projects in the CCS pipeline, up 60% since 2023 [160]. 50 of these CCS facilities are already in operation, with the remainder either under construction or in early development. The Institute for Energy Economics and Financial Analysis (IEEFA) anticipates the vast majority of these projects will never reach commercial operation [161].

Of these reported projects, the GCCSI has listed six commercial-scale CCUS projects for the steel industry that are in the development pipeline, in addition to one operational project [160]. These are summarised in Figure 2.2, provided by the IEEFA [162]. However, the lack of transparency on details for some of these projects has cast doubt on their development status and timeline, with crucial details undisclosed for capture capacity and storage type [162].

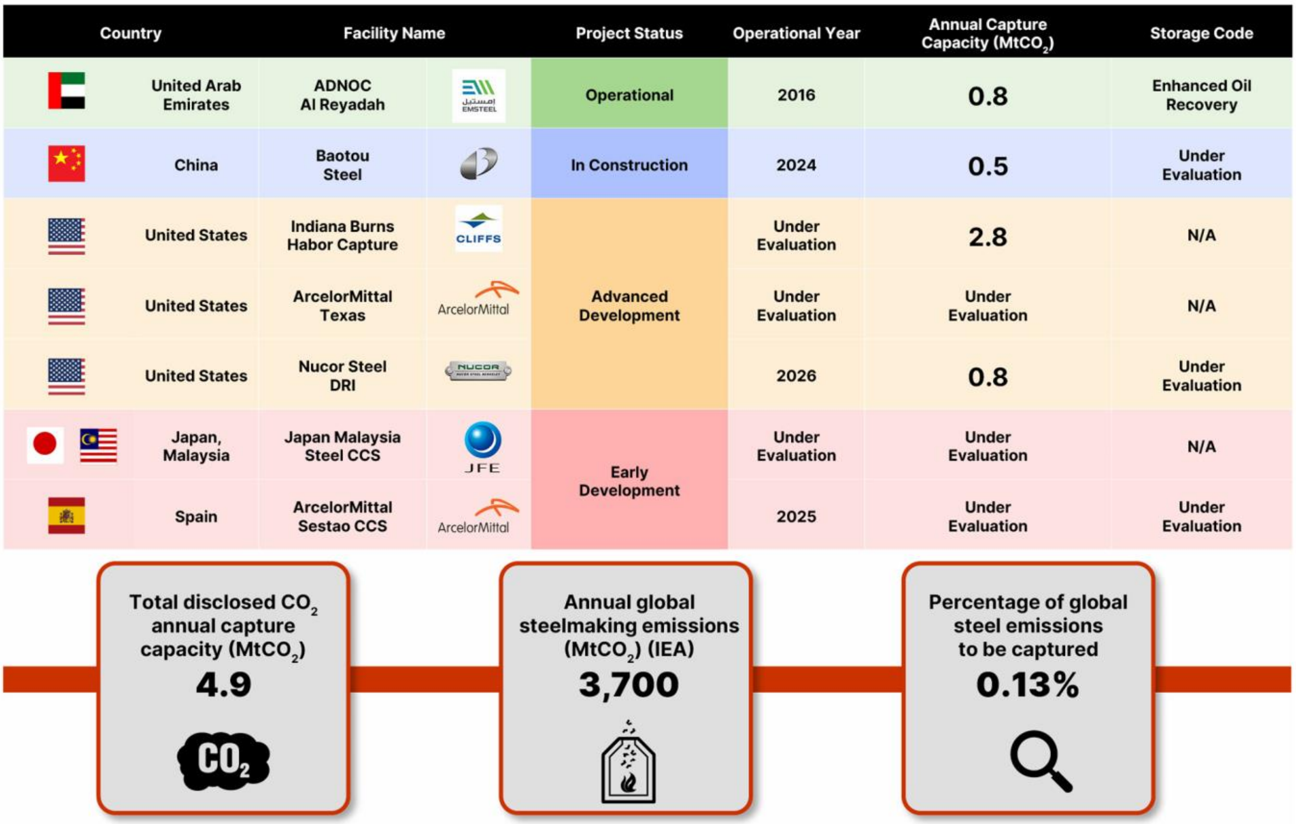

Country	Facility Name	Project Status	Operational Year	Annual Capture Capacity ($MtCO_2$)	Storage Code
United Arab Emirates	ADNOC Al Reyadah	Operational	2016	0.8	Enhanced Oil Recovery
China	Baotou Steel	In Construction	2024	0.5	Under Evaluation
United States	Indiana Burns Habor Capture	Advanced Development	Under Evaluation	2.8	N/A
United States	ArcelorMittal Texas		Under Evaluation	Under Evaluation	N/A
United States	Nucor Steel DRI		2026	0.8	Under Evaluation
Japan, Malaysia	Japan Malaysia Steel CCS	Early Development	Under Evaluation	Under Evaluation	N/A
Spain	ArcelorMittal Sestao CCS		2025	Under Evaluation	Under Evaluation

Total disclosed CO_2 annual capture capacity ($MtCO_2$)
4.9

Annual global steelmaking emissions ($MtCO_2$) (IEA)
3,700

Percentage of global steel emissions to be captured
0.13%

Figure 2.2: Status of global commercial-scale CCUS projects for iron and steelmaking. Source: IEEFA [162].

The Al Reyadah CCS facility in Abu Dhabi launched in 2016 and remains the first and only commercial-scale CCUS project for the steelmaking industry [163,164]. The plant uses MEA to capture CO_2 from a DRI-based steel plant owned by Emirates Steel Arkan for use in enhanced oil recovery operations in the Abu Dhabi National Oil Company's oil fields at a rate of injection of 0.8 $Mt{\cdot}CO_2$/year [164,165]. However, this capacity meant that the plant reduced less than 20% of emissions in 2020 and 2021, with this number rising only to 26.6% in 2023 after substantial implementation of green electricity from nuclear and solar power [161,162,166].

The IEEFA is of the opinion that CCUS is unlikely to play a role in the decarbonisation of steelmaking, due to an accumulated track record of underperformance and failure [161]. Despite this, steelmakers continue to back CCUS as a technology that will play a role in meeting their decarbonisation targets [162]. This suggests that CCUS still has the potential to be applied to steelmaking operations, but further development is required to minimise the financial and viability risks associated with the uniqueness of each CCUS project [161]. Several pilot plant studies have been conducted to assess the feasibility and performance of CCUS with steelmaking emissions, with some projects still ongoing.

2.4.1 Pilot-Scale CCUS Projects for Iron and Steelmaking

ArcelorMittal, along with partners MHI, BHP, and Mitsubishi Development began operating a pilot-scale carbon capture unit on BFG at ArcelorMittal's plant in Gent, Belgium in May 2024 [167]. It is being run in two phases, over a time period of one to two years, with the aim to test the feasibility of progress to full-scale deployment of the technology at the Gent site. The first phase focuses on capture from BFG at a rate of approximately 300 kg·CO_2/day, while the second phase will involve capture from the off gases in the hot strip mill reheating furnace [167]. The capture process utilises MHI's advanced KM CDR Process™, although the exact proprietary solvent is unspecified.

Tata Steel, partnered with Carbon Clean, commissioned India's first CO_2 capture plant in 2021 for handling BFG at Jamshedpur [168,169]. The modular skid is capable of capturing 5 tonnes·CO_2/day that is then used on site in a variety of applications. The solvent was not disclosed, although it is likely to be Carbon Clean's proprietary solvent APBS-CDRMAX®, which has been specifically formulated for industrial flue gases including steelmaking off-gases [170].

JSW Steel later partnered with both BHP and Carbon Clean to explore the feasibility of using Carbon Clean's CycloneCC modular technology [171,172] to capture up to 0.1 Mt·CO_2/year, the largest scale deployment of CycloneCC in steelmaking [173]. The CycloneCC RPB technology in combination with the APBS-CDRMAX® solvent aims to reduce the installed cost and unit footprint by up to 50%, with equipment sizes ten times smaller than conventional capture technologies.

The VALORCO project, coordinated by ArcelorMittal, aimed to reduce and valorise CO_2 emissions from the steel industry [174]. Three IFP Energies Nouvelles (IFPEN) processes, initially developed for CO_2 capture on coal power plants, were investigated for use on BFG: Hicapt™ process (MEA 30 wt.%), Hicapt+™ process (MEA 40 wt.%) and DMX™ process (demixing solvent, a blend of amines exhibiting phase change) [28]. Of the three processes, the DMX™ process was proven to be the most promising, having been tested with both BFG and top gas recycling (TGR) gas. Recovery costs of around €40/tonne·CO_2 were discussed as feasible, with the potential to reduce costs to €27/tonne·CO_2 by using waste heat integration.

This was followed by a pilot plant demonstration project in 2023 testing the DMX™ process with BFG from ArcelorMittal's plant in Dunkirk, France [175]. Coordinated by IFPEN, the project brought together 11 partners from research and industry. The aim of the study was to show the operability of the process, validate efficient energy performance, confirm solvent stability and achieve high purity of the captured CO_2. A series of operational tests were conducted with the unit operating 24/7, where the CO_2 capture efficiency exceeded 90% and yielded a CO_2 purity >99.5%. Furthermore, no solvent degradation was observed despite the presence of flue gas contaminants. The results were in line with expectations and confirmed the efficiency and energy performance of the technology [175].

The COURSE50 project, coordinated by Nippon Steel in 2008, aimed to reduce CO_2 emissions from the blast furnace by 30% through capture and suppression of CO_2 emissions [176]. Novel synthetic absorbents consisting of secondary alkanolamines were developed and tested with BFG from Nippon steel on pilot plants of two different sizes, with capacities of 1 and 30 tonne·CO_2/day, where an energy consumption of 2.5 GJ/ tonne·CO_2 was reported [176,177]. This was succeeded by the Super COURSE50 project, which aims for a 50% reduction in emissions through the use of hydrogen injection to the blast furnace. However, Nippon Steel has come under increasing scrutiny for their pessimistic decarbonisation target and slow progress compared to competitors, with some arguing it is on the wrong path for climate action [178,179]

While ongoing pilot plant research is well intentioned, the IEEFA notes a critical observation: there are still no commercial-scale CCUS plants for blast furnace-based steelmaking in operation anywhere in the world [162]. Many of the pilot-scale projects have focused on advanced and proprietary solvent use, sometimes including advanced process configurations, making it difficult to assess how much better performing these solvents are.

Therefore, establishing baseline performance data for process conditions typically encountered in the iron and steel industry is crucial for accurately benchmarking these advanced systems. This would be in the form of a conventional PB capture plant, utilising MEA.

2.5 The Challenge of Elevated CO_2 Concentrations

The primary challenge in benchmarking chemical absorption for the iron and steel industry is the lack of available and transparent pilot plant data in the open literature. Performance and technical specifications in studies and press releases from private companies are seldom disclosed in full, making direct comparison and the identification of further research avenues difficult.

A review of the broader CCS literature reveals a predominant focus on treating emissions from the power generation sector, driven by the urgent need to decarbonise the world's power systems [180]. Flue gas emissions from power generation, which are characterised by lower CO_2 concentrations, are distinctly different from those typically emitted from hard-to-abate industries. Typical CO_2 concentrations range from 10 to 15 mol.% for coal and 4 to 5 mol.% for natural gas flue gases [181]. In contrast, for the three primary hard-to-abate sectors [182], typical CO_2 emissions range from 14 to 33 mol.% in the cement industry [183], between 8 and 17 mol.% in the petrochemical industry [184,185], and up to 25 mol.% for the iron and steelmaking industry [4].

Pilot plant studies focused on these hard-to-abate industries are scarce. Consequently, there is a significant and critical lack of systematic, pilot-scale experimental data for the elevated CO_2 concentrations representative of these industrial process emissions. Crucially, in their review of large-scale pilot campaigns using MEA, Biermann et al. reported an absence of published pilot data for CO_2 concentrations above 15 mol.% [180]. While chemical absorption with MEA is considered a mature technology, it was originally developed for application to the power sector [186]. As a result, its validated application in other areas has been limited.

This highlights a clear opportunity to establish a novel performance baseline dataset that encompasses the typical CO_2 concentrations of process emissions from the iron and steel industry, while being transferable to other hard-to-abate sectors. While research into advanced process configurations continues [9], conventional packed bed systems remain the established industry standard and the logical starting point for creating a performance baseline.

Therefore, this thesis will focus on establishing a performance baseline concerning the capture of CO_2 from representative process emissions of the iron and steel industry. This will be achieved through a comprehensive experimental campaign using a standard MEA solvent in a conventional packed bed absorption system. This foundational knowledge base will enable the identification of key parametric trends, assisting in process optimisation and facilitating the confident design and scale-up of capture technologies for deployment in hard-to-abate industries.

Given the limited performance data available for CO_2 concentrations above 15 mol.%, simulation and modelling will first be utilised to predict initial operating conditions for the experimental campaign. As such, a review of available process simulation and modelling software is conducted to determine the most appropriate choice.

2.6 Process Simulation for Chemical Absorption Carbon Capture

Process modelling is a powerful tool for the evaluation and optimisation of carbon capture systems, offering a method to understand the complex interactions between process variables without the immediate cost and risk of experimentation. The fidelity of any such model, its ability to represent a meaningful simplification of reality, is contingent on its capability to accurately replicate key physical phenomena, which include thermodynamic, kinetic, and transport properties [187]. Inaccuracies in these areas can lead to significant discrepancies between simulated outcomes and real-world performances.

Consequently, the selection of an appropriate process simulation tool is a critical decision that shapes the scope, depth, and validity of the entire study. While many software packages appear similar, they possess crucial differences in their underlying mathematical frameworks and application-specific functionalities. Therefore, a thorough understanding of these respective strengths and limitations is essential to making an informed choice for modelling chemical absorption processes. Commercial process simulators generally use one of two primary solver methods: sequential-modular (SM) or equation-oriented (EO) [188]. The choice of architecture has profound implications on the capabilities of the simulator, particularly concerning optimisation, customisation, and dynamic analysis.

The sequential-modular approach is the more traditional and widely used architecture, employed by simulators such as Aspen Plus, Aspen HYSYS, ProMax, and CHEMCAD. In an SM framework, the process flowsheet is represented as a series of individual unit operations, known as modules or blocks, where the mathematical model for each unit is solved sequentially in the direction of the process flow. For flowsheets containing interconnected or recycle streams, the simulator must iterate by guessing the properties of the recycle stream, calculating through the loop, and comparing the calculated values with the initial guess, adjusting until convergence is achieved. This approach is highly robust, intuitive for process design, and efficient for standard steady-state simulations where well-defined unit operation models are available, but it can be less efficient for complex systems with strong interactions between units [188].

In contrast, the equation-oriented approach, as utilised by platforms such as Siemens gPROMS, treats the entire process flowsheet as a single, large system of simultaneous equations [188]. All the material and energy balance equations, thermodynamic relations, and kinetic and transport equations for all unit operations are collected and solved together. This method is computationally intensive but well-suited for complex plants with highly integrated systems, where multi-variable optimisation can be carried out efficiently [188]. Furthermore, the EO architecture is the natural choice for dynamic simulation, as it directly solves the time-dependent differential equations that describe the transient behaviour of a process.

2.6.1 Commercial Software for Process Simulation

Below is an overview of commonly used commercial process simulation software that could be utilised for the simulation of chemical absorption carbon capture.

2.6.1.1 Aspen Plus and Aspen HYSYS

AspenTech offers two of the most widely used process simulators in industry and academia: Aspen Plus and Aspen HYSYS [189]. While they share a common parent company and some functionalities, they were developed for different purposes and possess different strengths. Aspen Plus is broadly recognised as the industry-leading simulator for different process industries [190]. Its fundamental design is process-focused, making it proficient at handling systems with complex chemistry, non-ideal thermodynamic behaviour, and critically, electrolytes. Amine-based chemical absorption is an aqueous electrolyte system, and Aspen Plus excels at modelling such a system through use of its electrolyte non-random two-liquid (ELECNRTL) property method, which is specifically designed for electrolyte systems [191]. The software is extensively documented for carbon capture applications, featuring a dedicated “Electrolyte Wizard” for setting up complex chemistry, and the powerful RadFrac/RateSep model for rigorous, rate-based modelling of absorber and stripper columns.

Aspen HYSYS (an acronym for Hydrocarbon SYStem) was originally developed for and remains optimised for the oil and gas refining industries [192]. Its strength lies in simulating hydrocarbon-based systems and typically employs equation-of-state properties like Peng-Robinson or Soave-Redlich-Kwong. While AspenTech has incorporated an acid gas property package into HYSYS that utilises the ELECNRTL model for amine modelling, its core architecture and extensive property databases are less tailored to the specific challenges of aqueous electrolyte chemistry than those of Aspen Plus.

2.6.1.2 gPROMS

Siemens gPROMS (general PROcess Modelling System) is designed to capture deep process knowledge and create high-fidelity predictive models, referred to as “digital twins” [193]. Its equation-oriented architecture makes it exceptionally strong for custom model development, large-scale optimisation, and in particular, dynamic simulation. It is able to model the response of capture plants under transient conditions [194], such as fluctuating flue gas flow rates, which is a crucial consideration for real-world application.

While its power and flexibility are undeniable, gPROMS often requires the user to build models from fundamental equations, unlike sequential-modular simulators such as Aspen Plus. This can be a significant undertaking and may not be beneficial to projects focused on steady-state design.

2.6.1.3 ProMax

ProMax, from Bryan Research and Engineering, is widely regarded as the premier simulation software for acid gas removal, holding a dominant position in the natural gas processing and refining industries [195]. Key strengths include a comprehensive library of both generic and proprietary amine-based solvents, a proprietary Electrolytic-ELR thermodynamic model, and specialised models for mass and heat transfer in packed and trayed columns [195].

For its core applications, ProMax is unparalleled. However, its specialisation to hydrocarbons raises concern about its application to steelmaking emissions. Its performance and validation for the specific flue gas compositions found in the iron and steel industry are less extensively documented in the open literature compared to other simulators like Aspen Plus.

2.6.1.4 CHEMCAD

CHEMCAD from Chemstations is a versatile and customisable simulator that provides a comprehensive suite of chemical process simulation tools [196]. It includes models for both steady state and dynamic simulation, as well as specialised tools for heat exchanger design and batch processes. The software has documented capabilities for modelling chemical absorption [197] and is equipped to handle aqueous electrolyte systems. Despite its suitability as a capable and flexible tool, it is cited less frequently in literature compared to market leaders like Aspen Plus.

2.6.1.5 Simulation Software Selection

The academic and user communities generally agree that Aspen Plus is the most appropriate and robust process simulation tool for modelling chemical absorption systems, being extensively documented across the open literature [198]. Its proficiency in modelling aqueous electrolyte systems makes it suitable for representing MEA and other amine-based solvents. This, in addition to its ability to accurately model absorber and stripper columns, confirms its suitability for a study on conventional PB systems. Consequently, Aspen Plus has been selected as the process simulation tool for this thesis. The development and utilisation of the chemical absorption model will be guided by key publications identified in the literature, including studies by Zhang and Chen [199], Lim et al. [200], Plaza et al. [201], Harbou et al. [202], Garcia et al. [198], and others [26,87,194,203–205].

The resulting simulation model will represent the performance of a real-world conventional packed bed pilot plant using MEA. The model’s predictions will be analysed to identify parametric trends, which in turn will guide the initial starting conditions of a comprehensive experimental campaign. The outcomes of this campaign will then be used to further refine the simulation model, forming the foundation of a high-fidelity digital twin of the pilot plant. The specific aims and objectives of this thesis are outlined in the following section.

2.7 The Knowledge Gap, Research Novelty, Aim and Objectives

The Knowledge Gap

While several pilot campaigns have targeted steelmaking emissions, they have almost exclusively utilised proprietary or developmental solvents, such as DMX™, KS-21™, and APBS-CDRMAX®, whose performance data is often limited or not publicly available. Consequently, a critical knowledge gap exists: the absence of a fundamental performance benchmark for a conventional PB system using a standard, non-proprietary solvent, such as MEA, under elevated CO_2 conditions. This deficiency hinders the direct, objective comparison of novel capture technologies and limits process development for the decarbonisation of the iron and steel industry.

Novelty

The novelty of this research lies in its synergistic methodology, which combines rigorous process simulation with a targeted experimental campaign. This work will develop and validate a process simulation model in Aspen Plus to investigate performance under elevated CO_2 concentrations. The model's predictions will define the operational envelope of the pilot plant, informing initial starting conditions for a comprehensive experimental campaign to generate novel performance data. This new data will then be used to create a high-fidelity, calibrated simulation model, forming the foundation of a digital twin representation of the pilot plant. The models and methodologies developed in this thesis will be highly transferable, providing a robust framework for assessing capture technologies across other heavy industries.

Overall Aim

The overarching aim of this thesis is to establish a foundational understanding of, and subsequently optimise the performance of, conventional chemical absorption carbon capture systems treating flue gases with elevated CO_2 concentrations, representative of process emissions from the iron and steel industry.

Research Objectives

i) To develop and validate a representative process simulation model of a chemical absorption pilot plant in Aspen Plus.

ii) To systematically investigate the influence of key operational parameters on plant performance under a range of elevated CO_2 concentrations and process conditions using the validated simulation model.

iii) To generate a novel performance dataset for the capture of industrial process emissions by conducting a comprehensive experimental campaign on a conventional chemical absorption pilot plant.

iv) To create a calibrated, high-fidelity process simulation model using the novel experimental data, enhancing predictive accuracy and forming the foundation of a digital twin.

2.8 References for Chapter 2

[1] IEA. Energy Technology Perspectives 2020 – Analysis. IEA 2020. https://www.iea.org/reports/energy-technology-perspectives-2020.

[2] IEA. Iron and Steel Technology Roadmap – Analysis. IEA 2020. https://www.iea.org/reports/iron-and-steel-technology-roadmap.

[3] IEA. Net Zero by 2050 – Analysis. IEA 2021. https://www.iea.org/reports/net-zero-by-2050.

[4] Ramírez-Santos ÁA, Castel C, Favre E. A review of gas separation technologies within emission reduction programs in the iron and steel sector: Current application and development perspectives. Separation and Purification Technology 2018;194:425–42. https://doi.org/10.1016/j.seppur.2017.11.063.

[5] Finney KN, Akram M, Diego ME, Yang X, Pourkashanian M. Carbon Capture Technologies. Elsevier; 2019. https://doi.org/10.1016/B978-0-12-816229-3.00002-8.

[6] Akram M, Ali U, Best T, Blakey S, Finney KN, Pourkashanian M. Performance evaluation of PACT Pilot-plant for CO2 capture from gas turbines with Exhaust Gas Recycle. International Journal of Greenhouse Gas Control 2016;47:137–50. https://doi.org/10.1016/j.ijggc.2016.01.047.

[7] Kohl AL, Nielsen RB. Alkanolamines for Hydrogen Sulfide and Carbon Dioxide Removal. Gas Purification, Houston, Texas: Gulf Publishing Compancy; 1997, p. 41–174.

[8] Wang M, Joel AS, Ramshaw C, Eimer D, Musa NM. Process intensification for post-combustion CO2 capture with chemical absorption: A critical review. Applied Energy 2015;158:275–91. https://doi.org/10.1016/j.apenergy.2015.08.083.

[9] Oyenekan BA, Rochelle GT. Energy Performance of Stripper Configurations for CO2 Capture by Aqueous Amines. Industrial & Engineering Chemistry Research 2006;45:2457–64. https://doi.org/10.1021/ie050548k.

[10] Pudasainee D, Kurian V, Gupta R. Coal: Past, Present, and Future Sustainable Use. Future Energy, Elsevier; 2020, p. 21–48. https://doi.org/10.1016/B978-0-08-102886-5.00002-5.

[11] Salvinder KMS, Zabiri H, Taqvi SA, Ramasamy M, Isa F, Rozali NEM, et al. An overview on control strategies for CO2 capture using absorption/stripping system. Chemical Engineering Research and Design 2019;147:319–37. https://doi.org/10.1016/j.cherd.2019.04.034.

[12] Wang M, Lawal A, Stephenson P, Sidders J, Ramshaw C. Post-combustion CO2 capture with chemical absorption: A state-of-the-art review. Chemical Engineering Research and Design 2011;89:1609–24. https://doi.org/10.1016/j.cherd.2010.11.005.

[13] Tatarczuk A, Tańczyk M, Więcław-Solny L, Zdeb J. Pilot plant results of amine-based carbon capture with heat integrated stripper. Applied Energy 2024;367:123416. https://doi.org/10.1016/j.apenergy.2024.123416.

[14] Nwaoha C, Idem R, Supap T, Saiwan C, Tontiwachwuthikul P, Rongwong W, et al. Heat duty, heat of absorption, sensible heat and heat of vaporization of 2–Amino–2–Methyl–1–Propanol (AMP), Piperazine (PZ) and Monoethanolamine (MEA) tri–solvent blend for carbon dioxide (CO2) capture. Chemical Engineering Science 2017;170:26–35. https://doi.org/10.1016/j.ces.2017.03.025.

[15] Artanto Y, Jansen J, Pearson P, Do T, Cottrell A, Meuleman E, et al. Performance of MEA and amine-blends in the CSIRO PCC pilot plant at Loy Yang Power in Australia. Fuel 2012;101:264–75. https://doi.org/10.1016/j.fuel.2012.02.023.

[16] Oexmann J, Kather A. Minimising the regeneration heat duty of post-combustion CO2 capture by wet chemical absorption: The misguided focus on low heat of absorption solvents. International Journal of Greenhouse Gas Control 2010;4:36–43. https://doi.org/10.1016/j.ijggc.2009.09.010.

[17] Vinjarapu SHB, Regueira T, Neerup R, von Solms N, Fosbøl PL. Heat of absorption of CO2 in 30 wt% MEA with monoethyleneglycol and urea as vapour reduction additives. Energy 2024;293:130609. https://doi.org/10.1016/j.energy.2024.130609.

[18] N.Borhani T, Wang M. Role of solvents in CO2 capture processes: The review of selection and design methods. Renewable and Sustainable Energy Reviews 2019;114:109299. https://doi.org/10.1016/j.rser.2019.109299.

[19] Raksajati A, Ho M, Wiley D. Solvent Development for Post-Combustion CO_2 Capture: Recent Development and Opportunities. MATEC Web Conf 2018;156:03015. https://doi.org/10.1051/matecconf/201815603015.

[20] Hoff KA, Silva EFD, Kim I, Grimstvedt A, Ma'mun S. Solvent development in post combustion CO2 capture-Selection criteria and optimization of solvent performance, cost and environmental impact. Energy Procedia 2013;37:292–9. https://doi.org/10.1016/j.egypro.2013.05.114.

[21] Salazar J, Diwekar U, Joback K, Berger AH, Bhown AS. Solvent Selection for Post-Combustion CO2 Capture. Energy Procedia 2013;37:257–64. https://doi.org/10.1016/j.egypro.2013.05.110.

[22] Shadab F, Alkhatib III, Vega LF. Guiding the Selection of Novel Amines for CO2 Capture Using a Molecular-Based and Multicriteria Modeling Approach. Energy Fuels 2024;38:17805–21. https://doi.org/10.1021/acs.energyfuels.4c03210.

[23] Vega F, Sanna A, Navarrete B, Maroto-Valer MM, Cortés VJ. Degradation of amine-based solvents in CO2 capture process by chemical absorption. Greenhouse Gases: Science and Technology 2014;4:707–33. https://doi.org/10.1002/ghg.1446.

[24] Xin K, Gallucci F, Annaland MVS. Optimization of solvent properties for post-combustion CO2 capture using process simulation. International Journal of Greenhouse Gas Control 2020;99:103080. https://doi.org/10.1016/j.ijggc.2020.103080.

[25] Luis P. Use of monoethanolamine (MEA) for CO2 capture in a global scenario: Consequences and alternatives. Desalination 2016;380:93–9. https://doi.org/10.1016/j.desal.2015.08.004.

[26] Abu-Zahra MRM, Schneiders LHJ, Niederer JPM, Feron PHM, Versteeg GF. CO2 capture from power plants: Part I. A parametric study of the technical performance based on monoethanolamine. International Journal of Greenhouse Gas Control 2007;1:37–46. https://doi.org/10.1016/S1750-5836(06)00007-7.

[27] Yu C-H, Huang C-H, Tan C-S. A Review of CO2 Capture by Absorption and Adsorption. Aerosol and Air Quality Research 2012;12:745–69. https://doi.org/10.4209/aaqr.2012.05.0132.

[28] Dreillard M, Broutin P, Briot P, Huard T, Lettat A. Application of the DMXTM CO2 Capture Process in Steel Industry. Energy Procedia 2017;114:2573–89. https://doi.org/10.1016/j.egypro.2017.03.1415.

[29] Oko E, Zacchello B, Wang M, Fethi A. Process analysis and economic evaluation of mixed aqueous ionic liquid and monoethanolamine (MEA) solvent for CO2 capture from a coke oven plant. Greenhouse Gases: Science and Technology 2018;8:686–700. https://doi.org/10.1002/ghg.1772.

[30] Muchan P, Saiwan C, Narku-Tetteh J, Idem R, Supap T, Tontiwachwuthikul P. Screening tests of aqueous alkanolamine solutions based on primary, secondary, and tertiary structure for blended aqueous amine solution selection in post combustion CO2 capture. Chemical Engineering Science 2017;170:574–82. https://doi.org/10.1016/j.ces.2017.02.031.

[31] Vega F, Baena-Moreno FM, Gallego Fernández LM, Portillo E, Navarrete B, Zhang Z. Current status of CO2 chemical absorption research applied to CCS: Towards full deployment at industrial scale. Applied Energy 2020;260:114313. https://doi.org/10.1016/j.apenergy.2019.114313.

[32] Conway W, Bruggink S, Beyad Y, Luo W, Melián-Cabrera I, Puxty G, et al. CO2 absorption into aqueous amine blended solutions containing monoethanolamine (MEA), N,N-dimethylethanolamine (DMEA), N,N-diethylethanolamine (DEEA) and 2-amino-2-methyl-1-propanol (AMP) for post-combustion capture processes. Chemical Engineering Science 2015;126:446–54. https://doi.org/10.1016/j.ces.2014.12.053.

[33] Vaidya PD, Kenig EY. CO2-Alkanolamine Reaction Kinetics: A Review of Recent Studies. Chemical Engineering & Technology 2007;30:1467–74. https://doi.org/10.1002/ceat.200700268.

[34] Li J, You C, Chen L, Ye Y, Qi Z, Sundmacher K. Dynamics of CO2 Absorption and Desorption Processes in Alkanolamine with Cosolvent Polyethylene Glycol. Industrial & Engineering Chemistry Research 2012;51:12081–8. https://doi.org/10.1021/ie301164v.

[35] Bernhardsen IM, Knuutila HK. A review of potential amine solvents for CO2 absorption process: Absorption capacity, cyclic capacity and pKa. International Journal of Greenhouse Gas Control 2017;61:27–48. https://doi.org/10.1016/j.ijggc.2017.03.021.

[36] Putta KR, Pinto DDD, Svendsen HF, Knuutila HK. CO2 absorption into loaded aqueous MEA solutions: Kinetics assessment using penetration theory. International Journal of Greenhouse Gas Control 2016;53:338–53. https://doi.org/10.1016/j.ijggc.2016.08.009.

[37] Yildirim Ö, Kiss AA, Hüser N, Leßmann K, Kenig EY. Reactive absorption in chemical process industry: A review on current activities. Chemical Engineering Journal 2012;213:371–91. https://doi.org/10.1016/j.cej.2012.09.121.

[38] Lv B, Guo B, Zhou Z, Jing G. Mechanisms of CO2 Capture into Monoethanolamine Solution with Different CO2 Loading during the Absorption/Desorption Processes. Environmental Science & Technology 2015;49:10728–35. https://doi.org/10.1021/acs.est.5b02356.

[39] Chen M, Luo Q, Lin H, Sun Q, Gao H, Liu S, et al. A study on reaction mechanism and kinetics of CO2 and MEA/DEA-tertiary amines in non-aqueous and water-lean solutions. Chemical Engineering Science 2023;269:118431. https://doi.org/10.1016/j.ces.2022.118431.

[40] García-Abuín A, Gómez-Díaz D, López AB, Navaza JM, Rumbo A. NMR Characterization of Carbon Dioxide Chemical Absorption with Monoethanolamine, Diethanolamine, and Triethanolamine. Ind Eng Chem Res 2013;52:13432–8. https://doi.org/10.1021/ie4010496.

[41] Caplow M. Kinetics of carbamate formation and breakdown. J Am Chem Soc 1968;90:6795–803. https://doi.org/10.1021/ja01026a041.

[42] Crooks JE, Donnellan JP. Kinetics and mechanism of the reaction between carbon dioxide and amines in aqueous solution. J Chem Soc, Perkin Trans 2 1989:331. https://doi.org/10.1039/p29890000331.

[43] Donaldson TL, Nguyen YN. Carbon Dioxide Reaction Kinetics and Transport in Aqueous Amine Membranes. Ind Eng Chem Fund 1980;19:260–6. https://doi.org/10.1021/i160075a005.

[44] Danckwerts PV. The reaction of CO2 with ethanolamines. Chemical Engineering Science 1979;34:443–6. https://doi.org/10.1016/0009-2509(79)85087-3.

[45] Mahajani VV, Joshi JB. Kinetics of reactions between carbon dioxide and alkanolamines. Gas Separation & Purification 1988;2:50–64. https://doi.org/10.1016/0950-4214(88)80013-6.

[46] Versteeg GF, Van Dijck LAJ, Van Swaaij WPM. On the Kinectics Between CO2 and Alkanolamines both in Aqueous and Non-aqueous Solutions. An Overview. Chemical Engineering Communications 1996;144:113–58. https://doi.org/10.1080/00986449608936450.

[47] Aboudheir A, Tontiwachwuthikul P, Chakma A, Idem R. Kinetics of the reactive absorption of carbon dioxide in high CO2-loaded, concentrated aqueous monoethanolamine solutions. Chemical Engineering Science 2003;58:5195–210. https://doi.org/10.1016/j.ces.2003.08.014.

[48] Da Silva EF, Svendsen HF. Ab Initio Study of the Reaction of Carbamate Formation from CO_2 and Alkanolamines. Ind Eng Chem Res 2004;43:3413–8. https://doi.org/10.1021/ie030619k.

[49] Mahmud N, Benamor A, Nasser MS, Al-Marri MJ, Qiblawey H, Tontiwachwuthikul P. Reaction kinetics of carbon dioxide with aqueous solutions of l-Arginine, Glycine & Sarcosine using the stopped flow technique. International Journal of Greenhouse Gas Control 2017;63:47–58. https://doi.org/10.1016/j.ijggc.2017.05.012.

[50] Lim J, Scholes CA, Dumée LF, Kentish SE. Nanofiltration for the concentration of heat stable salts prior to MEA reclamation. International Journal of Greenhouse Gas Control 2014;30:34–41. https://doi.org/10.1016/j.ijggc.2014.08.020.

[51] Lepaumier H, Picq D, Carrette P-L. New Amines for CO2 Capture. II. Oxidative Degradation Mechanisms. Ind Eng Chem Res 2009;48:9068–75. https://doi.org/10.1021/ie9004749.

[52] Zoannou KS, Sapsford DJ, Griffiths AJ. Thermal degradation of monoethanolamine and its effect on CO2 capture capacity. International Journal of Greenhouse Gas Control 2013;17:423–30. https://doi.org/10.1016/j.ijggc.2013.05.026.

[53] Jason Daniel Davis. Thermal degradation of aqueous amines used for carbon dioxide capture. The University of Texas at Austin, 2009.

[54] Davis J, Rochelle G. Thermal degradation of monoethanolamine at stripper conditions. Energy Procedia 2009;1:327–33. https://doi.org/10.1016/j.egypro.2009.01.045.

[55] Rezazadeh F. Optimal Integration of Post-Combustion CO2 Capture Process with Natural Gas Fired Combined Cycle Power Plants. 2016, PhD Thesis, University of Leeds.

[56] Gouedard C, Picq D, Launay F, Carrette P-L. Amine degradation in CO2 capture. I. A review. International Journal of Greenhouse Gas Control 2012;10:244–70. https://doi.org/10.1016/j.ijggc.2012.06.015.

[57] Dickinson J, Percy A, Puxty G, Verheyen TV. Oxidative degradation of amine absorbents in carbon capture systems – A dynamic modelling approach. International Journal of Greenhouse Gas Control 2016;53:391–400. https://doi.org/10.1016/j.ijggc.2016.08.001.

[58] Goff GS. Oxidative Degradation of Aqueous Monoethanolamine in CO2 Capture Processes : Iron and Copper Catalysis , Inhibition , and O2 Mass Transfer. 2005, PhD Thesis, University of Texas: Austin 2005:283.

[59] Supap T, Idem R, Veawab A, Aroonwilas A, Tontiwachwuthikul P, Chakma A, et al. Kinetics of the Oxidative Degradation of Aqueous Monoethanolamine in a Flue Gas Treating Unit. Industrial & Engineering Chemistry Research 2001;40:3445–50. https://doi.org/10.1021/ie000957a.

[60] Chi S, Rochelle GT. Oxidative Degradation of Monoethanolamine. Industrial & Engineering Chemistry Research 2002;41:4178–86. https://doi.org/10.1021/ie010697c.

[61] Fredriksen SB, Jens KJ. Oxidative degradation of aqueous amine solutions of MEA, AMP, MDEA, Pz: A review. Energy Procedia 2013;37:1770–7. https://doi.org/10.1016/j.egypro.2013.06.053.

[62] Vevelstad SJ, Eide-Haugmo I, Da Silva EF, Svendsen HF. Degradation of MEA; A theoretical study. Energy Procedia 2011;4:1608–15. https://doi.org/10.1016/j.egypro.2011.02.031.

[63] Lepaumier H, da Silva EF, Einbu A, Grimstvedt A, Knudsen JN, Zahlsen K, et al. Comparison of MEA degradation in pilot-scale with lab-scale experiments. Energy Procedia 2011;4:1652–9. https://doi.org/10.1016/j.egypro.2011.02.037.

[64] Salih HA, Pokhrel J, Reinalda D, AlNashf I, Khaleel M, Vega LF, et al. Hybrid – Slurry/Nanofluid systems as alternative to conventional chemical absorption for carbon dioxide capture: A review. International Journal of Greenhouse Gas Control 2021;110:103415. https://doi.org/10.1016/j.ijggc.2021.103415.

[65] Thompson J, Nikolic H, Combs M, Bhatnagar S, Pelgen J, Abad K, et al. Solvent Degradation and Emissions from a 0.7MWe Pilot CO2 Capture System with Two-stage Stripping. Energy Procedia 2017;114:1297–306. https://doi.org/10.1016/j.egypro.2017.03.1242.

[66] Verma N, Verma A. Amine system problems arising from heat stable salts and solutions to improve system performance. Fuel Processing Technology 2009;90:483–9. https://doi.org/10.1016/j.fuproc.2009.02.002.

[67] Reynolds AJ, Verheyen TV, Meuleman E. Degradation of amine-based solvents. Absorption-Based Post-combustion Capture of Carbon Dioxide, Elsevier; 2016, p. 399–423. https://doi.org/10.1016/B978-0-08-100514-9.00016-0.

[68] Wang Y, Fang M, Huang Y, Wang T, Li S, Lu X, et al. Removal of heat stable salts from degraded amine solvent by “BMED+ED” two-stage electrodialysis unit. International Journal of Greenhouse Gas Control 2023;127:103939. https://doi.org/10.1016/j.ijggc.2023.103939.

[69] Morken AK, Pedersen S, Nesse SO, Flø NE, Johnsen K, Feste JK, et al. CO2 capture with monoethanolamine: Solvent management and environmental impacts during long term operation at the Technology Centre Mongstad (TCM). International Journal of Greenhouse Gas Control 2019;82:175–83. https://doi.org/10.1016/j.ijggc.2018.12.018.

[70] Morken AK, Pedersen S, Kleppe ER, Wisthaler A, Vernstad K, Ullestad Ø, et al. Degradation and Emission Results of Amine Plant Operations from MEA Testing at the CO2 Technology Centre Mongstad. Energy Procedia 2017;114:1245–62. https://doi.org/10.1016/j.egypro.2017.03.1379.

[71] Moser P, Wiechers G, Schmidt S, Garcia Moretz-Sohn Monteiro J, Charalambous C, Garcia S, et al. Results of the 18-month test with MEA at the post-combustion capture pilot plant at Niederaussem – new impetus to solvent management, emissions and dynamic behaviour. International Journal of Greenhouse Gas Control 2020;95:102945. https://doi.org/10.1016/j.ijggc.2019.102945.

[72] Neerup R, Rasmussen VE, Vinjarapu SHB, Larsen AH, Shi M, Andersen C, et al. Solvent degradation and emissions from a CO2 capture pilot at a waste-to-energy plant. Journal of Environmental Chemical Engineering 2023;11:111411. https://doi.org/10.1016/j.jece.2023.111411.

[73] Léonard G, Crosset C, Dumont M-N, Toye D. Designing Large-scale CO2 Capture Units with Assessment of Solvent Degradation. Energy Procedia 2014;63:1478–86. https://doi.org/10.1016/j.egypro.2014.11.157.

[74] Braakhuis L, Knuutila HK. Predicting solvent degradation in absorption–based CO2 capture from industrial flue gases. Chemical Engineering Science 2023;279:118940. https://doi.org/10.1016/j.ces.2023.118940.

[75] Fleury E, Kittel J, Vuillemin B, Oltra R, Ropital F. Corrosion in amine solvents used for the removal of acid gases. EUROCORR 2008 - European Corrosion Congress: Managing Corrosion for Sustainability, Book of Abstracts 2008:297.

[76] Lee I-Y, Lee JH, Kim J-H, Jang KR, Shim J-G. Effect of Corrosion Inhibitors on Oxidative Degradation of MEA in Carbon Dioxide Capture. Journal of Chemical Engineering of Japan 2011;44:273–7. https://doi.org/10.1252/jcej.10we289.

[77] Fine NA, Rochelle GT. Thermal Decomposition of N-nitrosopiperazine. Energy Procedia 2013;37:1678–86. https://doi.org/10.1016/j.egypro.2013.06.043.

[78] Knuutila H, Asif N, Vevelstad SJ, Svendsen HF. Formation and Destruction of NDELA in 30 wt% MEA (Monoethanolamine) and 50 wt% DEA (Diethanolamine) Solutions. Oil Gas Sci Technol – Rev IFP Energies Nouvelles 2014;69:805–20. https://doi.org/10.2516/ogst/2013168.

[79] Azzi M, White S. Emissions from amine-based post-combustion CO2 capture plants. Absorption-Based Post-combustion Capture of Carbon Dioxide, Elsevier; 2016, p. 487–504. https://doi.org/10.1016/B978-0-08-100514-9.00020-2.

[80] Fostås B, Gangstad A, Nenseter B, Pedersen S, Sjøvoll M, Sørensen AL. Effects of NOx in the flue gas degradation of MEA. Energy Procedia 2011;4:1566–73. https://doi.org/10.1016/j.egypro.2011.02.026.

[81] Sartori G, Savage DW. Sterically hindered amines for carbon dioxide removal from gases. Industrial & Engineering Chemistry Fundamentals 1983;22:239–49. https://doi.org/10.1021/i100010a016.

[82] Sartori G, Ho WS, Savage DW, Chludzinski GR, Wlechert S. Sterically-Hindered Amines for Acid-Gas Absorption. Separation and Purification Methods 1987;16:171–200. https://doi.org/10.1080/03602548708058543.

[83] CO_2 Capture Technology for Exhaust Gas KM CDR Process^{TM}. Energy Transition Mitsubishi Heavy Industries Group n.d. https://solutions.mhi.com/ccus/co2-capture-technology-for-exhaust-gas-kmcdr-process/.

[84] Miyamoto O, Maas C, Tsujiuchi T, Inui M, Hirata T, Tanaka H, et al. KM CDR ProcessTM Project Update and the New Novel Solvent Development. Energy Procedia 2017;114:5616–23. https://doi.org/10.1016/j.egypro.2017.03.1700.

[85] Mitsubishi Heavy Industries | Mitsubishi Heavy Industries Engineering Successfully CompletesTesting of New “KS-21^{TM}” Solvent for CO_2 Capture. Mitsubishi Heavy Industries, Ltd 2021. https://www.mhi.com/news/211019.html.

[86] Dutcher B, Fan M, Russell AG. Amine-Based CO2 Capture Technology Development from the Beginning of 2013—A Review. ACS Applied Materials & Interfaces 2015;7:2137–48. https://doi.org/10.1021/am507465f.

[87] Zhao B, Liu F, Cui Z, Liu C, Yue H, Tang S, et al. Enhancing the energetic efficiency of MDEA/PZ-based CO2 capture technology for a 650 MW power plant: Process improvement. Applied Energy 2017;185:362–75. https://doi.org/10.1016/j.apenergy.2016.11.009.

[88] Adeosun A, Abu-Zahra MRM. Evaluation of amine-blend solvent systems for CO2 post-combustion capture applications. Energy Procedia 2013;37:211–8. https://doi.org/10.1016/j.egypro.2013.05.104.

[89] Aroonwilas A, Veawab A. Integration of CO2 capture unit using blended MEA–AMP solution into coal-fired power plants. Energy Procedia 2009;1:4315–21. https://doi.org/10.1016/j.egypro.2009.02.244.

[90] Khan BA, Ullah A, Saleem MW, Khan AN, Faiq M, Haris M. Energy Minimization in Piperazine Promoted MDEA-Based CO2 Capture Process. Sustainability 2020;12:8524. https://doi.org/10.3390/su12208524.

[91] Papadopoulos AI, Tzirakis F, Tsivintzelis I, Seferlis P. Phase-Change Solvents and Processes for Postcombustion CO2 Capture: A Detailed Review. Industrial & Engineering Chemistry Research 2019;58:5088–111. https://doi.org/10.1021/acs.iecr.8b06279.

[92] Ye Q, Zhu L, Wang X, Lu Y. On the mechanisms of CO2 absorption and desorption with phase transitional solvents. International Journal of Greenhouse Gas Control 2017;56:278–88. https://doi.org/10.1016/j.ijggc.2016.11.027.

[93] Raksajati A, Ho MT, Wiley DE. Reducing The Cost of CO2 Capture From Flue Gases Using Phase-change Solvent Absorption. Energy Procedia 2014;63:2280–8. https://doi.org/10.1016/j.egypro.2014.11.247.

[94] Zhang S, Shen Y, Wang L, Chen J, Lu Y. Phase change solvents for post-combustion CO2 capture: Principle, advances, and challenges. Applied Energy 2019;239:876–97. https://doi.org/10.1016/j.apenergy.2019.01.242.

[95] Wang X, Li B. Phase-Change Solvents for CO2 Capture. Novel Materials for Carbon Dioxide Mitigation Technology, Elsevier; 2015, p. 3–22. https://doi.org/10.1016/B978-0-444-63259-3.00001-X.

[96] Heldebrant DJ, Koech PK, Glezakou V-A, Rousseau R, Malhotra D, Cantu DC. Water-Lean Solvents for Post-Combustion CO2 Capture: Fundamentals, Uncertainties, Opportunities, and Outlook. Chemical Reviews 2017;117:9594–624. https://doi.org/10.1021/acs.chemrev.6b00768.

[97] Wanderley RR, Yuan Y, Rochelle GT, Knuutila HK. CO2 solubility and mass transfer in water-lean solvents. Chemical Engineering Science 2019;202:403–16. https://doi.org/10.1016/j.ces.2019.03.052.

[98] Heldebrant DJ, Koech PK, Rousseau R, Glezakou V-A, Cantu D, Malhotra D, et al. Are Water-lean Solvent Systems Viable for Post-Combustion CO2 Capture? Energy Procedia 2017;114:756–63. https://doi.org/10.1016/j.egypro.2017.03.1218.

[99] Zheng RF, Barpaga D, Mathias PM, Malhotra D, Koech PK, Jiang Y, et al. A single-component water-lean post-combustion CO2 capture solvent with exceptionally low operational heat and total costs of capture – comprehensive experimental and theoretical evaluation. Energy & Environmental Science 2020;13:4106–13. https://doi.org/10.1039/D0EE02585B.

[100] Yuan Y, Rochelle G. Water-Lean Solvents for CO2 Capture Will Not Use Less Energy than Aqueous Amines. SSRN Electronic Journal 2020;2:2–4. https://doi.org/10.2139/ssrn.3366219.

[101] Shakerian F, Kim K-H, Szulejko JE, Park J-W. A comparative review between amines and ammonia as sorptive media for post-combustion CO 2 capture. Applied Energy 2015;148:10–22. https://doi.org/10.1016/j.apenergy.2015.03.026.

[102] Molina CT, Bouallou C. Assessment of different methods of CO2 capture in post-combustion using ammonia as solvent. Journal of Cleaner Production 2015;103:463–8. https://doi.org/10.1016/j.jclepro.2014.03.024.

[103] Bai H, Yeh AC. Removal of CO2 Greenhouse Gas by Ammonia Scrubbing. Industrial & Engineering Chemistry Research 1997;36:2490–3. https://doi.org/10.1021/ie960748j.

[104] Han K, Ahn CK, Lee MS, Rhee CH, Kim JY, Chun HD. Current status and challenges of the ammonia-based CO2 capture technologies toward commercialization. International Journal of Greenhouse Gas Control 2013;14:270–81. https://doi.org/10.1016/j.ijggc.2013.01.007.

[105] Kim JY, Han K, Chun HD. CO2 absorption with low concentration ammonia liquor. Energy Procedia 2009;1:757–62. https://doi.org/10.1016/j.egypro.2009.01.100.

[106] Rhee CH, Kim JY, Han K, Ahn CK, Chun HD. Process analysis for ammonia-based CO2 capture in ironmaking industry. Energy Procedia 2011;4:1486–93. https://doi.org/10.1016/j.egypro.2011.02.015.

[107] Kim JY, Han K, Ahn CK, Lee MS, Rhee CH, Chun HD. Operating Cost for CO2 Capture Process Using Aqueous Ammonia. Energy Procedia 2013;37:677–82. https://doi.org/10.1016/j.egypro.2013.05.156.

[108] Weiland R, Hatcher N, Alvis S. Pinched Performance: Part 1. Digital Refining 2015.

[109] Ralph Weiland, Nate Hatcher, Clay Jones. Rich-end, Lean-end, and Bulge Pinches in Amine Treating | Gas Processors Association Europe 2014.

[110] Bui M, Gunawan I, Verheyen TV, Meuleman E, Feron P. Dynamic Operation of Post-combustion CO2 Capture in Australian Coal-fired Power Plants. Energy Procedia 2014;63:1368–75. https://doi.org/10.1016/j.egypro.2014.11.146.

[111] Kvamsdal HM, Rochelle GT. Effects of the Temperature Bulge in CO2 Absorption from Flue Gas by Aqueous Monoethanolamine. Ind Eng Chem Res 2008;47:867–75. https://doi.org/10.1021/ie061651s.

[112] Hatcher N, Alvis S, Weiland R. Gas treating simulation – a holistic perspective part 2: carbon capture. Digital Refining 2013.

[113] Hatcher N, Alvis S, Weiland R. Gas treating simulation — a holistic perspective part 3: co2 removal in an LNG plant. Digital Refining 2013.

[114] Gibbins J. Amine stripper temperature profile a key to optimising net-zero performance in post-combustion carbon capture plants | LinkedIn. LinkedIn 2023. https://www.linkedin.com/pulse/amine-stripper-temperature-profile-key-optimising-net-zero-gibbins/.

[115] Michailos S, Gibbins J. A Modelling Study of Post-Combustion Capture Plant Process Conditions to Facilitate 95–99% CO2 Capture Levels From Gas Turbine Flue Gases. Frontiers in Energy Research 2022;10.

[116] Michailos S, Gibbins J. Effect of stripper pressure and low lean loadings on the performance of a PCC plant for 99% CO2 capture level. SSRN Electronic Journal 2022. https://doi.org/10.2139/ssrn.4283827.

[117] Warudkar SS, Cox KR, Wong MS, Hirasaki GJ. Influence of stripper operating parameters on the performance of amine absorption systems for post-combustion carbon capture: Part I. High pressure strippers. International Journal of Greenhouse Gas Control 2013;16:342–50. https://doi.org/10.1016/j.ijggc.2013.01.050.

[118] Kothandaraman A, Nord L, Bolland O, Herzog HJ, McRae GJ. Comparison of solvents for post-combustion capture of CO2 by chemical absorption. Energy Procedia 2009;1:1373–80. https://doi.org/10.1016/j.egypro.2009.01.180.

[119] Choi J, Cho H, Yun S, Jang MG, Oh SY, Binns M, et al. Process design and optimization of MEA-based CO2 capture processes for non-power industries. Energy 2019;185:971–80. https://doi.org/10.1016/j.energy.2019.07.092.

[120] Xue B, Yu Y, Chen J, Luo X, Wang M. A comparative study of MEA and DEA for post-combustion CO2 capture with different process configurations. International Journal of Coal Science and Technology 2017;4:15–24. https://doi.org/10.1007/s40789-016-0149-7.

[121] Le Moullec Y, Neveux T, Azki AA, Chikukwa A, Hoff KA. Process Modifications for Solvent-based Post Combustion CO2 Capture. Energy Procedia 2014;63:1470–7. https://doi.org/10.1016/j.egypro.2014.11.156.

[122] Le Moullec Y, Kanniche M. Screening of flowsheet modifications for an efficient monoethanolamine (MEA) based post-combustion CO2 capture. International Journal of Greenhouse Gas Control 2011;5:727–40. https://doi.org/10.1016/j.ijggc.2011.03.004.

[123] Karimi M, Hillestad M, Svendsen HF. Investigation of intercooling effect in CO2 capture energy consumption. Energy Procedia 2011;4:1601–7. https://doi.org/10.1016/j.egypro.2011.02.030.

[124] Tobiesen FA, Svendsen HF, Mejdell T. Modeling of blast furnace CO2 capture using amine absorbents. Industrial and Engineering Chemistry Research 2007;46:7811–9. https://doi.org/10.1021/ie061556j.

[125] Freguia S, Rochelle GT. Modeling of CO2 capture by aqueous monoethanolamine. AIChE Journal 2003;49:1676–86. https://doi.org/10.1002/aic.690490708.

[126] Chang H, Shih C. Simulation and Optimization for Power Plant Flue Gas CO2 Absorption-Stripping Systems. Separation Science and Technology 2005;40:877–909. https://doi.org/10.1081/SS-200048014.

[127] Aroonwilas A, Veawab A. Heat recovery gas absorption process. US Patent: US 20070221065, 2007.

[128] Rezazadeh F, Gale WF, Rochelle GT, Sachde D. Effectiveness of absorber intercooling for CO2 absorption from natural gas fired flue gases using monoethanolamine solvent. International Journal of Greenhouse Gas Control 2017;58:246–55. https://doi.org/10.1016/j.ijggc.2017.01.016.

[129] Ahn H, Luberti M, Liu Z, Brandani S. Process configuration studies of the amine capture process for coal-fired power plants. International Journal of Greenhouse Gas Control 2013;16:29–40. https://doi.org/10.1016/j.ijggc.2013.03.002.

[130] Shoeld M. Purification and separation of gaseous mixtures. US Patent: US 1971798A, 1934.

[131] Aroonwilas A, Veawab A. Integration of CO2 capture unit using single- and blended-amines into supercritical coal-fired power plants: Implications for emission and energy management. International Journal of Greenhouse Gas Control 2007;1:143–50. https://doi.org/10.1016/S1750-5836(07)00011-4.

[132] Leites IL, Sama DA, Lior N. The theory and practice of energy saving in the chemical industry: some methods for reducing thermodynamic irreversibility in chemical technology processes. Energy 2003;28:55–97. https://doi.org/10.1016/S0360-5442(02)00107-X.

[133] Towler GP, Shethna HK, Cole B, Hajdik B. Improved absorber-stripper technology for gas sweetening to ultra-low H2S concentrations. Proceedings, Annual Convention - Gas Processors Association, 1997, p. 93–100.

[134] Oexmann J, Kather A. Post-combustion CO2 capture in coal-fired power plants: Comparison of integrated chemical absorption processes with piperazine promoted potassium carbonate and MEA. Energy Procedia 2009;1:799–806. https://doi.org/10.1016/j.egypro.2009.01.106.

[135] Reddy S, Gillmartin J, Francuz V. Integrated Compressor/Stripper Configurations And Methods. US Patent: US 20090205946, 2009.

[136] Woodhouse S, Rushfeldt P. Absorbent Regeneration With Flashed Lean Solution And Heat Integration. US Patent: US 20100062926, 2010.

[137] Sanchez Fernandez E, Bergsma EJ, de Miguel Mercader F, Goetheer ELV, Vlugt TJH. Optimisation of lean vapour compression (LVC) as an option for post-combustion CO2 capture: Net present value maximisation. International Journal of Greenhouse Gas Control 2012;11:S114–21. https://doi.org/10.1016/j.ijggc.2012.09.007.

[138] Karimi M, Hillestad M, Svendsen HF. Capital costs and energy considerations of different alternative stripper configurations for post combustion CO2 capture. Chemical Engineering Research and Design 2011;89:1229–36. https://doi.org/10.1016/j.cherd.2011.03.005.

[139] Oyenekan BA, Rochelle GT. Alternative stripper configurations for CO2 capture by aqueous amines. AIChE Journal 2007;53:3144–54. https://doi.org/10.1002/aic.11316.

[140] Reay D. The role of process intensification in cutting greenhouse gas emissions. Applied Thermal Engineering 2008;28:2011–9. https://doi.org/10.1016/j.applthermaleng.2008.01.004.

[141] Rahmanian Nejat, Rehan Mohammad, Sumani Abdallah, Nizami Abdul-Sattar. Effect of packing structure on CO2 capturing process. Chemical Engineering Transactions 2018;70:1891–6. https://doi.org/10.3303/CET1870316.

[142] Michigan Engineering. Absorbers – Visual Encyclopedia of Chemical Engineering Equipment n.d. https://encyclopedia.che.engin.umich.edu/absorbers/.

[143] LianChuang. Structured Packings: Types, Characteristics, Applications, and Complete Guide n.d. https://www.chemicalpackings.com/article/structured-packing.html.

[144] LianChuang. Random Packing Types Materials Applications Selection for Random Packed Columns n.d. https://www.chemicalpackings.com/article/random-packings.html.

[145] EPCM. Absorption Column: Types and Designing Considerations n.d. https://epcmholdings.com/absorption-column-types-and-designing-considerations/.

[146] Colin Ramshaw, Roger H. Mallinson. Mass transfer process. US4283255A, n.d.

[147] Visscher F, Van Der Schaaf J, Nijhuis TA, Schouten JC. Rotating reactors – A review. Chemical Engineering Research and Design 2013;91:1923–40. https://doi.org/10.1016/j.cherd.2013.07.021.

[148] Shukla C, Mishra P, Dash SK. A review of process intensified CO2 capture in RPB for sustainability and contribution to industrial net zero. Front Energy Res 2023;11:1135188. https://doi.org/10.3389/fenrg.2023.1135188.

[149] Jung H, Park N, Lee JH. Evaluating the efficiency and cost-effectiveness of RPB-based CO2 capture: A comprehensive approach to simultaneous design and operating condition optimization. Applied Energy 2024;365:123251. https://doi.org/10.1016/j.apenergy.2024.123251.

[150] Lin C-C, Kuo Y-W. Mass transfer performance of rotating packed beds with blade packings in absorption of CO2 into MEA solution. International Journal of Heat and Mass Transfer 2016;97:712–8. https://doi.org/10.1016/j.ijheatmasstransfer.2016.02.033.

[151] Cheng H-H, Lai C-C, Tan C-S. Thermal regeneration of alkanolamine solutions in a rotating packed bed. International Journal of Greenhouse Gas Control 2013;16:206–16. https://doi.org/10.1016/j.ijggc.2013.03.022.

[152] Jassim MS, Rochelle G, Eimer D, Ramshaw C. Carbon dioxide absorption and desorption in aqueous monoethanolamine solutions in a rotating packed bed. Industrial and Engineering Chemistry Research 2007;46:2823–33. https://doi.org/10.1021/ie051104r.

[153] Adamu A, Russo-Abegão F, Boodhoo K. Process intensification technologies for CO2 capture and conversion – a review. BMC Chem Eng 2020;2:2. https://doi.org/10.1186/s42480-019-0026-4.

[154] Scott J. ACCSESS presented at RPB Colloquium 2022. Accsess 2022. https://www.projectaccsess.eu/2022/07/27/accsess-presented-at-rpb-colloquium-2022/.

[155] Lee JGM, Hendry J, Kolawole T, Schulz R, Rabold T. Pilot Scale Amine-Based Carbon Capture Using Rotating Packed Beds n.d.

[156] Oko E, Wang M, Joel AS. Current status and future development of solvent-based carbon capture. International Journal of Coal Science and Technology 2017;4:5–14. https://doi.org/10.1007/s40789-017-0159-0.

[157] Li Q, Flamant G, Yuan X, Neveu P, Luo L. Compact heat exchangers: A review and future applications for a new generation of high temperature solar receivers. Renewable and Sustainable Energy Reviews 2011;15:4855–75. https://doi.org/10.1016/j.rser.2011.07.066.

[158] Hesselgreaves JE, Law R, Reay D. Compact Heat Exchangers: Selection, Design and Operation. Butterworth-Heinemann; 2016.

[159] Tsuzuki N, Kato Y, Ishiduka T. High performance printed circuit heat exchanger. Applied Thermal Engineering 2007;27:1702–7. https://doi.org/10.1016/j.applthermaleng.2006.07.007.

[160] Global CCS Institute. Global Status of CCS 2024. 2024.

[161] Institute for Energy Economics and Financial Analysis. Carbon capture for steel? | IEEFA 2024. https://ieefa.org/resources/carbon-capture-steel.

[162] Nicholas S, Basirat S. Steel CCUS update: Carbon capture technology looks ever less convincing. 2024.

[163] Abu Zahra M. Perspective from Emirates Steel Project/UAE. Presentation from IEAGHG Workshop CCS Pathways to Commercialisation 2015.

[164] Sakaria D. Case Study: Al Reyadah CCUS Project 2017.

[165] Al Reyadah Carbon Capture, Use, and Storage (CCUS) Project | CSLForum n.d. https://www.cslforum.org/cslf/Projects/AlReyadah (accessed August 3, 2021).

[166] Emirates Steel Arkan. 2023 Sustainability Report. 2023.

[167] ArcelorMittal. Trial carbon capture unit begins operating on blast furnace at ArcelorMittal Gent, Belgium 2024. https://corporate.arcelormittal.com/media/news-articles/trial-carbon-capture-unit-begins-operating-on-blast-furnace-at-arcelormittal-gent-belgium.

[168] Carbon Clean. Carbon Clean provides India's first blast furnace carbon capture plant 2021. https://www.carbonclean.com/news/carbon-capture-plant-for-tata-steel.

[169] Tata Steel. Tata Steel commissions India's first plant for CO2 capture from Blast Furnace gas at Jamshedpur 2021. http://www.tatasteel.com/media/newsroom/press-releases/india/2021/tata-steel-commissions-india-s-first-plant-for-co2-capture-from-blast-furnace-gas-at-jamshedpur/.

[170] Carbon Clean. Proprietary carbon solvent technology n.d. https://www.carbonclean.com/technology/carbon-solvents.

[171] Carbon Clean. Innovative carbon capture for the steel industry n.d. https://www.carbonclean.com/insights/carbon-capture-steel-industry.

[172] Carbon Clean. Modular carbon capture systems for industry n.d. https://www.carbonclean.com/technology/modular.

[173] BHP. BHP, Carbon Clean, and JSW Steel sign agreement to explore Carbon Clean's CycloneCC technology 2024. https://www.bhp.com/news/articles/2024/10/bhp-carbon-clean-and-jsw-steel-sign-agreement-to-explore-carbon-cleans-cyclonecc-technology.

[174] CO2 Value Europe. VALORCO n.d. https://database.co2value.eu/projects/119.

[175] Carbon Capture Journal. CO2 capture from steel using the DMX process successful 2024. https://www.carboncapturejournal.com/news/co2-capture-from-steel-using-the-dmx-process-successful/6095.aspx?Category=all.

[176] Tonomura S. Outline of Course 50. Energy Procedia 2013;37:7160–7. https://doi.org/10.1016/j.egypro.2013.06.653.

[177] Chowdhury FA, Yamada H, Matsuzaki Y, Goto K, Higashii T, Onoda M. Development of Novel Synthetic Amine Absorbents for CO2 Capture. Energy Procedia 2014;63:572–9. https://doi.org/10.1016/j.egypro.2014.11.062.

[178] Steel Watch. Nippon Steel and hydrogen: Why Super COURSE50 is the wrong path for climate action. 2024.

[179] Transistion Asia. Japan's FY2024 Climate Actions: Corporate and Government Moves as well as Urgent Priorities. Transition Asia 2025. https://transitionasia.org/japans-fy2024-climate-actions-corporate-and-government-moves-as-well-as-urgent-priorities/.

[180] Biermann M, Normann F, Johnsson F, Hoballah R, Onarheim K. Capture of CO2 from Steam Reformer Flue Gases Using Monoethanolamine: Pilot Plant Validation and Process Design for Partial Capture. Ind Eng Chem Res 2022;61:14305–23. https://doi.org/10.1021/acs.iecr.2c02205.

[181] Global CCS Institute. CO2 Capture Tecnologies Post Combustion Capture (PCC). 2012.

[182] UNFCCC. Integrating hard-to-abate industries in the process of preparing and implementing NDCs. n.d.

[183] Bosoaga A, Masek O, Oakey JE. CO2 Capture Technologies for Cement Industry. Energy Procedia 2009;1:133–40. https://doi.org/10.1016/j.egypro.2009.01.020.

[184] Ma Q, Chang Y, Yuan B, Song Z, Xue J, Jiang Q. Utilizing carbon dioxide from refinery flue gas for methanol production: System design and assessment. Energy 2022;249:123602. https://doi.org/10.1016/j.energy.2022.123602.

[185] Songolzadeh M, Soleimani M, Takht Ravanchi M, Songolzadeh R. Carbon Dioxide Separation from Flue Gases: A Technological Review Emphasizing Reduction in Greenhouse Gas Emissions. The Scientific World Journal 2014;2014:1–34. https://doi.org/10.1155/2014/828131.

[186] Tatarczuk A, Spietz T, Więcław-Solny L, Krótki A, Chwoła T, Dobras S, et al. Enhancing CO2 Capture Efficiency: Advanced Modifications of Solvent-Based Absorption Process—Pilot Plant Insights. Energies 2025;18:2236. https://doi.org/10.3390/en18092236.

[187] Ali U. Process Simulation of Power Generation Systems with CO2 Capture 2017, PhD Thesis, University of Sheffield.

[188] MySEp. Process Simulation n.d. https://www.mysep.com/process-simulation.

[189] AspenTech. AspenTech Product Portfolio n.d. https://www.aspentech.com/en/products/full-product-listing.

[190] AspenTech. Aspen Plus n.d. https://www.aspentech.com/en/products/engineering/aspen-plus.

[191] Gilardi Matteo, Bisotti Filippo, Knuutila Hanna K., Tobiesen Andrew, Bonalumi Davide. Aspen Plus ENRTL Model for HS3 Blend, a Novel Solvent for CO2 Capture. Chemical Engineering Transactions 2023;100:271–6. https://doi.org/10.3303/cet23100046.

[192] AspenTech. Aspen HYSYS n.d. https://www.aspentech.com/en/products/engineering/aspen-hysys.

[193] Siemens. gPROMS Digital Process Design and Operation n.d. https://www.siemens.com/global/en/products/automation/industry-software/gproms-digital-process-design-and-operations.html.

[194] Harun N, Nittaya T, Douglas PL, Croiset E, Ricardez-Sandoval LA. Dynamic simulation of MEA absorption process for CO2 capture from power plants. International Journal of Greenhouse Gas Control 2012;10:295–309. https://doi.org/10.1016/j.ijggc.2012.06.017.

[195] Bryan Research & Engineering. ProMax - Acid Gas Removal n.d. https://www.bre.com/ProMax-Acid-Gas-Removal.aspx.

[196] Chemstations. CHEMCAD n.d. https://chemstations.com/chemcad.

[197] Chemstations. Power Plant Carbon Capture with CHEMCAD n.d.

[198] Garcia M, Knuutila HK, Gu S. ASPEN PLUS simulation model for CO2 removal with MEA: Validation of desorption model with experimental data. Journal of Environmental Chemical Engineering 2017;5:4693–701. https://doi.org/10.1016/j.jece.2017.08.024.

[199] Zhang Y, Chen CC. Modeling CO2 Absorption and Desorption by Aqueous Monoethanolamine Solution with Aspen Rate-based Model. Energy Procedia 2013;37:1584–96. https://doi.org/10.1016/j.egypro.2013.06.034.

[200] Lim Y, Kim J, Jung J, Lee CS, Han C. Modeling and Simulation of CO2 Capture Process for Coal- based Power Plant Using Amine Solvent in South Korea. Energy Procedia 2013;37:1855–62. https://doi.org/10.1016/j.egypro.2013.06.065.

[201] Plaza JM, Wagener DV, Rochelle GT. Modeling CO2 capture with aqueous monoethanolamine. Energy Procedia 2009;1:1171–8. https://doi.org/10.1016/j.egypro.2009.01.154.

[202] Von Harbou I, Imle M, Hasse H. Modeling and simulation of reactive absorption of CO2 with MEA: Results for four different packings on two different scales. Chemical Engineering Science 2014;105:179–90. https://doi.org/10.1016/j.ces.2013.11.005.

[203] Osagie E, Aliyu AM, Nnabuife SG, Omoregbe O, Etim V. Exergy Analysis and Evaluation of the Different Flowsheeting Configurations for CO2 Capture Plant Using 2-Amino-2-Methyl-1-Propanol (AMP). Processes 2019;7:391. https://doi.org/10.3390/pr7060391.

[204] Lee AS, Eslick JC, Miller DC, Kitchin JR. Comparisons of amine solvents for post-combustion CO2 capture: A multi-objective analysis approach. International Journal of Greenhouse Gas Control 2013;18:68–74. https://doi.org/10.1016/j.ijggc.2013.06.020.

[205] Rezazadeh F, Gale WF, Lin Y-J, Rochelle GT. Energy Performance of Advanced Reboiled and Flash Stripper Configurations for CO2 Capture Using Monoethanolamine. Industrial & Engineering Chemistry Research 2016;55:4622–31. https://doi.org/10.1021/acs.iecr.5b05005.

Chapter 3: Simulation Model Development and Performance Predictions

---

3.1 The TERC ACP and Need for Process Simulation

3.1.1 Introduction to the TERC ACP

The Translational Energy Research Centre (TERC) is part of the Energy Innovation Centre (EIC) in Sheffield, United Kingdom, and houses an industrial pilot-scale amine capture plant (ACP) designed for post-combustion CO_2 capture [1,2]. The pilot plant can capture approximately one tonne of CO_2 per day, handling gas flows of up to 250 Nm^3/h and can achieve >95% capture efficiencies using MEA under certain conditions.

The plant was originally designed to handle coal combustion flue gas before the closure of coal-fired power stations [3]. Previous projects have focused on process optimisation, solvent degradation studies, solvent development testing and aerosol emissions control [3–7]. Since the closure of UK coal-fired power stations, subsequent projects have rarely required flue gas flows with elevated CO_2 concentrations above 10 mol.%, which are typical of combustion and industrial processes. The development of a project that required high CO_2 concentration flue gases presented a unique opportunity to investigate the performance potential of the ACP in handling flue gases that are more typical of processes in the iron and steelmaking industry.

3.1.2 The TERC ACP Process Description

The operation of the TERC ACP for chemical absorption-based CO_2 capture from flue gases is described as follows. Flue gas is blown into the bottom of the absorber column by a fan, either from a synthetic gas mixing skid or a flue gas manifold that collects exhaust gases from various combustion and process plants. The flue gas flows upward through the structured packing of the column, where it contacts the counter-flowing lean solvent. The solvent reacts with the CO_2 in the flue gas, capturing it and becoming rich, that is, laden with the CO_2. The remaining flue gas exits the top of the absorber and passes through a two-stage water wash system to recover any residual solvent. The rich solvent is then pumped through a plate heat exchanger for preheating, before entering the top of the stripper column. The rich solvent flows down the stripper column into the reboiler and heats up, releasing the CO_2 through the reversible endothermic reaction. The reboiler is supplied with pressurised hot water (PHW) to provide heat. The released CO_2 exits the top of the stripper, passes through a cooler, and then a reflux drum to recover any vapourised water or solvent, which drains back into the stripper. The separated pure CO_2 then leaves the top of the reflux drum. The remaining hot solvent, now lean due to having less absorbed CO_2, exits the bottom of the reboiler and is pumped through the plate heat exchanger to preheat the incoming rich solvent. After passing through a cooler to reach the required temperature set point, the lean solvent re-enters the top of the absorber to repeat the cycle. The process operates in a closed loop, with minor losses of water and solvent replenished as needed.

The ACP was originally located at the Pilot-scale Advanced Capture Technology (PACT) facilities at the UK Carbon Capture and Storage Research Centre (UKCCSRC) and featured a different structural configuration for the absorber column. The stripper column, reboiler and cross-heat exchanger remain unchanged from the original PACT configuration to the new TERC ACP installation. The structural configuration of a plant significantly impacts optimisation, as variations in column diameter or height will impact performance [3]. Balancing flow, mass transport and energy demand variables are crucial for a given configuration. The key technical specifications of the ACP, including details for both TERC and PACT configurations, are summarised in Table 3.1. Operating ranges for key parameters of the ACP are presented in Table 3.2.

Table 3.1: Technical specifications of the ACP.

Equipment	Specification
Absorber Column (TERC)	Two 250 mm diameter columns, providing up to 12 m total packed height Packing: 4 x 3 m packed beds of Flexipac 350X structured packing 12 Resistance Temperature Detectors in each absorber column for temperature monitoring
Absorber Column (PACT)	Single column of 300 mm diameter with 8 m total height Packing: IMPT25 random packing 4 Resistance Temperature Detectors for temperature monitoring
Stripper Column	Single column of 300 mm diameter with 8 m total height Packing: IMPT25 random packing 9 Resistance Temperature Detectors for temperature monitoring
Cross-Heat Exchanger	Plate heat exchanger with Maximum heat duty up to 43 kW
Stripper Reboiler	Supplied with pressurised hot water Electric boiler heat duty up to 72 kW

Table 3.2: Parameter operating ranges of the ACP.

Parameter	Operational Range
Solvent Mass Flow Rate (CO_2 Free Basis)	300 – 1200 kg/h
Flue Gas Volumetric Flow Rate	100 – 250 Nm^3/h
Stripper Column Pressure	1.0 – 3.0 bara

3.1.3 The Need for Process Simulation

Pilot-scale experimental campaigns can be costly to undertake and are time, personnel and energy intensive, with little margin for error. When investigating a novel operating condition, it is essential to be well informed regarding the potential effects of changing operating parameters and aim to achieve optimised operation with the minimum number of experimental changes possible. Process simulation plays a crucial role alongside experimental work, offering the potential to accurately predict outcomes and even eliminate the need for a number of experimental trials. In most cases, simulation predictions provide informed starting points, with subsequent experimental results used to refine the simulation model through calibration. Following such a procedure to design an experimental programme to investigate capture from a flue gas stream with elevated CO_2 concentrations, a comprehensive process simulation of the ACP has been developed using Aspen Plus V11.0 as a prerequisite for conducting the experimental trials. The Aspen Plus flowsheet of the TERC ACP is presented in Figure 3.1.

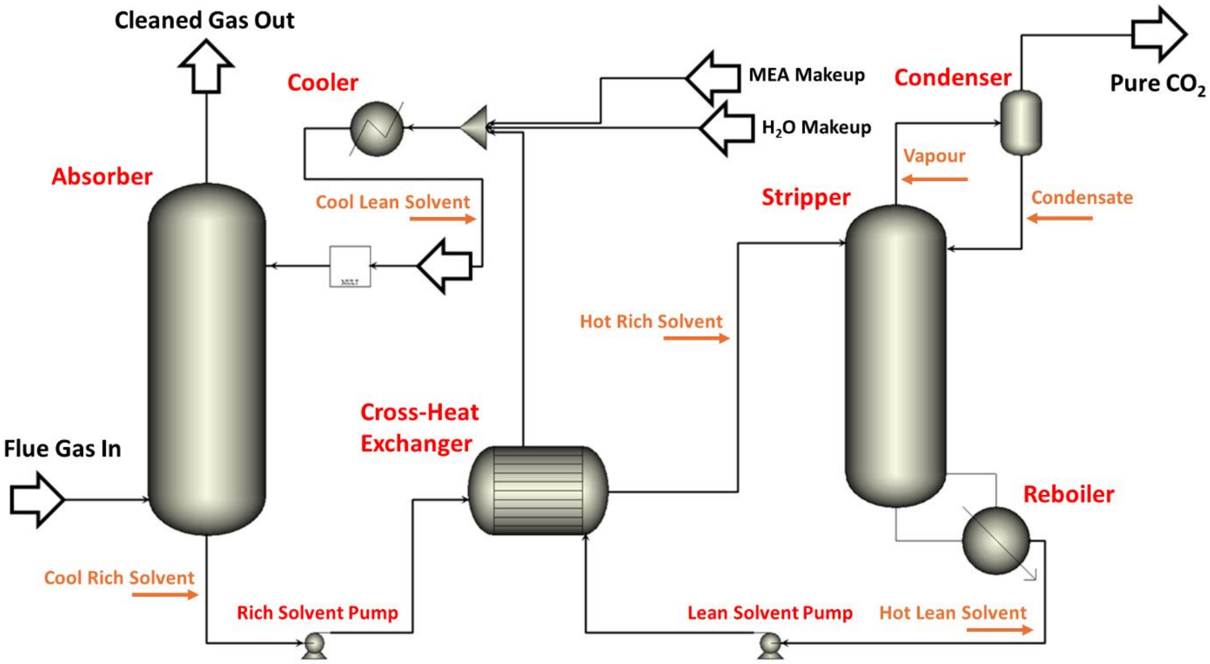

Figure 3.1: Process flow diagram of the TERC ACP Aspen Plus V11.0.

The following sections outline the development and validation of this simulation model, henceforth referred to as the Developed Carbon Capture (DCC) model. The DCC model was ultimately used to represent the TERC ACP configuration, assessing the plant's performance and capability in handling higher CO_2 concentrations than previously investigated. This model offered insights into the relationships between key parameters, enabling more efficient scenario predictions for capture plants without relying solely on iterative experimental testing. The DCC model will be further refined using data from experimental trials, enhancing the accuracy of its subsequent predictions to better align with experimental values.

3.2 DCC Model Development

3.2.1 Introduction

The foundations of the DCC model originate from the intrinsic Aspen Plus V11.0 configuration file "ENTRL-RK Rate Based MEA Model". This file contains an ACP model that has been validated against existing literature and has a user guide accompanying the file [8]. This model has been adapted to be representative of the TERC ACP. The adaptations were based upon a combination of interpreting literature and calibration against existing experimental data. The underlying chemical properties for components in the Aspen Plus database and the source literature upon which the original intrinsic file was based have been used without modification, because these have been validated against measurements and analyses from a range of experimental plants and chemical reaction modelling, as outlined in the user guide [8].

3.2.2 MEA Absorption Chemistry

The reaction chemistry for CO_2 absorption using MEA, as implemented in the DCC model, follows Equations (3.1) to (3.5), based on the work by Zhang and Chen [9]:

Water Dissociation
$$2H_2O \leftrightarrow H_3O^+ + OH^- \tag{3.1}$$

CO_2 Hydrolysis
$$CO_2 + 2H_2O \leftrightarrow HCO_3^- + H_3O^+ \tag{3.2}$$

Bicarbonate Dissociation
$$HCO_3^- + H_2O \leftrightarrow MEA + H_3O^+ \tag{3.3}$$

Carbamate Hydrolysis
$$MEACOO^- + H_2O \leftrightarrow MEA + HCO_3^- \tag{3.4}$$

MEA Protonation
$$MEAH^+ + H_2O \leftrightarrow MEA + HCO_3^- \tag{3.5}$$

3.2.3 Kinetic Model

The formations of bicarbonate and carbamate are kinetically limited. In Aspen Plus these are represented as twinned competing forward and reverse kinetic reactions. Equations (3.6) and (3.7) represent bicarbonate formation, whereas Equations (3.8) and (3.9) represent carbamate formation [9]:

Bicarbonate Formation
$$OH^- + CO_2 \rightarrow HCO_3^- \tag{3.6}$$
$$HCO_3 \rightarrow OH^- + CO_2 \tag{3.7}$$

Carbamate Formation
$$MEA + CO_2 + H_2O \rightarrow MEACOO^- + H_3O^+ \tag{3.8}$$
$$MEACOO^- + H_3O^+ \rightarrow MEA + CO_2 + H_2O \tag{3.9}$$

For kinetically limited reactions, Aspen Plus describes the reaction rates through power law expressions. The general power law expression is:

$$r = k\left(\frac{T_{\mathrm{abs}}}{T_0}\right)^n \exp\left[\left(\frac{-E}{R}\right)\cdot\left(\frac{1}{T_{\mathrm{abs}}}-\frac{1}{T_0}\right)\right]\prod_{\mathrm{i}=1}^{N}(x_{\mathrm{i}}\gamma_{\mathrm{i}})^{\beta_{\mathrm{i}}} \tag{3.10}$$

Where:

r = rate of reaction (dependent)

k = Arrhenius factor (dependent)

T_{abs} = absolute temperature (K)

T_0 = reference temperature (K)

n = temperature exponent

E = activation energy (kJ/mol)

R = universal gas constant (J/(mol·K))

N = number of species in the reaction

x_{i} = mole fraction of a specific component (mol/mol)

γ_{i} = activity coefficient of a specific component

β_{i} = the stoichiometric coefficient of a specific component in the reaction equation

A reduced power law expression was used because T_0 was not specified, and the temperature exponent n was set to zero. The pre-exponential factor and activation energy need to be specified. These parameters, shown in Table 3.3 are expressed as activity base rate constants calculated by Zhang and Chen [9], based on the molarity basis rate constants presented by Hikita et al. [10] and Pinsent et al. [11].

Table 3.3: Kinetic parameters used in Equation (3.10).

Related Species	Reaction No.	Reaction Direction	k kmol/m^3·s	E kJ/mol
HCO_3^-	(3.6)	Forward	1.33×10^{17}	55471
	(3.7)	Reverse	6.63×10^{16}	107417
$MEACOO^-$	(3.8)	Forward	3.02×10^{14}	41264
	(3.9)	Reverse (Absorbing Column)	5.52×10^{23}	69158
	(3.9)	Reverse (Stripping Column)	6.50×10^{27}	95384

3.2.4 Thermodynamic Model

The thermodynamics adopted for the DCC model are based on work conducted by Zhang et al. [12]. Here, an electrolyte non-random two-liquid (ELECNRTL) activity coefficient model accounted for liquid phase nonideality [13], and a perturbed-chain statistical associating fluid theory (PC-SAFT) equation of state (EOS) accounted for vapour phase properties [14,15].

3.2.5 Transport Property Models

Transport property models are required for rate-based process models to calculate the correlations of variables that describe phenomena such as heat transfer, mass transfer, interfacial areas, liquid holdup, pressure drop etc. [16]. Table 3.4 summarises the models used in Aspen Plus for the calculations in this work.

Table 3.4: Physical property models used in the simulation for liquid and gas phases.

Parameter	Liquid Model	Gas Model
Density	Clarke Density Model	PC-SAFT EOS Model
Viscosity	Jones-Dole Electrolyte Correction Model	Chapman-Enskog Wilke-Lee Model
Surface Tension	Onsager-Samaras Model	-
Thermal Conductivity	Riedel Electrolyte Correction Model	Stiel-Thodos Model
Binary Diffusivity	Nernst-Hartley Model	Chapman-Enskog Wilke-Lee Model

3.2.6 The Aspen Plus Radfrac™ Model

Based on the guidance provided by Madeddu et al. [17], the RadFrac™ model was chosen for the ACP absorber and stripper columns to accurately represent the fundamental properties governing their operation. This model describes the non-ideal thermodynamics, chemical reactions, interphase transfer, and component transport in different phases and fluid dynamics, making it suitable for a chemical absorption model. Key parameters needing to be defined for the model include: calculation approach, bulk fluid modelling, film modelling and the number of column stages.

3.2.6.1 Rate-Based Calculation Mode

Two different calculation approaches are available in the RadFrac™ model: “Equilibrium” and “Rated-Based” modes. It is widely agreed in the open literature that the “Rate-Based” approach is superior for most circumstances [16, 18–23]. The “Rate-Based Mode” accounts for mass transfer limitations caused by the presence of chemical reactions, based on Lewis and Whitman’s two-film theory [24]. This theory partitions the gas phase and liquid phase into bulk and film regions, separated by an interface. The driving force permits mass transfer of a gaseous species from the bulk gas, into the gas film, across the interface into the liquid film, and finally into the bulk liquid. In comparison, the “Equilibrium” mode tends to oversimplify complex separation processes and does not directly consider the column designs and operating conditions, often leading to inaccurate performance predictions. Consequently, the “Rate-Based Mode” has been chosen for this study to better represent mass transfer calculations.

3.2.6.2 Bulk Modelling

Only one input is required to describe the bulk: the “Flow Model” within the RadFrac™ settings. Among several available options, the “Mixed Flow” option, which assumes bulk conditions equal to the outlet conditions, was selected. This choice maintains the columns as a series of continuous stirred-tank reactors (CSTRs) [25], following the approach outlined by Zhang et al. [16] and Errico et al. [18].

3.2.6.3 Film Modelling

According to the two-film theory, reactions only occur in the film zones, creating a rapid, non-linear CO_2 mole fraction profile during the absorption process [26]. In the RadFrac™ model's Rate-Based mode, options are available to describe the resistances of the gas and liquid films. For the gaseous phase, where no reactions are occurring, diffusion resistance is accounted for using the "Consider Film" option. In the liquid film, where fast chemical reactions are present, the "Discretize Film" option is used to accurately describe the diffusion resistance and reaction profile by discretising the film. The fast reactions in the liquid film necessitate a small number of discretisation points near the gas-liquid interface. Based on recommendations by Madeddu et al. [25] and Kucka et al. [26], this work adopts five discretisation points for the DCC model. Additionally, "Geometric Discretization" is enabled, requiring further parametric specification.

The Reaction Condition Factor (RCF) weights the contributions of the interface and bulk conditions in the calculation of the reaction rate and empirical values are determined that have been demonstrated to adjust the reaction rates to represent measured conditions. Varying between 0 and 1, a larger value of the RCF is required when film reactions are rapid, and the bulk conditions must hold a higher weight. The RCF is set to 0.9 as agreed upon by Madeddu et al. [25] and Zhang et al. [16]. The Film Discretization Ratio (FDR) determines the width of the segments in the liquid film, with values larger than 1 shrinking the segments and moving them towards the interface. An FDR value of 10 was found to be a good balance between discretisation points and segment width [25].

3.2.6.4 Number of Stages

Determining the correct number of stages for accurate column simulation is challenging and often overlooked in open literature. Ideally, the number of stages should represent the profiles observed in experimental data. However, Madeddu et al. [25] note that there is no clear correlation between the number of stages and column height in various absorber setups, which complicates predicting the required stages for this work.

Madeddu et al. [25] also show that during a specific experimental run, accurate profile representation only emerged at higher stage counts, at least 80 stages were needed for profile overlap, and a temperature bulge in the profile appeared only after 30 stages. To avoid losing important details due to low resolution, 100 stages will be used in this work for both columns to ensure a higher resolution of the profiles.

3.2.7 DCC Model Development Summary

A summary of the key design parameters used in the development of the DCC model is presented in Table 3.5.

Table 3.5: Summary of key design parameters used in the simulation.

Parameter	ACP Model Basis	References
Modelling Approach	Rate-Based Approach	[24]
Number of Stages	100	[17]
Flow Model	Mixed	[16,18]
Film Resistance Options	Liquid Phase: "Discretize film" Vapour Phase: "Consider film"	[17]
Liquid Film Discretisation	Discretisation Points = 5 Discretisation Ratio = 10	[17,26]
Reaction Condition Factor	0.9	[16]
Mass Transfer Coefficient Model	Onda-68 (PACT) Brf-85 (TERC)	[27,28]
Heat Transfer Coefficient Model	Chilton and Colburn	[29]
Interfacial Area Model	Onda-68 (PACT) Brf-85 (TERC) Interfacial Area Tuning Factor = 1.2	[21,28]
Fractional Liquid Hold-Up Model	Stichlmair89	[30]
Flooding Method	Wallis	[31]

3.2.8 Introduction to the CCSI Model

During the development of the DCC model, an investigation into existing models in the open literature was conducted. One such model is the United States Department of Energy's Carbon Capture Simulation Initiative (CCSI) MEA Steady-State Model [32,33], proposed as the "gold standard" for a MEA-based capture system model and is compatible with Aspen Plus V10 and above. This comprehensive process model contains various user-developed models within its library, including physical property models for viscosity, density, surface tension and diffusivity, as well as models for hydraulics, interfacial interactions and reaction kinetics [32]. The CCSI model was developed and validated against the Pilot Solvent Test Unit (PSTU) at the National Carbon Capture Centre (NCCC) in Wilsonville, Alabama [34,35], with no additional tuning to enhance the model representation [32].

The physical property models for viscosity, density and surface tension in the system were developed as described by Morgan et. al. [36] and are implemented as FORTRAN user models. The thermodynamic framework is based on UT Austin's Phoenix Model [37], represented by the ELECNRTL method in Aspen Plus V11.0 and calibrated by fitting data for various components. The kinetic model adopted a simplified reaction system of two equilibrium reactions from the Phoenix model, and followed the methodology presented by Mathias and Gilmartin [38]:

$$2MEA + CO_2 \leftrightarrow MEA^{+} + MEACOO^{-} \quad \textbf{(3.11)}$$

$$MEA + CO_2 + H_2O \leftrightarrow MEA^{+} + HCO_3^{-} \quad \textbf{(3.12)}$$

The hydraulic models, which include pressure drop and hold-up, were developed by Chinen et al. [39]. The Billet and Schutes correlation was regressed using data from Tsai [40] for MellapakPlus™ 250Y packing, which is comparable to the MellapakPlus™ 252Y packing used in the PSTU at the NCCC. Parameters for the interfacial area, mass transfer coefficient and diffusivity models were evaluated using wetted wall column data from Dugas [41] and pilot plant data from Tobiesen et al. [23], achieved using the CCSI software Framework for Optimisation, Quantification of Uncertainty, and Surrogates (FOQUS) [42]. A list of suggested simulation variable ranges, based on those considered at the NCCC, are provided in Table 3.6.

Table 3.6: Suggested ranges for CCSI simulation variables [32].

Variable	Units	Range
Solvent Concentration	wt.%	25 – 35
Lean Solvent Loading	mol/mol	0.05 – 0.50
Lean Solvent Flow Rate	kg/h	3000 – 12000
Flue Gas Flow Rate	kg/h	1250 – 3000
Reboiler Heat Duty	kW	150 – 700

The underlying sub-models remained unchanged for this work, with the columns of the PACT/TERC ACP recreated to the same dimensions specified in Table 3.1. The absorber and stripper column models used MellapakPlus™ 252Y packing because the mass transfer and hydraulic models were developed specifically for this packing [32]. The absorber and stripper column models have 90 and 41 stages, respectively, unchanged to ensure proper model functionality. The absorber column included "Pumparounds", functioning as an intercooled absorber model, where a portion of the flowing solvent is removed from the absorber column and cooled before returning back to the column. The ACP does not have absorber intercooling, so these were set to a minimal flow rate of 0.01 kg/h to minimise their influence on performance because the CCSI model cannot run without them activated. Further details on the complete development of the CCSI model are available in the open literature [32].

3.2.9 Model Convergence Logic

The DCC and CCSI models have had two independent, sequential design specifications added to achieve model convergence. The first design specification ensured that the system achieved the target capture efficiency, calculated by measuring the difference in CO_2 mass flow rate between the incoming and exiting flue gas around the absorber, after contact with the lean solvent stream. If the specified capture efficiency was not achieved, the model iterated the CO_2 loading of the lean solvent stream to adjust the solvent cyclic capacity, which was defined as the difference between the rich and lean solvent CO_2 loadings for a given condition, allowing for more or less CO_2 capture to take place until the target was met.

The second design specification balanced the CO_2 loading of the hot lean solvent exiting the stripper column with the CO_2 loading of the lean solvent entering the absorber that achieved the target capture efficiency in the first design specification. The model compared the CO_2 loadings of both streams and adjusted the reboiler heat duty in the stripper column between iterations until the calculated loadings were equal. When both of these design specifications successfully converge in sequence the simulation functions as a closed loop representation of the target capture condition, allowing for results to be collected to describe the outcomes.

3.3 Model Validation

No single process simulation model can perfectly represent a given ACP, since each has its own strengths and limitations which will depend upon the basis against which the model was developed. Models can be refined for closer approximation of specific plants and operating conditions; therefore, it is essential to validate both the DCC and CCSI models against existing plant data to assess their accuracy and determine their suitability for process simulation predictions. The aim of validation was to identify which model was more representative of the TERC ACP, so it can be used to predict outcomes that will inform an experimental campaign. This experimental campaign would then be used to further refine the chosen model. Validation was conducted in two stages: first, the model was compared against published data from the ACP available in the open literature, and second, against new preliminary data following structural changes to the ACP.

3.3.1 PACT ACP Validation

The DCC and CCSI models were initially validated using existing PACT ACP data from a study by Akram et al. [3]. A capture efficiency of approximately 90% was achieved for each CO_2 concentration in the PACT campaign, by varying the solvent flow rate. For simulation purposes, trace compounds and elements were omitted from the flue gas, therefore comprising carbon dioxide, water, oxygen and nitrogen. The models achieved converged for all reported conditions. The complete results of the PACT ACP validation are presented in Table 3.7. Figure 3.2 presents the SRD results of the DCC and CCSI models for each CO_2 concentration case.

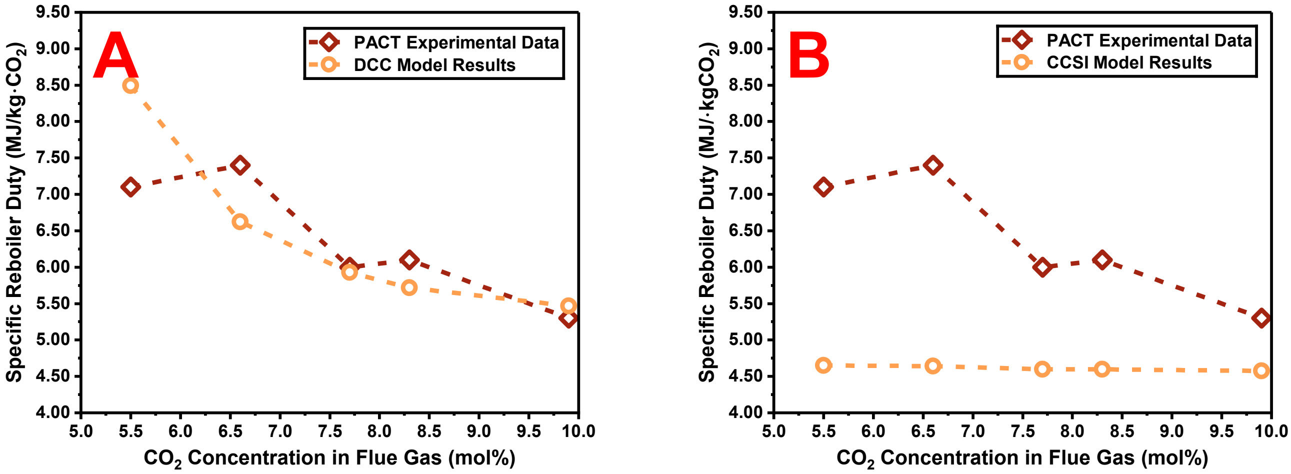

Figure 3.2: Specific reboiler duty against flue gas CO_2 concentration for: (A) PACT ACP and DCC model, and (B) PACT ACP and CCSI model.

The SRD predictions from the DCC model show good agreement with the experimental results in Figure 3.2A, with deviations generally decreasing as CO_2 concentration increases. This reduction enhances confidence in the model predictions to be extrapolated to higher CO_2 concentrations beyond the tested range. Akram et al. [3] discussed how solvent concentration affected SRD results, noting that the MEA concentrations in the 6.6 and 8.3 mol.% CO_2 cases were lower than expected. This was likely due to water transfer from the wash column to the absorber to compensate for evaporative losses, which dilutes the solvent concentration and removes energy from the system. The addition of cold water necessitates extra energy to maintain the process temperature, increasing the overall regeneration energy required for the diluted solvent, due to the consequent higher specific heat capacity. Since the DCC model does not account for water transfer, it predicts lower SRD values for these two cases.

The 5.5 mol.% CO_2 case exhibits a larger discrepancy in SRD from the experimental value. According to Akram et al. [3], a solvent flow of 400 kg/h is the minimum required for this column size and packing to avoid channelling. The DCC model overpredicts SRD at low solvent flow rates and fails to converge at rates significantly below 400 kg/h, due to the increasing proportion of water vapor generated in the reboiler. However, this limiting case does not reflect typical operating conditions, and the SRD results remain valid for the range of cases modelled.

The SRD predictions from the CCSI model show significant deviation from the experimental results, indicating a substantial error. The CCSI model consistently underpredicts the SRD in all cases and does not follow the expected trend. Notably, the predicted SRD remains constant despite variations in flue gas CO_2 concentration, as shown in Figure 3.2B. In contrast, the DCC model offers a much closer approximation to the experimental results.

The underlying absorption chemistry is fundamental to the capture process. The stoichiometry of the reaction between MEA and CO_2 shows that 2 moles of MEA react with 1 mole of CO_2, yielding a theoretical maximum CO_2 loading of 0.5 mol·CO_2/mol·MEA. However, CO_2 loadings higher than this can be observed owing to physical dissolution [43,44]. To determine which reaction model more accurately represented the absorption chemistry of CO_2 in MEA, the solvent loadings and capacities predicted by the DCC and CCSI models were compared with the experimental results, as presented in Figure 3.3.

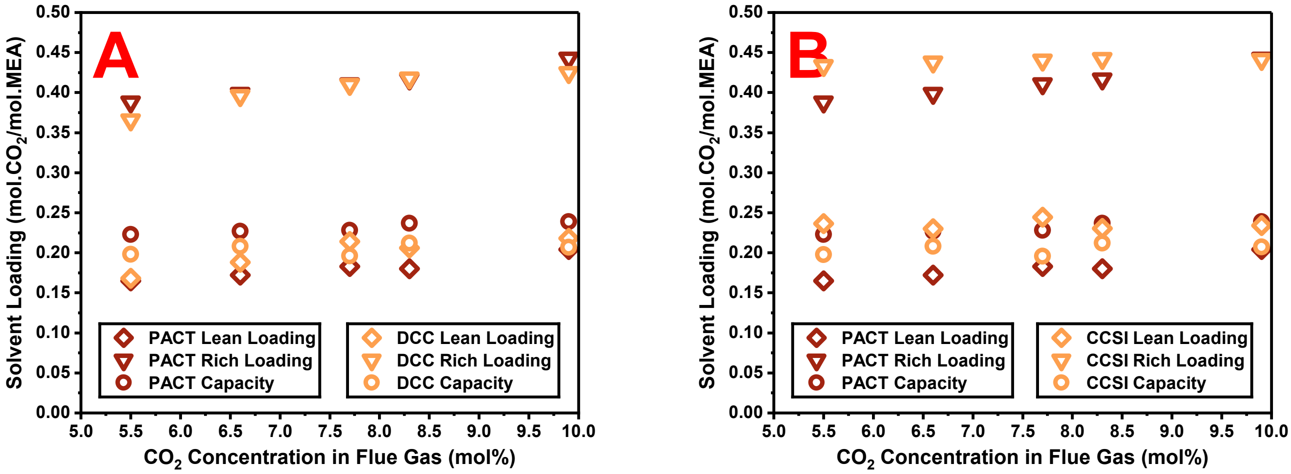

Figure 3.3: Comparison of solvent loadings and capacities against flue gas CO_2 concentration for: (A) PACT ACP and DCC model, and (B) PACT ACP and CCSI model.

Assessment of the DCC model revealed it accurately represented the PACT rich loadings, as shown in Figure 3.3A. The predicted rich loadings increased with CO_2 concentration, indicating that the solvent was not fully saturated with CO_2 while still achieving the target capture efficiency. The corresponding predicted lean loadings also increased with CO_2 concentration but had a higher level of deviation from the experimental values. This discrepancy is due to the DCC model's convergence logic, where the lean loading is iteratively adjusted until the target capture efficiency is achieved. Although the DCC model slightly overpredicted the lean loading, resulting in a slightly smaller solvent capacity compared to the reported PACT data, this overprediction is minimal. Coupled with the SRD in Figure 3.2A aligning well, this provided confidence in the DCC model predictions.

In comparison, the CCSI model deviated from the expected trend in Figure 3.3B by generally over predicting rich loadings. The predicted rich loadings remained constant despite the variation in flue gas concentration, suggesting that the solvent achieved a maximum loading dictated by the reaction chemistry. However, this led to the corresponding lean loadings being significantly overpredicted for each condition. Notably, the solvent capacities for both models were consistent across individual cases, achieving the same capture efficiency, confirming their direct relationship and resulting in similar mass balances. This consistency showed that the convergence logic of the model was effective, regardless of the reaction chemistry used. However, the difference in solvent loadings highlighted the variations in the reaction chemistry of the models. The DCC model, with its more comprehensive system of reaction equations, aligned more closely with the PACT data, compared to the simplified approach used in the CCSI model.

Column temperature profiles provide crucial insights into column operation, as discussed in Chapter 2. For simulation models to make accurate predictions, they must reproduce these temperature distributions with sufficient accuracy. Figure 3.4 presents the temperature profiles of the PACT experimental data, taken from Akram et al. [3] since the original data was unavailable for direct reconstruction.

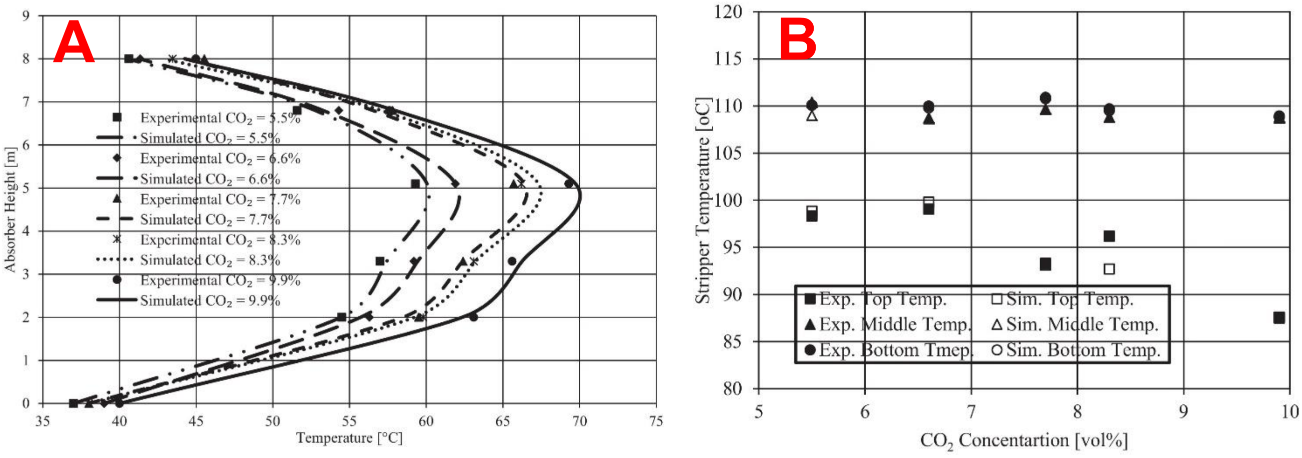

Figure 3.4: (A) absorber, and (B) stripper temperature profiles with varying flue gas CO_2 concentrations for the PACT ACP, graphs taken from Akram et al. [3].

The absorber temperature profile in Figure 3.4A was generated from temperature monitoring measurements, taken at various heights in the column, as well as in the inlet and outlet gas streams. In contrast, the stripper temperature profile in Figure 3.4B is less detailed, with measurements recorded only at the top, middle and bottom of the column. A separate process simulation model was developed in Aspen HYSYS by Akram et al. [3] to represent the PACT plant, with those comparative predictions also shown in Figure 3.4.

The absorber temperature profiles predicted by the DCC and CCSI models are presented in Figure 3.5.

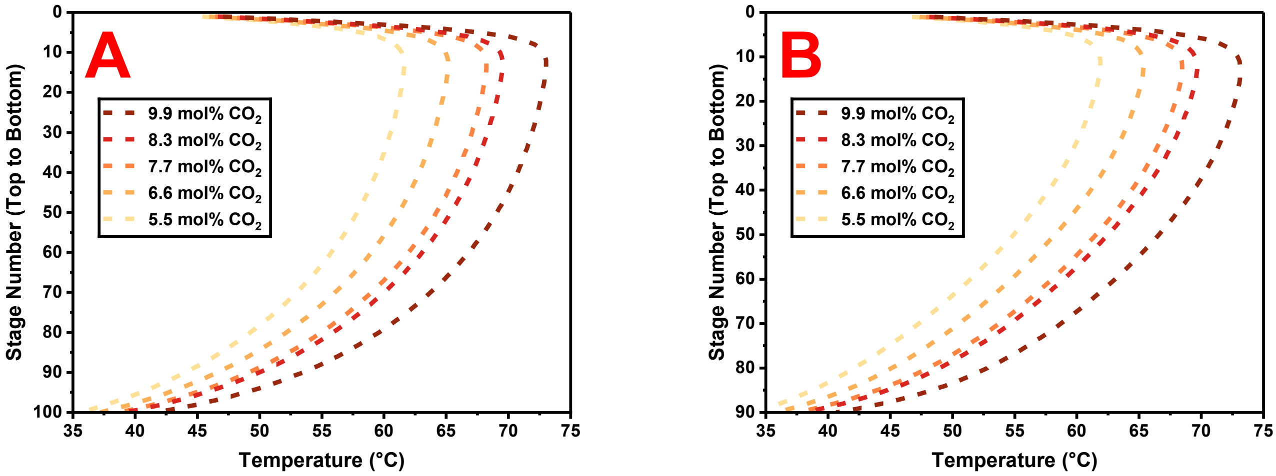

Figure 3.5: Predicted absorber temperature profiles with different flue gas CO_2 concentration cases using (A) the DCC model, and (B) the CCSI model.

The exothermic reaction between MEA and CO_2 creates a temperature bulge within the absorber column, indicating the region of highest reaction activity. The PACT absorber data presented by Akram et al. [3] suggests that this bulge is occurring just above the mid-point of the column, implying that the majority of the CO_2 absorption happens just below where the lean solvent enters the column, providing the maximum driving force for mass transfer.

In contrast, the DCC and CCSI models, as shown in Figure 3.5, depict an idealised version of this process, predicting the temperature bulge higher up the absorber than observed in the PACT data. This discrepancy is likely due to the flow model selected in Aspen Plus, where the vapour and liquid phases are well mixed throughout the absorber, and the absence of any liquid distributor representation within the column. Additionally, the difference in temperature bulge locations may arise from side reactions occurring experimentally [3], which are not accounted for in the models. The maximum predicted temperatures align with the experimental values but are overpredicted by approximately 3 °C for each idealised case. The temperature profiles between the DCC and CCSI models were consistent, suggesting that absorber temperature profiles can remain similar between models while achieving the same capture efficiencies, even when the underlying solvent loading chemistry differs.

The stripper temperature profiles predicted by the DCC and CCSI models are presented in Figure 3.6, with temperatures reported at the top, middle and bottom of the column to maintain consistency with Figure 3.4B.

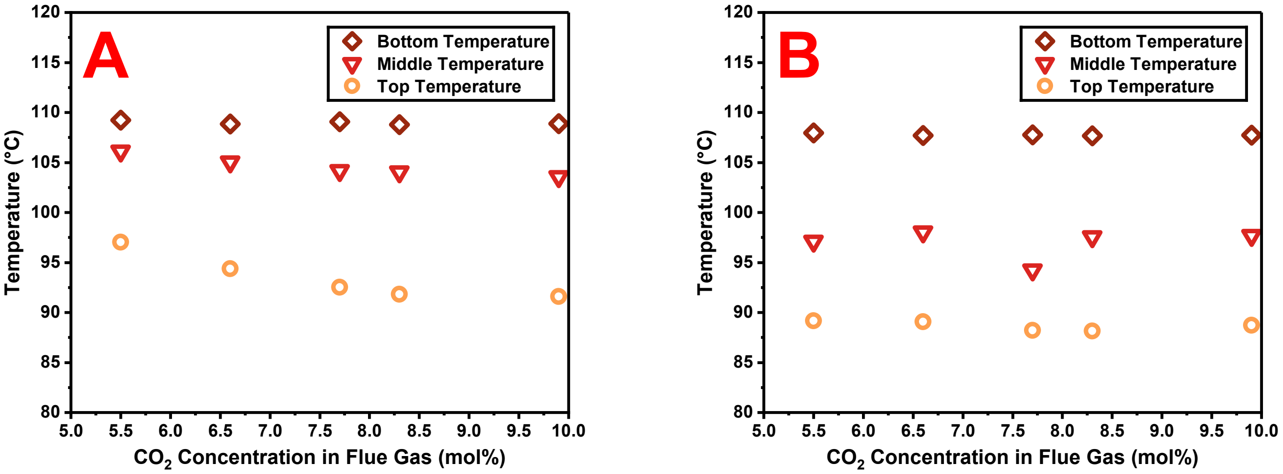

Figure 3.6: Predicted stripper temperature profiles with different flue gas CO_2 concentration cases using (A) the DCC model, and (B) the CCSI model.

The flue gas CO_2 concentration also influences the temperature profile of the stripper column, primarily due to the varying solvent flow rates needed to achieve the target capture efficiency. Figure 3.6A illustrates the DCC model predictions for different flue gas CO_2 concentrations at the same temperature distribution points as the PACT data. The DCC model confirmed a similar column top temperature trend as observed in the PACT data, where the temperature decreased as CO_2 concentration increased, resulting from the higher solvent flow rates required for CO_2 capture. The DCC model also predicted a gradual decrease in top temperature with increasing CO_2 concentration. The predicted bottom temperatures closely align with the PACT data, due to the stripper column pressure affecting the solvent boiling point. The predicted middle temperature was slightly lower than the PACT data, implying that the DCC model represented an idealised system with a smoother temperature gradient down the column, whereas the experimental data revealed operation towards the exponential region of the column.

In contrast, the CCSI model deviated significantly from the expected temperature profile, as shown in Figure 3.6B. The top and middle temperatures were underpredicted in all cases, indicating a much smoother temperature distribution descending the column than either the DCC model predicted, or the PACT data demonstrated.

Comparing the DCC and CCSI models with the PACT data demonstrated that the DCC model represented the experimental results more accurately than the CCSI model. The DCC model predicted representative SRD and chemistry data, with column temperature profiles that approximate the observed behaviour, albeit with an idealised stripper column temperature profile. In contrast, the CCSI model significantly underpredicted SRD, incurred solvent loadings that did not align with observed results and did not represent the stripper temperature profile accurately. Consequently, the decision has been made to focus on further developing the validated DCC model, rather than amending the CCSI model to represent the experimental PACT ACP conditions better.

Table 3.7: PACT ACP validation results.

Parameter	Units	PACT	DCC	CCSI	PACT	DCC	CCSI	PACT	DCC	CCSI	PACT	DCC	CCSI	PACT	DCC	CCSI
Flue Gas CO$_2$ Concentration	mol.%	5.5	5.5	5.5	6.6	6.6	6.6	7.7	7.7	7.7	8.3	8.3	8.3	9.9	9.9	9.9
Overall Solvent Mass Flow Rate	kg/h	400.00	400.32	406.55	488.00	489.65	494.12	567.00	571.06	574.97	604.00	607.36	610.55	721.00	723.21	725.75
Solvent MEA and H$_2$O Mass Flow Rate	kg/h	-	384.83	384.83	-	469.92	469.92	-	543.30	543.30	-	580.66	580.66	-	688.68	688.68
Solvent MEA Mass Flow Rate	kg/h	-	127.60	127.60	-	145.91	145.91	-	179.74	179.74	-	179.99	179.99	-	219.91	219.91
Solvent H$_2$O Mass Flow Rate	kg/h	-	257.23	257.23	-	324.01	324.01	-	363.56	363.56	-	400.66	400.66	-	468.77	468.77
Solvent CO$_2$ Mass Flow Rate	kg/h	-	15.49	21.72	-	19.74	24.20	-	27.76	31.67	-	26.71	29.89	-	34.53	37.07
Flue Gas Mass Flow Rate	kg/h	242.10	242.10	242.10	245.80	245.80	245.80	246.40	246.40	246.40	247.90	247.90	247.90	248.80	248.80	248.80
Flue Gas CO$_2$ Mass Flow Rate	kg/h	21.10	19.97	19.97	24.19	24.19	24.19	29.60	28.13	28.13	31.90	30.42	30.42	38.00	36.12	36.12
Flue Gas Volumetric Flow Rate	m^3/h	-	209.83	209.82	-	213.19	213.18	-	211.82	211.81	-	212.46	212.45	-	212.86	212.85
Liquid to Gas Ratio	kg/kg	1.65	1.65	1.68	2.00	1.99	2.01	2.30	2.32	2.33	2.40	2.45	2.46	2.90	2.91	2.92
Solvent to CO$_2$ Ratio	kg/kg	19.9	19.27	19.27	20.60	19.42	19.42	21.10	19.31	19.31	20.70	19.09	19.09	21.70	19.07	19.07
Flue Gas Temperature	°C	37	37	37	39	39	39	38	38	38	38	38	38	40	40	40
Lean Solvent Temperature	°C	40	40	40	40	40	40	40	40	40	40	40	40	40	40	40
Lean Solvent Concentration (CO$_2$ Free)	wt.%	31.9	31.9	31.4	29.9	29.8	29.5	31.7	31.5	31.3	29.8	29.7	29.5	30.5	30.4	30.3
Rich Solvent Concentration (CO$_2$ Free)	wt.%	30.80	31.68	31.23	27.80	29.58	29.34	30.60	31.19	31.00	27.50	29.34	29.21	29.10	30.03	29.93
Lean Solvent Loading	mol/mol	0.165	0.168	0.236	0.172	0.188	0.230	0.183	0.214	0.245	0.180	0.206	0.231	0.204	0.218	0.234
Rich Solvent Loading	mol/mol	0.388	0.366	0.434	0.399	0.396	0.438	0.411	0.410	0.440	0.417	0.418	0.442	0.443	0.425	0.441
Solvent Capacity	mol/mol	0.223	0.198	0.198	0.227	0.208	0.208	0.228	0.196	0.196	0.237	0.212	0.212	0.239	0.207	0.207
Absorber Bottom Temperature	°C	-	35.6	34.1	-	37.2	35.8	-	38.7	37.5	-	39.2	38.0	-	41.7	40.6
Cross-Heat Exchanger Duty	kW	-	20.16	19.53	-	24.43	23.62	-	26.84	25.70	-	28.70	27.57	-	32.92	31.36
Stripper Approach Temperature	°C	-	89.7	88.3	-	90.1	88.8	-	89.3	87.8	-	89.2	87.9	-	89.9	88.7
Stripper Bottom Temperature	°C	110.4	109.2	108.0	108.8	108.8	107.7	109.7	109.1	107.8	108.8	108.8	107.7	108.8	108.9	107.7
Stripper Pressure	bara	1.2	1.2	1.2	1.2	1.2	1.2	1.2	1.2	1.2	1.2	1.2	1.2	1.2	1.2	1.2
Stripper Reboiler Heat Duty	kW	40.00	42.61	23.44	48.60	40.23	28.18	45.00	41.73	32.37	49.40	43.59	35.07	48.50	49.83	41.74
Specific Reboiler Duty	MJ/kg·CO$_2$	7.10	8.49	4.65	7.40	6.62	4.64	6.00	5.93	4.60	6.10	5.72	4.60	5.30	5.47	4.58
Degree of Solvent Regeneration	%	57.50	53.97	45.54	56.90	52.57	47.48	55.50	47.73	44.46	56.80	50.71	47.89	54.00	48.74	46.97
CO$_2$ Capture Efficiency	%	90.80	90.80	90.80	90.30	90.30	90.30	90.00	90.00	90.00	90.20	90.20	90.20	90.80	90.81	90.80

3.3.2 TERC ACP Validation

Following validation of the DCC model against the PACT ACP, the model was updated to reflect the newer TERC configuration. This updated configuration was then validated against preliminary data from the TERC ACP. The test case involved a gas flow of 200 Nm^3/h with a CO_2 concentration of 5 mol.%, treated with a solvent flow of 300 kg/h containing 40 wt.% MEA. The stripper pressure was set at 1.5 bara, and the stripper reboiler duty was varied to achieve different steady state capture efficiencies around 90% capture. Both the lean solvent and flue gas temperatures were maintained at 40 °C. Flexipac 1X was selected as the packing material to represent the absorber column internals. This packing had the closest dimensions [45] to the absorber packing material used in reality, Flexipac 350X, which was not available in the Aspen Plus V11.0 database. For consistency between the PACT and TERC conditions, the absorber diameter was fixed at 300 mm and a sensitivity analysis conducted to assess the impact of changes in column diameter. The analysis demonstrated that the SRD would increase by a maximum of 1.7% for a column diameter of 250 mm, a change considered negligible.

While absorber and stripper column temperature profiles were unavailable for this preliminary trial, the calculated experimental SRD and chemistry data, along with the prior validation against the PACT ACP, provided sufficient confidence in the DCC model performance with the TERC ACP to use the predictions. Figure 3.7 presents the SRD for each capture efficiency, as well as solvent loadings data for one representative condition.

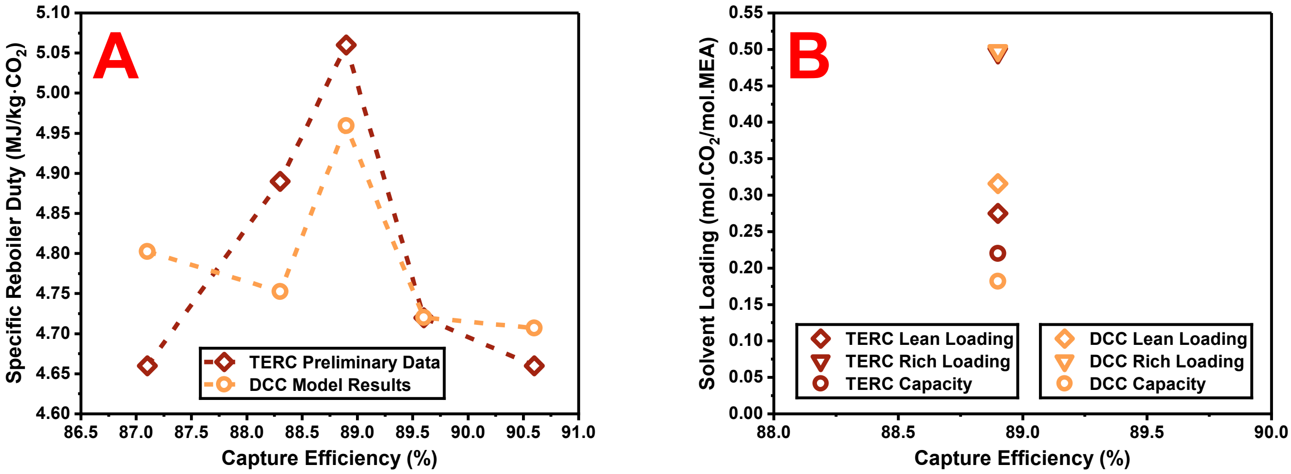

Figure 3.7: Specific reboiler duty against capture efficiency for (A) preliminary TERC ACP cases, with (B) corresponding solvent loadings data for 88.9% capture efficiency.

The SRD predictions from the DCC model closely aligned with the experimental results. The predicted solvent loadings for the TERC ACP corroborated the trends observed with the PACT ACP. While the predicted rich loading agreed with the TERC data sample, the lean loading was slightly over-predicted, resulting in a lower reported solvent capacity. The change in absorber column between PACT and TERC had negligible impact upon solvent loading predictions because the capture efficiency was imposed via design specifications as described in Section 3.2.9.

The SRD predictions for the TERC ACP were noticeably lower than those from the PACT validation, supporting the assertion by Akram et al. that a taller absorber with additional packing reduces SRD for the system [3]. Given that the DCC model performed well against the PACT absorber temperature profiles, it is reasonable to expect similar performance for the TERC absorber temperature profile predictions, given the accurate representation of the TERC absorber's height, diameter and packing in Aspen Plus.

The stripper column configuration remains unchanged between the PACT and TERC systems, meaning the conclusions from the PACT validation also apply to the TERC validation. The stripper column successfully modelled regeneration of the solvent to the correct lean loading with an SRD comparable to the preliminary TERC data, confirming the DCC model's robustness in handling different MEA concentrations and stripper column conditions.

With the validation of the DCC model complete, it was subsequently used in a sensitivity analysis to assess the impact of various operating parameters on the system, detailed in the following section.

3.4 Sensitivity Analysis

A sensitivity analysis was conducted to inform optimisation of the DCC model by systematically varying key input parameters and observing their effects on simulation outputs. The analysis used a base comparator condition detailed in Table 3.8, selected from a series of preliminary predictions and chosen because the parameters lay well within the plant operating limits, making it suitable for assessment across a range of operating conditions. The parameters listed in Table 3.9 were adjusted systematically to evaluate the impact upon predicted ACP performance.

Table 3.8: Base comparator case parameters for input to the DCC model.

Parameter	Units	Value
Flue Gas Volumetric Flow Rate	m^3/h	150
Flue Gas CO_2 Concentration	mol.%	20
Flue Gas Temperature	°C	40
Solvent MEA and H_2O Mass Flow Rate	kg/h	700
Solvent MEA Mass Flow Rate	kg/h	245
Solvent H_2O Mass Flow Rate	kg/h	455
Lean Solvent Concentration (CO_2 Free)	wt.%	35
Lean Solvent Temperature	°C	40
Stripper Pressure	bara	1.2
Cross Heat Exchanger Duty	kW	43
CO_2 Capture Efficiency	%	90

Table 3.9: Sensitivity analysis parameters and operating ranges investigated for the DCC model.

Parameter	Analysis Range
Flue Gas Composition	Air Basis, BFG, CO_2/N_2
Flue Gas Temperature	10 – 100 °C
Lean Solvent Temperature	10 – 60 °C
Lean Solvent Concentration	20 – 80 wt.%
Solvent Mass Flow Rate	500 – 1200 kg/h
CO_2 Capture Efficiency	20 – 95%
Stripper Pressure	1.0 – 2.0 bara

3.4.1 Flue Gas Composition

Before conducting the full sensitivity analysis, it was necessary to assess the variation in flue gas composition while keeping the CO_2 content fixed. This step aimed to identify any impacts that alternative flue gas compositions might have on the DCC model predictions. Three flue gases were evaluated: air with a CO_2 injection, a representative BFG composition, and a CO_2/N_2 blend. All three flue gases had a fixed H_2O content of 3.2 mol.%, based on the average in the study by Akram et al. [3]. Table 3.10 presents the key results from this analysis.

Table 3.10: Key results for DCC model sensitivity with respect to flue gas composition.

Parameter		Units	Flue Gas Basis		
			Air + CO_2	BFG	CO_2/N_2
Flue Gas Composition	CO_2	mol.%	20.00	20.00	20.00
	CO	mol.%	0.00	20.00	0.00
	H_2	mol.%	0.00	3.00	0.00
	H_2O	mol.%	3.20	3.20	3.20
	N_2	mol.%	60.52	53.80	76.80
	O_2	mol.%	16.28	0.00	0.00
Overall Solvent Mass Flow Rate		kg/h	744.26	744.26	744.26
Solvent CO_2 Mass Flow Rate		kg/h	44.26	44.26	44.26
Flue Gas Mass Flow Rate		kg/h	184.33	175.96	180.52
Flue Gas CO_2 Mass Flow Rate		kg/h	51.44	51.44	51.44
Liquid to Gas Ratio		kg/kg	4.04	4.23	4.12
Solvent to CO_2 Ratio		kg/kg	13.61	13.61	13.61
Rich Solvent Concentration (CO_2 Free)		wt.%	36.70	36.70	36.70
Lean Solvent Loading		mol/mol	0.251	0.251	0.251
Rich Solvent Loading		mol/mol	0.513	0.513	0.513
Solvent Capacity		mol/mol	0.263	0.263	0.263
Absorber Bottom Temperature		°C	42.5	42.5	42.5
Stripper Approach Temperature		°C	103.0	103.0	103.0
Stripper Bottom Temperature		°C	109.3	109.3	109.3
Stripper Reboiler Heat Duty		kW	47.28	47.28	47.28
Specific Reboiler Duty		MJ/kg·CO_2	3.67	3.67	3.67
Degree of Solvent Regeneration		%	51.16	51.16	51.16
CO_2 Capture Efficiency		%	90.00	90.00	90.00

The analysis demonstrated that varying the flue gas composition with a fixed CO_2 content had no impact on the model results, since all three compositions produced identical outcomes. The only exceptions are the flue gas mass flow rate and the corresponding L/G ratio, which varied based on the flue gas composition and consequent changes in mass. The solvent to CO_2 ratio, which directly compares the CO_2 content in the flue gas against the solvent flow rate, remains constant across all three compositions. This consistency is expected because the DCC model's chemistry only accounted for the CO_2 absorption into MEA, with no reactions involving other gases present. This finding indicated that the presence of the other gases considered did not affect any other predicted results. Practically, this means that any of the flue gas compositions can be used for modelling purposes and be considered representative. For the remainder of the modelling predictions, an air-based flue gas composition was utilised, given that experimental campaigns are likely to use an air or a CO_2/N_2 basis, due to the ease of creating these mixtures and the reduced health and explosive risks compared to using CO or H_2 in a pilot plant.

3.4.2 Flue Gas Temperature

The DCC model's sensitivity to flue gas temperature was assessed by varying the temperature from 10 to 100 °C in 10 °C increments, representing a typical operating range for the system. Although temperatures above 40 °C are uncommon due to the use of heat recovery systems to minimise energy wastage, the assessment extended up to 100 °C to evaluate the system's response without such a recovery system in place. To maintain consistent modelling conditions, the mass flow of the flue gas was kept constant for each assessed temperature, even as the volumetric flow varied with temperature. This approach ensured that the same mass flow of CO_2 in the flue gas was treated at each temperature. Figure 3.8 presents the results of four key performance metrics for assessment.

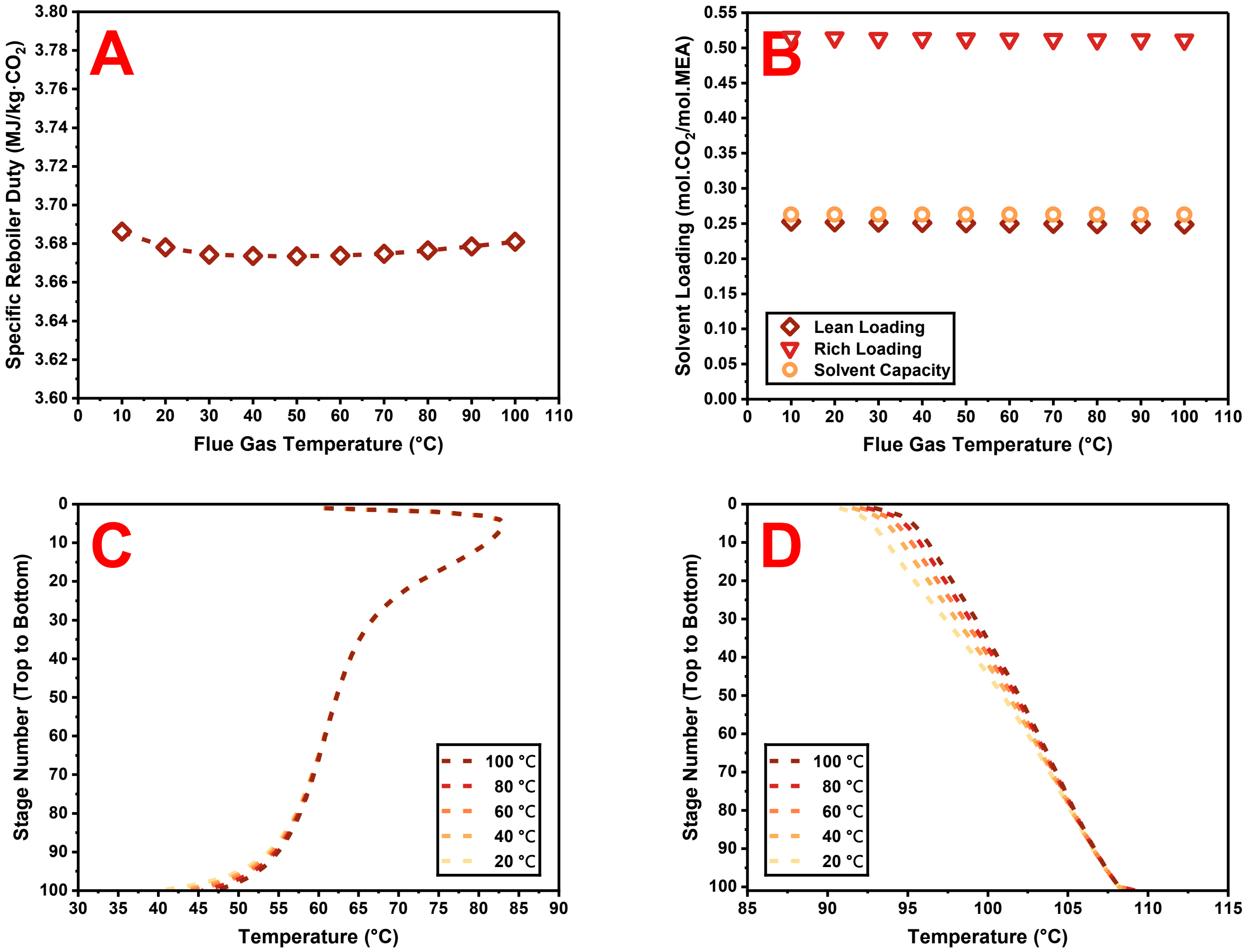

Figure 3.8: Key performance metrics for DCC model sensitivity with respect to flue gas temperature: (A) specific reboiler duty, (B) solvent loadings and capacity, (C) absorber temperature profiles, (D) stripper temperature profiles.

It is evident that varying the flue gas temperature had a negligible impact on the SRD for the system in Figure 3.8A. This is due to the higher specific heat capacity of the downflowing lean solvent compared to the rising flue gas, allowing a significant amount of energy exchange into the gas with minimal change in solvent temperature. This is shown in Figure 3.8C, where the absorber temperature profiles remain nearly identical for all flue gas temperatures modelled, until the bottom of the column, where a slight deviation occurs at the initial contact point between the gas and solvent. The temperature profiles exhibited rich-pinched behaviour, evident through peak temperatures near the top of the column, driven by the low L/G ratio of 4.04, which concentrates the exothermic CO_2 absorption reactions at the top.

The stripper temperature profiles in Figure 3.8D are also very similar between cases, with only a slight increase in top temperature as the flue gas temperature increased. This change is influenced by the absorber bottom temperature and the cross-heat exchanger. As the flue gas temperature increases, there is a small rise in absorber bottom temperature. The fixed heat input from the cross-heat exchanger then raises the stripper approach temperature, causing subtle changes in the stripper temperature profile. Despite these variations, the stripper temperature profiles converge into a consistent shape, resulting in nearly identical SRD values across the flue gas temperature range. The temperature profiles indicate operation around the inflection point, with temperatures increasing steadily down the column due to the smooth energy exchange from vapour to liquid.

Figure 3.8B shows that varying flue gas temperatures had little effect on the solvent loadings, with every case having consistent solvent capacity achieving 90% capture efficiency. The expected impact on reaction kinetics is minimal due to the significant thermal energy difference between the flue gas and lean solvent, which stabilises the solvent loadings and absorber temperature profiles.

In conclusion, flue gas temperature had negligible impact on DCC model predictions. Real-world plants should seek to recover useful heat from the flue gas before it enters the absorber column to avoid wasting energy.

3.4.3 Lean Solvent Temperature

The DCC model's sensitivity to lean solvent temperature was assessed by varying the temperature from 10 to 60 °C in 10 °C increments, representing a typical operating range for the system. Temperatures higher than 60 °C are uncommon, because the lean solvent typically passes through a cooler before entering the absorber column. Similarly, temperatures below 10 °C are rare, because the system's sensible heat maintains an ambient temperature above the freezing point of the lean solvent, preventing damage to the pipework. Figure 3.9 presents the results of four key performance metrics for assessment.

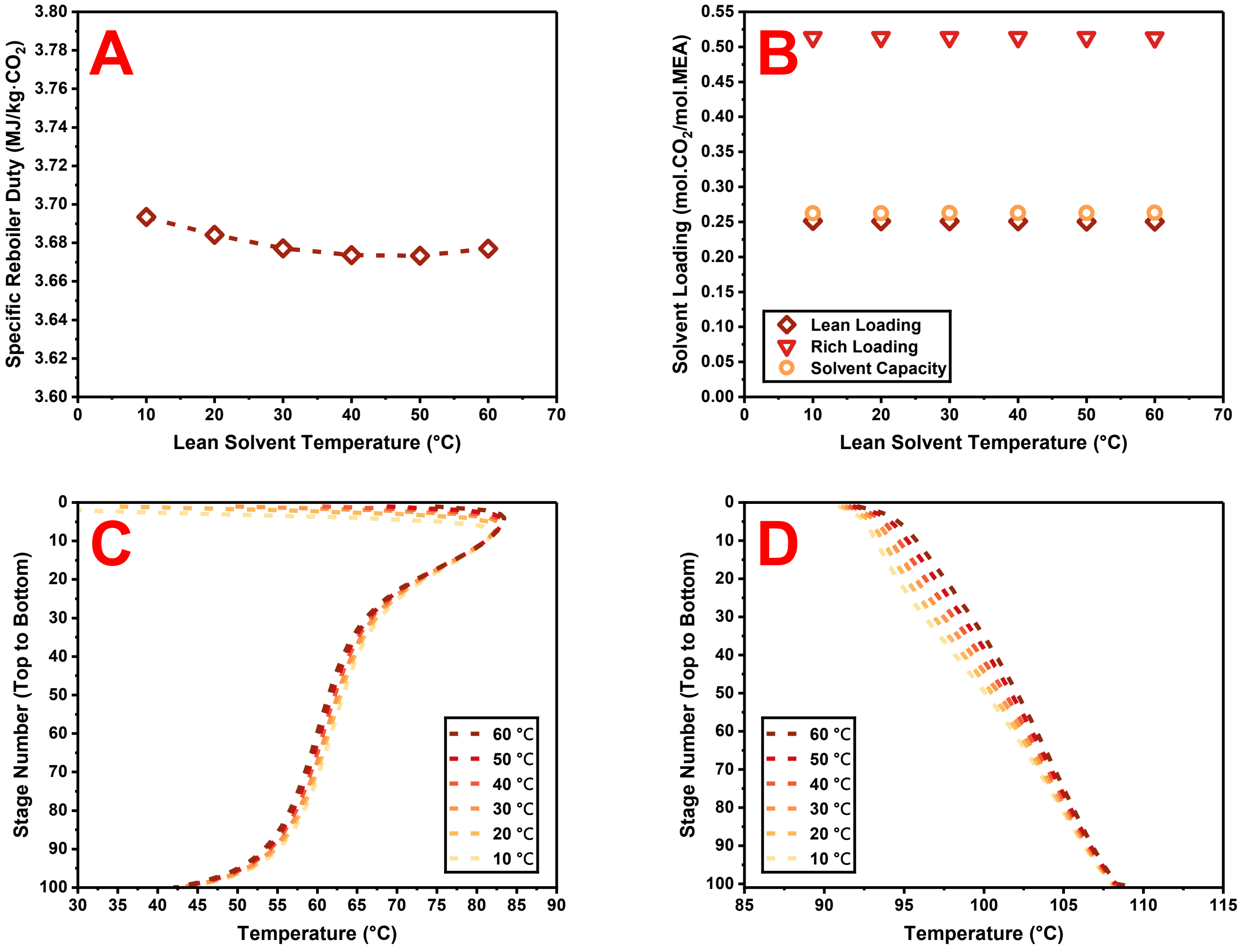

Figure 3.9: Key performance metrics for DCC model sensitivity with respect to lean solvent temperature: (A) specific reboiler duty, (B) solvent loadings and capacity, (C) absorber temperature profiles, (D) stripper temperature profiles.

It is evident that varying the lean solvent temperature has negligible impact on the system's SRD, as shown in Figure 3.9A, similar to the effects observed with flue gas temperature. Figure 3.9B demonstrates that solvent loadings remain consistent across different lean solvent temperatures, indicating minimal impact on reaction kinetics in achieving the target capture efficiency. The absorber column temperatures in Figure 3.9C are also similar across cases, exhibiting rich-pinched behaviour primarily influenced by the unchanged L/G ratio of 4.04, with only minor effects from solvent temperature. When the lean solvent contacts the flue gas at the top of the absorber column, the exothermic reaction rapidly heats the solvent. Changes in solvent temperature affected the temperature profile due to the solvent's higher specific heat capacity compared to the flue gas, but this temperature effect is minor. A cooler solvent results in a slightly lower peak temperature and lower peak height within the column, as it takes longer to heat up. This reduces the residence time for the flue gas to cool the descending rich solvent, leading to an increase in the absorber bottom temperature. If the reaction kinetics are affected by the changes in lean solvent temperature, their impact on the temperature profile is overshadowed by the effects of the L/G ratio and specific heat capacity of the solvent.

The stripper temperature profiles in Figure 3.9D resemble those in Figure 3.8D, showing divergence near the top of the column across different lean solvent temperature before converging towards the bottom. The system's SRD remained optimised, with the stripper operating near the inflection point, as variations in lean solvent temperature were not substantial enough to affect overall performance.

In conclusion, lean solvent temperature had negligible impact on the DCC model predictions, similarly to flue gas temperature. Thus, real-world plants should recover useful heat from the lean solvent before it enters the absorber column to avoid energy wastage.

3.4.4 Lean Solvent Concentration

The DCC model’s sensitivity to lean solvent concentration was assessed by varying the solvent concentration from 20 to 80 wt.% in 5 wt.% increments, covering the theoretical operating range for the system. Concentrations above 40 wt.% are less common due to the increasing corrosiveness of the solvent, the system damage incurred likely outweighing any benefits offered. However, higher solvent concentrations are feasible in alternative capture units such as RPBs, so they were included for assessment. The DCC model does not account for degradation products or system damage, instead presenting an idealised scenario where detrimental effects of solvent corrosiveness were neglected. Figure 3.10 presents the results of four key performance metrics for assessment.

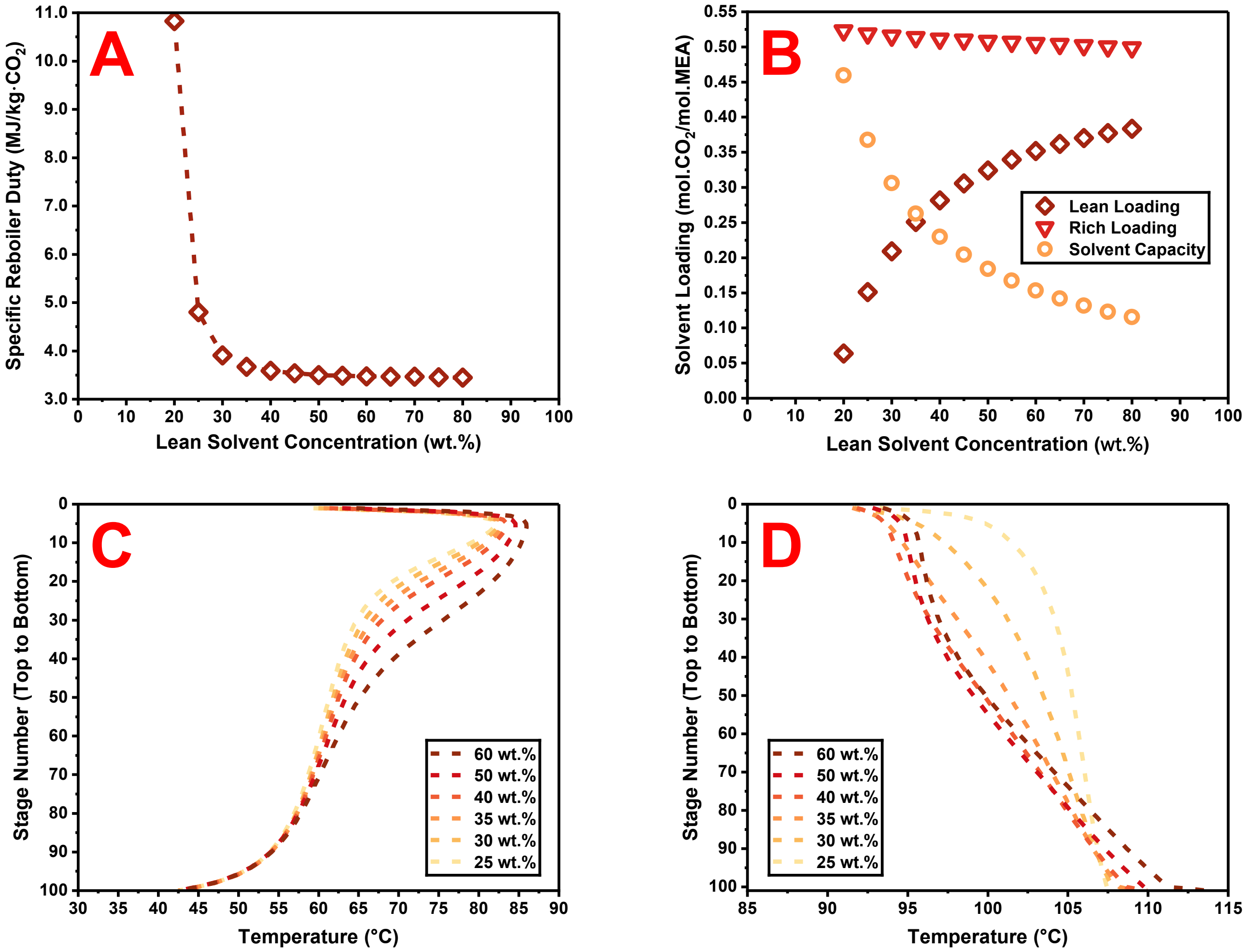

Figure 3.10: Key performance metrics for DCC model sensitivity with respect to lean solvent concentration: (A) specific reboiler duty, (B) solvent loadings and capacity, (C) absorber temperature profiles, (D) stripper temperature profile.

Varying the lean solvent concentration significantly impacts the system’s SRD, as shown in Figure 3.10A. At low solvent concentrations the SRD required to achieve the target capture efficiency is extremely high. As concentration increases, the SRD drops sharply, until reaching a concentration of around 40 wt.%. Beyond this point, further increases in concentration leads to diminishing returns on SRD. This trend can be explained by the solvent loadings and capacities shown in Figure 3.10B. At a low solvent concentration of 20 wt.%, achieving the target capture efficiency requires a very high solvent capacity, necessitating an extremely low lean loading. Lowering the lean loading is energy intensive, demanding a higher reboiler duty and resulting in a high SRD. As solvent concentration increases, more MEA is available to capture CO_2, reducing the required solvent capacity, lean loading and associated reboiler duty. Additionally, less water is present as the solvent concentration increases, meaning less energy wasted on heating and vaporising water, further reducing SRD. This effect on SRD diminishes with further increases in solvent concentration because of the heat of absorption associated with the solvent regeneration, which still requires a large baseline energy input to liberate the CO_2 from the solvent.

The absorber temperature profiles in Figure 3.10C supported this explanation, showing rich-pinched behaviour primarily driven by the unchanged L/G ratio of 4.04, with additional effects from varying solvent concentration. At low solvent concentrations, the MEA completed reactions with CO_2 near the top of the column to achieve the required solvent capacity for the target capture efficiency. As the solvent concentration increased, lean loading rose, reducing the solvent capacity and causing CO_2 absorption to extend further down the column. This shift in the exothermic reaction zone led to higher temperatures further down the column, before cooling and converging into similar absorber bottom temperatures between the solvent concentrations.

The stripper temperature profiles in Figure 3.10D illustrate why SRD is extremely high at low solvent concentrations. For a concentration of 35 wt.%, the system operates near the inflection point, minimising the SRD. At solvent concentrations above 35 wt.% the system begins to transition into the baseline region but does not have a significant impact on the SRD, as discussed above. For concentrations below 35 wt.%, however, the system enters the exponential region, where a high energy input is demanded to regenerate the solvent to lower lean loadings, which leads to an increasing amount of water vapour generated by the reboiler as a consequence. This vapour cannot fully condense within the column, wasting its energy of vaporisation and causing the SRD to spike.

In conclusion, lean solvent concentration significantly influences DCC model predictions. However, practical considerations must be made in real-world plants, as higher solvent concentrations are corrosive and will damage the system. Typically, a concentration between 30 and 40 wt.% is selected, depending on capture requirements.

3.4.5 Solvent Mass Flow Rate

The DCC model's sensitivity to solvent mass flow rate was assessed by varying the pure solvent flow rate, defined as the combined mass flow of MEA and water and excluding the CO_2 associated with the lean loading, from 500 to 1200 kg/h in 100 kg/h increments (50 kg/h increments near the optimal flow rate), representing a typical operating range for the system. The upper operational limit of 1200 kg/h, as specified by the TERC ACP, was initially assessed, then gradually reduced until it was clear that the minimum SRD, indicative of the optimal solvent flow rate, had been surpassed. Figure 3.11 presents the results of four key performance metrics for assessment.

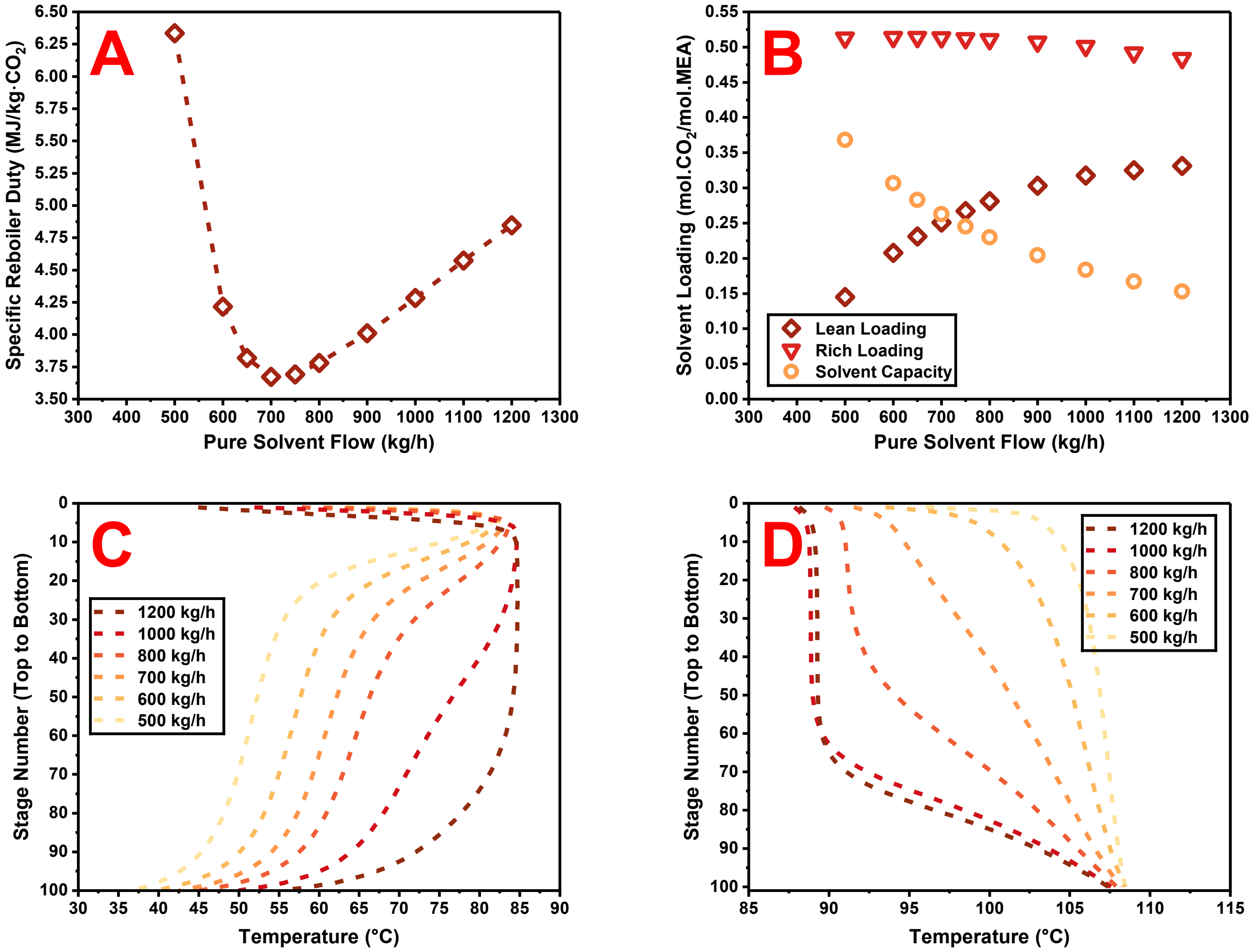

Figure 3.11: Key performance metrics for DCC model sensitivity with respect to pure solvent mass flow rate: (A) specific reboiler duty, (B) solvent loadings and capacity, (C) absorber temperature profiles, (D) stripper temperature profiles.

The L/G ratio is a crucial factor in CO_2 capture, so it unsurprising that changing the solvent mass flow rate significantly impacts the SRD, as shown in Figure 3.11A. The optimal pure solvent flow rate, where the SRD was minimised, approximated 700 kg/h. Below this rate, SRD increases sharply as the system requires a larger solvent capacity, achieved by reducing lean loading to meet the target capture efficiency, as evident in Figure 3.11B. This effect is similar to lowering the lean solvent concentration, as seen in Figure 3.10. Increasing the pure solvent flow rate above the 700 kg/h optimal also raises the SRD, primarily due to energy wastage from heating and vaporising the additional water in the solvent flow. The solvent loadings and capacities in Figure 3.11B resemble those in Figure 3.10B, reflecting a similar balance of loadings achieved either by increasing solvent flow or solvent concentration.

The absorber temperature profiles in Figure 3.11C show a transition from rich-pinched to bulge-pinched as the solvent flow rate increases. This occurs because the principal reaction region shifts downward in the column with increasing solvent flow, resulting in a pronounced temperature bulge in the middle of the column at the limits of operation.

The stripper temperature profiles in Figure 3.11D illustrate the three typical operational behaviours across the solvent flow range. At the optimal pure solvent flow rate of 700 kg/h, the stripper operates at the inflection point, with a smooth energy transition and temperature rise from top to bottom, minimising the SRD. Below the optimal flow rate, the profiles shift to the exponential region due to excessive water vapour generation, leading to a rapid SRD increase as the column struggles to regenerate the solvent. Above the optimal flow rate, the profiles enter the baseline region, with minimal temperature variation until the lower column stages, where a rapid temperature rise occurs. This occurs because the increasing mass flow rate of incoming rich solvent causes the vapour to condense near the bottom of the column. As a result, more energy is required to heat and vaporise the additional water present along with the MEA, thereby increasing the SRD.

In conclusion, that solvent mass flow rate significantly influences DCC model predictions, highlighting the importance of quickly optimising solvent flow in real-world plants to avoid excessive energy wastage. Identification of the optimal solvent flow rate, and the corresponding L/G ratios, are an essential part of this work and cannot be generalised from this sensitivity analysis alone. The optimal solvent flow depends on the mass of CO_2 needing to be captured, influenced by the flue gas volumetric flow and composition, which is explored later in this chapter.

3.4.6 CO_2 Capture Efficiency

The DCC model's sensitivity to CO_2 capture efficiency was assessed by varying the efficiency from 20 to 95 wt.% in 5% increments, with larger 10% increments below 50% capture efficiency, representing a typical operating range for the system. The capture efficiency was adjusted by varying the heat duty of the stripper reboiler, which influenced the lean loading, thereby giving different solvent capacities. Figure 3.12 presents the results of four key performance metrics for assessment.

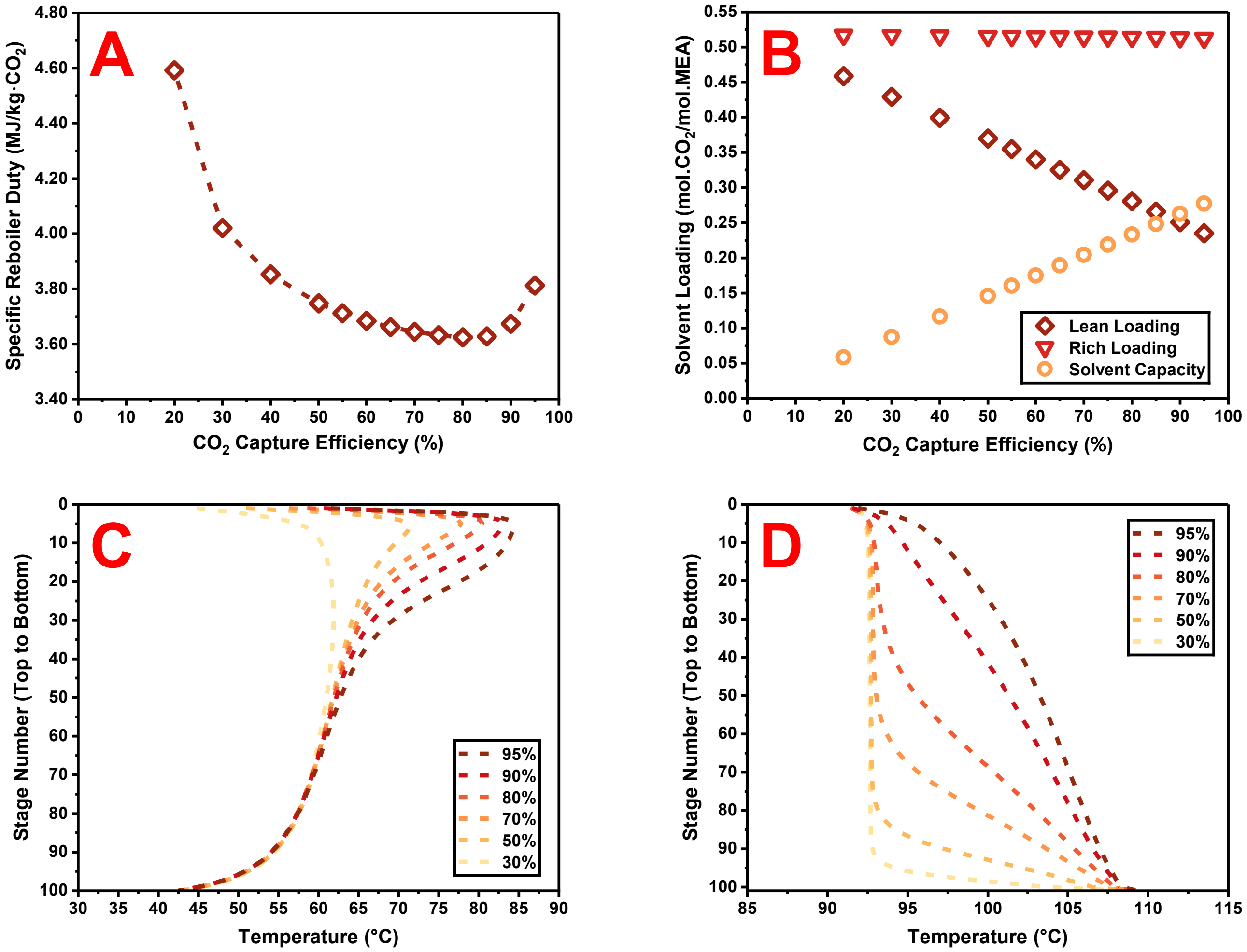

Figure 3.12: Key performance metrics for DCC model sensitivity with respect to CO_2 capture efficiency: (A) specific reboiler duty, (B) solvent loadings and capacity, (C) absorber temperature profiles, (D) stripper temperature profiles.

The impact of capture efficiency on the system's SRD was significant, where the SRD significantly increased at the extreme ends of capture efficiency potential, as shown in Figure 3.12A. Irrespective of the capture efficiency achieved, a considerable input of baseline energy is required to heat and regenerate the solvent. At low capture efficiencies, the SRD is high because the energy input is not offset by substantial CO_2 capture, resulting in inefficient operation. As the capture efficiency increases, the process becomes more SRD efficient, with the initial energy input spread over more captured CO_2. The SRD reaches its minimum at around 80% capture efficiency, with only a slight increase observed when targeting 90% capture efficiency. Achieving capture efficiencies above 90% becomes increasingly challenging, requiring disproportionately more energy from the reboiler to reduce the lean solvent loading even further and increase the solvent capacity, which arises from the generation of additional water vapour and results in a sharp rise in SRD. The trends for lean loading and solvent capacity with respect to capture efficiency are presented in Figure 3.12B, reflecting the necessary increase in solvent capacity for increasing capture efficiency. The inverse relationship between solvent capacity and lean loading is critical to understanding how the system adapts to different target efficiencies with a constant L/G ratio.

The absorber temperature profiles in Figure 3.12C align with the observed trend in solvent capacity. At high capture efficiencies, the increased solvent capacity and corresponding low lean loadings create an environment of high reactivity at the top of the column where most of the CO_2 is absorbed, resulting in a sharp rich-pinched temperature profile. As capture efficiency decreased from 95% to 30%, the absorber temperature profile evolved from a distinct rich-pinched profile to a less defined one, resembling a bulge-pinched profile but with a lower peak temperature than typically observed in such scenarios, due to significantly less CO_2 being captured. The capture efficiency decreased by increasing the lean loading, constraining the solvent capacity and leading to a cooler, less active reaction zone, which produced a rich-pinched profile with a lower peak temperature. All temperature profiles converged near the bottom of the column as reactions ceased, and the solvent is cooled by the incoming flue gas.

The stripper temperature profiles in Figure 3.12D illustrate how changes in capture efficiency influence column operation. For the base case with 90% capture efficiency at the optimal solvent flow rate, the stripper temperature profile is at the inflection point. Adjusting the lean loading, thereby the solvent capacity, to achieve different capture efficiencies corresponds to capturing different mass flows of CO_2. Lower capture efficiency related to a lower mass flow of CO_2, causing the temperature profiles to shift into the baseline region due to excessive amount of solvent circulated compared to the mass necessary to achieve capture for the reduced amount of CO_2. In contrast, capture efficiencies above 90% reflect a higher mass flow of CO_2, requiring a lower lean loading. This results in a shift of the temperature profile towards the exponential region, as the system generates additional water vapour when regenerating the solvent to a lower lean loading.

In conclusion, CO_2 capture efficiency must be carefully considered when assessing flue gas treatment. Operating at a fixed solvent flow rate while varying capture efficiency is energetically inefficient regarding SRD. Instead, adjusting the solvent flow rate based on the mass flow of CO_2 needing to be captured is preferable. Practically, this means that the capture efficiency should be selected and fixed to eliminate it as a variable.

3.4.7 Stripper Column Pressure

The DCC model's sensitivity to stripper column pressure was assessed by varying the pressure from 1.0 to 2.0 bara in 0.1 bara increments, representing a typical operating range for the system. Figure 3.13 presents the results of four key performance metrics for assessment.

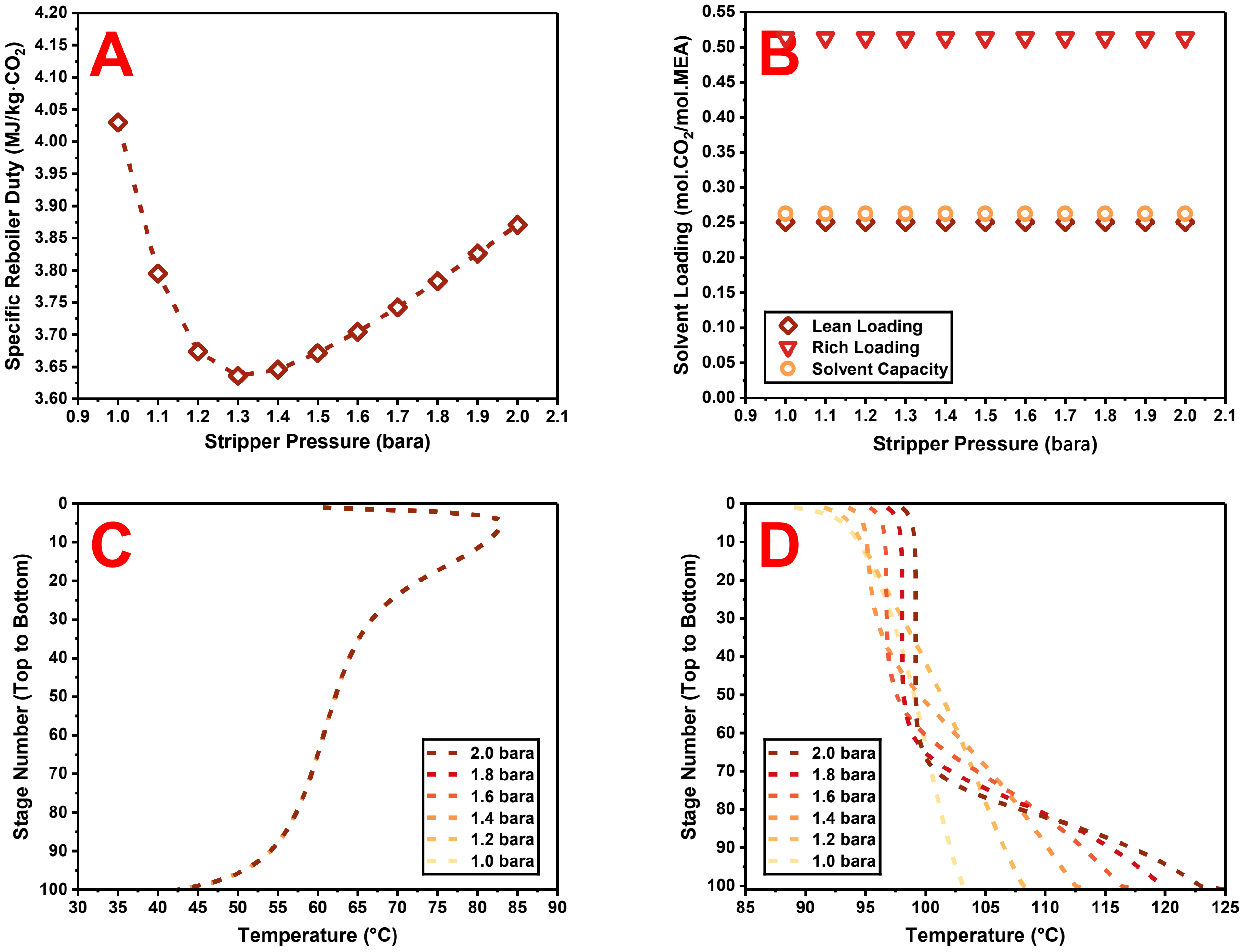

Figure 3.13: Key performance metrics for DCC model sensitivity with respect to stripper column pressure: (A) specific reboiler duty, (B) solvent loadings and capacity, (C) absorber temperature profiles, (D) stripper temperature profiles.

The stripper column pressure is a crucial factor to consider when optimising CO_2 capture, as it significantly impacts the SRD, as shown in Figure 3.13A. It has a significant impact on the SRD alongside the solvent concentration and the solvent mass flow rate for a capture efficiency of 90%. Evidently, the reaction chemistry remains unaffected by changes in stripper pressure, as shown in Figure 3.13B, where the same capture efficiency is achieved across all cases. This outcome is expected since the chemistry is dictated within the absorber column, which, as Figure 3.13C shows, is also unaffected by changes in stripper pressure, as the process units are fundamentally separated. These observations indicate that changes in stripper pressure only directly affect the stripper temperature profiles and the corresponding SRD, as illustrated in Figures 3.13A and 3.13D. However, an additional fact must be considered to fully understand the implications.

As the stripper pressure increases, the bottom temperature increases due to the effect of pressure on the boiling point of the solvent mixture, as shown in Figure 3.13D. This results in a hotter lean solvent stream exiting the stripper and passing through the cross-heat exchanger to preheat the incoming rich solvent. For this analysis, the cross-heat exchanger heat duty is set to a maximum of 43 kW to represent the TERC ACP, which imposes a constraint on the stripper approach temperature. Consequently, the rich solvent enters the top of the stripper at similar temperatures for all pressures above 1.3 bara, requiring an increasing SRD as pressure rises to bring the solvent up to temperature. The deviation observed in top temperatures at stage 0 in Figure 3.13D is due to the incoming condensed solvent mixing with the rich solvent, but the rich solvent enters the stripper at the same temperature for all cases. This constrained evaluation is useful for operating the TERC ACP and other real-world scenarios running at maximum cross-heat exchanger capacity but disguises the true impact of the stripper pressure. If the cross-heat exchanger's heat duty were adjustable to minimise the approach temperature, it is expected that the SRD would continue to decrease with increasing pressure. Ultimately, this demonstrates that the optimal stripper pressure is dependent on the cross-heat exchanger's capacity. As the pressure increases, the hot rich and hot lean approach temperature widens, resulting in a higher SRD for CO_2 capture.

Despite these considerations, valuable insights can still be drawn from the constrained system. An optimal stripper pressure of 1.3 bara, as shown in Figure 3.13A, aligns with a stripper temperature profile in Figure 3.13D that falls between 1.2 and 1.4 bara. This pressure approximates the inflection point of the stripper, reinforcing the concept that the optimal SRD occurs at the inflection point, influenced by the cross-heat exchanger. As pressure and bottom temperature increase, the temperature profiles shift into the baseline region because heat transfer between the steam and incoming rich solvent occurs increasingly towards the bottom of the column.

In conclusion, stripper column pressure is a key factor in system optimisation, but it is heavily influenced by the heat duty of the cross-heat exchanger. The optimal stripper pressure seeks to minimises the SRD subject to the heat duty constraint of the cross-heat exchanger.

3.4.8 Optimisation of an Example Case

Understanding the individual effects of different parameters on the system is important, but it is crucial to also comprehend how these parameters interact with each other for effective optimisation of the system. The order in which variables are optimised must be logical and practical, mirroring real-world adjustments during system optimisation. The process could follow the below steps, where the reboiler heat duty is monitored for each change:

i) Begin with a basic setup: fixed flue gas conditions, an initial solvent flow and initial stripper pressure.

ii) Adjust the solvent concentration to at least 30 wt.% with makeup solvent.

iii) Find the optimal L/G ratio at the target capture efficiency for the chosen solvent concentration.

iv) Adjust the stripper pressure to allow further refinement of the solvent flow rate.

v) Refine the solvent flow rate to maximise heat integration from the cross-heat exchanger.

vi) Adjust the lean solvent temperature, if necessary.

vii) Adjust the flue gas temperature, if possible.

If the cross-heat exchanger is at full capacity, it may also be possible to fix the stripper pressure first, simplifying the solvent flow rate selection to a single step.

An example demonstrates how this optimisation process could be carried out. Table 3.11 shows the optimisation for a 150 m^3/h gas flow with 20 mol.% CO_2, where the flue gas mass flow is held constant. Parameters were tuned sequentially to achieve the lowest SRD in each step. The table should be read from left to right, tracking the optimisation progress. Additionally, Figure 3.14 presents the absorber and stripper temperature profiles for each optimisation step, reading top to bottom in the plot legends.

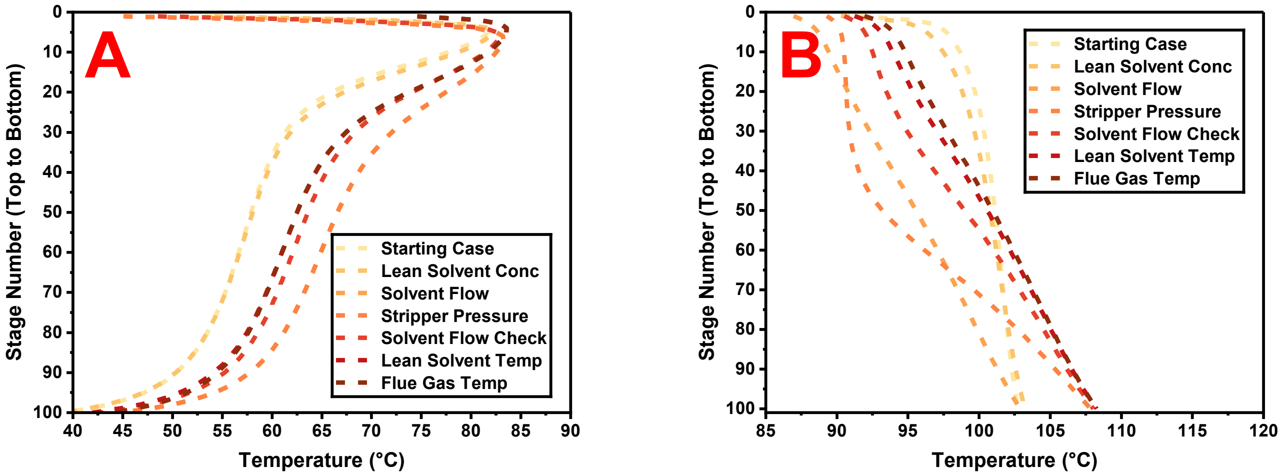

Figure 3.14: Optimisation of an example case with (A) absorber temperature profiles and (B) stripper temperature profiles.

Table 3.11: Optimisation of an example case.

Parameter	Units	Starting Case	Solvent Concentration	Solvent Flow	Stripper Pressure	Solvent Flow Check	Solvent Temp	Flue Gas Temp
Flue Gas CO_2 Concentration	mol.%	20	20	20	20	20	20	20
Overall Solvent Mass Flow Rate	kg/h	620.69	631.52	856.81	856.80	772.50	772.42	772.24
Solvent MEA and H_2O Mass Flow Rate	kg/h	600.00	600.00	800.00	800.00	725.00	725.00	725.00
Solvent MEA Mass Flow Rate	kg/h	180.00	210.00	280.00	280.00	253.75	253.75	253.75
Solvent H_2O Mass Flow Rate	kg/h	420.00	390.00	520.00	520.00	471.25	471.25	471.25
Solvent CO_2 Mass Flow Rate	kg/h	20.69	31.52	56.81	56.80	47.50	47.42	47.24
Flue Gas Mass Flow Rate	kg/h	184.33	184.33	184.33	184.33	184.33	184.33	184.33
Flue Gas CO_2 Mass Flow Rate	kg/h	51.44	51.44	51.44	51.44	51.44	51.44	51.44
Flue Gas Volumetric Flow Rate	m^3/h	150	150	150	150	150	150	150
Liquid to Gas Ratio	kg/kg	3.37	3.43	4.65	4.65	4.19	4.19	4.19
Solvent to CO_2 Ratio	kg/kg	11.66	11.66	15.55	15.55	14.09	14.09	14.09
Flue Gas Temperature	°C	30	30	30	30	30	30	60
Lean Solvent Temperature	°C	30	30	30	30	30	60	60
Lean Solvent Concentration (CO_2 Free)	wt.%	30	35	35	35	35	35	35
Rich Solvent Concentration (CO_2 Free)	wt.%	32.88	36.60	37.47	35.80	36.06	37.74	37.75
Lean Solvent Loading	mol/mol	0.160	0.208	0.282	0.282	0.260	0.259	0.258
Rich Solvent Loading	mol/mol	0.517	0.515	0.511	0.511	0.513	0.513	0.512
Solvent Capacity	mol/mol	0.357	0.306	0.230	0.230	0.253	0.254	0.254
Absorber Bottom Temperature	°C	39.2	39.1	44.8	44.8	42.8	41.9	44.1
Cross-Heat Exchanger Duty	kW	38	38	43	43	43	43	43
Stripper Approach Temperature	°C	101.2	102.1	98.1	98.1	101.1	102.6	103.9
Stripper Bottom Temperature	°C	103.6	104.2	103.9	109.1	109.2	109.4	109.4
Stripper Pressure	bara	1	1	1	1.2	1.2	1.2	1.2
Stripper Reboiler Heat Duty	kW	80.35	64.07	48.78	49.11	47.44	47.03	46.97
Specific Reboiler Duty	$MJ/kg{\cdot}CO_2$	6.25	4.98	3.79	3.82	3.69	3.65	3.65
Degree of Solvent Regeneration	%	69.13	59.53	44.92	44.93	49.38	49.46	49.56
CO_2 Capture Efficiency	%	90.00	90.00	89.99	90.01	90.00	89.99	89.99

The initial condition assumed an MEA concentration of 30 wt.%, a pure solvent flow of 600 kg/h, and a stripper pressure close to atmospheric. This produced a low lean solvent loading to achieve 90% capture efficiency but a correspondingly high SRD. The absorber exhibited a rich-pinched temperature profile, while the stripper operated in the exponential region.

Increasing the solvent concentration to 35 wt.% reduced the SRD from 6.25 to 4.98 MJ/kg·CO_2, a reduction of 20.3%, without significantly increasing corrosion risk. The lean loading increased from 0.160 to 0.208, reducing the solvent cyclic capacity from 0.357 to 0.306 for the same capture efficiency, while absorber and stripper temperature profiles remained largely unchanged.

Optimising the pure solvent flow rate yielded optimal performance at 800 kg/h with an SRD of 3.79 MJ/kg·CO_2, giving an overall SRD reduction of 39.4% from the initial condition. The lean loading increased from to 0.282, further reducing solvent capacity to 0.230. The absorber remained rich-pinched, though temperatures below stage 20 increased by approximately 10 °C, and the stripper profile shifted from the exponential region to the inflection point.

Pressuring the stripper to 1.2 bara increased the bottom temperature but produced little SRD change. However, this enabled further solvent-flow optimisation. The solvent loadings and absorber temperatures were unaffected by the pressurisation, while the stripper profile shifted towards the baseline region, indicating potential for additional SRD reduction.

Fine tuning the pure solvent flow rate to 725 kg/h reduced the SRD to 3.69 MJ/kg·CO_2, an overall SRD reduction of 41.0%. This condition maximised the cross-heat exchanger capacity and minimised the approach temperature between the hot rich and hot lean solvent. Absorber temperatures below stage 20 decreased by approximately 5 °C, while the stripper operation returned to the inflection point. The lean loading decreased to 0.260, increasing the solvent capacity to 0.253.

Adjusting the lean solvent and flue gas temperatures produced only minor additional SRD reductions. At 60 °C for both streams, the final SRD reached 3.65 MJ/kg·CO_2, a total reduction of 41.6% from the initial 6.25 MJ/kg·CO_2, with minimal changes to temperature profiles or solvent loadings.

Overall, this optimisation example demonstrates how operational parameters interact to govern SRD, illustrating how significant energy reductions can be achieved through relatively simple operational adjustments. Process optimisation is therefore a critical aspect of plant operation, enabling energy requirements to be minimised under varying capture conditions. The approach described above can be applied to any flue gas flow rate and composition considered within a conventional PB chemical absorption system. Additional steps may be required depending on the structural configuration of the plant, but the underlying principles remain unchanged.

3.4.9 Model Validation and Sensitivity Summary

The DCC model has been successfully validated for use in performance predictions of the TERC ACP. Having established its predictive accuracy and sensitivity to parameter variation, it will now be employed to conduct the primary simulation study of this thesis. The following sections present the results of this comprehensive modelling study, designed to identify key performance trends and establish operational guidelines under elevated CO_2 conditions. These findings will, in turn, inform the initial conditions and anticipated outcomes of the subsequent experimental campaign.

3.5 Modelling Predictions for Flue Gases with Elevated CO_2

The validated DCC model was used to conduct a comprehensive performance study of the TERC ACP treating flue gases with elevated CO_2 concentrations representative of iron and steelmaking process emissions. The study examined parameters critical to optimising energy consumption and capture efficiency, including: flue gas and solvent flow rates, CO_2 concentration, stripper pressure, and cross-heat exchanger capacity. Trend analysis across these parameters identified optimal operating conditions and provided insight into the underlying process behaviour.

Key results include: SRD trends, optimal L/G ratios, solvent loadings, and the influence of cross-heat exchanger performance and stripper pressure, supported by the analysis of column temperature profiles. The findings demonstrate the interdependence of solvent flow, lean loading, and heat duty in minimising SRD and defining optimal operation, forming the basis for the design and initial conditions of the subsequent experimental campaign.

In the analyses presented in the remainder of this chapter, solvent flow rates are reported on a pure solvent basis, such that the mass of the CO_2 associated with the lean loading is excluded. Consequently, liquid to gas ratios are also expressed on a pure solvent basis as L_{pure}/G, defined as the mass flow rate of CO_2-free liquid solvent relative to the mass flow rate of flue gas. This basis enables controlled variation of solvent circulation independent of lean solvent loading. In contrast, liquid to gas ratios reported for experimental work in the following chapter are expressed on the conventional circulating solvent basis, L/G, which includes the mass of CO_2 associated with the lean loading. The distinction between these two definitions is maintained throughout this thesis and should be considered when comparing quantitative values. However, the qualitative trends observed are unaffected by the choice of basis.

3.5.1 Analysis and Discussion for 90% Capture Efficiency Conditions

A comparison of SRD for a range of solvent flow rates and CO_2 concentrations is presented in Figure 3.15 for three representative gas flow rates, 130, 170, and 210 Nm^3/h, encompassing the majority of the TERC ACP operating envelope and enabling parametric predictions under typical operating conditions. The targeted capture efficiency was 90%, with simulation convergence achieved using the design specifications outlined in Section 3.2.9. CO_2 concentrations ranged from 10 to 25 mol.% in 5% increments for all gas flow rates, with the flue gas water content fixed at 3.2 mol.% based on the validation in Section 3.3. The remaining gas comprised oxygen and nitrogen in the same ratio as in air, representative of the synthetic gas composition planned for use in the experimental campaign. The pure solvent flow rates ranged from 300 to 1200 kg/h to reflect the TERC ACP's operating range. The MEA concentration in the lean solvent was fixed at 35 wt.%, on a CO_2 free basis. The temperatures of the lean solvent stream and flue gas stream were fixed at 40 °C. The stripper pressure was kept constant at 1.2 bara. The cross-heat exchanger minimised the approach temperature between the hot rich and hot lean solvent flows until a heat duty of 43 kW was achieved, representative of the maximum heat exchanger capacity.

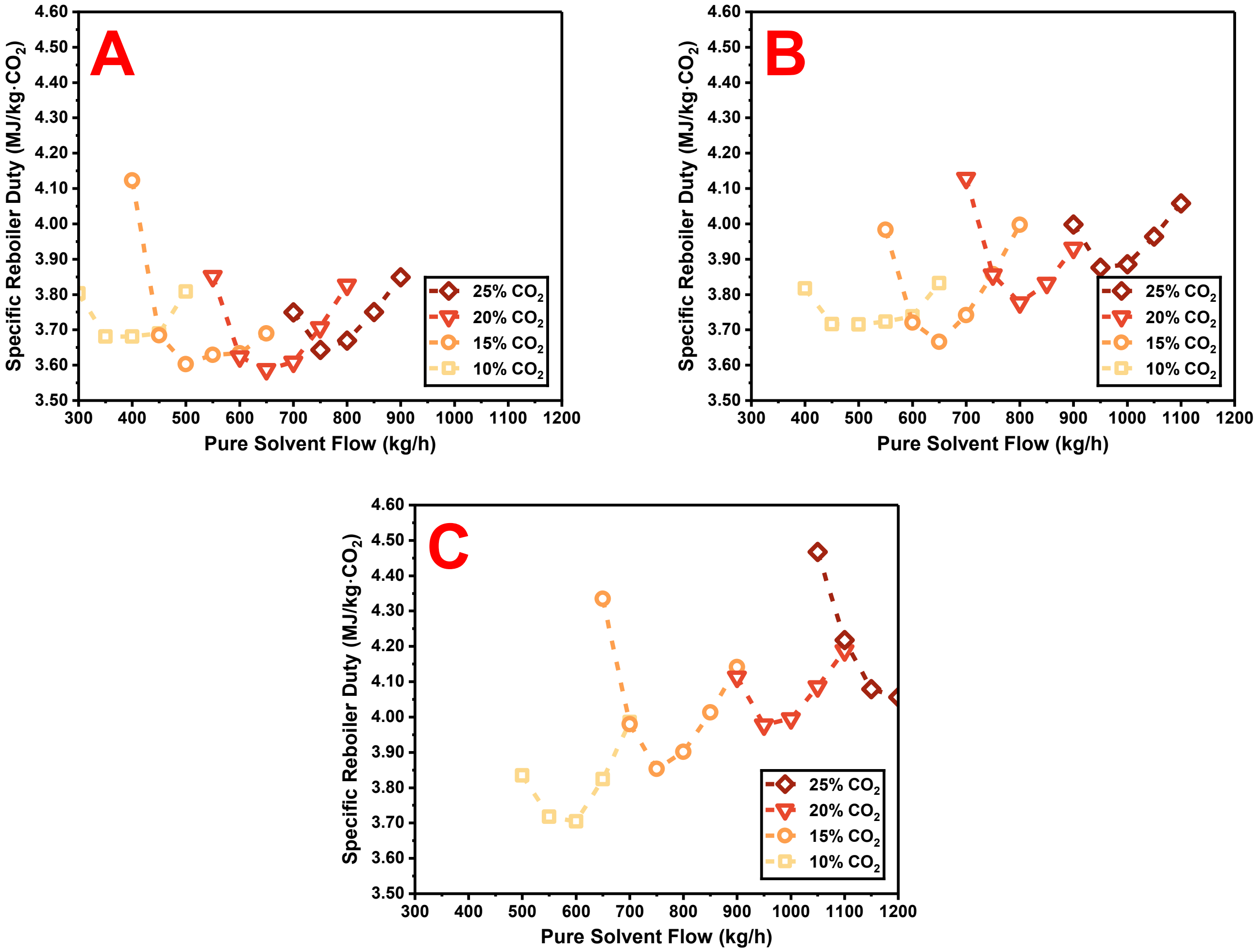

Figure 3.15: Specific reboiler duty against pure solvent flow rate for gas flow rates: (A) 130 Nm^3/h, (B) 170 Nm^3/h, and (C) 210 Nm^3/h for a range of CO_2 concentrations at 90% capture efficiency.

The model predicted a near optimal pure solvent flow rate, and corresponding L_{pure}/G ratio, for all combinations of gas flow rates and CO_2 concentrations, identified as the minimum SRD in Figure 3.15 for each trend. The optimal L_{pure}/G ratio achieves the target capture efficiency while minimising the reboiler heat duty, reflecting the minimised system energy demand for solvent regeneration. Therefore, the optimal L_{pure}/G ratio corresponds to the minimum SRD for capture from a given flue gas condition.

Figure 3.15 provides insight into how the CO_2 concentration of the flue gas relates to the minimum SRD for different gas flow rates. For a gas flow rate of 130 Nm^3/h in Figure 3.15A, the minimum SRD decreased as CO_2 concentration rose from 10 to 20 mol.%, before increasing at 25 mol.%. Similarly, for a gas flow rate of 170 Nm^3/h in Figure 3.15B, the minimum SRD decreased when the CO_2 concentration increased from 10 to 15 mol.%, before increasing again at higher CO_2 concentrations. However, for a gas flow rate of 210 Nm^3/h in Figure 3.15C, the SRD demonstrably increased with increasing CO_2 concentration. This occurs due to the cross-heat exchanger reaching its maximum capacity. As both gas flow rate and CO_2 concentration increase, a higher solvent flow rate is needed to achieve the optimal L_{pure}/G ratio. Consequently, more heat transfer occurs within the cross-heat exchanger, until the maximum heat duty of 43 kW is reached.

Once this limit is reached, the maximum heat transfer occurs in the exchanger, which leads to the widening of the approach temperature with further increases in solvent flow rate because the rich solvent is not preheated efficiently. As a result, the rich solvent enters the top of the stripper at a lower temperature, demanding additional heat input from the stripper reboiler for solvent regeneration. The incremental SRD increase for optimal L_{pure}/G ratios of different CO_2 concentrations in Figure 3.15C corresponds to the additional sensible heat required as solvent flow surpasses the cross-heat exchanger’s capacity. This is crucial for real-world applications because cross-heat exchangers are likely to operate at maximum capacity when handling higher CO_2 concentrations and the associated increased solvent flow rates. Understanding this impact on the SRD is essential for accurate interpretation of the DCC model data.

The predictions presented in Figure 3.15A show that lower solvent flow rates achieved the minimum possible approach temperature with a cross-heat exchanger duty below 43 kW, except at 25 mol.% CO_2, where the heat duty would have slightly exceeded 43 kW if not constrained. This allowed the rich solvent to enter the stripper at the highest possible temperature, resulting in similar optimal SRD values across different CO_2 concentrations at 130 Nm^3/h. These findings indicate that increasing CO_2 concentration does not necessarily increase SRD, which depends on total gas and solvent flow rates, and cross-heat exchanger capacity.

The predictions presented in Figure 3.15B have a range of cross-heat exchanger capacities. For CO_2 concentrations of 10 and 15 mol.%, heat duty remained below 43 kW, while for 20 and 25 mol.%, heat duty was fixed at 43 kW, explaining the rise in SRD with higher CO_2 concentrations. When accounting for the cross-heat exchanger limit, it was clear that increasing total gas flow rates increased the SRD for the same CO_2 concentration, driven by the higher solvent flow required to capture the increased gas flow. This increased the mass of water to be heated and vaporised during regeneration, thereby increasing reboiler duty.

A key trend was observed in the L_{pure}/G ratios across Figure 3.15, showing little variation in optimal L_{pure}/G ratios for the same CO_2 concentrations, regardless of gas flow rate, SRD, or cross-heat exchanger effects. This allows simplification of the data, where only CO_2 concentration needs to be considered to set initial plant operation conditions to achieve 90% capture efficiency. This trend became apparent due to the consistent composition of the modelled flue gas. In real-world applications, the flue gas composition may fluctuate, affecting the mass flow rate of the flue gas and making the L_{pure}/G and conventional L/G ratios less reliable for predictions. The solvent/CO_2 ratio, an extension of the L_{pure}/G ratio, isolates the CO_2 content of the flue gas for comparison and is defined as the mass flow rate of CO_2-free liquid solvent relative to the mass flow rate of CO_2 in the flue gas. This ratio allows for the correct selection of solvent flow rate, regardless of the flue gas composition, providing that the CO_2 concentration is known. The predicted optimal L_{pure}/G and solvent/CO_2 ratios for CO_2 concentrations between 10 and 25 mol.%, achieving 90% capture efficiency, are presented in Table 3.12.

Table 3.12: Optimal L_{pure}/G and solvent/CO_2 ratios for different CO_2 concentrations for gas flow rates of 130, 170, and 210 Nm^3/h achieving 90% capture efficiency using 35 wt.% MEA.

CO_2 Concentration mol.%	130 Nm^3/h		170 Nm^3/h		210 Nm^3/h	
	L_{pure}/G Ratio	Solvent/CO_2 Ratio	L_{pure}/G Ratio	Solvent/CO_2 Ratio	L_{pure}/G Ratio	Solvent/CO_2 Ratio
10	2.5	17.1	2.5	17.1	2.5	17.1
15	3.2	14.9	3.2	14.9	3.2	14.9
20	3.9	14.0	3.9	14.0	3.9	14.0
25	4.6	13.5	4.6	13.5	4.6	13.5

The predicted optimal L_{pure}/G ratio for a given CO_2 concentration remained constant across the gas flow rates of 130, 170 and 210 Nm^3/h, as shown in Table 3.12. This consistency was also observed with the solvent/CO_2 ratio. The optimal L_{pure}/G ratio exhibited a linear increase with CO_2 concentration, increasing by approximately 0.7 for each 5% rise of CO_2 concentration, from 10 to 25 mol.%. This trend allows for the prediction of optimal L_{pure}/G ratios to achieve 90% capture efficiency for gas flow rates within the 130 to 210 Nm^3/h range, and potentially beyond, with caution regarding gas composition. It was evident that the solvent/CO_2 ratio decreased as CO_2 concentration increased. The rate at which the solvent/CO_2 ratio decreased between CO_2 concentrations was not linear, unlike those observed with the L_{pure}/G ratio. This is explained after analysis of the solvent loadings data for these identified optimal ratios, presented in Table 3.13.

Table 3.13: Solvent loadings data at optimal L_{pure}/G ratios for different CO_2 concentrations for gas flow rates of 130, 170, and 210 Nm^3/h achieving 90% capture efficiency using 35 wt.% MEA.

CO_2 Concentration mol.%	Lean Loading			Rich Loading			Solvent Capacity		
	130 Nm^3/h	170 Nm^3/h	210 Nm^3/h	130 Nm^3/h	170 Nm^3/h	210 Nm^3/h	130 Nm^3/h	170 Nm^3/h	210 Nm^3/h
10	0.294	0.293	0.291	0.505	0.503	0.503	0.210	0.210	0.211
15	0.271	0.268	0.266	0.510	0.508	0.506	0.239	0.240	0.240
20	0.259	0.256	0.254	0.514	0.512	0.510	0.255	0.256	0.256
25	0.252	0.247	0.247	0.517	0.514	0.512	0.265	0.267	0.265

The lean and rich loadings, along with the corresponding solvent cyclic capacities, for gas flow rates of 130, 170 and 210 Nm^3/h are presented in Table 3.13. The lean loadings decrease from approximately 0.29 to 0.25 as CO_2 concentration increases from 10 to 25 mol.%, while the rich loadings remain just above 0.5, indicating that maximum solvent saturation has taken place. The predicted solvent capacity rises with increasing CO_2 concentration due to the greater amount of CO_2 needing to be captured.

The solvent capacity was found to be independent of total gas flow for a given CO_2 concentration. Notably, the percentage difference in solvent capacities with increasing CO_2 concentration closely aligns with the percentage difference in solvent/CO_2 ratios from Table 3.12. These findings are presented in Table 3.14.

Table 3.14: Comparison of percentage differences between solvent capacity and solvent/CO_2 ratio with respect to flue gas CO_2 concentration, achieving 90% capture efficiency using 35 wt.% MEA.

CO_2 Concentration mol.%	Solvent Capacity		CO_2 Concentration mol.%	Solvent/CO_2 Ratio	
	Value	Increasing % Difference		Value	Increasing % Difference
10	0.210	-	25	13.5	-
15	0.240	12.5	20	14.0	3.6
20	0.256	6.3	15	14.9	6.0
25	0.265	3.4	10	17.1	12.9

It is evident that the solvent/CO_2 ratio governs the solvent capacity required to achieve 90% capture efficiency across different flue gas CO_2 concentrations. A lower solvent/CO_2 ratio results in a larger solvent capacity, indicating an inverse relationship. Since the solvent/CO_2 ratio is linked to the corresponding L_{pure}/G ratio, it can be inferred that the L_{pure}/G ratio also informs the solvent capacity. Therefore, the linear trend of the L_{pure}/G ratio can be used to predict conditions for achieving 90% capture efficiency across varying CO_2 concentrations when the remaining flue gas composition is a consistent basis. For alternative flue gas compositions with known CO_2 concentrations, the solvent/CO_2 ratio may be used for predictions instead of the L_{pure}/G ratio because the flue gas mass flow rate will vary with composition. Predictions using either method can be verified using solvent loadings data.

The preceding analyses support the conclusion that the optimal solvent/CO_2 ratio, solvent capacity, and consequently the optimal L_{pure}/G ratio, are independent of gas flow rate. Instead, they are determined to be solely a function of capture efficiency and flue gas CO_2 concentration.

The SRD values corresponding to each identified optimal L_{pure}/G ratio are presented in Table 3.15 for the different CO_2 concentrations achieving 90% capture efficiency using 35 wt.% MEA.

Table 3.15: SRD at identified optimal L_{pure}/G and solvent/CO_2 ratios for different CO_2 concentrations for gas flow rates of 130, 170, and 210 Nm^3/h achieving 90% capture efficiency using 35 wt.% MEA.

CO_2 Concentration mol.%	**L_{pure}/G Ratio**	**Solvent/CO_2 Ratio**	**SRD MJ/kg·CO_2**		
			130 Nm^3/h	**170 Nm^3/h**	**210 Nm^3/h**
10	2.5	17.1	3.68	3.71	3.74
15	3.2	14.9	3.60	3.67	3.91
20	3.9	14.0	3.59	3.78	4.00
25	4.6	13.5	3.64	3.88	4.07

Table 3.15 provides insight that led to two main conclusions. Firstly, for a specific CO_2 concentration, the SRD at the optimal L_{pure}/G ratio increases with gas flow rate. This outcome was expected, because higher gas flow rates require increased solvent flow to maintain the same L_{pure}/G ratio. This results in additional water needing to be heated and vapourised, contributing to additional energy consumption. Secondly, for a constant gas flow rate, the trend of SRD with increasing CO_2 concentration is less predictable. This variability was due to the cross-heat exchanger reaching its maximum heat duty under certain capture conditions. Both conclusions align with and reinforce the earlier discussion related to Table 3.12.

3.5.2 *Analysis and Discussion for 95% Capture Efficiency Conditions*

The UK Environment Agency now considers 95% capture efficiency as the attainable standard for new capture plants to meet net zero targets by 2050, shifting from the previous industry target of 90% [46]. To assess the TERC ACP's capability at this higher capture efficiency, the cases investigated in Section 3.5.1 were repeated, this time targeting a 95% capture efficiency. An increase in capture efficiency leads to a higher solvent regeneration energy, as additional CO_2 must be liberated from the solvent in the stripper. The consequent increase in SRD due to the change from 90 to 95% capture efficiency was deemed an acceptable energy burden by Michailos and Gibbins [47] despite the increasing difficulty of capturing CO_2 beyond 90% efficiency under all modelled conditions.

A comparison of SRD for a range of solvent flow rates and CO_2 concentrations is presented in Figure 3.16 for three representative gas flow rates, 130, 170, and 210 Nm^3/h, achieving 95% capture efficiency. The parameters used to model the 90% capture efficiency conditions in Section 3.5.1 were also applied to the higher capture efficiency conditions. Simulation convergence was achieved using the design specifications outlined in Section 3.2.9.

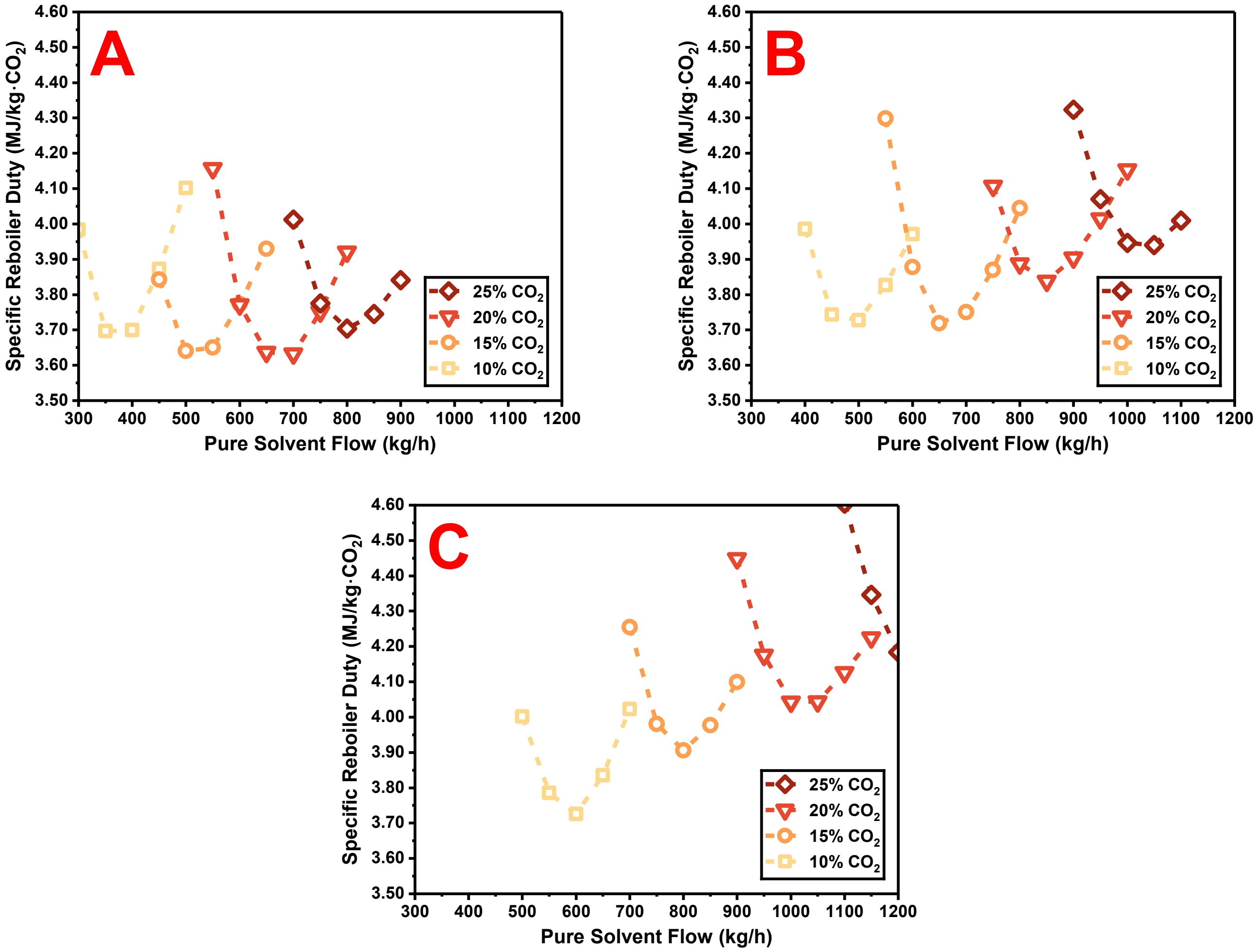

Figure 3.16: Specific reboiler duty against pure solvent flow rate for gas flow rates: (A) 130 Nm^3/h, (B) 170 Nm^3/h, and (C) 210 Nm^3/h for a range of CO_2 concentrations at 95% capture efficiency.

An analysis of the trends across the three gas flow rates shown in Figure 3.16 revealed consistency with those observed in Figure 3.15. In Figure 3.16A, the different plots exhibit similar SRDs at their respective optimal L_{pure}/G ratios, primarily due to most of the conditions operating below the maximum heat duty capacity of the cross-heat exchanger. The separation between the plots is determined by the L_{pure}/G ratios required for each CO_2 concentration. In Figure 3.16B, representing 170 Nm^3/h gas flow, the SRDs for CO_2 concentrations of 10 and 15 mol.% remain below the cross-heat exchanger's maximum heat duty, while the 20 and 25 mol.% cases operate at maximum heat duty, resulting in the noticeable incremental changes in SRD between the plots. This trend is most pronounced in Figure 3.16C, where gas flow rates of 210 Nm^3/h are considered. Here, all four CO_2 concentration conditions are operating at maximum cross-heat exchanger duty, leading to a clear separation among the plots. Subsequently, the optimal L_{pure}/G ratios and solvent/CO_2 ratios for CO_2 concentrations ranging from 10 to 25 mol.% at 95% capture efficiency were identified, with the results presented in Table 3.16.

Table 3.16: Optimal L_{pure}/G and solvent/CO_2 ratios for different CO_2 concentrations for gas flow rates of 130, 170, and 210 Nm^3/h achieving 95% capture efficiency using 35 wt.% MEA.

CO_2 Concentration mol.%	130 Nm^3/h		170 Nm^3/h		210 Nm^3/h	
	L_{pure}/G Ratio	Solvent/CO_2 Ratio	L_{pure}/G Ratio	Solvent/CO_2 Ratio	L_{pure}/G Ratio	Solvent/CO_2 Ratio
10	2.5	17.1	2.5	17.1	2.5	17.1
15	3.2	14.9	3.2	14.9	3.2	14.9
20	4.0	14.3	4.0	14.3	4.0	14.3
25	4.9	14.4	4.9	14.4	4.9	14.4

It is clear that the trends observed for 90% capture efficiency remain valid at 95% capture efficiency, with the predicted optimal L_{pure}/G ratios and corresponding solvent/CO_2 ratios showing independence from gas flow rate across varying flue gas CO_2 concentrations. The solvent loadings data for 95% capture efficiency cases, presented in Table 3.17, are compared with the optimal L_{pure}/G ratios in Table 3.16.

Table 3.17: Solvent loadings data at optimal L_{pure}/G ratios for different CO_2 concentrations for gas flow rates of 130, 170, and 210 Nm^3/h achieving 95% capture efficiency using 35 wt.% MEA.

CO_2 Concentration mol.%	Lean Loading			Rich Loading			Solvent Capacity		
	130 Nm^3/h	170 Nm^3/h	210 Nm^3/h	130 Nm^3/h	170 Nm^3/h	210 Nm^3/h	130 Nm^3/h	170 Nm^3/h	210 Nm^3/h
10	0.281	0.280	0.278	0.503	0.501	0.500	0.222	0.221	0.221
15	0.257	0.253	0.252	0.509	0.507	0.505	0.253	0.254	0.253
20	0.250	0.247	0.245	0.513	0.510	0.508	0.263	0.263	0.263
25	0.252	0.249	0.247	0.514	0.511	0.509	0.262	0.262	0.262

While rich loadings are similar between 90% and 95% capture efficiencies, it is evident that lower lean loadings, typically from 0.28 to 0.25, are required to achieve higher capture efficiencies, resulting in slightly larger solvent capacities. At CO_2 concentrations of 20 and 25 mol.% a higher L_{pure}/G ratio is observed for 95% capture efficiency compared to 90% to achieve a minimal SRD. This suggests a minimum lean loading of approximately 0.25 is optimal for minimising the SRD, which leads to a solvent capacity slightly above 0.26.

Additionally, the analysis of solvent capacities and solvent/CO_2 ratios for 95% capture efficiency reaffirms the inverse relationship observed in Table 3.14, reinforcing the previous conclusion that the solvent/CO_2 ratio governed the required solvent capacity for a target capture efficiency. These findings are presented in Table 3.18.

Table 3.18: Comparison of percentage differences between solvent capacity and solvent/CO_2 ratio with respect to flue gas CO_2 concentration, achieving 95% capture efficiency using 35 wt.% MEA.

CO_2 Concentration mol.%	Solvent Capacity		CO_2 Concentration mol.%	Solvent/CO_2 Ratio	
	Value	Increasing % Difference		Value	Increasing % Difference
10	0.221	-	25	14.4	-
15	0.253	12.6	20	14.3	-0.7
20	0.263	3.8	15	14.9	4.0
25	0.262	-0.4	10	17.1	12.9

The SRD values corresponding to each identified optimal L_{pure}/G ratio are presented in Table 3.19 for the different CO_2 concentrations achieving 95% capture efficiency using 35 wt.% MEA.

Table 3.19: SRDs at identified optimal L_{pure}/G and solvent/CO_2 ratios for different CO_2 concentrations for gas flow rates of 130, 170, and 210 Nm^3/h achieving 95% capture efficiency using 35 wt.% MEA.

CO_2 Concentration mol.%	L_{pure}/G Ratio	Solvent/CO_2 Ratio	SRD MJ/kg·CO_2		
			130 Nm^3/h	170 Nm^3/h	210 Nm^3/h
10	2.5	17.1	3.70	3.72	3.76
15	3.2	14.9	3.64	3.72	3.91
20	4.0	14.3	3.64	3.84	4.03
25	4.9	14.4	3.71	3.94	4.13

The SRD trends observed in Table 3.19 for 95% capture efficiency align with those noted for the 90% capture efficiency conditions, showing these trends are consistent across different capture efficiencies and are not limited to a specific target capture efficiency.

3.5.3 Comparison Between 90% and 95% Capture Efficiency Conditions

A comparison of SRD across different capture efficiency targets was conducted to identify any trends or potential inconsistencies within the simulations. Table 3.20 presents the collected SRD results for both 90% and 95% capture efficiencies across the three tested gas flow rates, each with varying CO_2 concentrations.

Table 3.20: SRDs at identified optimal L_{pure}/G and solvent/CO_2 ratios for different CO_2 concentrations for gas flow rates of 130, 170, and 210 Nm^3/h achieving 90% and 95% capture efficiency using 35 wt.% MEA.

CO_2 Concentration mol.%	SRD MJ/kg·CO_2					
	130 Nm^3/h		170 Nm^3/h		210 Nm^3/h	
	90% Capture	95% Capture	90% Capture	95% Capture	90% Capture	95% Capture
10	3.68	3.70	3.71	3.72	3.74	3.76
15	3.60	3.64	3.67	3.72	3.91	3.91
20	3.59	3.64	3.78	3.84	4.00	4.03
25	3.64	3.71	3.88	3.94	4.07	4.13

Furthermore, Table 3.21 consolidates data on optimal L_{pure}/G ratios, solvent/CO_2 ratios, lean loadings, and solvent capacities for different CO_2 concentrations at both 90% and 95% capture efficiencies, these results being independent of total gas flow rate.

Table 3.21: Optimal L_{pure}/G ratios, solvent/CO_2 ratios, lean loadings and solvent capacities for different CO_2 concentrations for 90% and 95% capture efficiency using 35 wt.% MEA.

CO_2 Concentration mol.%	90% Capture Efficiency				95% Capture Efficiency			
	L_{pure}/G Ratio	Solvent/ CO_2 Ratio	Lean Loading	Solvent Capacity	L_{pure}/G Ratio	Solvent/ CO_2 Ratio	Lean Loading	Solvent Capacity
10	2.5	17.1	0.294	0.210	2.5	17.1	0.281	0.221
15	3.2	14.9	0.271	0.240	3.2	14.9	0.257	0.253
20	3.9	14.0	0.259	0.256	4.0	14.3	0.250	0.263
25	4.6	13.5	0.252	0.265	4.9	14.4	0.252	0.262

An analysis of the SRD across all gas flows in Table 3.20 reveals that the SRD for 95% capture efficiency consistently showed a slight increase compared to the 90% cases at the minimum L_{pure}/G ratios for each CO_2 concentration. Specifically, for a gas flow rate of 130 Nm^3/h, the SRD increase ranged from 0.54% to 1.92% for CO_2 concentrations between 10 to 25 mol.%. For a gas flow rate of 170 Nm^3/h, this increase ranged from 0.26% to 1.54%, while for 210 Nm^3/h, the range spanned 0.2% to 1.47% over the same CO_2 concentrations. Given the relatively small increase in SRD, targeting a higher capture efficiency may therefore be justified to enhance decarbonisation with only a minimal additional energy penalty, consistent with the findings of Michailos and Gibbins [47]. This could be done in straightforward manner, as the results indicate that the optimal L_{pure}/G and solvent/CO_2 ratios for 95% capture efficiency are consistently equal to, or only slightly higher than those for 90% capture efficiency, depending on the optimal lean loading.

For CO_2 concentrations of 10 and 15 mol.%, the higher SRD for 95% capture efficiency is related to the lower lean loading required for the capture, as seen in Table 3.21, which demands a greater heat input to achieve. Despite this, the optimal L_{pure}/G ratios remain consistent across both 90% and 95% capture cases for these CO_2 concentrations. In contrast, for CO_2 concentrations of 20 and 25 mol.%, the higher SRD requirement for 95% capture is attributed to an increase in the L_{pure}/G ratio, as reflected in Table 3.21. The divergence stems from the system's heat and mass balance, which aims to achieve a lean loading of approximately 0.25, necessitating a higher solvent flow. While this arrangement results in a more efficient SRD compared to a lower L_{pure}/G ratio, the overall SRD increases relative to the 90% capture cases due to the extra energy required to heat and vaporise the additional water. Achieving a lean loading of 0.25 leads to a solvent capacity slightly exceeding 0.26, which is evidently the optimal configuration once the concentration of CO_2 is sufficiently high. This trend is less pronounced at lower CO_2 concentrations, where smaller solvent capacities suffice for optimal capture. At higher CO_2 mass flows in the flue gas, the model adjusts the optimal L_{pure}/G ratio to meet the observed solvent capacity of approximately 0.26.

While these results were intended for comparison with open literature, many studies, such as the rigorous work by Tobiesen et al. [48], focus on a limited number of flue gas conditions, making direct comparisons challenging. This highlights the novelty and broader scope that this investigation afforded. Several studies have utilised the findings by Mangalapally and Hasse [49] as the basis for simulation work. Although their findings offered limited overlap with this study, their "Series B" flue gas, with a CO_2 concentration of 10 mol.% identified an optimal L/G ratio of 2.5 for achieving 90% capture efficiency. This is consistent with the L_{pure}/G value determined for the TERC ACP, although the corresponding L/G ratio is slightly higher at 2.68. Additionally, the predicted SRD in this study is lower than that reported by Mangalapally and Hasse, at 3.6 versus 4.1 MJ/kg·CO_2.

In real-world applications, the CO_2 concentration of the flue gas should first be confirmed, followed by the desired capture efficiency. This will guide the selection of L_{pure}/G or solvent/CO_2 ratio when using 35 wt.% MEA solvent. Solvent loadings data can then be used to describe the system and verify the solvent capacity predictions, ensuring the desired capture efficiency is achieved.

While the values presented in Table 3.21 provide useful initial estimates for handling gases with varying CO_2 concentrations, they offer limited insight into why these specific L_{pure}/G ratios are optimal for the given conditions. This behaviour is explained through column temperature profiles, which are examined in the following section.

3.6 Simulated Column Profiles

3.6.1 Absorber and Stripper Temperature Profiles

Column profiles provide crucial insights into system operation, aiding in diagnostics and optimisation, as previously discussed in Chapter 2. While composition profiles provide a comprehensive understanding, temperature profiles offer a simple, practical indicator of operation, enabling easier comparison to real-world systems [50]. The required solvent flows and corresponding L/G ratios for achieving different absorber and stripper operations depends on plant design and dimensions, which must be well understood.

Absorber columns operate in one of three modes: rich-pinched, lean-pinched, and bulge-pinched [51]. These modes depend on the system's L/G ratio, which governs where the driving force for mass transfer occurs. Low L/G ratios lead to rich-pinched operation, while high L/G ratios result in lean-pinched operation. The bulge-pinched zone lies between these extremes and represents a transition region. Ideally, operation should remain in the rich or lean-pinched modes, as bulge-pinched operation has poor energy efficiency for the same amount of CO_2 capture [52].

In stripper columns, three distinct regions of operation are identified: the exponential region, the inflection point and the baseline region, all governed by the amount of water vapour generated from the reboiler. Low L/G ratios produce high water vapour amounts that cannot fully condense within the column, leading to operation in the exponential region [47,53]. In contrast, high L/G ratios have low amounts of water vapour that fully condense near the bottom of the column, corresponding to the baseline region [47,54]. The inflection point represents the ideal L/G ratio, minimising the SRD by balancing heat and mass transfer, with water vapour condensing progressively along the column, completing just before the top [53]. This point marks the transition between the exponential and baseline regions, and process optimisation should aim to operate the stripper at, or near, the inflection point. Notably, all three stripper zones can occur within the same absorber operating mode.

Figure 3.17 presents the column temperature profiles for different L_{pure}/G ratios for three representative gas flow rates of 130, 170 and 210 Nm^3/h, respectively, across a range of L_{pure}/G ratios between 2.35 and 7.50 for pure solvent flows ranging from 400 to 1200 kg/h. All flue gas flows had a CO_2 concentration of 20 mol.% and achieved 90% capture efficiency. The lean solvent concentration was fixed at 35 wt.% MEA, on a CO_2 free basis, with both lean solvent and flue gas streams maintained at 40 °C. The stripper pressure was kept constant at 1.2 bara and the cross-heat exchanger minimised the approach temperature between the hot rich and hot lean solvent flows until a heat duty of 43 kW was achieved, representative of the maximum heat exchanger capacity. The SRD of these cases was first presented in Figure 3.15.

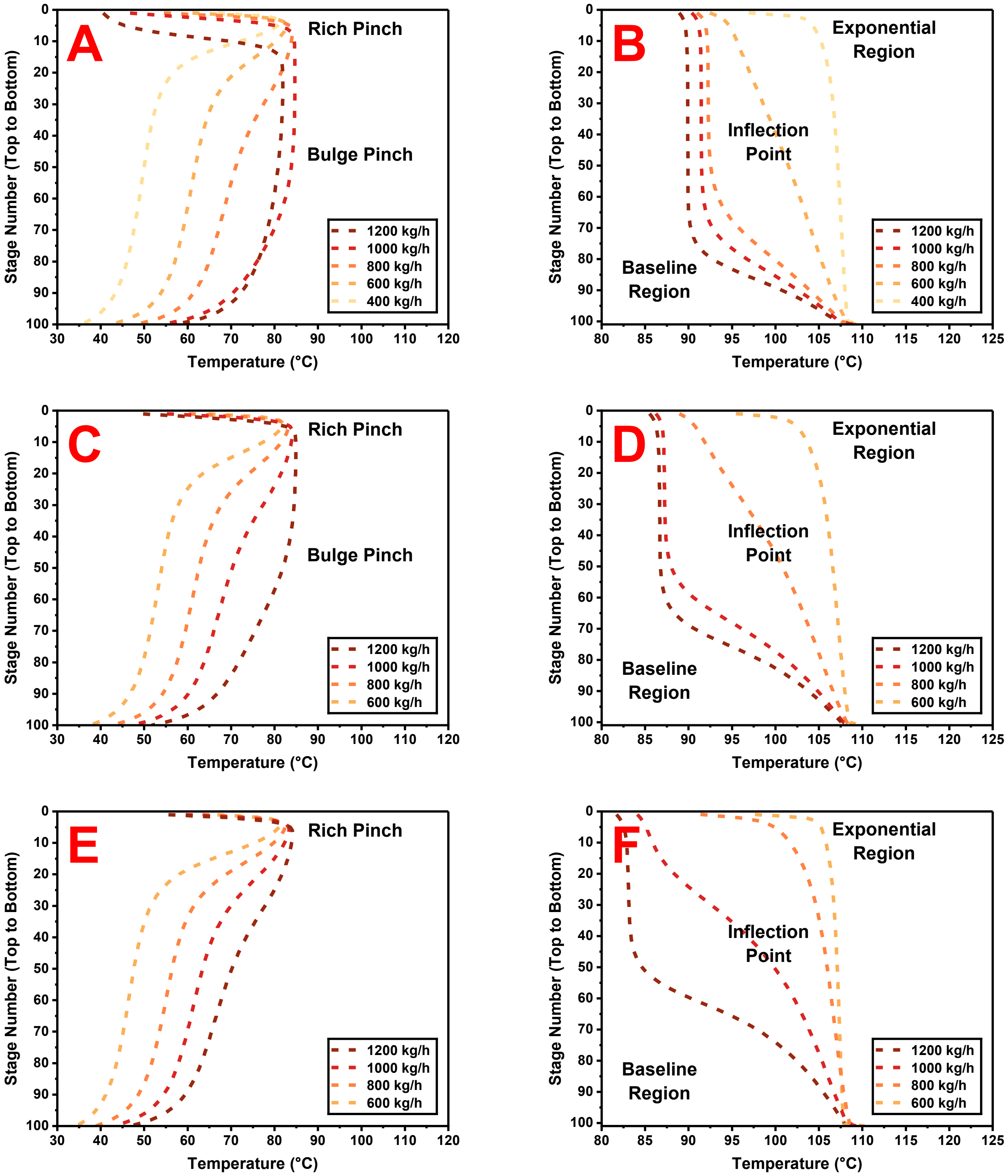

Figure 3.17: Column temperature profiles with a CO_2 concentration of 20 mol.%, using 35 wt.% MEA pure solvent flow rates to achieve 90% capture efficiency. Absorber profiles are in the left column and stripper profiles in the right column. Gas flow rates: (A, B) 130 Nm^3/h, (C, D) 170 Nm^3/h, and (E, F) 210 Nm^3/h.

At lower pure solvent flow rates, rich-pinched behaviour is observed in the absorber columns, characterised by a temperature bulge near the top of the column. As solvent flow increases, profiles began transitioning toward bulge-pinched states, more pronounced with decreasing gas flow rate, owing to the higher L_{pure}/G ratios possible, and most apparent in the 130 Nm^3/h cases. For a gas flow of 170 Nm^3/h, the emerging bulge-pinched state was only seen at a pure solvent flow of 1200 kg/h with an L_{pure}/G ratio of 5.75, while the same pure solvent flow rate for a gas flow of 210 Nm^3/h only sees slight flattening of the temperature profile, corresponding to an L_{pure}/G ratio of 4.65. To avoid bulge-pinched operation when handling flue gas with 20 mol.% CO_2, an L_{pure}/G ratio below 5.00 is recommended.

The corresponding stripper temperature profiles for the same gas flows are presented in Figures 3.17B, 3.17D, and 3.17F, highlighting the three distinct operating zones across the same range of solvent flows. The inflection point, which minimises the SRD, corresponds to an L_{pure}/G ratio of 3.9, as identified in Table 3.12. This aligns with the 1000 kg/h trendline for 210 Nm^3/h, the 800 kg/h trendline for 170 Nm^3/h and approximates the 600 kg/h trendline for 130 Nm^3/h. Across all gas flows, the inflection point is distinctive, showing a uniform temperature increase down the column, reflecting the optimised energy transfer into the solvent. These optimal profiles correspond to rich-pinched absorber behaviour, confirming efficient energy use while avoiding bulge-pinched operation in the absorber.

The relationship between solvent flow, L_{pure}/G ratio and SRD becomes clear when comparing the stripper temperature profiles to the corresponding SRD graphs in Figure 3.15. Increasing the pure solvent flow from the optimal raises the L_{pure}/G ratio, pushing the stripper into the baseline region and increasing the SRD. In contrast, reducing the pure solvent flow lowers the L_{pure}/G ratio, moving the stripper into the exponential region, which also raises the SRD. This understanding provides a more complete perspective on system performance beyond basic energy plots. With these insights, column temperature profiles for different CO_2 concentrations across different pure solvent flow rates can be analysed for further system optimisation.

3.6.2 Absorber and Stripper Composition Profiles

Following the initial examination of a broad range of column temperature profiles, a representative example was selected to explore the underlying physical chemistry contributing to the temperature distributions. The chosen condition had a gas flow rate of 170 Nm^3/h with a CO_2 concentration of 20 mol.% and was earlier depicted in Figures 3.17C and 3.17D. This condition was analysed with pure solvent flow rates of 600, 800 and 1000 kg/h, representing the exponential region, approximate inflection point, and baseline region of the stripper column, respectively.

Figure 3.18 presents various parameter profiles for the absorber column, emphasising how the solvent flow rate governs where CO_2 capture occurs and contributes to the observed temperature distributions. Figure 3.18A presents the absorber temperature profiles for reference and Figure 3.18B highlights the mass transfer of CO_2 from the flue gas into the solvent via absorption reactions, where higher values indicate faster absorption. The CO_2 vapour composition profiles in Figure 3.18C are used to provide an in-depth view of CO_2 concentrations along the height of the column, while Figure 3.18D simplifies this by presenting the mass flow rate of CO_2 in the vapour phase.

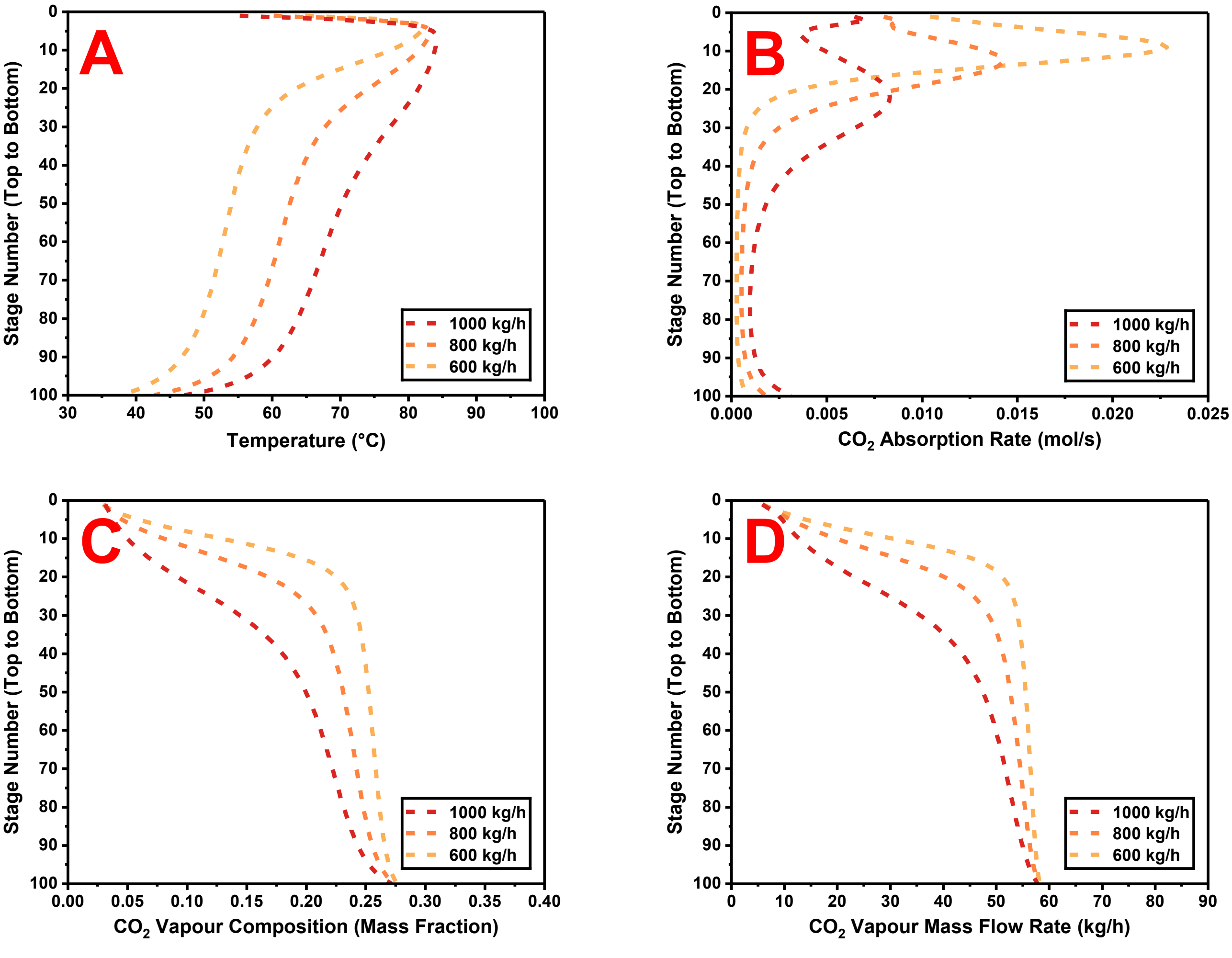

Figure 3.18: Absorber column profiles with different pure solvent flow rates for a gas flow rate of 170 Nm^3/h with a CO_2 concentration of 20 mol.%, achieving 90% capture efficiency using 35 wt.% MEA. (A) Temperature, (B) CO_2 absorption rate, (C) CO_2 vapour composition, and (D) CO_2 vapour mass flow rate.

It is evident that the trends in CO_2 vapour mass fraction profiles align with the temperature profiles. In all solvent flow rates examined, a notable decrease in CO_2 concentration is observed just below the corresponding temperature peaks. This indicates the location of intense reaction activity is towards the top of the column, driven by the exothermic nature of CO_2 absorption. As CO_2 absorption progressed and reaction activity slowed, less energy was generated for heating and temperatures decreased towards the bottom of the column.

At the lowest tested pure solvent flow rate of 600 kg/h, reaction activity intensifies above stage 20, aligning with a steep decline in CO_2 mass flow rate across the same stages. This results in a rapid temperature increase near the top of the column, creating the distinctive appearance of a rich-pinched profile.

When the pure solvent flow rate was increased to 800 kg/h, the driving force for absorption began to migrate downward, beginning above stage 30, which distributed the reaction zone wider and lowered the peak reaction rate near the top of the column. This shift caused the CO_2 mass flow rate to decline at a lower height in the column and in a more gradual manner. Consequently, the corresponding temperature profile became overall hotter than in the 600 kg/h case yet retained the characteristics of a rich-pinched absorber.

With a further increase in pure solvent flow rate to 1000 kg/h, the system transitions toward a bulge-pinched state. The peak reaction zone continues to shift downward and spread more extensively along the height of the column. This resulted in a broader reaction zone with a distinct bulge shape between stages 10 and 40, producing a smoother decline in CO_2 mass flow rate as the flue gas rose through the column. This corresponds to a smoother temperature profile that is overall hotter than those observed at lower solvent flow rates but was missing a sharp temperature peak. Although the 1000 kg/h temperature profile suggests an emerging bulge-pinched state when compared with lower flow rates, this may not be immediately evident when viewed in isolation. However, the additional context provided by the composition and reaction plots reinforced the conclusion that this transition is indeed occurring.

With the absorber column's behaviour verified and understood, these foundational insights were applied to the stripper column to investigate its operational principles. Figure 3.19 presents various parameter profiles for the stripper column, emphasising how changes in solvent flow rate influences where CO_2 stripping occurs and contributes to the observed temperature distributions during regeneration. Figure 3.19A presents the stripper temperature profiles for reference and Figure 3.19B displays the CO_2 production within the column via desorption reactions, where positive values indicate CO_2 production and negative values signal reabsorption into the solvent. Figures 3.19C and 3.19D depict the vapour composition profiles of CO_2 and H_2O, respectively, while Figures 3.19D and 3.19F simplify these compositions as mass flow rates of CO_2 and H_2O.

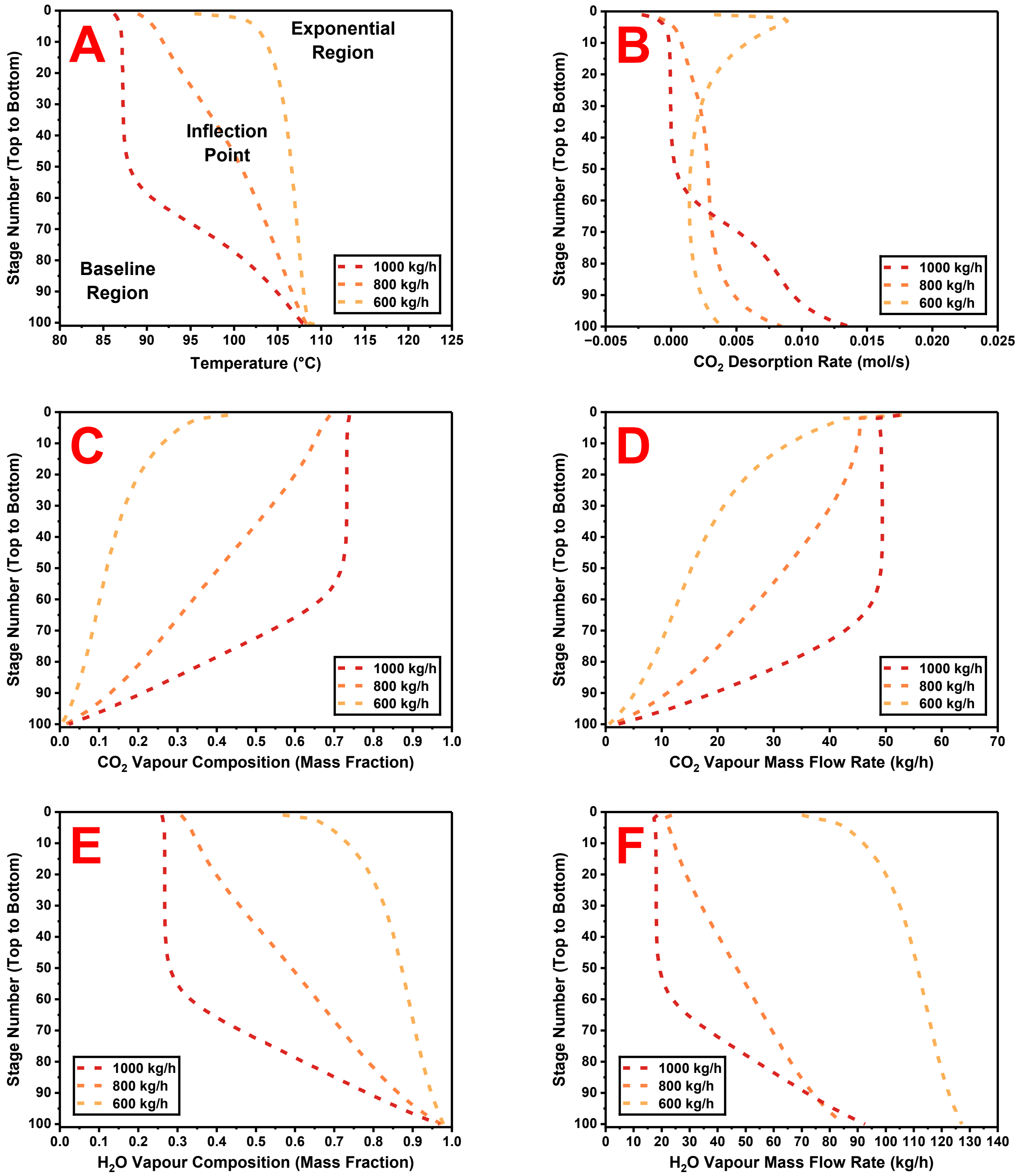

Figure 3.19: Stripper column profiles with different pure solvent flow rates for a gas flow rate of 170 Nm^3/h with a CO_2 concentration of 20 mol.%, achieving 90% capture efficiency using 35 wt.% MEA. (A) Temperature, (B) CO_2 desorption rate, (C) CO_2 vapour composition, (D) CO_2 vapour mass flow rate, (E) H_2O vapour composition, and (F) H_2O vapour mass flow rate.

In contrast to the absorber column, the trend in CO_2 vapour mass fraction within the stripper is inversely related to the temperature profile, as depicted in the relationship between Figures 3.19C and 3.19A. The water vapour profile shown in Figure 3.19E, however, closely aligns with the observed temperature trends, indicating a direct relationship between the two trends. As water vapour ascends the stripper column, it condenses on contact with the solvent mixture, releasing heat to drive the endothermic reaction that liberates CO_2. This relationship is evident in Figure 3.19B, where desorption rates correspond to the speed in which water vapour amounts decrease. In summary, when the H_2O mass fraction declines, the total CO_2 mass fraction increases. Despite the differences in solvent flow rates, the total mass flow rate of CO_2 exiting the top of the stripper column remained the same, due to the fixed capture efficiency target of 90%.

At a pure solvent flow rate of 600 kg/h, Figure 3.19F shows substantial water vapour generation at the base of the column. This vapour condenses gradually up the column, sustaining high temperatures until rapid condensation occurs near the top. This results in a sharp increase in CO_2 liberation, as observed in Figure 3.19B, while a significant portion of water vapour exits the column. The excess water vapour generated in the reboiler results from a high energy input required to attain a leaner solvent loading to achieve capture efficiency targets, with the high temperatures preventing the reabsorption of CO_2. This balance of behaviours is characteristic of operation in the exponential region.

Increasing the pure solvent flow rate to 800 kg/h reduces the production of water vapour in the reboiler, where less energy is required to strip the solvent to a higher lean loading and release the same amount of CO_2. At this solvent flow rate, the system achieved a balance between mass and energy, resulting in steady water condensation across the column's height. Here, the water mass fraction gradually decreases while CO_2 is liberated at a comparable rate. This leads to minimal water vapour exiting the column and a smooth temperature profile, characteristic of operation at the inflection point.

A further increase in pure solvent flow rate to 1000 kg/h allows the solvent to have an even higher level of lean loading for the same CO_2 capture. This increased flow rate pushes the water condensation zone lower in the column, where maximum condensation completes by stage 50. Beyond this point, no further water condensation occurs, and CO_2 liberation ceases, with some CO_2 even reabsorbing due to the reduced temperature. The rapid temperature increase at the bottom of the column signals baseline operation.

In conclusion, this analysis of the absorber and stripper temperature profiles clarifies the reasons behind these parametric trends, confirming their practical application for monitoring and optimising column performance.

3.6.3 Optimal Liquid to Gas Ratio Temperature Profiles

With the occurrence of operational modes of absorption and stripping columns understood, the temperature profiles of predicted optimal L_{pure}/G ratios were assessed to confirm if they are indeed optimal. Figure 3.20 presents the column temperature profiles for the optimal L_{pure}/G ratios presented previously in Table 3.21.

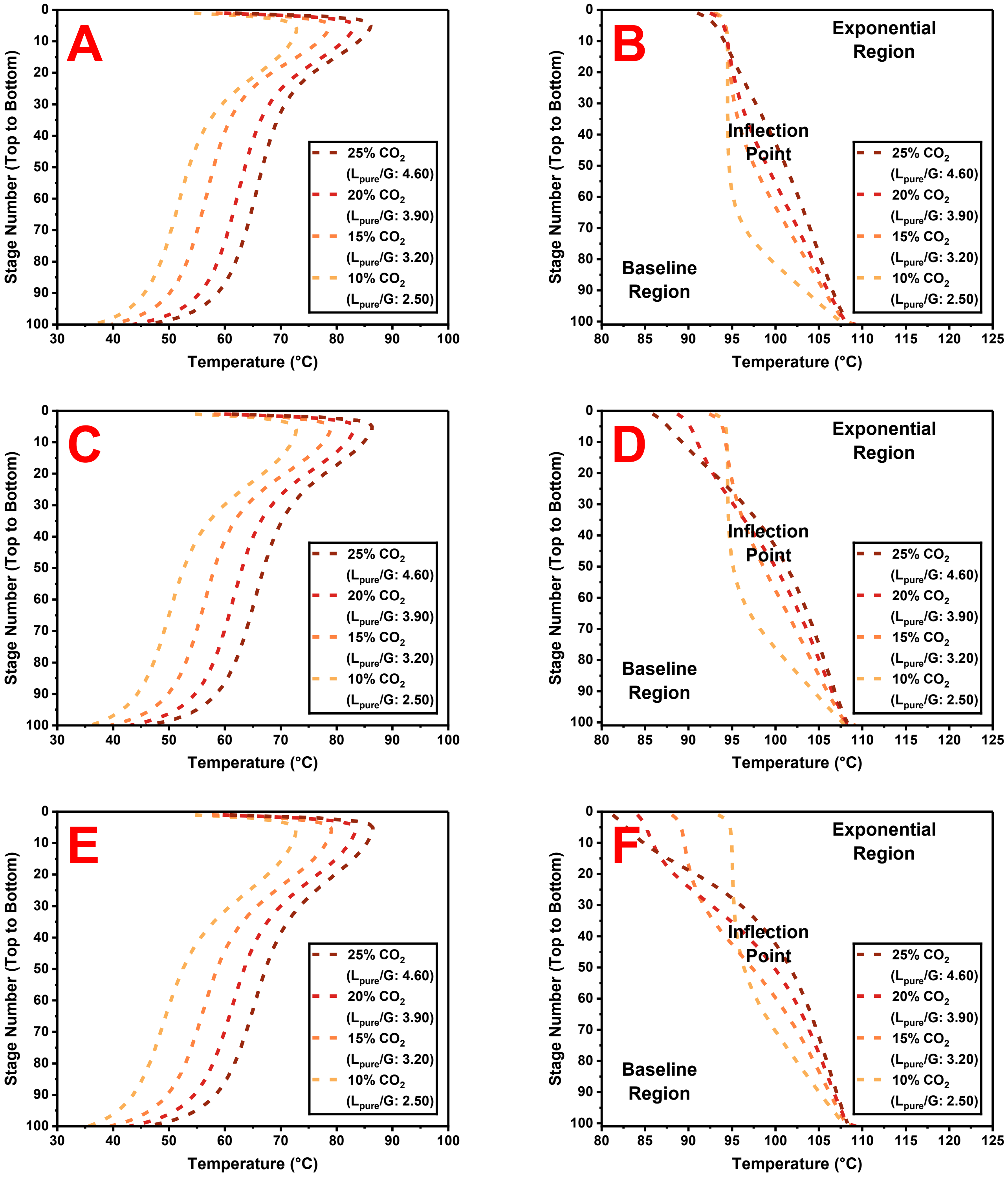

Figure 3.20: Optimal temperature profiles with varying CO_2 concentrations, treated with 35 wt.% MEA to achieve 90% capture efficiency. Absorber profiles are in the left column and stripper profiles in the right column. Gas flow rates: (A, B) 130 Nm^3/h, (C, D) 170 Nm^3/h, and (E, F) 210 Nm^3/h.

Figures 3.20A, 3.20C, and 3.20E present absorber temperature profiles for gas flow rates of 130, 170 and 210 Nm^3/h, respectively, at optimal L_{pure}/G ratios for flue gas CO_2 concentrations ranging from 10 to 25 mol.% in 5% increments. Across all gas flows, the absorber exhibits rich-pinched behaviour, with the same general shape for every case, where increasing CO_2 concentration in the flue gas resulted in adjacent profiles at higher average temperatures. The observed temperature differences arise from the increasing exothermic reaction energy with respect to increasing CO_2 concentration. Despite variations in gas flow rate, the temperature profiles are nearly identical, reaffirming that the optimal L_{pure}/G ratio is independent of the gas flow rate and is solely a function of capture efficiency and CO_2 concentration. This confirms that the TERC ACP operates optimally with a rich-pinched absorber, where Figure 3.17 has already shown that the absorber does not typically operate in a bulge or lean-pinched state due to the constraint of the maximum solvent flow rate.

The corresponding stripper temperature profiles for the same conditions as the absorber are presented in Figures 3.20B, 3.20D, and 3.20F, which should approximate the inflection point if they are optimised. While most cases align with this expectation, discrepancies in the top temperatures of the stripper column emerge before settling into an optimised profile. These variations are due to the heat duty limitation of the cross-heat exchanger. For the 130 Nm^3/h conditions, the exchanger effectively minimises the approach temperature between the hot rich and hot lean solvents, resulting in similar top temperatures. However, in the 170 Nm^3/h conditions, the exchanger struggles to minimise the approach temperature when the CO_2 concentration exceeded 15 mol.%, indicating it is operating at maximum capacity. This caused the top temperatures to separate, with cooling observed as CO_2 concentration and solvent flow increased. This effect was most pronounced in the 210 Nm^3/h conditions, where the exchanger was at maximum capacity across all CO_2 concentrations, resulting in a widening approach temperature as CO_2 concentration and solvent flow increase. These variations caused the observed "crossover" profiles in Figures 3.20D and 3.20F. However, after the first 30 stages of the column the profiles converged towards the inflection point, validating the L_{pure}/G ratios as optimal.

In an ideal system, a cross-heat exchanger with a much larger heat duty would minimise the approach temperature for the higher solvent flows, so that higher gas flow rates would have similar temperatures at the top of the column. However, the observed crossover temperature profiles reflect real-world conditions in which a stripper column operates with the maximum cross-heat exchanger duty. Understanding these effects is crucial for accurately characterising column behaviour and optimising system performance.

A potential discrepancy in the optimal L_{pure}/G ratio was noted for the 10 mol.% CO_2 cases, where the temperature profile appears to shift from the inflection point to the baseline region as gas flow decreased. This raised the question of whether different L_{pure}/G ratios may be required for low CO_2 concentrations at varying gas flows. However, a review of the SRD versus solvent flow graphs in Figure 3.15 revealed a flat SRD curve across a small solvent flow range for gas flows of 130 and 170 Nm^3/h. The variation in SRD across a 100 kg/h change in pure solvent flow is less than 0.3%, indicating flexibility in operating points for low gas flow rates and CO_2 concentrations. Thus, close-to-optimal SRD can be achieved for these conditions even when the system does not operate precisely at the inflection point, easing implementation in real-world plants. Finally, all cases discussed thus far assumed a constant stripper pressure of 1.2 bara. The impact of stripper pressure on system optimisation is explored in the following section.

3.7 Stripping Column Pressure Implications

The impact of stripper pressure on SRD was analysed across different CO_2 capture efficiencies, gas flow rates, and CO_2 concentrations. Stripper pressure directly influences both the bottom temperature and overall temperature distribution within the column. As pressure increases, the solvent's boiling point rises, resulting in higher reboiler-generated vapour temperatures. Consequently, higher stripper pressures lead to elevated bottom temperatures, which in turn affect the efficiency of the endothermic reactions required to release the CO_2 from the solvent.

Figure 3.21 presents stripper pressure cases ranging from 1.0 bara to 2.0 bara for different gas flow rates at a CO_2 concentration of 20 mol.%, achieving 90% capture efficiency for a solvent concentration of 35 wt.% MEA. The L_{pure}/G ratio was set to 3.9, which was the identified optimum for a stripper pressure of 1.2 bara. Figure 3.21A shows predictions when the exchanger was constrained to a maximum heat duty of 43 kW, representative of the TERC ACP, while Figure 3.21B shows predictions with a minimum approach temperature between the hot rich and the hot lean solvent, representing an idealised system without a heat duty constraint.

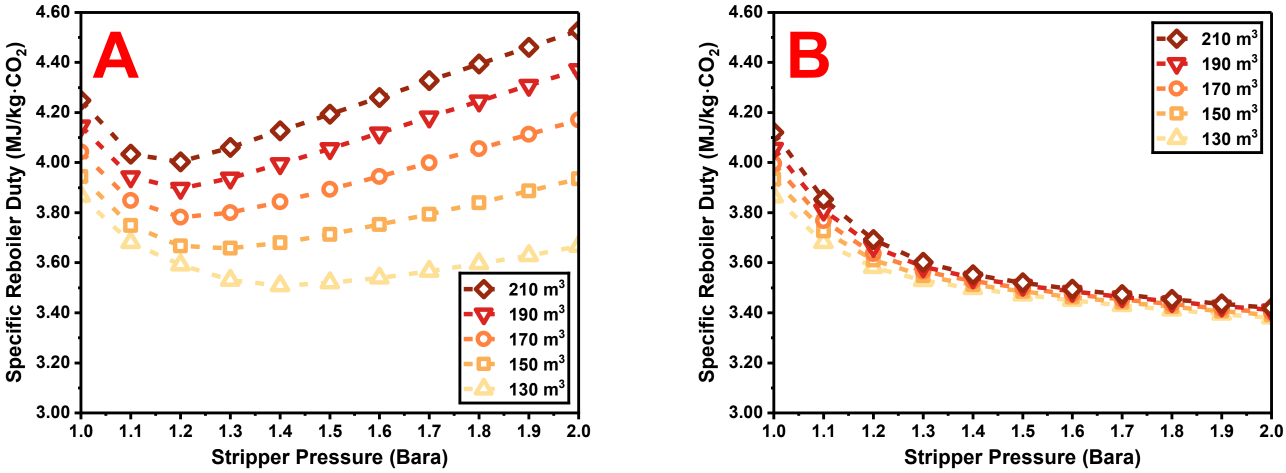

Figure 3.21: Specific reboiler duty against stripper pressure for various gas flow rates with a CO_2 concentration of 20 mol.%, achieving 90% capture efficiency at an L_{pure}/G ratio of 3.9 for (A) a cross-heat exchanger duty of 43 kW, and (B) minimised hot rich and hot lean solvent approach temperature.

The key observation of Figure 3.21A is that the SRD increases significantly unless the optimal stripper pressure is precisely identified for a given scenario. At 90% capture efficiency, the optimal stripper pressure is approximately 1.2 to 1.4 bara, where the optimal pressure slightly increased with decreasing gas flow rates. Similar trends were observed when achieving 95% capture, with the optimal stripper pressure range increasing slightly to 1.3 to 1.5 bara. This indicates that operation with slightly higher stripper pressures on the TERC ACP may be advantageous for reducing SRD at higher capture efficiencies or lower gas flow rates. However, the general increase in SRD with stripper pressure is attributed to the constrained heat duty of the cross-heat exchanger.

As the stripper pressure increases, the bottom temperature increases, driven by the elevated boiling point of the solvent mixture under higher pressure. At the maximum capacity of the cross-heat exchanger, the approach temperature widens with increasing pressure, as the preheating of the rich solvent becomes constrained. This results in similar entry temperatures for the solvent at the top of the stripper, regardless of pressure, but requires a higher energy demand to bring the solvent to the boiling point, thereby increasing SRD. This constrained scenario, while representative of real-world systems operating at maximum exchanger capacity, disguises the true impact of pressure on energy demand. To gain a clearer understanding of how stripper pressure affects SRD without the limitations of constrained heat integration, a second set of conditions was modelled using a minimised approach temperature between the hot rich and the hot lean solvents. These results are presented in Figure 3.21B. In this idealised system, the effect of increasing stripper pressure on SRD was clear: higher pressure consistently lowers SRD. This highlights the critical role of heat integration in minimising SRD, and the importance of using a cross-heat exchanger capable of achieving the lowest possible approach temperature wherever possible.

With the influence of the cross-heat exchanger on SRD under varying pressure now understood, stripper column temperature profiles are evaluated for both scenarios: fixed exchanger heat duty and minimised approach temperature. These are presented in Figure 3.22. The selected conditions include a gas flow rate of 210 Nm^3/h with a CO_2 concentration of 20 mol.% achieving 90% capture efficiency at an L_{pure}/G ratio of 3.9. Figure 3.22A presents the temperature profiles when the cross-heat exchanger was constrained to 43 kW, while Figure 3.22B presents the profiles under a minimum approach temperature, both with varying stripper pressure ranging from 1.0 to 2.0 bara.

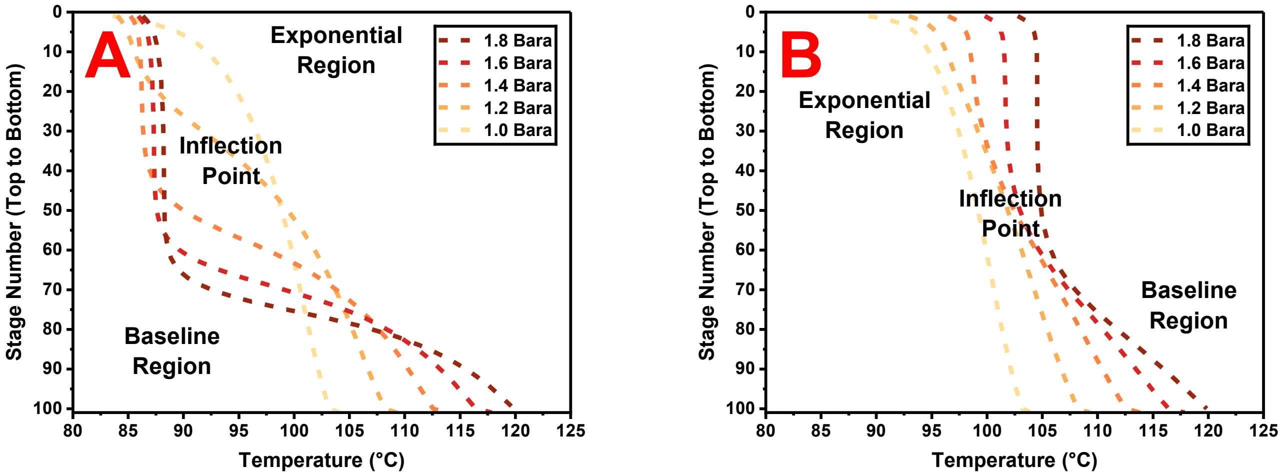

Figure 3.22: Stripper temperature profiles with gas flow of 210 Nm^3/h with a CO_2 concentration of 20 mol.% for a range of stripper pressures achieving 90% capture efficiency at an L_{pure}/G ratio of 3.9 for (A) a cross-heat exchanger duty of 43 kW, and (B) minimised hot rich and hot lean solvent approach temperature.

The SRD, cross-heat exchanger duty and the temperature of the rich solvent entering the top of the stripper for the same conditions depicted in Figure 3.22 are presented in Table 3.22.

Table 3.22: SRD, cross-heat exchanger duty, and hot rich solvent temperature across a range of stripper pressures for a constrained heat exchanger and an unconstrained heat exchanger with a minimised temperature approach. Cases conducted at an L/G ratio of 3.9 for a gas flow of 210 Nm^3/h gas with a CO_2 concentration of 20 mol.% achieving 90% capture efficiency, with solvent concentration of 35 wt.% MEA.

Stripper Pressure Bara	Constrained Heat Exchanger			Minimised Temperature Approach		
	SRD MJ/kg·CO_2	Cross-Heat Exchanger Duty kW	Rich Solvent Temp °C	SRD MJ/kg·CO_2	Cross-Heat Exchanger Duty kW	Rich Solvent Temp °C
1.0	4.25	43	86.89	4.12	60.39	102.62
1.2	4.00	43	86.89	3.69	65.63	105.74
1.4	4.13	43	86.89	3.55	70.24	108.22
1.6	4.26	43	86.89	3.49	74.35	110.27
1.8	4.40	43	86.89	3.45	78.08	111.99

A stripper pressure of 1.2 bara in Figure 3.22A approximates the inflection point for the constrained system, corresponding to the minimal SRD observed for the same gas flow in Figure 3.21A. When the stripper pressure increases beyond this optimal magnitude, the system operation shifts from the inflection point into the baseline region. In this region, the temperature profiles exhibit little variation from the top of the column down to the progressively lower stages, where the increasingly hot vapour mixture rapidly condenses. This condensation causes a significant temperature increase in the downflowing rich solvent. In contrast, when stripper pressure decreases from the optimal operating condition, the solvent boiling point drops, shifting the system towards the exponential region. In this region, an increasing portion of the vapour fails to condense within the stripper column, resulting in a higher water concentration at the top of the column and increased SRD requirements for CO_2 capture.

The main difference between Figures 3.22A and 3.22B lies in the nature of the cross-heat exchanger, which influences the temperature of the rich solvent entering the top of the stripper column, highlighted in Table 3.22 across different pressures. Figure 3.22A reflects real-world conditions where the heat integration is constrained by the capacity of the cross-heat exchanger, leading to a fixed temperature of the rich solvent entering the stripper, irrespective of pressure. In contrast, Figure 3.22B represents an idealised system with maximum heat integration, showing the increasing temperature of the hot rich solvent entering the top of the column as stripper pressure rises.

While Figure 3.22B exhibits the three distinct operating regions of the stripper column, the SRD continues to decrease with rising pressure due to optimal heat integration, shown in Table 3.22. Consequently, identification of the optimal operating conditions based solely on the temperature profile becomes less straightforward in the idealised system. This indicates that the existence of an optimal inflection point is a characteristic of systems with constrained heat integration, a scenario more representative of real-world operations. In an idealised system, the selection of pressure would be governed by the highest stripper bottom temperature achievable before the onset of significant thermal degradation of the solvent, typically reported to be around 130 °C [3,55].

The effect of different flue gas CO_2 concentrations under varying stripper pressure is now assessed. A range of stripper pressures from 1.0 to 2.0 bara were evaluated for different CO_2 concentrations at a gas flow rate of 170 Nm^3/h, each operating at its optimal L_{pure}/G ratio as identified for a stripper pressure of 1.2 bara. The results are presented in Figure 3.23, where Figure 3.23A represents a constrained system with the cross-heat exchanger fixed at a maximum heat duty of 43 kW, and Figure 3.23B depicts an idealised system with a minimum approach temperature between the hot rich and hot lean solvents.

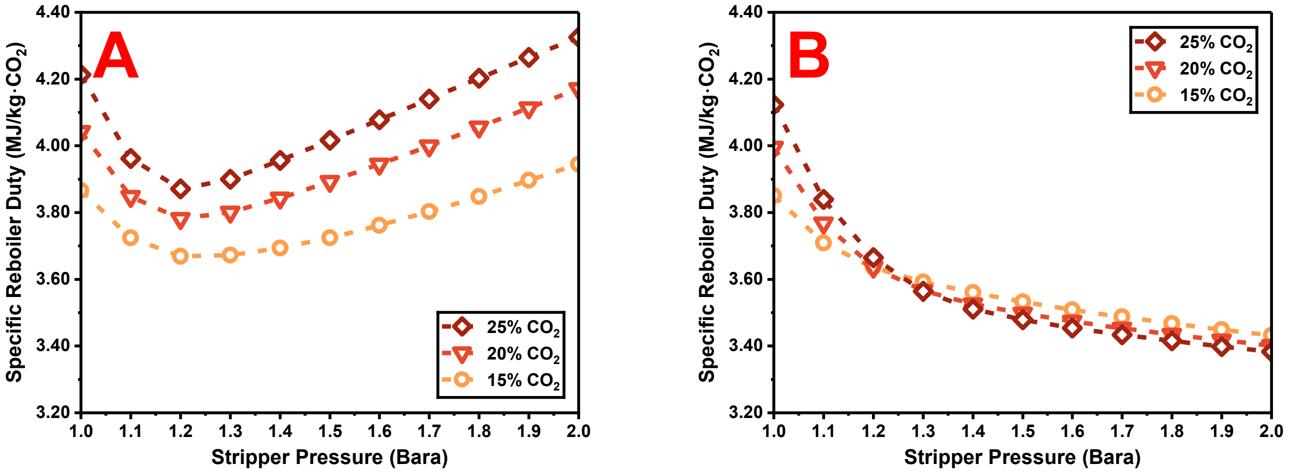

Figure 3.23: Specific reboiler duty against stripper pressure for 170 Nm^3/h gas flow rates with a range of CO_2 concentrations achieving 90% capture efficiency at identified optimal L_{pure}/G ratios for (A) a cross-heat exchanger duty of 43 kW and, (B) minimised hot rich and hot lean approach temperature.

Figure 3.23A shows a clear trend where increasing CO_2 concentration consistently results in higher SRD values at any given pressure, demonstrated by the absence of crossover among the plots. The trends align with those observed in Figure 3.21A, confirming that the increase in SRD with stripper pressure stems from the fixed heat capacity of the cross-heat exchanger. For the TERC ACP, an optimal stripping pressure range between 1.2 and 1.3 bara is observed, consistent with the analysis of Figure 3.21A. This range positions the stripper to operate around the inflection point, minimising the SRD as observed in Figure 3.22A. Figure 3.23B, which represents scenarios using the minimum approach temperature, corroborates the results from Figure 3.21B, showing a consistent decrease in SRD with increasing stripper pressure, and implies that SRD also decreases with increasing CO_2 concentration for given pressures above 1.2 bara.

Optimising the stripper pressure is a complex, multi-objective problem influenced by factors including the L/G ratio, CO_2 concentration of the gas, heat integration capacity, and desired capture efficiency. The optimisation seeks to minimise the total energy consumption of the system subject to the heat duty constraint of the cross-heat exchanger.

In systems equipped with high capacity cross-heat exchangers, optimisation is simplified because the hot rich solvent can enter the stripper at the highest feasible temperature. However, this is rarely achievable in practice for real-world systems due to equipment and cost limitations. Recognising the constraints imposed by the cross-heat exchanger's capacity, and its impact on overall energy performance, is therefore crucial for accurate system optimisation.

3.8 Conclusions for Chapter 3

In this chapter, a process simulation model was developed in Aspen Plus V11.0 to accurately represent the TERC ACP. The DCC model builds upon the framework of an intrinsic MEA steady-state model within Aspen Plus, incorporating data and insights from open literature to improve the representation of the ACP. A comparison was made with an alternative CCSI model, and both models were validated against existing data for the PACT ACP configuration. The DCC model proved superior to its CCSI alternative, more closely aligning with the SRD and solvent loadings of the experimental results and better representing the column temperature profiles. Further validation was conducted on the DCC model using preliminary data from the TERC ACP, which showed promising initial results, increasing confidence in the model's ability to predict performance for future experimental campaigns.

A sensitivity analysis was then carried out on the DCC model to examine the influence of different parameters on the model's performance. Solvent concentration, solvent flow rate, and stripper pressure were found to significantly impact ACP operation, while the temperature of the flue gas and lean solvent had less influence. An example case demonstrated how optimisation could reduce the SRD of the condition by 41.6%.

The validated DCC model was then successfully used to perform a comprehensive modelling study across a range of conditions representing the operational envelope of the TERC ACP under elevated CO_2 conditions. The optimal operating conditions predicted by the DCC model allowed for a detailed insight into parametric trends and their relationships to each other, leading to a deeper understanding of the underlying process phenomena.

The following main conclusions can be drawn from the results:

- Optimal L_{pure}/G ratios are independent of gas flow rates and are instead a function of capture efficiency and CO_2 concentration. This was apparent through investigation of the solvent loadings required for a target capture efficiency, which had the same solvent capacities at different gas flow rates for a specified CO_2 concentration and capture efficiency.
- Optimal L_{pure}/G ratios of all test cases occurred within a range of 2.5 to 4.6 for 90% capture efficiency and 2.5 to 4.9 for 95% capture efficiency across the range of flue gas CO_2 concentrations.
- For the optimal L_{pure}/G ratios of all test cases the associated lean solvent loadings occurred within a range of 0.247 to 0.294, and the associated rich solvent loadings occurred within a range of 0.500 to 0.517.
- Optimal L_{pure}/G ratios may be used for initial predictions in systems with similar flue gas composition to the one described for this work.
- Optimal L_{pure}/G ratios have a corresponding solvent/CO_2 ratio that is closely linked to the solvent capacity, a relationship that is not evident through L_{pure}/G ratio alone.

- Optimal solvent/CO_2 ratios of all test cases occurred within a range of 17.1 to 13.5 for 90% capture efficiency, and 17.1 to 14.3 for 95% capture efficiency across the range of flue gas CO_2 concentrations.
- Optimal solvent/CO_2 ratios may be used more generally for initial predictions where the flue gas composition differs from this work, provided that the CO_2 concentration in the flue gas is known.
- For lower flue gas CO_2 concentrations of 10 and 15 mol.% the predicted values for optimal L_{pure}/G and solvent/CO_2 ratios are the same for both 90 and 95% capture efficiency.
- For higher flue gas CO_2 concentrations of 20 and 25 mol.% the predicted optimal L_{pure}/G and solvent/CO_2 ratios were observed to be slightly higher for 95% capture efficiency over 90% capture efficiency. For these cases the lean solvent loading approximated 0.25, inferred to be the optimal for the system.
- The heat duty of the cross-heat exchanger affected the SRD for higher gas flow rates but not the predicted solvent loadings.
- Absorber and stripper temperature profiles were verified using composition profiles of CO_2 and H_2O in the vapour phase, alongside reaction rates to show the energy transfer and subsequent temperature changes.
- Absorber column temperature profiles should be assessed as an initial starting point to ensure that the mode of operation falls in either a rich-pinched or lean-pinched scenario, always avoiding bulge-pinched operating conditions. When possible, absorber column composition profiles should ultimately be used to identify and assess the status of pinches in the absorber column to aid detailed system optimisation.
- Stripper column temperature profiles should be observed, and adjustments made to ensure that the system operates as close to the inflection point as possible, thereby achieving a minimum SRD for systems with constrained heat integration. Operating regimes outside of the inflection point for constrained heat systems incur an SRD penalty but may not be the case for idealised heat integration. The baseline region is generally associated with high L/G ratios, and the exponential region is associated with low L/G ratios.
- The minimal SRD of a case may appear flat over a range of solvent flow rates. The optimal L/G ratio can be confirmed through assessment of stripper temperature profiles and calibrated to achieve the inflection point.
- Evaluating the impact of heat duty from the cross-heat exchanger is essential to correctly understand stripper column temperatures. At a minimum approach temperature in an ideal system, the hot rich solvent enters the top of the stripper at the maximum possible temperature, and the operating regimes will be evident across different L/G ratios. With constrained heat integration, typical of real plants, the temperature of the hot rich solvent entering the stripper will vary in accordance with the solvent flow rate and the L/G ratio, imposing different stripper temperature profiles.

- The cross-heat exchanger can mask the impact of stripper pressure. In a constrained system there is an optimal stripper pressure associated with the cross-heat exchanger that leads to a minimum SRD. For an ideal system with a minimum approach temperature for the cross-heat exchanger, increasing stripper pressure results in decreasing SRD.
- Optimisation of the stripping column pressure is a multi-objective problem, where the L/G ratio, CO_2 concentration of the gas stream, amount of heat integration, and desired capture efficiency all influence the ideal stripper pressure. A stripper pressure between 1.2 to 1.4 bara closely approximates operation around the inflection point for the TERC ACP.

The results from this modelling study were used to guide the initial conditions for an experimental campaign on the TERC ACP, detailed in the next chapter. This chapter forms the initial part of the synergistic methodology to combine process simulation and experimental work to provide a novel performance baseline of a conventional PB capture plant using MEA for the treatment of flue gases with elevated CO_2 concentrations. While this work is primarily focusing on CO_2 concentrations typical of the iron and steel industry, the findings from this study can be applied to other hard-to-abate heavy industries and used more broadly on alternative chemical absorption capture plants.

3.9 References for Chapter 3

[1] TERC. Carbon Capture Equipment 2023. https://terc.ac.uk/equipment/carbon-capture-equipment/.

[2] ECCSEL ERIC. Amine Capture Plant 2023. https://www.eccsel.org/catalogue/313.

[3] Akram M, Ali U, Best T, Blakey S, Finney KN, Pourkashanian M. Performance evaluation of PACT Pilot-plant for CO2 capture from gas turbines with Exhaust Gas Recycle. International Journal of Greenhouse Gas Control 2016;47:137–50. https://doi.org/10.1016/j.ijggc.2016.01.047.

[4] Akram M, Milkowski K, Gibbins J, Pourkashanian M. Comparative energy and environmental performance of 40 % and 30 % monoethanolamine at PACT pilot plant. International Journal of Greenhouse Gas Control 2020;95:102946. https://doi.org/10.1016/j.ijggc.2019.102946.

[5] Akram M, Jinadasa MHWN, Tait P, Lucquiaud M, Milkowski K, Szuhanszki J, et al. Application of Raman spectroscopy to real-time monitoring of CO2 capture at PACT pilot plant; Part 1: Plant operational data. International Journal of Greenhouse Gas Control 2020;95:102969. https://doi.org/10.1016/j.ijggc.2020.102969.

[6] Tait P, Buschle B, Milkowski K, Akram M, Pourkashanian M, Lucquiaud M. Flexible operation of post-combustion CO2 capture at pilot scale with demonstration of capture-efficiency control using online solvent measurements. International Journal of Greenhouse Gas Control 2018;71:253–77. https://doi.org/10.1016/j.ijggc.2018.02.023.

[7] Akram M, Skylogianni E, Veronezi Figueiredo R, Monteiro J, Grimstvedt A, Vevelstad SJ, et al. Comparison of TERC and TNO's LR2 CO2 capture rigs for normal and accelerated degradation 2022. https://doi.org/10.2139/ssrn.4279777.

[8] Aspen Technology I. Rate-Based Model of the CO2 Capture Process by MEA using Aspen Plus Aspen Plus. 2008.

[9] Zhang Y, Chen CC. Modeling CO2 Absorption and Desorption by Aqueous Monoethanolamine Solution with Aspen Rate-based Model. Energy Procedia 2013;37:1584–96. https://doi.org/10.1016/j.egypro.2013.06.034.

[10] Hikita H, Asai S, Ishikawa H, Honda M. The kinetics of reactions of carbon dioxide with monoethanolamine, diethanolamine and triethanolamine by a rapid mixing method. The Chemical Engineering Journal 1977;13:7–12. https://doi.org/10.1016/0300-9467(77)80002-6.

[11] Pinsent BRW, Pearson L, Roughton FJW. The kinetics of combination of carbon dioxide with hydroxide ions. Trans Faraday Soc 1956;52:1512. https://doi.org/10.1039/tf9565201512.

[12] Zhang Y, Que H, Chen C-C. Thermodynamic modeling for CO2 absorption in aqueous MEA solution with electrolyte NRTL model. Fluid Phase Equilibria 2011;311:67–75. https://doi.org/10.1016/j.fluid.2011.08.025.

[13] Song Y, Chen CC. Symmetric Electrolyte Nonrandom Two-Liquid Activity Coefficient Model. Industrial and Engineering Chemistry Research 2009;48:7788–97. https://doi.org/10.1021/ie9004578.

[14] Gross J, Sadowski G. Perturbed-chain SAFT: An equation of state based on a perturbation theory for chain molecules. Industrial and Engineering Chemistry Research 2001;40:1244–60. https://doi.org/10.1021/ie0003887.

[15] Gross J, Sadowski G. Application of the perturbed-chain SAFT equation of state to associating systems. Industrial and Engineering Chemistry Research 2002;41:5510–5. https://doi.org/10.1021/ie010954d.

[16] Zhang Y, Chen H, Chen CC, Plaza JM, Dugas R, Rochelle GT. Rate-based process modeling study of CO2 Capture with aqueous monoethanolamine solution. Industrial and Engineering Chemistry Research 2009;48:9233–46. https://doi.org/10.1021/ie900068k.

[17] Madeddu C, Errico M, Baratti R. CO2 Capture by Reactive Absorption-Stripping: Modeling, Analysis and Design. Cham: Springer International Publishing; 2019. https://doi.org/10.1007/978-3-030-04579-1.

[18] Errico M, Madeddu C, Pinna D, Baratti R. Model calibration for the carbon dioxide-amine absorption system. Applied Energy 2016;183:958–68. https://doi.org/10.1016/j.apenergy.2016.09.036.

[19] Faramarzi L, Kontogeorgis GM, Michelsen ML, Thomsen K, Stenby EH. Absorber model for CO2 capture by monoethanolamine. Industrial and Engineering Chemistry Research 2010;49:3751–9. https://doi.org/10.1021/ie901671f.

[20] Lawal A, Wang M, Stephenson P, Yeung H. Dynamic modelling of CO2 absorption for post combustion capture in coal-fired power plants. Fuel 2009;88:2455–62. https://doi.org/10.1016/j.fuel.2008.11.009.

[21] Mores P, Scenna N, Mussati S. A rate based model of a packed column for CO2 absorption using aqueous monoethanolamine solution. International Journal of Greenhouse Gas Control 2012;6:21–36. https://doi.org/10.1016/j.ijggc.2011.10.012.

[22] Plaza JM, Van Wagener D, Rochelle GT. Modeling CO2 capture with aqueous monoethanolamine. International Journal of Greenhouse Gas Control 2010;4:161–6. https://doi.org/10.1016/j.ijggc.2009.09.017.

[23] Tobiesen FA, Svendsen HF, Juliussen O. Experimental validation of a rigorous absorber model for CO2 postcombustion capture. AIChE Journal 2007;53:846–65. https://doi.org/10.1002/aic.11133.

[24] Lewis WK, Whitman WG. Principles of Gas Absorption. Industrial and Engineering Chemistry 1924;16:1215–20. https://doi.org/10.1021/ie50180a002.

[25] Madeddu C, Errico M, Baratti R. CO2 Capture by Reactive Absorption-Stripping. Cham: Springer International Publishing; 2019. https://doi.org/10.1007/978-3-030-04579-1.

[26] Kucka L, Müller I, Kenig EY, Górak A. On the modelling and simulation of sour gas absorption by aqueous amine solutions. Chemical Engineering Science 2003;16:3571–8. https://doi.org/10.1016/S0009-2509(03)00255-0.

[27] Onda K, Takeuchi H, Okumoto Y. Mass Transfer Coefficients Between Gas and Liquid Phases in Packed Columns. J Chem Eng Japan / JCEJ 1968;1:56–62. https://doi.org/10.1252/jcej.1.56.

[28] Bravo J, Rocha JA, Fair J. Mass transfer in gauze packings. Hydrocarbon Processing 1985.

[29] Chilton TH, Colburn AP. Mass Transfer (Absorption) Coefficients: Prediction from Data on Heat Transfer and Fluid Friction. Industrial and Engineering Chemistry 1934;26:1183–7. https://doi.org/10.1021/ie50299a012.

[30] Stichlmair J, Bravo JL, Fair JR. General model for prediction of pressure drop and capacity of countercurrent gas/liquid packed columns. Gas Separation & Purification 1989;3:19–28. https://doi.org/10.1016/0950-4214(89)80016-7.

[31] McNulty K, Hsieh C. Hydraulic Performance and Efficiency of Koch Flexipac Structured Packings. AIChE National Meeting, LA, CA: 1982.

[32] Morgan J, Soares Chinen A, Omell B, Bhattacharyya D, Deshpande A. MEA Steady-State Model — MEA Steady-State Model 3.2 documentation. CCSI Carbon Capture Sumulation for Industry Impact n.d. https://mea-ssm.readthedocs.io/en/latest/index.html.

[33] Morgan J, Omell B, Bhattacharyya D, Deshpande A. GitHub - CCSI-Toolset/MEA_ssm: MEA Steady State Model. CCSI-Toolset/MEA_ssm n.d. https://github.com/CCSI-Toolset/MEA_ssm.

[34] Morgan JC, Soares Chinen A, Omell B, Bhattacharyya D, Tong C, Miller DC, et al. Development of a Rigorous Modeling Framework for Solvent-Based CO2 Capture. Part 2: Steady-State Validation and Uncertainty Quantification with Pilot Plant Data. Ind Eng Chem Res 2018;57:10464–81. https://doi.org/10.1021/acs.iecr.8b01472.

[35] Morgan JC, Chinen AS, Anderson-Cook C, Tong C, Carroll J, Saha C, et al. Development of a framework for sequential Bayesian design of experiments: Application to a pilot-scale solvent-based CO2 capture process. Applied Energy 2020;262:114533. https://doi.org/10.1016/j.apenergy.2020.114533.

[36] Morgan JC, Bhattacharyya D, Tong C, Miller DC. Uncertainty quantification of property models: Methodology and its application to CO2-loaded aqueous MEA solutions. AIChE Journal 2015;61:1822–39. https://doi.org/10.1002/aic.14762.

[37] Plaza JM. Modeling of carbon dioxide absorption using aqueous monoethanolamine, piperazine and promoted potassium carbonate. 2012.

[38] Mathias PM, Gilmartin JP. Quantitative Evaluation of the Effect of Uncertainty in Property Models on the Simulated Performance of Solvent-Based CO2-Capture. Energy Procedia 2014;63:1171–85. https://doi.org/10.1016/j.egypro.2014.11.127.

[39] Soares Chinen A, Morgan JC, Omell B, Bhattacharyya D, Tong C, Miller DC. Development of a Rigorous Modeling Framework for Solvent-Based CO2 Capture. 1. Hydraulic and Mass Transfer Models and Their Uncertainty Quantification. Ind Eng Chem Res 2018;57:10448–63. https://doi.org/10.1021/acs.iecr.8b01471.

[40] Tsai RE. Mass transfer area of structured packing. thesis. 2010.

[41] Dugas RE. Carbon Dioxide Absorption , Desorption , and Diffusion in Aqueous Piperazine and Monoethanolamine. 2009.

[42] FOQUS 2024. https://github.com/CCSI-Toolset/FOQUS.

[43] Zhu K, Yue C, Wei Z, Huang J, Hu M, Ji Y, et al. Experimental and Thermodynamic Investigation on CO2 Absorption in Aqueous MEA Solutions. Advances in Materials Science and Engineering 2022;2022:6278342. https://doi.org/10.1155/2022/6278342.

[44] Rieder A, Unterberger S. EnBW's Post-Combustion Capture Pilot Plant at Heilbronn–Results of the First Year's Testing Programme. Energy Procedia 2013;37:6464–72. https://doi.org/10.1016/j.egypro.2013.06.576.

[45] Koch-Glitsch. Structured Packing 2024. https://www.koch-glitsch.com/technical-documents/brochures/structured-packing-brochure.

[46] Gibbins J, Lucquiaud M. BAT Review for New-Build and Retrofit Post-Combustion Carbon Dioxide Capture Using Amine-Based Technologies for Power and CHP Plants Fuelled by Gas and Biomass as an Emerging Technology under the IED for the UK Ver.1.0. UKCCSRC 2021.

[47] Michailos S, Gibbins J. A Modelling Study of Post-Combustion Capture Plant Process Conditions to Facilitate 95–99% CO2 Capture Levels From Gas Turbine Flue Gases. Frontiers in Energy Research 2022;10.

[48] Tobiesen FA, Juliussen O, Svendsen HF. Experimental validation of a rigorous desorber model for CO2 post-combustion capture. Chemical Engineering Science 2008;63:2641–56. https://doi.org/10.1016/j.ces.2008.02.011.

[49] Mangalapally HP, Hasse H. Pilot plant study of post-combustion carbon dioxide capture by reactive absorption: Methodology, comparison of different structured packings, and comprehensive results for monoethanolamine. Chemical Engineering Research and Design 2011;89:1216–28. https://doi.org/10.1016/j.cherd.2011.01.013.

[50] Weiland R, Hatcher N, Alvis S. Pinched Performance: Part 1. Digital Refining 2015.

[51] Bui M, Gunawan I, Verheyen TV, Meuleman E, Feron P. Dynamic Operation of Post-combustion CO2 Capture in Australian Coal-fired Power Plants. Energy Procedia 2014;63:1368–75. https://doi.org/10.1016/j.egypro.2014.11.146.

[52] Hatcher N, Alvis S, Weiland R. Gas treating simulation – a holistic perspective part 2: carbon capture. Digital Refining 2013.

[53] Michailos S, Gibbins J. Effect of stripper pressure and low lean loadings on the performance of a PCC plant for 99% CO2 capture level. SSRN Electronic Journal 2022. https://doi.org/10.2139/ssrn.4283827.

[54] Gibbins J. Amine stripper temperature profile a key to optimising net-zero performance in post-combustion carbon capture plants | LinkedIn. LinkedIn 2023. https://www.linkedin.com/pulse/amine-stripper-temperature-profile-key-optimising-net-zero-gibbins/.

[55] Rezazadeh F. Optimal Integration of Post-Combustion CO2 Capture Process with Natural Gas Fired Combined Cycle Power Plants 2016, PhD Thesis, University of Leeds.

Chapter 4: Experimental Performance Campaign for Elevated CO_2 Conditions

4.1 Experimental Campaign Overview

This chapter details an experimental campaign conducted on the Amine Capture Plant (ACP) at the Translational Energy Research Centre (TERC), Sheffield, pictured in Figure 4.1. The objective was to evaluate the plant's capture performance across a range of flue gas compositions representative of emissions from industrial processes in the iron and steel industry. In the open literature, very few pilot-scale studies have been conducted with elevated flue gas CO_2 concentrations typical of industrial process, highlighting a critical knowledge gap in the practical application of carbon capture using chemical absorption.

Figure 4.1: Photograph of the TERC ACP.

Most of the studies on the TERC ACP have been performed with flue gas CO_2 concentrations up to 10 mol.%, typical of fossil fuel combustion waste gases. However, the Developed Carbon Capture (DCC) model developed in the preceding chapter suggests that the ACP can achieve capture efficiencies of 90% or higher at significantly higher CO_2 concentrations, provided the flue gas volumetric flow rate and reboiler duty remain sufficiently low. Accordingly, the experimental conditions in this study were guided by DCC model predictions. Tests were conducted at flue gas CO_2 concentrations of 10, 15, 20 and 25 mol.%, with a fixed flow rate of 150 Nm^3/h. The target capture efficiency across all conditions was 90%, using a monoethanolamine (MEA) solvent concentration of 35 wt.%.

This study establishes novel baseline data for chemical absorption-based carbon capture using a conventional packed bed (PB) system without advanced process modifications, using a standard MEA solvent. This enables straightforward comparison with future studies and lays the groundwork for improving the capture process to reduce the overall energy demand. The experimental data offers insights into the expected capabilities of real-world PB capture systems and helps to define optimal operating conditions to enhance capture performance. In addition, this work extends the proven operating range of the TERC ACP, facilitating future investigations under high-CO_2 conditions.

Finally, the data will be used to refine the DCC model into a calibrated simulation tailored to the TERC ACP, forming the foundation for developing a digital twin representation of the plant. This simulation will be capable of delivering rapid results while reducing reliance on costly and time-intensive experimental work.

The following sections describe the experimental setup and methodology, followed by performance assessment including comparison with DCC model predictions and existing literature. Solvent regeneration energy requirements and system heat losses are also analysed for each condition.

4.2 Pilot Plant Technical Specifications

4.2.1 Process Description of the TERC ACP

The design of the TERC ACP is based on a conventional amine-based CO_2 capture plant, with the simplified layout presented in Figure 4.2. The ACP is integrated with various combustion units at TERC, including a grate boiler waste-to-energy plant, a combined heat and power (CHP) gasifier, and a CHP gas turbine, with additional connections available for visiting or future units. The plant is designed to capture up to one tonne of CO_2 per day, with the capacity to scrub between 100 to 250 Nm^3/h of flue gas. A general process description was briefly introduced in Chapter 3 but omitted technical specifications not pertinent to the development of the DCC model. These are now described in detail below [1–6].

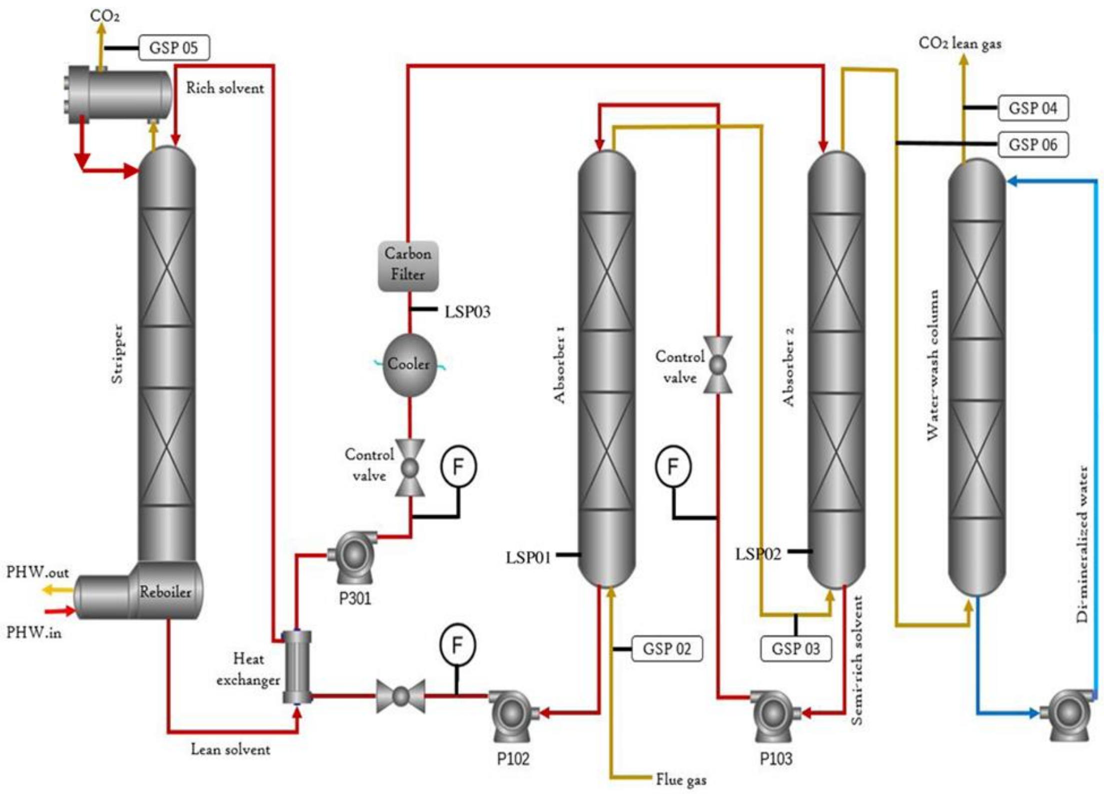

Figure 4.2: Simplified flow diagram of the TERC ACP [7].

Flue gas may be sourced from an integrated combustion unit or a synthetic gas mixing skid comprising three bulk gas streams: CO_2, N_2 and air. CO_2 and N_2 are supplied from cryogenic storage tanks. It also has the capability to inject trace gases such as NO_x and SO_x, enabling a wide range of flue gas compositions to be simulated. The plant is also equipped with a flue gas desulphurisation (FGD) unit capable of removing acid gases such as SO_2 and HCl to concentrations below 10 ppm before the absorber, to minimise solvent degradation and system corrosion. For this experimental campaign, the FGD was bypassed, because clean flue gas was supplied by the gas skid. Using synthetic flue gas reduces operating costs and improves gas composition consistency. Throughout the campaign, the flue gas flow rate was maintained at 150 Nm^3/h, while the CO_2 partial pressure was varied across test conditions. The remaining balance of the gas mixture was made up with air to maintain the constant total flow rate.

Regardless of source, all flue gases pass through a booster fan to deliver it to the absorber and the rest of the capture plant. A pitot tube, along with temperature and pressure sensors, measures the gas flow at the absorber inlet. The absorber consists of two identical columns, each containing two packed beds, 3 m high and 250 mm in diameter, filled with Flexipac 350X structured packing from Koch Glitsch. Bucket-type liquid distributors are located at the solvent inlets at the top of each column, with liquid redistributors located between the two packed beds in each column. Gas distributors are located at the gas inlet at the bottom of each column. For this study, the absorber columns were operated in series with counter-current flow, though parallel and single column flow configurations are also possible. The absorbers operate at atmospheric pressure.

Flue gas flows upward through the packing, while solvent flows downward, allowing CO_2 to react with the lean solvent upon contact. The structured packing increases contact area, enhancing mass transfer and absorption rates. The absorption process is exothermic, with the thermal profile monitored using 12 resistance temperature detectors (RTDs) distributed along each absorber column. Partially cleaned flue gas from absorber 1 enters absorber 2, where the absorption process continues. Simultaneously, semi-lean, partially laden solvent exits absorber 2 and enters the top of absorber 1, becoming CO_2-rich by the time it reaches the sump at the bottom of the column.

Lean solvent entering the absorber is temperature and flow controlled. A Coriolis flow meter measures the mass flow, regulated by a variable speed drive pump. Similarly, the rich solvent leaving the absorber is also measured with a Coriolis meter. Its level in the sump is controlled using a separate pump to ensure steady state operation. The rich solvent is then preheated via a plate type cross-heat exchanger, using heat from the regenerated lean solvent returning from the reboiler. The preheated rich solvent enters the top of the stripper column, where it is further heated to a temperature between 110 and 125 °C, depending on the stripper pressure. This elevated temperature reverses the absorption process in an endothermic reaction, releasing the captured CO_2 and regenerating the solvent. The stripper column is 7.5 m high and 300 mm in diameter, packed with IMTP25 random packing from Koch Glitsch. The stripper thermal profile is monitored using nine RTDs distributed across the column.

Solvent regeneration is driven by heat input from the reboiler, a horizontal vessel equipped with a shell and tube heat exchanger located at the bottom of the stripper. Pressurised hot water (PHW), supplied by an electrically heated boiler, circulates through the tubes in a closed loop. The PHW is maintained at 4.8 to 5.0 bara and a temperature of approximately 125 ° C. Changes in PHW flow rate or temperature directly influence solvent regeneration and capture efficiency. For this campaign, the PHW temperature was varied to achieve the target capture efficiency of 90%.

Heat transfer from the PHW to the solvent in the reboiler produces steam. The steam travels up the stripper column, reducing the CO_2 partial pressure in the vapour phase and increasing the driving force for desorption. The stripper packing increases surface area to enhance CO_2 desorption. When the steam contacts the packing and the falling rich solvent, a portion of it condenses, transferring latent heat into the solvent, supplying energy for the endothermic desorption reaction to liberate CO_2. The resulting CO_2, along with excess steam and trace solvent vapours, exits the top of the stripper and passes through an air cooler and reflux condenser. CO_2 is vented through the top of the reflux vessel via pressure control valves that regulate the system pressure, before exiting the top of the plant. In the future this may be directed to a carbon capture utilisation (CCU) plant. Condensed water and solvent from the reflux vessel are returned to the top of the stripper to maintain the mass balance of the solvent loop. Regenerated hot lean solvent from the reboiler sump passes through the cross-heat exchanger to preheat the incoming rich solvent. Thermocouples monitor inlet and outlet temperatures. The now warm lean solvent temperature is further cooled to 40 °C by passing through an air cooler with a valve-controlled bypass. A temperature sensor at the main and bypass stream mixing point informs the valve position, thereby controlling the flow rate of these streams to maintain a constant temperature. After cooling, the lean solvent passes through a carbon filter filled with acid-washed activated carbon to remove solvent degradation products before re-entering the absorber, completing the cycle. Lean and rich solvent samples are taken downstream of their corresponding solvent pumps to monitor the CO_2 loading levels and solvent concentrations.

The cleaned flue gas exiting the second absorber passes through a water wash column, packed with IMTP25 random packing, also 7.5 m high and 300 mm in diameter. The water wash removes entrained solvent droplets carried over by the flue gas, minimising contaminant emissions from the ACP. The gas exits the absorber saturated with water, causing gradual water loss from the solvent circuit. To compensate, water is periodically transferred from the wash column to the sump of the first absorber and then pumped to the stripper in an automated process. This maintains overall water and solvent balance. The water wash is replenished with fresh demineralised water as needed. Similarly, solvent concentration is maintained by periodic addition of fresh solvent.

A summary of the technical specifications and operating parameter ranges for the TERC ACP are presented in Table 4.1 and Table 4.2, respectively.

Table 4.1: Technical specifications of the TERC ACP.

Equipment	Specification
Absorber Column	Two 250 mm diameter columns, providing up to 12 m total packed height Packing: 4 x 3 m packed beds of Flexipac 350X structured packing 12 Resistance Temperature Detectors in each absorber column for temperature monitoring
Stripper Column	Single column of 300 mm diameter with 8 m total height Packing: IMPT25 random packing 9 Resistance Temperature Detectors for temperature monitoring
Cross-Heat Exchanger	Plate heat exchanger Maximum heat duty up to 43 kW
Stripper Reboiler	Supplied with pressurised hot water Electric boiler heat duty up to 72 kW

Table 4.2: Parameter operating ranges of the TERC ACP.

Parameter	Operational Range
Solvent Mass Flow Rate (CO_2 Free Basis)	300 – 1200 kg/h
Flue Gas Volumetric Flow Rate	100 – 250 Nm^3/h
Stripper Column Pressure	1.0 – 3.0 bara

4.3 Methodology

4.3.1 *Sampling and Measurements Overview*

The following key measurements were recorded at various locations on the ACP during the testing period:

- Temperature, flow and pressure readings were taken across all units and pipelines, including the PHW reboiler system, to enable a complete specification and operational overview of the plant.
- Flue gas compositions were measured at six locations using a Gasmet FTIR analyser.
- Solvent samples were analysed using a Mettler Toledo auto-titrator.

These three sets of measurements were then used to calculate key performance indicators for each capture condition, including specific reboiler duty (SRD), CO_2 capture efficiency, liquid to gas (L/G) ratios, solvent concentrations, and solvent CO_2 loadings.

4.3.2 *Process Data Analysis*

Accurate measurement of the incoming and outgoing flue gas is essential for calculating capture performance. Volumetric flow rate, temperature, and pressure are recorded at the absorber gas inlet, whereas only temperature and pressure measurements are recorded at the absorber outlet. The omission of a gas flow rate measurement is intentional, because the presence of water vapour in the exiting flue gas could damage an installed flow meter.

Measurements from the PHW circuit are also necessary to determine the reboiler duty. With the volumetric flow rate and pressure of the PHW held constant during testing, the amount of heat transferred to the solvent in the reboiler is directly proportional to the temperature differential between the inlet and outlet PHW streams. The specific heat capacity and density of PHW at each capture condition were obtained using the "COOLPROP" Microsoft Excel add-in [8], based on the recorded temperature and pressure data.

Temperature measurements along the length of the absorber and stripper columns were used to construct column temperature profiles. These profiles provide insight into system operating modes and aid diagnostic analyses [9–11].

4.3.3 *Flue Gas Analysis*

Fourier Transform Infrared (FTIR) spectroscopy is used for flue gas analysis on the TERC ACP. In this method, infrared (IR) radiation is passed through a heated sample of flue gas. The gas absorbs IR radiation at specific wavelengths characteristic of its molecular structure and functional groups [12]. Because absorption at each wavelength is proportional to the concentration of the corresponding molecule, FTIR can be used to both identify and quantify species in the sample. Unknown samples can typically be characterised by comparing their absorption spectra to a database of reference IR spectra, enabling molecular identification.

Flue gas analysis on the TERC ACP is performed using a Gasmet DX4000 FTIR analyser, depicted in Figure 4.3. The sampling sequence and duration are user defined through the FTIR software. The system allows for gas analysis at six different locations on the ACP, as detailed in Table 4.3.

Figure 4.3: Photograph of the Gasmet DX4000 FTIR analyser used for gas analysis.

Table 4.3: Description of flue gas sampling points, labelled in Figure 4.2.

Label	Location on the Plant
GSP01	FGD inlet
GSP02	Inlet of absorber 1 (FGD outlet)
GSP03	Inlet of absorber 2 (absorber 1 outlet)
GSP04	Water wash inlet (absorber 2 outlet)
GSP05	Outlet of stripper (product CO_2 stream)
GSP06	Water wash outlet

Flue gas samples are extracted using isokinetic sampling probes and delivered to the FTIR via heated filters, heated sampling lines, and a heated cabinet containing solenoid valves for switching between sampling points. The entire sampling system, including the FTIR instrument, is maintained at 180 °C to prevent condensation. Condensation is detrimental to the FTIR cell, where moisture will gradually dissolve the cell material and change the absorption characteristics, which leads to incorrect absorption spectra and false identification of samples.

The FTIR analysis software is calibrated for 16 typical combustion gases and monoethanolamine (MEA), with capacity for up to 50 species per sample. Additional compounds can be added to the calibration as needed.

In this study, the Gasmet FTIR was used to monitor the changes in flue gas composition between two key locations: GSP02 (inlet of absorber 1) and GSP04 (outlet of absorber 2). Continuous real-time monitoring flue gas compositions of enabled identification of steady state conditions, defined by a stable outlet composition. Data collected during steady state periods were averaged over 15 second intervals, chosen to reduce measurement variation, and used for capture performance calculations.

4.3.4 Solvent Analysis

Solvent concentration and CO_2 loadings were determined from solvent samples taken at three sampling locations, as described in Table 4.4.

Table 4.4: Description of solvent sampling points, labelled in Figure 4.2.

Label	Location on the Plant
LSP01	Rich solvent from the outlet of absorber 1
LSP02	Semi-rich solvent from the outlet of absorber 2
LSP03	Lean solvent from the outlet of the stripper

Analysis involved two chemical titrations, conducted using a T9 Mettler Toledo auto-titrator, pictured in Figure 4.4. The titrations were performed in “semi-automatic” mode, where sample preparation and mass measurements were done manually. Results were recorded using Mettler Toledo’s LabX software. For this study, only the lean and rich solvent streams were sampled for analysis.

Figure 4.4: Photograph of the auto-titrator system for solvent analysis.

Additional solvent properties, dissolved oxygen and iron concentrations, can also be measured to monitor solvent degradation. Installed optical probes determine dissolved oxygen content of the solvent, while iron content is analysed manually from collected samples. However, these measurements were omitted for this campaign as this study was focused on performance assessment, and not solvent degradation.

4.4 Operating Procedures

4.4.1 Standard Operating Procedure

The procedure below assumes that the ACP has already been filled with solvent and demineralised water to the correct sump levels, with the solvent concentration adjusted to the required specification.

i) The water wash pump, lean solvent cooler and stripper condenser are started to ensure all systems are operational.

ii) The electric boiler for the PHW is then turned on, with an initial temperature set point of 120 °C used for system warm up. As the PHW heats and circulates through the reboiler loop it begins transferring heat to the solvent in the reboiler.

iii) The required solvent flow rates are then configured for the following pumps, in sequence: (1) stripper to absorber 2, (2) absorber 2 to absorber 1, and (3) absorber 1 to the stripper. Once the solvent temperature in the reboiler reaches 80 °C these pumps are started in order, initiating solvent circulation through the plant.

iv) After the solvent circulation stabilises, the flue gas booster fan is switched on and the desired gas flow rate is set, pushing flue gas through the absorber and contacting the flowing solvent.

v) CO_2 injection from the gas skid is then initiated and adjusted to achieve the required concentration for each capture condition. Stabilisation of CO_2 levels is necessary before steady state operation can be confirmed.

The plant can be placed in automatic mode to maintain steady state operation at a fixed solvent flow rate. This is achieved by using the parameter “average total mass” in the ACP control system, a value calculated from solvent flows, sump liquid levels and liquid holdups, as a control setpoint. This value gradually decreases over time, triggering a water transfer from the water wash column once the average total mass drops more than 2 to 3% below the setpoint. Caution is required when enabling automatic control before the system has reached operating temperature because solvent expansion arising from heating affects measurement readings. This means that the average total mass value is variable until the operating temperature is achieved and cannot be used as a set point to maintain a fixed solvent flow rate. Stripper pressure is controlled using one of two control valves located at the top of the stripper column. For this experimental campaign, the stripper pressure was fixed at 1.2 bara.

4.4.2 Capture Condition Procedure

Once steady state has been achieved at a given solvent flow rate, the capture rate of CO_2 can be measured. This evaluation begins by determining the composition of the flue gas entering the absorber using FTIR analysis to measure the CO_2 concentration. After confirming that the inlet concentration is stable, the sampling system is used to monitor the CO_2 concentration in the flue gas exiting the absorber.

For a given capture efficiency, the expected CO_2 concentration in the exiting flue gas can be estimated using the CO_2 concentration of the incoming flue gas and the corresponding CO_2 removal fraction, as described below:

$$c_{\mathrm{CO_2,removed,vol.\%}} = c_{\mathrm{CO_2,0,vol.\%}} \cdot k_{\mathrm{removal}} \tag{4.1}$$

$$c_{\mathrm{CO_2,remaining,vol.\%}} = c_{\mathrm{CO_2,0,vol.\%}} - c_{\mathrm{CO_2,removed,vol.\%}} \tag{4.2}$$

$$c_{\mathrm{exit\ gas,vol.\%}} = 100\% - c_{\mathrm{CO_2,removed,vol.\%}} \tag{4.3}$$

$$c_{\mathrm{CO_2,1,vol.\%}} = \frac{c_{\mathrm{CO_2,remaining,vol.\%}}}{c_{\mathrm{exit\ gas,vol.\%}}} \cdot 100 \tag{4.4}$$

Where:

$c_{\mathrm{CO_2,removed,vol.\%}}$ = captured CO_2 (vol.%)

$c_{\mathrm{CO_2,0,vol.\%}}$ = initial CO_2 percentage in the flue gas (vol.%)

k_{removal} = CO_2 removal fraction (e.g. 0.9 for 90% capture)

$c_{\mathrm{CO_2,remaining,vol.\%}}$ = uncaptured CO_2 (vol.%)

$c_{\mathrm{exit\ gas,vol.\%}}$ = exiting gas volume as a percentage of the inlet flue gas (vol.%)

$c_{\mathrm{CO_2,1,vol.\%}}$ = volume of CO_2 in the exiting flue gas (vol.%)

Once the target CO_2 concentration for the exiting flue gas stream has been calculated, the system can be adjusted to achieve this at the required solvent flow rate. This is done by incrementally adjusting the temperature of the reboiler, which subsequently alters the temperature of the PHW, since its flow rate remains constant. When the target CO_2 concentration was achieved, or as close as reasonably practicable within the time constraints of the experimental campaign, the system was maintained at steady state for approximately one hour and the data was then averaged to smooth out any residual fluctuations. At the end of the steady state period, samples of the lean and rich solvent were taken for analysis. The system was then adjusted to the next capture condition. The specific capture conditions investigated in this experimental campaign are detailed in the experimental matrix presented in Section 4.7.

4.4.3 Data Processing Procedure

The data obtained from the experimental campaign is processed in the following order:

i) The recorded sampling time of the solvent samples marks the endpoint of the gas outlet steady state period for each specific capture condition.

ii) FTIR data is then used to identify the duration and timestamps of the gas outlet steady state period. This involves assessing the CO_2 concentration in the exiting flue gas and identifying periods of stability with minimal fluctuation. The FTIR data for CO_2 and H_2O is averaged over this identified time period.

iii) FTIR data for CO_2 and H_2O content in the inlet flue gas is also collected and averaged over an identified gas inlet steady state period.

iv) Process data is collected and averaged for the same identified steady state periods.

v) Capture efficiency and the SRD can be calculated by combining the FTIR and process data.

vi) The lean and rich solvent sample data is analysed to determine the MEA and CO_2 concentrations, as well as the CO_2 loading.

vii) Finally, by integrating the solvent analysis results with the process data, the mass flow rates of individual solvent components can be estimated, enabling a full specification of the system.

The detailed calculations used to analyse the collected process data are described in the next section.

4.5 Data Calculations

4.5.1 Capture Efficiency Calculations

The calculation of CO_2 capture efficiency is carried out around the absorber using Method 3 as described by Thimsen et al. [13]. This method requires determining the CO_2 mass flow rates in the inlet and outlet flue gas streams, which is achieved through combining FTIR data with flue gas process measurements.

Although the flue gas from the synthetic gas mixing skid is controlled to maintain a constant volumetric flow rate, slight variations in temperature and pressure can influence the actual volume. These fluctuations are recorded, and the Ideal Gas Law is applied to appropriately scale the volume flow to account for these changes:

$$P_{\mathrm{gas}} \cdot V_{\mathrm{gas}} = n_{\mathrm{gas}} \cdot R \cdot T_{\mathrm{gas}} \tag{4.5}$$

Where:

P_{gas} = pressure of the flue gas (Pa)

V_{gas} = volume of the flue gas (m^3)

n_{gas} = number of moles of flue gas (mol)

R = universal gas constant (J/(mol·K))

T_{gas} = temperature of the flue gas (K)

Assuming a fixed molar gas flow and a constant value for R, the relationship between two gas states, designated as conditions 1 and 2, can be simplified as follows:

$$\frac{P_{\mathrm{gas},1} \cdot V_{\mathrm{gas},1}}{T_{\mathrm{gas},1}} = \frac{P_{\mathrm{gas},2} \cdot V_{\mathrm{gas},2}}{T_{\mathrm{gas},2}} \tag{4.6}$$

This equation can be rearranged to solve for the new volume:

$$V_{\mathrm{gas},2} = V_{\mathrm{gas},1} \cdot \frac{P_{\mathrm{gas},1} \cdot T_{\mathrm{gas},2}}{P_{\mathrm{gas},2} \cdot T_{\mathrm{gas},1}} \tag{4.7}$$

The FTIR data provides volume fractions of CO_2 and H_2O in the flue gas, with the remaining composition assumed to consist of N_2, O_2, and Ar in ratios typical of air:

$$y_{\mathrm{i}} = k_{\mathrm{air,i}} \cdot \left(1 - y_{\mathrm{CO_2}} - y_{\mathrm{H_2O}}\right) \tag{4.8}$$

Where:

y_{i} = volume fraction of a specific component in the flue gas

$k_{\mathrm{air,i}}$ = air scaling factor for specific component in the flue gas, where N_2 = 0.781, O_2 = 0.21, and Ar = 0.009

$y_{\mathrm{CO_2}}$= volume fraction of CO_2 in the flue gas

$y_{\mathrm{H_2O}}$= volume fraction of H_2O in the flue gas

The molar quantities of individual components can be calculated using the molar gas volume equation in combination with their respective volume fractions:

$$n_\mathrm{i} = y_\mathrm{i} \cdot \frac{V_\mathrm{gas}}{0.0224} \tag{4.9}$$

Where:

n_i = number of moles of a specific component in the flue gas (mol)

The mass of each component can be calculated by multiplying its molar amount by its molecular weight:

$$m_\mathrm{i} = n_\mathrm{i} \cdot \frac{MW_\mathrm{i}}{1000} \tag{4.10}$$

Where:

m_i = mass of a specific component (kg)

MW_i = molecular weight of a specific component (g/mol)

From these equations, the mass flow rates of each component in the flue gas entering the absorber are now known. The next step is to determine the mass flow rate of each component leaving the top of the absorber column, after CO_2 absorption. This cannot be calculated using the same method as before, since there is no gas flow measurement at the absorber outlet. Instead, the outlet gas flow rate is determined through a mass balance around the absorber.

To perform this mass balance, it is assumed that no absorption of N_2, O_2 or Ar occurs within the solvent, meaning that the same molar flow rates of these components exit the absorber as entered. Based on this assumption, the outlet volumes of these three components can be directly calculated:

$$V_\mathrm{i} = n_\mathrm{i} \cdot 0.0224 \tag{4.11}$$

Where:

V_i = volume of a specific component in the flue gas (m^3)

The FTIR data provides the volume fractions of CO_2 and H_2O in the exiting flue gas. Therefore Equation (4.8) can once again be applied to determine the volume fractions of N_2, O_2, and Ar. With the known outlet volumes of N_2, O_2, and Ar, along with the volume fractions of all five components, it becomes possible to calculate a preliminary estimate of the total volume of the exiting flue gas:

$$V_\mathrm{exit\ gas,1} = \frac{V_{\mathrm{N_2}} + V_{\mathrm{O_2}} + V_\mathrm{Ar}}{1 - y_{\mathrm{CO_2}} - y_{\mathrm{H_2O}}} \tag{4.12}$$

Where:

$V_\mathrm{exit\ gas,1}$ = preliminary volume of exiting flue gas (m^3)

The exiting flue gas volume is also influenced by small variations in temperature and pressure. As such, the actual gas volume is calculated in the same manner as shown in Equation (4.7):

$$V_{\text{exit gas,2}} = V_{\text{exit gas,1}} \cdot \frac{P_{\text{exit gas,1}} \cdot T_{\text{exit gas,2}}}{P_{\text{exit gas,2}} \cdot T_{\text{exit gas,1}}} \tag{4.13}$$

Where:

$V_{\text{exit gas,2}}$ = final volume of exiting flue gas (m^3)

With the actual volume of the exiting flue gas known, the molar and mass amounts of CO_2 and H_2O can be calculated using Equations (4.9) and (4.10), respectively. This fully specifies the composition of the exiting flue gas, with all components having defined volume fractions, volumes, and masses. All calculations are carried out under the assumption of steady state conditions, with quantities expressed as flow rates over time, where applicable.

The mass of captured CO_2 is determined as the difference between the CO_2 mass flow rates in the flue gas at the inlet and outlet out the absorber column:

$$\dot{m}_{\text{CO}_2\text{,captured}} = \dot{m}_{\text{CO}_2\text{,in}} - \dot{m}_{\text{CO}_2\text{,out}} \tag{4.14}$$

Where:

$\dot{m}_{\text{CO}_2\text{,captured}}$ = mass flow rate of captured CO_2 (kg/h)

$\dot{m}_{\text{CO}_2\text{,in}}$= mass flow rate of CO_2 entering the absorber (kg/h)

$\dot{m}_{\text{CO}_2\text{,out}}$ = mass flow rate of CO_2 exiting the absorber (kg/h)

Accordingly, the capture efficiency for a given capture condition can be determined by calculating the percentage difference between the mass of captured CO_2 and the CO_2 mass flow at the absorber inlet:

$$\eta_{\text{capture}} = \frac{\dot{m}_{\text{CO}_2\text{,captured}}}{\dot{m}_{\text{CO}_2\text{,in}}} \cdot 100 \tag{4.15}$$

Where:

η_{capture} = capture efficiency of CO_2 (%)

4.5.2 Specific Reboiler Heat Duty Calculations

Heat is supplied to the stripper via the PHW circulating through the reboiler at the bottom of the column. The heater is operated from the control room, where the flow rate, temperature, and pressure of the PHW are controlled. Although the heater has a maximum electrical input of 72 kW, not all of this energy is transferred from the PHW into solvent. The mass flow rate of the PHW is calculated using the following equation:

$$\dot{m}_{\text{PHW}} = \rho_{\text{PHW}} \cdot \dot{V}_{\text{PHW}} \tag{4.16}$$

Where:

$\dot{m}_{\text{PHW}}$ = mass flow rate of the PHW (kg/h)

ρ_{PHW} = density of the PHW at the average temperature (kg/m^3)

$\dot{V}_{\text{PHW}}$ = volumetric flow rate of the PHW (m^3/h)

The reboiler heat duty is calculated from the temperature difference of the PHW using the following equation:

$$Q_{\mathrm{reboiler}} = \dot{m}_{\mathrm{PHW}} \cdot C_{\mathrm{p,PHW}} \cdot \left(T_{\mathrm{PHW,in}} - T_{\mathrm{PHW,out}}\right) \quad \textbf{(4.17)}$$

Where:

Q_{reboiler} = reboiler heat duty (kJ/h)

$C_{\mathrm{p,PHW}}$ = specific heat capacity of the PHW (kJ/(kg·K))

$T_{\mathrm{PHW,in}}$ = inlet temperature of the PHW (°C)

$T_{\mathrm{PHW,out}}$ = outlet temperature of the PHW (°C)

The specific reboiler duty, defined as the amount of energy required by the reboiler to release a unit mass of CO$_2$, is calculated by dividing the total energy input by the mass of CO$_2$ captured:

$$q_{\mathrm{reboiler}} = \frac{Q_{\mathrm{reboiler}}}{\dot{m}_{\mathrm{CO_2,captured}} \cdot 10^3} \quad \textbf{(4.18)}$$

Where:

q_{reboiler} = specific reboiler duty (MJ/(kg·CO$_2$))

The SRD is a key performance metric, allowing straightforward comparisons of different operating conditions.

4.5.3 Solvent Concentration Calculation

The first titration determines the solvent concentration using water and hydrochloric acid. A 1 mL of sample of solvent is injected into 50 mL of water and titrated with 0.2 M hydrochloric acid until a pH endpoint of 4.8 is reached. The MEA concentration is then calculated as follows:

$$c_{\mathrm{MEA,wt.\%}} = \frac{M_{\mathrm{HCl}} \cdot V_{\mathrm{HCl}} \cdot MW_{\mathrm{MEA}} \cdot 100}{m_{\mathrm{sample,1}} \cdot 1000} \quad \textbf{(4.19)}$$

Where:

$c_{\mathrm{MEA,wt.\%}}$ = concentration of MEA in the solvent by mass (wt.%)

M_{HCl} = molarity of HCl (mol/L)

V_{HCl} = volume of HCL required for titration (mL)

MW_{MEA} = molecular weight of MEA (g/mol)

$m_{\mathrm{sample,1}}$ = mass of first solvent sample (g)

4.5.4 CO$_2$ Concentration Calculation

The second titration determines the acid CO$_2$ content using methanol and sodium hydroxide. First, 50 mL of methanol is titrated with 0.5 M sodium hydroxide until a pH of 11.2 is reached. A 1 mL sample of solvent is then added, lowering the pH, after which titration continues with 0.5M sodium hydroxide until the pH returns to 11.2. The CO_2 concentration is then calculated as follows:

$$c_{\mathrm{CO_2,wt.\%}} = \frac{M_{\mathrm{NaOH}} \cdot V_{\mathrm{NaOH}} \cdot MW_{\mathrm{CO_2}} \cdot 100}{m_{\mathrm{sample,2}} \cdot 1000} \tag{4.20}$$

Where:

$c_{\mathrm{CO_2,wt.\%}}$ = concentration of captured CO_2 in the solvent by mass (wt.%)

M_{NaOH} = molarity of NaOH (mol/L)

V_{NaOH} = volume of NaOH required for titration (mL)

$MW_{\mathrm{CO_2}}$ = molecular weight of CO_2 (g/mol)

$m_{\mathrm{sample,2}}$ = mass of second solvent sample (g)

4.5.5 Solvent Loading Calculations

Once the concentrations of both MEA and CO_2 are known, the final CO_2 loading in the solvent can be determined using the following equation:

$$\lambda = \frac{c_{\mathrm{CO_2,wt.\%}} \cdot MW_{\mathrm{MEA}}}{c_{\mathrm{MEA,wt.\%}} \cdot MW_{\mathrm{CO_2}}} \tag{4.21}$$

Where:

λ = CO_2 loading in the solvent (mol·CO_2/mol·MEA)

Equation (4.21) may also be expressed as a combination of Equations (4.19) and (4.20):

$$\lambda = \frac{M_{\mathrm{NaOH}} \cdot V_{\mathrm{NaOH}} \cdot m_{\mathrm{sample,1}}}{M_{\mathrm{HCl}} \cdot V_{\mathrm{HCl}} \cdot m_{\mathrm{sample,2}}} \tag{4.22}$$

4.5.6 Solvent Component Mass Flow Calculations

Although the lean solvent flow rate is carefully controlled, the exact mass flow rates of the individual components within the solvent are not directly measured. By combining the results from the solvent analysis with the known solvent flow data, it is possible to estimate the mass fractions and corresponding mass flow rates of MEA, H_2O and CO_2. These calculations assume that the solvent consists of apparent components, rather than their true electrolyte forms. The procedure begins by assuming one mole of MEA in the solvent, against which the molar amounts of H_2O and CO_2 are scaled. The lean solvent loading, determined from the chemistry analysis, is expressed in units of mol·CO_2/mol·MEA, leaving the molar quantity of H_2O as the only unknown. Each of these molar quantities is then multiplied by their respective molecular weights to obtain initial mass values, with both the molar and mass quantities of H_2O still to be determined:

$$m_{\mathrm{MEA},0} = 1 \cdot MW_{\mathrm{MEA}} \tag{4.23}$$

$$m_{\mathrm{CO_2},0} = \lambda \cdot MW_{\mathrm{CO_2}} \tag{4.24}$$

$$m_{\mathrm{H_2O},0} = n_{\mathrm{H_2O},0} \cdot MW_{\mathrm{H_2O}} \tag{4.25}$$

Where:

$m_{\mathrm{MEA},0}$= initial mass of MEA (kg)

$m_{\mathrm{CO_2},0}$= initial mass of CO_2 (kg)

$m_{\mathrm{H_2O},0}$ = initial mass of H_2O (kg)

$n_{\mathrm{H_2O},0}$ = initial moles of H_2O (mol)

$MW_{\mathrm{H_2O}}$ = molecular weight of H_2O (g/mol)

The MEA concentration derived from the chemistry analysis accounts for both CO_2 and H_2O in the solvent. Expressed as a weight percentage, it reflects the proportion of MEA relative to the total initial mass of all components in the solvent:

$$c_{\mathrm{MEA,wt.\%}} = \frac{m_{\mathrm{MEA},0} \cdot 100}{m_{\mathrm{MEA},0} + m_{\mathrm{CO_2},0} + m_{\mathrm{H_2O},0}} \tag{4.26}$$

The initial mass of H_2O can be determined by rearranging Equation (4.26) accordingly:

$$m_{\mathrm{H_2O},0} = \frac{\left(m_{\mathrm{MEA},0} \cdot 100\right) - c_{\mathrm{MEA,wt.\%}} \cdot m_{\mathrm{MEA},0} - c_{\mathrm{MEA}} \cdot m_{\mathrm{CO_2},0}}{c_{\mathrm{MEA,wt.\%}}} \tag{4.27}$$

Once the mass is known, the initial molar quantity of H_2O can be found by dividing this value by the molecular weight of H_2O, as per the rearranged form of Equation (4.25):

$$n_{\mathrm{H_2O},0} = \frac{m_{\mathrm{H_2O},0}}{MW_{\mathrm{H_2O}}} \tag{4.28}$$

To verify the accuracy of these initial mass estimates, the CO_2 concentration obtained from the chemistry analysis is validated. Similar to Equation (4.26), the CO_2 concentration is expressed as the proportion of CO_2 relative to the total initial solvent mass. This calculated value should align closely with the CO_2 concentration determined analytically.

$$c_{\mathrm{CO_2,wt.\%}} = \frac{m_{\mathrm{CO_2},0} \cdot 100}{m_{\mathrm{CO_2},0} + m_{\mathrm{MEA},0} + m_{\mathrm{H_2O},0}} \tag{4.29}$$

Finally, once the CO_2 concentration has been validated, the initial masses of MEA, CO_2 and H_2O are scaled by a single “solvent flow rate scaling factor”. This factor ensures that the total of the scaled component mass flow rates matches the target solvent flow rate from the process data, while preserving the calculated mass fractions. The resulting mass flow rates for each component are then recorded in the results tables.

$$\dot{m}_{\mathrm{i}} = m_{\mathrm{i,0}} \cdot k_{\mathrm{solvent}} \tag{4.30}$$

$$\dot{m}_{\mathrm{solvent}} = \dot{m}_{\mathrm{MEA}} + \dot{m}_{\mathrm{CO_2}} + \dot{m}_{\mathrm{H_2O}} \tag{4.31}$$

Where:

$\dot{m}_{\mathrm{i}}$ = mass flow rate of a specific component (kg/h)

$m_{\mathrm{i,0}}$ = initial mass of specific component (kg)

k_{solvent} = solvent flow rate scaling factor (1/h)

$\dot{m}_{\mathrm{solvent}}$ = total mass flow rate of the solvent (kg/h)

$\dot{m}_{\mathrm{MEA}}$ = mass flow rate of MEA (kg/h)

$\dot{m}_{\mathrm{CO_2}}$ = mass flow rate of CO_2 (kg/h)

$\dot{m}_{\mathrm{H_2O}}$ = mass flow rate of H_2O (kg/h)

This process can also be applied to the rich solvent flow to validate the MEA and CO_2 concentrations corresponding to the observed rich loading. For completeness, the component mass flow rates in the rich solvent can be calculated in the same manner.

It was observed that the rich solvent flows exhibited minor reductions in the mass flow rates of MEA and H_2O compared to the lean solvent flows, with H_2O losses being more pronounced. These discrepancies are primarily attributed to evaporative losses within the absorber column, driven by the exothermic nature of the CO_2 absorption.

When the component mass flow rates for both lean and rich solvent streams are known, an alternative method for calculating CO_2 capture efficiency equation becomes possible. The difference between the CO_2 mass flow rates of the two streams can be converted to a capture efficiency, providing a supplementary method and point of comparison to the primary approach outlined in Equation (4.15). It was evident that the capture efficiency values resulting from this supplementary method were typically lower than those obtained using FTIR data. This difference arises because the primary approach relies on process data averaged over a defined steady state period, whereas the alternative method uses instantaneous values from chemical analysis. The averaging process smooths out fluctuations and can obscure transient variations or anomalies captured during the measurement period. It was noted that longer steady state periods tended to amplify discrepancies between the two methods, suggesting that shorter averaging windows could improve alignment. Nevertheless, the capture efficiency calculated using Equation (4.15) was selected as the primary value for reporting, as this approach was considered more robust and reliable for the present analysis. To support this selection, an uncertainty analysis framework was developed to assess the validity of the calculated experimental results, as detailed in the following section.

4.6 Uncertainty Analysis Framework

To complement the primary experimental calculations, an uncertainty analysis was performed to quantify the propagation of uncertainty through to the final calculated results. This involved consideration into Type A and Type B uncertainties [14]. The analysis follows a single sigma (1σ) framework, where the uncertainty represents one standard deviation from the mean.

Two distinct types of uncertainty are defined:

1) Absolute uncertainty: the margin of error in a measurement, expressed in the same units as the measurement itself (e.g., ±0.5 kg/h).
2) Relative uncertainty: the uncertainty expressed as a unitless fraction or a percentage of the mean value, enabling comparisons of precision across different measurements.

The propagation of uncertainty was based on the following key assumptions:

- The uncertainty for any averaged measured variable was taken as the statistical uncertainty (Type A), represented by the standard deviation of the corresponding set of raw data points. This applied to mass flow rates of the solvent, volume flow rates of the flue gas and PHW, stream and column temperatures, inlet and outlet gas pressures, and gas compositions recorded by the FTIR.
- Instrumental uncertainty (Type B), arising from the measurement devices themselves, is specified by manufacturer data sheets and varies between device types and models. High-end Coriolis flow meters typically exhibit uncertainties on the order of 0.05 to 0.2% uncertainty [15–17], while Class A RTDs are rated at ±0.15 °C according to European standards [18]. In the present measurements, the Type A standard uncertainties obtained from repeated measurements typically exceeded the Type B uncertainties by more than an order of magnitude. The resulting contribution of instrumental effects in the final uncertainty was therefore negligible. Consequently, instrumental uncertainty was omitted from the analysis to maintain focus on the dominant statistical uncertainty.
- Physical properties such as specific heat capacities, densities, molecular weights, and enthalpies of vaporisation or condensation were treated as reference values with uncertainties negligible relative to the experimental measurement uncertainty. Their contribution to the overall uncertainty was therefore assumed to be insignificant and was not included in the analysis.
- Instantaneous single measurements, such as those derived from solvent analysis, were treated as having negligible uncertainty. The random uncertainty associated with operator handling cannot be reliably quantified from single observations, and these specific measurements do not propagate into subsequent

calculated quantities. Consequently, sample collection was assumed to be done in an ideal manner with negligible uncertainty and was excluded from the analysis.

- The final derived uncertainties are therefore considered to provide a conservative estimate of the uncertainty across the experimental campaign. Although a more detailed investigation could attempt to quantify the excluded components, these are not expected to significantly influence the final reported uncertainties or the resulting conclusions, as the dominant contributions arise from the statistical variability of the measured data.

Standard rules for the propagation of uncertainty were applied, depending on the mathematical operations involved. For addition or subtraction, absolute uncertainties are used. When a result, (X), is calculated from the sum or difference of other values (e.g., $X = Y \pm Z$ ...), the combined absolute uncertainty is the square root of the sum of the squares of the individual absolute uncertainties:

$$u(X) = \sqrt{u(Y)^2 + u(Z)^2 \dots} \qquad \textbf{(4.32)}$$

Where:

u = absolute uncertainty of a value (same units as the mean value)

For multiplication or division, relative uncertainties are used. When a result, (X), is calculated from the product or quotient of other values (e.g., $X = Y \cdot Z$ or $X = Y/Z$), the combined relative uncertainty is the square root of the sum of the squares of the individual relative uncertainties:

$$u_{\mathrm{rel}}(X) = \sqrt{u_{\mathrm{rel}}(Y)^2 + u_{\mathrm{rel}}(Z)^2 \dots} \qquad \textbf{(4.33)}$$

Where:

u_{rel} = relative uncertainty of a mean value (unitless, %)

The relative uncertainty of a given value is calculated by dividing its absolute uncertainty by its mean value:

$$u_{\mathrm{rel}}(Y) = \frac{u(Y)}{Y}, u_{\mathrm{rel}}(Z) = \frac{u(Z)}{Z} \dots \qquad \textbf{(4.34)}$$

The final absolute uncertainty of the result is then found by multiplying the relative uncertainty by the mean value of the result:

$$u(X) = u_{\mathrm{rel}}(X) \cdot X \qquad \textbf{(4.35)}$$

The calculated uncertainties enable the evaluation of experimental results for reliability and consistency. These uncertainty values are used throughout this chapter in accordance with the methodology outlined above.

4.7 Experimental Matrix

The experimental matrix in Table 4.5 was developed based on the modelling predictions detailed in Chapter 3, with the goal of identifying the minimum L/G ratio required to achieve a capture efficiency of 90% for each flue gas CO_2 concentration. Four CO_2 concentrations were investigated: 25, 20, 15, and 10 mol.%. These were produced as synthetic flue gas using the gas skid, comprising controlled mixtures of CO_2 and air. The flue gas flow rate was maintained at 150 Nm^3/h throughout all capture conditions.

The number of capture conditions investigated had to be limited due to time constraints during the campaign. Therefore, the selected solvent flow rates focused on capturing the optimal L/G ratios predicted by the DCC model. Greater emphasis was placed on higher CO_2 concentrations, beginning with the investigation of 25 mol.% conditions.

Each change in capture condition required an adjustment in either the flue gas CO_2 concentration or the lean solvent flow rate and in some cases, both of these parameters. These changes necessitated time to re-establish steady state. To minimise the waiting period between conditions and to reduce step change impacts, the conditions were adjusted in a logical, descending order, from the highest CO_2 concentrations and solvent flow rates to the lowest. Lowering the solvent flow typically requires a lower reboiler duty, and steadily decreasing the input energy is more stable than increasing it, allowing a new steady state condition to be achieved more easily.

Table 4.5: Experimental matrix of solvent flow rates and CO_2 concentrations in gas flows of 150 Nm^3/h.

Solvent Flow kg/h	**CO_2 Concentration**			
	25 mol.%	**20 mol.%**	**15 mol.%**	**10 mol.%**
1200	✓	✓		
1100	✓	✓		
1000	✓	✓		
900	✓	✓	✓	
800	✓	✓	✓	
700			✓	✓
600			✓	✓
500			✓	✓
400				✓
300				✓

Solvent mass flow rates in the ACP are measured using Coriolis meters, which account for the total mass, including absorbed CO_2. As a result, the individual mass flow rates of MEA, H_2O and CO_2 in the solvent needed to be determined from the solvent analysis, using the methodology outlined in Section 4.5.6.

4.8 Experimental Results

4.8.1 *Introduction to the Experimental Results*

This section presents the results and discussion for each capture condition tested during the experimental campaign. It also outlines the key limitations encountered throughout the study. All results were processed using the methodologies detailed in the preceding sections and are organised into distinct sets based on the CO_2 concentration in the flue gas. This approach enables a clearer understanding of the system performance by highlighting trends and relationships between key variables, facilitating more meaningful analysis. Where appropriate, these result sets are brought together to provide an overall assessment of the capture system behaviour.

Throughout this study, capture conditions are labelled using a two-part naming convention: the first number indicates the flue gas CO_2 concentration in mol.%, and the second number represents the solvent flow rate in kg/h. For example, condition 25_1100 corresponds to a CO_2 concentration of 25 mol.% treated with 1100 kg/h solvent.

4.8.2 *Limitations During the Campaign*

The nature of pilot-scale research often results in unexpected challenges that only become apparent during the experimental campaign, particularly during data collection and subsequent analysis. Due to time and financial constraints, the trials could not be repeated, meaning these limitations must be thoroughly documented to understand their potential impact on the results presented. The following bullet points outline the key limitations encountered, their possible effects, and any action taken to mitigate these issues:

i) Missing chemistry data samples.

The testing period included overnight and weekend operation via remote plant operation. As a result, chemistry data was not collected for certain conditions, making it impossible to fully specify these capture points. These conditions were excluded from the final dataset, and only those with complete data are included in the analysis.

ii) Error in cross-heat exchanger temperature readings.

During analysis, it became evident that the inlet and outlet temperature readings for the cross-heat exchanger were consistently too cold. A post-campaign investigation revealed that the RTDs were inadequately insulated, with part of the sensor exposed to ambient conditions. This caused an unknown underreporting of temperatures, making the readings unsuitable for use. While these values are not critical for the primary analysis, they do prevent accurate calculation of the cross-heat exchanger duty and approach temperature between the hot rich and hot lean solvent streams. Consequently, these temperature readings were omitted from the results tables. Where needed, the temperature of the rich solvent entering the stripper was assumed to be the same as the stripper top temperature.

iii) Absorber bottom temperature probe not functional.

The bottom RTD in absorber 1 was non-functional and marked for replacement. While this affects the completeness of the absorber temperature profile, nearby RTDs toward the bottom of the column showed very similar values, suggesting minimal vertical temperature variation in this section. The nearest adjacent RTD was used to represent the bottom temperature.

iv) Systematic error in an absorber temperature probe.

One RTD in absorber 2, located just above the redistributor, consistently reported temperatures higher than expected across all capture conditions. This anomaly is not consistent with typical absorber profiles and is likely due to a calibration issue. As such, this reading was excluded from all absorber temperature profile plots.

v) Not all flue gas CO_2 concentrations identified the optimal L/G ratio.

It was evident that the optimal L/G ratio was not able to be identified for all flue gas CO_2 concentrations. This was a result of overestimating the anticipated optimal L/G ratio and trialling solvent flow rates around this expectation. Consequently, solvent flow rates are too high for some flue gas CO_2 concentrations.

vi) Solvent flow rate increments were too wide around the optimal L/G ratio.

Capture conditions were tested using solvent flow rate increments of 100 kg/h. while this step size was sufficient to explore general trends, it is too wide when approaching the optimal L/G ratio. Ideally smaller solvent flow rate increments would have been made around the anticipated optimal L/G ratio to capture it properly, but this was limited due to time.

vii) Not all conditions achieved 90% capture efficiency.

Some capture conditions did not reach the target capture efficiency of 90%. In these conditions, the reboiler had already reached its maximum heat duty, meaning further heat input was not possible. Despite this, all investigated capture conditions achieved capture efficiencies between approximately 84.1% and 91.4%, representing a sufficiently narrow range to enable valid comparisons between conditions.

4.8.3 25% CO_2 Flue Gas Capture Conditions

The solvent flow rates that achieved steady state conditions with a flue gas CO_2 concentration of 25 mol.% and were specified fully were: 800, 900, 1000, and 1100 kg/h. The 1200 kg/h condition was omitted due to missing chemistry data. The results for the capture conditions are presented in Table 4.6, with key performance metrics illustrated in Figure 4.5.

Table 4.6: Results summary for complete capture conditions with a flue gas CO_2 concentration of 25 mol.%.

Parameter	**Units**	**Capture Conditions**			
		25_800	**25_900**	**25_1000**	**25_1100**
Flue Gas CO_2 Concentration	mol.%	24.24	24.99	24.99	24.99
Overall Solvent Mass Flow Rate	kg/h	800	900	1000	1100
Pure Solvent Mass Flow Rate	kg/h	758	843	936	1024
Solvent MEA Mass Flow Rate	kg/h	263.39	290.30	320.82	351.95
Solvent H_2O Mass Flow Rate	kg/h	495.05	552.38	615.38	671.73
Solvent CO_2 Mass Flow Rate	kg/h	41.56	57.31	63.80	76.33
Flue Gas Mass Flow Rate	kg/h	223.36	224.32	223.47	223.70
Flue Gas CO_2 Mass Flow Rate	kg/h	72.66	74.99	74.71	74.78
Flue Gas Volumetric Flow Rate	Nm^3/h	153	153	152	152
Liquid (Pure) to Gas Ratio	kg/kg	3.40	3.76	4.19	4.58
Liquid to Gas Ratio	kg/kg	3.58	4.01	4.47	4.92
Solvent to CO_2 Ratio	kg/kg	10.44	11.24	12.53	13.69
Flue Gas Temperature	°C	11.7	12.1	11.1	11.4
Lean Solvent Temperature	°C	33.9	37.1	37.3	38.1
Lean Solvent Concentration	wt.%	32.92	32.26	32.08	32.00
Rich Solvent Concentration	wt.%	30.05	30.59	30.52	30.42
Lean Solvent Loading	mol/mol	0.219	0.274	0.276	0.301
Rich Solvent Loading	mol/mol	0.542	0.545	0.539	0.521
Solvent Capacity	mol/mol	0.323	0.271	0.263	0.220
Absorber Bottom Temperature	°C	37.6	45.5	45.7	47.86
Stripper Top Temperature	°C	73.2	75.8	75.8	76.4
Stripper Bottom Temperature	°C	112.0	111.7	110.9	110.1
Stripper Pressure	bara	1.2	1.2	1.2	1.2
PHW Volumetric Flow Rate	m^3/h	11.81	11.82	11.81	11.82
PHW Inlet Temperature	°C	120.5	120.4	119.1	118.5
PHW Outlet Temperature	°C	115.1	114.9	113.7	113.0
Stripper Reboiler Heat Duty	kW	70.96	72.42	71.60	72.30
Specific Reboiler Duty	$MJ/kg.CO_2$	4.05	3.83	4.04	4.14
Degree of Solvent Regeneration	%	59.59	49.72	48.79	42.23
Captured CO_2 Mass Flow Rate	kg/h	63.02	68.15	63.76	62.91
CO_2 Capture Efficiency	%	86.73	90.88	85.35	84.12

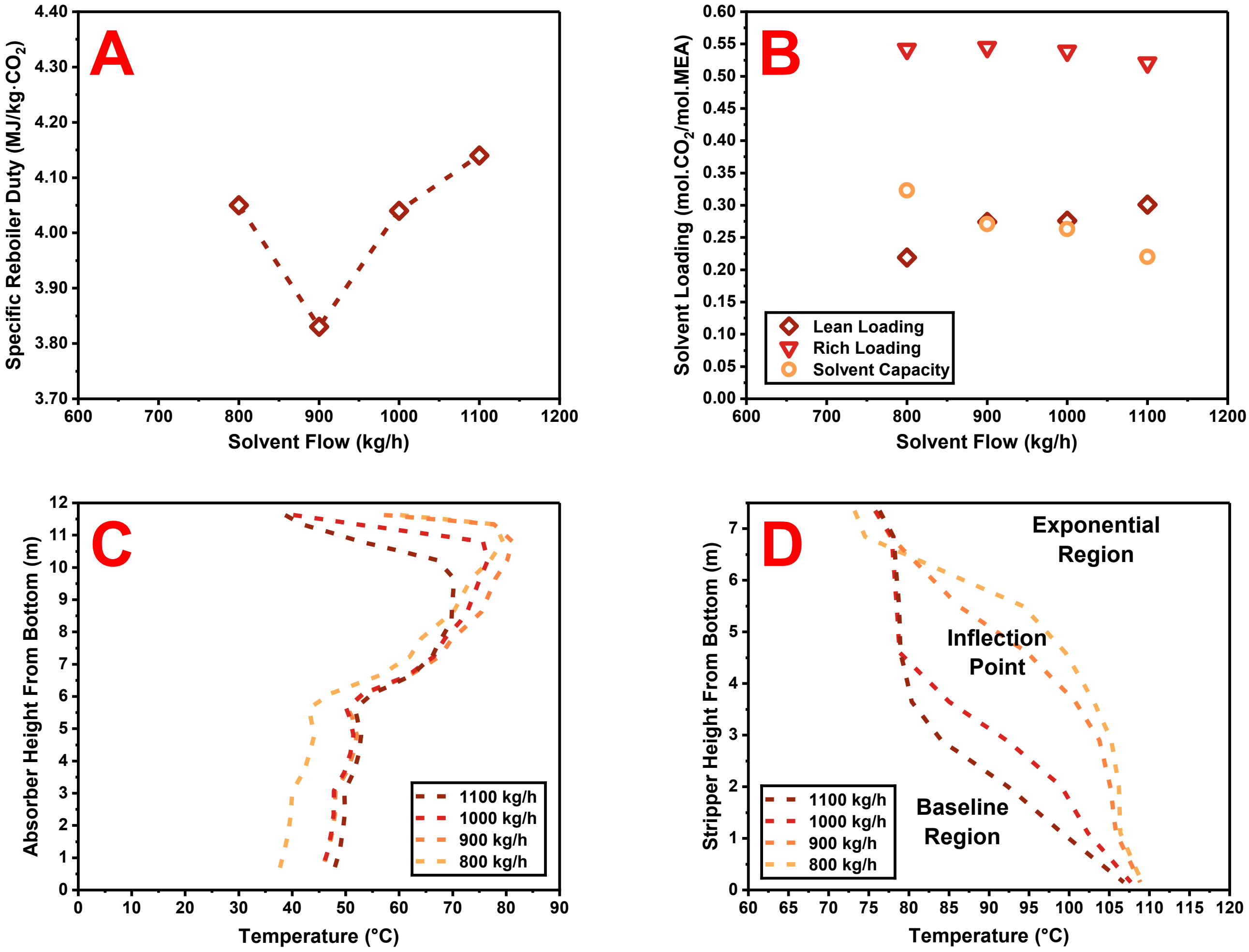

Figure 4.5: Key performance metrics for solvent flow rates treating 150 Nm^3/h flue gas containing 25 mol.% CO_2, targeting 90% capture efficiency: (A) specific reboiler duty, (B) solvent loadings and capacity, (C) absorber temperature profiles, and (D) stripper temperature.

The tested range of solvent flow rates successfully captured the approximate location of the optimal L/G ratio, as indicated by the minimum observed SRD of 3.83 MJ/kg·CO_2 at a solvent flow of 900 kg/h in Figure 4.5A. The optimal L/G ratio of 4.01 corresponded to a lean solvent concentration of 32.26 wt.% MEA, which considered the mass of CO_2 in the solvent in its calculation in addition to the MEA and H_2O. This equates to a pure solvent flow rate of approximately 843 kg/h with an L_{pure}/G ratio of 3.76. The SRD values at solvent flow rates of 800 and 1000 kg/h are similar, supporting the conclusion that 900 kg/h, situated at the midpoint between these two points, represents a near optimal condition. The rich solvent concentration for the optimal L/G ratio is 30.59 wt.% MEA, which is lower than the lean solvent concentration, resulting from the increased proportion of CO_2 in the flowing solvent. This trend is consistent across the complete set of experimental results.

Notably, only the 900 kg/h condition achieved the target capture efficiency, with a value of 90.88%. The other conditions achieved slightly lower capture efficiencies, around 85%. The results confirm that the reboiler was operating at maximum heat input for each condition, with the cross-heat exchanger also assumed to be operating at its maximum duty. This indicates that, except at 900 kg/h, the system was unable to deliver sufficient thermal energy to reach 90% capture, implying that the 900 kg/h condition offers more favourable heat integration. For higher solvent flow rates, the mass of solvent flow is too high for the maximum reboiler duty to heat sufficiently regenerate the solvent enough to achieve 90% capture. As lower solvent flow rates, the depth of regeneration required to achieve 90% capture efficiency is more energy intensive, which is also too high for the maximum reboiler duty. For the 900 kg/h condition, a 5% increase in CO_2 capture efficiency relative to other capture conditions, combined with improved heat utilisation, results in a lower, optimal SRD for this capture condition.

The analysis of solvent loadings in Figure 4.5B show that rich solvent loadings remain high and relatively constant across the tested range, indicating that maximum CO_2 absorption was consistently achieved. The rich solvent loading decreases slightly with increasing solvent flow, ranging from approximately 0.54 to 0.52. Values exceeding 0.5 are indicative of some physical dissolution of CO_2 into the MEA, in addition to chemical absorption. This suggests once maximum chemical absorption has occurred, the extent of physical dissolution becomes more dependent on solvent residence time within the absorber column.

In contrast, lean loading increases with solvent flow, rising from approximately 0.22 to 0.30 as flow increases from 800 to 1100 kg/h. This trend reflects a reduction in solvent regeneration depth at higher flow rates, because less solvent cyclic capacity is required to meet the capture target when more solvent is circulating. The lean loading at 900 kg/h is notably higher than expected based on this trend, nearly equal to that observed at 1000 kg/h. This anomaly suggests a possible measurement error. While the solvent cyclic capacity for the 900 kg/h condition remains greater than that at 1000 kg/h, this does not compensate for the difference in capture efficiency and solvent flow rate. From the observed trend in Figure 4.5B it would be expected that the lean loading of the 900 kg/h condition would approximate 0.25, which aligns with predictions from the DCC model in Chapter 3.

Detailed discussion of column temperature profiles has been provided previously in Chapter 2, where such profiles offer crucial insights into system operation, optimisation and problem diagnosis [9,10,19].

The absorber temperature profiles shown in Figure 4.5C align well with expectations. As solvent flow increases, the temperature profiles evolve from a rich-pinched state towards a bulge-pinched profile. This shift indicates that the driving force for CO_2 absorption moves lower in the column with increased solvent flow, distributing the reaction zone and flattening the temperature peak, consistent with the behaviour discussed in Chapter 2. At absorber heights of 6 m and below in Figure 4.5C, which correspond to absorber 1 when the TERC ACP operates in series configuration, minimal temperature variation is observed across all flow conditions. This suggests that the majority of CO_2 absorption occurs in absorber 2. The limited temperature profile changes between flow conditions in absorber 1 are likely due to a combination of ambient temperature effects and the thermal content carried by the solvent flow.

The stripper temperature profiles in Figure 4.5D illustrate the distinct operating zones typical of a stripping column [11]. As discussed in Chapter 2, “high” solvent flow rates lead to baseline operation, while “low” flow rates result in exponential operation. The transition between these two regions, known as the inflection point, is characterised by a smooth, continuous temperature rise from the top to the bottom of the column and corresponds to the minimum SRD for a given capture condition. Based on Figure 4.5D, the 900 kg/h condition closely approximates the inflection point, and agrees with the observations from Figure 4.5A where the minimum SRD was identified. At higher solvent flow rates of 1000 and 1100 kg/h, the system enters the baseline region, increasing SRD due to the additional energy required to heat higher solvent flows. Conversely, decreasing solvent flow below 900 kg/h, as seen at 800 kg/h, shifts the operation into the exponential region, which also increases the SRD due to the excessive amounts of steam generated as solvent flow rate reduces.

4.8.4 20% CO_2 Flue Gas Capture Conditions

The solvent flow rates that achieved steady state conditions with a flue gas CO_2 concentration of 20 mol.% and were specified fully were: 800, 900, 1000, 1100, and 1200 kg/h. The results for the capture conditions are presented in Table 4.7 with key performance metrics illustrated in Figure 4.6.

Table 4.7: Results summary for complete capture conditions with a flue gas CO_2 concentration of 20 mol.%.

Parameter	**Units**	**Capture Conditions**				
		20_800	**20_900**	**20_1000**	**20_1100**	**20_1200**
Flue Gas CO_2 Concentration	mol.%	20.18	20.18	20.11	20.11	20.07
Overall Solvent Mass Flow Rate	kg/h	800	900	1000	1100	1200
Pure Solvent Mass Flow Rate	kg/h	748	838	926	1015	1104
Solvent MEA Mass Flow Rate	kg/h	267.38	297.78	329.94	362.49	396.34
Solvent H_2O Mass Flow Rate	kg/h	480.61	539.78	595.89	652.88	708.00
Solvent CO_2 Mass Flow Rate	kg/h	52.02	62.44	74.17	84.62	95.67
Flue Gas Mass Flow Rate	kg/h	216.87	217.45	217.63	218.15	219.30
Flue Gas CO_2 Mass Flow Rate	kg/h	59.78	59.94	59.78	59.92	60.18
Flue Gas Volumetric Flow Rate	Nm^3/h	151	151	151	152	153
Liquid (Pure) to Gas Ratio	kg/kg	3.45	3.85	4.25	4.65	5.04
Liquid to Gas Ratio	kg/kg	3.69	4.14	4.59	5.04	5.47
Solvent to CO_2 Ratio	kg/kg	12.51	13.97	15.49	16.95	18.35
Flue Gas Temperature	°C	8.9	9.4	9.9	10.8	12.5
Lean Solvent Temperature	°C	30.3	31.1	33.5	35.9	37.4
Lean Solvent Concentration	wt.%	33.42	33.09	32.99	32.95	33.03
Rich Solvent Concentration	wt.%	31.43	31.20	31.43	31.74	31.36
Lean Solvent Loading	mol/mol	0.270	0.291	0.312	0.324	0.335
Rich Solvent Loading	mol/mol	0.517	0.521	0.533	0.504	0.508
Solvent Capacity	mol/mol	0.247	0.230	0.221	0.180	0.173
Absorber Bottom Temperature	°C	45.7	43.3	48.0	53.4	52.4
Stripper Top Temperature	°C	74.7	73.3	75.3	78.9	78.7
Stripper Bottom Temperature	°C	110.57	110.1	109.3	108.9	108.3
Stripper Pressure	bara	1.2	1.2	1.2	1.2	1.2
PHW Volumetric Flow Rate	m^3/h	11.77	11.75	11.75	11.75	11.76
PHW Inlet Temperature	°C	117.0	116.9	116.5	116.0	115.6
PHW Outlet Temperature	°C	112.5	112.2	111.6	111.2	110.7
Stripper Reboiler Heat Duty	kW	58.54	62.00	63.63	63.13	65.14
Specific Reboiler Duty	MJ/kg.CO_2	3.86	4.12	4.22	4.24	4.37
Degree of Solvent Regeneration	%	47.78	44.15	41.46	35.71	34.06
Captured CO_2 Mass Flow Rate	kg/h	54.63	54.21	54.28	53.59	53.61
CO_2 Capture Efficiency	%	91.39	90.45	90.79	89.43	89.09

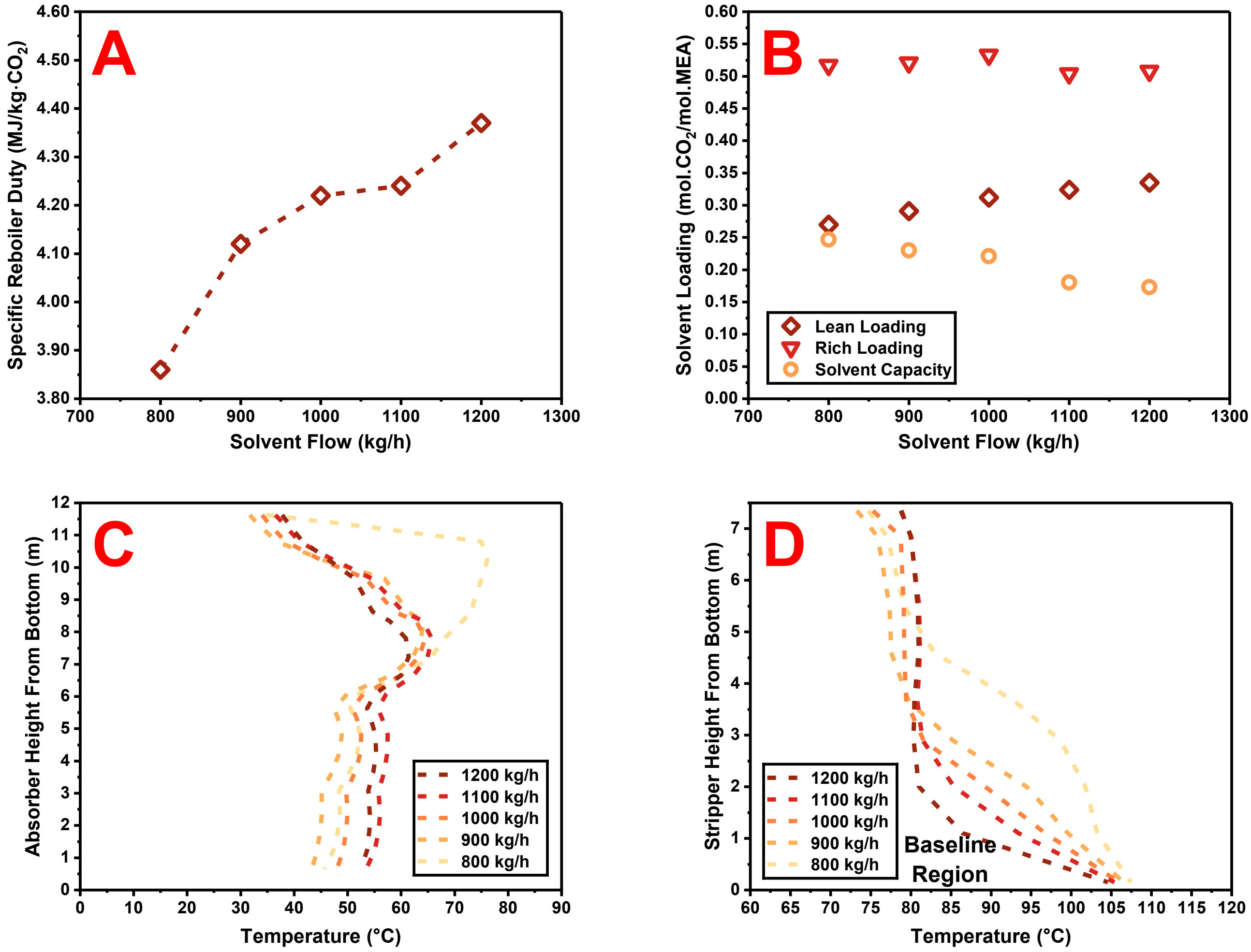

Figure 4.6: Key performance metrics for solvent flow rates treating 150 Nm^3/h flue gas containing 20 mol.% CO_2, targeting 90% capture efficiency: (A) specific reboiler duty, (B) solvent loadings and capacity, (C) absorber temperature profiles, and (D) stripper temperature.

The tested solvent flow rate range for 20 mol.% CO_2 matched that used for 25 mol.% CO_2. As shown in Figure 4.6A, the optimal L/G ratio was not clearly identified for the 20 mol.% conditions, as the SRD continues to decrease with decreasing solvent flow. At the lowest tested flow rate of 800 kg/h, an SRD of 3.86 MJ/kg·CO_2 was recorded, which is comparable to the minimum SRD of 3.83 MJ/kg·CO_2 observed at 900 kg/h for the 25 mol.% condition. This similarity supports the expectation from the DCC model that optimal SRD values are similar across different CO_2 concentrations as described in Chapter 3. These results suggest that the 800 kg/h condition may be near the L/G ratio at which the minimum SRD occurred for 20 mol.% CO_2, although the true optimal was probably below the tested range. A more appropriate flow range for future testing would span 600 to 1000 kg/h, expected to capture the minimum SRD. However, all tested flow rates for 20 mol.% approximated the target capture efficiency of 90%, owing to the required reboiler duty being well below the maximum heat input.

The solvent loadings shown in Figure 4.6B generally follow expected trends. Lean loading increases steadily with increasing solvent flow rate, while rich loading decreases slightly. Rich loadings range from 0.533 to 0.504 across the tested flow rates. This decrease is consistent with a reduction in residence time and corresponding decrease in physical dissolution at higher flow rates. The rich loading at 1000 kg/h is notably higher than expected from the observed trend and appears to be a measurement anomaly. Overall, the solvent capacity decreases with increasing solvent flow rate, as expected. Notably, at a flow rate of 800 kg/h, the lean loading is 0.27, closely matching the DCC model prediction of 0.26 for optimal operation, as shown in Chapter 3. This supports the inference that 800 kg/h is near the optimal, although a further reduction in solvent flow is required to precisely identify the optimal L/G ratio for which the minimum SRD occurs. Based on the experimental lean loading trend, this is expected to occur around 750 kg/h.

The absorber temperature profiles in Figure 4.6C reveal notable behaviour. For solvent flow rates between 900 and 1200 kg/h, the profiles converge and shift towards a bulge-pinched state as flow increases. In contrast, the 800 kg/h condition exhibits a rich-pinched profile, indicating a higher concentration of reaction activity near the top of the column with a lower solvent flow rate. However, comparison to a secondary, but ultimately unused steady state capture condition for a solvent flow rate of 800 kg/h revealed an absorber temperature profile similar to the higher solvent flow rate conditions. This discrepancy can be explained with reference to the capture efficiencies of the conditions, where the primary reported condition had a capture efficiency of 91.39%, the highest of any condition tested experimentally, and the secondary condition had a lower capture efficiency of approximately 89%. The higher capture efficiency was the reason the primary reported value was chosen. This seemingly small increase in capture efficiency is crucial to the change in absorber behaviour for the same solvent flow rate. As capture efficiency increases above 90% it becomes increasingly harder for the solvent to absorb CO_2 as the partial pressure of CO_2 in the flue gas decreases. This means that the reaction zone is forced higher into the column to enable absorption of additional CO_2, and generates additional heat from the exothermic reaction, giving the characteristic shape of a rich-pinched absorber.

As with the 25 mol.% CO_2 conditions, minimal temperature variation is observed in absorber 1 across all conditions, indicating that most CO_2 absorption continues to occur in absorber 2. The limited profile changes in absorber 1 are attributed to ambient temperature effects and thermal content carried by the solvent flow.

The stripper temperature profiles shown in Figure 4.6D also align with expectations. Across all conditions, the stripper appears to operate within the baseline region, with operation gradually approaching the inflection point as solvent flow decreases. Flow rates at 900 kg/h and above push the stripper deeper into the baseline region, increasing the SRD due to the additional energy required to heat higher solvent flows. The 800 kg/h condition deviates from this trend, appearing closer to the inflection point, but is still above the optimal flow rate. This observation is consistent with the lean solvent loading data and further supports the need for testing lower solvent flow rates to precisely identify the inflection point and corresponding minimum SRD.

4.8.5 15% CO_2 Flue Gas Capture Conditions

The solvent flow rates that achieved steady state conditions with a flue gas CO_2 concentration of 15 mol.% and were specified fully were: 600, 700, and 800 kg/h. The 900 and 500 kg/h conditions were omitted due to missing chemistry data. The results for the capture conditions are presented in Table 4.8, with key performance metrics illustrated in Figure 4.7.

Table 4.8: Results summary for complete capture conditions with a flue gas CO_2 concentration of 15 mol.%.

Parameter	Units	Capture Conditions		
		15_600	15_700	15_800
Flue Gas CO_2 Concentration	mol.%	15.14	15.00	15.04
Overall Solvent Mass Flow Rate	kg/h	600	700	800
Pure Solvent Mass Flow Rate	kg/h	562	652	740
Solvent MEA Mass Flow Rate	kg/h	198.32	230.51	261.38
Solvent H_2O Mass Flow Rate	kg/h	363.82	421.16	478.74
Solvent CO_2 Mass Flow Rate	kg/h	37.87	48.33	59.89
Flue Gas Mass Flow Rate	kg/h	213.32	212.55	211.41
Flue Gas CO_2 Mass Flow Rate	kg/h	45.18	44.62	44.49
Flue Gas Volumetric Flow Rate	Nm^3/h	152	151	151
Liquid (Pure) to Gas Ratio	kg/kg	2.64	3.07	3.50
Liquid to Gas Ratio	kg/kg	2.81	3.29	3.78
Solvent to CO_2 Ratio	kg/kg	12.44	14.60	16.64
Flue Gas Temperature	°C	12.4	11.0	9.2
Lean Solvent Temperature	°C	28.2	30.3	31.9
Lean Solvent Concentration	wt.%	33.05	32.93	32.67
Rich Solvent Concentration	wt.%	31.49	31.20	31.67
Lean Solvent Loading	mol/mol	0.265	0.291	0.318
Rich Solvent Loading	mol/mol	0.539	0.531	0.533
Solvent Capacity	mol/mol	0.274	0.240	0.215
Absorber Bottom Temperature	°C	39.4	46.6	47.6
Stripper Top Temperature	°C	74.5	77.3	78.4
Stripper Bottom Temperature	°C	110.9	111.3	110.2
Stripper Pressure	bara	1.2	1.2	1.2
PHW Volumetric Flow Rate	m^3/h	11.75	11.76	11.78
PHW Inlet Temperature	°C	115.6	116.0	115.4
PHW Outlet Temperature	°C	112.3	112.6	111.8
Stripper Reboiler Heat Duty	kW	42.97	45.15	47.53
Specific Reboiler Duty	MJ/kg.CO_2	3.79	4.05	4.21
Degree of Solvent Regeneration	%	50.83	45.20	40.34
Captured CO_2 Mass Flow Rate	kg/h	40.78	40.17	40.65
CO_2 Capture Efficiency	%	90.26	90.02	91.37

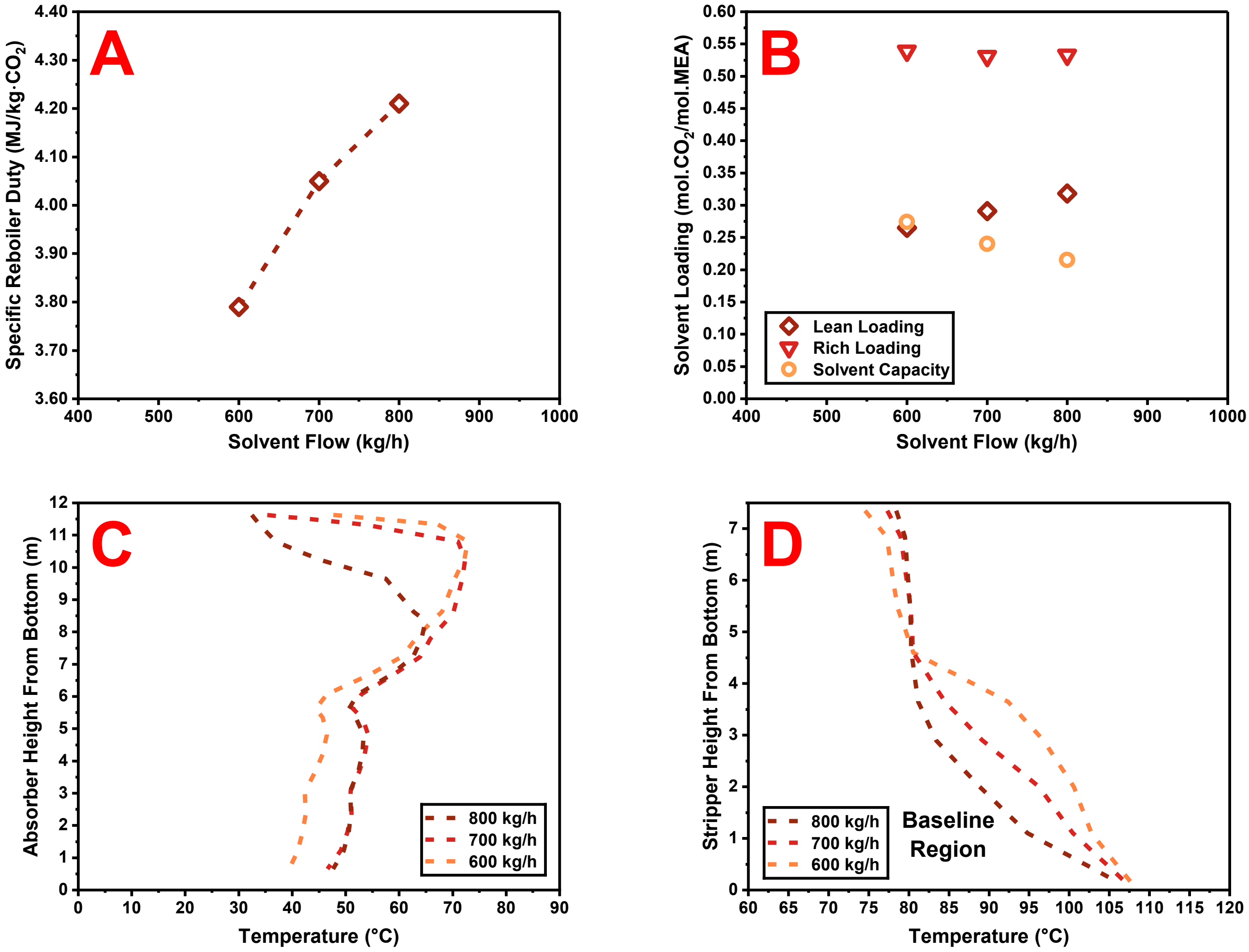

Figure 4.7: Key performance metrics for solvent flow rates treating 150 Nm^3/h flue gas containing 15 mol.% CO_2, targeting 90% capture efficiency: (A) specific reboiler duty, (B) solvent loadings and capacity, (C) absorber temperature profiles, and (D) stripper temperature.

The tested solvent flow rates for the 15 mol.% CO_2 condition were limited to three cases, as shown in Figure 4.7A. Similar to the 20 mol.% CO_2 results, the optimal L/G ratio was not clearly captured within the tested range. The lowest SRD recorded was 3.79 MJ/kg·CO_2 at a solvent flow of 600 kg/h, which may approximate the minimal L/G ratio, though the limited number of data points prevents a definitive conclusion. As expected, increasing the solvent flow rate above 600 kg/h resulted in higher SRD values. All three conditions achieved or exceeded the target 90% capture efficiency.

The solvent loadings shown in Figure 4.7B follow expected trends. Lean solvent loading increases steadily with solvent flow, while rich solvent decreases slightly, although some variation is observed. Overall, the solvent capacity decreases with increasing flow, consistent with the reduction in regeneration extent at higher circulation rates. According to the DCC model, the optimal lean loading for 15 mol.% CO_2 is predicted to be approximately 0.27, as shown in Chapter 3. In comparison, the lean loading measured at 600 kg/h was 0.265, suggesting a slight deviation from model predictions. One interpretation is that the minimum SRD could occur at a solvent flow marginally above 600 kg/h, or above a pure solvent flow rate of 562 kg/h, which would align with the DCC model predictions for this case. However, this assumes that SRD values increase at flow rates below 600 kg/h, which is not supported by the available temperature profile data.

Absorber temperature profiles shown in Figure 4.7C reinforce earlier observations. At solvent flow rates of 600 and 700 kg/h, the system operates in a rich-pinched state, while at higher flow rates, the profiles begin evolving towards a bulge-pinched state. This progression mirrors the behaviour observed for higher CO_2 concentrations and reflects the movement of the primary absorption zone lower in the column as solvent flow increases. In absorber 1, temperature profiles remain largely unchanged across the conditions, consistent with previous conclusions that minimal CO_2 absorption occurs in this column. The observed temperature profiles are instead attributed to ambient temperature effects and thermal content carried by the solvent flow.

The stripper temperature profiles shown in Figure 4.7D indicate that all conditions tested tend towards the baseline operating region. As solvent flow decreases, the system begins to approach the inflection point, though it is not yet reached at 600 kg/h. These findings do not support the earlier consideration that the minimum SRD may occur at a slightly higher flow rate than 600 kg/h, as suggested by the lean loading comparison to the DCC model. Instead, extrapolation of the temperature profile trend suggest that a solvent flow rate of approximately 500 kg/h would be closer to the inflection point and would therefore minimise the SRD for the 15 mol.% CO_2 condition.

4.8.6 10% CO_2 Flue Gas Capture Conditions

The solvent flow rates that achieved steady state conditions with a flue gas CO_2 concentration of 10 mol.% and were specified fully were: 300, 400, 500, and 700 kg/h. The 600 kg/h condition was omitted due to missing chemistry data. The results for the capture conditions are presented in Table 4.9, with key performance metrics illustrated in Figure 4.8.

Table 4.9: Results summary for complete capture conditions with a flue gas CO_2 concentration of 10 mol.%.

Parameter	Units	Capture Conditions			
		10_300	10_400	10_500	10_700
Flue Gas CO_2 Concentration	mol.%	10.15	10.01	10.03	10.01
Overall Solvent Mass Flow Rate	kg/h	300	400	500	700
Pure Solvent Mass Flow Rate	kg/h	290	381	468	650
Solvent MEA Mass Flow Rate	kg/h	94.55	116.91	153.37	199.30
Solvent H_2O Mass Flow Rate	kg/h	195.50	264.56	314.14	450.87
Solvent CO_2 Mass Flow Rate	kg/h	9.95	18.53	32.49	49.83
Flue Gas Mass Flow Rate	kg/h	204.01	202.28	204.73	204.72
Flue Gas CO_2 Mass Flow Rate	kg/h	29.64	28.99	29.40	29.34
Flue Gas Volumetric Flow Rate	Nm^3/h	149	147	149	149
Liquid (Pure) to Gas Ratio	kg/kg	1.42	1.89	2.28	3.18
Liquid to Gas Ratio	kg/kg	1.47	1.98	2.44	3.42
Solvent to CO_2 Ratio	kg/kg	9.79	13.16	15.90	22.16
Flue Gas Temperature	°C	6.2	3.8	7.9	7.2
Lean Solvent Temperature	°C	28.7	29.5	35.2	36.6
Lean Solvent Concentration	wt.%	31.52	29.23	30.67	28.47
Rich Solvent Concentration	wt.%	30.66	27.32	29.37	27.47
Lean Solvent Loading	mol/mol	0.146	0.220	0.294	0.347
Rich Solvent Loading	mol/mol	0.504	0.544	0.535	0.539
Solvent Capacity	mol/mol	0.358	0.324	0.241	0.192
Absorber Bottom Temperature	°C	16.1	22.7	36.9	40.8
Stripper Top Temperature	°C	99.0	75.6	75.6	76.5
Stripper Bottom Temperature	°C	111.4	110.7	110.3	108.3
Stripper Pressure	bara	1.2	1.2	1.2	1.2
PHW Volumetric Flow Rate	m^3/h	11.76	11.79	11.80	11.76
PHW Inlet Temperature	°C	117.2	113.7	113.2	111.9
PHW Outlet Temperature	°C	113.3	111.3	110.9	109.2
Stripper Reboiler Heat Duty	kW	51.97	30.96	30.24	35.48
Specific Reboiler Duty	MJ/kg.CO_2	7.15	4.29	4.13	4.83
Degree of Solvent Regeneration	%	71.03	59.56	45.05	35.62
Captured CO_2 Mass Flow Rate	kg/h	26.16	26.12	26.36	26.45
CO_2 Capture Efficiency	%	88.26	89.57	89.66	90.18

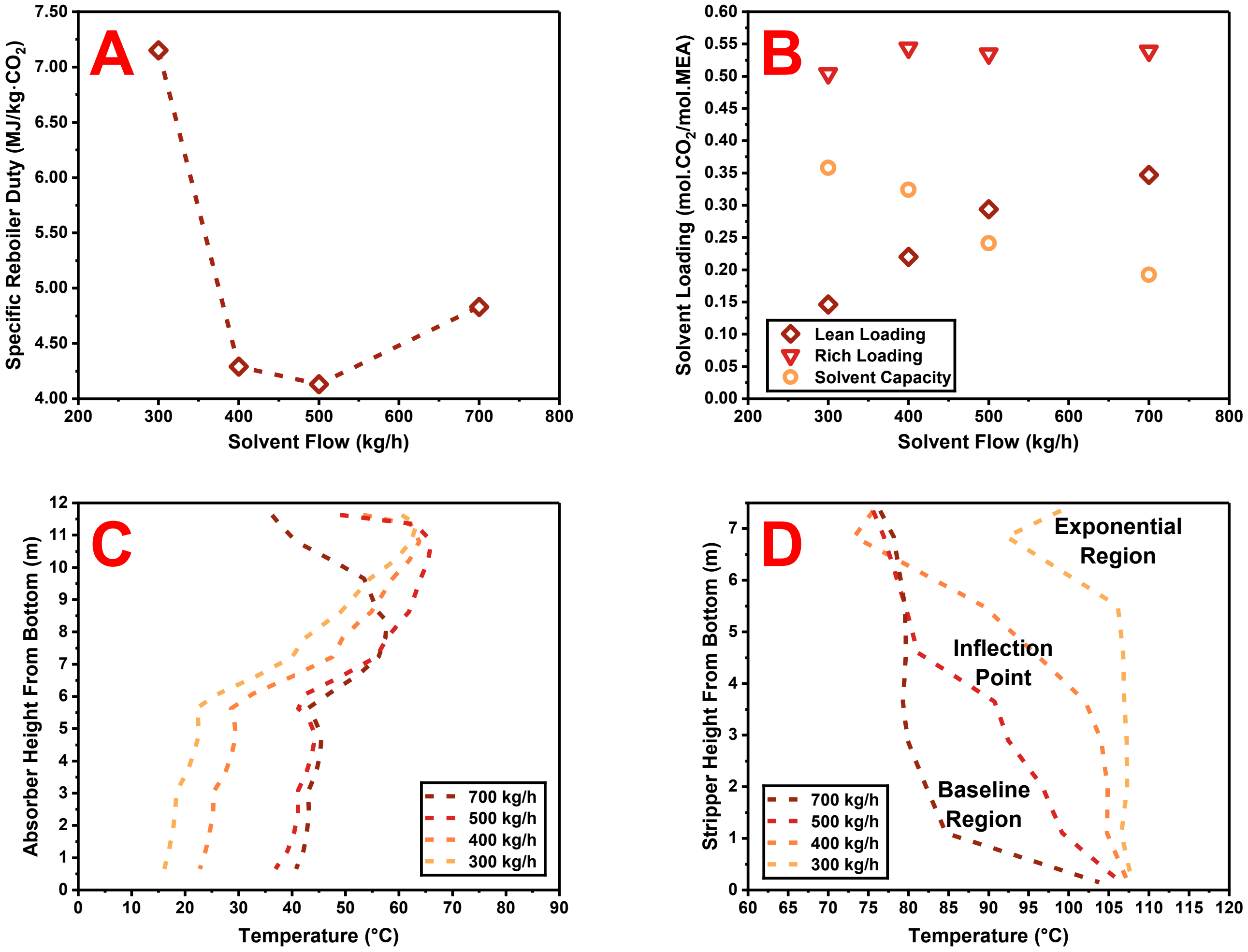

Figure 4.8: Key performance metrics for solvent flow rates treating 150 Nm^3/h flue gas containing 10 mol.% CO_2, targeting 90% capture efficiency: (A) specific reboiler duty, (B) solvent loadings and capacity, (C) absorber temperature profiles, and (D) stripper temperature.

The tested solvent flow rates for the 10 mol.% CO_2 condition covered the lower end of the operating range of the plant and approached the limits of successful CO_2 capture on this facility, spanning from 700 kg/h down to a minimum of 300 kg/h. As shown in Figure 4.8A, the minimum SRD recorded was 4.13 MJ/kg·CO_2 at a solvent flow rate 500 kg/h, corresponding to a L/G ratio of 2.44 with a lean solvent concentration of 30.67 wt.% MEA. This equates to a pure solvent flow rate of approximately 468 kg/h with an L_{pure}/G ratio of 2.28. Notably, this minimum SRD is higher than the values calculated/expected at the optimal L/G ratios for 25, 20 and 15 mol.% CO_2 conditions. This trend aligns with predictions from the DCC model in Chapter 3 and reflects the increasing energy penalty associated with capturing CO_2 from dilute flue gas streams. The system becomes less thermodynamically efficient as it removes smaller amounts of CO_2, resulting in a higher SRD. A similar trend can be observed across the different CO_2 concentrations tested by Akram et al [3]. All tested conditions achieved approximately 90% capture efficiency, with the exception of the 300 kg/h flow rate, which fell slightly short at 88.26%.

The solvent loadings shown in Figure 4.8B exhibit behaviour that diverges slightly from trends observed at higher CO_2 concentrations. Both rich and lean loadings increase with solvent flow rate, however, the increase in rich loading occurs more gradually. The rich loading at 300 kg/h appears uncharacteristically low compared to the other solvent flow rates, as evidenced by the respective differences in solvent capacity between 500 and 400 kg/h, and 400 and 300 kg/h. Extrapolating this trend to 300 kg/h suggests a solvent capacity of approximately 0.407, which would correspond to a rich loading of around 0.553. A lower solvent flow rate also increases the residence time in the column, which leads to a higher rich loading. These discrepancies indicate that the rich loading measurement for the 300 kg/h condition is likely anomalous. Irrespective of this, the expected correlation between lean and rich loadings holds true, with solvent capacity decreasing as solvent flow increases. Notably, the lean solvent loading of 0.294 at the 500 kg/h condition precisely matches the optimal lean loading predicted by the DCC model, further reinforcing the conclusion that this flow rate is near optimal.

The absorber temperature profiles in Figure 4.8C clearly reflect the transition in operating behaviour. At 300 and 400 kg/h, the system exhibits rich-pinched operation, with a concentrated reaction zone near the top of the column. As solvent flow increases beyond 500 kg/h, the temperature profiles evolve towards a bulge-pinched state as the driving force for reaction moves lower in the column. Observations of absorber 1 continue to support previous conclusions: the shape and magnitude of temperature profiles remain largely unchanged, indicating minimal CO_2 absorption occurs in this section. Differences between flow rates are again attributed to ambient conditions and heat carried by the solvent.

Figure 4.8D shows that all three stripper operating regions are represented in the temperature profiles across the tested solvent flow rates. The 500 kg/h flow rate corresponds closely to the inflection point, with 400 kg/h transitioning into the exponential region and 300 kg/h operating deeply within it. In contrast, the 700 kg/h condition clearly falls within the baseline region. The high SRD associated with the 300 kg/h condition is primarily due to this exponential behaviour, where excessive steam generation accompanies the solvent regeneration, increasing the energy demand.

An additional feature observed in the stripper temperature profiles is a distinct dip at a height of 7 m for the 300 and 400 kg/h solvent flow rates. This decrease is attributed to the introduction of cold condensate from the reflux condenser, which mixes with the hot rich solvent stream in proximity to the temperature probe. This effect is more pronounced at lower flow rates due to the relatively higher condensate flows and is not clearly captured at higher solvent flow conditions.

4.8.7 Collated Results

With trends for individual CO$_2$ concentration analysed across a range of conditions, the results can now be collated to provide an overview of overall system performance. The goal is to identify broader patterns that may support performance predictions and validate expected system behaviour. This comparison across a broad range of conditions reveals insights that may otherwise be lost within individual case analyses.

For consistency and clarity in these comparisons, the 10 mol.% CO$_2$ condition at 300 kg/h solvent flow has been omitted. As discussed in Section 4.8.6, this point lies at an extreme end of the operating range and is clearly suboptimal. Including it would obscure meaningful trends among the other data points, so it was excluded to improve the clarity of trends that emerged amongst the remaining data points.

Figure 4.9 presents the SRD plotted against both L/G ratio and solvent/CO$_2$ ratio for the conditions targeting 90% capture efficiency. The solvent/CO$_2$ ratio enables more generalised comparison by relating the CO$_2$-free solvent mass flow to the isolated CO$_2$ content of the flue gas. As described previously in Chapter 3, this normalisation eliminates the influence of varying flue gas compositions, allowing for clearer trend identification and direct comparison to real plant data.

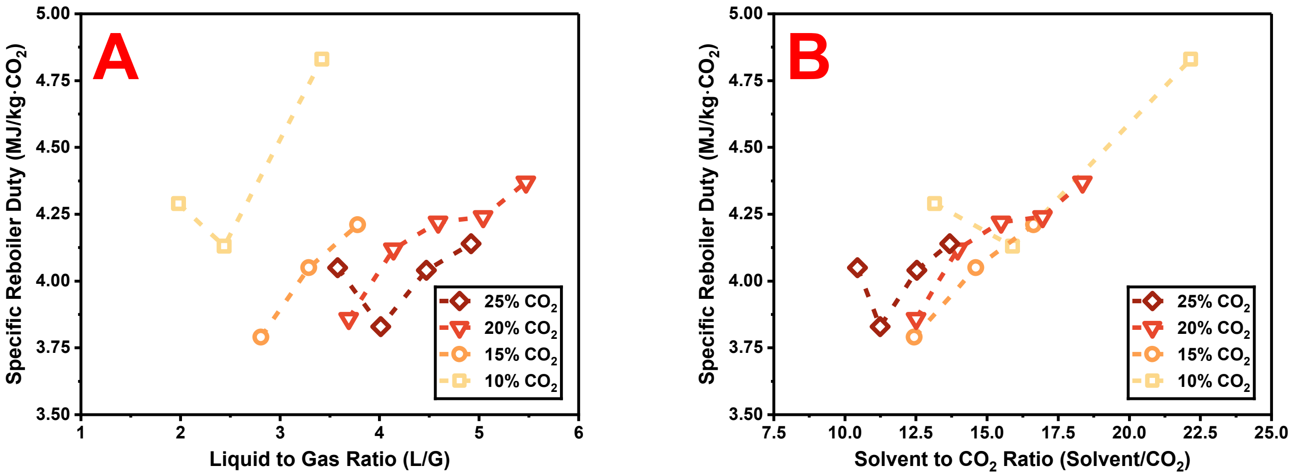

Figure 4.9: Specific reboiler duty against: (A) liquid to gas ratio and (B) solvent/CO$_2$ ratio, for solvent flow rates treating 150 Nm^3/h flue gas containing different CO$_2$ concentrations, targeting 90% capture efficiency.

Figure 4.9A presents SRD as a function of L/G ratio across the different capture conditions. It is evident that the 10 mol.% CO$_2$ trend exhibits a higher SRD around its optimal L/G ratio compared to the higher CO$_2$ concentrations. The minimum SRDs of the 10 and 25 mol.% CO$_2$ plots approximate the inflection points of the stripper, and therefore the optimal L/G ratios for the respective flue gas CO$_2$ concentration. The minimum SRD of the 25 mol.% plot is 3.83 MJ/kg·CO$_2$, compared to 4.13 MJ/kg·CO$_2$ for the 10 mol.% plot. This represents a 7.3% reduction in SRD between the two optimal conditions. As discussed in Section 4.8.6, this difference suggests that capture at 10 mol.% CO$_2$ is less thermodynamically efficient, as it removes smaller amounts of CO$_2$. This results in higher energy usage for less CO_2 captured overall, increasing the SRD. Increasing CO_2 concentrations above 10 mol.% evidently becomes more thermodynamically efficient when achieving 90% capture efficiency, lowering the SRD at the respective optimal L/G ratios. Further increases in flue gas CO_2 concentration will eventually surpass a minimum SRD attainable on the capture plant, where the SRD will begin increasing once more as the system approaches its limits of operation and becomes less thermodynamically efficient again. Based on observations from Figure 4.9A, it is likely that the minimum SRD for the optimal L/G ratio of the 25 mol.% CO_2 conditions is larger than the absolute minimum SRD possible on the capture plant. This is because the 15 and 20 mol.% CO_2 conditions, at their lowest tested solvent flow rates, had similar SRD values to the optimal SRD for the 25 mol.% CO_2 conditions. As the 15 and 20 mol.% CO_2 conditions have most likely not achieved their optimal L/G ratios, as discussed in Sections 4.8.4 and 4.8.5, it is probable that lower SRD values can be achieved. Both conditions still operate within the stripper's baseline region at their lowest recorded L/G ratios, indicating further reductions in L/G ratio would yield lower SRD values. Therefore, it is expected that the optimal SRD values for the 15 and 20 mol.% CO_2 conditions will fall below that of the 25 mol.% optimal, representing an even greater improvement over the 10 mol.% CO_2 optimal.

These trends are consistent with the predictions made using the DCC model in Chapter 3, where simulations across a range of gas and solvent flow rates indicated a similar pattern. The SRD at optimal L_{pure}/G ratios initially decreases with increasing CO_2 concentration before rising again as system limitations are approached, particularly when the maximum heat duty on the cross-heat exchanger is reached, which reduces thermal efficiency.

Figure 4.9B shows SRD plotted against the solvent/CO_2 ratio for the same conditions. Unlike in Figure 4.9A, where higher CO_2 concentrations correspond to increased L/G ratios, the solvent/CO_2 ratio decreases with increasing CO_2 concentration. This trend is consistent across all conditions and is primarily due to the greater volume of CO_2 requiring capture at higher concentrations. It reflects the solvent capacity needed to achieve the target capture efficiency at different solvent flow rates, where lower solvent/CO_2 ratios indicate more efficient solvent use. This corresponds to more thermodynamically efficient capture at higher CO_2 concentrations and is the reason the SRD values typically decrease with decreasing solvent/CO_2 ratio.

Comparing these experimental trends with DCC model predictions indicates that the model tends to overestimate the L/G ratios at which optimal SRD occurs. This discrepancy suggests that the model chemistry does not perfectly reflect the behaviour of the experimental system, where a slightly higher solvent flow rate is required in the DCC model to achieve the lean loading associated with minimum SRD. To investigate this further, the lean solvent loading is compared against both L/G and solvent/CO_2 ratios in Figure 4.10 for the range of tested conditions.

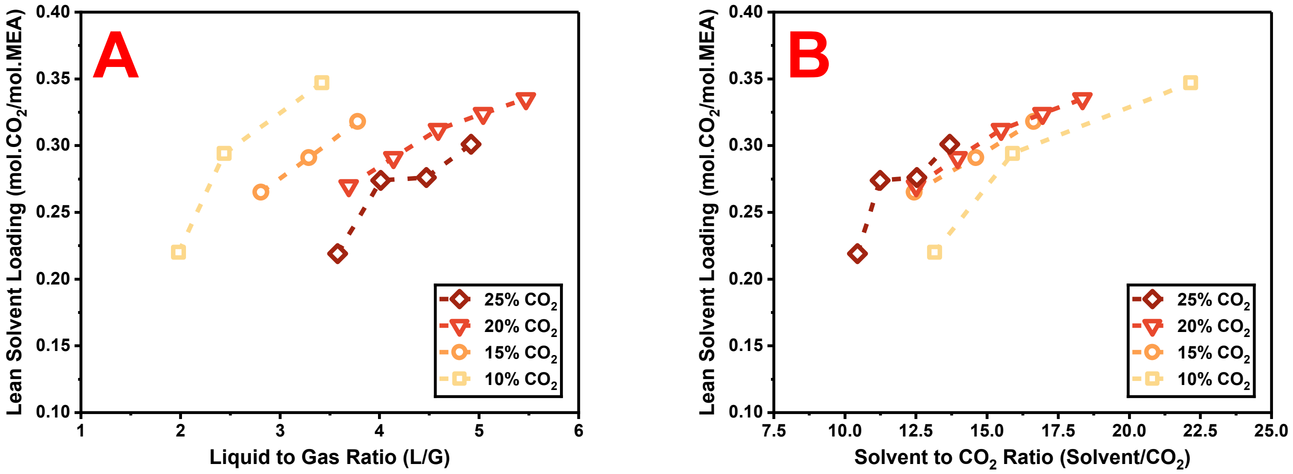

Figure 4.10: Lean solvent loading against: (A) liquid to gas ratio and (B) solvent/CO_2 ratio, for solvent flow rates treating 150 Nm^3/h flue gas containing different CO_2 concentrations, targeting 90% capture efficiency.

Figure 4.10A presents the lean solvent loading plotted against the L/G ratio across the different capture conditions. As expected, the trendlines exhibit a near linear increase with incremental changes in L/G ratio, reflecting the link between solvent flow rate and solvent loadings for a fixed CO_2 capture amount. A crucial observation is the distinct difference in lean loadings for similar L/G ratios across the CO_2 concentrations. For the same L/G ratio, the difference in lean loading between adjacent CO_2 concentrations is approximately 0.05, highlighting the increased solvent capacity required to achieve the target capture efficiency as CO_2 concentration increases.

Additionally, for similar lean loadings, a noticeable difference in the L/G ratios required across different CO_2 concentrations is also evident. At a given lean loading, the L/G ratio varies by approximately 0.8 between adjacent trendlines, reflecting the increased solvent flow required at higher CO_2 concentrations to maintain the same solvent cyclic capacity. An exception to this pattern is observed for the 25 mol.% CO_2 condition at an L/G ratio of 4.01, which is likely due to a measurement anomaly, as previously discussed in Section 4.8.3.

Good agreement was observed between the experimental lean loadings at the optimal L/G ratios and the DCC model predictions for each flue gas CO_2 concentration. The experimental lean loadings were measured at the optimal L/G ratios for the 25 and 10 mol.% CO_2 conditions and extrapolated from the experimental data for the 20 and 15 mol.% CO_2 conditions. This indicates that the model chemistry accurately predicts the optimal lean loading values, but at different L/G ratios to those observed experimentally. For the same L/G ratio, the DCC model predicts a lower lean loading than observed in the experimental data. This indicates that the model requires refinement to align both the predicted L/G ratio and lean loading with experimental observations to reduce discrepancies and achieve better agreement with experimental data.

Figure 4.10B presents the lean loading plotted against the solvent/CO_2 ratio for the same capture conditions. Similarly to the observations from Figure 4.10B, increasing CO_2 concentration results in a decreasing solvent/CO_2

ratio. Furthermore, the difference in solvent/CO_2 ratio between data points diminishes as CO_2 concentration increases. For the 25 mol.% CO_2 conditions, the average difference in solvent/CO_2 ratio between data points is approximately 1.1. For the 20, 15 and 10 mol.% conditions, the corresponding averages are 1.5, 2.1 and 3.1 respectively.

At a given solvent/CO_2 ratio, the corresponding lean loading increases with CO_2 concentration. For example, three points, one each from the 25, 20 and 15 mol.% CO_2 conditions, at a solvent/CO_2 ratio of approximately 12.5 show a difference in lean loading of approximately 0.05 between them. While fewer points share similar solvent/CO_2 ratios compared to the L/G ratios in Figure 4.10A, similar inter-trend observations hold.

Identifying the optimal operating conditions for each flue gas CO_2 concentration involved determining the solvent flow rate at which the SRD is minimised. As solvent flow rate changes, the stripper transitions between the baseline and exponential operating regions. The point of inflection between these regions corresponds to the minimum SRD and has an associated lean solvent loading and total solvent capacity.

By plotting SRD against lean loading, it becomes possible to estimate the expected lean loading for a given SRD value. Similarly, plotting SRD against solvent capacity enables estimation of the solvent capacity required to achieve a particular SRD. Figure 4.11 presents the SRD plotted against both lean loading and solvent capacity across for the various capture conditions.

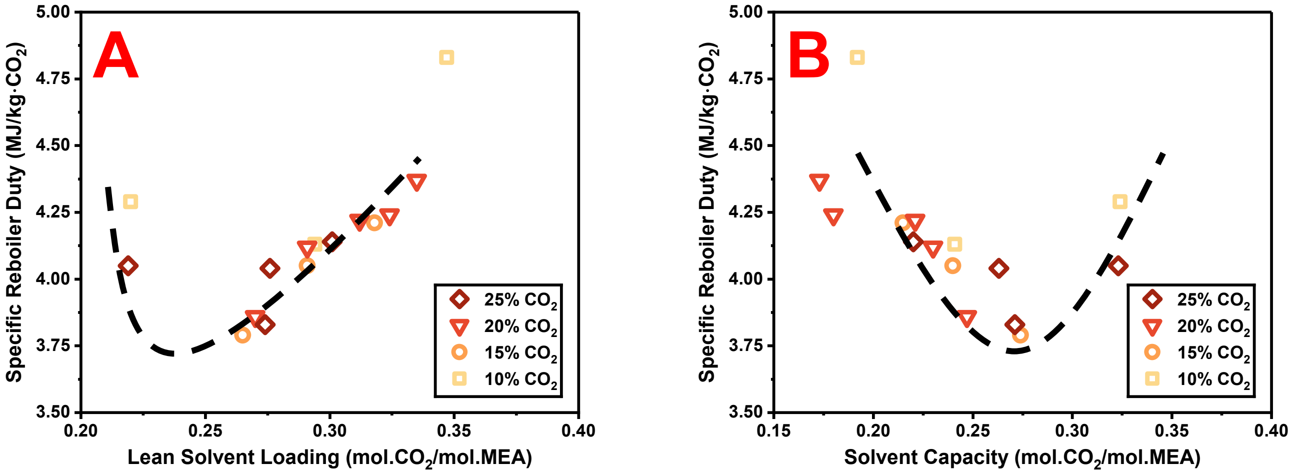

Figure 4.11: Specific reboiler duty against: (A) lean solvent loading and (B) solvent capacity, for solvent flow rates treating 150 Nm^3/h flue gas containing different CO_2 concentrations, targeting 90% capture efficiency.

The dashed lines in Figure 4.11 represent partial trendlines, derived from experimental data and corrected based on expected system performance to represent ideal operating conditions. In Figure 4.11A, data points to the right of the minimum primarily correspond to conditions within the baseline region of stripper operation, while points to the left reflect the exponential region. In Figure 4.11B, this trend is reversed: points to the left of the minimum are in the baseline region, and those to the right are in the exponential region.

Figure 4.11A shows that, as solvent flow decreases and the system transitions from baseline operation towards the inflection point, both lean loading and SRD decrease until a minimum SRD is reached at an optimal lean loading. The partial trendline suggests that, for the TERC ACP achieving 90% capture efficiency, this optimum occurs at a lean loading of approximately 0.23, indicating that the optimal L/G ratio for a given condition should achieve a lean loading near this value. Of the three points exhibiting the lowest SRD values on the plot, it is known that the 15 and 20 mol.% CO_2 conditions have not yet reached their minimum SRD or optimal lean loading, while the lean loading for the 25 mol.% CO_2 condition appears to be recorded too high. At their respective optimal conditions, these data points are expected to shift leftward and downward on the plot, reducing lean loading and SRD, and aligning more closely with the trendline and DCC model predictions. The optimal lean loading for the 10 mol.% CO_2 condition lies close to the trendline, but the associated SRD remains significantly higher, as discussed earlier.

To better account for variation in rich loading, Figure 4.11B plots SRD against solvent capacity. The same three lowest SRD points lie near the trendline minimum, suggesting that, for optimal L/G ratios, the solvent capacity converges at approximately 0.275. For optimal lean loading, the 15 and 20 mol.% CO_2 conditions are expected to exhibit slightly higher solvent capacities and lower SRD values. Similarly, with corrected lean loading, the 25 mol.% CO_2 point would likely shift to a higher solvent capacity, aligning more closely with the trendline. The optimal 10 mol.% CO_2 condition, however, remains an outlier with a significantly higher SRD, and does not follow the same trend. Instead, the trendline is more representative of systems operating at higher CO_2 concentrations.

Finally, the trendlines in both subfigures suggest that the minimum achievable SRD for 90% capture efficiency on the TERC ACP is approximately 3.70 MJ/kg·CO_2 for the described operational setup. Achieving an SRD below this predicted minimum would require significant operational changes, which are discussed in more detail in Section 4.10.

4.8.8 Uncertainty Analysis for the Primary Experimental Results

A statistical uncertainty analysis was conducted for the primary experimental results, following the methodology outlined in Section 4.6. Four key performance indicators were evaluated to assess the reliability of the results:

- Reboiler duty, Q_{reboiler}
- Mass of captured CO_2, $\dot{m}_{\text{CO}_2\text{,captured}}$
- Capture efficiency, η_{capture}
- SRD, q_{reboiler}

The relative uncertainties for each parameter are presented in Table 4.10 for all tested capture conditions.

The relative uncertainty in the reboiler duty, Q_{reboiler}, ranged from ±3.23% to ±6.87%, with an average of ±4.80%, indicating a relatively stable and accurate measurement of the total energy input across all capture conditions. This narrow margin of uncertainty is primarily attributed to the temperature measurements of the PHW, which carried a relative uncertainty approximately ten times greater than the PHW mass flow rate.

The uncertainty in the mass of captured CO_2, $\dot{m}_{\text{CO}_2\text{,captured}}$, was consistently the lowest among all four parameters, ranging from ±0.51% to ±1.53%, with an average of ±1.02%. This very low uncertainty reflects the high precision of the underlying measurements, namely gas flow rates, pressure and temperature readings, and FTIR gas compositions, under steady state conditions. Despite being derived through a multi-step calculation, the propagation of uncertainty remained minimal, providing strong confidence in the accuracy of these results.

Similarly, the uncertainty in the capture efficiency, η_{capture}, was also very low, ranging from ±0.62% to ±1.64%, with an average of ±1.10%. As this metric is derived from the mass of captured CO_2, its uncertainty is directly governed by the precision of that parameter, further reflecting the reliability of the CO_2 capture calculation.

The relative uncertainty in the SRD, q_{reboiler}, was slightly higher than that of the reboiler duty, ranging from ±3.27% to ±6.94%, with an average of ±4.92%. Since the SRD is calculated by dividing the reboiler duty by the mass of captured CO_2, its uncertainty is a combination of both terms. However, the analysis shows that the uncertainty in the SRD is overwhelmingly dominated by the uncertainty in the reboiler duty, as the contribution from the mass of captured CO_2 is comparatively negligible.

Overall, this uncertainty analysis confirms that the key performance indicators of the primary experimental results are both reliable and accurate, with quantifiable margins of error. These values form a reliable foundation for the subsequent uncertainty analyses related to energy balances and solvent regeneration calculations presented later in this chapter.

Table 4.10: Relative uncertainties in the primary experimental results for different capture conditions.

Parameter	Units	Capture Condition															
		25_800	25_900	25_1000	25_1100	20_800	20_900	20_1000	20_1100	20_1200	15_600	15_700	15_800	10_300	10_400	10_500	10_700
$Q_{reboiler}$	±%	4.44	3.89	3.39	4.64	6.87	3.36	3.23	3.42	3.28	5.49	4.41	5.38	5.62	6.55	6.87	5.95
$\dot{m}_{CO_2,captured}$	±%	1.49	1.39	0.93	1.15	0.99	0.65	0.51	0.60	0.86	1.53	0.90	1.14	0.75	0.95	0.98	1.45
$\eta_{capture}$	±%	1.64	1.60	0.90	1.05	0.98	0.71	0.62	0.68	0.98	1.54	1.08	1.24	0.86	1.13	1.05	1.50
$q_{reboiler}$	±%	4.68	4.13	3.52	4.78	6.94	3.42	3.27	3.47	3.39	5.70	4.51	5.50	5.67	6.62	6.94	6.13

4.8.9 Experimental Results Discussion

Comparison of SRD and solvent loadings to previous studies on the TERC ACP is challenging due to the various changes the plant has undergone over the years. Many earlier studies reporting SRD were performed on the PACT configuration of the ACP, where some presented SRD only in a normalised format, comparing results to a chosen base case rather than providing absolute values [2,20].

The published work by Akram et al. [3], previously used to validate the DCC model, reports SRD values across tested capture conditions. A comparable condition from both the Akram study and the current work involves a 10 mol.% CO_2 concentration with a 700 kg/h solvent flow rate. For this study, the SRD of this condition was 4.86 MJ/kg·CO_2 for a gas flow rate of 150 Nm^3/h, whereas for the reference condition the reported SRD was slightly higher at 5.2 MJ/kg·CO_2 for a gas flow rate of 210 Nm^3/h. The main difference between the two studies is the absorber configuration, where Akram et al. used a single 8 m column, and this study used the updated configuration with two 6 m absorbers placed in series. The higher reboiler duty reported by Akram et al. is a result of the difference in rich solvent loading levels and how the system had to compensate to achieve the target capture efficiency.

In this study, the absorbers in series have a combined larger height than the original absorber and are fitted with liquid redistributors at the top and midpoint of each column to improve contact between liquid and gas. This led to a high rich loading of 0.539 for the capture condition. As a result, the level of regeneration needed to achieve 90% capture efficiency required a lean solvent loading of 0.347.

In the original study, the shorter singular absorber was fitted with continuous packing. Combined with a higher flue gas flow this led to a shorter residence time of gas and solvent in the column, reducing contact between liquid and gas and the extent of absorption, leading to a reduced rich loading of 0.443. Consequently, a much lower lean loading of 0.204 was needed in order to achieving 90% capture efficiency, which demanded a higher energy input to the system, therefore increasing the overall SRD.

Additionally, the difference between solvent cyclic capacities is evident. In this work, a capacity of 0.192 was required to achieve 90% capture efficiency, whereas a larger capacity of 0.239 was needed in the reference condition. The reasons for this are twofold. Firstly, the original study used a lower MEA concentration of 30 wt.%, compared to 35 wt.% in this work. This would demand a larger solvent capacity for the same mass of CO_2 captured. Secondly, the original study used a higher gas flow rate of 210 Nm^3/hr, compared to 150 Nm^3/hr in this study. The additional mass of CO_2 required a larger solvent capacity for the same solvent flow rate. These effects combined lead to the observed difference in solvent capacity between the two studies.

These factors collectively contributed to a higher reboiler duty of 48.5 kW in the reference condition, compared to 35.5 kW in the current work. The observed difference in SRD between the two cases is therefore reasonable and consistent with differences in process configuration and operating conditions.

In the broader literature, relatively few studies have investigated higher flue gas CO_2 concentrations using MEA solvent, making direct comparison of operating points difficult. Ideally, comparisons require that the study targets a 90% capture efficiency, uses MEA at a comparable concentration, and operates within the CO_2 concentration range explored in this work. When one or more of these conditions are not met, comparison becomes challenging.

A pivotal campaign was conducted using an Aker Carbon Capture mobile test unit (MTU) to treat flue gas from a steam reformer at the Preem refinery in Lysekil, Sweden [21]. The MTU is comparable in size to the TERC ACP, featuring a variable absorber height of either 11 m or 18 m, with a diameter of 0.4 m. The desorber is 8 m tall, with a diameter of 0.32 m. Although the exact column packing type was confidential, it was represented in a complementary modelling study using Flexipac 2X. The campaign operated for a total of 508 hours, treating flue gas with CO_2 concentrations ranging from 18 to 20 mol.%, using 30 wt.% MEA. At an absorber height of 18 m, the MTU achieved approximately 90% capture efficiency with an average minimum SRD of 3.7 MJ/kg·CO_2 at an optimal reboiler temperature of 120 °C. Reducing the absorber height to 11 m increased the relative SRD by approximately 0.1 MJ/kg·CO_2. This observation aligns closely with the SRD value of 3.86 MJ/kg·CO_2 recorded for the 20_800 capture condition in this study, which is just above the optimal L/G ratio, providing strong validation for the calculated results.

Crucially, in their review of large-scale pilot campaigns that used MEA solvent, Biermann et al. reported they were unable to find any MEA pilot data for CO_2 concentrations above 15 mol.% [21], underscoring the novelty and value of this study to engineering research. As a result, other pilot-scale studies available in the open literature focus on flue gas CO_2 concentrations below 15 mol.%.

In an earlier significant study, Notz et al. conducted a comprehensive pilot plant study at the University of Kaiserslautern using MEA, focusing on the plant's operational behaviour under a wide range of conditions [22]. Through eight sensitivity analyses, a total of 47 capture conditions were investigated, establishing valuable baseline knowledge that continues to inform studies to this day. The pilot plant used in their work was significantly smaller than the TERC ACP, with absorber and stripper columns approximately one third of the height and half the diameter. It also utilised an integrated evaporator in the base of the stripper column to generate steam, rather than a reboiler.

However, the operating conditions explored in their study fall outside the range tested in the current work. At their highest CO_2 concentration of 13.4 mol.%, the capture efficiency was only 43.67%. At 10.9 mol.% CO_2, the capture efficiency increased slightly to 51.32%. These values are well below the 90% target used throughout this study, and as such, a direct comparison of SRD or solvent loadings are not meaningful.

However, an earlier study by Mangalapally and Hasse, conducted on the same pilot plant, identified conditions more directly comparable to the present work [23]. In that study, two CO_2 concentrations were investigated across a range of operating parameters, including variation of the L/G ratio by adjusting the solvent flow rate. For their "Series B" flue gas, comprising 10 mol% CO_2, they reported an optimal L/G ratio of 2.5 using 30 wt.% MEA when targeting 90% capture efficiency, with an SRD of 4.1 MJ/kg·CO_2. This aligns closely with the corresponding case in the present study, where the optimal L/G ratio was observed at 2.44 with a recorded MEA concentration of 30.67 wt.%, equivalent to a CO_2-free solvent concentration of 32.81 wt.%, which gave an SRD of 4.13 MJ/kg·CO_2 for the same CO_2 concentration.

A recent study by Krótki et al. [24] investigated different solvents using a capture plant configuration comparable in size and capacity to the TERC ACP, but with the addition of a rich solvent split in the stripper column. The tested flue gas contained 13.2 mol.% CO_2, with a mass flow rate of 285 kg/h, and a target capture efficiency of 90%. When using MEA, the study identified an optimal L/G ratio of 3.4, with an SRD of approximately 4.0 MJ/kg·CO_2. This condition falls between two cases tested in the present study: the 10 mol.% CO_2 case with a 500 kg/h solvent flow rate, and the 15 mol.% CO_2 case with a 600 kg/h solvent flow rate. The former achieved a minimum SRD of 4.13 MJ/kg·CO_2 at an L/G ratio of 2.44, while the latter remained above its optimal L/G ratio, reporting an SRD of 3.79 MJ/kg·CO_2 at an L/G ratio of 2.81.

Although the SRD values are broadly consistent across studies, the L/G ratios observed in this work are lower than those reported by Krótki et al. This difference is likely attributable to variations in plant configuration and operating conditions, which influence solvent loadings and the associated energy demand for solvent regeneration. However, this assumption is based on their reported results for aqueous 2-(2-aminoethylamino)ethanol (AEEA), and since MEA solvent loading values were not provided, the impact cannot be further investigated.

A study by Kwak et al. [25] investigated CO_2 capture at a flue gas concentration of 15.2 mol.% using a pilot plant capable of capturing two tonnes of CO_2 per day. The gas flow rate was 350 Sm^3/h, with a capture efficiency of 90% and an MEA concentration of 30 wt.%. The plant's absorber and stripper columns were larger than those of the TERC ACP: the absorber measured 23.5 m in height and 0.4 m in diameter, while the stripper was 17 m tall with a diameter of 0.35 m. The study identified an optimal L/G ratio of 3.7, corresponding to a solvent flow rate of 1300 kg/h, with an SRD of 3.92 MJ/kg·CO_2. While this SRD is comparable to that of the 15_600 condition in the present study (3.79 MJ/kg·CO_2), the optimal L/G ratio is significantly higher (3.7 vs 2.81), aligning more closely with the findings reported by Krótki et al. The reported rich and lean loadings were 0.5 and 0.15, respectively, both lower than the corresponding values of 0.539 and 0.265 observed in the present study.

These lower solvent loadings are likely a consequence of the plant operating parameters, where higher solvent and gas flow rates could reduce the residence time available for CO_2 absorption. This is similar to the earlier discussion regarding the PACT ACP, where limited rich loading due to shorter residence time was offset by deeper solvent regeneration to lower lean loadings. A lower lean loading leads to faster CO_2 absorption, enabling the 90% capture efficiency to still be met even if the rich solvent isn't fully saturated.

Additionally, the solvent capacity in the Kwak study was larger, at 0.35 compared to 0.274 in the present study. The larger capacity suggests that, for their specific plant design and operating conditions, achieving a larger capacity was more energy efficient than operating at a smaller capacity with a higher L/G ratio.

Knudsen et al., as part of the CASTOR project, investigated 30 wt.% MEA as a baseline solvent for comparison against other novel solvents, achieving 90% capture efficiency from a flue gas containing 12. Mol.% CO_2 [26]. The absorber column was approximately 17 m tall with a diameter of 1.1 m, and the stripper column was 10 m tall with an additional 3 m water wash section, also with a 1.1 m diameter. The study identified an optimal L/G ratio of 2.45, with an SRD of 3.6 MJ/kg·CO_2. This L/G ratio is more consistent with the values observed for the 10 and 15 mol.% conditions in the present study, however, the lower SRD suggests a more energy efficient setup for the CASTOR pilot plant. MEA solvent loadings were not directly reported by Knudsen et al., limiting further comparison.

In summary, direct comparison between pilot studies is challenging due to a range of factors, including variations in absorber and stripper dimensions, flue gas composition and flow rates, solvent types and concentrations, and plant configurations, which may incorporate advanced process modifications such as rich solvent splits. These variables significantly influence key operational parameters, including solvent loadings and regeneration energy requirements, making strict performance benchmarking difficult. Nevertheless, by carefully accounting for these differences, meaningful qualitative comparisons can still be drawn.

Despite differences in absolute performance metrics, the observed trends in this work, such as the relationships between L/G ratio, solvent loadings, and SRD, are broadly consistent with expected behaviour. As anticipated, operation at the optimal L/G ratio minimises SRD, with the solvent capacity requirements for a given capture efficiency strongly influencing the degree of solvent regeneration and the associated energy demand. Column temperature profiles across the absorber and stripper further support these findings, reflecting the interaction between CO_2 absorption and ease of solvent regeneration across the range of tested conditions.

With relatively few pilot plant studies available in the open literature, this work provides valuable new data to address a recognised gap in CO_2 capture research, particularly for flue gas CO_2 concentrations above 15 mol.%, as highlighted in the review by Biermann et al. [21]. Importantly, the TERC ACP employs a conventional PB absorber without advanced process modifications, offering a practical and accessible reference point for future pilot plant studies. As interest grows in capturing CO_2 from industrial process emissions with higher CO_2 concentrations, such datasets will be essential for benchmarking, model validation, and technology development.

In the following sections, detailed energy balances around the stripper are performed for each capture condition to determine the corresponding steam requirements during solvent regeneration. From this, the solvent regeneration energy is evaluated by quantifying the contributions of each component in the solvent regeneration energy equation.

4.9 System Energy Balance for Capture Conditions

4.9.1 Introduction to the Energy Balance

Following the analysis of the experimental data, an energy balance was conducted around the stripper for each capture condition. The energy content of each process stream, along with other relevant parameters, was determined as part of this assessment. The system boundaries and stream configuration are illustrated in Figure 4.12, where each stream is labelled with its composition and assigned a unique number used consistently throughout the calculations.

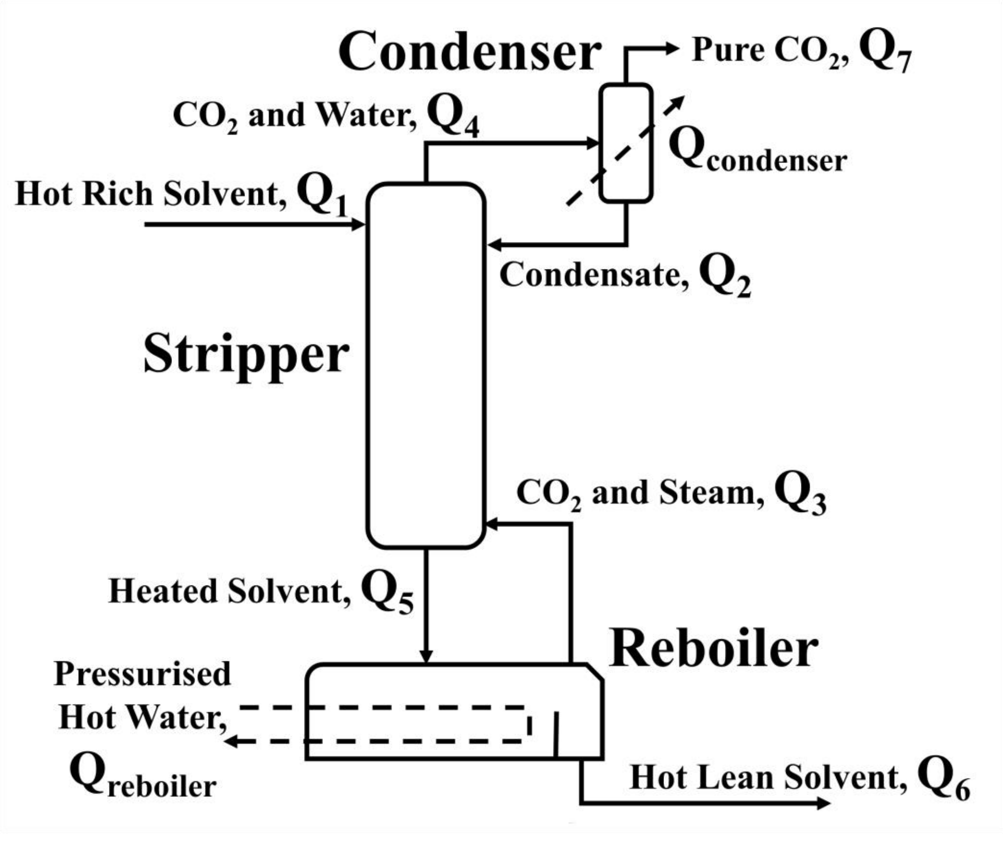

Figure 4.12: Energy balance around the overall stripper system.

The methodology employed for this energy balance was originally described by Akram et al [3], with the following list of assumptions required for a consistent calculation basis:

- All captured CO_2 is fully desorbed from the solvent within the reboiler.
- Steam generation occurs exclusively within the reboiler.
- MEA remains entirely in the liquid phase and does not undergo vaporisation at any point.
- The temperatures of the gaseous and liquid streams at the bottom of the column are equilibrated.
- The stripper overhead stream is taken to be CO_2 saturated with water at the corresponding exit temperature.
- All latent heat of the condensing steam is assumed to have transferred to the rich solvent within the column.
- The condensate leaving the condenser is pure water; no reabsorption of CO_2 occurs.

Two additional assumptions are made in this work due to limitations in the recorded process data:

- The condenser is assumed to remove 100% of the water from the CO_2.
- The temperature of the incoming rich solvent stream is assumed to be equal to the top RTD of the stripper.

4.9.2 Calculation Basis and Reference Values

The following subsections derive the equations used throughout the system energy balance.

4.9.2.1 General Stream Energy Calculations

$$Q_\mathrm{j} = \dot{m}_\mathrm{j} \cdot C_\mathrm{p,j} \cdot \Delta T_\mathrm{j} \tag{4.36}$$

Where:

Q_j = amount of energy flowing in a specific stream (kJ/h)

$\dot{m}_\mathrm{j}$ = mass flow rate of a specific stream (kg/h)

$C_\mathrm{p,j}$ = specific heat capacity of a specific stream ((kJ/(kg·K))

ΔT_j = temperature change of a specific stream (K)

In some cases, it is necessary to calculate the energy contribution of a specific component within a given stream:

$$Q_\mathrm{i} = \dot{m}_\mathrm{i} \cdot C_\mathrm{p,i} \cdot \Delta T_\mathrm{i} \tag{4.37}$$

Where:

Q_i = amount of energy flowing in a specific component (kJ/h)

$C_\mathrm{p,i}$ = specific heat capacity of a specific component ((kJ/(kg·K))

ΔT_i = temperature change of a specific component (K)

Unless otherwise stated, energy calculations are made to a reference of 0 °C, meaning that the temperature difference, ΔT_i, refers to the actual temperature of the stream in Celsius.

4.9.2.2 Specific Heat Capacities

The specific heat capacities of the streams have been determined using several approaches:

- For streams containing MEA (streams 1, 5, and 6), specific heat capacities were provided by Aspen Plus at the relevant temperature and composition [27].
- For stream 7, composed entirely of CO_2, the specific heat capacity was calculated via linear interpolation of tabulated values from The Engineering Toolbox [28].
- For stream 2, which consists solely of condensed water, the specific heat capacity was obtained using the CoolProp Microsoft Excel add-in [8].
- For mixed streams containing both CO_2 and water/steam (streams 3 and 4), the specific heat capacity was estimated using the rule of mixtures, where the overall value is calculated as a weighted average of the component heat capacities:

$$C_{\mathrm{p},3} \; or \; C_{\mathrm{p},4} = C_{\mathrm{p,avg}} = \sum (w_{\mathrm{i}} \cdot C_{\mathrm{p,i}}) \tag{4.38}$$

Where:

$C_{\mathrm{p,avg}}$ = average specific heat capacity of the stream (kJ/(kg·K))

w_{i} = mass fraction of a specific component (kg/kg)

4.9.2.3 Latent Heat of Vaporisation

The heat of vaporisation considered in this energy balance is solely that of water. This is because MEA has a significantly higher boiling point (~170 °C) compared to water (~100 °C at atmospheric pressure), and it is therefore assumed that no MEA vaporises within the system [29–31].

The enthalpy of vaporisation is calculated as the difference between the specific enthalpy of saturated vapour and saturated liquid at the relevant temperature, with values provided by the CoolProp add-in:

$$h_{\mathrm{fg}} = h_{\mathrm{g}} - h_{\mathrm{f}} \tag{4.39}$$

Where:

h_{fg} = specific enthalpy of vaporisation/condensation (kJ/kg)

h_{g} = specific enthalpy of saturated vapour (kJ/kg)

h_{f} = specific enthalpy of saturated liquid (kJ/kg)

The latent heat of condensation is also calculated using Equation (4.39), but with the sign reversed to reflect the opposing phase change process.

4.9.3 Condenser Duty Calculations

To perform the energy balance around the entire stripper system, the energy contributions of the streams associated with the condenser must first be calculated. Figure 4.13 illustrates the boundary applied for the local energy balance around the condenser.

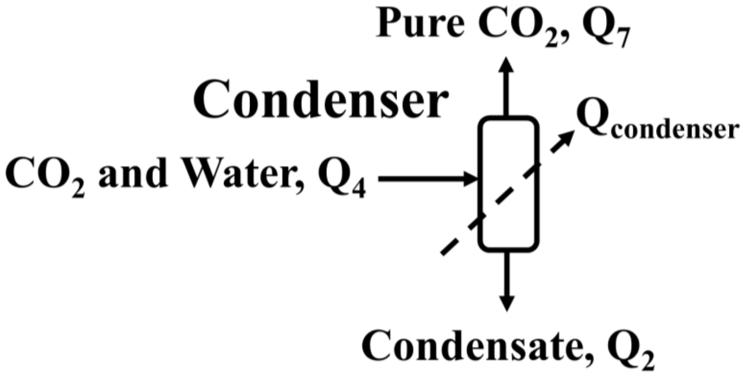

Figure 4.13: Energy balance around the condenser.

The hot vapour (stream 4) enters the condenser and is cooled, where all entrained liquid water is assumed to separate from the CO_2 and exits as condensate in stream 2. This simplification allows for the masses of steam generation and condensing steam within the stripper column to be estimated while balancing the stream masses and energies around the system boundaries. In reality, a very small amount of water would leave the top of the condenser with the CO_2 under saturation at the lower temperature, with a mass fraction typically <0.01. The remaining pure CO_2 exits the top of the condenser in stream 7.

The condenser duty is calculated by taking the difference between the energy of the inlet and outlet streams:

$$Q_{\text{condenser}} = Q_4 - Q_2 - Q_7 \tag{4.40}$$

Where:

$Q_{\text{condenser}}$ = energy removed by the condenser (kJ/h)

The mass flow rates of the relevant streams are required to determine the energy content of each. The mass of captured CO_2 is known from Section 4.5.1, calculated as the difference between the CO_2 mass flow entering and exiting the absorber. As the system is at steady state, this calculated value must be equal to the amount of pure CO_2 exiting the condenser in stream 7. Given the assumption that no CO_2 absorbs into the condensate, the CO_2 mass in the incoming vapour stream is considered equal to that in the outlet stream from the condenser.

The mass of water in stream 4 can then be inferred by assuming the CO_2 is saturated with water at the corresponding temperatures. Using saturation temperature tables [32], the saturation pressure of water at a given temperature is obtained using linear interpolation between the two nearest data points. This enables calculation of the mole fraction of water in the stream:

$$x_{\mathrm{H_2O}} = \frac{P_{\mathrm{saturation}}}{P_{\mathrm{reboiler}}} \tag{4.41}$$

Where:

$x_{\mathrm{H_2O}}$ = mole fraction of water in the stream (mol/mol)

$P_{\mathrm{saturation}}$ = saturation pressure at the corresponding temperature (kPa)

P_{reboiler} = pressure of the reboiler (kPa)

This mole fraction can then be converted to a mass fraction:

$$w_{\mathrm{H_2O}} = \frac{x_{\mathrm{H_2O}} \cdot MW_{\mathrm{H_2O}}}{x_{\mathrm{H_2O}} \cdot MW_{\mathrm{H_2O}} + \left(1 - x_{\mathrm{H_2O}}\right) \cdot MW_{\mathrm{CO_2}}} \tag{4.42}$$

Where:

$w_{\mathrm{H_2O}}$ = mass fraction of water (kg/kg)

The mass fraction allows for the mass flow rate of stream 4 to calculated:

$$\dot{m}_4 = \frac{\dot{m}_{4,\mathrm{CO_2}}}{1 - w_{\mathrm{H_2O}}} \tag{4.43}$$

The mass flow rate of the condensate is equal to the difference between the mass flow rates of streams 4 and 7:

$$\dot{m}_2 = \dot{m}_4 - \dot{m}_7 \tag{4.44}$$

With the mass flow rates of all streams around the condenser now known, Equations (4.36) and (4.38) can be used to calculate Q_4 and Equation (4.37) can be used to calculate Q_2 and Q_7.

4.9.4 Steam Production Calculations

The energy balance around the stripper column may now be determined. Figure 4.14 presents the boundary around the column for the local energy balance. Hot rich solvent enters the stripper near the top of the column in stream 1 and falls down the column, where it mixes with the condensate coming from two sources: external condensate coming from the condenser in stream 2, and internal condensate from the steam within the column condensing, supplied by the reboiler in stream 3. The heated solvent at the bottom of the column leaves to the reboiler in stream 5. The CO_2 and any remaining water exit the top of the stripper in stream 4.

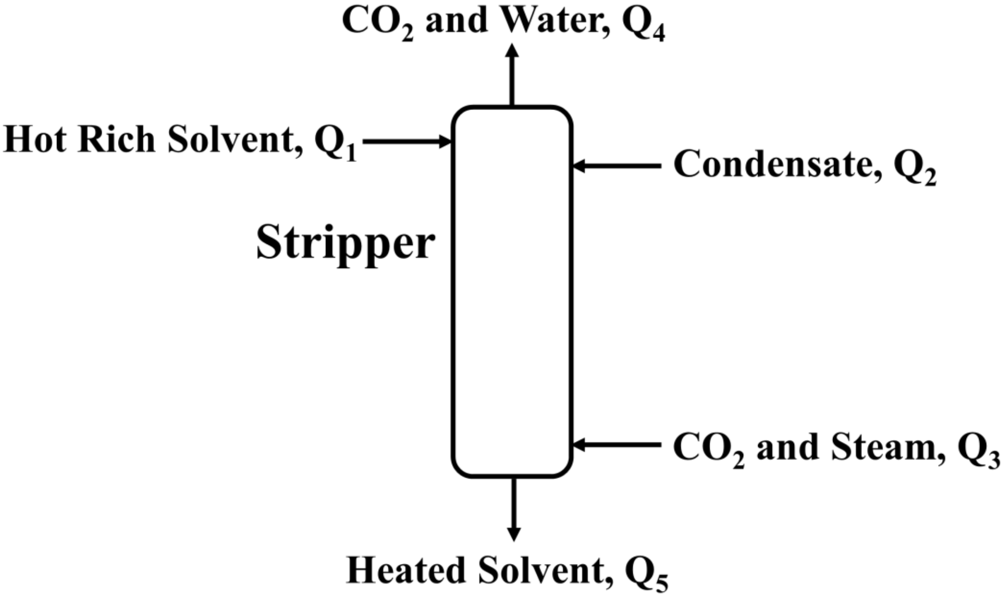

Figure 4.14: Energy balance around the stripper column.

The overall energy balance around the stripper is expressed as:

$$\text{Energy In} = \text{Energy Out}$$
$$Q_1 + Q_2 + Q_3 = Q_4 + Q_5 \tag{4.45}$$

From the condenser duty calculations, Q_2 and Q_4 are already known, and Equation (4.36) can be used to calculate Q_1. Determining the correct values of Q_3 and Q_5 is less straightforward. Q_3 includes the steam generated in the reboiler, which condenses within the column as it rises. This internal condensate leaves the bottom of the stripper in stream 5 and falls into the reboiler, contributing to the energy of Q_5. The exact amount of steam that condenses within the column is initially unknown, affecting both the mass and energy balances of streams 3 and 5.

The overall mass balance around the stripper column is given by:

$$\dot{m}_1 + \dot{m}_2 + \dot{m}_3 = \dot{m}_4 + \dot{m}_5 \tag{4.46}$$

At steady state, both mass and energy must balance around the system boundaries. Determining the amount of steam produced by the reboiler is critical to achieving this balance.

The energy content of stream 3 leaving the reboiler and entering the bottom of the stripper is evaluated as the sum of the energy contributions from both CO_2 and steam at the temperature of the reboiler:

$$Q_3 = Q_{3,\mathrm{CO_2}} + Q_{3,\mathrm{H_2O}} \tag{4.47}$$

$Q_{3,\mathrm{CO_2}}$ can be determined using Equation (4.37), while $Q_{3,\mathrm{H_2O}}$ is determined using the following calculation:

$$Q_{3,\mathrm{H_2O}} = Q_{\mathrm{steam}} = \dot{m}_{\mathrm{steam}} \cdot h_{\mathrm{g}} \tag{4.48}$$

Where:

Q_{steam} = energy of flowing steam (kJ)

$\dot{m}_{\mathrm{steam}}$ = mass flow rate of steam (kg/h)

This allows the energy balance from Equation (4.45) to be rewritten as:

$$Q_1 + Q_2 + Q_{3,\mathrm{CO_2}} + \dot{m}_{\mathrm{steam}} \cdot h_{\mathrm{g}} = Q_4 + Q_5 \tag{4.49}$$

Rearranging Equation (4.49) enables the mass flow rate of steam produced by the reboiler to be determined:

$$\dot{m}_{\mathrm{steam}} = \frac{Q_4 + Q_5 - Q_1 - Q_2 - Q_{3,\mathrm{CO_2}}}{h_{\mathrm{g}}} \tag{4.50}$$

When an initial mass flow rate estimate is provided to determine Q_5 using Equation (4.36), preliminary values for $\dot{m}_{\mathrm{steam}}$ and Q_3 can be found using Equations (4.50) and (4.47). However, this does not ensure that the mass and energy balances across the system are aligned. Accurate determination of Q_5 requires an iterative approach to appropriately reconcile the mass and energy flows between streams 3 and 5, ensuring that the correct amount of steam is condenses within the stripper column. The system of equations used to achieve this balance is as follows:

$$\dot{m}_{\mathrm{steam}} = \dot{m}_5 - \dot{m}_1 = \dot{m}_3 - \dot{m}_7 \tag{4.51}$$

Changing the estimate of $\dot{m}_5$ affects the amount of steam that is generated, which in turn affects the value of $\dot{m}_3$. The system becomes balanced once the amount of steam generated is equivalent to the difference in the mass flow rate between the solvent at the bottom of the stripper falling into the reboiler, $\dot{m}_5$, and the incoming rich solvent, $\dot{m}_1$. As it is assumed that all of the water leaving the top of the stripper is returned to the column as condensate, then the difference in mass flow rate between the hot vapour leaving the reboiler, $\dot{m}_3$, and the pure CO_2 leaving the condenser, $\dot{m}_7$, should also equal the amount of steam generated. Consequently, Microsoft Excel's Solver tool was used to balance Equation (4.51) and determine the mass of generated steam by iterating $\dot{m}_5$. Equation (4.49) was then verified to ensure consistency with the new values. At this point, both mass and energy flows were balanced around the system boundary illustrated in Figure 4.14. Stream 6 is the remaining stream depicted in Figure 4.12 as the hot lean solvent leaving the reboiler, where its energy content was determined using Equation (4.36).

4.9.5 Additional Calculations

The energy used for the desorption reaction is calculated indirectly around the whole stripper, using the following equation [3]:

$$Q_{\mathrm{de}} = Q_{\mathrm{reboiler}} + Q_1 - Q_{\mathrm{condenser}} - Q_6 - Q_7 \tag{4.52}$$

Where:

Q_{de} = desorption energy (kJ/h)

This indirect method will be highly dependent on the accuracy of which the other energy terms have been calculated, where any uncertainty will propagate into the desorption energy value.

The specific steam generation (SSG) value is the ratio between the mass of steam generated and the mass of captured CO_2:

$$SSG = \frac{\dot{m}_{\mathrm{steam}}}{\dot{m}_{\mathrm{CO_2,captured}}} \tag{4.53}$$

Where:

SSG = specific steam generation (kg/kg)

A mass balance was performed around the whole system to compare the recorded average flow values:

$$\begin{gathered} \text{Mass In} = \text{Mass Out} \\ \dot{m}_1 = \dot{m}_6 + \dot{m}_7 \end{gathered} \tag{4.54}$$

It was noted that a small discrepancy existed between the total mass flow entering and leaving the system. Across the different capture conditions, this imbalance ranged from 10.8 to 21.9 kg/h of apparent excess mass leaving the system. An uncertainty analysis was performed on the mass flow rates, and it was found that the absolute uncertainty of the difference in mass flow rates ranged from ±2.4 to ±32.7 kg/h. For the majority of capture conditions, the absolute uncertainty approximated the difference in mass flow rate, showing that the imbalance is not statistically significant and falls within the expected range of experimental variation. It was found that the uncertainty of $\dot{m}_1$ dominated the uncertainty calculations, at approximately 20 times the combined uncertainty of $\dot{m}_6$ and $\dot{m}_7$. This shows that the total uncertainty in the mass balance comes almost entirely from the uncertainty in the mass flow measurement of stream 1.

Further investigation of the ACP revealed that some Coriolis flow meters required calibration, contributing to these flow rate deviations. Additionally, the method used to maintain solvent levels in the stripper sump permits a degree of accumulation or depletion, even at steady state, which was reflected in the process data. This mass imbalance discrepancy had no significant impact on the overall energy balance calculations around the stripper as stream 6 is outside of the main energy balance calculations.

The final results of the stripper energy balance are presented in Table 4.11. Anomalies were identified for capture condition 10_300, where the mass balance calculation showed more vapour exiting the column than was generated by the reboiler, an impossible result. This discrepancy originated from the saturation temperature used for calculating water content in the saturated CO_2 stream. At a stripper top temperature of 99 °C, the CO_2 could theoretically carry a much higher water content, causing the energy balance methodology to break down. The stripper temperature profile for this condition remained above 105 °C over most of the column height, placing it deep into the exponential region of operation. Under such conditions, the simplifying assumption that all latent heat from the steam is transferred to the rich solvent becomes invalid. As a result, the energy balance for condition 10_300 was excluded from further analysis.

A statistical uncertainty analysis was conducted for the energy balance calculations, following the methodology outlined in Section 4.6. Each stream was evaluated based on uncertainties in the mass flow rates and temperatures, along with the absolute uncertainties in the masses of captured CO_2 and reboiler heat duties. The resulting relative uncertainties are presented as percentages in Table 4.12.

4.9.6 Energy Balance Discussion and Uncertainty Analysis

The energy balance analysis reveals several important trends across the evaluated energy terms. For the major streams: Q_1, Q_3, Q_5, and Q_6, as well as the heat duty input Q_{reboiler}, steam generation $\dot{m}_{\text{steam}}$, and steam energy Q_{steam}, two primary patterns emerge. Firstly, energy values generally increase with rising flue gas CO_2 concentrations, reflecting the additional energy demand required for deeper solvent regeneration to capture additional CO_2. Secondly, energy values also increase with solvent flow rate, due to the increased mass of water that must be heated to achieve the target capture efficiency.

The relative uncertainty for Q_{reboiler} remains unchanged from the previous analysis, ranging from ±3.23% and ±6.87%, indicating a relatively stable and reliable measurement of the total energy input. Relative uncertainties for Q_1 and Q_5 vary across conditions but are typically below ±1.6%, demonstrating high confidence in these values. For $\dot{m}_{\text{steam}}$ and Q_{steam}, relative uncertainties ranged from ±0.67% to ±11.96%, showing how variability in the process data propagates through the energy balance. Greater process stability generally reduces data variability, leading to lower propagated uncertainty. Similarly, Q_3 exhibits moderate relative uncertainty, ranging from ±0.65% to ±11.50%, due to the combination of uncertainty in both steam generation and captured CO_2. By contrast, Q_6 has the lowest uncertainty of any term, consistently below ±0.1%, due to tightly controlled lean solvent flow rates, boosting confidence in the energy values associated with this stream.

For minor streams: Q_2, Q_4, Q_7, $Q_{\mathrm{CO_2}}$, and $Q_{\mathrm{condenser}}$, similar trends are present but exhibit more relative fluctuation. These values are several orders of magnitude smaller than the major energy streams, making them more susceptible to measurement noise, which can obscure parameter trends.

Uncertainties in these minor streams are predominantly governed by the uncertainty in the mass of captured CO_2, generally ranging between ±0.5% to ±1.5%. For Q_2 and Q_7, their absolute values are so small that they have a negligible impact on the overall energy balance and its uncertainty. This supports the simplification assumption that 100% of the water is removed from the CO_2 stream in the condenser for the purpose of energy calculations.

The desorption energy, Q_{de}, shows broadly similar values for each flue gas CO_2 concentration. This is expected, as the amount of CO_2 captured is generally consistent for each flue gas CO_2 concentrations, with the exception of 25 mol.% CO_2. Notably, Q_{de} exhibits the highest uncertainty among all calculated energy terms, ranging from ±7.33% to ±18.50%, due to its derivation from multiple large, uncertain components. This suggest that the indirect method used to estimate the energy desorption is not the most reliable method and should be interpreted with caution.

The SSG ranges from 0.86 to 1.50, with an average value of 1.06 across all capture conditions. For most conditions, the mass of generated steam and the mass of captured CO_2 are similar. However, an increase in SSG is observed as the solvent flow rate increases for each respective flue gas CO_2 concentration, confirming that higher solvent flow rates generate more steam due to additional water mass. The relative uncertainty in SSG is similar to that of Q_3, as both depend on propagated uncertainties from steam generation and CO_2 capture calculations.

Overall, the uncertainty analysis reveals that mass flow rate uncertainties, for solvent, steam, and captured CO_2, are the dominant contributors to propagated error. These uncertainties can be up to 40 times larger than corresponding uncertainties in temperature measurements, making flow rate precision critical to improving result reliability.

Finally, it is important to note that the current methodology does not account for heat losses within the system, as it only evaluates energy associated with defined process streams. A more comprehensive investigation is required to quantify these losses. This is addressed in the next section, where the individual components of solvent regeneration energy are calculated directly using the energy balance results, supported by experimental data and associated uncertainty analyses.

Table 4.11: Energy balances across the stripper for different capture conditions.

Parameter	Units	Capture Condition														
		25_800	25_900	25_1000	25_1100	20_800	20_900	20_1000	20_1100	20_1200	15_600	15_700	15_800	10_400	10_500	10_700
Q1	MJ/h	196.8	229.7	254.2	280.9	197.9	218.1	249.1	287.8	312.5	148.9	179.6	207.6	103.1	125.0	182.9
Q2	MJ/h	0.5	0.6	0.5	0.5	0.1	0.2	0.1	0.2	0.2	0.1	0.2	0.2	0.1	0.1	0.1
Q3	MJ/h	156.5	164.7	174.8	184.5	142.7	163.3	166.8	163.2	173.3	109.0	118.7	125.9	71.7	85.1	109.7
Q4	MJ/h	7.5	8.9	8.4	8.4	6.9	6.4	7.0	8.0	8.0	5.1	5.7	6.1	3.4	3.4	3.6
Q5	MJ/h	346.3	386.0	421.1	457.5	333.8	375.2	409.0	443.2	443.2	253.0	292.8	327.6	171.4	206.6	289.0
Q6	MJ/h	316.5	354.6	384.2	415.5	305.0	338.4	369.9	402.0	433.3	229.8	264.7	298.0	158.0	189.5	260.7
Q7	MJ/h	0.5	0.6	0.5	0.5	0.1	0.2	0.1	0.1	0.2	0.2	0.1	0.1	0.1	0.1	0.1
$Q_{reboiler}$	MJ/h	255.5	260.7	257.8	260.3	210.7	223.2	229.1	227.3	234.5	154.7	162.5	171.1	111.5	108.9	127.7
$Q_{condenser}$	MJ/h	6.4	7.8	7.4	7.4	6.7	6.1	6.8	7.7	7.6	4.8	5.4	5.8	3.3	3.4	3.5
Q_{de}	MJ/h	128.9	127.4	119.9	117.8	96.8	96.6	101.4	105.3	105.9	68.8	71.9	74.8	53.3	41.0	46.3
$m_{CO_2,captured}$	kg/h	63.0	68.2	63.8	62.9	54.6	54.2	54.3	53.6	53.6	40.8	40.2	40.6	26.0	26.4	26.5
Q_{CO_2}	MJ/h	6.5	7.0	6.5	6.4	5.6	5.5	5.5	5.4	5.4	4.2	4.1	4.1	2.7	2.7	2.6
$\dot{m}_{steam}$	kg/h	55.7	58.5	62.5	66.2	50.9	58.6	60.0	58.7	62.5	38.9	42.5	45.2	25.7	30.6	39.8
Q_{steam}	MJ/h	149.9	157.6	168.3	178.1	137.1	157.8	161.3	157.8	167.9	104.8	114.6	121.8	69.1	82.4	107.0
SSG	kg/kg	0.9	0.9	1.0	1.1	0.9	1.1	1.1	1.1	1.2	1.0	1.1	1.1	1.0	1.2	1.5

Table 4.12: Relative uncertainties in the energy balances across the stripper for different capture conditions.

Parameter	Units	Capture Condition														
		25_800	25_900	25_1000	25_1100	20_800	20_900	20_1000	20_1100	20_1200	15_600	15_700	15_800	10_400	10_500	10_700
Q1	±%	3.87	3.14	0.91	1.45	0.35	1.35	0.26	1.55	1.52	4.46	1.90	0.38	0.58	0.90	2.11
Q2	±%	1.50	1.39	0.94	1.15	0.99	0.65	0.51	0.62	0.86	1.53	0.91	1.14	0.95	1.00	1.47
Q3	±%	9.36	8.19	2.46	4.01	0.89	3.42	0.65	4.85	4.83	11.50	5.27	1.11	1.53	2.42	6.28
Q4	±%	1.53	1.40	0.94	1.17	0.99	0.66	0.52	0.61	0.86	1.54	0.91	1.14	0.95	0.99	1.48
Q5	±%	3.61	2.95	0.86	1.35	0.32	1.27	0.22	1.47	1.44	4.20	1.79	0.35	0.54	0.84	1.97
Q6	±%	0.06	0.05	0.05	0.05	0.05	0.04	0.04	0.04	0.04	0.06	0.06	0.05	0.09	0.08	0.06
Q7	±%	1.50	1.39	0.94	1.15	0.99	0.65	0.51	0.62	0.86	1.53	0.91	1.14	0.95	1.00	1.47
$Q_{reboiler}$	±%	4.44	3.89	3.39	4.64	6.87	3.36	3.23	3.42	3.28	5.49	4.41	5.38	6.55	6.87	5.95
$Q_{condenser}$	±%	1.78	1.62	1.07	1.33	1.02	0.70	0.54	0.64	0.91	1.64	0.96	1.21	0.97	1.01	1.53
Q_{de}	±%	10.60	9.77	7.56	10.81	14.96	8.35	7.33	8.51	8.54	15.66	11.06	12.35	13.79	18.50	18.39
$m_{CO2,captured}$	±%	1.49	1.39	0.93	1.15	0.99	0.65	0.51	0.60	0.86	1.53	0.90	1.14	0.95	0.98	1.45
Q_{CO2}	±%	1.49	1.39	0.94	1.15	0.99	0.65	0.51	0.60	0.86	1.53	0.90	1.14	0.95	0.98	1.45
$\dot{m}_{steam}$	±%	9.77	8.56	2.56	4.15	0.93	3.54	0.67	5.01	4.99	11.96	5.46	1.15	1.59	2.50	6.43
Q_{steam}	±%	9.77	8.56	2.56	4.15	0.93	3.54	0.67	5.01	4.99	11.96	5.46	1.15	1.59	2.50	6.43
SSG	±%	11.19	10.09	2.78	4.10	1.45	3.33	0.76	4.61	4.34	12.63	5.23	1.45	1.87	2.31	4.38

4.10 Solvent Regeneration Energy

4.10.1 Introduction to the Regeneration Energy

The regeneration energy of a solvent is defined as the total energy required to convert rich solvent into lean solvent by liberating the absorbed CO_2. This process typically involves three distinct components: the sensible heat required to raise the solvent to the appropriate temperature, the vaporisation energy necessary to generate steam, and the heat of desorption associated with the liberation of the absorbed CO_2 [30,31,33–35].

Conventionally, regeneration energy is expressed as the sum of these three contributions:

$$Q_{\text{regen}} = Q_{\text{sens}} + Q_{\text{vap}} + Q_{\text{react}} \tag{4.55}$$

Where:

Q_{regen} = conventional regeneration energy (kJ/h)

Q_{sens} = total sensible heat of the solvent (kJ/h)

Q_{vap} = total energy required to vaporise the solvent from liquid (kJ/h)

Q_{react} = total energy required in the desorption reaction (kJ/h)

Q_{vap} can sometimes refer to the energy of the steam leaving the top of the stripper column, as this removes the need to determine the steam produced in the reboiler [22,30]. For this work, Q_{vap} refers to the vaporisation energy of the total generated steam, as per Equation (4.50).

An increase in any of these components leads to a corresponding rise in the total regeneration energy [30]. It is therefore essential to minimise the energy demand of each component where possible [36]. Strategies for reducing the contribution of each element are discussed in the subsections that follow.

The specific regeneration energy, defined as the amount of energy required to release a unit mass of CO_2, is calculated by dividing the regeneration energy by the mass of CO_2 captured [35]:

$$q_{\text{regen}} = \frac{Q_{\text{regen}}}{m_{CO_2}} \tag{4.56}$$

Where:

q_{regen} = specific regeneration energy (MJ/kg·CO_2)

Equation (4.56) appears similar to Equation (4.18), but the two differ in purpose and interpretation. While Equation (4.56) represents the sum of specific energy contributions required for CO_2 desorption, Equation (4.18) considers the actual energy input to the system via the reboiler.

A key limitation of Equation (4.55) is that it neglects internal energy sources typically present in a real stripping column that act as heat recovery. The total heat recovery partially offsets the energy demands to minimise the solvent regeneration energy. As such, heat recovery must be accounted for in any accurate calculation of the net regeneration energy. The net regeneration energy equation is therefore:

$$Q_{\text{regen,net}} = Q_{\text{sens}} + Q_{\text{vap}} + Q_{\text{react}} - Q_{\text{recovery}} \tag{4.57}$$

Where:

$Q_{\text{regen,net}}$ = net regeneration energy (kJ/h)

Q_{recovery} = total energy of internal heat recovery (kJ/h)

Under steady state conditions the mass flow rate of captured CO_2 is stable for a stable reboiler duty. This means that the regeneration energy required for that condition must be less than the energy supplied by the reboiler. In a real system, however, there will be generalised heat losses across the system. This means that under steady state conditions, the reboiler duty must be equal to the net regeneration energy plus any heat losses [22,30]:

$$Q_{\text{reboiler}} = Q_{\text{regen,net}} + Q_{\text{losses}} \tag{4.58}$$

Where:

Q_{losses} = generalised heat losses across the system (kJ/h)

The fully realised regeneration energy equation for a real steady state condition becomes:

$$Q_{\text{reboiler}} = Q_{\text{sens}} + Q_{\text{vap}} + Q_{\text{react}} - Q_{\text{recovery}} + Q_{\text{losses}} \tag{4.59}$$

Each of the terms in Equation (4.57) must be independently evaluated using a combination of thermodynamic data from open literature and estimations obtained from process simulation tools such as Aspen Plus.

The final results of the regeneration energy calculations, along with other key values, are presented in Table 4.13 for the different capture conditions. The corresponding relative uncertainties of the regeneration energy calculations are presented in Table 4.14.

The following subsections outline the methodology used in this work to evaluate each energy component, with corresponding results and uncertainty analyses for the different capture conditions.

4.10.2 Sensible Heat of Solvent

The sensible heat of the solvent is the energy required to heat the rich solvent up to the reboiler temperature. It is a significant energy demand for the system and is the crucial reason that a cross-heat exchanger is used to recover heat, such that the rich solvent enters the top of the stripper at a much higher temperature without requiring additional energy input from the reboiler. This reduces the sensible heat required to raise the pre-heated rich solvent up to the reboiler temperature. In this study, the sensible heat of solvent has been broken into different contributions, with the total sensible heat being the summation of four distinct terms [30,37]:

$$Q_{\text{sens}} = Q_{\text{sens,rich}} + Q_{\text{sens,column}} + Q_{\text{sens,condenser}} + Q_{\text{sens,bottom}} \tag{4.60}$$

Where:

$Q_{\text{sens,rich}}$ = sensible heat to get the hot rich solvent component to the stripper bottom temperature (kJ/h)

$Q_{\text{sens,column}}$ = sensible heat to get the column steam condensate to the stripper bottom temperature (kJ/h)

$Q_{\text{sens,condenser}}$ = sensible heat to get the condenser steam condensate to the stripper bottom temperature (kJ/h)

$Q_{\text{sens,bottom}}$ = sensible heat to get the total solvent at the stripper bottom to the reboiler core temperature (kJ/h)

Each term in Equation (4.60) is evaluated using Equation (4.36). The specific heat capacities are determined at the average temperature corresponding to the respective temperature change for each component. The specific heat capacity values for the condensate terms are obtained using the COOLPROP add-in, while those for the solvent terms are provided by Aspen Plus.

Figure 4.15 compares the calculated sensible heat of the solvent against the L/G ratio and solvent/CO_2 ratio for each capture condition.

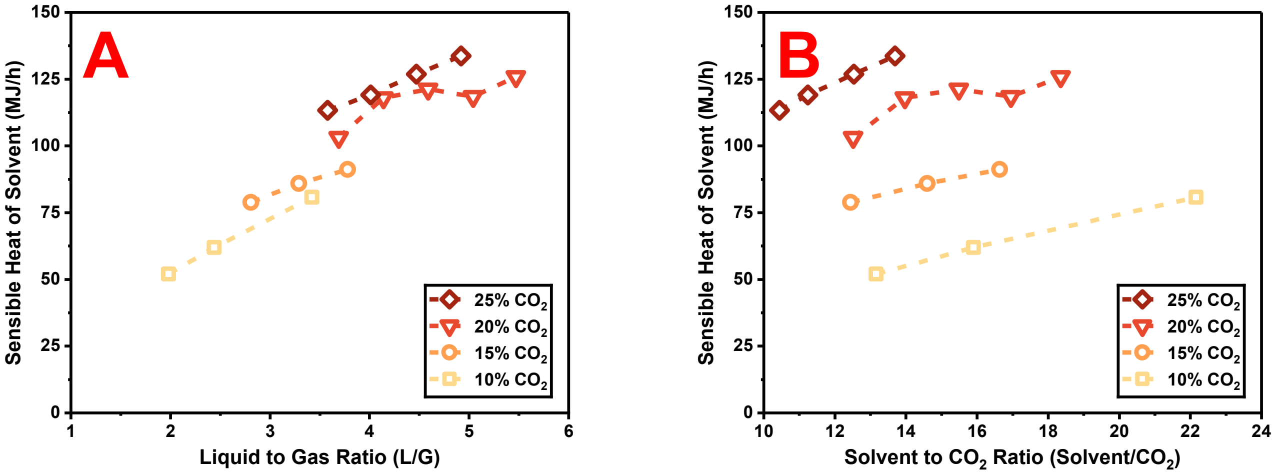

Figure 4.15: Solvent sensible heat against: (A) liquid to gas ratio and (B) solvent/CO_2 ratio, for solvent flow rates treating 150 Nm^3/h flue gas containing different CO_2 concentrations, targeting 90% capture efficiency.

Figure 4.15 clearly demonstrates the expected trend where the sensible heat of the solvent increases with solvent flow rate, consistent across all CO_2 concentrations. A greater mass of solvent requires more energy to reach the operating temperature. Notably, cases 20_900 and 20_1000 report slightly elevated sensible heat values. Further examination revealed that the top of the stripper column was marginally cooler in these cases, requiring additional energy to achieve the reboiler core temperature.

Additionally, Figure 4.15 shows that higher flue gas CO_2 concentrations result in greater sensible heat requirements at the same L/G and solvent/CO_2 ratios. At constant solvent/CO_2 ratios, increasing the flue gas CO_2 concentration requires a higher solvent flow rate to maintain the target capture efficiency, leading to increased L/G ratios, as shown in Figure 4.15A. The larger circulating solvent mass must be heated to the operating temperature, thereby increasing the sensible heat requirement. This trend is more clearly illustrated in Figure 4.15B at a solvent/CO_2 ratio of approximately 12.5, where maintaining a constant ratio across different flue gas CO_2 concentrations necessitates a proportional increase in solvent mass flow, and consequently greater sensible heat.

However, an increase in sensible heat with flue-gas concentration is also observed at constant solvent flow rates (e.g., the 10_700 and 15_700 conditions, and the 20_800 and 25_800 conditions). This behaviour is related to changes in lean solvent loading and solvent composition. As flue gas CO_2 concentration increases, the required lean loading decreases for the same total solvent flow rate. For example, the lean loading decreases from 0.270 in the 20_800 condition to 0.219 in the 25_800 condition, despite both operating at a lean solvent flow rate of 800 kg/h. This reduction in lean loading increases the relative mass fraction of MEA and water in the circulating solvent, effectively increasing the mass of "pure solvent" that must be heated. In addition, higher CO_2 concentrations result in greater captured CO_2 mass (54.63 kg/h for 20_800 compared with 63.02 kg/h for 25_800), which also contributes to the increased sensible heat requirement.

Many studies have investigated enhanced heat integration through advanced structural configurations aimed at minimising the sensible heat required for solvent regeneration [36]. Process modifications such as absorber intercooling [38–40], rich solvent splits [41,42], solvent split flows [38,43–45], lean vapour compression [41,42,46,47], among others, have been shown to improve energy efficiency by reducing sensible heat demands. A more detailed discussion of various capture plant configurations is provided in Chapter 2.

The relative uncertainty of the total sensible heat, $Q_{\mathrm{sens,solvent}}$, ranged from ±0.89% to ±4.64%, with an average of ±2.24%. This indicates that the sensible heat calculation is generally reliable and reasonably precise across the different capture conditions. The largest contributor to this uncertainty was consistently the rich solvent component, $Q_{\mathrm{sens,rich}}$. This is attributed to the uncertainty in the rich solvent mass flow rate which, as discussed previously, is a more significant source of uncertainty than the temperature measurements. Therefore, achieving a steadier rich solvent mass flow would be the most effective way to reduce the uncertainty in the overall sensible heat calculation.

4.10.3 Solvent Vaporisation

The vaporisation energy is the energy required to generate steam in the reboiler. The steam serves a critical physical function: as it rises through the stripper column, it reduces the partial pressure of CO_2 in the vapour phase. According to the principles of vapour-liquid equilibrium (VLE), this lower partial pressure creates a larger driving force for CO_2 to desorb from the liquid solvent, allowing for regeneration to occur at a given temperature [22,48]. Fundamentally, the steam "strips" the CO_2 out of the solvent.

The vaporisation energy is calculated by multiplying the mass of steam generated in the reboiler by the enthalpy of vaporisation at the reboiler core temperature:

$$Q_{\text{vap}} = \dot{m}_{\text{steam}} \cdot h_{\text{fg}} \tag{4.61}$$

Figure 4.16 compares vaporisation energy against the L/G ratio and solvent/CO_2 ratio for each capture condition.

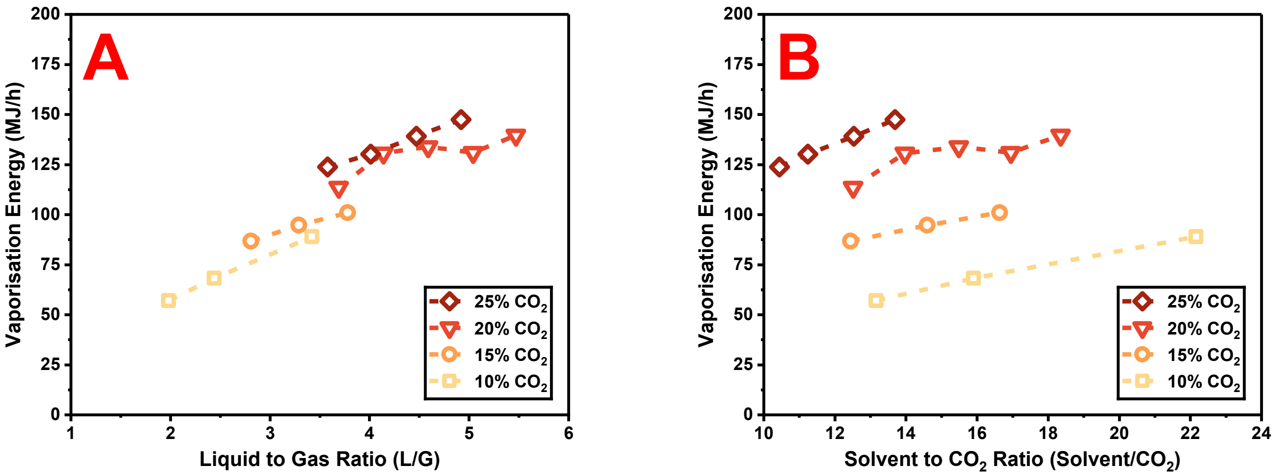

Figure 4.16: Vaporisation energy against: (A) liquid to gas ratio and (B) solvent/CO_2 ratio, solvent flow rates treating 150 Nm^3/h flue gas containing different CO_2 concentrations, targeting 90% capture efficiency.

In general, Figure 4.16 shows that vaporisation energy increases with solvent flow rate, since a higher flow results in more water in the solvent needing to be vaporised. Additionally, vaporisation energy increases with the CO_2 concentration of the flue gas, most apparent at similar L/G and solvent/CO_2 ratios. This is due to a deeper solvent regeneration requirement to achieve the lower lead loadings necessary for achieving the target capture efficiency at higher flue gas CO_2 concentrations, which demands more energy, and is predominantly supplied by an increased supply of stripping steam. Table 4.11 shows how the mass of steam increases with flue gas CO_2 concentration for the same solvent flow rate.

The observed trends are remarkably similar to those of the solvent sensible heats in Figure 4.15, and in fact the actual values are largely similar for each component. Once again, conditions 20_900 and 20_1000 display slightly elevated vaporisation energies compared to the expected trend. This is due to a slightly higher production of steam for these conditions, as per the system energy balance in Table 4.11, leading to larger reported vaporisation energies.

Reducing the required vaporisation energy is primarily achieved through process optimisation, as stripping steam must be generated to drive the desorption reaction and regenerate the solvent. Operating as close as possible to the inflection point minimises the amount of steam leaving the top of the column [11]. Although solvent regeneration inherently requires vaporisation of water, and therefore a minimum steam duty is unavoidable, optimal operation promotes complete condensation of this steam along the total height of the stripper column, thereby reducing the overall vaporisation energy requirement.

The relative uncertainty of the vaporisation energy, Q_{vap}, is significant, ranging from ±0.67% to ±11.96%, with an average of ±4.62%. This uncertainty is governed entirely by the uncertainty in the calculated mass of generated steam, as the enthalpy of vaporisation is treated as an exact value. The higher variability in the steam mass uncertainty stems from it being a derived value from the main energy balance, which accumulates the uncertainties from the larger process streams. Consequently, the only way to reduce the uncertainty in the vaporisation energy is to improve the stability of the solvent flows and temperature measurements that underpin the entire energy balance.

4.10.4 Heat of Desorption

The absorption process is an exothermic chemical reaction, where CO_2 reacts with MEA to form carbamates, bicarbonates and carbonates, releasing energy in the form of heat. The quantification of this energy release is referred to as the heat of absorption, typically expressed per unit of absorbed CO_2 [30]. This process is reversible with the application of heat, meaning that the liberation of CO_2 and the regeneration of solvent constitute an endothermic reaction associated with a corresponding heat of desorption. Studies investigating this heat of reaction, also referred to as the reaction enthalpy, commonly assume that the heat of desorption is equal in magnitude to the heat of absorption [30,31,34].

The reaction enthalpy can vary significantly depending on process conditions. Numerous studies have been conducted to quantify the reaction enthalpy under various conditions, typically determined empirically or experimentally, covering variables such as solvent type, solvent loading, temperature, pressure, concentration and the presence of solvent additives [35,49–57].

Quantification of the reaction enthalpy of MEA is useful for understanding solvent performance, however, reducing it is less straightforward. Researchers have explored alternative solvents as a viable solution. Investigations into alternative solvents, such as piperazine [53], hindered amines [54], tertiary amines [56], solvent blends [58,59], and more, have shown that these solvents may offer significantly lower heats of reaction compared to MEA. However, these alternative solvents present their own challenges, which must be addressed through further research before they can see widespread adoption.

Several companies have also developed propriety solvents for carbon capture that show promise in testing campaigns. Solvents such as KS-1™ by Mitsubishi Heavy Industries (MHI) [60] and APBS-CDRMax® by Carbon Clean Solutions Limited (CCSL) [61] have been used in comparative studies and have demonstrated improved energy efficiency, solvent capacity, and reduced corrosiveness against MEA.

Many modern studies reference the works of Kim et al. as the standard comparison for the heat of absorption of CO_2 with MEA, owing to the rigorous experimental approach and methodology applied in their research.

Accordingly, this work refers to the newer experimental data published by Kim et al. in 2014 [49], with specific reference to the data provided in their Appendix A1 for a 30 wt.% MEA solution.

Kim et al. identified several notable trends that are particularly relevant. Firstly, their data shows that the heat of absorption increases with temperature for a for a given CO_2 loading, enabling interpolation of values at intermediate temperatures not explicitly tested. Secondly, for CO_2 loadings below 0.25 mol·CO_2/mol·MEA, the heat of absorption increases with MEA concentration. However, above this point, the values for 30 wt.% and 70 wt.% MEA converge, supporting direct comparison to this study's use of 35 wt.% MEA. Thirdly, the heat of absorption decreases sharply for CO_2 loadings above 0.5 mol·CO_2/mol·MEA, because above this stoichiometric maximum additional CO_2 is absorbed physically rather than chemically, reducing the energy required for desorption.

According to Kim et al., at 120 °C with 30 wt.% MEA, a CO_2 loading of 0.25 corresponds to a heat of absorption of 100.77 kJ/mol·CO_2, dropping to approximately 88 kJ/mol·CO_2 at 80°C. For higher loadings of 0.5 and 0.55, the heat of absorption is lower, at 73.71 and 58.94 kJ/mol·CO_2, respectively, for 80 °C. While no direct data is provided at 120 °C for these higher loadings, it can be inferred that the values would be slightly higher than those at 80 °C.

In this study, most capture conditions have lean loadings greater than 0.25 and rich loadings between 0.5 and 0.55. Accordingly, a reasonable portion of the CO_2 regeneration begins at loadings above the stoichiometric threshold, where the heat of absorption is lower. As the solvent regenerates towards lower lean loadings, the heat of absorption increases. This means that the average heat of absorption depends on the initial rich loading and extent of regeneration. Based on the trends from Kim et al., average heats of absorption in the range of 80 and 90 kJ/mol·CO_2 are expected for the capture conditions tested in this study.

The average heat of absorption was estimated using the 80 °C absorption data from Kim et al. for each capture condition, based on the corresponding lean and rich solvent loading and the total amount of CO_2 absorbed. A segmental integration approach was applied using discretised loading intervals across the solvent loading range. For each segment, the energy demand was calculated using the tabulated absorption values or interpolated values based on the rich solvent loading. The total absorption energy was then divided by the total moles of CO_2 captured to obtain the average heat of absorption.

The calculated average heats of absorption ranged from 80.96 to 84.68 kJ/mol·CO_2, with an overall average of 83.29 kJ/mol·CO_2 across all capture conditions. These results align closely with the trends and magnitudes reported by Kim et al., providing confidence in the method and the values used for this work.

The desorption energy can be calculated by the amount of CO_2 captured multiplied by the average heat of absorption:

$$Q_{\mathrm{react}} = \frac{\dot{m}_{\mathrm{CO_2,captured}}}{MW_{\mathrm{CO_2}}} \cdot H_{\mathrm{abs}} \quad \textbf{(4.62)}$$

Where:

H_{abs} = average specific enthalpy of absorption/desorption (kJ/mol·CO₂)

Figure 4.17 compares reaction energy against the L/G ratio and solvent/CO₂ ratio for each capture condition.

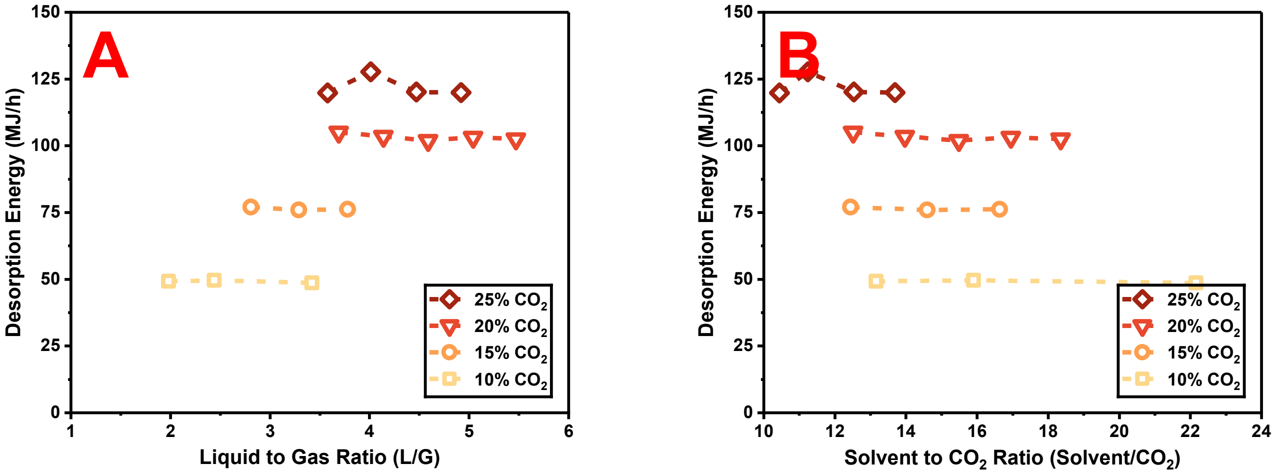

Figure 4.17: Desorption energy against: (A) liquid to gas ratio and (B) solvent/CO₂ ratio, solvent flow rates treating 150 Nm³/h flue gas containing different CO₂ concentrations, targeting 90% capture efficiency.

The desorption energies presented in Figure 4.17 are used to assess the validity of the methodology applied in their calculation. For a given CO₂ concentration, the reaction energy should remain broadly consistent across different solvent flow rates, as the same quantity of CO₂ is being liberated from the solvent. Figure 4.17 confirms this is true across the 10, 15 and 20 mol.% CO₂ concentrations, as expected. For the 25 mol.% CO₂ conditions, it must be considered that only the 25_900 capture condition achieved 90% capture efficiency. The other solvent flow rates all reported slightly lower capture efficiency ranging from approximately 84 to 87%, leading to lower desorption energies for these conditions.

The reaction energy increases with CO₂ concentration, resulting from increased amount of CO₂ needing liberation from the solvent. It is evident that the difference in average desorption energies between 15 and 10 mol.% CO₂ conditions is the same as the difference in average desorption energies between 20 and 15 mol.% CO₂ conditions, showing that the step increase in CO₂ concentration directly correlates to the increase in desorption energy. In fact, the difference between the average desorption energy for the 20 mol.% CO₂ conditions and the desorption energy of the 25_900 condition closely approximates the difference between the other step changes, further reinforcing this conclusion.

A comparison of the desorption energy values directly calculated here, Q_{react}, to the indirect desorption energy values from the earlier energy balance, Q_{de}, found they are generally similar across the different capture conditions, as shown in Figure 4.18.

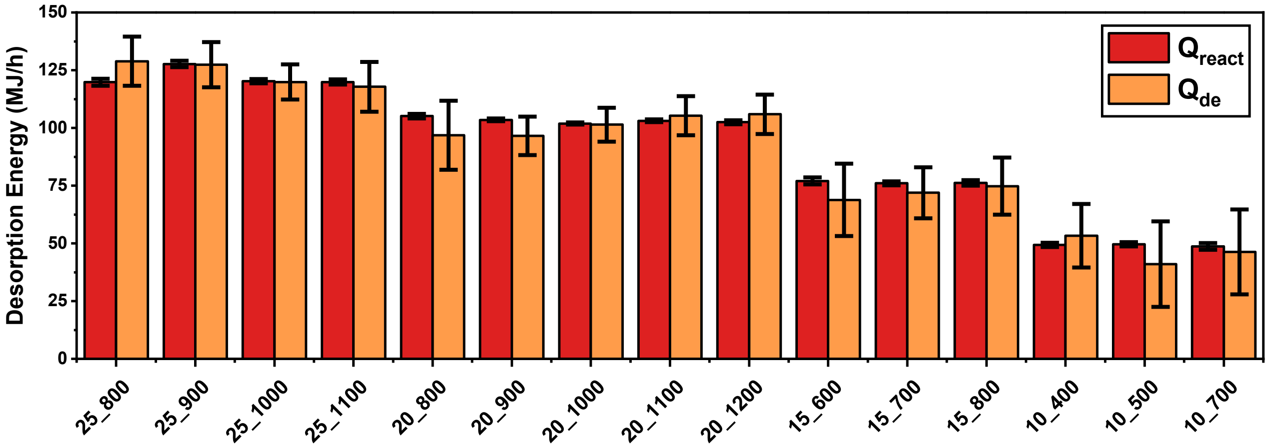

Figure 4.18: Comparison of desorption energy values given by Q_{react} and Q_{de} for different capture conditions. Error bars represent the propagated combined standard uncertainty (±1σ) for each value.

The relative uncertainty in the Q_{react} values ranged from ±0.51% to ±1.53%, with an average of 1.03%, giving a high level of confidence in the Q_{react} desorption energy values. This is due to the uncertainty being governed entirely by the uncertainty in the calculated mass of captured CO_2, which is a precise and reliable measurement.

Meanwhile, the relative uncertainty of the Q_{de} values ranged from ±7.33% to ±18.50%, which accounts for the deviation between the two values for a given capture condition. This suggests that the indirect method of calculating the desorption energy is typically acceptable, but care must be taken when drawing conclusions from these values, especially for capture conditions that have a higher level of uncertainty in their measurements.

4.10.5 Heat Recovery

The heat recovery of the system can be split into its different contributions. For this work, this is considered as three components. The largest component accounts for the energy recovery through condensing steam in the column. As steam rises through the column, it gradually condenses, releasing latent heat that heats the downflowing rich solvent. The second and third components are minor contributions in the form of sensible heat. As the steam and liberated CO_2 rise up the column, they undergo a small temperature drop, transferring sensible heat to the solvent. The heat recovery in this work is therefore expressed as:

$$Q_{\mathrm{recovery}} = Q_{\mathrm{cond}} + Q_{\mathrm{sens,CO_2}} + Q_{\mathrm{sens,steam}} \tag{4.63}$$

Where:

Q_{cond} = energy released from steam condensation within the column (kJ)

$Q_{\mathrm{sens,CO_2}}$ = sensible heat transferred from the cooling of CO_2 within the column (kJ)

$Q_{\mathrm{sens,steam}}$ = sensible heat transferred from the cooling of steam within the column (kJ)

As steam rises in the column and cools, it begins to condense and lose its latent heat when it reaches the saturation temperature, given as 104.78 °C at 1.2 bara. The energy associated with the portion of steam condensing within the column is determined by multiplying the mass of condensing steam by the enthalpy of condensation at the corresponding saturation temperature:

$$Q_{\mathrm{cond}} = \dot{m}_{\mathrm{steam,cond}} \cdot h_{\mathrm{fg}} \tag{4.64}$$

Figure 4.19 compares condensation energy against the L/G ratio and solvent/CO_2 ratio for each capture condition.

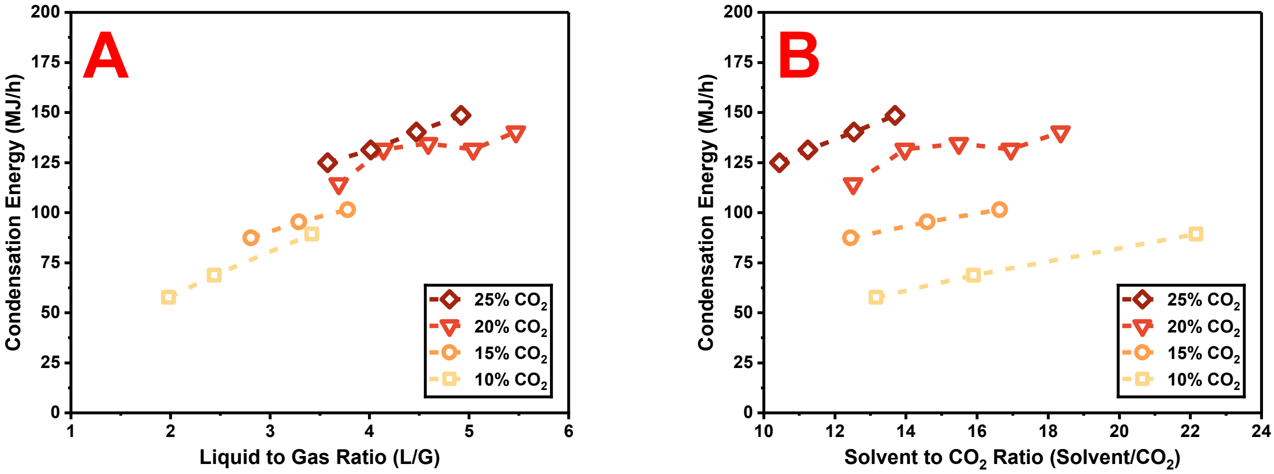

Figure 4.19: Condensation energy against: (A) liquid to gas ratio and (B) solvent/CO_2 ratio, solvent flow rates treating 150 Nm^3/h flue gas containing different CO_2 concentrations, targeting 90% capture efficiency.

The trends observed in condensation energy closely align to those of vaporisation energy in Figure 4.16. This similarity is expected, because all of the steam is assumed to transfer its latent heat to the descending rich solvent in the column. This means that Q_{vap} and Q_{cond} functionally cancel each other out, reflecting the internal energy transfers occurring through phase change within the column.

The sensible heat contribution from the cooling of liberated CO_2 within the column, $Q_{\mathrm{sens,CO_2}}$, is calculated using Equation (4.37), considering the temperature difference between the reboiler core and the top of the column. The specific heat capacity is evaluated at the average of these two temperatures. Figure 4.20 compares the sensible heat contributions of cooling CO_2 against the L/G ratio and solvent/CO_2 ratio for each capture condition.

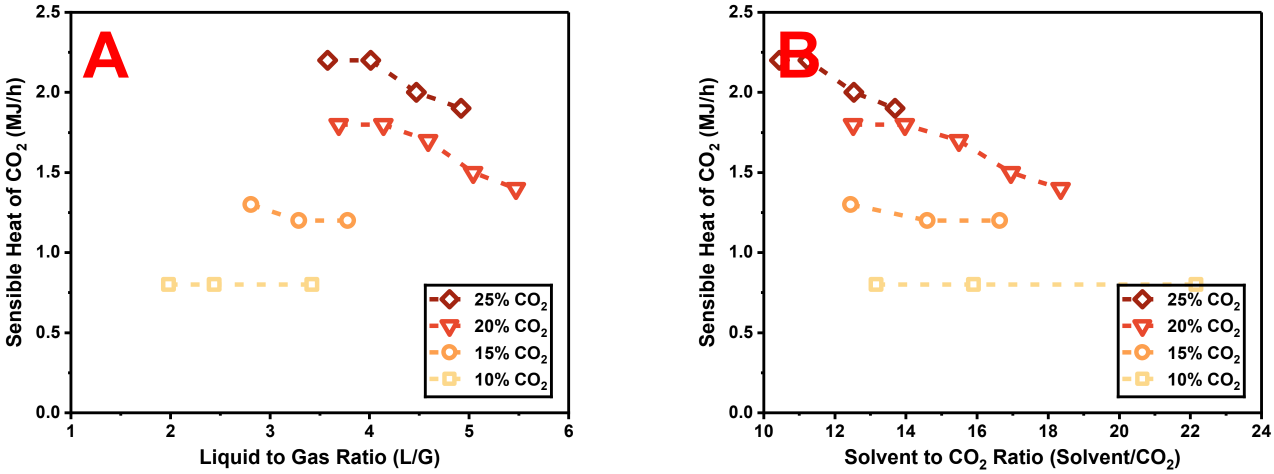

Figure 4.20: Sensible heat of CO_2 against: (A) liquid to gas ratio and (B) solvent/CO_2 ratio, solvent flow rates treating 150 Nm^3/h flue gas containing different CO_2 concentrations, targeting 90% capture efficiency.

The sensible heat from the cooling of steam, $Q_{\text{sens,steam}}$, is determined as the sum of two components:

$$Q_{\text{sens,steam}} = Q_{\text{top,H}_2\text{O}} + Q_{\text{column,steam}} \tag{4.65}$$

Where:

$Q_{\text{top,H}_2\text{O}}$ = sensible heat transferred from the water that exits the top of the stripper (kJ/h)

$Q_{\text{column,steam}}$ = sensible heat transferred from the steam cooling to the saturation temperature (kJ/h)

For Equation (4.65), each term is evaluated using Equation (4.37). The temperature change for $Q_{\text{top,H}_2\text{O}}$ corresponds to the difference between the saturation temperature and the top of the column, while for $Q_{\text{column,steam}}$, the temperature change corresponds to the difference between the reboiler core temperature and the saturation temperature. The specific heat capacities for each term are evaluated at the respective average temperatures.

Figure 4.21 compares the sensible heat contribution of cooling steam against the L/G ratio and solvent/CO_2 ratio for each capture condition.

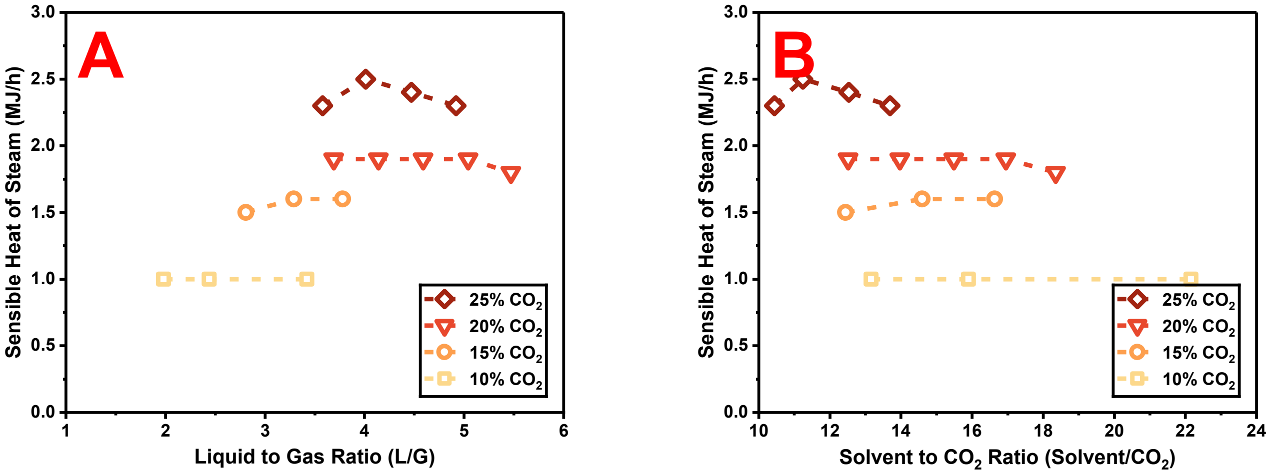

Figure 4.21: Sensible heat of steam against: (A) liquid to gas ratio and (B) solvent/CO_2 ratio, solvent flow rates treating 150 Nm^3/h flue gas containing different CO_2 concentrations, targeting 90% capture efficiency.

It can be seen that the sensible heat terms remain largely constant at a given CO_2 concentration, owing to similar levels of CO_2 capture, where variations primarily arise from minor differences in stripper top and reboiler temperatures. The sensible heats increase with CO_2 concentration due to higher mass flows of CO_2 and steam for these conditions. However, the heat recovery from the sensible heat of rising CO_2 and steam is insignificant compared to the heat recovery from condensing steam, with the sum of the two sensible heat terms always amounting to <4% of the condensing steam energy. That is not to say that they are negligible, however, as they play a small, but essential part in the overall regeneration energy calculation, crucial to determining the heat loss of the system.

The relative uncertainty of the total internal heat recovery, Q_{recovery}, ranged from ±0.66% to ±11.58%, with an average of ±4.48%. This uncertainty is overwhelmingly dominated by the contribution from the condensation energy term, Q_{cond}, which was calculated using the same principle as the vaporisation energy. Since the enthalpy of condensation is treated as an exact value, the uncertainty is governed entirely by the uncertainty in the mass of generated steam, as has been discussed previously. The contributions from the sensible heat of the cooling vapours were, by comparison, negligible and had only a slight impact on the final uncertainty.

4.10.6 Net Regeneration Energy, System Heat Loss, and Energy Distribution

With all components of the net regeneration energy, $Q_{\text{regen,net}}$, determined, they can be summed and compared against the calculated reboiler duty, Q_{reboiler}. If the net regeneration energy is less than the reboiler duty for a given capture condition, then the calculations are deemed reasonable according to the outlined methodology. The results of this comparison for each capture condition are presented in Figure 4.22.

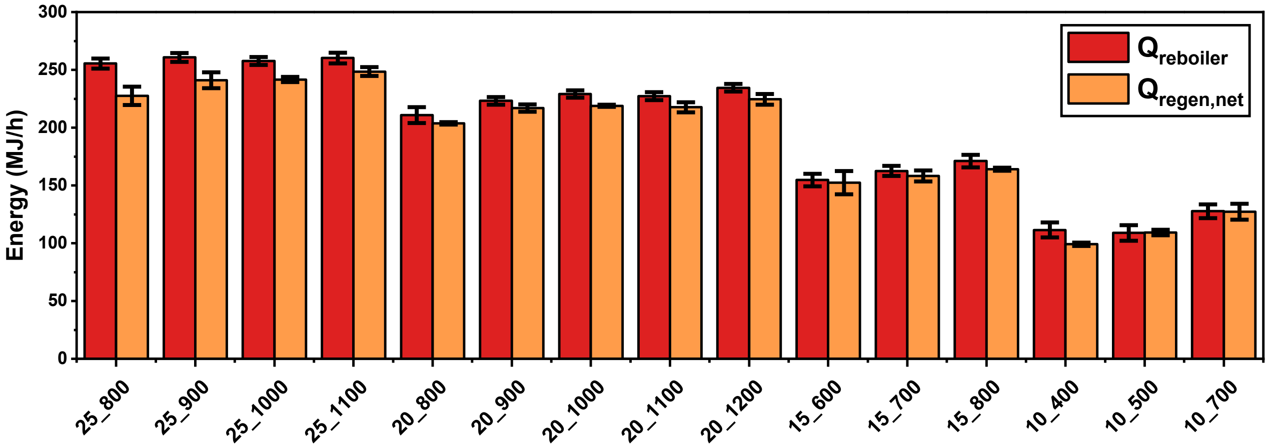

Figure 4.22: Comparison of energy values given by Q_{reboiler} and $Q_{\text{regen,net}}$ for different capture conditions. Error bars represent the propagated combined standard uncertainty (±1σ) for each value.

As shown in Figure 4.22, the calculated net regeneration energy closely tracks the reboiler duty and is slightly lower in almost all cases, with the difference representing the generalised heat loss of the system. The validity of the presented values is reinforced by the uncertainty analysis.

The relative uncertainty of the net regeneration energy, $Q_{\text{regen,net}}$, ranged from ±0.92% to ±9.94%, with an average of ±4.11%. In contrast, the relative uncertainty of the reboiler duty, Q_{reboiler}, ranged from ±3.23% to ±6.87%, with an average of ±4.74%. Both terms have a similar average level of uncertainty, giving confidence in the calculated energy values and the methodologies used to determine them. This validates that all major energy requirements and internal heat recovery pathways have been successfully accounted for in the analysis.

However, a key finding of the uncertainty analysis is the consistency of the two terms. The uncertainty of the net regeneration has a wider range than the reboiler duty, which is more stable. This demonstrates that while the overall methodology is sound, the calculated net regeneration energy is highly sensitive to experimental variations of a given operating condition, whereas the determination of the reboiler duty is a more reliable calculation. Condition 10_500 is the sole exception where the calculated regeneration energy slightly exceeds that of the reboiler duty, which falls within the margin of experimental uncertainty.

With the energies of the reboiler duty and the net regeneration energy validated, the generalised heat loss of the system can be assessed, and is found indirectly by rearranging Equation (4.58) as follows:

$$Q_{\text{losses}} = Q_{\text{reboiler}} - Q_{\text{regen,net}} \tag{4.66}$$

The calculated generalised heat loss ranged from -0.3 to 27.9 MJ/h, with an average of 9.7 MJ/h. Expressed as a percentage of the corresponding reboiler duty, these losses ranged from -0.31% to 11.11%, with an average of 4.52%. As a negative system heat loss is not physically meaningful, an uncertainty analysis was performed to assess the validity of these results. The relative uncertainty associated with Q_{losses} was substantial, ranging from ±60.7% to ±2383.08%, with an average of ±463.84%. This indicates that the calculated heat loss is small compared with the propagated experimental uncertainty, which in many cases significantly exceeds the magnitude of the heat loss itself.

For example, condition 10_500 yielded an apparent negative heat loss of -333 kJ/h with an absolute uncertainty of 7937 kJ/h, corresponding to a relative uncertainty of ±2383.08%. Here the heat loss is indistinguishable from a significant positive value or from zero. In contrast, condition 25_1000 produced a calculated heat loss of 16127 kJ/h with an absolute uncertainty of 10293 kJ/h, giving a relative uncertainty of 63.82%. This comparison demonstrates that the relative uncertainty becomes disproportionately large when the apparent heat loss approaches zero.

Two principal conclusions can therefore be drawn. Firstly, the overall energy balance methodology is considered valid, as the small magnitude of the calculated heat loss suggests that the dominant energy contributions have been appropriately accounted for. Second, although the heat loss is consistently minor, its exact value cannot be determined with statistical confidence due to the propagation of uncertainties from the larger measured energy terms. Collectively, these results indicate that system heat losses are small but cannot be quantified precisely within the experimental uncertainty of the present measurements.

With the values of the individual energy components now validated, an analysis of the conventional regeneration energy, Q_{regen}, was performed to determine the relative contribution of its three main components: sensible heat, Q_{sens}, vaporisation energy, Q_{vap}, and the heat of desorption, Q_{react}. The energy distribution of the components, expressed as percentages of $Q_{\text{regen,}}$, is presented in Figure 4.23 for each capture condition.

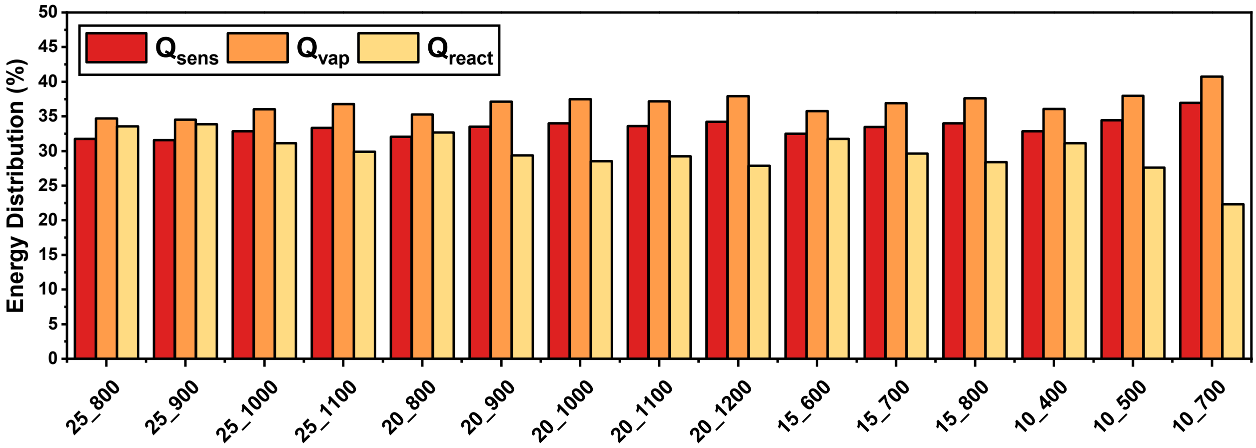

Figure 4.23: Energy distribution of Q$_{sens}$, Q$_{vap}$, and Q$_{react}$ as percentages of the conventional regeneration energy for different capture conditions.

Figure 4.23 shows that the energy distribution is broadly similar across capture conditions, with minor differences in energy demand between respective components. The analysis shows that the vaporisation energy is the dominant component, consistently representing the largest portion of the energy demand in all conditions. Typically, the sensible heat is the second largest contributor, while the heat of desorption constitutes the smallest share.

As the solvent flow rate increases for a given CO$_2$ concentration, the distribution between the terms becomes more pronounced. Both Q_{sens} and Q_{vap} increase substantially, as more energy is required to both heat and vaporise the increasing mass flow of solvent, as shown previously in Figure 4.15 and Figure 4.16. In contrast, Q_{react}, remains relatively stable for a given CO$_2$ concentration, as shown in Figure 4.17.

This breakdown underscores the importance of system optimisation to improve the energy efficiency of the system by minimising wasted heat. An effective optimisation strategy must target both the sensible heat and the vaporisation energy. The sensible heat can be reduced using enhanced heat integration, such as lowering the hot rich and hot lean temperature approach of the cross-heat exchanger, or with advanced structural configurations, in order to increase the incoming temperature of the rich solvent and reduce its share of the energy distribution. The vaporisation energy is best optimised by operating as close to the inflection point as possible, which will reduce its share of the energy distribution. A combined approach targeting both improved heat recovery and optimising operating conditions is critical to reducing the overall regeneration energy consumption.

Table 4.13: Regeneration energy components and other key values for different capture conditions.

Parameter	Units	Capture Condition														
		25_800	25_900	25_1000	25_1100	20_800	20_900	20_1000	20_1100	20_1200	15_600	15_700	15_800	10_400	10_500	10_700
Q_{sens}	MJ/h	113.3	119.1	126.9	133.7	103.1	118.0	121.3	118.5	125.9	78.8	85.9	91.2	52.0	61.9	80.7
$Q_{sens,rich}$	MJ/h	99.0	102.8	108.9	114.3	88.6	101.4	103.8	98.7	104.3	67.8	70.5	74.7	44.2	52.2	66.5
$Q_{sens,column}$	MJ/h	4.4	5.6	5.2	5.2	4.5	4.0	4.5	5.4	5.3	3.3	3.8	4.1	2.2	2.2	2.3
$Q_{sens,condenser}$	MJ/h	0.8	0.7	0.6	0.4	0.4	0.3	0.2	0.1	0.0	0.3	0.3	0.1	0.2	0.1	-0.1
$Q_{sens,bottom}$	MJ/h	8.9	9.8	12.0	13.6	9.5	12.2	12.6	14.1	16.2	7.2	11.2	12.1	5.2	7.1	11.9
Q_{vap}	MJ/h	123.8	130.2	139.2	147.5	113.5	130.7	133.8	131.0	139.6	86.7	94.7	100.9	57.1	68.2	89.0
Q_{react}	MJ/h	119.8	127.7	120.2	119.9	105.1	103.5	101.9	103.1	102.5	77.0	76.0	76.2	49.3	49.6	48.7
H_{abs}	kJ/mol·CO_2	83.68	82.49	82.93	83.85	84.67	84.04	82.61	84.68	84.13	83.15	83.27	82.46	83.52	82.88	80.96
$Q_{recovery}$	MJ/h	129.3	136.0	144.6	152.6	118.0	135.2	138.1	135.0	143.4	90.1	98.3	104.2	59.3	70.5	91.0
Q_{cond}	MJ/h	124.9	131.3	140.2	148.5	114.3	131.6	134.5	131.7	140.2	87.4	95.4	101.5	57.6	68.7	89.3
$Q_{CO2,cool}$	MJ/h	2.2	2.2	2.0	1.9	1.8	1.8	1.7	1.5	1.4	1.3	1.2	1.2	0.8	0.8	0.8
$Q_{sens,steam}$	MJ/h	2.3	2.5	2.4	2.3	1.9	1.9	1.9	1.9	1.8	1.5	1.6	1.6	1.0	1.0	1.0
$Q_{reboiler}$	MJ/h	255.5	260.7	257.8	260.3	210.7	223.2	229.1	227.3	234.5	154.7	162.5	171.1	111.5	108.9	127.7
$Q_{regen,net}$	MJ/h	227.6	241.0	241.6	248.4	203.7	217.0	218.9	217.6	224.5	152.4	158.3	163.9	99.1	109.2	127.2
Q_{losses}	MJ/h	27.9	19.7	16.1	11.8	7.0	6.2	10.2	9.7	10.0	2.3	4.2	7.2	12.4	-0.3	0.5
Q_{losses}	% of $Q_{reboiler}$	10.92	7.56	6.26	4.55	3.33	2.77	4.45	4.26	4.28	1.49	2.59	4.21	11.11	-0.31	0.39

Table 4.14: Relative uncertainties of the regeneration energy components for different capture conditions.

Parameter	**Units**	**Capture Condition**														
		25_800	**25_900**	**25_1000**	**25_1100**	**20_800**	**20_900**	**20_1000**	**20_1100**	**20_1200**	**15_600**	**15_700**	**15_800**	**10_400**	**10_500**	**10_700**
Q_{sens}	±%	4.63	3.42	1.27	2.70	0.89	1.69	1.21	2.10	2.03	4.26	1.84	1.25	1.07	1.61	3.69
Q_{vap}	±%	9.77	8.56	2.56	4.15	0.93	3.54	0.67	5.01	4.99	11.96	5.46	1.15	1.59	2.50	6.43
Q_{react}	±%	1.49	1.39	0.93	1.15	0.99	0.65	0.51	0.60	0.86	1.53	0.90	1.14	0.95	0.98	1.45
$Q_{recovery}$	±%	9.43	8.26	2.48	4.04	0.90	3.45	0.66	4.89	4.87	11.58	5.30	1.12	1.55	2.44	6.31
$Q_{regen,net}$	±%	7.93	6.82	2.24	3.83	1.00	3.18	0.92	4.44	4.56	9.94	4.76	1.33	1.50	2.44	6.81
Q_{losses}	±%	76.36	97.92	63.82	129.69	208.41	164.59	75.33	128.12	127.46	751.61	247.42	131.43	60.17	2383.08	2312.12

4.10.7 Regeneration Energy Discussion

Regeneration energies and their individual components are highly specific to the capture condition being studied. Each energy component, whether sensible heat, vaporisation energy, or desorption energy, is influenced by factors including pilot plant configuration, operating conditions, and control strategies. As a result, direct comparison to values in the open literature is challenging. Instead, this discussion focuses on comparing methodologies used across different studies to assess the reasonableness of the approach adopted here.

In the comprehensive study by Notz et al. [22] an energy balance was conducted around the system for each capture condition, and regeneration energy terms were determined directly, similar in principle to this work, but with notable methodological differences.

For instance, Notz et al. reported the sensible heat in two components: one for heating the incoming rich solvent and another for the returning condensate. This work instead summed up all solvent sensible heat components into a single value. Their vaporisation energy was simplified by quantifying only the energy of the steam exiting the top of the stripper, eliminating the need to calculate both the amount of vapour generated and the associated condensation energy. Consequently, their vaporisation energy values differ significantly from those in this study, as this work considers the vaporisation energy of the total mass of generated steam in the reboiler.

Furthermore, Notz et al. assumed that the heat of absorption is independent of CO_2 loading up to 0.5 $mol \cdot CO_2/mol \cdot MEA$, a simplification compared to the more recent work of Kim et al. [49]. Their overall methodology is described in greater detail in an earlier publication [62]. Additionally, as previously mentioned, their study focused on operating conditions that fall outside the range explored in this work, with capture efficiencies well below the 90% target applied here. This makes direct quantitative comparison of regeneration energies challenging due to differing foundational assumptions and capture conditions.

Notz et al. concluded that the heat of reaction and vaporisation energy are the main contributors to the regeneration energy, followed by the sensible heat. In contrast, this study finds that the different contributors are similar in size, but with a consistent order, highest to lowest, of vaporisation energy, followed by sensible heat, with the heat of reaction contributing the least, an outcome largely driven by methodological and operational differences. For example, Notz et al. reported rich solvent temperatures of approximately 110 °C entering the stripper, compared to 76 °C in this study, reducing their sensible heat requirements significantly. Differences in how and where vaporisation energy is quantified (e.g., reboiler vs stripper top) also contribute to these contrasts.

Tatarczuk et al. conducted a recent study focused on heat integration strategies to improve stripper energy efficiency [30]. Their approach to calculating regeneration energy components was also direct, and their treatment of the sensible heat aligned closely with the methodology used in this study, accounting for all relevant streams via mass and energy balances.

Their findings show that sensible heat increases with solvent flow rate, which is consistent with this study's results. However, their vaporisation energy calculation followed the simplification used by Notz et al., considering only the vapour exiting the top of the stripper and omitting the condensation energy term. They observed that vaporisation energy decreased with increasing solvent flow rate, attributing this to a declining stripper top temperature and corresponding reduction in water vapour content.

This trend is not reflected in this study. Assuming the vapour exiting the stripper is saturated with water, the amount of water vapour remains relatively constant across different solvent flow rates. This discrepancy likely arises from a more consistent stripper top temperature observed in this study, in addition to most conditions operating within the stripper baseline region, meaning that even with similar calculation methods, different trends would be obtained due to differences in operating behaviour.

Tatarczuk et al. assumed a fixed heat of absorption value of 84.68 kJ/mol·CO_2 (1924 kJ/kg·CO_2) to calculate desorption energy, based on the work by Brúder et al. [63], which is just above the average value of 83.29 kJ/mol·CO_2 used in this work. They reported that desorption energy was independent of solvent flow rate, but this assumption is an oversimplification. As discussed earlier, the heat of desorption depends on solvent loading, which in turn varies with solvent flow rate for a given capture efficiency. Thus, the desorption energy would be expected to change under different flow conditions, and their fixed value introduces inaccuracies across varying capture conditions.

Li et al used pilot plant data from the Tarong power station in Queensland, Australia, to develop a rate-based Aspen Plus model for regeneration energy reduction studies [64]. They picked a representative capture condition from the pilot plant study to determine a baseline energy assessment that included sensible heat, desorption, and vaporisation energy.

The sensible heat calculation was performed similarly to this study, using flow rates, temperatures, and specific heat capacities to determine the required energy. The desorption energy was calculated using a method from Que and Chen [65] while vaporisation energy followed the same simplification used by Notz et al. [22] and Tatarczuk et al. [30], focusing on vapour exiting the stripper.

Interestingly, Li et al. found that desorption energy was the largest contributor to the overall regeneration energy, followed by sensible heat and then vaporisation energy. This contrasts with both Notz et al. and the current study, underscoring that the regeneration energy breakdown is highly context-dependent and specific to each plant and its operating conditions.

Finding studies that provide a complete, transparent, experimentally derived quantitative breakdown of the regeneration energy proved challenging, as many studies primarily focus on the SRD as the primary performance indicator. However, for the limited studies that have provided this type of analysis, they showed consistent principles in regeneration energy analysis despite some methodological differences. The methods employed across studies, particularly the direct calculation approach, are broadly similar and enable insights into each component of the energy requirement. Comparisons highlighted the importance of plant-specific behaviour and the need for methodological transparency in energy analysis.

This work contributes a detailed breakdown of regeneration energy components using a consistent methodology that accounts for the complex interplay of process parameters. The component-level breakdown presented here can guide future optimisation efforts, whether through process control adjustments or structural design modifications, to further reduce the energy penalty associated with solvent regeneration. Additionally, the uncertainty analysis gave crucial insight into which energy components have the most confidence in their calculation, versus those that have more variability due to the propagation of uncertainties in their calculation, which must be considered when averaging process data over a steady state period.

4.10.8 Heat Loss Discussion

Heat losses are an unavoidable consequence of operating any thermal process. Even in advanced process configurations, complete thermal retention within process streams is unattainable, and a portion of energy will inevitably dissipate to the surrounding environment. The extent of these losses is influenced by multiple factors, including but not limited to: plant scale and design, operational performance, insulation quality, and prevailing ambient conditions. Quantifying heat loss provides valuable insight into the thermal performance of the system. If losses fall within expected bounds, they can be considered an acceptable operational burden. However, deviations from typical values may warrant further investigation to identify inefficiencies or areas for process improvement.

Typical heat loss values for chemical absorption plants are not widely reported in the open literature. Furthermore, studies that do report heat losses often employ varying methodologies, either directly or indirectly determining system losses. Indirect methods, such as those used in this work, as well as in studies by Owrang and Svendsen [66], and Babu and Rochelle [67], estimate total system heat loss based on energy balances from process data. In contrast, direct methods, as applied by Notz et al. [22] and Tatarczuk et al. [30], measure heat loss from individual process units and pipework. Although direct methods offer a more rigorous approach that can pinpoint problematic equipment, they are time consuming and require extensive data collected under a variety of operating conditions to fully characterise the system's sensitivity to heat loss. Indirect methods, by contrast, use energy balances from process data to infer generalised heat losses, but they cannot specify where losses occur with certainty. While methodologies vary, the literature consistently reports heat losses representing a large fraction of the total reboiler duty.

The study by Owrang and Svendsen estimated heat losses from a lab-scale capture plant by calculating the difference between the reboiler heat duty and the energy removed through steam condensation in the heat exchangers [66]. Twenty experiments were conducted across different reboiler duties and water flow rates, with distilled water used in place of a chemical solvent. Total heat losses ranged from 15% to 79% of the reboiler duty, although most cases fell within a 15% to 34% range. Their results showed that total heat loss was largely independent of reboiler duty and instead correlated with water flow rate: as flow rate increased, heat losses also increased due to decreased condensate recovery in the heat exchangers. This behaviour is analogous to stripper system operation deeper into the baseline region as the L/G ratio increases, consistent with the observations made across cases in this study.

Similarly, a study by Babu and Rochelle at the National Carbon Capture Centre (NCCC) evaluated heat losses when operating an advanced stripper system with piperazine [67]. They reported an average measured heat loss of 0.38 $MJ/kg{\cdot}CO_2$, equating to approximately 30% of the gross heating rate. This value was subsequently used to inform correction factors within their modelling framework. The stripper dimensions in the NCCC study are comparable to those of the TERC ACP, suggesting that TERC ACP retains heat better than the stripper at the NCCC. This could be due to several factors, including but not limited to: pilot plant insulation, process efficiency, and process optimisation.

The study by Notz et al. initially determined heat losses from the pilot plant using an indirect method similar to the methodology applied in this work [22]. By considering the entire capture system as a black box at steady state, they observed that the total heat removed by the system's heat exchangers did not match the heat supplied by the evaporator. This energy gap was attributed to system heat losses, consistent with the boundary-based energy gap methodology used in this study around the stripper. Beyond the overall balance, Notz et al. also estimated direct heat losses from individual process units and connecting pipework, following methodologies developed in earlier work by the same primary author [62]. In their regeneration energy equation, Notz et al. introduced an explicit heat loss term, treating part of the reboiler duty as heat lost to the environment, similar to Equation (4.59) in this work. They applied a correction by subtracting these direct heat losses from the gross evaporator duty when calculating the SRD and reported total SRD values both with and without correction for heat losses.

The heat losses reported by Notz et al. were upwards of 26% of the corresponding reboiler duty, although significant variability was observed between different cases. In contrast, the values obtained in the present work in Table 4.13 are generally lower, reaching up to 11.11% of the reboiler duty, with an average of 4.52%.

This can primarily be attributed to difference in capture plant scale, considered a key contributing factor to system heat losses. As plant size increases, the surface area-to-volume ratio decreases, typically leading to lower relative heat losses [30]. With the TERC ACP columns approximately three times taller and twice the diameter of those at the University of Kaiserslautern, the surface area-to-volume ratio of the TERC ACP is roughly one-third that of the Kaiserslautern plant, confirming that lower relative heat losses should occur.

However, there are other differences between the two studies that suggest that the relative heat loss of the TERC ACP is still higher than it could be. Differences in operating flow rates could contribute to increased heat loss, as previously discussed with respect to Owrang and Svendsen's findings. The TERC ACP can handle nearly four times the maximum solvent flow rate of the Kaiserslautern plant, which could lead to increased heat losses. Furthermore, external ambient conditions could be considered: the TERC ACP is located outdoors, and the experimental campaign was conducted during winter months, where lower ambient temperatures and poor weather conditions could enhance heat loss. In contrast, the Kaiserslautern plant operated within an indoor environment, providing more thermally stable conditions.

Despite this, the TERC ACP exhibits much lower heat losses relative to the Kaiserslautern plant, suggesting that the surface area-to-volume ratio is a primary driver of differences in system heat loss, and significantly outweighs the impact of other negative influences on heat loss.

In the study by Tatarczuk et al. part of the study involved evaluation of system heat losses. This was done by defining four system boundaries, each encompassing different process units. Heat balances were derived for each boundary, allowing the calculation of heat losses associated with individual units. Reported heat losses ranged from 20% to 27% of the reboiler duty [30]. Tatarczuk et al. further noted that heat losses could reach up to 35% depending on the structural configuration of the plant [58,68], which are much larger than those reported in this study. It is also noted that Tatarczuk et al. incorporated an explicit heat loss term within the regeneration energy equation, following a methodology similar to that of Notz et al. [22] and this study.

In conclusion, system heat losses represent an inherent limitation on the energy efficiency of thermal plants and must be minimised wherever practicable. Heat loss mitigation should be a core consideration in the design of any future capture plant, where standardised insulation protocols and heat recovery designs should be prioritised to minimise reboiler demand and lower operating costs. Where possible, detailed thermal loss audits for process units and pipework under varying conditions should be conducted to establish baseline references for ongoing plant operation and maintenance.

Although the absolute magnitude of heat losses will inevitably be specific to each capture plant, expressing these losses as a percentage of reboiler duty enables meaningful comparison across different systems. The heat loses observed for the TERC ACP in Table 4.13 are generally much lower than typical values reported in the open literature, suggesting that the TERC ACP is a well-insulated and efficient pilot-plant. This study also underscores the importance of heat loss management, where strategies to minimise system heat losses should be paramount in the design stage of any capture plant. Significant thermal efficiency improvements can be made through targeted design optimisation and enhanced system insulation, with further savings possible when operation uses optimised process conditions.

4.11 Conclusions for Chapter 4

This chapter has presented a comprehensive analysis of a pilot-scale experimental campaign investigating post-combustion and process CO_2 capture from elevated CO_2 concentrations, representative of industrial sectors with significant and hard-to-abate process emissions, such as iron and steel. This work has generated novel performance data using 35 wt.% MEA as a benchmark solvent across a wide range of flue gas CO_2 concentrations. This unique dataset fills a critical gap in the literature, where limited attention has previously been given to practical capture performance under such elevated CO_2 conditions using a conventional PB system. As such, it provides a valuable baseline for comparison in future studies targeting clean-up of industrial emissions.

Through detailed evaluation of L/G ratios, lean and rich solvent loadings, and column temperature profiles, the analysis identified trends toward optimal SRD conditions for each CO_2 concentration. Although optimal conditions could not be identified for every CO_2 concentration, the experimental insights confirmed fundamental relationships between operating parameters. These findings offer practical guidance for tuning solvent flow rates in industrial capture plant operating scenarios and establish a foundation for benchmarking alternative solvents or advanced plant configurations.

A detailed breakdown of solvent regeneration energy into its constituent components: sensible heat, vaporisation, desorption, heat recovery, and heat losses allowed for meaningful insights to be gained for each capture condition. This analysis revealed that regeneration energy is highly sensitive to operational parameters, and that its magnitude and distribution are influenced significantly by capture plant structure and the assumptions embedded within energy estimation methods. Steam generation and sensible heat were found to be the dominant contributors to overall energy demand, while the desorption energy offered a lower contribution of energy. Comparison to literature, including studies by Notz et al., Tatarczuk et al., and Li et al., highlighted that although methods and terminology may vary, consistent analytical frameworks are emerging, reinforcing the credibility of this study’s approach.

Furthermore, indirect estimation of system heat losses offered a broader perspective on plant-level energy efficiency. Results showed that the TERC ACP exhibits much lower heat losses comparable to those reported in other pilot-scale facilities, but still with room for improvement. These losses highlight the importance of both process optimisation and system-level integration in driving down the energy penalty associated with CO_2 capture.

In summary, the experimental campaign presented in this chapter not only validates the performance of MEA under elevated CO_2 capture conditions but also provides novel process data and methodological insights that are transferable to the wider research community and to inform the design and operation of potential capture plant deployment at larger scale. These findings support further optimisation efforts through process or structural modification and serve as a crucial input to simulation and modelling efforts.

The process data and insights generated here can now be utilised to develop and calibrate the DCC model to provide the foundation upon which a digital twin representation of the TERC ACP can be constructed. This forms the basis of the next chapter, where the model is refined and validated against these experimental results to enable accurate predictions and scenario analysis for the TERC ACP.

4.12 References for Chapter 4

[1] Rezazadeh F, Gale WF, Akram M, Hughes KJ, Pourkashanian M. Performance evaluation and optimisation of post combustion CO2 capture processes for natural gas applications at pilot scale via a verified rate-based model. International Journal of Greenhouse Gas Control 2016;53:243–53. https://doi.org/10.1016/j.ijggc.2016.08.003.

[2] Akram M, Milkowski K, Gibbins J, Pourkashanian M. Comparative energy and environmental performance of 40 % and 30 % monoethanolamine at PACT pilot plant. International Journal of Greenhouse Gas Control 2020;95:102946. https://doi.org/10.1016/j.ijggc.2019.102946.

[3] Akram M, Ali U, Best T, Blakey S, Finney KN, Pourkashanian M. Performance evaluation of PACT Pilot-plant for CO2 capture from gas turbines with Exhaust Gas Recycle. International Journal of Greenhouse Gas Control 2016;47:137–50. https://doi.org/10.1016/j.ijggc.2016.01.047.

[4] Akram M, Gheit A, Milkowski K, Gale W, Pourkashanian M. Comparison of conventional and process intensified next generation RPB absorbers for decarbonisation of the steel industry. Fuel 2025;388:134484. https://doi.org/10.1016/j.fuel.2025.134484.

[5] The University of Sheffield. Standard Operating Procedure for Amine Capture Plant (ACP) 2023.

[6] The University of Sheffield. TERC Pilot Plant Training Course: Amine Capture Plant 2024.

[7] Akram M, Milkowski K, Gibbins J, Pourkashanian M. Controlling capture plants to avoid CO2 emissions penalties during peak load demand. International Journal of Greenhouse Gas Control 2021;106:103285. https://doi.org/10.1016/j.ijggc.2021.103285.

[8] Bell IH, Wronski J, Quoilin S, Lemort V. Pure and Pseudo-pure Fluid Thermophysical Property Evaluation and the Open-Source Thermophysical Property Library CoolProp. Ind Eng Chem Res 2014;53:2498–508. https://doi.org/10.1021/ie4033999.

[9] Weiland R, Hatcher N, Alvis S. Pinched Performance: Part 1. Digital Refining 2015.

[10] Hatcher N, Alvis S, Weiland R. Gas treating simulation – a holistic perspective part 2: carbon capture. Digital Refining 2013.

[11] Gibbins J. Amine stripper temperature profile a key to optimising net-zero performance in post-combustion carbon capture plants | LinkedIn. LinkedIn 2023. https://www.linkedin.com/pulse/amine-stripper-temperature-profile-key-optimising-net-zero-gibbins/ (accessed January 28, 2024).

[12] Mathias J. How Does FTIR Analysis Work? Innovatech Labs 2022. https://www.innovatechlabs.com/newsroom/672/stuff-works-ftir-analysis/ (accessed May 1, 2025).

[13] Thimsen D, Maxson A, Smith V, Cents T, Falk-Pedersen O, Gorset O, et al. Results from MEA testing at the CO2 Technology Centre Mongstad. Part I: Post-Combustion CO2 capture testing methodology. Energy Procedia 2014;63:5938–58. https://doi.org/10.1016/j.egypro.2014.11.630.

[14] Rishi S. The Guide to the expression of uncertainty in measurement (GUM)—the new approach. A Practical Handbook on Measurement Uncertainty: FAQs and fundamentals for metrologists, IOP Publishing; 2024. https://doi.org/10.1088/978-0-7503-6462-1ch6.

[15] Proline Promass F 500 Coriolis flowmeter. Endress 2026. https://www.us.endress.com/en/field-instruments-overview/flow-measurement-product-overview/coriolis-flowmeter-promass-f500-8f5b (accessed February 5, 2026).

[16] Emerson. Micro Motion^{TM} ELITE^{TM} Coriolis Flow and Density Meters 2024.

[17] Yokogawa. ROTAMASS Total Insight Coriolis Mass Flow and Density Meter Addendum to General Specifications for Prime 1H 2019.

[18] Omega. RTD/Pt100 Selection Guide n.d.

[19] Hatcher N, Alvis S, Weiland R. Gas treating simulation — a holistic perspective part 3: CO2 removal in an LNG plant. Digital Refining 2013.

[20] Aliyu AA, Akram M, Hughes KJ, Ma L, Ingham DB, Pourkashanian M. Investigation into simulating Selective Exhaust Gas Recirculation and varying Pressurized Hot Water temperature on the performance of the Pilot-scale Advanced CO2 Capture Plant with 40 wt(%) MEA. International Journal of Greenhouse Gas Control 2021;107:103287. https://doi.org/10.1016/j.ijggc.2021.103287.

[21] Biermann M, Normann F, Johnsson F, Hoballah R, Onarheim K. Capture of CO2 from Steam Reformer Flue Gases Using Monoethanolamine: Pilot Plant Validation and Process Design for Partial Capture. Ind Eng Chem Res 2022;61:14305–23. https://doi.org/10.1021/acs.iecr.2c02205.

[22] Notz R, Mangalapally HP, Hasse H. Post combustion CO2 capture by reactive absorption: Pilot plant description and results of systematic studies with MEA. International Journal of Greenhouse Gas Control 2012;6:84–112. https://doi.org/10.1016/j.ijggc.2011.11.004.

[23] Mangalapally HP, Hasse H. Pilot plant study of post-combustion carbon dioxide capture by reactive absorption: Methodology, comparison of different structured packings, and comprehensive results for monoethanolamine. Chemical Engineering Research and Design 2011;89:1216–28. https://doi.org/10.1016/j.cherd.2011.01.013.

[24] Krótki A, Więcław-Solny L, Tatarczuk A, Spietz T, Chwoła T, Dobras S. A pilot study comparing MEA and AEEA solvents in carbon capture. International Journal of Greenhouse Gas Control 2023;126:103891. https://doi.org/10.1016/j.ijggc.2023.103891.

[25] Kwak NS, Lee JH, Lee IY, Jang KR, Shim JG. A study of the CO2 capture pilot plant by amine absorption. Energy 2012;47:41–6. https://doi.org/10.1016/j.energy.2012.07.016.

[26] Knudsen JN, Jensen JN, Vilhelmsen P-J, Biede O. Experience with CO2 capture from coal flue gas in pilot-scale: Testing of different amine solvents. Energy Procedia 2009;1:783–90. https://doi.org/10.1016/j.egypro.2009.01.104.

[27] AspenTech. Aspen Plus V11 n.d.

[28] The Engineering Toolbox. Carbon Dioxide - Specific Heat of Gas vs. Temperature 2005. https://www.engineeringtoolbox.com/carbon-dioxide-d_974.html (accessed May 1, 2025).

[29] PubChem. Monoethanolamine n.d. https://pubchem.ncbi.nlm.nih.gov/compound/700 (accessed May 1, 2025).

[30] Tatarczuk A, Tańczyk M, Więcław-Solny L, Zdeb J. Pilot plant results of amine-based carbon capture with heat integrated stripper. Applied Energy 2024;367:123416. https://doi.org/10.1016/j.apenergy.2024.123416.

[31] Nwaoha C, Idem R, Supap T, Saiwan C, Tontiwachwuthikul P, Rongwong W, et al. Heat duty, heat of absorption, sensible heat and heat of vaporization of 2–Amino–2–Methyl–1–Propanol (AMP), Piperazine (PZ) and Monoethanolamine (MEA) tri–solvent blend for carbon dioxide (CO2) capture. Chemical Engineering Science 2017;170:26–35. https://doi.org/10.1016/j.ces.2017.03.025.

[32] Entry EB. Steam Table. Thermopedia, Begel House Inc.; 2011. https://doi.org/10.1615/atoz.s.steam_tables.

[33] Artanto Y, Jansen J, Pearson P, Do T, Cottrell A, Meuleman E, et al. Performance of MEA and amine-blends in the CSIRO PCC pilot plant at Loy Yang Power in Australia. Fuel 2012;101:264–75. https://doi.org/10.1016/j.fuel.2012.02.023.

[34] Oexmann J, Kather A. Minimising the regeneration heat duty of post-combustion CO2 capture by wet chemical absorption: The misguided focus on low heat of absorption solvents. International Journal of Greenhouse Gas Control 2010;4:36–43. https://doi.org/10.1016/j.ijggc.2009.09.010.

[35] Vinjarapu SHB, Regueira T, Neerup R, von Solms N, Fosbøl PL. Heat of absorption of CO2 in 30 wt% MEA with monoethyleneglycol and urea as vapour reduction additives. Energy 2024;293:130609. https://doi.org/10.1016/j.energy.2024.130609.

[36] Sultan H, Quach T-Q, Muhammad HA, Bhatti UH, Lee YD, Hong MG, et al. Advanced post combustion CO2 capture process – A systematic approach to minimize thermal energy requirement. Applied Thermal Engineering 2021;184:116285. https://doi.org/10.1016/j.applthermaleng.2020.116285.

[37] Leites IL, Sama DA, Lior N. The theory and practice of energy saving in the chemical industry: some methods for reducing thermodynamic irreversibility in chemical technology processes. Energy 2003;28:55–97. https://doi.org/10.1016/S0360-5442(02)00107-x.

[38] Le Moullec Y, Neveux T, Azki AA, Chikukwa A, Hoff KA. Process Modifications for Solvent-based Post Combustion CO2 Capture. Energy Procedia 2014;63:1470–7. https://doi.org/10.1016/j.egypro.2014.11.156.

[39] Karimi M, Hillestad M, Svendsen HF. Investigation of intercooling effect in CO2 capture energy consumption. Energy Procedia 2011;4:1601–7. https://doi.org/10.1016/j.egypro.2011.02.030.

[40] Tobiesen FA, Svendsen HF, Mejdell T. Modeling of blast furnace CO2 capture using amine absorbents. Industrial and Engineering Chemistry Research 2007;46:7811–9. https://doi.org/10.1021/ie061556j.

[41] Xue B, Yu Y, Chen J, Luo X, Wang M. A comparative study of MEA and DEA for post-combustion CO2 capture with different process configurations. International Journal of Coal Science and Technology 2017;4:15–24. https://doi.org/10.1007/s40789-016-0149-7.

[42] Le Moullec Y, Kanniche M. Screening of flowsheet modifications for an efficient monoethanolamine (MEA) based post-combustion CO2 capture. International Journal of Greenhouse Gas Control 2011;5:727–40. https://doi.org/10.1016/j.ijggc.2011.03.004.

[43] Chang H, Shih C. Simulation and Optimization for Power Plant Flue Gas CO 2 Absorption-Stripping Systems. Separation Science and Technology 2005;40:877–909. https://doi.org/10.1081/SS-200048014.

[44] Ahn H, Luberti M, Liu Z, Brandani S. Process configuration studies of the amine capture process for coal-fired power plants. International Journal of Greenhouse Gas Control 2013;16:29–40. https://doi.org/10.1016/j.ijggc.2013.03.002.

[45] Shoeld M. Purification and separation of gaseous mixtures. US Patent: US 1971798A, 1934.

[46] Reddy S, Gillmartin J, Francuz V. Integrated Compressor/Stripper Configurations And Methods. US Patent: US 20090205946, 2009.

[47] Woodhouse S, Rushfeldt P. Absorbent Regeneration With Flashed Lean Solution And Heat Integration. US Patent: US 20100062926, 2010.

[48] Mullen D, Braakhuis L, Knuutila HK, Gibbins J, Lucquiaud M. Monoethanolamine Degradation Rates in Post-combustion CO2 Capture Plants with the Capture of 100% of the Added CO2. Ind Eng Chem Res 2024;63:13677–91. https://doi.org/10.1021/acs.iecr.4c01525.

[49] Kim I, Hoff KA, Mejdell T. Heat of Absorption of CO2 with Aqueous Solutions of MEA: New Experimental Data. Energy Procedia 2014;63:1446–55. https://doi.org/10.1016/j.egypro.2014.11.154.

[50] Kim I, Hoff KA, Hessen ET, Haug-Warberg T, Svendsen HF. Enthalpy of absorption of CO2 with alkanolamine solutions predicted from reaction equilibrium constants. Chemical Engineering Science 2009;64:2027–38. https://doi.org/10.1016/j.ces.2008.12.037.

[51] Kim I, Svendsen HF. Heat of Absorption of Carbon Dioxide (CO2) in Monoethanolamine (MEA) and 2-(Aminoethyl)ethanolamine (AEEA) Solutions. Ind Eng Chem Res 2007;46:5803–9. https://doi.org/10.1021/ie0616489.

[52] Jou F-Y, Otto FD, Mather AE. Vapor-Liquid Equilibrium of Carbon Dioxide in Aqueous Mixtures of Monoethanolamine and Methyldiethanolamine. Ind Eng Chem Res 1994;33:2002–5. https://doi.org/10.1021/ie00032a016.

[53] Liu J, Wang S, Svendsen HF, Idrees MU, Kim I, Chen C. Heat of absorption of CO2 in aqueous ammonia, piperazine solutions and their mixtures. International Journal of Greenhouse Gas Control 2012;9:148–59. https://doi.org/10.1016/j.ijggc.2012.03.013.

[54] Chowdhury FA, Okabe H, Yamada H, Onoda M, Fujioka Y. Synthesis and selection of hindered new amine absorbents for CO2 capture. Energy Procedia 2011;4:201–8. https://doi.org/10.1016/j.egypro.2011.01.042.

[55] Wanderley RR, Pinto DDD, Knuutila HK. Investigating opportunities for water-lean solvents in CO2 capture: VLE and heat of absorption in water-lean solvents containing MEA. Separation and Purification Technology 2020;231:115883. https://doi.org/10.1016/j.seppur.2019.115883.

[56] Arshad MW, von Solms N, Thomsen K, Svendsen HF. Heat of Absorption of CO2 in Aqueous Solutions of DEEA, MAPA and their Mixture. Energy Procedia 2013;37:1532–42. https://doi.org/10.1016/j.egypro.2013.06.029.

[57] McCann N, Maeder M, Attalla M. Simulation of Enthalpy and Capacity of CO2 Absorption by Aqueous Amine Systems. Ind Eng Chem Res 2008;47:2002–9. https://doi.org/10.1021/ie070619a.

[58] Mangalapally HP, Notz R, Asprion N, Sieder G, Garcia H, Hasse H. Pilot plant study of four new solvents for post combustion carbon dioxide capture by reactive absorption and comparison to MEA. International Journal of Greenhouse Gas Control 2012;8:205–16. https://doi.org/10.1016/j.ijggc.2012.02.014.

[59] Mun J-H, Shin B-J, Kim S-M, Kyun You J, Cheol Park Y, Chun D-H, et al. Optimal MEA/DIPA/water blending ratio for minimizing regeneration energy in absorption-based carbon capture process: Experimental CO2 solubility and thermodynamic modeling. Chemical Engineering Journal 2022;444:136523. https://doi.org/10.1016/j.cej.2022.136523.

[60] Miyamoto O, Maas C, Tsujiuchi T, Inui M, Hirata T, Tanaka H, et al. KM CDR ProcessTM Project Update and the New Novel Solvent Development. Energy Procedia 2017;114:5616–23. https://doi.org/10.1016/j.egypro.2017.03.1700.

[61] Frimpong RA, Nikolic H, Bahr D, Kiran G, Liu K. Pilot scale testing of an advanced solvent in a 0.7 MWe post-combustion CO2 capture unit. International Journal of Greenhouse Gas Control 2021;106:103290. https://doi.org/10.1016/j.ijggc.2021.103290.

[62] Notz RJ. CO2-Abtrennung Aus Kraftwerksabgasen Mittels Reaktivabsorption. Berlin, Germany: Logos Verlag Berlin; 2010.

[63] Brúder P, Grimstvedt A, Mejdell T, Svendsen HF. CO2 capture into aqueous solutions of piperazine activated 2-amino-2-methyl-1-propanol. Chemical Engineering Science 2011;66:6193–8. https://doi.org/10.1016/j.ces.2011.08.051.

[64] Li K, Cousins A, Yu H, Feron P, Tade M, Luo W, et al. Systematic study of aqueous monoethanolamine-based CO2 capture process: model development and process improvement. Energy Science & Engineering 2016;4:23–39. https://doi.org/10.1002/ese3.101.

[65] Que H, Chen C-C. Thermodynamic Modeling of the NH3–CO2–H2O System with Electrolyte NRTL Model. Ind Eng Chem Res 2011;50:11406–21. https://doi.org/10.1021/ie201276m.

[66] Owrang F, Svendsen HF. Estimating the heat losses from a laboratory pilot plant for CO2 absorption. 2010 2nd International Conference on Chemical, Biological and Environmental Engineering, 2010, p. 180–3. https://doi.org/10.1109/icbee.2010.5649674.

[67] Suresh Babu A, Rochelle GT. Heat Loss and Energy Use in Pilot Plant Testing of Piperazine With the Advanced Stripper 2021. https://doi.org/10.2139/ssrn.3811548.

[68] Dugas RE. Pilot plant study of carbon dioxide capture by aqueous monoethanolamine 2006.

Chapter 5: Simulation Model Enhancement and Utilisation

5.1 Introduction to the ECC Model

The performance assessment campaign for the TERC ACP described in the preceding chapter provided insights into capture conditions for a range of flue gas CO_2 concentrations in a gas flow of 150 Nm^3/h, with varying solvent flow rates targeting 90% capture efficiency. The tested ranges were informed by earlier predictions made by the DCC model in Chapter 3. Throughout the analysis of the experimental results, several comparisons were made with the preliminary DCC model predictions. It became apparent that, while the DCC model provided suitable initial conditions for the campaign, the model would benefit from further refinement to better represent the TERC ACP and enhance performance predictions.

The process data obtained from the experimental campaign can be used to calibrate and improve the DCC model, providing the foundation for a digital twin representation of the TERC ACP. This calibrated model, henceforth referred to as the Enhanced Carbon Capture (ECC) model, is designed to predict the expected SRD, solvent loadings, and column temperature profiles under various capture conditions at elevated flue gas CO_2 concentrations. This will reduce reliance on costly and time-intensive experimental campaigns, enabling rapid acquisition of results for specified capture conditions.

The following sections describe the development of the ECC model, beginning with the initial comparison between the experimental campaign and the DCC model to identify areas for improvements, followed by a detailed investigation to achieve improved alignment with the TERC ACP, and culminating in the application of the ECC model to predict capture conditions beyond the scope of the experimental campaign.

5.2 Comparison of Experimental Results to DCC Model

The results obtained from the experimental campaign were replicated using the initial DCC model. The flue gas and solvent analyses provided composition data for the flue gas and lean solvent streams, respectively, while averaged process data supplied the temperatures and pressures for the capture conditions. The hot rich solvent entering the top of the stripper was assumed to be the same temperature as the top RTD measurement, consistent with the methodology used in the Chapter 4 energy balances. This assumption was necessary because the experimental temperature measurements around the cross-heat exchanger were found to be unreliable, while accurate representation of its performance is critical for model convergence

In the DCC model, the capture efficiency of the experimental condition is achieved by iteratively adjusting the lean loading of the lean solvent, which in turn alters the solvent's cyclic capacity to reach the target capture efficiency. The stripper reboiler duty is then iteratively adjusted until the lean loading of the regenerated solvent is equal to that of the input lean solvent, thereby completing the solvent loop. The results of the simulation are subsequently collected for comparison.

As in the preceding chapter, capture conditions are labelled using a two-part naming convention: the first number indicates the flue gas CO_2 concentration in mol.%, and the second number represents the solvent flow rate in kg/h. For example, case 25_1100 corresponds to a flue gas concentration of 25 mol.% CO_2 treated with 1100 kg/h solvent.

5.2.1 Specific Reboiler Duty

Figure 5.1 presents the relationship of SRD with varying solvent flow rates across different flue gas CO_2 concentrations tested on the TERC ACP, comparing experimental values with simulation predictions by the DCC model. The solvent flow rates refer to the lean solvent streams and include the residual mass of CO_2 absorbed in the solvent representing the lean loading. Due to the way the DCC model adjusts the lean loading to achieve the target capture efficiency, the simulated solvent flow rates are marginally different to the experimental values with no significant effect upon the results.

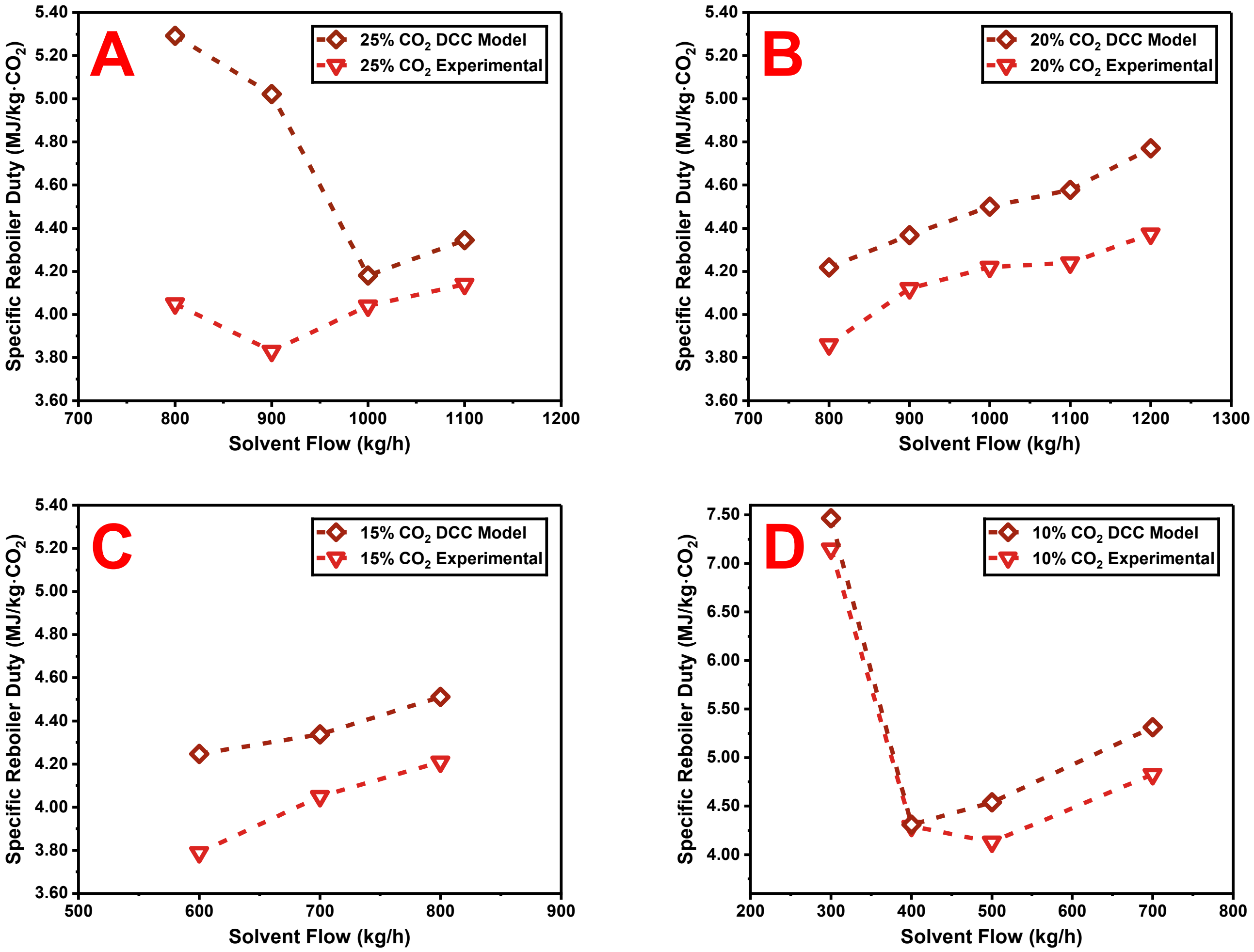

Figure 5.1: SRD against solvent flow rate for different CO_2 concentrations in a 150 Nm^3/h gas flow targeting 90% capture efficiency: (A) 25 mol.% CO_2, (B) 20 mol.% CO_2, (C) 15 mol.% CO_2, and (D) 10 mol.% CO_2.

From Figure 5.1, it is evident that the DCC model performs better for some flue gas CO_2 concentrations than for others. For Figures 5.1B and 5.1C, representing flue gas CO_2 concentrations of 20 and 15 mol.% respectively, the overall trend of SRD with solvent flow rate correlates well between simulated and experimental values. However, for Figure 5.1A, representing 25 mol.% CO_2, the DCC model deviates significantly from the experimental SRD values at solvent flow rates of 800 and 900 kg/h. This indicates that while the DCC model represents a step forward in process modelling of the TERC ACP, it has limitations in its predictive abilities that affords scope for improvement.

The DCC model predicts the minimum SRD to occur at a solvent flow rate of approximately 1000 kg/h, which is clearly inconsistent with the experimental data. For Figure 5.1D, the DCC model generally aligns with the trend of experimental SRD values, but incorrectly predicts the minimum SRD shown for the experimental data at approximately 500 kg/h.

For all capture conditions presented in Figure 5.1, the DCC model overestimates the SRD required for capture to varying degrees. Figure 5.2 shows the difference in SRD between the experimental and simulated results for all capture conditions.

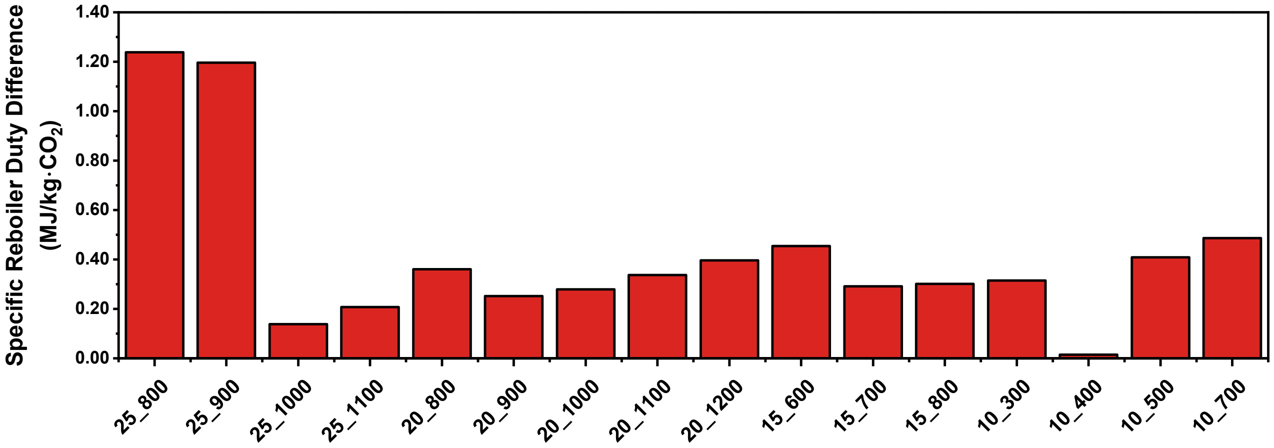

Figure 5.2: Difference in SRD between DCC model simulations and experimental results for capture conditions targeting 90% capture efficiency from a 150 Nm^3/h gas flow.

The difference between the simulated and experimental SRD values across the capture conditions ranges from 0.015 to 1.239 $MJ/kg{\cdot}CO_2$, with the smallest and largest differences occurring at conditions 10_400 and 25_800, respectively. The average difference across all capture conditions is 0.417 $MJ/kg{\cdot}CO_2$. This indicates that while the model achieved generally good representation of the experimental conditions across a wide range of conditions, it became less accurate towards the limits of the tested range.

Improvements to the DCC model should aim to reduce the SRD differences between simulated and experimental values, with particular emphasis on conditions 25_800 and 25_900, which exhibit the largest deviations. A maximum average SRD difference of 0.2 $MJ/kg{\cdot}CO_2$ is proposed as the target for the ECC model, equivalent to a 5% deviation from an empirical baseline SRD of 4.0 $MJ/kg{\cdot}CO_2$ for the TERC ACP. Achieving this target would yield improvements in 14 of the 16 conditions, with SRD differences reduced by at least 50% in 6 conditions and at least 30% in 10 conditions.

5.2.2 *Solvent Loadings*

Figure 5.3 presents the CO_2 loadings against the solvent flow rates for the same conditions shown in Figure 5.1. The lean and rich loadings, in addition to the solvent cyclic capacity, are presented as both experimental and simulated results for each capture condition, labelled in the legend as TERC and DCC, respectively.

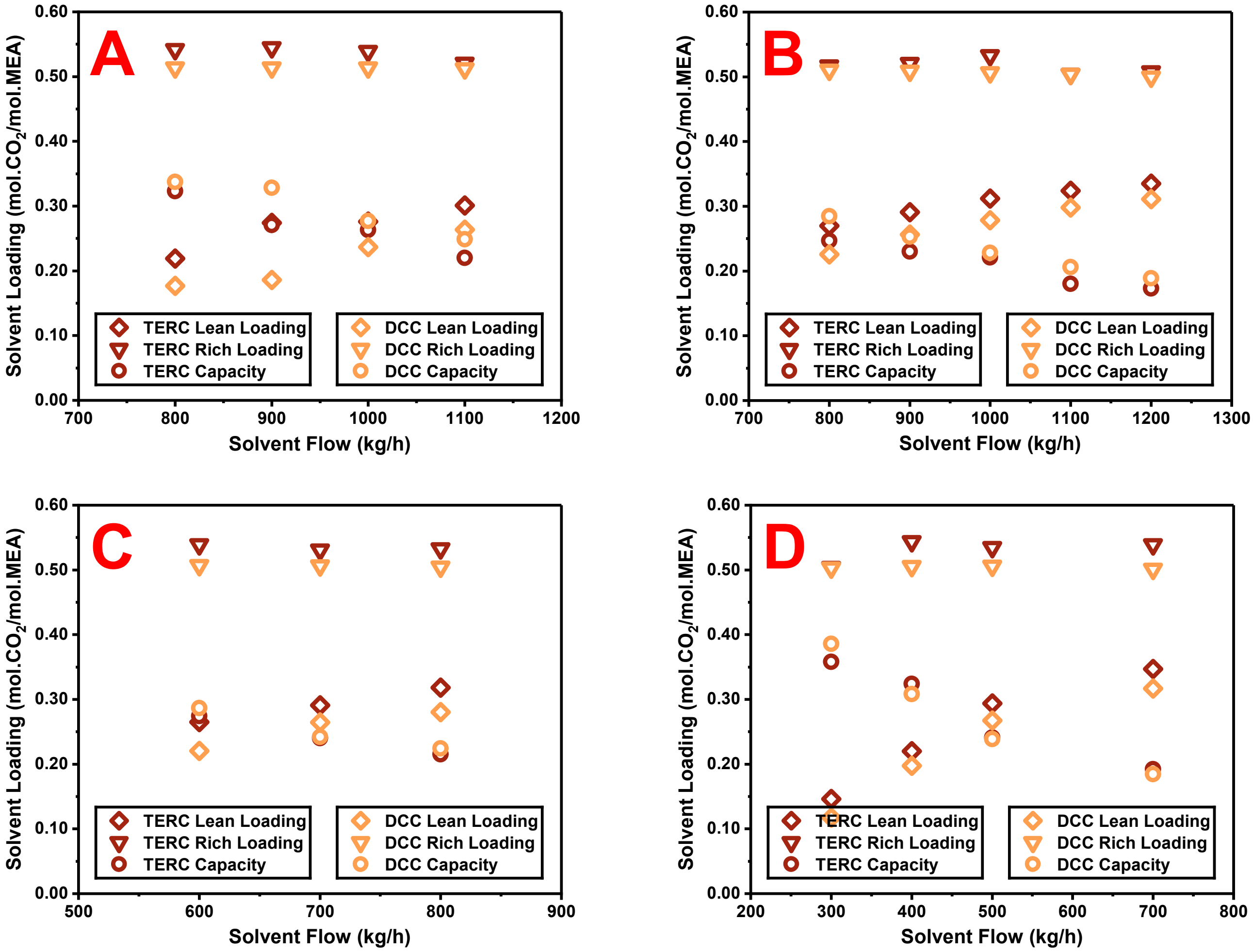

Figure 5.3: Solvent loadings against solvent flow rate for different CO_2 concentrations in a 150 Nm^3/h gas flow targeting 90% capture efficiency: (A) 25 mol.% CO_2, (B) 20 mol.% CO_2, (C) 15 mol.% CO_2, and (D) 10 mol.% CO_2.

The variations of experimental and modelled solvent loadings with solvent flow rates had similar trends for each of the three variables. The lean loading increases and cyclic capacity decreases with increasing solvent flow rate, while rich loading remains relatively stable for each flue gas CO_2 concentration. It is evident, however, that the DCC model underestimates both the lean and rich loading values compared to those measured experimentally. This is examined further in Figure 5.4, which shows the differences in solvent loadings for all capture conditions between the experimental and simulated results.

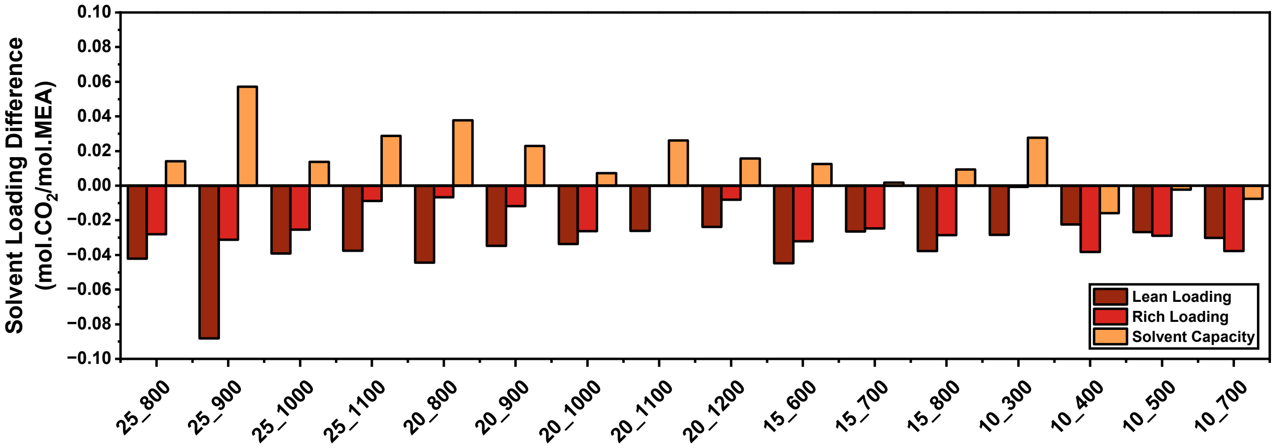

Figure 5.4: Difference in solvent loadings between DCC model simulations and experimental results for capture conditions targeting 90% capture efficiency from a 150 Nm^3/h gas flow.

Figure 5.4 confirms that the DCC model underestimates the lean and rich solvent loadings for all conditions, as the differences relative to the experimental values are negative. For the lean loadings, the difference between the simulated and experimental values ranges from 0.0223 to 0.0883, with the smallest and largest differences occurring at conditions 10_400 and 25_900, respectively. The average difference across all capture conditions is 0.0367. Improvements to the DCC model should aim to reduce the lean loading difference by increasing the lean loading for a given capture condition. A maximum average lean loading difference of 0.01 is proposed as the target for the ECC model, equivalent to approximately a 4% deviation from an empirical baseline lean loading of 0.23, representing the expected lean loading of the TERC ACP identified in Chapter 4. Achieving this target would improve performance across all 16 conditions, with lean loading differences reduced by at least 70% in 9 conditions, and at least 60% in 14 conditions.

For the rich loadings, the difference between the simulated and experimental values ranges from 0.0000 to 0.0383, with the smallest and largest differences occurring at conditions 20_1100 and 10_400, respectively. The average difference across all capture conditions is 0.0211. The rich loading differences are generally less varied than the lean loading differences, as the solvent neared complete saturation for each capture condition, but they cannot be directly controlled in the DCC model because they result from the absorption reactions. It is assumed that any improvements made to the lean loadings will also influence the rich loadings. Consequently, the target for improvement in the ECC model is the same as that for the lean loadings: a maximum average rich loading difference of 0.01. Achieving this target improve performance for 11 of the 16 conditions, with rich loading differences reduced by at least 60% in 10 conditions.

The solvent cyclic capacity shows more variation between conditions: it typically overestimates the capacity at flue gas CO_2 concentrations of 25 and 20 mol.%, aligns more closely with the experimental capacity for 15 mol.%

conditions, and generally underestimates the capacity for 10 mol.% conditions. The solvent capacity is not directly controlled, as it is calculated as the difference between the rich and lean loadings. These differences reflect the inherent uncertainty in experimental measurements compared to the ideal conditions assumed by the simulation. The solvent capacity is therefore not expected to match precisely unless fundamental changes to the simulation absorption chemistry are introduced. Consequently, no specific improvement target is set for the ECC model regarding solvent capacity, as it is inherently dependent on the solvent loadings given by the absorption chemistry.

5.2.3 Absorber Temperature Profiles

Figure 5.5 presents the absorber temperature profiles for the conditions presented in Figure 5.1. The left column presents experimental data, and the right column shows the corresponding simulation results. Each row represents a different flue gas CO_2 concentration, starting with 25 mol.% in the top row and decreasing by 5 mol.% for each subsequent row.

Several general observations can be made when comparing the experimental data with the simulation results. Firstly, the peak temperature in the simulations is consistently higher than that observed experimentally, and the peak is located slightly higher in the absorber column. This difference in peak location is likely due to the position where the lean solvent stream enters the absorber: in the DCC model, the lean solvent enters at the very top of the column, whereas in reality the stream enters slightly lower. Nevertheless, the peak location in the simulations is always towards the top of the column, consistent with the experimental peak occurring in absorber 2 on the TERC ACP. The difference in peak temperature may result from real-world heat losses or from how the reaction chemistry is represented by Aspen Plus.

The simulated temperature profiles are more uniform and regular than the experimental profiles, which show greater variation. This is inevitable, as the simulated profiles are an idealised and simplified representation of the capture plant. While the experimental conditions clearly evolve from a rich-pinched to a bulge-pinched state with increasing solvent flow rate, this trend is not generally reproduced in the simulations, except for the 10 mol.% CO_2 conditions in Figure 5.5H. The DCC model naturally represents an idealised version of the TERC ACP absorber columns and does not account for mechanical features present in the actual column, such as bucket distributors, which complicates accurate representation in a simulation environment.

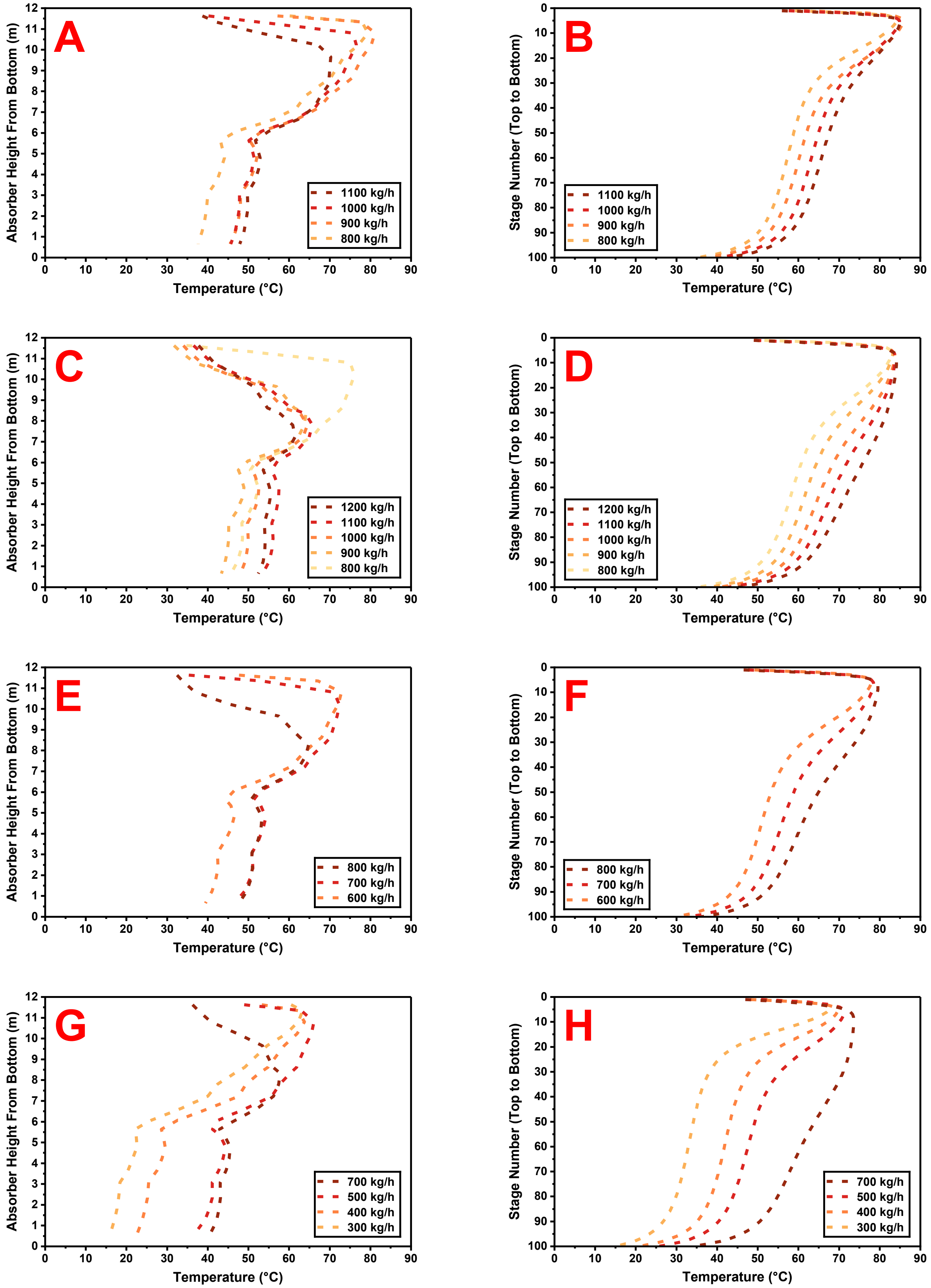

Figure 5.5: Absorber temperature profiles from experimental measurements and DCC model predictions. Each row corresponds to a different flue gas CO_2 concentration, with experimental data on the left, and simulated results on the right: (A, B) 25 mol.% CO_2, (C, D) 20 mol.% CO_2, (E, F) 15 mol.% CO_2, and (G, H) 10 mol.% CO_2.

To quantitatively assess how well the DCC model is at representing the temperature profiles of the TERC absorber, the mean absolute percentage error (MAPE) was calculated for the temperature profiles. This was determined by taking the experimental temperature values measured by the absorber RTDs and calculating the absolute error of the simulated values at the same column height, before averaging the total error across the column:

$$Column\ MAPE = 100 \cdot \frac{1}{n}\sum_{\mathrm{i}=1}^{n} \frac{|A_{\mathrm{i}} - S_{\mathrm{i}}|}{A_{\mathrm{i}}} \tag{5.1}$$

Where:

A = actual temperature of a column RTD (°C)

S = simulated temperature at the same height as the RTD (°C)

Figure 5.6 presents the absorber MAPEs between the experimental and modelled results for the different capture conditions.

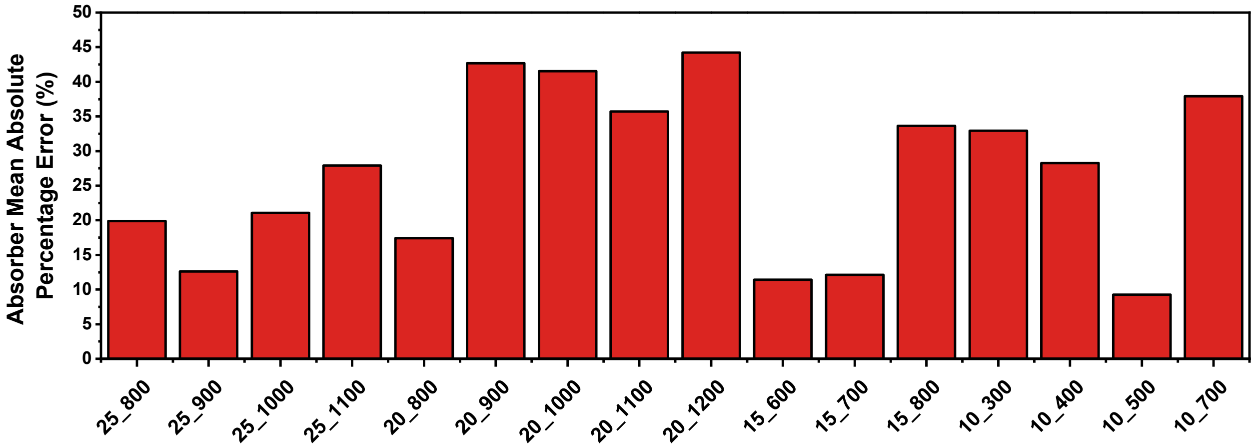

Figure 5.6: Difference in absorber MAPE between DCC model simulations and experimental results for capture conditions targeting 90% capture efficiency from a 150 Nm^3/h gas flow.

Figure 5.6 confirms that there are substantial differences in the MAPEs between the simulated and experimental absorber temperature profiles across the capture conditions. The absorber MAPE ranges from 9.28% to 44.21%, with the lowest and highest MAPEs occurring at conditions 10_500 and 20_1200, respectively. The average absorber MAPE across all capture conditions is 26.79%. Improvements to the DCC model should aim to more accurately capture the transition from rich-pinched to bulge-pinched profiles and improve the accuracy of the predicted peak temperature and its location. A maximum average absorber MAPE of 10% is proposed as the target for the ECC model. This threshold is nominal, chosen to ensure the predicted temperature profiles are sufficiently accurate to inform operational decisions, while balancing achievable accuracy with the limitations of available data. Achieving this target would yield improvements in 15 of the 16 conditions, with MAPE reduced by at least 70% in 6 conditions, and at least 50% in 10 conditions.

5.2.4 Stripper Temperature Profiles

Figure 5.7 presents the stripper temperature profiles for the conditions presented in Figure 5.1. The left column presents experimental data, and the right column shows the corresponding simulation results. Each row represents a different flue gas CO_2 concentration, starting with 25 mol.% in the top row and decreasing by 5 mol.% for each subsequent row.

It is evident that there is a disconnect between the experimental and simulated temperature profiles for a given capture condition. For example, conditions 25_900 and 25_800 appear in the exponential region in the simulated profiles in Figure 5.7B, whereas they approximate the inflection point in the experimental profiles in Figure 5.7A.

There is a degree of sparsity between RTD measurements on the column, particularly towards the top of the column, where RTDs are first located at simulation equivalent stages 2, 9 and then 27, representing the largest gap between RTD sensors on the column, providing some uncertainty in the experimental temperature profile shape near the top of the column. The true profile shapes are unlikely to be far from those plotted, especially for those in the baseline region where the temperature is similar until further down the column, however it does marginally affect profiles that shift into the exponential region. However, profiles can only be made from the recorded data, with the profile shape between sensors inferred based on expected operating conditions.

This disparity contributes to the differences in SRD for these conditions, as shown in Figure 5.1A. Similar mismatches are observed for the temperature profiles of the 20 and 15 mol.% CO_2 conditions, where the simulated profiles are not consistent with the solvent flow rates. The solvent loadings also contribute to these discrepancies: lower lean and rich loadings increase the energy required for solvent regeneration, shifting the profiles towards the exponential region, as observed. The simulated 10 mol.% CO_2 temperature profiles align more closely with the experimental profiles in the exponential region for conditions 10_400 and 10_300, which helps explain why the SRDs agree more closely in Figure 5.1D at lower flow rates, though a disconnect remains at higher flow rates.

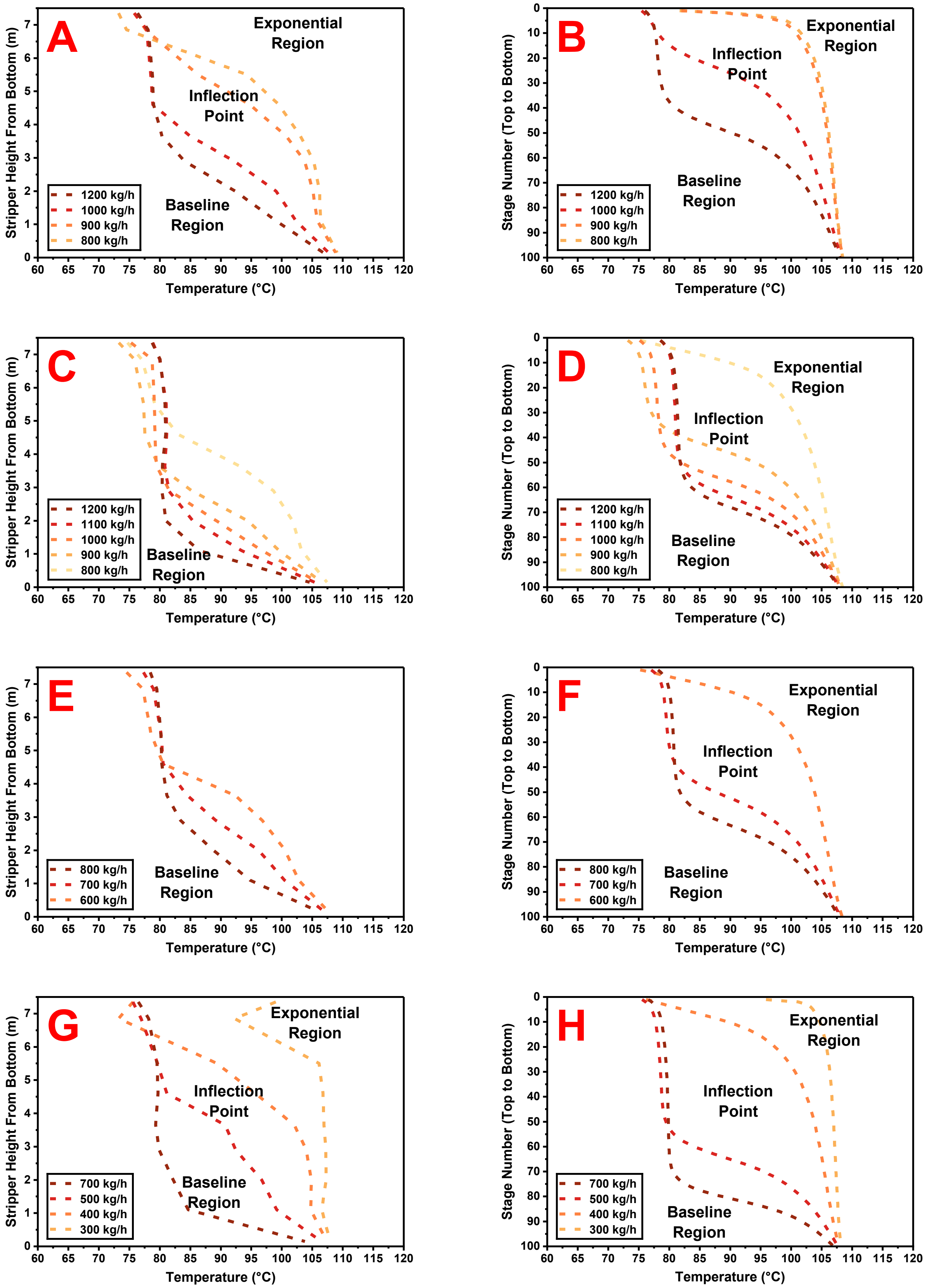

Figure 5.7: Stripper temperature profiles from experimental measurements and DCC model predictions. Each row corresponds to a different flue gas CO_2 concentration, with experimental data on the left, and simulated results on the right: (A, B) 25 mol.% CO_2, (C, D) 20 mol.% CO_2, (E, F) 15 mol.% CO_2, and (G, H) 10 mol.% CO_2.

As with the absorber, the stripper profiles have been quantitatively evaluated by calculating the MAPE between the experimental and simulated profiles. This was done using Equation (5.1) with the stripper RTD measurements and the simulated stage temperatures at the corresponding column heights. Figure 5.8 presents the stripper MAPEs for the different capture conditions.

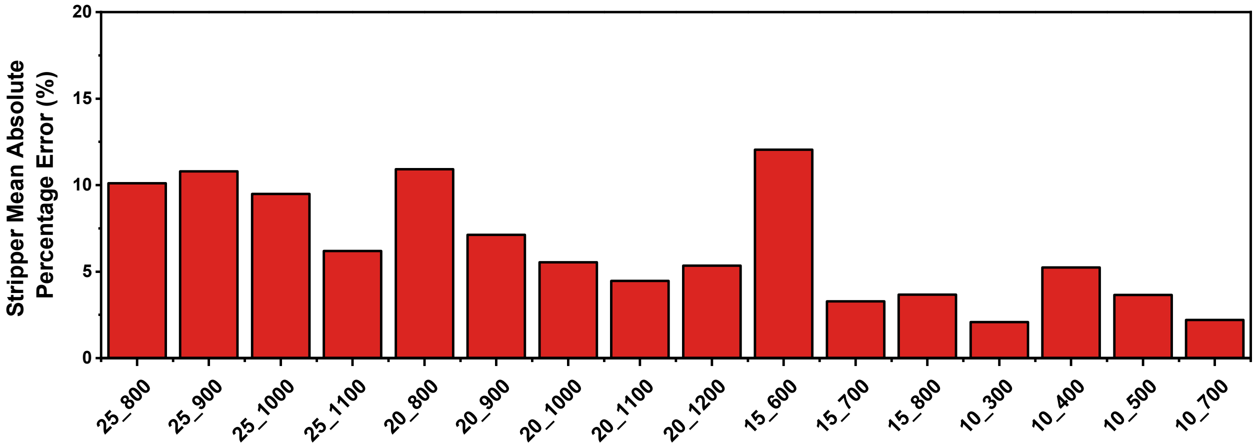

Figure 5.8: Difference in stripper MAPE between DCC model simulations and experimental results for capture conditions targeting 90% capture efficiency from a 150 Nm^3/h gas flow.

Figure 5.8 shows that there is generally less variation in the MAPEs between the simulated and experimental stripper temperature profiles compared to the absorber. The stripper MAPE ranges from 2.09% to 12.04%, with the lowest and highest MAPEs occurring at conditions 10_300 and 15_600, respectively. The average stripper MAPE across all capture conditions is 6.38%. Improvements to the DCC model should focus on aligning the simulated stripper temperature profiles more closely with the experimental profiles for each capture condition, thereby improving accuracy and reliability for predicting performance under different, untested conditions. A maximum average stripper MAPE of 5% is proposed as the target for the ECC model. This threshold is nominal, chosen to ensure high accuracy in predictions given that stripper profiles are critical for understanding system performance and optimisation. Achieving this target would yield improvements in 10 of the 16 conditions, with MAPE reduced by at least 50% in 4 conditions, and at least 20% in 7 conditions.

5.2.5 DCC Model Comparison Summary

Overall, the DCC model performed well in providing initial conditions and estimates for the experimental campaign on the TERC ACP. However, it can be further refined into a more accurate representation of the plant through systematic calibration against the collected experimental data. The preceding analysis has identified specific areas where the model underperforms, enabling the definition of clear performance improvement targets for the development of the ECC model. Table 5.1 summarises these performance improvement targets. The complete results of the simulated capture conditions provided by the DCC model are presented in Table 5.2, together with the calculated column MAPEs and absolute differences from key experimental values.

Table 5.1: Summary of performance improvement targets for the ECC model.

Parameter	Units	Average Improvement Target
SRD Difference	MJ/kg·CO_2	0.2
Lean Loading Difference	mol·CO_2/mol·MEA	0.01
Rich Loading Difference	mol·CO_2/mol·MEA	0.01
Absorber MAPE	%	10
Stripper MAPE	%	5

The following sections describe the development of the ECC model, including an evaluation of alternative column packing arrangements and their impact on performance for each capture condition. This investigation supports the fine-tuning of the ECC model into a plant-specific simulation calibrated for the TERC ACP, while the methodology employed provides a generalised, transferable framework for improving predictive models of comparable chemical absorption plants.

Table 5.2: DCC model simulation results of the experimental capture conditions.

Parameter	Units	25_800	25_900	25_1000	25_1100	20_800	20_900	20_1000	20_1100	20_1200	15_600	15_700	15_800	10_300	10_400	10_500	10_700
CO_2 in Flue Gas	vol.%	24.42	24.99	24.99	24.99	20.18	20.18	20.11	20.11	20.07	15.14	15.00	15.04	10.15	10.01	10.03	10.01
H_2O in Flue Gas	vol.%	0.78	0.78	0.78	0.78	0.52	0.52	0.43	0.43	0.67	0.74	0.69	0.65	0.50	0.37	0.43	0.37
Overall Solvent Mass Flow	kg/h	791.99	881.53	990.94	1090.49	791.44	892.53	992.01	1093.18	1193.22	593.61	695.60	794.21	298.06	398.12	497.04	695.67
Solvent MEA + H_2O Flow	kg/h	758.44	842.68	936.20	1023.68	747.99	837.56	925.83	1015.37	1104.34	562.14	651.67	740.12	290.05	381.47	467.51	650.17
Solvent MEA Mass Flow	kg/h	263.39	290.30	320.82	351.95	267.38	297.78	329.94	362.49	396.34	198.32	230.51	261.38	94.55	116.91	153.37	199.30
Solvent H_2O Mass Flow	kg/h	495.05	552.38	615.38	671.73	480.61	539.78	595.89	652.88	708.00	363.82	421.16	478.74	195.50	264.56	314.14	450.87
Solvent CO_2 Mass Flow	kg/h	33.55	38.85	54.74	66.81	43.45	54.97	66.18	77.81	88.88	31.47	43.93	54.09	8.01	16.65	29.53	45.50
Flue Gas Mass Flow	kg/h	222.48	223.08	221.62	221.62	214.99	214.99	214.98	216.41	217.75	211.29	209.69	209.68	201.94	199.19	201.87	201.90
Flue Gas CO_2 Mass Flow	kg/h	73.64	75.36	74.87	74.87	59.93	59.93	59.72	60.12	60.43	45.30	44.57	44.67	29.73	28.94	29.39	29.33
Flue Gas Volumetric Flow	m^3/h	159.90	160.09	158.49	158.67	155.97	156.21	156.52	158.07	160.17	159.17	157.25	156.17	152.38	149.07	153.34	152.95
Liquid to Gas Ratio	kg/kg	3.56	3.95	4.47	4.92	3.68	4.15	4.61	5.05	5.48	2.81	3.32	3.79	1.48	2.00	2.46	3.45
Solvent to CO_2 Ratio	kg/kg	10.30	11.18	12.50	13.67	12.48	13.98	15.50	16.89	18.27	12.41	14.62	16.57	9.76	13.18	15.91	22.17
Flue Gas Temperature	°C	11.74	12.08	11.07	11.40	8.93	9.37	9.92	10.84	12.55	12.45	11.01	9.17	6.16	3.83	7.92	7.21
Lean Solvent Temperature	°C	33.90	37.08	37.31	38.11	30.25	31.13	33.46	35.87	37.39	28.25	30.33	31.88	28.70	29.54	35.16	36.61
Lean Solvent Concentration	wt.%	33.27	32.95	32.39	32.29	33.80	33.38	33.28	33.17	33.23	33.43	33.15	32.93	31.74	29.38	30.87	28.66
Rich Solvent Concentration	wt.%	32.43	32.19	31.67	31.58	32.89	32.49	32.46	32.43	32.50	32.65	32.44	32.23	31.24	28.98	30.65	28.37
Lean Loading	mol/mol	0.1768	0.1857	0.2368	0.2635	0.2255	0.2562	0.2784	0.2979	0.3112	0.2203	0.2645	0.2802	0.1176	0.1977	0.2673	0.3168
Rich Loading	mol/mol	0.5140	0.5138	0.5136	0.5122	0.5102	0.5092	0.5067	0.5040	0.4999	0.5068	0.5063	0.5045	0.5033	0.5057	0.5060	0.5012
Loading Capacity	mol/mol	0.3371	0.3281	0.2768	0.2487	0.2847	0.2529	0.2283	0.2061	0.1887	0.2866	0.2418	0.2243	0.3857	0.3081	0.2387	0.1843
Absorber Bottom Temperature	°C	35.20	37.56	40.27	42.43	35.24	38.11	40.54	42.74	45.13	29.65	33.12	36.11	14.91	20.68	25.59	33.89
Cross Heat Exchanger Duty	kW	27.36	30.69	32.35	34.08	28.38	28.71	31.59	36.28	36.98	24.12	27.93	30.71	22.94	20.26	22.53	27.79
Cross Heat Exchanger Temperature Approach	°C	36.61	33.97	33.64	33.04	35.02	36.32	34.26	30.60	30.72	35.17	32.24	31.02	10.74	33.42	33.64	32.34
Stripper Bottom Temperature	°C	109.59	109.50	109.22	109.12	109.49	109.30	109.22	109.15	109.12	109.45	109.26	109.15	109.53	108.84	108.94	108.46
Stripper Pressure	Bara	1.2	1.2	1.2	1.2	1.2	1.2	1.2	1.2	1.2	1.2	1.2	1.2	1.2	1.2	1.2	1.2
Stripper Reboiler Heat Duty	kW	93.95	95.60	74.24	76.05	64.21	65.81	67.81	68.34	71.37	48.27	48.36	51.17	54.44	31.03	33.24	39.06
SRD	MJ/kg·CO_2	5.29	5.02	4.18	4.34	4.22	4.37	4.50	4.58	4.77	4.25	4.34	4.51	7.47	4.31	4.54	5.31
Degree of Regeneration	%	65.60	63.85	53.89	48.56	55.80	49.68	45.06	40.88	37.74	56.54	47.76	43.03	76.64	60.91	47.18	36.78
CO_2 Capture Efficiency	%	86.73	90.87	85.34	84.13	91.38	90.44	90.78	89.43	89.09	90.26	90.01	91.37	88.26	89.57	89.66	90.18
Lean Loading Difference	mol/mol	0.0422	0.0883	0.0392	0.0375	0.0445	0.0348	0.0336	0.0261	0.0238	0.0447	0.0265	0.0378	0.0284	0.0223	0.0267	0.0302
Rich Loading Difference	mol/mol	0.0280	0.0312	0.0254	0.0088	0.0068	0.0118	0.0263	0.0000	0.0081	0.0322	0.0247	0.0285	0.0007	0.0383	0.0290	0.0378
Solvent Capacity Difference	mol/mol	0.0141	0.0571	0.0138	0.0287	0.0377	0.0229	0.0073	0.0261	0.0157	0.0126	0.0018	0.0093	0.0277	0.0159	0.0023	0.0077
SRD Difference	MJ/kg·CO_2	1.24	1.20	0.14	0.21	0.36	0.25	0.28	0.34	0.40	0.45	0.29	0.30	0.31	0.02	0.41	0.49
Absorber MAPE	%	19.88	12.61	21.09	27.89	17.42	42.67	41.55	35.73	44.21	11.43	12.11	33.64	32.92	28.28	9.28	37.92
Stripper MAPE	%	10.10	10.80	9.49	6.19	10.91	7.12	5.54	4.47	5.34	12.04	3.28	3.67	2.09	5.23	3.66	2.20

5.3 Alternative Packing Configurations

5.3.1 Alternative Packing Hypothesis

In a real-world experimental campaign, various process inefficiencies inherently affect the obtained process data, causing deviations from ideal conditions. By contrast, a process simulation generally assumes ideal behaviour unless specific inefficiencies are explicitly incorporated. The influence of factors such as gas impurities, system corrosion, or heat losses is difficult to quantify without extensive, targeted measurements, and their precise impact on the process data cannot easily be determined. The data required for such an in-depth characterisation was not available from the present experimental campaign and would necessitate a dedicated investigation to obtain. As a result, it was anticipated that the simulation might be unable to sufficiently replicate all capture conditions using the actual column packing configurations used in the TERC ACP, where the ideal simulation results deviate too far from the experimental values.

The physical characteristics of the column packing, such as specific surface area and void fraction, are used by the simulation model to calculate key hydrodynamic and mass transfer parameters, including the effective interfacial area for gas-liquid contact and the liquid holdup within the column [1,2]. These calculated parameters, in turn, influence the SRD requirements, solvent loadings, and column temperature profiles for a given capture condition [2].

For example, Rahmanian et al. [2] highlight that packings with higher surface areas facilitate more efficient mass transfer. While the fundamental reaction kinetics remain unchanged, the extent of reaction increases, resulting in a higher rich solvent loading and consequently a lower SRD requirement. A larger surface area also distributes the mass transfer and reactions more effectively along the columns, altering the shape of the temperature profiles.

It was hypothesised that an alternative column packing configuration, selected from the options available within Aspen Plus, might enable the simulation results to represent the experimental data better and simplify the simulation tuning process.

However, identifying such an alternative is not straightforward. Aspen Plus offers an extensive database of column packings. At the most basic level, users must choose between packed and trayed column internals. For packed columns, which the TERC ACP uses, a wide range of industrially relevant packings is available. Each packing type can then be customised by selecting a vendor-specific version, material, and size. Figure 5.9 shows an example of the column internals selection screen in Aspen Plus.

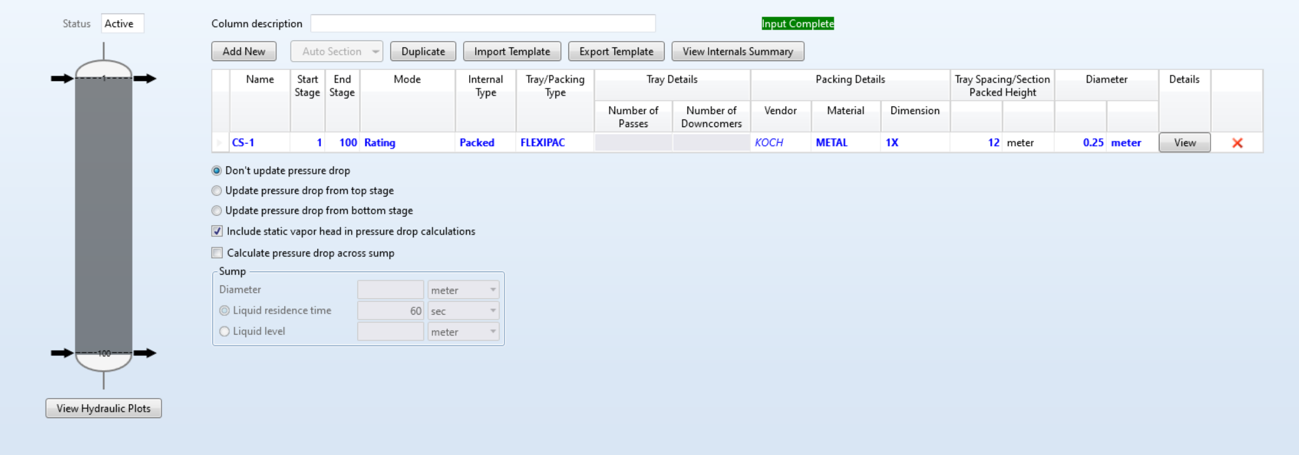

Status: Active

Column description:

Name	Start Stage	End Stage	Mode	Internal Type	Tray/Packing Type	Tray Details		Packing Details			Tray Spacing/Section Packed Height		Diameter		Details	
						Number of Passes	Number of Downcomers	Vendor	Material	Dimension						
CS-1	1	100	Rating	Packed	FLEXIPAC			KOCH	METAL	1X	12	meter	0.25	meter	View	✕

● Don't update pressure drop
○ Update pressure drop from top stage
○ Update pressure drop from bottom stage
☑ Include static vapor head in pressure drop calculations
☐ Calculate pressure drop across sump

Sump
Diameter: meter
◎ Liquid residence time: 60 sec
○ Liquid level: meter

Figure 5.9: Screenshot of example absorber column internals options in Aspen Plus V11.0.

Consequently, the total number of possible packing configurations for each column exceeds 20,000, with no clear guidance on which combinations are likely to yield the best match with experimental results. Manually testing each option was impractical. Instead, a coding-based approach was developed to automate the evaluation of different packing configurations and to identify those offering improved agreement with the experimental data.

The following section provides an overview of the developed automation script and explains how it was used to screen and select promising packing arrangements for the ECC model.

5.3.2 *Python Automation Script Development*

An automation script was developed in Python to control Aspen Plus to systematically test every feasible column packing configuration within the underlying DCC model. This script was co-developed with Vincent Bailey Ladd and served primarily to generate the results discussed throughout this section. Guidance on interfacing Python to Aspen Plus was drawn from Richard Wolfgang ten Hagen's Aspen Plus Python Interface project [3], publicly available on GitHub. The foundation of the automation methodology was developed by Vincent Bailey Ladd, incorporating adapted code from Zihao Wang [4]. While the optimisation approach was collaborative, all simulation results and interpretations presented here are my own.

The automation script used Windows specific programming to control Aspen Plus [5,6]. Aspen Plus includes a feature known as the "variable explorer", a hierarchical structure providing access to every variable, parameter, and status indicator within the simulation [7]. By referencing specific nodes within this structure, the script could systematically modify inputs and monitor simulation status, enabling full control over the DCC model.

To begin, the script loaded the appropriate Aspen Plus file for each capture condition and systematically cycled through all feasible packing configurations, varying packing name, vendor, material, and dimension. Any tuning factors in the DCC model were reset to 1.0 to ensure a neutral baseline across all simulations. Additionally, the absorber column's diameter was adjusted from 300 mm to 250 mm to match the current TERC ACP specifications. The simulation convergence tolerance was also reduced from four to three decimal places to avoid flat response convergence errors that occasionally arose under tighter tolerances.

Before each run, the script checked whether the simulation inputs were complete by querying the hexadecimal status of the \data node in the variable explorer. If the inputs were valid, the simulation proceeded, otherwise that configuration was skipped due to unresolved input requirements.

Once initiated, the model iterated the lean solvent loading to achieve the target capture efficiency, then modified the reboiler duty to match the specified lean loading. After the run, the script again checked the \data node for errors. Simulations that failed to complete successfully were closed without saving results, and the model was reloaded with the next packing configuration. In the case of non-converging simulations, a timeout safeguard adapted from the work by Zihao Wang [4] was used to abort runs that exceeded a 15-minute execution window, thereby avoiding infinite convergence loops.

For simulations that completed successfully, the script extracted the key process outputs, compared them statistically to the experimental results, and generated visualisations of the absorber and stripper temperature profiles. Statistical analysis was performed using the NumPy, pandas, and SciPy packages available for Python [8–10]. All outputs were automatically organised into structured folders, and a master Excel file was compiled, consolidating the results from every successful run across all capture conditions.

Simulations were run on a machine equipped with a 13th Gen Intel® Core™ i9-13900k 3.00 GHz CPU and 64.0 GB of RAM. This setup enabled up to 20 instances of Aspen Plus to be executed in parallel [11] and reduced the average processing time to approximately 150 seconds per simulation. A flowchart detailing the automation sequence is provided in the blue pathway of Figure 5.10.

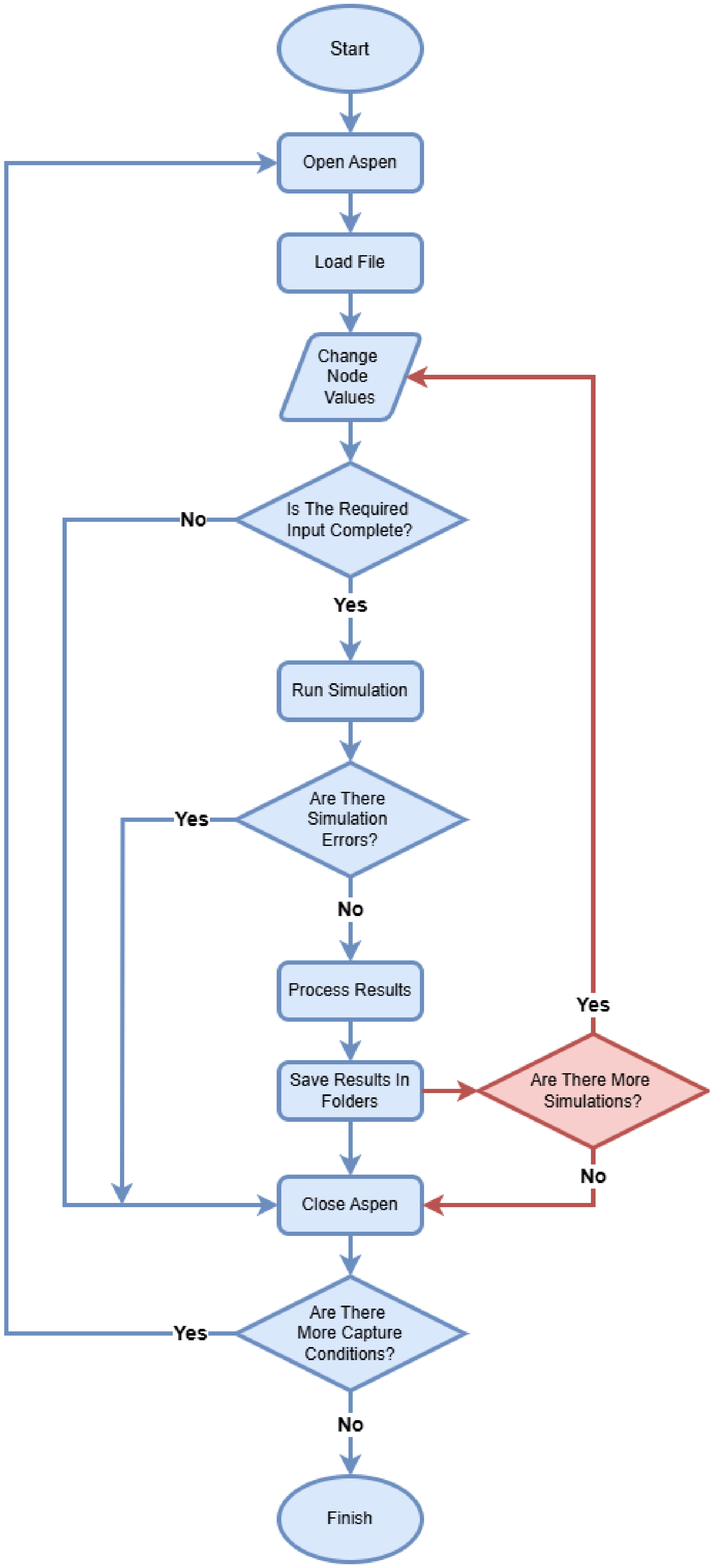

Figure 5.10: Flowchart of the developed Python script. The blue pathway represents the initial column packing testing and the red pathway represents subsequent tuning factor testing for the selected packings.

5.3.3 Optimal Packing Configuration Identification

Preliminary testing showed that packing configurations influenced the absorber and stripper column in distinct ways. In the absorber, the packing primarily affected the lean solvent loading associated with the target capture efficiency and the MAPE of the absorber temperature profile. Since lean loading in turn impacts SRD, the absorber packing indirectly influenced energy consumption. In contrast, the stripper packing directly affected the SRD and the MAPE of the stripper temperature profile but had no influence on lean loading due to how the design specifications of the simulation achieve convergence.

These differences made it necessary to optimise the absorber and stripper packings independently. The absorber packing was varied first, while holding the stripper packing constant to isolate its effects. Once optimal absorber packings were identified, a similar process was repeated for the stripper. Each column had 508 unique packing configurations available in Aspen Plus, leading to 8128 simulations per column across 16 capture conditions, or a total of 16,258 simulations for the full investigation. From these simulations, the top-performing packings for each column were identified and then tested in all possible combinations to determine the best overall pairings. These combinations advanced to the next stage for fine-tuning. The general selection workflow is outlined in Figure 5.11.

Figure 5.11: Alternative packing arrangement investigation overview.

Absorber packings were ranked based on the absolute difference between simulated and experimental lean loading, considered a critical metric for reflecting true solvent chemistry. A dense ranking system was used to prevent distortions caused by closely matched entries (e.g., 1st, 2nd, 2nd 3rd rather than 1st, 2nd, 2nd, 4th). Not all packing choices led to converged models across all 16 conditions, so results were processed using Excel PIVOT tables to calculate both occurrence counts and summed ranks. Average rankings were then computed and ordered numerically from lowest (best match) to highest.

Flexipac 1X metal packing by Koch Glitsch, representing the packing used in the original experimental campaign, served as the average ranking baseline. Only absorber packings with lower average rank scores and at least 14 successful occurrences out of 16 were retained, to eliminate the majority of unsuccessful packings with poorer performance than the baseline packing. This left 13 viable absorber packings for further consideration, including the reference case.

Stripper packings were ranked using the same dense ranking method but based on the difference between simulated and experimental SRD. Many packings converged across all conditions, so the selection was restricted to those that succeeded for all 16 simulations. A nominal summed rank threshold of 1000 was applied, as it provided a clear cutoff without the need for average rankings. This yielded 22 stripper packings for further analysis, including the reference IMTP 25 mm packing.

With 13 absorber and 22 packings selected, a total of 286 unique combinations were tested across all 16 capture conditions, amounting to 4576 additional simulations. These were ranked across four criteria: lean loading difference, SRD difference, absorber MAPE, and stripper MAPE.

No single packing combination ranked best across all metrics, therefore, a second stage of ranking was developed, where each individual parameter rank was combined into a composite rank. It became clear that absorber MAPE rankings conflicted significantly with the other three metrics, skewing results. Since the simulations always achieved the target capture efficiency, the absorber could be treated as a “black box”, making its temperature profile less critical than the resulting lean loading. Absorber MAPE was therefore removed from the final composite ranking.

The final ranking considered the lean loading difference, SRD difference, and stripper MAPE. Ranking ties caused by minor differences (e.g., same geometry, different material) were manually pruned to enhance clarity. The top packings selected, including the original experimental packing configuration, are listed in Table 5.3.

Table 5.3: Column packing configurations selected for tuning.

Number	Packing Configuration (Name/Vendor/Material/Dimension)	
	Absorber	Stripper
1	Mellapak/Sulzer/Standard/750Y	Raschig/Norton/Metal-16/0.625 in or 16 mm
2	Mellapak/Sulzer/Standard/750Y	Raschig/Norton/Ceramic/0.625 in or 16 mm
3	CY/Sulzer/Standard/Standard	Raschig/Norton/Metal-16/0.625 in or 16 mm
4	CY/Sulzer/Standard/Standard	IMTP/Generic/Metal/0.625 in or 16 mm
5	Flexipac/Koch/Metal/1X	IMTP/Koch/Metal/1 in or 25 mm

Two absorber packing styles, Mellapak and CY, outperformed Flexipac 1X in the untuned simulations. For the stripper, Raschig and IMTP styles emerged as top performers. The inclusion of an IMTP packing among the top stripper candidates suggests that the stripper column in the DCC model more closely represents the TERC ACP configuration than the absorber column, consistent with the MAPE comparisons shown in in Figures 5.6 and 5.8.

With the optimal packing configurations identified, the next step was to fine-tune the simulations to better align with experimental results. Aspen Plus offers several tuning parameters for this purpose, and preliminary sensitivity analyses were conducted to assess their influence before defining the final tuning scope.

5.4 Aspen Plus Tuning Factors

5.4.1 Tuning Factor Scope

Aspen Plus provides four distinct scale factors for rate-based modelling in packed columns: interfacial area (IA) factor, heat transfer factor, liquid mass transfer coefficient factor, and vapor mass transfer coefficient factor. In addition, the liquid holdup (LH) scale factor was also evaluated. Each of these factors was investigated for potential inclusion in the tuning process. Only tuning factors directly related to the column packings were considered, deliberately avoiding any that would alter the underlying reaction chemistry. This approach ensured focus on tuning packing-dependent parameters only.

The required sensitivity analyses were conducted using a modified version of the automation script described earlier. In this configuration, the simulation file was not closed and reopened between tuning factor iterations, thereby retaining the simulation history file, shown as the red pathway in Figure 5.10. Preserving the history improved convergence behaviour, as restarting from a fresh instance (blue pathway) frequently caused convergence issues at higher tuning factor values, where the solution was too far from the initial conditions.

5.4.2 Interfacial Area

In a packed absorption column, the interfacial area refers to the effective wetted surface area where the liquid solvent and gas stream come into direct contact, enabling the mass transfer of CO_2 to take place. It is widely recognised as the primary bottleneck in the absorption process. Since the overall absorption rate is directly proportional to the IA, simulation predictions are highly sensitive to its value [12,13], with a larger IA allowing for a greater mass transfer rate [14].

Due to real-world inefficiencies that can lead to deviations from idealised performance, it is common practice to adjust the IA within simulation models to better align with actual plant data. Several studies have explicitly documented this approach. For example, Øi et al. found an IA of 0.55 to provide the best fit when validating models against data from the Technology Centre Mongstad (TCM) [15]. In a subsequent study, Øi and Fagerhaim varied the IA from 0.29 to 1.0 across different scenarios when fitting to further TCM data [16]. Separately, Li et al. adjusted the IA from 1.0 to 2.0 in their comparison of simulation and experimental results from the coal-fired Tarong power station in Queensland, Australia, identifying 1.8 as providing good agreement [17]. In another calibration study, Errico et al. used an IA of 1.2 to correct for an underestimation of effective wetted area in their MEA system model [18]. These examples demonstrate that IA adjustment is a critical and widely accepted step in aligning CO_2-MEA absorption simulations with real plant performance, and as such, it was included in the tuning process.

A preliminary sensitivity analysis was conducted to confirm these effects. The IA scale factor was varied from 1.0 to 5.0 in 0.1 increments for the absorber, and from 0.5 to 5.0 for the stripper. Each column was assessed independently with no other changes to the simulation. The results showed that in the absorber, increasing IA generally improved most key performance indicators, with the exception of the absorber MAPE, which worsened. This highlights a critical trade-off in model tuning: while a higher IA increases the column's efficiency, it also alters the reaction rate distribution along the column, affecting the extent of reaction and therefore the solvent loadings. Since the absorber temperature profile is a direct consequence of this distribution, the new profile may deviate more from the experimental data.

In contrast, varying the stripper IA had no impact on solvent loadings, which are determined solely by absorber performance and then matched via the reboiler duty. Instead, changes to the stripper IA affected the rate of desorption, leading to inconsistent changes in SRD and stripper MAPE across different conditions, further highlighting the complexity of these interactions.

5.4.3 Heat Transfer Factor

The heat transfer factor was found to have a negligible effect on the simulation results. This is because heat transfer is not the rate-limiting step in the absorption process. Instead, the dominant factors are the reaction kinetics and the IA [12]. The significant heat observed in the column arises from the rapid, exothermic reaction between CO_2 and MEA, rather than limitations in the system's ability to dissipate heat [19]. As a result, modifying the heat transfer factor does not meaningfully affect the CO_2 capture performance in the simulation, and so was removed from consideration.

5.4.4 Mass Transfer Coefficient Factors

The effects of the liquid and vapour mass transfer coefficient factors are inherently complex due to the influence of chemically enhanced mass transfer. In CO_2 absorption systems, the overall mass transfer rate is not directly proportional to the mass transfer coefficient. Instead, it is governed by the product of the mass transfer coefficient and an enhancement factor, which quantifies how much the chemical reaction accelerates the absorption rate compared to purely physical absorption [20,21].

The enhancement factor itself is a non-linear function of the Hatta number, representing the ratio of the maximum reaction rate within the liquid film to the maximum diffusion rate through the film [12]. As such, applying a scalar adjustment to the mass transfer coefficients alters the Hatta number, which in turn modifies the enhancement factor in a complex and non-linear manner along the column that depends on local temperature and concentrations [12].

Because of this complex interrelationship, tuning the mass transfer coefficient factors lacks transparency and predictability, making them unsuitable for systematic or interpretable model calibration. As a result, these factors were excluded from the tuning process.

5.4.5 Liquid Holdup

The primary role of liquid holdup is to govern the residence time of the liquid phase within a packed column. It is closely linked to reaction conversion, interfacial mass transfer, and overall energy consumption [22]. A packing configuration that produces a higher LH physically retains a larger volume of solvent within the column [23,24]. For a given solvent flow rate, this directly translates into a longer residence time. A longer residence time enhances gas-liquid contact and promotes mass transfer, increasing the extent of reaction and producing higher rich loadings [23,25,26].

To quantify the impact of LH, a preliminary sensitivity analysis was conducted. The LH scale factor in the absorber was varied from 1 to 40 in increments of 1.

The analysis showed that increasing the LH scale factor generally improved the model's alignment with experimental data, particularly with respect to stripper performance and overall energy consumption. As the LH scale factor increased, CO_2 loadings rose, and the SRD decreased. This resulted in better agreement with the stripper temperature profile and improved the stripper MAPE. The effect was more consistent at higher flue gas CO_2 concentrations, which correlated with solvent flow rates above 800 kg/h.

However, a critical trade-off was again observed: while the stripper model improved, the absorber MAPE became inconsistent and frequently worsened. This outcome is a logical consequence of the model's constraints. With the CO_2 capture rate fixed, the model must achieve this target regardless of internal changes. By increasing the LH, the residence time and extent of reaction are enhanced, increasing the solvent loading levels. A higher rich loading leads to a higher lean loading for the same capture efficiency, which lowers the SRD and generally improves alignment of the stripper profile. However, because the absorber temperature profile is a direct result of the exothermic reaction rate, it must adjust to whatever conditions are necessary to meet the fixed capture target, even if those conditions deviate from the experimental data.

This reinforces the rationale behind treating the absorber as a black box in this context and focusing the model calibration on accurately predicting SRD and solvent loadings, rather than replicating the absorber temperature profile in detail.

5.4.6 Tuning Factor Conclusion

After evaluating the different options within the tuning process scope, it was decided to focus on tuning the liquid holdup and interfacial area of the columns. These two factors were selected due to their significant influence on mass transfer, residence time, and ultimately the ability to adjust solvent loadings and energy consumption in the simulation. In contrast, tuning other parameters, such as the heat and mass transfer coefficients, were found to have negligible impact or introduce complex, non-transparent behaviour.

As LH and IA are governed by empirical hydraulic and mass transfer correlations that vary with packing geometry, the calculated values are packing specific [27]. Consequently, the associated tuning factors must be determined separately for each packing configuration. The following section outlines the methodology used to optimise these factors across the range of capture conditions considered in this study.

5.5 Simulation Tuning

5.5.1 Tuning Approach

Tuning began with the absorber, aiming to align the simulated lean and rich loadings as closely as reasonably possible with experimental values. This prioritisation reflects the role of the absorber in setting the solvent chemistry in the simulation model: although the underlying absorption chemistry model remains unchanged, modifications to the absorber, particularly its packing configuration, directly influences the resulting solvent loadings. Where feasible, absorber MAPE was also improved, but this was treated as a secondary objective. Once the absorber tuning was completed, the stripper column was tuned to improve both the SRD and stripper MAPE. These two parameters are strongly linked, so improvements to one were expected to benefit the other.

Initial testing showed that changes in LH had a more pronounced effect on simulation results than IA. Therefore, LH was adjusted first for the absorber, followed by IA. This process was then repeated for the stripper. Once tuning was finalised, all capture conditions were re-run using the updated simulation models, and results were compared against the improvement targets summarised in Table 5.1. The overall tuning workflow is outlined in Figure 5.12, forming the foundation for the ECC model development.

Figure 5.12: Fine tuning process steps to develop ECC model.

All tuning steps were performed using the Python automation script via the red pathway shown in Figure 5.10. In this configuration, the simulation file remained open after convergence, enabling rapid parameter updates and improved convergence stability between successive runs.

5.5.2 Absorber Liquid Holdup Tuning

The five packing configurations listed in Table 5.3 were assessed by varying the absorber LH from 1 to 15 in increments of 1, across all 16 capture conditions. Once the automation script completed, the simulation results were checked for convergence errors. It became apparent that packing configurations 2 and 4 failed to converge under the 25_1100 capture condition, even after manual intervention. As 25_1100 represents a condition towards the upper operating range for solvent flow rate, important for simulating capture from high flue gas CO_2 concentrations, it was essential that the model could converge under this condition. Consequently, packing configurations 2 and 4 were removed from further consideration.

Of the remaining three configurations, packing configurations 1 and 3 exhibited near identical performance across the range of absorber LHs, with less than 1% variation in results. To eliminate redundancy in the tuning process, packing configuration 3 was also removed. This left two packing configurations, 1 and 5, for continued analysis. These are henceforth referred to as the alternative packing (configuration 1) and the original packing (configuration 5).

These two packing configurations were evaluated in more detail against the five performance targets outlined in Table 5.1. The analysis below explores how the differences between simulated and experimental values changed with increasing LH, identifying trends that guided selection of an optimal LH that balances performance across all capture conditions.

For both packings, alignment of the SRD with experimental values generally improved with increasing LH across capture conditions with 25, 20, and 15 mol.% CO_2, except for the 25_800 condition with the alternative packing, where SRD alignment worsened after initially improving. In contrast, 10 mol.% CO_2 conditions showed inconsistent SRD behaviour: 10_300 and 10_400, which operated at lower solvent flow rates, showed rapid worsening SRD alignment with increasing LH, whereas 10_500 and 10_700 showed only marginal improvements with less benefit compared to higher CO_2 concentrations.

Lean loading trends closely followed SRD patterns. For both packings, increasing LH improved alignment to experimental lean loading values under 25, 20, and 15 mol.% CO_2 conditions. The exception was 20_1200 for the alternative packing, where lean loading alignment began to worsen after reaching an optimal LH. For these higher

CO_2 concentrations, LH values above 12 offered the best alignment. In contrast, for 10 mol.% CO_2 conditions, the optimal LH varied widely between 3 and 10, with no consistent pattern.

Rich loading for the alternative packing was relatively insensitive to increasing LH, with no clear trends across conditions. For the original packing, improvements were observed at higher CO_2 concentrations, but again, performance under 10 mol.% conditions generally worsened as LH increased.

Absorber MAPE results displayed inconsistent behaviour across both packing configurations, with no clear correlation to LH. Stripper MAPE typically worsened slowly with increasing LH for both packings, although the changes were modest.

Overall, the 10 mol.% CO_2 conditions were the most problematic, exhibiting erratic performance and weak correlations. It was suspected that the model struggled with simulation stability at lower solvent flow rates, which are characteristic of these conditions. In contrast, higher flow rates, typical of higher CO_2 concentrations, showed better stability and more consistent tuning behaviour. As a result, the 10 mol.% capture conditions were excluded from further tuning efforts. This suggests that it is difficult to tune a simulation model that can accurately represent the extremes of operational ranges in addition to the main operational envelope of the capture plant, and that compromises must be made to focus on specific operating conditions for the best representation of real-world conditions. Consequently, the tuning process was focused on flue gas concentrations of 15 mol.% and above.

Selecting the best overall LH required balancing trade-offs across the five parameters in Table 5.1. Of these, lean loading and SRD were prioritised, as they showed the greatest sensitivity to LH and were most critical to model fidelity. Based on this, an absorber LH of 15 was selected for both the original and alternative packing configurations.

With the absorber LH established, the simulation files for the remaining capture conditions were updated accordingly, and tuning proceeded to the next parameter: absorber IA.

5.5.3 Absorber Interfacial Area Tuning

The absorber IA was varied from 1.0 to 5.0 in increments of 0.1 across the remaining 12 capture conditions, corresponding to flue gas CO_2 concentrations of 25, 20 and 15 mol.%. In this tuning stage, all 12 capture conditions converged successfully across most IA values, enabling straightforward analysis of the resulting trends.

For the original packing, the SRD improved consistently with increasing IA across all capture conditions. For the alternative packing, most conditions followed the same trend, with the exception of 25_800 and 25_900. With 25_800, SRD alignment worsened immediately as IA increased. For 25_900, SRD initially improved before reaching a minimum deviation, and then worsened with further increases in IA.

Lean loading alignment generally improved with increasing IA across both packings. However, two conditions were the exception to this, where 20_1200 and 15_700 showed a worsening lean loading alignment from the outset for both packing configurations.

Rich loading alignment varied more substantially between capture conditions, with only four showing consistent improvement across both packings: 25_900, 25_1000, 20_1000, and 15_800. The remaining eight conditions worsened in alignment as IA increased.

It was observed that changes in SRD and solvent loadings resulting from adjustments to IA were relatively small compared to those achieved through absorber LH tuning, indicating that LH has a stronger influence on simulation results than IA, consistent with preliminary testing.

The effect of IA on absorber MAPE was inconsistent. For both packings, absorber MAPE improved at higher solvent flow rates within each flue gas CO_2 concentration but worsened at lower solvent flow rates. No single IA value improved absorber MAPE across all capture conditions. As such, absorber MAPE was excluded from consideration in IA selection. Improving the absorber MAPE requires further investigation to correctly adjust the column temperature profile, which falls outside the current tuning scope. Stripper MAPE showed negligible variation with changing IA for both packings. Most conditions experienced either no change, or only minor deviations, confirming that the absorber IA has minimal influence on stripper performance.

Given these findings, the absorber IA selection was based solely on its effect on SRD and solvent loadings. For the original packing, selection was relatively straightforward. As SRD alignment improved for all conditions, and lean loading alignment improved in most, an IA of 5.0 was selected. This value offered the greatest overall improvement with minimal detrimental effects on problematic conditions.

For the alternative packing, the absorber IA selection required more careful consideration. While most conditions improved with increasing IA, the 25_800 and 25_900 capture conditions worsened at different respective IA values. To strike a balance, focus was placed on optimising SRD alignment for the 25_900 condition, as it lies near the expected inflection point of the system and should therefore exhibit the lowest SRD. The optimal IA for 25_900 condition was 2.3, which had the best SRD alignment. While SRD alignment at 25_800 worsened slightly at this IA, the trade-off was considered acceptable, as the model is expected to transition into the exponential region at this point with higher SRD. Moreover, an IA of 2.3 provided modest improvements to SRD and solvent loadings across the remaining conditions.

With absorber tuning now completed, attention tuned to the stripper tuning phase, beginning with the adjustment of stripper LH using the updated simulation files incorporating the tuned absorber settings.

5.5.4 Stripper Liquid Holdup Tuning

The stripper LH was varied from 1 to 15 in increments of 1 across the 12 capture conditions with flue gas CO_2 concentrations of 25, 20 and 15 mol.%. All conditions converged successfully across most LH values, enabling straightforward analysis of the resulting trends.

As expected, changes to the stripper LH did not affect the solvent CO_2 loadings or the absorber MAPE for any condition. This is because the stripper does not directly influence the absorption process in the simulation. Instead, the simulation adjusts the reboiler duty to equal the lean loading in the outgoing hot lean solvent to that of the absorber lean loading, representing a closed-loop solvent circulation. Accordingly, the only parameters impacted by stripper tuning are those directly associated with the stripper: the SRD and the stripper MAPE.

For both packing configurations, increasing the stripper LH generally led to slight improvements in SRD alignment. However, two capture conditions exhibited more pronounced responses. For the 25_800 condition, SRD alignment rapidly worsened with increasing LH, particularly for the original packing. For the 25_900 condition, SRD alignment improved significantly with increasing LH for the original packing, but worsened for the alternative packing, highlighting subtle behavioural differences between the packing configurations.

In general, increasing the stripper LH worsened the stripper MAPE for capture conditions with lower solvent flow rates, primarily found in the 15 and 20 mol.% CO_2 conditions. In contrast, for conditions with higher solvent flow rates, namely the 25 mol.% CO_2 conditions and the upper end of the 20 mol.% CO_2 conditions, the stripper MAPE improved with increasing LH. However, a few exceptions to this pattern were noted. For the 15_800 condition, stripper MAPE improved with increasing LH in the original packing, while remaining unaffected in the alternative packing. For the 25_1000 and 20_1000 conditions, the stripper MAPE worsened with increasing LH in the alternative packing but improved in the original packing.

The stripper LH selection aimed to balance improvements in both SRD and stripper MAPE across all conditions. However, no single LH value produced universal improvement. The conflicting trends observed in 25_800 and 25_900, which had already influenced absorber IA selection, were again central to the decision-making process. Ultimately, the final selection was an LH of 4 for the original packing, and an LH of 5 for the alternative packing.

Following this, the simulation files were updated accordingly. The tuning process then proceeded to the final step: assessment of the impact of stripper IA on model performance across the capture conditions.

5.5.5 Stripper Interfacial Area Tuning

The stripper IA was varied from 0.5 to 5.0 in increments of 0.1 across the 12 capture conditions with flue gas CO_2 concentrations of 25, 20 and 15 mol.%. All conditions converged successfully across most IA values, enabling straightforward analysis of the resulting trends. As with the stripper LH tuning, changes to the stripper IA did not affect the solvent loadings or absorber MAPE. The only parameters influenced were the SRD and stripper MAPE.

For both packing configurations, SRD alignment was relatively insensitive to IA variation above 1.0, with worsening that was largely negligible. However, when stripper IA dropped below 1.0, SRD alignment improved more drastically, with optimal alignment occurring closer to 0.5, suggesting this lower range held the more potential for improvement. Once again, the 25_800 and 25_900 conditions complicated the selection. Lowering IA improved SRD alignment for 25_800, but worsened it for 25_900, indicating a trade-off was necessary.

The stripper MAPE followed similar trends, but with greater sensitivity. Above an IA of 1.0, the stripper MAPE generally worsened more rapidly than SRD. While values below 1.0 tended to improve MAPE, several conditions deviated from this trend. For the original packing, conditions, 25_800, 25_900, 20_1100, and 20_1200 had minimum MAPE values at stripper IAs between 1.4 and 1.7. For the alternative packing, conditions 20_1100 and 20_1200 showed best alignment at stripper IAs of 1.3 and 1.4, respectively.

As no single IA value provided universal improvement across all capture conditions, a balanced approach was necessary. The selection prioritised stripper MAPE, given how rapidly it could worsen with poorly chosen IA values. The SRD results, especially for 25_800 and 25_900, were also considered. Ultimately, the final selection kept the IA at 1.0 for the original packing and set the IA to 0.8 for the alternative packing. With this final tuning step complete, all simulation files were updated with the selected stripper IA values.

5.5.6 Tuning Summary

A summary of the tuning choices for all investigated parameters is presented in Table 5.4, concluding the full model tuning process originally outlined in Figure 5.12.

Table 5.4: Summary of selected tuning factors for the two column packing configurations.

Tuning Factors	**Packing Configuration**	
	Original Packing	**Alternative Packing**
Absorber Packing	Flexipac/Koch/Metal/1X	Mellapak/Sulzer/Standard/750Y
Absorber LH	15	15
Absorber IA	5.0	2.3
Stripper Packing	IMTP/Koch/Metal/1 in or 25 mm	Raschig/Norton/Metal-16/0.625 in or 16 mm
Stripper LH	4	5
Stripper IA	1.0	0.8

With the liquid holdups and interfacial areas selected for both columns across the two packing configurations, the simulations are now ready for performance assessment. Each capture condition can now be evaluated for how closely it aligns with the experimental data. To quantify the improvements achieved through the tuning process, the results will be compared against those from the initial DCC model, providing a clear benchmark for relative model performance.

5.6 Comparison of Tuned Column Packing Configurations

With both the original and alternative packing configurations now tuned, their performance must be assessed against the experimental data. For reference, results from the initial DCC model are also included to evaluate the extent of improvements achieved through the tuning process. The DCC model had all tuning parameters set to 1 except for the absorber IA, which was set to 1.2. This configuration is described in detail in Chapter 3.

The evaluation of model performance is based on the established improvement targets outlined in Table 5.1, which serve as the benchmark for assessing the effectiveness of the tuning conducted on both packing configurations.

5.6.1 Specific Reboiler Duty Comparison

The SRD differences are first assessed across the 12 capture conditions to determine whether energy demand aligns more closely with experimental values following tuning. Figure 5.13 presents the absolute SRD differences between the different packing configurations and the experimental data.

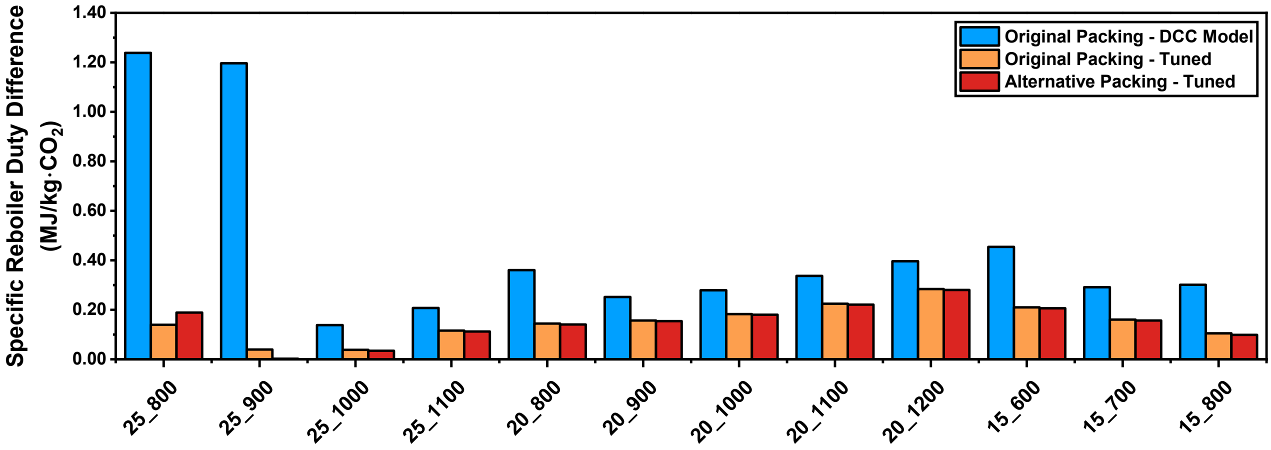

Figure 5.13: Difference in SRD between different column packing configurations and experimental results for capture conditions targeting 90% capture efficiency from a 150 Nm^3/h gas flow.

Both tuned packing configurations significantly reduced SRD differences relative to the DCC model across all capture conditions. The greatest improvements occurred at the outlier conditions, 25_800 and 25_900, which were particularly problematic in the DCC model. While the tuned packings show close agreement across most conditions, they begin to diverge at the same 25_800 and 25_900 conditions, a result of the compromises made during tuning. As discussed previously, tuning was prioritised to bring 25_900 as close to the experimental value as possible, due to its role as the system's approximate inflection point.

The average absolute SRD differences across the 12 capture conditions are:

- DCC model: 0.454 $MJ/kg{\cdot}CO_2$
- Tuned original packing: 0.150 $MJ/kg{\cdot}CO_2$
- Tuned alternative packing: 0.148 $MJ/kg{\cdot}CO_2$

The target for improvement was to reduce the average absolute SRD difference to within 0.2 MJ/kg·CO_2. As shown, the tuned packings fall well within this threshold, indicating that the tuning process has successfully met the SRD alignment goal.

Figure 5.14 presents the actual SRD values for each capture condition, comparing the two tuned packings, the DCC model, and the experimental results.

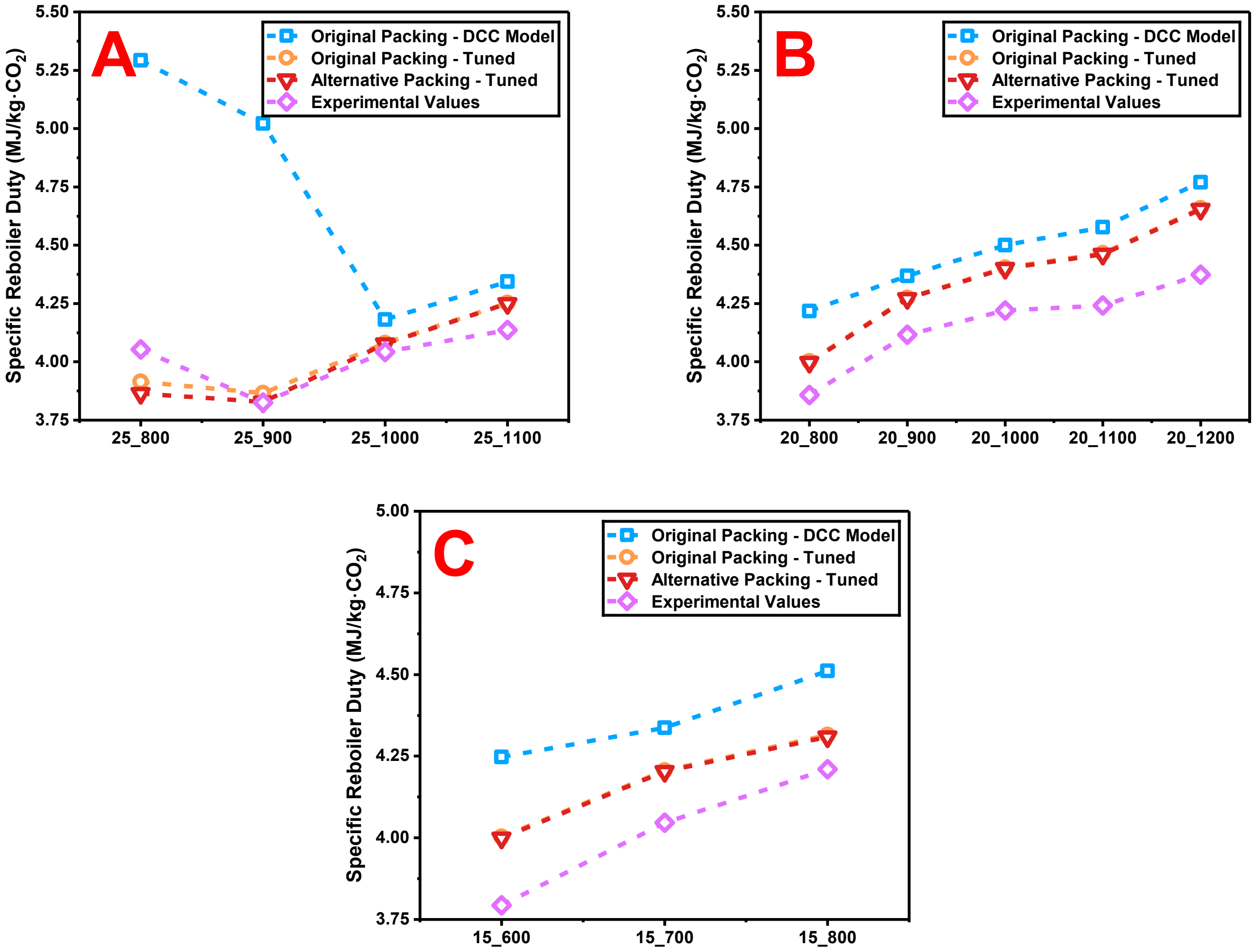

Figure 5.14: SRD against solvent flow rate for different CO_2 concentrations in a 150 Nm^3/h gas flow targeting 90% capture efficiency: (A) 25 mol.% CO_2, (B) 20 mol.% CO_2, and (C) 15 mol.% CO_2.

From Figure 5.14, it is evident that the tuned original and alternative packing configurations yield nearly identical SRD values across most conditions, with such consistency between these conditions that the results from the original packing are often visually overlaid by those from the alternative packing. The DCC model consistently overestimated SRD across all capture conditions, particularly for 25_800 and 25_900. In contrast, the tuned configurations still slightly overestimate SRD at the 20 and 15 mol.% CO_2 conditions but show close alignment with experimental values at 25 mol.% CO_2. Furthermore, the shape of the trendlines for the tuned packings closely follows the experimental trends, reinforcing the improvement in model accuracy.

5.6.2 Lean Loading Comparison

Next, the lean solvent loadings are assessed for each capture condition to evaluate whether the absorption chemistry of the models aligns more closely with experimental values following tuning. Figure 5.15 presents the absolute lean loading differences between the different packing configurations and the experimental data.

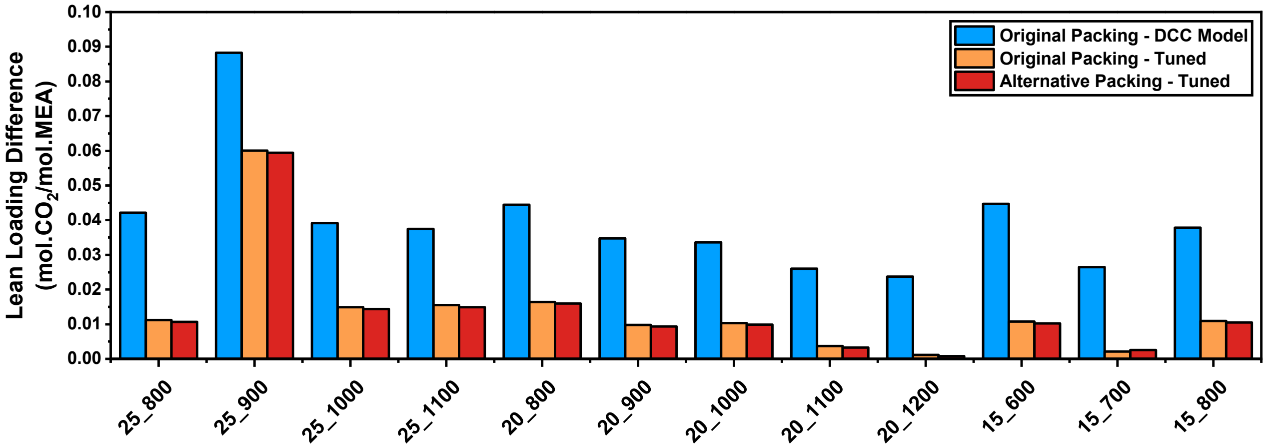

Figure 5.15: Difference in lean solvent loading between different column packing configurations and experimental results for capture conditions targeting 90% capture efficiency from a 150 Nm^3/h gas flow.

From Figure 5.15, it is evident that the tuned packing configurations demonstrate a significantly improved alignment to the experimental values, with the lean loading differences notably reduced across all 12 capture conditions compared to the DCC model. The tuned original and alternative packings display a near-identical performance, with very similar lean loading differences for each case.

The average absolute lean loading differences across the 12 capture conditions are:

- DCC model: 0.0399
- Tuned original packing: 0.0139
- Tuned alternative packing: 0.0135

The target for improvement was to reduce the average absolute lean loading difference to within 0.01. As shown, the tuned packings fall just outside this threshold. However, earlier discussions in Chapter 4 identified the lean loading of the 25_900 capture condition as potentially anomalous, due to being significantly higher than expected. When this condition is omitted from the average, the adjusted values improve to:

- Tuned original packing: 0.0097
- Tuned alternative packing: 0.0093

With this consideration, the lean loading values are within the targeted improvement threshold of 0.01, indicating that the tuning process has successfully met the lean loading alignment goal.

Figure 5.16 presents the actual lean loading values for each capture condition, comparing the two tuned packings, the DCC model, and the experimental results.

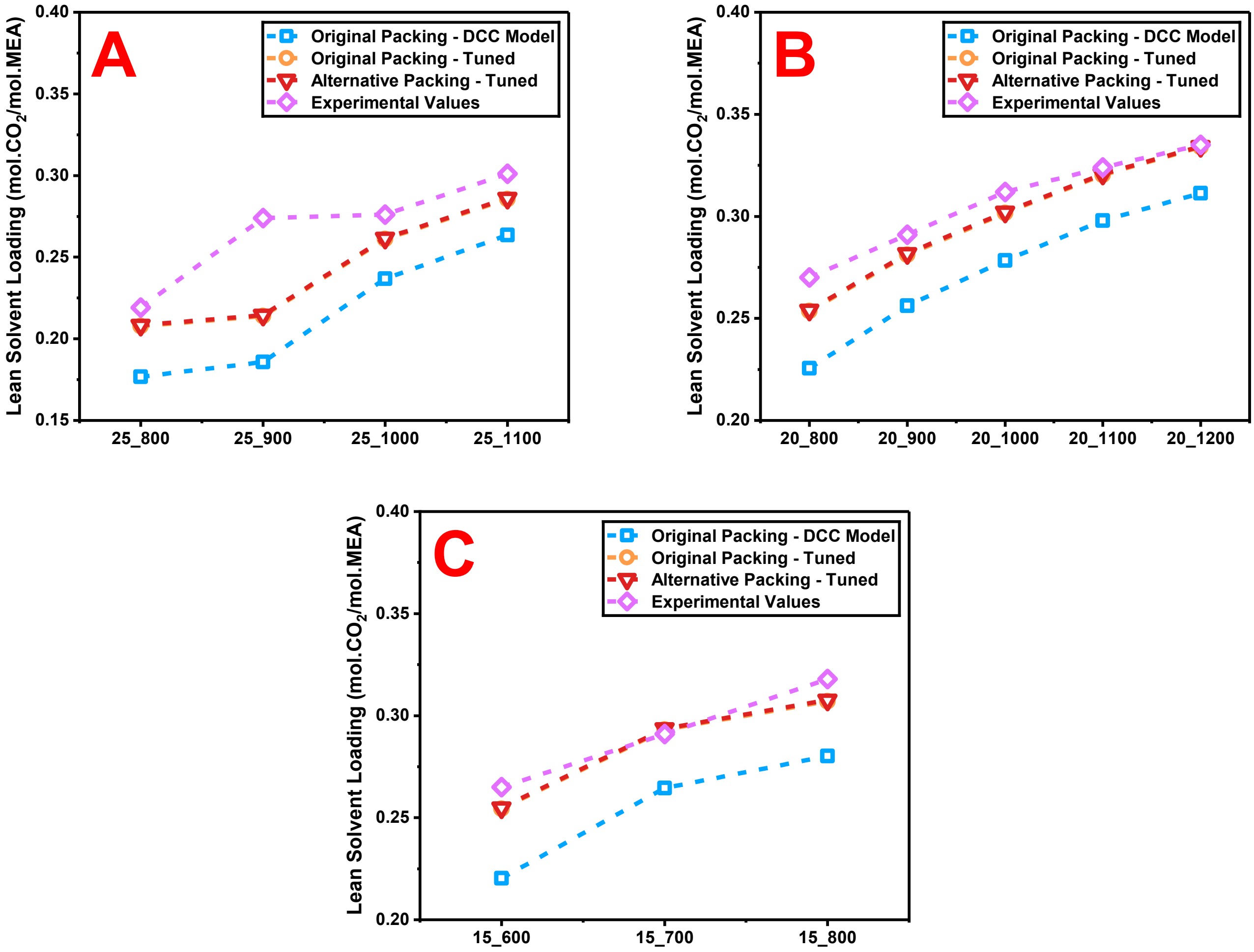

Figure 5.16: Lean solvent loading against solvent flow rate for different CO_2 concentrations in a 150 Nm^3/h gas flow targeting 90% capture efficiency: (A) 25 mol.% CO_2, (B) 20 mol.% CO_2, and (C) 15 mol.% CO_2.

From Figure 5.16, the tuned original and alternative packing configurations are again very closely aligned, with the original packing trends often overlaid by the alternative packing trends due to their proximity. Across all conditions, the tuned packings consistently predict higher lean loadings than the DCC model, bringing them closer to the experimental values. The overall shape and trend of the simulated lean loadings is preserved after tuning, which supports the quality of the model adjustments.

While the tuned configurations still slightly underpredict lean loading on average, the difference lies within the acceptable target range for improvement. Furthermore, Figure 5.16A highlights the outlier behaviour of the 25_900 condition, reinforcing the idea that its experimental lean loading value may be anomalous.

5.6.3 Rich Loading Comparison

Following the assessment of lean solvent loading, the rich solvent loadings are assessed for each capture condition. Figure 5.17 presents the absolute rich loading differences between the different packing configurations and the experimental data.

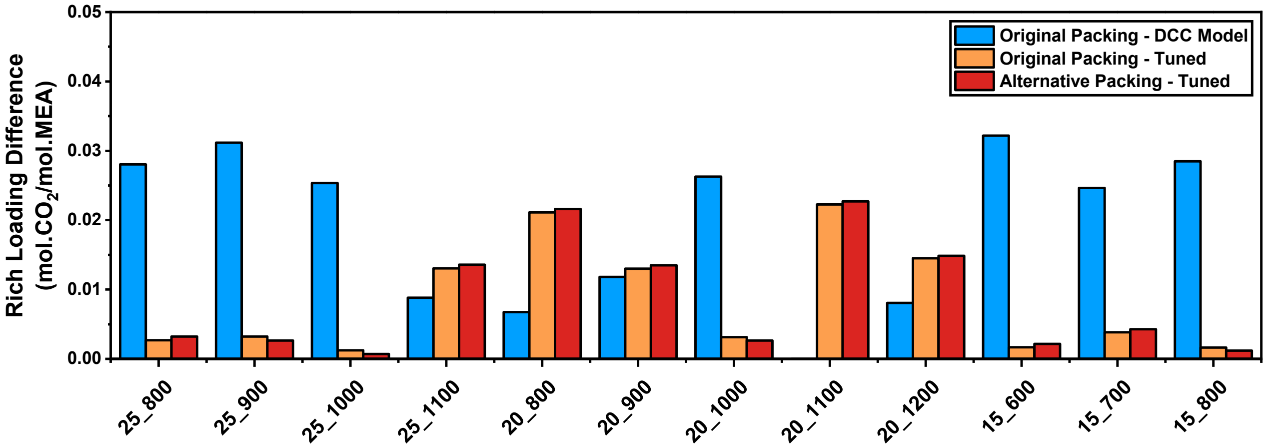

Figure 5.17: Difference in rich solvent loading between different column packing configurations and experimental results for capture conditions targeting 90% capture efficiency from a 150 Nm^3/h gas flow.

From Figure 5.17, it is evident that the tuned packing configurations achieved improved alignment with experimental values in 8 out of the 12 capture conditions. While the improvements are more varied than those observed for lean loading, the overall average absolute differences remain lower. In contrast to the lean loading, the DCC model was already reasonably close to the experimental values in some conditions, which meant the margin for improvement was smaller.

The average absolute rich loading differences across the 12 capture conditions are:

- DCC model: 0.0193
- Tuned original packing: 0.0084
- Tuned alternative packing: 0.0086

The target for improvement was to reduce the average absolute rich loading difference to within 0.01. As shown, the tuned packings fall within this threshold, indicating that the tuning process has successfully met the rich loading alignment goal.

Figure 5.18 presents the actual values of rich solvent loadings for each capture condition, comparing the two tuned packings, the DCC model, and the experimental results.

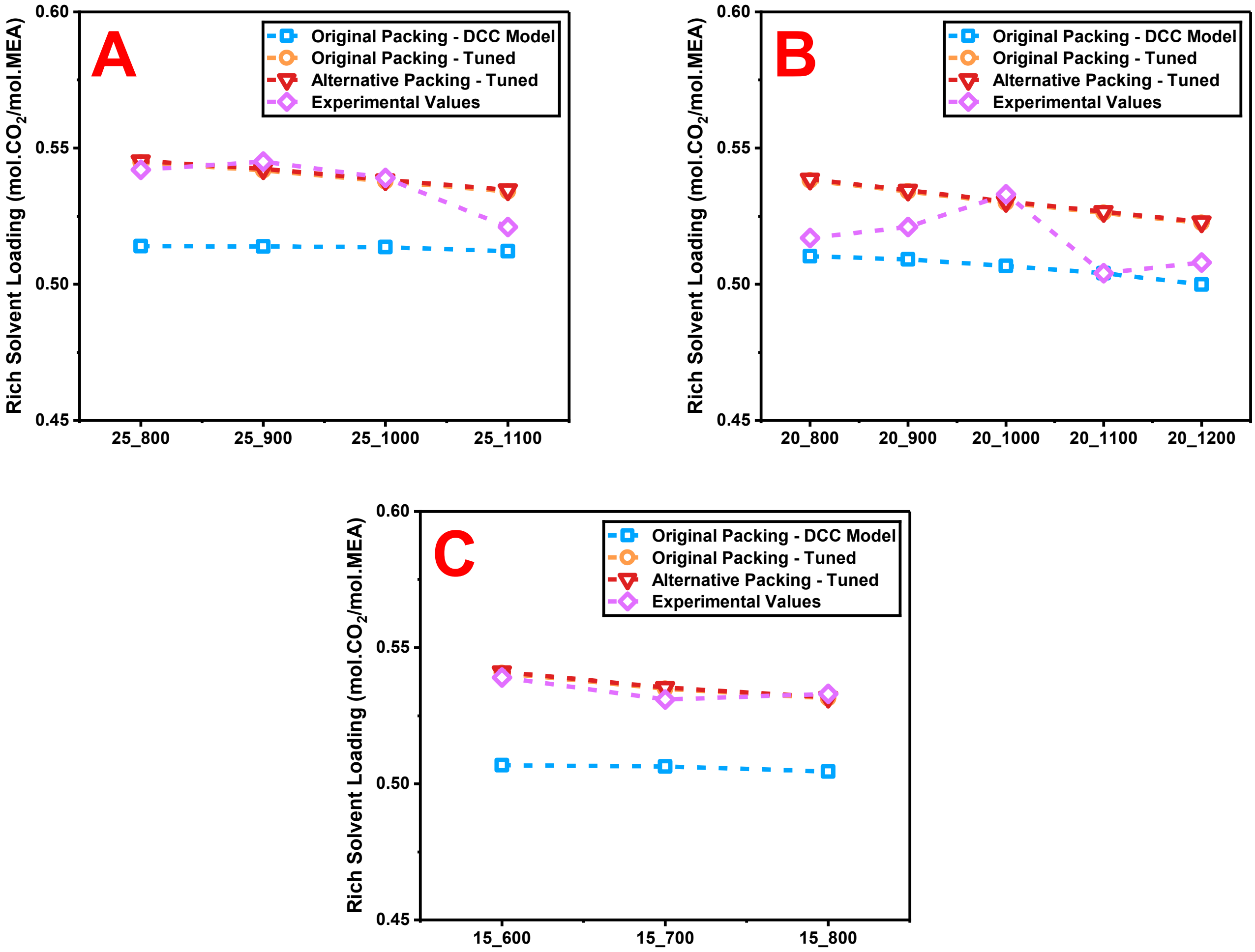

Figure 5.18: Rich solvent loading against solvent flow rate for different CO_2 concentrations in a 150 Nm^3/h gas flow targeting 90% capture efficiency: (A) 25 mol.% CO_2, (B) 20 mol.% CO_2, and (C) 15 mol.% CO_2.

From Figure 5.18, it can be seen that the tuned original and alternative packing configurations produce nearly identical values, with the alternative packing trends often overlaying the original packing trends due to their proximity. The shape of the trendlines is preserved across the tuning, consistent with the behaviour observed for the lean loading results. Figure 5.18A shows good agreement between tuned packings and experimental values across the 25 mol.% CO_2 conditions, though the experimental value at 25_1100 appears lower than expected. The good agreement is also demonstrated in Figure 5.18C for the 15 mol.% CO_2 conditions, with the tuned packings offering a clear improvement over the DCC model.

Figure 5.18B indicates, however, that for the 20 mol.% CO_2 conditions, the tuned packings slightly overpredict the rich loadings compared to experimental values. Notably, the 20_1000 condition, previously thought to have an overly high experimental rich loading, aligns closely with the tuned packings. This suggests the experimental rich loadings for the remaining 20 mol.% CO_2 conditions may actually be somewhat low, especially compared to the other CO_2 conditions. Despite these inconsistencies in experimental values, the tuned packings provide rich loadings that are within target range and follow expected loading behaviour, reinforcing confidence in the tuning outcomes.

5.6.4 Solvent Cyclic Capacity Comparison

The solvent cyclic capacities are assessed for each capture condition to ensure the solvent loading changes have not affected the capacity of the solvent. Figure 5.19 presents the absolute solvent cyclic capacity differences between the different packing configurations and the experimental data.

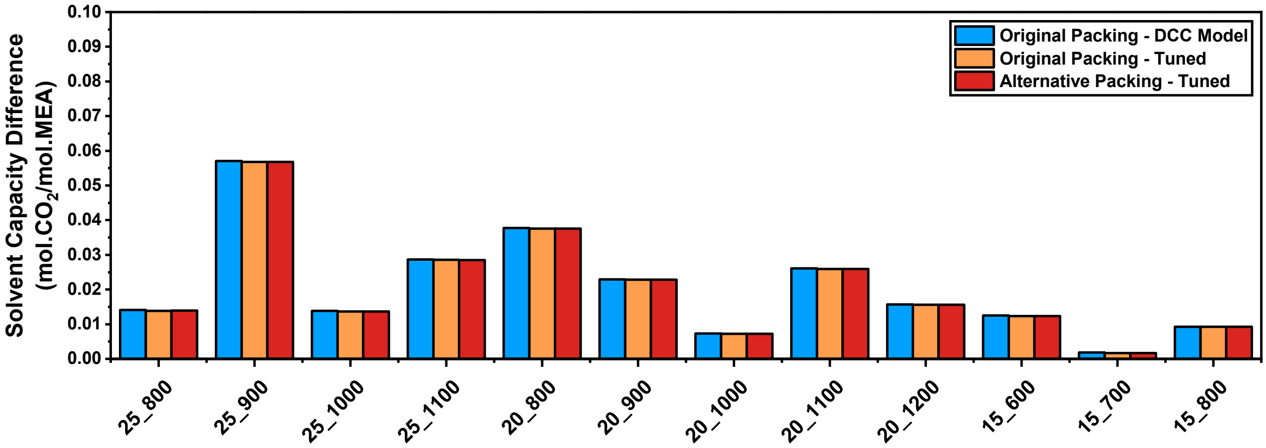

Figure 5.19: Difference in solvent cyclic capacity between different column packing configurations and experimental results for capture conditions targeting 90% capture efficiency from a 150 Nm^3/h gas flow.

As expected, Figure 5.19 confirms that the tuning of the column packings did not affect the fundamental solvent chemistry of the simulation models. The DCC model and tuned packing configurations produce near identical solvent cyclic capacity differences across all 12 capture conditions. This result was anticipated because the solvent cyclic capacity is primarily governed by the capture efficiency achieved at each condition and so would be the same for each packing configuration.

5.6.5 Absorber Temperature Profile Comparison

With the SRD and the solvent loadings assessed, attention now turns to the absorber column temperature profiles. Figure 5.20 presents the absorber MAPEs between the different packing configurations and the experimental data.

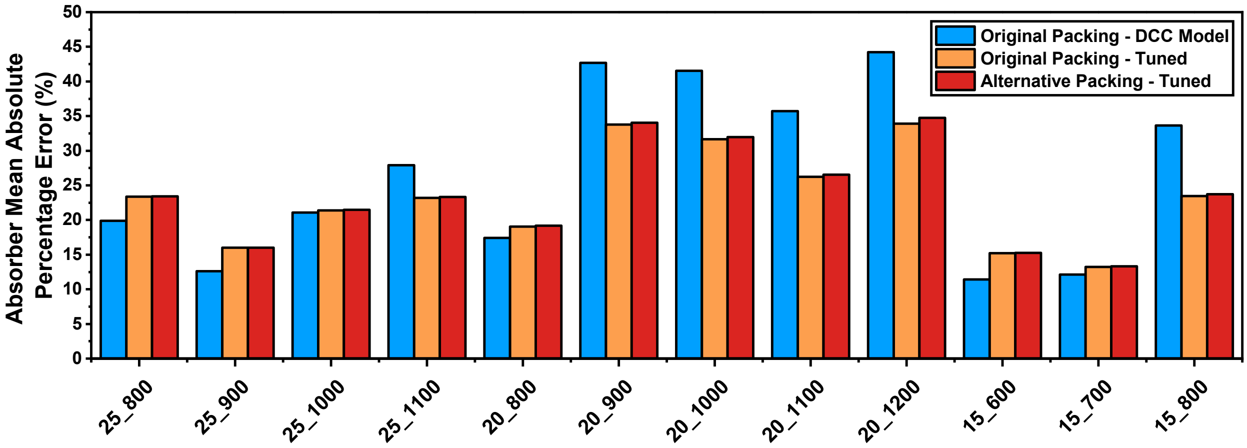

Figure 5.20: Absorber MAPEs between different column packing configurations and experimental results for capture conditions targeting 90% capture efficiency from a 150 Nm^3/h gas flow.

As previously noted during the tuning process, improving absorber temperature profile alignment often came into direct conflict with optimising other parameters such as the lean solvent loading and SRD. In its current state, the simulated absorber column struggles to replicate the experimental absorber temperature profiles across all 12 capture conditions. Figure 5.20 shows that the tuned packing configurations only offer marginal improvements in absorber MAPE for half of the capture conditions. For the remaining conditions, tuning has led to worse absorber MAPE compared to the DCC model.

The average absorber MAPE across all capture conditions are:

- DCC model: 26.69%
- Tuned original packing: 23.37%
- Tuned alternative packing: 23.58%

The target for improvement was to reduce the absorber MAPE to within 10%, meaning that none of the packing configurations achieved the desired improvement. Despite these shortcomings, the simulation still achieves the required capture efficiency around the absorber column across all conditions, with improved solvent loadings and SRD as previously discussed. This reinforces the notion that the absorber can be treated as a functional black box, where the internal temperature distribution may not match the experimental measurements precisely, but the overall system performance is maintained.

Figure 5.21 presents the absorber temperature profiles for three different capture conditions to illustrate the discrepancies in profile shape for the different packing configurations and experimental results.

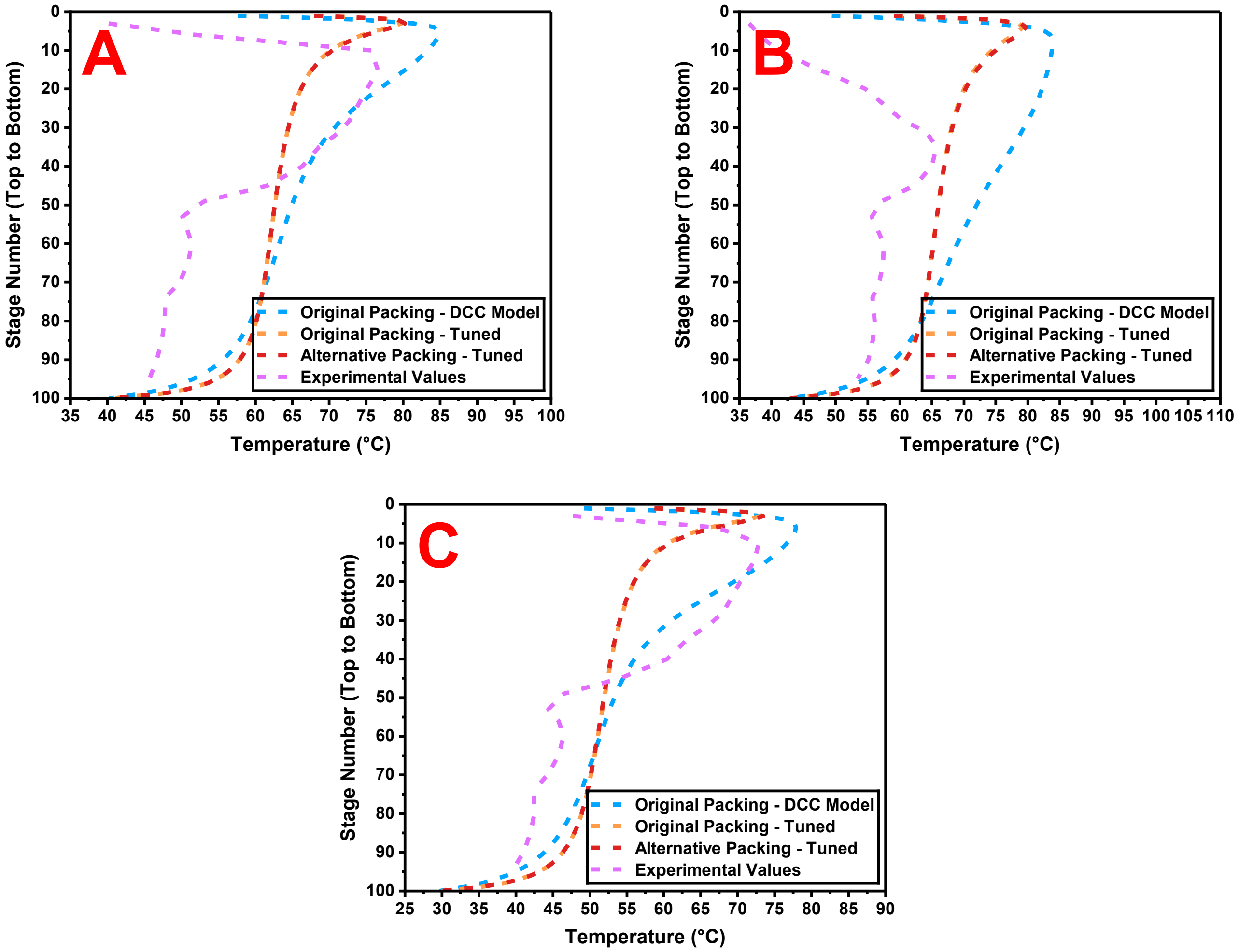

Figure 5.21: Absorber temperature profiles for different column packing configurations and experimental results for capture conditions: (A) 25_1000, (B) 20_1100, and (C) 15_600.

From Figure 5.21, several trends are evident. The profile of the tuned original packing is overlaid by the profile of the tuned alternative packing due to them producing virtually identical temperature profiles. These profiles exhibit rich-pinched behaviour with a sharp temperature peak at the very top of the absorber, followed by rapid cooling. This indicates that the reaction zone is compressed into the very top of the column.

In contrast, the DCC model produces broader, smoother temperature profiles, suggesting a wider reaction zone across the upper section of the absorber. For condition 15_600, the DCC model profile more closely resembles the experimental temperature profile, despite its higher MAPE.

For conditions 25_1000 and 20_1100, the tuned packing configurations yield lower MAPE values, but their profile shapes do not align with the experimental profiles, highlighting a limitation in using MAPE as a standalone metric.

This comparison reveals that the MAPE alone may be insufficient to assess temperature profile alignment, as different profile shapes can produce similar MAPE values. Therefore, visual inspection remains a critical tool in evaluating simulation accuracy, particularly when temperature gradients and reaction zones are involved.

5.6.6 Stripper Temperature Profile Comparison

With the limitations of MAPE highlighted in the absorber analysis, where a lower MAPE did not necessarily indicate realistic temperature profile shapes, the stripper temperature profiles are now assessed using both MAPE values and direct visual inspection. Figure 5.22 presents the stripper MAPEs between the different packing configurations and the experimental data.

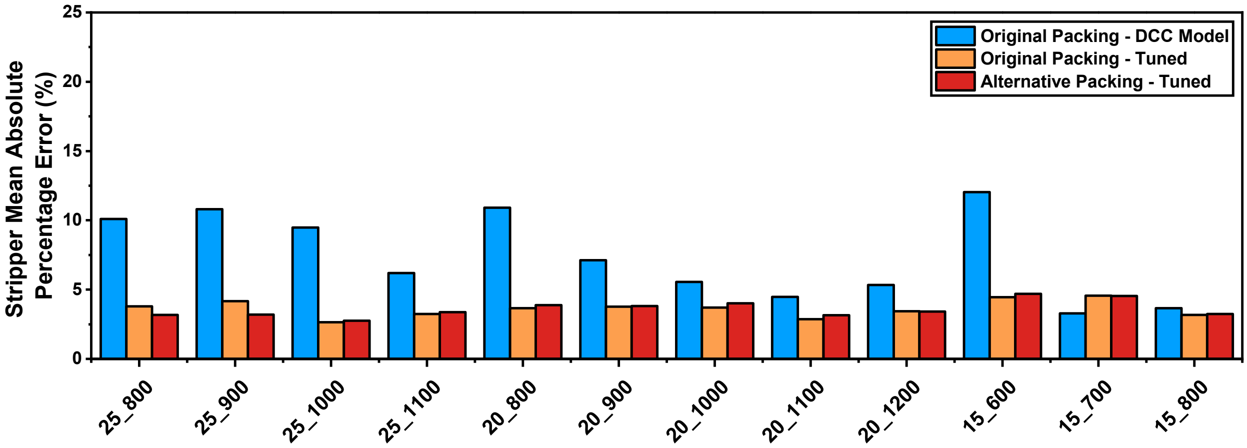

Figure 5.22: Stripper MAPEs between different column packing configurations and experimental results for capture conditions targeting 90% capture efficiency from a 150 Nm^3/h gas flow.

Unlike with the absorber column, stripper MAPEs demonstrate a clear and consistent improvement following packing tuning. Figure 5.22 shows the tuned packing configurations yield lower MAPE values than the DCC model for 11 out of 12 capture conditions, implying a strong enhancement in stripper temperature profile alignment.

The average stripper MAPE across all capture conditions are:

- DCC model: 7.41%
- Tuned original packing: 3.62%
- Tuned alternative packing: 3.60%

The target for improvement was to reduce the stripper MAPE to within 5%. As shown, the tuned packings fall well within this threshold, indicating that the tuning process has successfully met the stripper MAPE alignment goal. These improvements can be attributed in part to the improved alignment of solvent loadings, which directly influence SRD and the associated stripper temperature profiles for each condition.

While MAPE provides a useful performance indicator, visualising the actual temperature profile remains essential for interpreting how closely the model reflects real column behaviour. Subtle differences in the shape of the profile can reflect different thermodynamic and kinetic behaviours within the stripper, which will not be evident from MAPE values alone. Having an improved temperature profile fit allows for better insight into the column operation, where it is possible to optimise a capture condition based on information from the stripper temperature profile alone.

Figure 5.23 presents the stripper temperature profiles of three different capture conditions, selected to illustrate improvements and remaining limitations in the simulations across the different packing configurations.

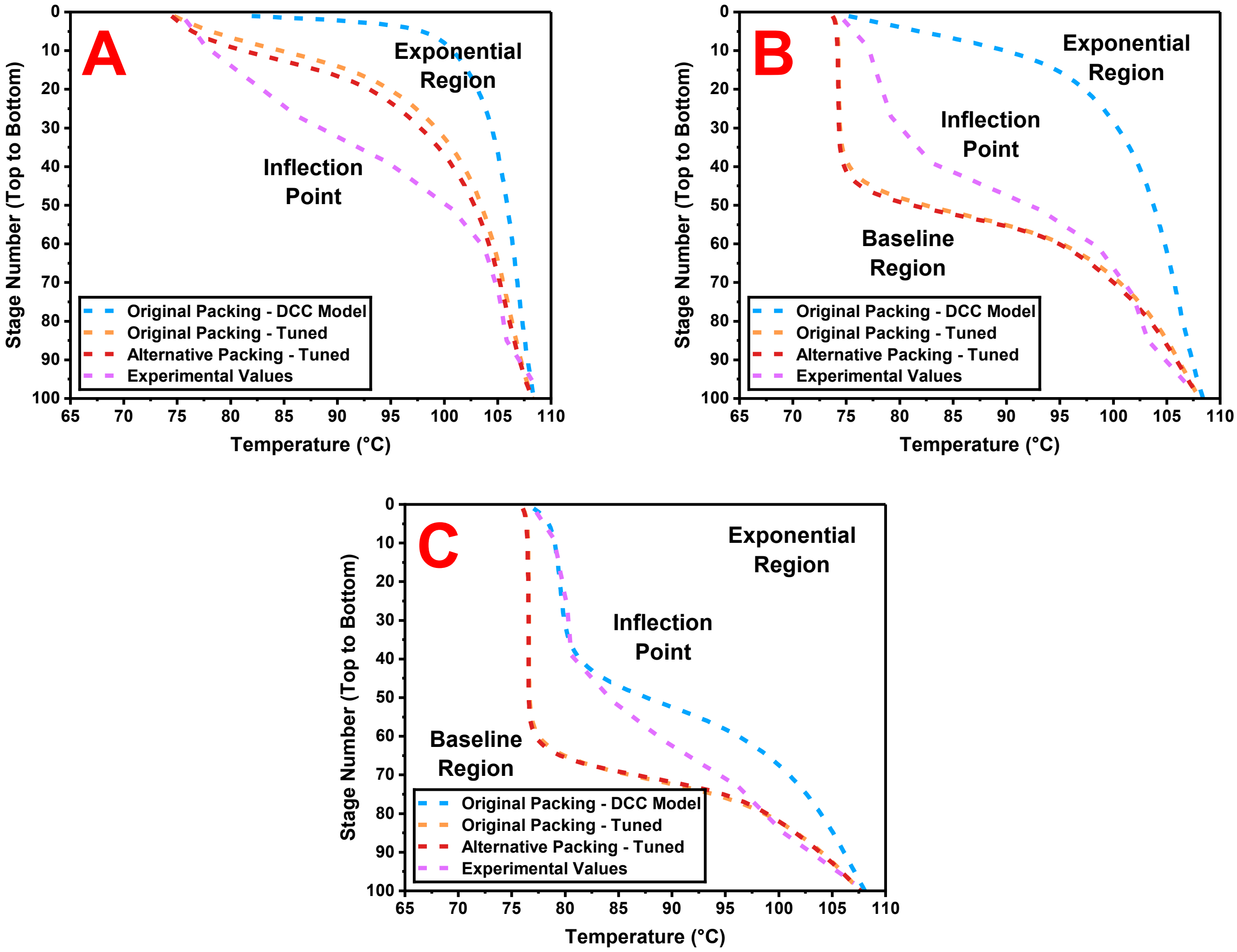

Figure 5.23: Stripper temperature profiles for different column packing configurations and experimental results for capture conditions: (A) 25_900, (B) 20_800, and (C) 15_700.

In Figure 5.23, just like with the absorber temperature profiles previously, the profile of the tuned original packing is overlaid by the profile of the tuned alternative packing due to them producing virtually identical temperature profiles.

For capture conditions 25_900 and 20_800, the tuned packings show clear improvements in temperature profile alignment, moving away from the exponential regions occupied by the DCC model. For 25_900, the tuned packing profiles shift towards the inflection point of the experimental profile, better representing the expected temperature gradient in the stripper. For 20_800, the tuned packing profiles reside in the baseline region of the stripper in agreement with the experimental profile, whereas the DCC model sits in the exponential region, indicating a fundamental issue with how the DCC model represents the capture condition.

In contrast, capture condition 15_700 was chosen as the only condition where the DCC model yields a lower MAPE than the tuned packings. The DCC model aligns more closely with the experimental profile towards the top of the column but diverges across the middle and bottom sections. The tuned packings deviate near the top but align more closely near the bottom. Despite a higher MAPE, the tuned packings are considered more representative of the expected baseline operation, particularly across the column's midsection, where the DCC model drifts toward the exponential region.

In summary, the stripper MAPEs suggest strong improvements with tuning, and the visual inspection confirms that these improvements generally reflect more realistic and representative temperature profiles within the stripper. This combined approach of using both numerical and graphical evaluations when assessing simulated column temperature profiles greatly increases confidence in the accuracy of simulated outcomes.

5.6.7 Selecting the Optimal Packing Configuration for the ECC Model

Comparing the two tuned packing configurations against the experimental data from the TERC ACP reveals that both configurations perform remarkably similarly. Each tuned packing delivers improved SRD, solvent loadings, and stripper temperature profiles compared to the DCC model, meeting the established performance improvement targets across all key metrics

Initially it was hypothesised that the alternative packing configuration might outperform the actual packing used in the absorber, by theoretically having a foundation in the un-tuned packing that more closely aligned to the real-world experimental conditions. However, the close alignment between the tuned original and tuned alternative packings was an unexpected result.

This outcome has notable implications:

- Firstly, it demonstrates that a packing configuration can be effectively tuned to closely match experimental values even if it is not the actual packing employed in the real-world system. This is valuable in cases where Aspen Plus may lack the exact packing data, in the case of new products entering the market for use.
- Secondly, it suggests that modelling efforts should prioritise tuning the real packing configuration rather than exploring alternative packings, since the latter does not provide a significant accuracy advantage once tuning is applied.

Future work should consider investigating additional tuning parameters omitted from this study, to determine if they might differentiate the packings more clearly. Further simulation modifications to the absorber column itself could also be explored to improve agreement with experimental results.

The purpose of this study was to inform the packing choice within the ECC model, tuned specifically for the TERC ACP, to provide rapid simulation results for capture conditions with elevated flue gas CO_2 concentrations and reduce reliance on extensive experimental campaigns. Considering the results, the tuned original packing configuration was selected for use in the ECC model because the tuned alternative packing did not provide substantial additional benefits. Table 5.5 presents the full results of the simulated capture conditions using the tuned original packing within the ECC model, including column MAPEs and absolute differences relative to experimental data.

In the following section, the ECC model is applied to extend the scope of the experimental campaign, filling gaps between capture conditions and providing predictions for flue gas compositions containing 30 mol.% CO_2, which were beyond the scope of the original experimental campaign.

Table 5.5: ECC model simulation results of the experimental capture conditions.

Parameter	Units	25_800	25_900	25_1000	25_1100	20_800	20_900	20_1000	20_1100	20_1200	15_600	15_700	15_800
CO_2 in Flue Gas	vol.%	24.42	24.99	24.99	24.99	20.18	20.18	20.11	20.11	20.07	15.14	15.00	15.04
H_2O in Flue Gas	vol.%	0.78	0.78	0.78	0.78	0.52	0.52	0.43	0.43	0.67	0.74	0.69	0.65
Overall Solvent Mass Flow	kg/h	797.88	887.43	996.56	1096.08	796.84	897.89	997.54	1099.02	1199.69	598.47	700.35	797.95
Solvent MEA + H_2O Flow	kg/h	758.44	842.68	936.2	1023.68	747.99	837.56	925.83	1015.37	1104.34	562.14	651.67	740.12
Solvent MEA Mass Flow	kg/h	263.39	290.3	320.82	351.95	267.38	297.78	329.94	362.49	396.34	198.32	230.51	261.38
Solvent H_2O Mass Flow	kg/h	495.05	552.38	615.38	671.73	480.61	539.78	595.89	652.88	708	363.82	421.16	478.74
Solvent CO_2 Mass Flow	kg/h	39.44	44.75	60.36	72.40	48.85	60.33	71.71	83.65	95.35	36.33	48.68	57.83
Flue Gas Mass Flow	kg/h	222.48	223.08	221.62	221.62	214.99	214.99	214.98	216.41	217.75	211.29	209.69	216.86
Flue Gas CO_2 Mass Flow	kg/h	73.64	75.36	74.87	74.87	59.93	59.93	59.72	60.12	60.43	45.30	44.57	46.20
Flue Gas Volumetric Flow	m^3/h	159.90	160.09	158.49	158.67	155.97	156.21	156.52	158.07	160.17	159.17	157.25	161.51
Liquid to Gas Ratio	kg/kg	3.59	3.98	4.50	4.95	3.71	4.18	4.64	5.08	5.51	2.83	3.34	3.68
Solvent to CO_2 Ratio	kg/kg	10.30	11.18	12.50	13.67	12.48	13.98	15.50	16.89	18.27	12.41	14.62	16.02
Flue Gas Temperature	°C	11.74	12.08	11.07	11.40	8.93	9.37	9.92	10.84	12.55	12.45	11.01	9.17
Lean Solvent Temperature	°C	33.90	37.08	37.31	38.11	30.25	31.13	33.46	35.87	37.39	28.25	30.33	31.88
Lean Solvent Concentration	wt.%	33.03	32.73	32.21	32.13	33.57	33.18	33.09	33.00	33.05	33.15	32.93	32.77
Rich Solvent Concentration	wt.%	32.12	31.91	31.43	31.36	32.60	32.24	32.22	32.20	32.28	32.30	32.15	32.03
Lean Loading	mol/mol	0.2078	0.2140	0.2611	0.2855	0.2536	0.2812	0.3016	0.3203	0.3339	0.2543	0.2931	0.3071
Rich Loading	mol/mol	0.5447	0.5418	0.5378	0.5341	0.5381	0.5340	0.5299	0.5262	0.5225	0.5407	0.5348	0.5314
Loading Capacity	mol/mol	0.3369	0.3278	0.2766	0.2485	0.2845	0.2528	0.2282	0.2060	0.1886	0.2864	0.2417	0.2243
Absorber Bottom Temperature	°C	35.43	37.75	40.49	42.69	35.43	38.29	40.68	42.86	45.11	29.88	33.29	35.32
Cross Heat Exchanger Duty	kW	26.78	30.12	31.77	33.47	27.84	28.18	31.08	35.80	36.62	23.63	27.47	30.80
Cross Heat Exchanger Temperature Approach	°C	36.45	33.83	33.54	32.94	34.90	36.20	34.13	30.47	30.57	35.03	32.10	30.92
Stripper Bottom Temperature	°C	109.45	109.38	109.13	109.04	109.37	109.20	109.13	109.07	109.04	109.31	109.15	109.08
Stripper Pressure	Bara	1.2	1.2	1.2	1.2	1.2	1.2	1.2	1.2	1.2	1.2	1.2	1.2
Stripper Reboiler Heat Duty	kW	69.46	73.58	72.44	74.43	60.89	64.37	66.34	66.70	69.65	45.47	46.89	50.60
SRD	MJ/kg·CO_2	3.91	3.87	4.08	4.25	4.00	4.27	4.40	4.47	4.66	4.00	4.21	4.31
Degree of Regeneration	%	61.85	60.51	51.44	46.54	52.87	47.35	43.07	39.14	36.10	52.97	45.19	42.21
CO_2 Capture Efficiency	%	86.73	90.88	85.35	84.13	91.39	90.46	90.80	89.43	89.09	90.26	90.02	91.38
Lean Loading Difference	mol/mol	0.0112	0.0600	0.0149	0.0155	0.0164	0.0098	0.0104	0.0037	0.0011	0.0107	0.0021	0.0109
Rich Loading Difference	mol/mol	0.0027	0.0032	0.0012	0.0131	0.0211	0.0130	0.0031	0.0222	0.0145	0.0017	0.0038	0.0016
Solvent Capacity Difference	mol/mol	0.0139	0.0568	0.0136	0.0285	0.0375	0.0228	0.0072	0.0260	0.0156	0.0124	0.0017	0.0093
SRD Difference	MJ/kg·CO_2	0.1397	0.0398	0.0377	0.1160	0.1450	0.1572	0.1831	0.2244	0.2845	0.2095	0.1602	0.1049
Absorber MAPE	%	23.35	15.99	21.36	23.18	19.05	33.79	31.66	26.22	33.89	15.23	13.23	23.46
Stripper MAPE	%	3.80	4.17	2.64	3.24	3.65	3.76	3.70	2.87	3.44	4.45	4.57	3.18

5.7 Expanding Experimental Campaign Results with ECC Model Predictions

With the ECC model calibrated to the experimental data of the performance campaign on the TERC ACP, it was first employed to extend these experimental results by making predictions between the tested capture conditions.

The Python automation script was used to automate predictions, using an Excel file as a controller to input parameters into the various model nodes. Inputs were derived from the existing experimental dataset, with key variables such as lean solvent concentration, lean solvent and flue gas temperatures, and gas compositions averaged across the capture conditions for each flue gas CO_2 concentration. The flue gas flow rate was held constant at 150 Nm^3/h. The temperature of the rich solvent entering the top of the stripper was fixed at 76 °C across all simulations, based on the experimentally recorded stripper top temperatures. Reasonable initial estimates for the lean solvent CO_2 content and reboiler duty were provided to ensure model convergence.

Simulations were performed incrementally in solvent flow rate steps of 25 kg/h of pure solvent, resulting in a resolution approximately four times finer than that achieved experimentally. A capture efficiency target of 90% was set for all simulation capture conditions.

Since the completion of the experimental campaign, the electric boiler supplying the PHW was upgraded, and can now supply a heat duty of 96 kW, up from 72 kW in the original boiler. Accordingly, all presented simulation results from the ECC model correspond to cases achieving 90% capture efficiency with a reboiler duty below the new 96 kW limit, which can theoretically be run on the TERC ACP without issue.

5.7.1 SRD Predictions

Figure 5.24 presents the SRD against solvent flow rate for different flue gas CO_2 concentrations for ECC model predictions and experimental values from the TERC ACP. The solvent flow rates include the mass of CO_2 that make up the lean loading for each capture condition.

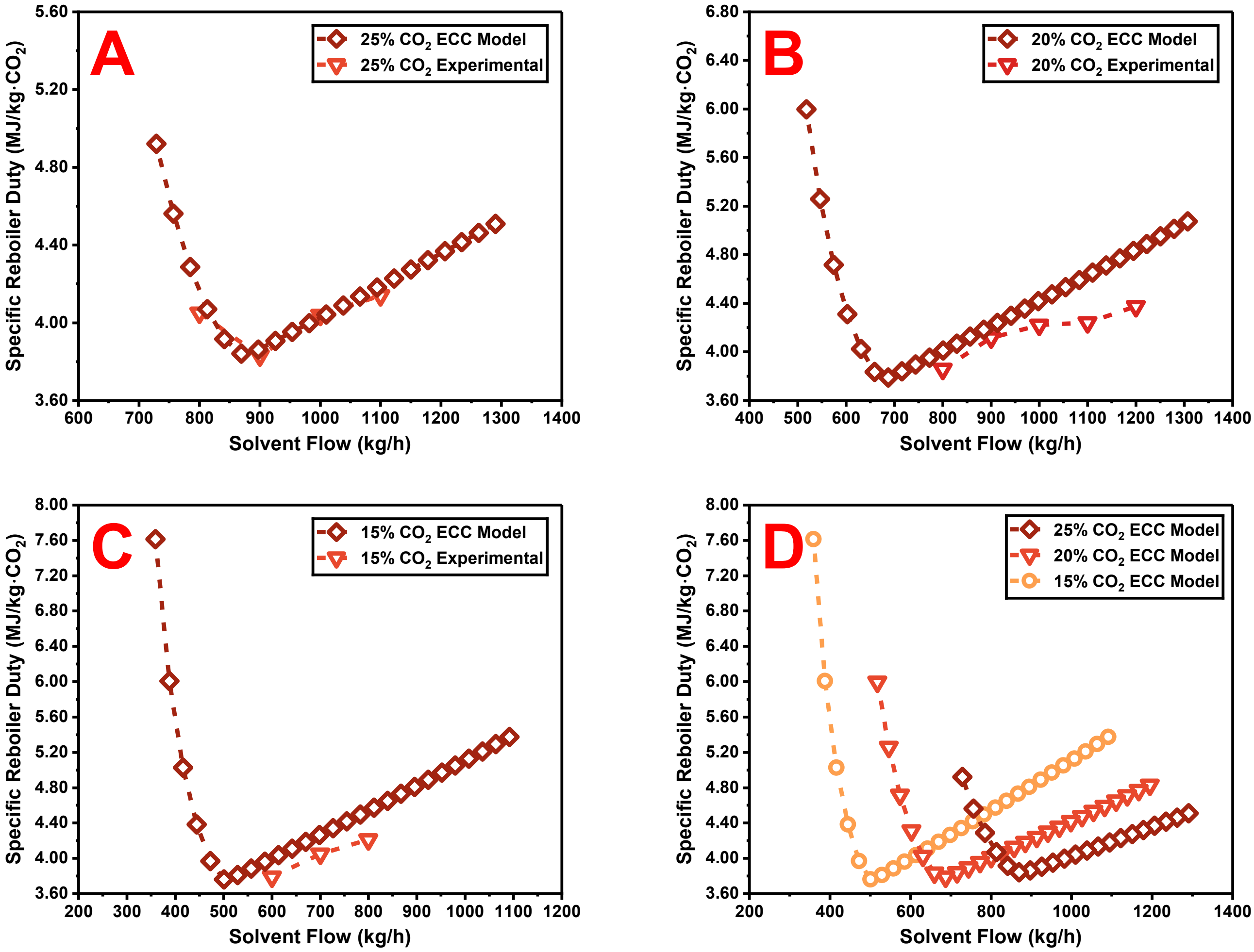

Figure 5.24: SRD against solvent flow rate for different CO_2 concentrations in a 150 Nm^3/h gas flow targeting 90% capture efficiency for ECC model predictions and experimental results: (A) 25 mol.% CO_2, (B) 20 mol.% CO_2, (C) 15 mol.% CO_2, and (D) All ECC model predictions.

For the 25 mol.% CO_2 conditions presented in Figure 5.24A, the ECC model shows strong alignment with the experimental SRD values. As previously discussed, the 25_900 capture condition was thought to approximate the inflection point and minimum SRD for this CO_2 concentration. The ECC model supports this, predicting the minimum SRD to occur at approximately 869 kg/h of total solvent flow, equivalent to an L/G ratio of 4.0 and 825 kg/h of pure solvent. The true minimum likely falls between 870 and 900 kg/h.

For the 20 mol.% CO_2 conditions presented in Figure 5.24B, the ECC model predicts values below the experimental range, successfully identifying a minimum SRD not achieved during the experimental campaign The predicted minimum occurs at approximately 688 kg/h of total solvent flow, equivalent to an L/G ratio of 3.22 and

650 kg/h of pure solvent. This aligns with the downward trend observed with the experimental results, though the predicted minimum is slightly below the 750 kg/h estimate made previously in the experimental analysis using lean loading trends from the DCC model.

Similarly for the 15 mol.% CO_2 conditions presented in Figure 5.24C, the ECC model enabled extrapolation of the predictions beyond tested conditions and identifies the location of the minimum SRD. The predicted minimum occurs at approximately 501 kg/h, equivalent to an L/G of 2.41 and 475 kg/h of pure solvent. This aligns well with earlier experimental analysis, which suggested 500 kg/h as the optimal flow rate.

Although the ECC model slightly overpredicts SRD for the 15 and 20 mol.% CO_2 conditions compared to the experimental values, the differences remain within the average acceptable threshold of 0.2 MJ/kg·CO_2. These minor deviations do not affect the identification of the optimal solvent flow rate and confirm that the model is suitably calibrated for predictive use.

A consistent and important trend across all flue gas CO_2 concentrations is the steep rise in SRD when solvent flow rates drop below the optimum. This sharp increase is attributed to deeper operation in the exponential region of the stripper, where lower solvent flow rates lead to inefficient heat use and excess steam generation by the reboiler. In contrast, increases in flow above the optimum shifts the system into the baseline region, resulting in more moderate, linear SRD increases.

The combined predictions across all flue gas CO_2 concentrations in Figure 5.24D form a reference baseline for performance. Based on the trends and predicted minima, the ECC model suggests that the TERC ACP can achieve 90% capture efficiency on flue gas containing 30 mol.% CO_2 within the solvent operating limit, with the optimum SRD occurring at approximately 1050 kg/h, just below the system's upper flow limit.

5.7.2 Solvent Loadings Predictions

Figure 5.25 presents solvent loadings against solvent flow rate for different flue gas CO_2 concentrations for ECC model predictions and experimental values from the TERC ACP.

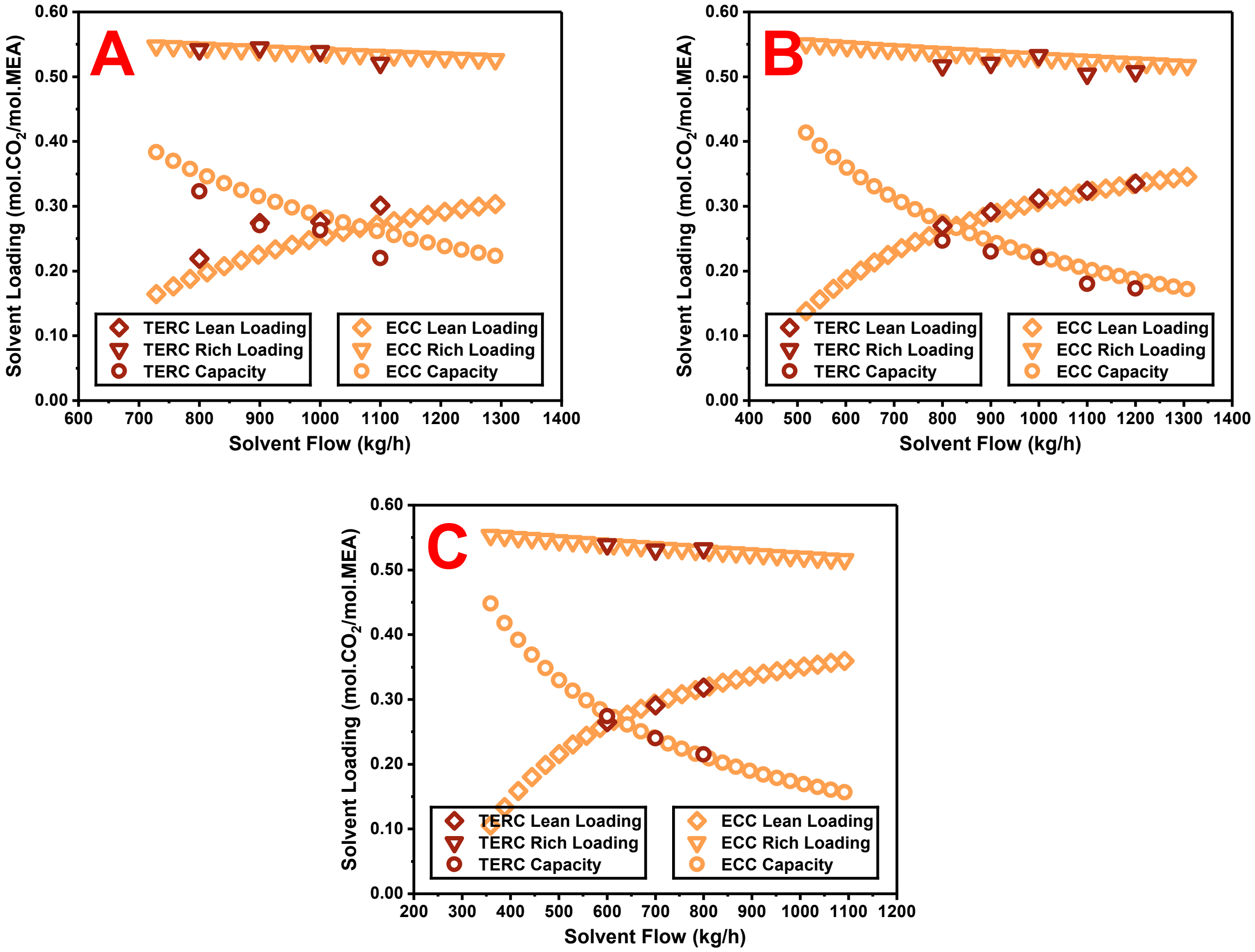

Figure 5.25: Solvent loadings against solvent flow rate for different CO_2 concentrations in a 150 Nm^3/h gas flow targeting 90% capture efficiency for ECC model predictions and experimental results: (A) 25 mol.% CO_2, (B) 20 mol.% CO_2, and (C) 15 mol.% CO_2.

The lean solvent loadings predicted by the ECC model for flue gas CO_2 concentrations of 20 and 15 mol.% show excellent agreement with experimental values in Figures 5.25B and 5.25C, respectively. In both cases, the experimental data closely overlays the predicted trends, which naturally extrapolate into reliable trendlines for estimating lean loadings at varying solvent flow rates. For the 25 mol.% CO_2 conditions in Figure 5.25A, the predicted lean loading trend lies slightly below the experimental values. This discrepancy is attributable to two main factors: first, the previously discussed anomaly in the lean loading for the 25_900 condition, which appears to be uncharacteristically high; and second, the fact that the other 25 mol.% CO_2 conditions did not achieve 90% Capture efficiency. If 90% capture efficiency had been attained experimentally, the expected lean loading would have been slightly lower, aligning more closely with ECC model predictions.

The rich loading predictions for the 15 mol.% CO_2 conditions align well with the experimental data, resulting in a good match for solvent cyclic capacity as well. For the 25 mol.% CO_2 conditions, the rich loading predictions also correspond well with experimental values, but the mismatch in lean loadings leads to slight deviations in predicted solvent capacity. If the experimental cases had achieved the target capture efficiency, the predicted solvent capacities would likely fall into closer alignment. For the 20 mol.% CO_2 conditions, most experimental rich loadings fall below the ECC model predictions, with the exception of the 20_1000 condition. As discussed earlier, this may point to possible uncertainties in the measured experimental rich loadings. These differences in rich loading also result in solvent capacity values that diverge from the ECC model predictions.

Overall, the extrapolated solvent loading trends predicted by the ECC model show strong agreement with the experimental dataset. This consistency builds confidence in the model's validity and supports its use for interpolating and predicting performance across a broader range of conditions. A comparison of the SRD against lean loading values, presented in Figure 5.26, provides insight into the optimal lean loading under varying flue gas CO_2 conditions.

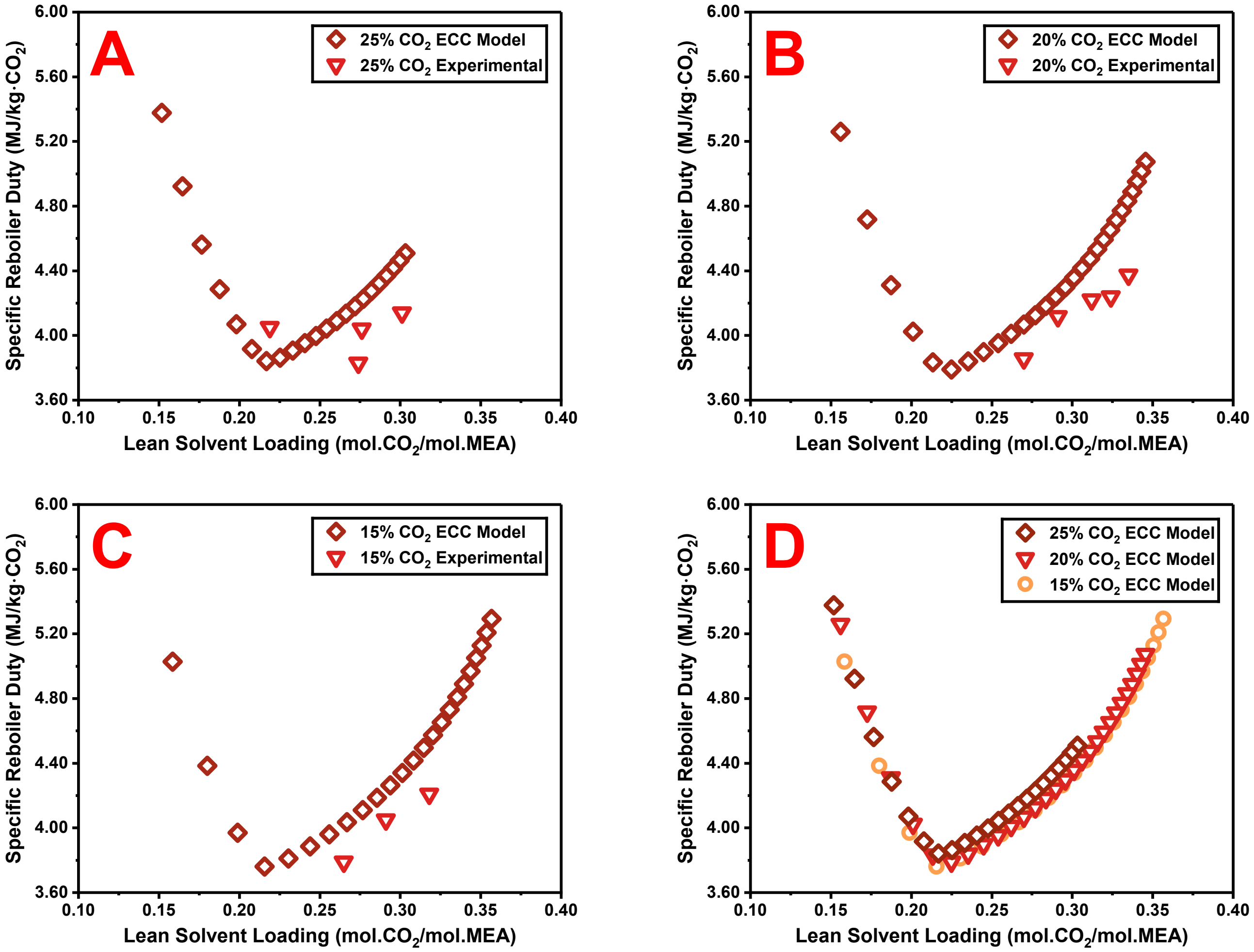

Figure 5.26: SRD against lean solvent loading for different CO_2 concentrations in a 150 Nm^3/h gas flow targeting 90% capture efficiency for ECC model predictions and experimental results: (A) 25 mol.% CO_2, (B) 20 mol.% CO_2, (C) 15 mol.% CO_2, and (D) All ECC model predictions.

Figure 5.26 enables the identification of the optimal lean loading values that correspond to the minimum SRD. For the different flue gas CO_2 concentrations, the optimal lean loadings are approximately: 0.217 for 25 mol.%, 0.225 for 20 mol.%, and 0.216 for 15 mol.%. The slight variation observed for the 20 mol.% CO_2 condition is likely attributable to the 25 kg/h solvent flow rate increment used in the simulations. A finer resolution would likely bring the 20 mol.% condition into even closer alignment with the others. However, the overall values suggest that the optimal lean loading for the TERC ACP is largely independent of the flue gas CO_2 concentration, agreeing with the conclusion in the preceding chapter. The average value of these optimal lean loadings approximates 0.22, which is within 0.01 of the predicted optimal lean loading of 0.23 for the TERC ACP, as discussed in Chapter 4.

The simulated trend lines follow the experimental data reasonably well. For the 20 and 15 mol.% CO_2 conditions, experimental lean loadings at minimum SRD are expected to fall within 0.01 of the ECC model predictions. As previously discussed, the 25 mol.% CO_2 experimental results are less representative due to varying capture efficiencies and a likely erroneous lean loading measurement. Nevertheless, the predicted trend for this condition is considered reliable based on the strong agreement observed for the other CO_2 concentrations.

Figure 5.26 also reinforces the earlier observation that SRD increases rapidly when solvent flow falls below the optimum, which is characteristic of lower lean loadings, and indicative of conditions where the stripper column operates in the exponential region. In contrast, increases in solvent flow above the optimum, which is characteristic of higher lean loadings, shift the system deeper into the baseline region, where SRD rises more gradually for the same incremental solvent flow change.

Finally, the combined comparison in Figure 5.26D demonstrates that all three CO_2 concentrations exhibit similar SRD-lean loading profiles, with only minor deviations. These arise due to the higher SRD associated with increased CO_2 concentrations: at a given lean loading, a higher solvent flow rate is needed to achieve 90% capture when flue gas CO_2 concentration increases. This leads to a greater water circulation and a higher energy requirement in the reboiler, reflected in the elevated SRD values.

5.7.3 *Stripper Temperature Profile Predictions*

Finally, the stripper temperature profiles predicted by the ECC model are compared with experimental profiles from the TERC ACP across the different flue gas CO_2 concentrations, presented in Figure 5.27. For the experimental and simulated profiles, the legend refers to the total lean solvent flow rate, including the CO_2 mass.

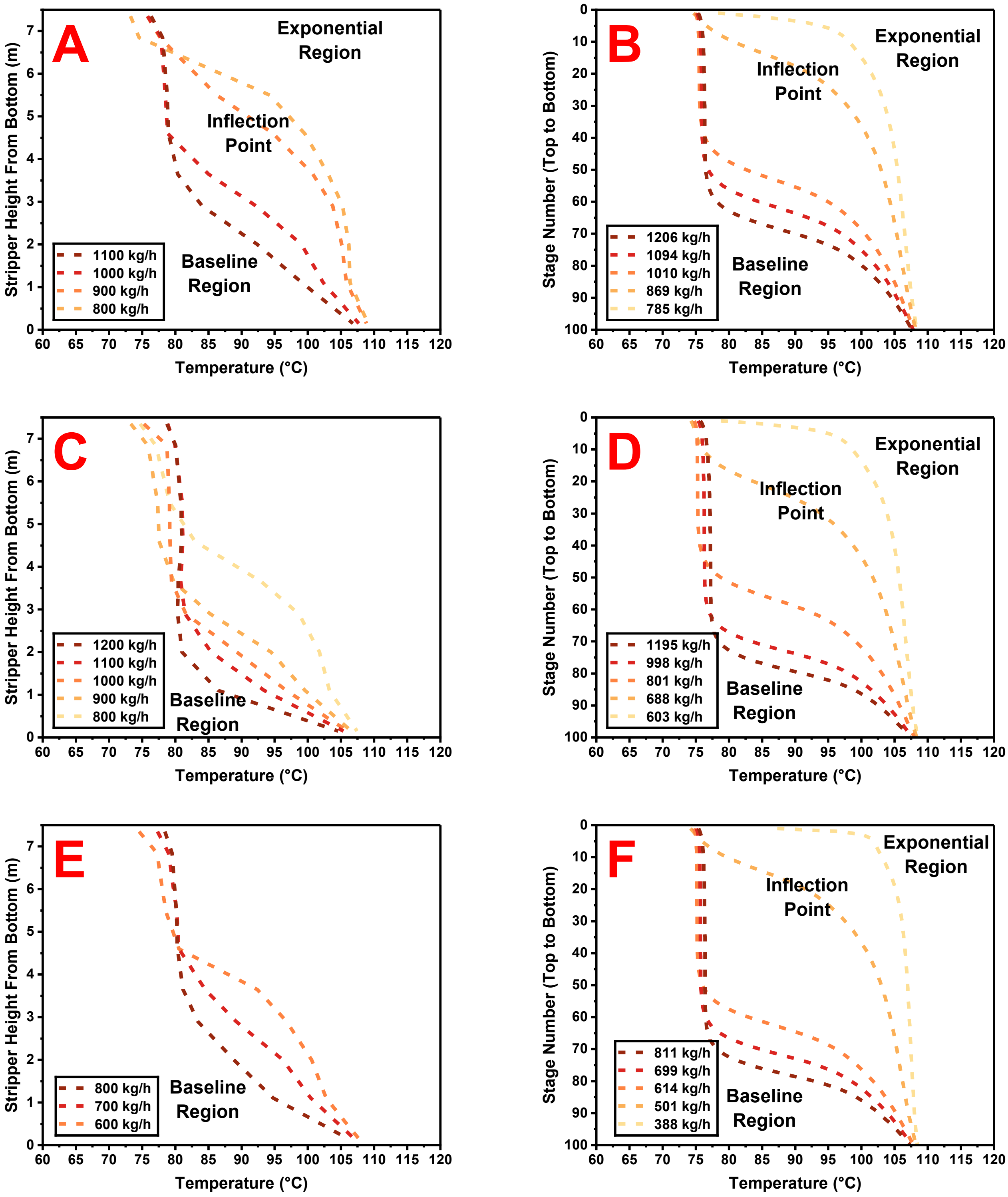

Figure 5.27: Stripper temperature profiles from experimental measurements and ECC model predictions. Each row corresponds to a different flue gas CO_2 concentration, with experimental data on the left, and simulated results on the right: (A, B) 25 mol.% CO_2, (C, D) 20 mol.% CO_2, and (E, F) 15 mol.% CO_2.

Figures 5.27A and 5.27B present profiles for 25 mol.% CO_2 conditions at solvent flow rates close to those tested experimentally, allowing for a direct comparison between predicted and actual temperature distributions. A key observation is that the ECC model predicts a more rapid increase in temperature towards the bottom of the column, particularly around stage 60, resulting in a more horizontal profile in this region. This suggests that, in reality, solvent heating is distributed across a larger portion of the column than the simulation predicts. While the location of the simulated inflection point is broadly similar to the experimental data, its shape gives the impression that it falls deeper into the exponential region, an artefact of the idealised nature of process simulation rather than a true shift in its position. At a lower solvent flow rate of 785 kg/h, the simulated profile clearly shifts deeper into the exponential region. The predicted profiles remain smooth and consistent across the flow rate range due to the idealised nature of the ECC model, which does not capture operational fluctuations or equipment limitations.

Figures 5.27C and 5.27D present profiles for 20 mol.% CO_2 conditions. In this case, the ECC model covers a broader range of solvent flows to fully capture the transition through the stripper operating regions. The same trends observed for 25 mol.% CO_2 apply here: the simulated profiles exhibit a steeper temperature rise concentrated in fewer stages towards the bottom of the column, and the inflection point again appears slightly shifted toward the exponential region, which is an artefact of the model. Reducing the solvent flow rate below the optimum shifts the profile into the exponential region, matching the trend observed in the 25 mol.% CO_2 profiles.

Similarly, Figures 5.27E and 5.27F display the profiles for the 15 mol.% CO_2 conditions, and the same behavioural patterns persist. Across all CO_2 concentrations, the ECC model consistently predicts similar temperature profile shapes across the range of solvent flows.

This consistency is particularly useful for guiding future simulations. Despite minor discrepancies in the absolute position or gradients, the ECC model reliably reproduces the overall shape and trends of the stripper temperature profile. This makes it a valuable tool for identifying the operating region, optimising flow rates, and guiding process adjustments, even in the absence of experimental data.

5.7.4 Expanding Experimental Campaign Results Conclusion

The ECC model has successfully expanded the results of the experimental campaign into a more detailed and continuous dataset, enabling clearer identification of performance trends and key operational parameters, particularly around SRD, lean loading, and stripper column behaviour, that were previously unattainable due to experimental constraints. Across all examined flue gas CO_2 concentrations, the ECC model showed strong agreement with experimental data, increasing confidence in its use for performance predictions.

This validation demonstrates that the ECC model is a reliable predictive tool for the TERC ACP, capable of reducing dependence on time-consuming and resource-intensive experiments to identify optimal operating conditions. As additional data becomes available, especially under more varied operating conditions, the model can be further refined and expanded, progressing towards a true digital twin of the pilot plant.

In the meantime, the ECC model is now ready to be used for predictive work under new conditions, starting with a higher flue gas CO_2 concentration of 30 mol.%. At the time of the original campaign, limitations in the electric boiler heat duty prevented such experiments. Now, with the upgraded boiler offering a heat duty of 96 kW, 90% capture efficiency is expected to be achievable for a flue gas flow rate of 150 Nm^3/h within the solvent flow rate operating range.

5.8 ECC Model Predictions for Capture Conditions with 30 mol.% CO_2

Predictions for flue gas containing 30 mol.% CO_2 were carried out under conditions chosen to reflect those of the original experimental campaign. Since the campaign took place in winter, the flue gas temperature was set to a typical UK temperature of 10 °C. The lean solvent temperature was based on an average of the values used across all previous flue gas CO_2 conditions, set at 33.5 °C. A 35 wt.% MEA solvent concentration was used, with solvent flow rates investigated in increments of 25 kg/h of pure solvent. The temperature of the rich solvent entering the stripper was fixed at 76 °C. The flue gas water content was set to 0.7 mol.% and the flue gas flow was fixed at 150 Nm^3/h. The stripper pressure remained at 1.2 bara, and simulations were configured to achieve 90% capture efficiency.

Figure 5.28 presents the key simulation results generated for these conditions. Only those simulations with reboiler duty requirements below 96 kW are shown, as these are realistically achievable on the TERC ACP following the boiler upgrade.

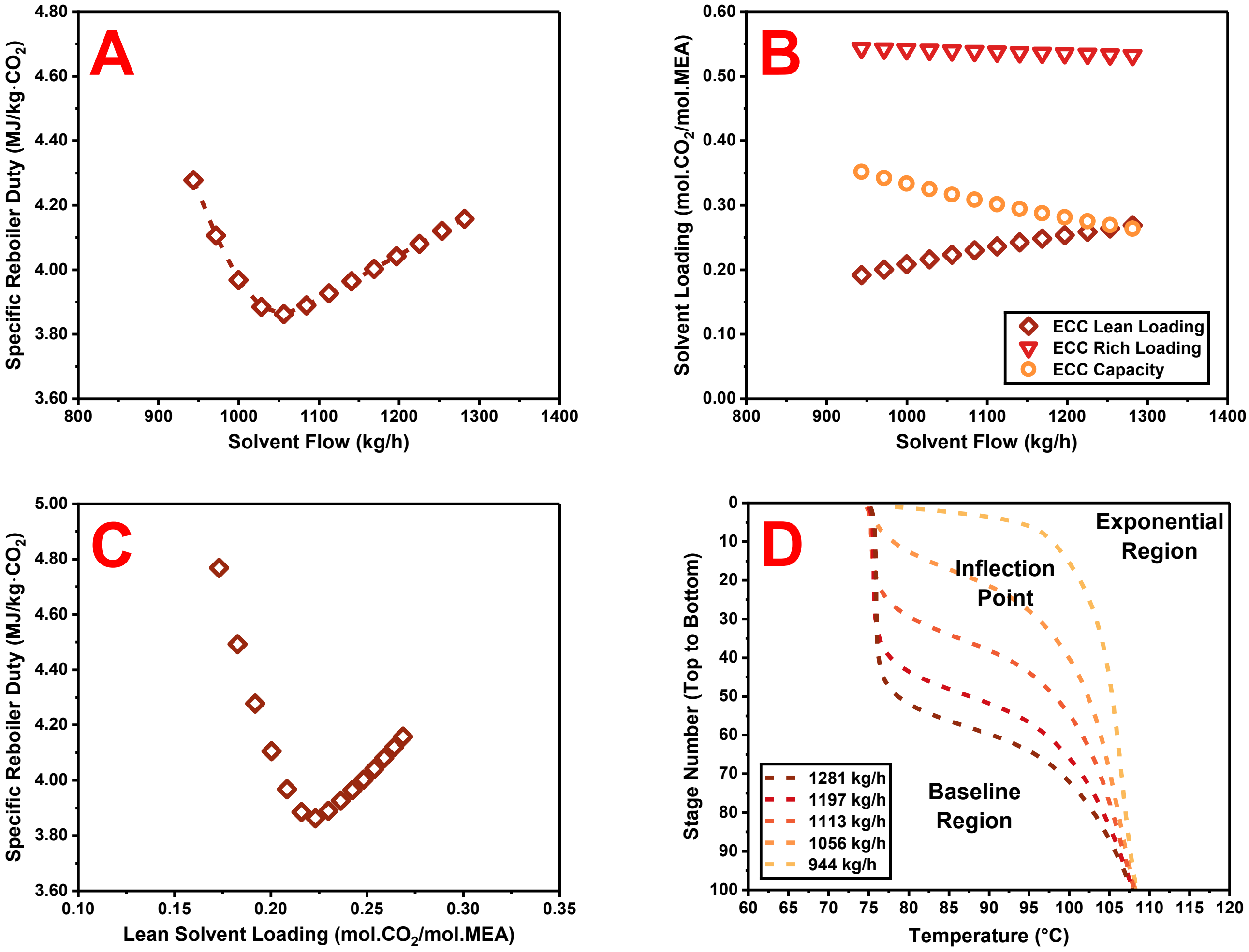

Figure 5.28: Predictions by the ECC model for a 150 Nm^3/h gas flow containing 30 mol.% CO$_2$, targeting 90% capture efficiency: (A) SRD against solvent flow rate, (B) Solvent loadings against solvent flow rate, (C) SRD against lean solvent loading, and (D) Stripper temperature profiles.

Figure 5.28A confirms an earlier hypothesis regarding the optimal solvent flow rate for minimum SRD when treating 30 mol.% CO$_2$ flue gas, where the minimum SRD is predicted to occur at a solvent flow rate of approximately 1050 kg/h. Solvent loadings are shown in Figure 5.28B, and appear as approximately linear trendlines due to the narrower flow rate range simulated on either side of the optimum, compared with the broader range examined in Figure 5.24. Figure 5.28C shows that the optimal lean loading associated with the minimum SRD is approximately 0.223, consistent with values previously presented in Figure 5.26.The stripper temperature profiles shown in Figure 5.28D exhibit the same trends and behaviours as those observed in earlier simulations in Figure 5.27, reinforcing confidence in the model's accuracy.

The complete results predicted by the ECC model for the 30 mol.% CO$_2$ conditions are presented in Table 5.6. These results are in strong agreement with the trends validated in earlier sections against experimental data, providing further confidence in their accuracy. The ability to generate these results rapidly using the developed Python automation script, with minimal user input, highlights the practical utility and robustness of the tool. This script will be invaluable for ongoing ECC model development, allowing easy adjustment of underlying Aspen Plus files.

Table 5.6: ECC model simulation results for flue gas CO_2 concentrations of 30 mol.%, under similar conditions to the experimental campaign.

Parameter	Units	Capture Conditions												
CO_2 in Flue Gas	vol.%	30.00	30.00	30.00	30.00	30.00	30.00	30.00	30.00	30.00	30.00	30.00	30.00	30.00
H_2O in Flue Gas	vol.%	0.70	0.70	0.70	0.70	0.70	0.70	0.70	0.70	0.70	0.70	0.70	0.70	0.70
Overall Solvent Mass Flow	kg/h	943.53	971.73	999.91	1028.09	1056.26	1084.42	1112.58	1140.72	1168.85	1196.98	1225.10	1253.22	1281.31
Solvent MEA + H_2O Flow	kg/h	900.00	925.00	950.00	975.00	1000.00	1025.00	1050.00	1075.00	1100.00	1125.00	1150.00	1175.00	1200.00
Solvent MEA Mass Flow	kg/h	315.00	323.75	332.50	341.25	350.00	358.75	367.50	376.25	385.00	393.75	402.50	411.25	420.00
Solvent H_2O Mass Flow	kg/h	585.00	601.25	617.50	633.75	650.00	666.25	682.50	698.75	715.00	731.25	747.50	763.75	780.00
Solvent CO_2 Mass Flow	kg/h	43.53	46.73	49.91	53.09	56.26	59.42	62.58	65.72	68.85	71.98	75.10	78.22	81.31
Flue Gas Mass Flow	kg/h	223.70	223.70	223.70	223.70	223.70	223.70	223.70	223.70	223.70	223.70	223.70	223.70	223.70
Flue Gas CO_2 Mass Flow	kg/h	88.63	88.63	88.63	88.63	88.63	88.63	88.63	88.63	88.63	88.63	88.63	88.63	88.63
Flue Gas Volumetric Flow	m^3/h	155.68	155.68	155.68	155.68	155.68	155.68	155.68	155.68	155.68	155.68	155.68	155.68	155.68
Liquid to Gas Ratio	kg/kg	4.22	4.34	4.47	4.60	4.72	4.85	4.97	5.10	5.23	5.35	5.48	5.60	5.73
Solvent to CO_2 Ratio	kg/kg	10.15	10.44	10.72	11.00	11.28	11.56	11.85	12.13	12.41	12.69	12.98	13.26	13.54
Flue Gas Temperature	°C	10.00	10.00	10.00	10.00	10.00	10.00	10.00	10.00	10.00	10.00	10.00	10.00	10.00
Lean Solvent Temperature	°C	33.50	33.50	33.50	33.50	33.50	33.50	33.50	33.50	33.50	33.50	33.50	33.50	33.50
Lean Solvent Concentration	wt.%	33.40	33.33	33.27	33.21	33.15	33.10	33.05	33.00	32.95	32.91	32.87	32.83	32.79
Rich Solvent Concentration	wt.%	32.31	32.24	32.18	32.12	32.06	32.00	31.95	31.90	31.85	31.80	31.76	31.71	31.67
Lean Loading	mol/mol	0.1918	0.2003	0.2083	0.2159	0.2231	0.2299	0.2363	0.2424	0.2482	0.2537	0.2590	0.2640	0.2687
Rich Loading	mol/mol	0.5437	0.5426	0.5416	0.5407	0.5397	0.5387	0.5378	0.5369	0.5360	0.5351	0.5342	0.5333	0.5325
Loading Capacity	mol/mol	0.3518	0.3423	0.3333	0.3247	0.3166	0.3088	0.3015	0.2945	0.2878	0.2813	0.2752	0.2694	0.2638
Absorber Bottom Temperature	°C	39.20	39.87	40.53	41.17	41.80	42.40	43.00	43.58	44.15	44.70	45.24	45.77	46.29
Cross Heat Exchanger Duty	kW	31.10	31.52	31.91	32.29	32.65	32.99	33.31	33.63	33.92	34.20	34.47	34.72	34.96
Cross Heat Exchanger Temperature Approach	°C	33.77	33.73	33.68	33.64	33.60	33.57	33.54	33.51	33.48	33.46	33.44	33.41	33.39
Stripper Bottom Temperature	°C	109.55	109.50	109.45	109.41	109.37	109.34	109.30	109.27	109.24	109.22	109.19	109.16	109.14
Stripper Pressure	Bara	1.2	1.2	1.2	1.2	1.2	1.2	1.2	1.2	1.2	1.2	1.2	1.2	1.2
Stripper Reboiler Heat Duty	kW	94.80	91.04	87.92	86.11	85.61	86.25	87.04	87.92	88.78	89.64	90.50	91.31	92.23
SRD	$MJ/kg{\cdot}CO_2$	4.28	4.11	3.97	3.88	3.86	3.89	3.93	3.96	4.00	4.04	4.08	4.12	4.16
Degree of Regeneration	%	64.72	63.08	61.54	60.06	58.66	57.33	56.06	54.84	53.69	52.58	51.52	50.50	49.53
CO_2 Capture Efficiency	%	90.00	90.00	90.01	90.00	90.00	90.00	89.99	89.99	90.00	89.99	90.00	89.99	90.00

5.9 Conclusions for Chapter 5

This chapter presented a comprehensive enhancement of the DCC model into a calibrated simulation tool capable of accurately predicting the performance of the TERC ACP under elevated CO_2 flue gas conditions. Through detailed comparison with experimental data, limitations in the original model were identified, particularly in its ability to reproduce solvent loadings and energy demands at higher CO_2 concentrations.

To address these limitations, a wide-ranging investigation of alternative column packing configurations available within Aspen Plus was conducted to evaluate whether acceptable substitutes existed that better represented experimental values. This was motivated by the fact that different packing exhibit varying physical characteristics, which significantly influence liquid holdup and interfacial area, two crucial factors that became central in the model tuning process.

These packing configurations were evaluated through an automated simulation framework, developed in Python, which enabled systematic testing and tuning of hundreds of configurations. This automation tool proved critical in efficiently managing the simulation campaign, allowing for rapid results acquisition and streamlined analysis.

The model tuning process focused on two key parameters: liquid holdup and interfacial area. These were selected due to their physical relevance to packing behaviour, their direct influence on model performance, and the transparency with which their effects could be interpreted. Other tuning factors, such as heat and mass transfer coefficients, were excluded due to either negligible impact or complex, non-linear behaviours that made them unsuitable for systematic model calibration.

Following tuning, two final packing configurations emerged as top performers, including the packing used in the DCC model that was representative of the structured packing used in the TERC ACP. These were evaluated against experimental data for capture conditions with flue gas CO_2 concentrations of 15 mol.% and above. Both achieved strong agreement for SRD, solvent loadings, and stripper temperature profiles. While the absorber temperature profile did not meet the target accuracy, this was an understood compromise, stemming from the logic used in the simulation convergence. As the absorber was treated as a black box for tuning purposes, this limitation did not impact the overall predictive capability of the model.

The original packing configuration, once tuned, was selected for use in the ECC model. This model was then used to interpolate performance between experimental capture conditions and extrapolate to a new flue gas CO_2 concentration of 30 mol.%, yielding results consistent with theoretical expectations. The ECC model now serves as a powerful tool for predictive analysis, reducing the need for costly experimental campaigns and accelerating system design, evaluation, and optimisation.

Crucially, the approach developed here, including targeted tuning, data-driven automation, and systematic performance validation, can be easily applied to other Aspen Plus-based CO_2 capture systems. This positions the ECC model and the Python automation script not only as a valuable tool set for the TERC ACP, but also as a transferable framework applicable to other real-world capture plants.

This work also serves as a foundational step towards a full digital twin representation of the TERC ACP, one capable of adapting and improving as further experimental data becomes available.

5.10 References for Chapter 5

[1] Otitoju O, Oko E, Wang M. Modelling, scale-up and techno-economic assessment of rotating packed bed absorber for CO2 capture from a 250 MWe combined cycle gas turbine power plant. Applied Energy 2023;335:120747. https://doi.org/10.1016/j.apenergy.2023.120747.

[2] Rahmanian Nejat, Rehan Mohammad, Sumani Abdallah, Nizami Abdul-Sattar. Effect of packing structure on CO2 capturing process. Chemical Engineering Transactions 2018;70:1891–6. https://doi.org/10.3303/cet1870316.

[3] ten Hagen RW. AspenPlus Python Interface (Version 2.1) 2022. https://github.com/YouMayCallMeJesus/AspenPlus-Python-Interface.

[4] Wang Z. zwang1995/Aspen-Plus-Automation 2025. https://github.com/zwang1995/Aspen-Plus-Automation.

[5] Mark Hammond. pywin32: Python for Window Extensions 2025. https://github.com/mhammond/pywin32.

[6] John Kitchin. Running Aspen via Python. The Kitchin Research Group 2013. https://kitchingroup.cheme.cmu.edu/blog/2013/06/14/Running-Aspen-via-Python/.

[7] Suardi M. Optimize process simulation with Python-Aspen integration. Eni digiTALKS 2022. https://medium.com/eni-digitalks/optimize-process-simulation-with-python-aspen-integration-e343bbab1aa0.

[8] Harris CR, Millman KJ, van der Walt SJ, Gommers R, Virtanen P, Cournapeau D, et al. Array programming with NumPy. Nature 2020;585:357–62. https://doi.org/10.1038/s41586-020-2649-2.

[9] pandas 2025. https://pandas.pydata.org.

[10] SciPy 2025. https://scipy.org.

[11] Joblib Developers. Joblib: Running Python functions as Pipeline Jobs. Joblib 2025. https://joblib.readthedocs.io/en/stable/.

[12] Guan H, Ye L, Wang Y, Shen F, He Y. Dynamic Modeling and Sensitivity Analysis for an MEA-Based CO2 Capture Absorber. Intelligent Automation & Soft Computing 2023;36:3535–50. https://doi.org/10.32604/iasc.2023.036399.

[13] Fu Y, Bao J, Singh RK, Zheng RF, Anderson-Cook CM, Bhat KS, et al. The influence of random packed column parameters on the liquid holdup and interfacial area. AIChE Journal 2022;68:e17691. https://doi.org/10.1002/aic.17691.

[14] Lu X, Xie P, Ingham DB, Ma L, Pourkashanian M. Modelling of CO2 absorption in a rotating packed bed using an Eulerian porous media approach. Chemical Engineering Science 2019;199:302–18. https://doi.org/10.1016/j.ces.2019.01.029.

[15] Øi LE, Sætre KA, Hamborg ES. Comparison of simulation tools to fit and predict performance data of CO2 absorption into monoethanol amine at CO2 Technology Centre Mongstad (TCM), 2018, p. 230–5. https://doi.org/10.3384/ecp18153230.

[16] Øi LE, Fagerheim S. Simulation of CO2 Absorption at TCM Mongstad for Performance Data Fitting and Prediction, 2021, p. 332–7. https://doi.org/10.3384/ecp20176332.

[17] Li K, Cousins A, Yu H, Feron P, Tade M, Luo W, et al. Systematic study of aqueous monoethanolamine-based CO2 capture process: model development and process improvement. Energy Science & Engineering 2016;4:23–39. https://doi.org/10.1002/ese3.101.

[18] Errico M, Madeddu C, Pinna D, Baratti R. Model calibration for the carbon dioxide-amine absorption system. Applied Energy 2016;183:958–68. https://doi.org/10.1016/j.apenergy.2016.09.036.

[19] Guo Liheng, Ding Yudong, Li Xiaoqiang, Zhu Xun, Liao Qiang, Yuan Shaojun. Simulation and optimization study on aqueous mea-based co2 capture process. Chemical Engineering Transactions 2018;70:751–6. https://doi.org/10.3303/cet1870126.

[20] Putta KR, Tobiesen FA, Svendsen HF, Knuutila HK. Applicability of enhancement factor models for CO2 absorption into aqueous MEA solutions. Applied Energy 2017;206:765–83. https://doi.org/10.1016/j.apenergy.2017.08.173.

[21] Pan W, Galvin J, Huang WL, Xu Z, Sun X, Fan Z, et al. Device-scale CFD modeling of gas-liquid multiphase flow and amine absorption for CO_2 capture. Greenhouse Gases 2018;8:603–20. https://doi.org/10.1002/ghg.1770.

[22] Iliuta I, Larachi F, Grandjean BPA. Pressure Drop and Liquid Holdup in Trickle Flow Reactors: Improved Ergun Constants and Slip Correlations for the Slit Model. Ind Eng Chem Res 1998;37:4542–50. https://doi.org/10.1021/ie980394r.

[23] Guo J, Al-Dahhan M. Liquid holdup and pressure drop in the gas–liquid cocurrent downflow packed-bed reactor under elevated pressures. Chemical Engineering Science 2004;59:5387–93. https://doi.org/10.1016/j.ces.2004.07.106.

[24] Zhou T, Hu J, Zhang H, Li H, Sang L. CO2 absorption enhancement with MEA in micropacked bed reactors: Mass transfer experiment and model study. Separation and Purification Technology 2024;339:126722. https://doi.org/10.1016/j.seppur.2024.126722.

[25] Tan LS, Shariff AM, Lau KK, Bustam MA. Factors affecting CO2 absorption efficiency in packed column: A review. Journal of Industrial and Engineering Chemistry 2012;18:1874–83. https://doi.org/10.1016/j.jiec.2012.05.013.

[26] Mores P, Scenna N, Mussati S. A rate based model of a packed column for CO2 absorption using aqueous monoethanolamine solution. International Journal of Greenhouse Gas Control 2012;6:21–36. https://doi.org/10.1016/j.ijggc.2011.10.012.

[27] Billet R, Schultes M. Prediction of Mass Transfer Columns with Dumped and Arranged Packings. Chemical Engineering Research and Design 1999;77:498–504. https://doi.org/10.1205/026387699526520.

Chapter 6: Conclusions and Recommendations for Future Work

6.1 Thesis Reflection

This thesis has presented a comprehensive investigation into the practical application of chemical absorption for treating flue gases with elevated CO_2 concentrations, characteristic of process emissions from hard-to-abate industrial sectors, such as the iron and steel industry. Performance data from real-world capture plants operating at CO_2 concentrations above 15 mol.% remains scarce in the open literature, highlighting a critical knowledge gap in the field of chemical absorption-based carbon capture.

To address this gap, a synergistic methodology combining rigorous process simulation and a targeted experimental campaign was employed. An initial predictive model, the Developed Carbon Capture (DCC) model, was developed in Aspen Plus to identify optimal operating conditions, which then guided an experimental campaign conducted on the Amine Capture Plant (ACP) at the Translational Energy Research Centre (TERC) in Sheffield, UK. This established novel baseline performance data that was then used to calibrate and enhance the simulation model, resulting in the ECC model. The calibration process is a transferable framework that can be applied to other chemical absorption systems. The ECC model forms the foundation of a digital twin of the TERC ACP and can be used for performance predictions without the need for costly and time-intensive experimental work.

This concluding chapter summarises the key findings from the research, drawing overarching conclusions about the operational characteristics and performance of the TERC ACP treating flue gases with elevated CO_2 concentrations, with insights that can be generalised to other capture systems. Finally, the recommendations for future research are proposed to build upon these findings and further advance the optimisation of chemical absorption-based carbon capture for industrial emissions.

6.2 Summary of Key Findings

The key findings from the three core research chapters are summarised in the following subsections.

6.2.1 Simulation Model Development and Performance Predictions

Chapter 3 detailed the development and utilisation of the DCC model, a process simulation model created in Aspen Plus V11.0 to represent the TERC ACP. The DCC model was built upon a foundation of established MEA absorption chemistry, kinetics, and thermodynamics, and was compared against another simulation model available in the open literature. It was validated against existing plant data from the older PACT configuration in addition to preliminary data from the TERC configuration, demonstrating its capability to accurately predict key performance indicators such as solvent loadings and SRD. A sensitivity analysis revealed which were the most influential parameters affecting system performance.

The validated model was then used to predict ACP performance across a wide range of operating conditions. Solvent flow rate, gas flow rate, and CO_2 concentrations were all varied for 90 and 95% capture efficiency to create a comprehensive MEA performance dataset from which trends could be identified. The heat duty of the cross-heat exchanger on the system was also investigated, in addition to the stripper pressure. The results from this investigation were used to guide the chosen capture conditions for the experimental campaign.

The main conclusions from this body of simulation work are as follows:

i) Model Development and Validation

The DCC model was developed in Aspen Plus by adapting by adapting an intrinsic MEA-based model, which was enhanced with established data from the open literature. The model was validated against historical experimental data from the PACT pilot plant configuration, where it was also compared to an alternative open source CCSI model. The DCC model demonstrated superior performance by more closely matching the experimental CO_2 loadings and SRD than the CCSI model. The model's accuracy was further confirmed against preliminary data from the current TERC ACP configuration, establishing it as a reliable tool for the predictive studies required to inform a future experimental campaign.

ii) Parameter Sensitivity and Optimisation Potential

A comprehensive sensitivity analysis identified the most influential parameters on plant performance. It revealed that solvent concentration, solvent mass flow, and stripper pressure had significant impacts on model predictions, while the temperatures of the flue gas and solvent flow had negligible effect. An example optimisation case demonstrated that tuning these key parameters could reduce the SRD by over 41% from an initial non-optimised state, highlighting the significant potential for energy savings. Crucially, the insights from this analysis directly informed the design of the subsequent experimental campaign, for which a solvent concentration of 35 wt.% and a stripper pressure of 1.2 bara were selected.

iii) Predictive Trends for Optimal L/G Ratios

A critical conclusion was drawn from the predictive modelling when the optimal L_{pure}/G ratio was found to be independent of the total gas flow rate and instead is a function of CO_2 concentration and capture efficiency. This was evident through assessment of the solvent cyclic capacity at the optimal L_{pure}/G ratio across different gas flow rates, which was the same for a given flue gas CO_2 concentration and capture efficiency. For flue gas concentrations ranging from 10 to 25 mol.% CO_2, the optimal L_{pure}/G ratios ranged from 2.5 to 4.6 for 90% capture efficiency, with slightly higher values required for 95% capture efficiency. The solvent/CO_2 ratios were also reported for the conditions, ranging from 17.1 to 13.5 for the same conditions at 90% capture efficiency. These solvent/CO_2 ratios provide generalisable performance metrics for comparison with other capture systems, as they isolate the relationship between pure solvent flow and the mass flow of CO_2 in the flue gas. This is particularly useful when flue gas composition varies for industrial process emissions, enabling consistent benchmarking across different operating conditions.

iv) Predictive Trends for Solvent Loadings and Capacities

The simulations provided detailed insight into the solvent loading behaviour observed for optimal L_{pure}/G ratios, revealing that the necessary loadings and capacity are a function of the flue gas CO_2 concentration but are independent of gas flow rate. At these optimal conditions, as the flue gas CO_2 concentration increased from 10 to 25 mol.%, the required lean loading was predicted to decrease from 0.294 to 0.247, while the rich loading remained consistently high and relatively static across conditions, ranging between 0.500 to 0.517. Consequently, the solvent cyclic capacity also increased from 0.210 to 0.265, reflecting the capacity required to capture a greater mass of CO_2 from more concentrated gas streams. However, when the flue gas CO_2 concentration was fixed, and the gas flow rate varied, the optimal L_{pure}/G ratios all had very similar corresponding lean and rich loadings. In fact, the solvent capacity was found to be identical for each gas flow rate, confirming independence from the gas flow rate.

v) Column Temperature Profiles and Operational Mode Predictions

Analysis of the simulated column temperature profiles revealed the fundamental relationship between the L/G ratio, the location of the reaction zones, and the resulting operational modes of the absorber and stripper. Absorber operation transitions from a rich-pinch at low L/G ratios to a lean-pinch at high L/G ratios, with an inefficient bulge-pinch in between. The simulations for the TERC ACP revealed that optimal performance was consistently achieved in a rich-pinched state.

The optimal L/G ratio occurs when the stripper operates at the inflection point, which is characterised by a smooth temperature gradient across the height of the column and represents the most efficient heat transfer, thereby minimising the SRD. Deviation from this point incurs an energy penalty, where higher solvent flow rates shift operation into the baseline region, while lower solvent flow rates move it into the exponential region, both of which have easily identifiable temperature profiles. This finding establishes the stripper temperature profile as a key diagnostic tool, providing a theoretical framework for optimising the solvent flow rate for capture.

vi) Impact of Cross-Heat Exchanger and Stripper Pressure on Performance

The simulations underscored the critical impact of real-world system constraints on energy consumption, particularly the interaction between the cross-heat exchanger and stripper pressure. The DCC model predicted that the minimum SRD values for different flue gas CO_2 concentrations remained broadly similar until the cross-heat exchanger reached its maximum heat duty. Reaching the maximum heat duty happens through increases in solvent flow rate, required for an increase in overall flue gas flow rate or CO_2 concentration, as well as increases in lean solvent temperature resulting from increased stripper pressure. Once the duty limit is reached, the preheating of the rich solvent becomes constrained with any further increase in lean solvent flow rate or its temperature, leading to a direct increase in SRD due to the greater sensible heat required to reach the reboiler temperature.

Consequently, the optimal stripper pressure is dependent on the cross-heat exchanger capacity, an observation evident for all real-world capture systems which utilise a cross-heat exchanger. For the TERC ACP, the optimal pressure was predicted to be between 1.2 to 1.4 bara, a range that balances thermal efficiency with the cross-heat exchanger's maximum heat duty and ultimately informed the condition for the experimental campaign. Operation outside of this range increases the SRD. This behaviour contrasts sharply with that of an ideal, unconstrained system, where the SRD would continuously decrease with rising pressure, as the rich solvent could always be preheated to a maximum theoretical temperature, minimising the sensible heat required.

vii) Foundation for Experimental Work

The predictive findings from this simulation work provided the essential guidance for the subsequent experimental campaign. The DCC model established the initial operating conditions and performance benchmarks against which the experimental results would be compared, forming a direct bridge between the theoretical and practical phases of this research. Furthermore, key parametric relationships identified for system optimisation are novel and transferable, providing useful guidance for the optimisation of other chemical absorption plants and treating flue gases with high CO_2 concentrations.

6.2.2 Experimental Performance Campaign for Elevated CO_2 Conditions

Chapter 4 presented a comprehensive analysis of a novel pilot-scale experimental campaign on the TERC ACP, focused on establishing baseline performance for chemical absorption capture using MEA from flue gases with elevated CO_2 concentrations. This investigation addressed a critical knowledge gap, as performance data for conventional MEA-based systems is scarce in the open literature for flue gas CO_2 concentrations above 15 mol.%. Performance data was obtained for solvent flow rates ranging from 300 to 1200 kg/h, treating a flue gas flow rate of 150 Nm^3/h with varying CO_2 concentrations of 25, 20, 15, and 10 mol.%. The MEA concentration was 35 wt.% and the stripper pressure was fixed at 1.2 bara. A capture efficiency of 90% was targeted for each capture condition.

Following the primary data analysis, a detailed energy balance was conducted around the stripper to determine the mass of steam generated for each capture condition. This was then used to calculate the solvent regeneration energy and quantify its constituent components for each capture condition, including an evaluation of generalised heat losses from the system. A rigorous statistical uncertainty analysis was applied throughout to ensure the reliability and accuracy of the presented results.

The main conclusions from the experimental campaign are as follows:

i) Novel Performance Data

The campaign successfully generated novel and valuable baseline performance data for carbon capture from flue gases with elevated CO_2 concentrations ranging from 10 to 25 mol.% CO_2, using a conventional PB system with standard MEA solvent. The investigation was comprehensive, establishing clear trends across a range of key performance indicators including L/G and solvent/CO_2 ratios, solvent loadings and cyclic capacities, reboiler duties, and column temperature profiles, with the findings providing practical guidance for the tuning of industrial-scale capture plants. As a result, this work provides a straightforward and accessible reference point for any future pilot plant studies that is essential for benchmarking, process validation, and technology development in the field of industrial carbon capture.

ii) Optimal Operating Conditions and SRD Trends

The optimal L/G ratio for a given flue gas CO_2 concentration corresponds to the location of the minimum SRD, which was successfully identified for 10 and 25 mol.% CO_2 conditions during the campaign. Under the process conditions tested, the minimum SRD for the 10 mol.% CO_2 condition, 4.13 MJ/kg·CO_2, was notably higher than the 3.83 MJ/kg·CO_2 observed for the 25 mol.% CO_2 condition. This reveals a complex relationship where the lowest possible SRD for the plant, inferred from experimental trends to be between 3.70 and 3.75 MJ/kg·CO_2, is expected to occur in the intermediate 15 to 20 mol.% CO_2 concentration range.

This trend reflects a compromise between energy penalties incurred at the extremes of the solvent flow operating range. At low solvent flows typical of dilute streams like the 10 mol.% CO_2 condition, a significant thermodynamic penalty arises from the high energy input required for a relatively small amount of CO_2 capture. Conversely, at the high solvent flows typical of concentrated streams like the 25 mol.% CO_2 condition, the energy penalty stems from heating and vaporising the larger mass of water in the solvent. The results indicate that the penalty of operating at low solvent flows is greater than at high solvent flows, and that minimising the overall SRD requires operating in a "sweet spot" towards the middle of the solvent flow range where the reboiler duty is comfortably below its maximum. This corresponds to the anticipated optimal L/G ratios for flue gas concentrations of 15 and 20 mol.% CO_2.

iii) Solvent Loadings and Column Behaviour

Analysis of the solvent loadings confirmed expectations, where the lean loading would increase with increasing solvent flow rate, while the rich loading would remain fairly static. The solvent cyclic capacity varied with both solvent flow rate and flue gas CO_2 concentration and is characteristic of the target capture efficiency. To achieve the target capture efficiency for a given condition the heat input from the reboiler was adjusted. This dictated the lean loading level and therefore the extent of solvent regeneration, which in turn produced the required solvent capacity for capture. The optimal lean loading is that of the solvent at the optimal L/G ratio for a given flue gas CO_2 concentration. An overall optimal lean loading for the TERC ACP was also investigated by comparing the SRD against lean loading for all capture conditions and was inferred to be approximately 0.23 $mol{\cdot}CO_2/mol{\cdot}MEA$.

Column temperature profiles provided critical insight into the operational modes of the absorber and stripper, which can be used to aid system diagnostics and to guide system optimisation. The absorber typically operated with a rich-pinch, characteristic of relatively low solvent flow rates, but this evolved into a bulge-pinch as solvent flow rate increased for some flue gas CO_2 concentrations. The stripper typically operated in the baseline region at high solvent flows but shifted towards the inflection point and into the exponential region as the solvent flow rate decreased. System optimisation heavily revolves around achieving stripper operation at the inflection point, as this indicates the optimal L/G ratio has been achieved. Consequently, the stripper temperature profile is a powerful tool for real-time monitoring and solvent flow control to minimise the energy demand of the system.

iv) Regeneration Energy and System Efficiency

An energy balance performed around the stripper enabled the mass of generated steam to be calculated for each capture condition. The required mass of steam was found to increase with both solvent flow and CO_2 concentration, reflecting the energy needed to heat the additional solvent mass and the extent of solvent regeneration required to achieve the target capture efficiency. Following this, a comprehensive breakdown of the solvent regeneration energy into its constituent components was conducted. Direct calculations of the sensible heat, vaporisation energy, desorption energy, and heat recovery were performed, which allowed for the generalised heat loss of the system to be estimated indirectly.

The analysis revealed that the vaporisation energy and sensible heat were the dominant contributors to the overall energy demand, both increasing with solvent flow rate and CO_2 concentration. In contrast, the desorption energy remained relatively for a given CO_2 concentration. The minimisation of SRD is therefore primarily driven by reductions in vaporisation energy and sensible heat, underscoring the critical importance of heat integration and process optimisation. Furthermore, the calculated system heat losses were typically low compared to pilot plants reported in the literature, suggesting that the TERC ACP is a well-insulated and thermally efficient system.

v) Statistical Uncertainty and Data Reliability

A rigorous statistical uncertainty analysis was conducted to validate the experimental results and quantify the reliability of derived values. The analysis of the primary performance indicators confirmed that the mass of captured CO_2 and corresponding capture efficiency were determined with high precision, exhibiting a low relative uncertainty averaging approximately ±1%. In contrast, the uncertainty in the reboiler duty and the resulting SRD was slightly higher, averaging approximately ±5%, and was found to be dominated by statistical variations in the temperature measurements of the PHW system.

The uncertainty framework was extended to the detailed energy balance and the constituent components of the solvent regeneration energy. It was revealed that directly calculated energy components, such as the sensible heat and desorption energy, were typically accurate with a narrow margin of uncertainty, whereas indirectly calculated components, such as the mass of generated steam and the system heat loss, carried a much higher degree of propagated uncertainty. The results confirmed that while heat losses were minor, the exact calculated values were not statistically reliable. Overall, the uncertainty analysis verified the accuracy of the core experimental findings while providing crucial content for the reliability of the derived energy calculations.

vi) Foundation for Enhanced Simulations

The rich dataset and process insights generated from the experimental work served as the essential foundation for the subsequent calibration and enhancement of the DCC model, paving the way for the development of a predictive digital twin representation of the TERC ACP.

6.2.3 Simulation Model Enhancement and Utilisation

Chapter 5 focused on enhancing the DCC model by calibrating it against the experimental data from the preceding chapter, resulting in the creation of a tuned simulation known as the Enhanced Carbon Capture (ECC) model. The enhancement process involved a systematic investigation into alternative column packing configurations and the subsequent tuning of key hydrodynamic parameters, the liquid holdup and the interfacial area, to improve the simulation's fidelity to the TERC ACP's performance.

This extensive tuning campaign, involving thousands of individual simulations, was enabled by a novel Python automation framework developed to interface with and control Aspen Plus. The successfully calibrated ECC model was then used to expand upon the experimental results by identifying the optimal L/G ratios for the 15 and 20 mol.% CO_2 conditions and extrapolating to predict performance for a novel 30 mol.% CO_2 flue gas condition.

The main conclusions from this model enhancement and application work are as follows:

i) Model Calibration Targets and the "Black Box" Principle

To guide the calibration process, the initial DCC model was used to recreate the experimental capture conditions, revealing several systematic weaknesses. While useful for preliminary predictions, the DCC model consistently overestimated the SRD and underestimated the lean solvent loading for every capture condition. Additionally, the predicted optimal L/G ratios deviated from the experimental findings. Based on these deviations, a clear set of quantitative improvement targets was established to benchmark the success of the simulation enhancement process.

A critical conclusion from the tuning process was that achieving a perfect match for all improvement targets was not necessary for creating a reliable system-level model. It became clear that it was not possible to resolve the large discrepancy in the absorber temperature profile without compromising more crucial performance indicators like solvent loadings and SRD. Therefore, it was concluded that the absorber could be treated as a "black box", where as long as the model accurately predicted the key system outputs (solvent loadings, capture efficiency, SRD, and stripper temperature profile), the internal inaccuracies of the absorber temperature profile were an acceptable trade-off.

ii) Development of a Novel Automation Script

A key component of this work was the development of a Python automation script to overcome the prohibitive time and complexity of manually tuning the simulation model. This novel tool, which interfaced directly with Aspen Plus, was essential for the simulation enhancement process. It enabled an extensive and systematic tuning campaign, automatically executing over 20,000 unique simulations to compare alternative packing configurations and iterate through tuning factors to identify an optimal model configuration. Beyond running simulations, the automation script managed the entire workflow by extracting process data, performing statistical analysis, and generating visualisations. It was later used to rapidly produce the expanded dataset and novel predictions for the experimental campaign. The automation script is a powerful and transferable tool that can be utilised to calibrate and control other process simulations of chemical absorption plants, thereby increasing research productivity and efficiency.

iii) Insights into Model Tuning Parameters

A crucial conclusion from the tuning process is that the specific choice of column packing configuration within the simulation is less critical than the ability to correctly tune its associated hydrodynamic parameters. This was demonstrated when the tuned original packing configuration ultimately performed as well as the best identified alternative, offering a key insight for future modelling efforts. This finding is highly valuable, as it suggests that a model can be accurately calibrated to experimental performance even if a plant uses a proprietary or unlisted packing by tuning the parameters of an alternative packing.

The extensive tuning process identified liquid holdup and interfacial area as the most transparent and influential parameters for model calibration, as they directly govern solvent residence time and the effective wetted surface area for CO_2 absorption, respectively. In contrast, the heat transfer factor had a negligible effect as the process is not heat-transfer limited, while the mass transfer coefficient factors for the liquid and vapour exhibited complex, non-linear behaviour, making them unsuitable for interpretable model calibration.

iv) Validation and Predictive Power of the ECC Model

The simulation tuning process was successful, producing the final ECC model with significantly improved predictive accuracy for flue gas CO_2 concentrations of 15 mol.% and above. The model met most pre-defined improvement targets: the average absolute difference in SRD was reduced below 0.2 MJ/kg·CO_2, the average difference in both lean and rich solvent loadings was reduced to approximately 0.01 mol·CO_2/mol·MEA, and the average MAPE for the stripper temperature profiles was reduced to approximately 3.6%.

This validated model was then applied as a predictive tool. It expanded the experimental campaign by simulating additional solvent flow rates between capture conditions, creating a comprehensive MEA performance dataset. These simulations identified the optimal L/G ratios for the 15 and 20 mol.% CO_2 conditions, an outcome not achieved experimentally, and provided greater insight into key performance indicators. The ECC model was then used to extrapolate beyond the experimental range, making novel predictions for a flue gas CO_2 concentration of 30 mol.%, which was now feasible due to an electric boiler upgrade. The predicted results were consistent with trends from lower CO_2 concentrations, giving confidence in their validity. The ECC model establishes itself as the foundation for a digital twin representation of the TERC ACP, reducing the need for costly and time-consuming experimental campaigns and enabling further refinement as new data becomes available.

6.3 Overall Thesis Conclusions

This thesis has successfully demonstrated the viability of using chemical absorption carbon capture in the treatment of industrial process emissions with elevated CO_2 concentrations, a critical step towards the decarbonisation of hard-to-abate industrial sectors, such as the iron and steel industry.

The following overarching conclusions can be drawn from this work:

i) Establishment of Novel Performance Benchmarks for Elevated-CO_2 Capture

Novel performance benchmarks were established for treating flue gas with high concentrations CO_2 of up to 25 mol.%. This work provides a comprehensive baseline dataset for a conventional packed bed capture system using standard MEA solvent without advanced process modifications, offering crucial reference points for future system optimisation and technology development. The dataset is extensive, covering detailed process operating data, system energy balances, and a component-level breakdown of the solvent regeneration energy. All calculations and methodologies have been clearly outlined to ensure the findings are transparent and can be easily translated to other capture systems.

ii) Identification of Key Operational Principles for System Optimisation

Key operational principles and parametric relationships were identified across the findings of this thesis, creating a focused understanding of how to control and optimise the capture system. It was concluded that identification of the optimal L/G ratios requires a comprehensive understanding of how parameters are inherently interlinked. The optimisation pathway is governed by the physical limitations of the plant, particularly the maximum heat duties of the reboiler and cross-heat exchanger, which are stressed differently depending on the solvent flow rate required for a given flue gas flow and its CO_2 concentration. These constraints dictate the overall energy performance of the system, influencing how secondary parameters like stripper pressure are set to support the primary objective of optimising the solvent flow rate and minimising energy consumption.

iii) Demonstration of a Synergistic Methodology Combining Simulation and Experimentation

This thesis demonstrated the power of a synergistic methodology that combines process simulation with novel experimentation for effective process optimisation and characterisation. It was successfully shown that an initial, uncalibrated model can effectively guide a targeted experimental campaign by predicting key operational capabilities. In turn, the novel dataset from the experiments is essential for the calibration of the simulation to create a refined predictive model of the capture plant. This iterative approach maximises the value of both simulation and physical testing, leading to insights that neither could achieve alone.

6.4 Recommendations for Future Work

Building upon the findings of this thesis, the recommendations for future work are separated into experimental-based work and simulation-based work, detailed in the subsections below. By pursuing these avenues of research, the foundational work can be expanded to further accelerate the development and deployment of chemical absorption carbon capture technologies for the decarbonisation of industrial processes around the world.

6.4.1 Future Experimental Work

Further experimental work is recommended to validate the parametric trends identified in the process simulation predictions and to build upon the findings of this thesis by exploring new directions. The following topics are recommended for investigation:

i) Testing of Advanced Solvents

This study focused exclusively on establishing a performance benchmark with standard MEA solvent. The performance data can now serve as a crucial benchmark for comparison against advanced or proprietary solvents. A dedicated campaign would provide valuable comparative data on absorption efficiency, solvent capacity, and solvent regeneration energy requirements under elevated CO_2 conditions. This is particularly important for assessing the heat of desorption, as this significant component of the regeneration energy can only be reduced through the use of alternative solvents. However, optimal capture conditions will vary between solvents, influencing the energy requirements of the other regeneration energy components, meaning that a comprehensive study must be conducted to determine which solvents have a net lower energy consumption for capture.

ii) Validation of Gas Flow Rate and Stripper Pressure Effects

The experimental campaign investigated a fixed flue gas flow rate of 150 Nm^3/h with a stripper pressure of 1.2 bara. Future campaigns should explore a wider range of these parameters within the TERC ACP’s capabilities to obtain a more comprehensive performance map and to experimentally validate the parametric trends predicted by the simulation work.

iii) Further Increases in Flue Gas CO_2 Concentration

The ECC model demonstrated the capability of the TERC ACP to handle flue gas CO_2 concentrations of 30 mol.% and potentially higher. Performing experiments at these conditions is a logical next step and would serve as a critical validation of the model’s extrapolative power. This would also further expand the novel MEA performance data to cover the majority of industrial process emissions, providing additional benchmark data for conventional capture systems, which remains limited in the open literature.

iv) Identifying Optimal Operating Conditions

While this investigation identified the regions of optimal performance, the exact minimum SRD for the 15 and 20 mol.% CO_2 conditions were not identified during the experimental campaign. Future work should include targeted tests with finer solvent flow rate increments around the optimal L/G ratios predicted by the ECC model. This would help to precisely locate the minimum SRD and provide the final data points required for a complete validation of the ECC model's predictive accuracy.

v) Characterisation of System Constraints

The simulations highlighted the critical role of the cross-heat exchanger on overall energy consumption, yet the experimental campaign noted unreliable temperature data for this unit. A dedicated experimental series to accurately measure the heat exchanger's duty and temperature approach under various conditions would clarify its performance. This would provide crucial data for validating the model's treatment of this key physical constraint.

vi) Direct Quantification of System Heat Loss

The energy balance analysis in the thesis estimated the overall system heat loss indirectly, noting that while the losses appeared to be low, the exact values had a high degree of statistical uncertainty. A dedicated investigation could be conducted concurrently with any other experimental campaign to directly measure heat losses from individual plant components under a range of operating and ambient conditions. This would provide a more precise quantification of the TERC ACP's thermal efficiency and enable the development of a detailed thermal loss model. Such a model would improve the accuracy of the overall system energy balance and help identify specific areas for insulation or operational improvements to further reduce the energy penalty of capture.

vii) Investigating the Impact of Flue Gas Contaminants

The experimental work in this thesis deliberately used clean, synthetic flue gas to establish a performance baseline, and the plant's FGD unit was bypassed. A critical next step for industrial application is to conduct a long-term campaign to investigate the impact of common flue gas contaminants, such as NO_x, SO_x, and metal particulates, on the capture process. Such a study would provide essential data on solvent degradation rates, emissions formation, and the overall performance and stability of the system under more realistic industrial conditions. As the composition of industrial process emissions is dependent on the source, performance data could be obtained for process emissions beyond the iron and steel industry, such as the cement and chemicals industry, providing novel baseline data for chemical absorption carbon capture from different industries.

viii) Dynamic and Flexible Operation Studies

The investigations in this thesis were conducted exclusively at steady state conditions to establish baseline performance. A crucial area for future research is to characterise the dynamic operational capabilities of the TERC ACP. This would involve experimental campaigns focused on startup and shutdown procedures, as well as transient response tests to assess how the plant performs and can respond to rapid changes in flue gas flow rate and CO_2 concentration. Such studies are essential for understanding how the capture plant would integrate real-world industrial processes that have variable loads, and the data would be critical for developing dynamic simulation models and advanced control strategies for flexible, load-following operation.

6.4.2 Future Simulation Work

Expansion of the simulation investigation is recommended to further develop the ECC model towards a true digital twin of the TERC ACP. Further calibration will be possible as more experimental data is obtained, which will continue to increase confidence in the performance predictions of the ECC model. The following topics are recommended for investigation:

i) Enhancing the Column Models (Opening the “Black Box”)

A key conclusion of the model enhancement work was that the absorber column had to be treated as a “black box” to achieve accurate system-level predictions, as its internal temperature profile was not physically accurate. Future work should focus on developing a more rigorous absorber model using regressed data from experiments. This would involve moving beyond standard correlations to incorporate more detailed hydrodynamics, such as liquid distribution and residence time effects, and could include adjustments to the underlying absorption chemistry to improve the physical realism of the temperature profiles. A similar approach could then be applied to the stripper column to further refine its alignment with experimental observations.

ii) Refinement of Model Convergence Logic

The simulation model operates using a set of design specifications to achieve convergence by iterating specific parameters. This process involves setting a target capture efficiency, which the model used to determine the required lean loading and, subsequently, the reboiler heat duty needed to achieve that level of regeneration. An observed weakness in this logic is that the model is set up to ignore the physical heat duty limitation of the reboiler. It calculates the ideal energy input to meet the capture target, even if that duty exceeds the plant’s physical capabilities. A more comprehensive model could be developed by reversing this logic. Future work should implement a new convergence path where the maximum heat duty is set as a fixed input. The model would then calculate the achievable lean loading based on this energy constraint and use that to determine the final, realistic capture efficiency. This would resolve the current limitation where the model can report a successful 90% capture efficiency around the absorber while simultaneously requiring a reboiler duty that is physically impossible to deliver in practice.

iii) Modelling of Additional Reactions

The ECC model was intentionally developed to simulate CO_2 capture under ideal conditions using clean flue gas, mirroring the experiment campaign's baseline approach. A critical area for future work is to expand the model's chemical framework to include side reactions caused by common industrial contaminants, such as NO_x, SO_x, and metal particulates. Incorporating these reactions would enable the development of more comprehensive, process-specific models for any industrial process, as long as the flue gas composition is considered. This would allow performance predictions to be made across a broad spectrum of industrial sectors and provide crucial insights for the successful deployment of carbon capture technologies into different industries.

iv) Developing a Digital Twin and Creating a Comprehensive Performance Map

The current ECC model provides a validated but ultimately incomplete performance map for the TERC ACP, as it is based on a specific set of experimental conditions. A continuous cycle of development is recommended, where the model is iteratively recalibrated using data generated from other research avenues in this section, such as those involving contaminants and improved column representation. The ultimate objective is to use the Python automation framework to generate a comprehensive, multi-dimensional performance map that covers the entire operational envelope of the plant. Such a map would chart the complex relationship between all key input variables and performance indicators, forming the core of a true digital twin representation. This would enable advanced, multi-parameter optimisation, inform the design of sophisticated control strategies for variable loads, and significantly reduce reliance on further experimental campaigns.

v) Developing a Dynamic Process Model

The current ECC model is a steady state representation of the TERC ACP, which is ideal for evaluating performance for constant conditions but cannot simulate real-world operational changes. A crucial area for future work would be to develop a dynamic version of the ECC model, using data from the proposed dynamic experimental campaign. This data would be critical for building and validating this dynamic model, which would cover transient operations such as startup and shutdown procedures and the plant's response to rapid changes in flue gas load. This in turn would enable the development of advanced and flexible control strategies for load-following operation.

vi) Modelling of Alternative Solvents

While modelling alternative solvents is challenging due to the need for extensive physical and chemical data, it is a valuable direction for future research. Future work could proceed along two avenues. The first involves focusing on publicly documented alternative solvents such as DEA or MDEA, for which intrinsic Aspen Plus data exists. The model development framework in this thesis could be adapted to these solvents and then validated against data from an experimental campaign. The second avenue involves direct collaboration with industrial solvent developers. While the data for proprietary solvents is often confidential, future research projects could be structured under nondisclosure agreements to develop and validate high-fidelity models for these advanced solvents, accelerating their path to commercial deployment and demonstrating the real-world utility of the TERC ACP and its digital twin.

vii) Expansion of the Automation Framework

The Python automation script developed for this work proved to be a powerful tool for research. Future work could focus on transforming it into a more general and user-friendly platform. This would involve enhancing its modularity to allow for easier adaptation to different Aspen Plus flowsheets and developing a graphical user interface (GUI) to make it accessible to non-expert programmers, broadening its usability. Furthermore, its analytical power could be significantly increased by integrating advanced machine learning or mathematical optimisation algorithms. This would enable true multi-parameter optimisation, potentially uncovering complex interactions between tuning factors and identifying optimal process conditions more efficiently.